

Seismic History Matching Using Binary Images

Dennis Obidegwu

Thesis presented for the degree of Doctor of Philosophy

Heriot-Watt University
Institute of Petroleum Engineering
School of Energy, Geoscience, Infrastructure and Society

December 2015

The copyright in this thesis is owned by the author. Any quotation from the thesis or use of any of the information contained in it must acknowledge this thesis as the source of the quotation or information.

Abstract

The ability to predict the flow of multiple fluids in a reservoir, and update the reservoir in a timely efficient manner is the dream of every reservoir engineer, and has been the bane of much research in the oil and gas industry. This is highly sought after because it enables efficient reservoir monitoring, management and planning. However this requires some level of skill and precision as well as the ability to interpret and input data from different sources into the model. In order to predict the flow of multiple fluids in a reservoir, the relative permeability of these fluids has to be determined. In this thesis, 4D seismic data is used to estimate some endpoints of the relative permeability curve (S_{gc} and S_{gmax}), whereby multiple seismic surveys are employed in association with the production history, depletion mechanism, geological and structural effects as well as reservoir simulation predictions. The multiple survey 4D seismic data is interpreted so as to decipher instances of critical gas saturation as well as maximum gas saturation effects, these are then quantitatively analysed, and a relationship between the ratio of their amplitudes and gas saturation are used to estimate the values.

In addition, integrating 4D seismic data with production data in a quantitative manner in a reservoir model improves the model's capability and reduces the uncertainty, however doing this is quite a challenging problem. This thesis addresses this challenge by utilising a binary approach which circumvents the full rock physics modelling approach. The binary approach is developed and tested where gas and water saturation from 4D seismic data and the reservoir simulation model are converted to binary indicators. Different metrics for quantifying the binary misfit in terms of their strengths and short comings are analysed, and the *Current* measurement metric and Hamming distance exhibit better capabilities than the Hausdorff distance and Mutual Information measurements. The binary

approach is then tested on a synthetic model in order to validate its use, as well as show its functionality in a practical setting. In the synthetic study, three different scenarios are analysed – the gas exsolution scenarios, the water evolution scenarios, and a combination of gas exsolution and water evolution, and the results show that the binary approach provides a quick and efficient method of assessing reservoir parameters. The binary approach is then implemented on a real field data from the United Kingdom Continental Shelf (UKCS), where 104 uncertain reservoir parameters are initially assessed. An initial ensemble of fluid flow simulation models is created where the full range of uncertain parameters are acknowledged using experimental design methods, and an evolutionary algorithm is used for optimization in the history matching process. It is found that the primary control parameters for the binary seismic gas match are the permeability and critical gas saturation, while the volumetric parameters are important for the binary seismic water match in this particular reservoir. This binary approach is then compared to a conventional seismic modelling approximation approach, where the results show that the binary approach gives a good match to gas saturation distribution and water saturation distribution, and the reservoir parameters converge towards a solution. The conventional approach captures some signals of hardening and softening in the seismic data, however most parameters do not fully converge towards a solution, and hence in summary, the binary approach seems more suitable as a quick look reservoir management tool.

Dedication

This thesis is dedicated to my family.

Acknowledgement

I would like to thank my supervisor, Colin MacBeth for his wonderful guidance and support throughout my PhD work. I regard him as a genius, not only for his scientific technical ability, but also for his great managerial skill in organising the biannual sponsors' meeting, and coordinating students coming from a wide range of multicultural and multidisciplinary background, on a wide range of topics. I specially thank Romain Chassagne and Sergey Kurelenkov for the co-supervision of the project. I thank Ilya Fursov, Hamed Amini, Romain Chassagne, Reza Falahat and Eric Mackay for the great technical discussion sessions. I appreciate all staff and students of the Institute of Petroleum Engineering, Heriot-Watt University. Special thanks to my PhD examiners – Denis José Schiozer, Alessandra Davolio and Maria-Daphne Mangriotis for taking their time to examine the thesis, as well as their valuable insights and feedback.

I thank the Edinburgh Time Lapse Project (ETLP) PhaseV and its sponsors (BG, BP, Chevron, ConocoPhillips, Eni, ExxonMobil, Hess, Ikon, Landmark, Maersk, Nexen, Norsar, Peroro, Petrobras, RSI, Shell, Statoil, Suncor, TAQA, TGS and Total) for funding my research. I am grateful to the Society of Exploration Geophysicist (SEG) for awarding me the prestigious SEG/EAGE/LeonThomsen/BP endowed scholarship fund for academic excellence in 2013. Thanks to BP for providing the data used in this thesis, and also thanks to Nigel Robinson, Chris Macdonald, Susan Fowler, Peter Allan, Linda Hodgson and Brian Davies, all from BP for discussion on the data. Thanks to Schlumberger for the use of PETREL, Eclipse, and MEPO software; also to Niels Kueck for timely MEPO software support. Special thanks to Nicolas Bruneau for guiding my feeble arms towards the mastery of Python programming language used in this thesis.

I will like to show my appreciation to all ETLP colleagues I came in contact with during my PhD: Colin MacBeth, Asghar Shams, Karl Stephen, Yi Huang, Alejandro Garcia, Hamed Amini, Yesser Hajnasser, Erick Alvarez, Reza Falahat, Sergey Kurelenkov, Valery Rukavishnikov, Ilya Fursov, Dhiman Mondal, Sean Shuzhe Tian, Olarinre Salako, David Zhen Yin, Lu Ji, Zein Wijaya, Ricardo Rangel, Angel Briceno, MingYi Wong, Veronica Omofoma, Mathieu Chamberfort, Maria-Daphne Mangriotis, Phung Nguyen, Romain Chassagne, Niki Obiwulu, Justin Chong Geng and Juliana Santos. Also, thanks to Mustapha Lamorde for the thesis formatting guidelines.

I will like to express my gratitude to Sean Ferris, Jonathan Brain, Kurt Rattansingh, Andrew Wilson and Linda Hodgson for organising discussion and visits to Chevron, Shell, BG Group, NexenCnooc, and BP respectively. This interaction played a key role in shaping this thesis, and enabled a better understanding of the practical applications and challenges.

I am very grateful to my parents – Dr and Mrs Obidegwu, and to my siblings – Uzo and family, Chinwe and family, and Uche and family for their unwavering support, love and constant encouragement. Warm appreciation to Nenye for being there for me.

All thanks to God for life, health, wisdom and for the ability to succeed with this PhD.

Dennis Obidegwu, December 2015

Declaration Statement

ACADEMIC REGISTRY Research Thesis Submission



Name:	Dennis Obidegwu		
School/PGI:	School of Energy, Geoscience, Infrastructure and Society/ Institute of Petroleum Engineering		
Version: <i>(i.e. First, Resubmission, Final)</i>	Final	Degree Sought: <i>(Award and subject area)</i>	PhD, Petroleum Engineering

Declaration

In accordance with the appropriate regulations I hereby submit my thesis and I declare that:

- 1) the thesis embodies the results of my own work and has been composed by myself
- 2) where appropriate, I have made acknowledgement of the work of others and have made reference to work carried out in collaboration with other persons
- 3) the thesis is the correct version of the thesis for submission and is the same version as any electronic versions submitted*.
- 4) my thesis for the award referred to, deposited in the Heriot-Watt University Library, should be made available for loan or photocopying and be available via the Institutional Repository, subject to such conditions as the Librarian may require
- 5) I understand that as a student of the University I am required to abide by the Regulations of the University and to conform to its discipline.

* Please note that it is the responsibility of the candidate to ensure that the correct version of the thesis is submitted.

Signature of Candidate:		Date:	21/12/2015
-------------------------	--	-------	------------

Submission

Submitted by (name in capitals):		
Signature of Individual submitting:		
Date Submitted:		

For Completion in Student Service Centre

Received in the SSC by <i>(name in capitals)</i> :			
Method of Submission <i>(Handed in to SSC; posted through internal/external mail):</i>			
E-thesis submitted <i>(mandatory for final theses)</i>			
Signature:		Date:	

Table of Contents

Abstract	i
Dedication	iii
Acknowledgement	iv
Declaration Statement	vi
Table of Contents	vii
List of Tables	xi
List of Figures	xiii
List of Appendix Figures	xxv
List of Symbols and Acronyms	xxvii
List of Publications	xxx
List of Awards	xxxii
Chapter 1	1
Introduction	1
1.1 Overview	2
1.1.1 Time Lapse Seismic Data.....	3
1.1.2 Quantitative Integration of 4D Seismic Data	4
1.1.3 Objective Function	8
1.1.4 History Matching and Uncertainty Quantification.....	10
1.1.5 Upscaling.....	11
1.1.6 4D Seismic Data and Reservoir Engineering Concepts	11
1.1.7 Seismic Response to Reservoir Activities.....	14
1.1.8 Gas and Oil Relative Permeability	18
1.2 Motivation of this Research.....	22
1.3 Objectives of this Research	23
1.4 Contributions of this Work.....	24
1.5 Thesis Outline.....	25
Chapter 2	27
Quantitative Analysis of Gas Volumes in a UKCS Field	27
2.1 Background to the Schiehallion Field	28
2.2 The Reservoir Mechanisms	31
2.2.1 Gas Exsolution	31
2.2.2 Gas Dissolution	34
2.3 Description of Gas Exsolution and Dissolution	36

2.4	Field Regional Analysis	40
2.5	Quantitative Analysis for S_{gc} and S_{gmax}	44
2.6	Quantitative Analysis of Gas Volumes	51
2.7	Discussion.....	56
2.7.1	Values for the Critical and Maximum Gas Saturation	57
2.7.2	Timing of the Seismic Surveys	60
2.8	Summary.....	63
	Chapter 3	64
	SHM Using Binary Images - Development	64
3.1	Binary Measurement Metrics	65
3.2	Clustering and Thresholding	67
3.2.1	Hamming Distance.....	79
3.2.2	Hausdorff Distance.....	80
3.2.3	Mutual Information	81
3.2.4	Current Measurement Metric	82
3.3	Analysis on Test Case Scenarios	83
3.4	Summary.....	92
	Chapter 4	94
	SHM Using Binary Images - Validation	94
4.1	Field Description	95
4.2	Gas Exsolution Scenarios	97
4.3	Water Evolution Scenarios	103
4.4	Combined Gas Exsolution and Water Evolution Scenarios	109
4.5	Summary.....	116
	Chapter 5	118
	Binary SAHM of Gas and Water in a UKCS Field	118
5.1	Introduction	119
5.2	Field Description	121
5.3	Simulation Model Conditioning.....	122
5.4	4D Seismic Data Conditioning.....	125
5.4.1	Clustering and Thresholding.....	125
5.5	Binary Objective Function	129
5.6	Setting the Scene	130
5.7	Model Parameterisation.....	134

5.8	Application of Binary SAHM	137
5.8.1	HM to Production Data only	142
5.8.2	Binary SAHM Using Hamming Distance	146
5.8.2.1	HM to Binary Seismic Gas only	147
5.8.2.2	HM to Binary Seismic Water only	155
5.8.2.3	HM to Production Data and Binary Seismic (Gas and Water).....	157
5.8.3	Binary SAHM Using Current Measurement Metric	159
5.8.3.1	HM to Binary Seismic Gas only	159
5.8.3.2	HM to Binary Seismic Water only	167
5.8.3.3	HM to Production Data and Binary Seismic (Gas and Water).....	169
5.8.4	Forecast Analysis	171
5.9	Summary.....	173
Chapter 6		175
Comparative Analysis of Binary and Conventional SAHM		175
6.1	Introduction	176
6.2	Conventional SAHM	177
6.2.1	Seismic Modelling Approximation	180
6.3	Application of Conventional SAHM.....	189
6.3.1	HM to Seismic.....	192
6.3.2	HM to Production Data and Seismic.....	194
6.4	Forecast Analysis.....	198
6.5	Comparative Analysis	199
6.6	Summary.....	203
Chapter 7		204
Conclusions and Recommendations		204
7.1	Conclusions	205
7.2	Recommendations for Future Research.....	209
7.2.1	Workflow Modification for Geological Model Updating	209
7.2.2	Different Scales of Analysis.....	212
7.2.2.1	Simulation Scale and Seismic Scale.....	212
7.2.2.2	Depth Averaged Maps and Volumetric	214
7.2.2.3	Similar Objective Function.....	215
7.2.3	Utilization of Ambiguous Signal	217
7.3	Final Remarks.....	219

Appendix A	220
A.1 Fluid Property Changes at, and near to, Critical Gas Saturation.....	220
Appendix B	222
B.1 Prediction of the 4D Seismic Amplitude Response to Gas Exsolution and Dissolution	222
B.2 Preproduction	224
B.3 After Gas Exsolution	225
B.4 After Gas Dissolution	227
Appendix C	228
C.1 Production Profiles	228
Appendix D	233
D.1 <i>k</i> -means Clustering	233
Appendix E	235
E.1 Misfit Analysis	235
Appendix F	237
F.1 Python Program Script	237
Appendix G	253
G.1 Publications	253
References	325

List of Tables

Table 1.1 Global objective functions (Bertolini and Schiozer, 2011). 8 different objective functions are analysed for history matching.	9
Table 1.2 The endpoint parameters and shape factor parameters used in creating relative permeability curves (Li et al., 2012).....	18
Table 2.1 Rock and fluid seismic/acoustic properties for the field.....	45
Table 2.2 Amplitude values for the regions of the field sector in which oil-filled sands are saturated with gas at critical gas saturation ($A(S_{gc})$) and maximum gas saturation ($A(S_{gmax})$). D_1 and D_2 correspond to the ratios defined in equation (2.3) and equation (2.4), from which the time-lapse metric in Figure 2.11 can be formed. ...	49
Table 2.3 Critical gas-saturation values for a range of studies (horizontal bars) compared to the results from the 4D seismic estimates (entry number 22).....	59
Table 4.1 The Hamming distance and <i>Current</i> measurement metric objective function for the different perturbations (A to D) for the gas exsolution scenarios. The values that have been normalised are plotted in Figure 4.5.	102
Table 4.2 The Hamming distance and <i>Current</i> measurement metric objective function for the different perturbations (E to H) for the water evolution scenarios. The values which have been normalised are plotted in Figure 4.9.	109
Table 4.3 The Hamming distance and <i>Current</i> measurement metric objective function for the different perturbations (I to L) for the combined gas exsolution and water evolution scenarios. $H(S_g)$ and $C(S_g)$ are the Hamming distance and <i>Current</i> measurement metric for matching to gas only, $H(S_w)$ and $C(S_w)$ are the Hamming distance and <i>Current</i> measurement metric for matching to water only, while H and C are the Hamming distance and <i>Current</i> measurement metric for matching to gas and water together. The normalised values are plotted in Figure 4.13.	114
Table 5.1 The parameters of the different upscaled models as compared to the initial model. Model 5 was selected as the most suitable model for the history matching exercise in terms of run time efficiency and simulation accuracy. The measurement analysis of the different misfit is in Appendix E.	123
Table 5.2 Model Parameterization for history matching the reservoir. The global parameters are parameters that are perturbed over the entire reservoir, while the	

regional parameters are parameters that are perturbed over selected regions/geobodies.	136
Table 5.3 Forecast misfit for the average of the improved models. The well data misfit is calculated using the least squares error, and the seismic misfit (gas and water) is calculated using the Hamming distance.	171
Table 5.4 Percentage improvement to the initial base case model using the Hamming distance as the binary seismic objective function.	172
Table 5.5 Forecast misfit for the average of the improved models. The well data misfit is calculated using the least squares error, and the seismic misfit (gas and water) is calculated using the Hamming distance.	172
Table 5.6 Percentage improvement to the initial base case model using the Hamming distance as the binary seismic objective function.	173
Table 6.1 The coefficients for equation (6.1) for different time steps, as well as the corresponding coefficient of determination, R^2	181
Table 6.2 The coefficients for equation (6.2) for different time steps, as well as the corresponding coefficient of determination, R^2	186
Table 6.3 Forecast misfit for the average of the improved models. The well data misfit is calculated using the least squares error, and the seismic misfit is from seismic modelling.	199
Table 6.4 Percentage improvement to the initial base case model.	199

List of Figures

Figure 1.1 Distribution of measurements in time and space. The well data is sparsely distributed in space, while the time frequency is high. The seismic data has the opposite characterisation, with high frequency in space but a lower frequency in time. The two data sources give complimentary information in the time and space domain (Nielsen et al., 2010).....	4
Figure 1.2 The different domains at which seismic history matching can be explored – the simulation model domain, the impedance domain, and the seismic domain.....	6
Figure 1.3 A 4D seismic data example of gas exsolution and dissolution from the Foinaven field, UKCS. Amplitude maps are generated for the 1993 baseline survey prior to production, then again in 1999 following gas exsolution after one year of production, and finally in 2000 after dissolution due to repressurization, gas migration and production. The mapped anomalies visibly expand due to the liberated gas, then contract upon pressure increase (Marsh et al., 2001)..	13
Figure 1.4 Generalised plots of P-wave velocity change in the different reservoir production scenarios, (a) gas injection, (b) gas out of solution, (c) water flood and (d) gas production (Huang, 2011).....	16
Figure 1.5 Quantitative representation of impedance response to different reservoir mechanisms (Amini, 2014).....	17
Figure 1.6 Schematic of a 2-phase and 3-phase fluid flow system, and an oil-gas relative permeability curve for a 3-phase system	19
Figure 1.7 Different sources of inputs for generating relative permeability curves. 4D seismic data is highlighted as a potential addition.....	21
Figure 2.1 The Schiehallion oil field location in the United Kingdom Continental Shelf (UKCS) highlighting a cross-section (A to A') of segment 1 showing the T31 which is the reservoir of interest (Martin and Macdonald, 2010).	29
Figure 2.2 Vertical-section from the 1996 preproduction coloured inversion seismic data, showing the reservoir structure. Troughs in dark red represent the sand bodies, whilst peaks in grey represent the shales. The top and base of the sand layers are picked as zero crossings by the data provider (Amini, 2014).....	30

Figure 2.3 Pressure-temperature phase envelope for the field based on measured oil compositional data from the data provider. The initial reservoir pressure is 2900 psi (19.99 MPa) and the temperature is 120 °F (48.89 °C), and so the oil is already very close to bubble point.	32
Figure 2.4 Schematic illustrating the three main stages of gas exsolution and dissolution (repressurization) that are being examined, and their consequent effect on the reservoir saturation conditions. (a) Initial preproduction state: live oil and no free gas; (b) after gas exsolution and mobilization of the free gas (note the trapped gas under low NTG pockets or structure); (c) oil production, repressurization by water injection and gas-cap shrinkage due to production. In this latter case, it is highly likely that the residual gas may be reduced to zero by the repressurization.....	33
Figure 2.5 A pore-scale description of the six saturation states relevant to the calculation of the seismic response from the exsolution and dissolution scenarios shown in Figure 2.4. S_{gr} refers to the residual gas saturation after gas-cap contraction and S_{gc} to the critical gas saturation.	35
Figure 2.6 Amplitude maps (using the sum of negative amplitudes attribute) for seismic surveys at times 1996 (production was in 1998), 1999, 2000 and 2002. The anomalies are related to gas or oil accumulations in the reservoir sand deposits....	37
Figure 2.7 Amplitude maps (using the sum of negative amplitudes attribute) for seismic surveys at times 2004, 2006, and 2008. The anomalies are related to gas or oil accumulations in the reservoir sand deposits. Also shown is a contour map indicating the time structure of the top T31a reservoir horizon.	38
Figure 2.8 (a) Labelling of main sand bodies highlighting the position of the injector wells and producer wells. The solid stars and circles correspond to the well TD (b) Timelines of activity for the wells showing when they are put on production/injection and shut-in, relative to the seismic data baseline and monitor surveys. The red lines represent the producer wells, while the blue lines represent the injector wells.	41
Figure 2.9 (a) Sub-regions of sand bodies used for the calculation of time-lapse amplitudes and gas-saturation analysis. (b) Seismic amplitude variations with survey time, together with inferred amplitude levels for maximum and critical gas saturations (dotted horizontal lines). Thin coloured lines correspond to the	

individual sub-region results, whilst the solid black line is the average of these values.	43
Figure 2.10 Schematic illustrating the three main reservoir states that are being examined to compute their corresponding impedances.(a) Initial preproduction state: live oil and no free gas; (b) after some oil production activity, gas exsolution to critical gas saturation; (c) Further oil production leads to just gas and residual oil, i.e. secondary gas cap.	46
Figure 2.11 Estimate of amplitude change with critical gas saturation and no gas in the oil sands, normalized by the expected amplitude change when going from oil to maximum gas saturation in the gas cap.	47
Figure 2.12 (a) Schematic illustration of the pressure dependence of the solution gas–oil ratio, R_s , for a black oil. The ratio decreases as pressure drops below bubble point until the monitor state is reached at point B. Repressurization increases R_s again but as less gas is available to dissolve in the gas, the R_s behaviour reaches a plateau at a lower constant value and point C is reached. (b) R_s values predicted for the study area from fluid-flow simulation (black line and circles) versus the variation estimated from the 4D seismic data for low (red), medium (green) and high (blue) cases derived from varied STOIP.	55
Figure 2.13 Timing of the physics of nucleation and development of gas exsolution in a hydrocarbon oil. Timings are based on simulation model studies for this field.	61
Figure 3.1 4-D seismic data in “black and white” format (Landa, 1997). Saturation representation displayed in binary format.	66
Figure 3.2 Saturation differences after binary processing from (a) the true model (b) the initial model (c) the updated model (Jin et al., 2012b).	66
Figure 3.3 Illustration of the clustering of 4D seismic data into two classes (Tillier et al., 2013).	67
Figure 3.4 Illustration of the different levels of clustering achieved by implementing the k -means clustering algorithm.	68
Figure 3.5 Test cases model 1 and 2 with different threshold levels to quantify the accuracy of misfit through the matching process. Three threshold levels are	

presented from the top to the bottom, the last one has no threshold (full level) as it is the initial continuous image.	70
Figure 3.6 Test cases model 3 and 4 with different threshold levels to quantify the accuracy of misfit through the matching process. Three threshold levels are presented from the top to the bottom, the last one has no threshold (full level) as it is the initial continuous image.	71
Figure 3.7 Test cases seismic model 1 and 2 with different threshold levels to quantify the accuracy of misfit through the matching process. Three threshold levels are presented from the top to the bottom, the last one has no threshold (full level) as it is the initial continuous image.	72
Figure 3.8 Test cases seismic model 3 and 4 with different threshold levels to quantify the accuracy of misfit through the matching process. Three threshold levels are presented from the top to the bottom, the last one has no threshold (full level) as it is the initial continuous image.	73
Figure 3.9 Normalised search space applied to different threshold levels.....	75
Figure 3.10 Normalised search space applied to different threshold levels.....	76
Figure 3.11 Standard deviation for Models 1, 2, 3 and 4 as a function of different threshold levels.	78
Figure 3.12 Hamming Distance “D” between original and forged images (Zhao et al., 2010).	79
Figure 3.13 Different scenarios to test the metrics.	85
Figure 3.14 Different scenarios to test the metrics	86
Figure 3.15 Different scenarios to test the metrics	87
Figure 3.16 Results of the performance of the different tested metrics on the different selected scenarios.....	90
Figure 3.17 Results of the performance of the different tested metrics on the different selected scenarios.....	91
Figure 3.18 Results of the performance of the different tested metrics on the different selected scenarios.....	92

Figure 4.1 Heterogeneous properties (horizontal permeability, vertical permeability, porosity and NTG) of the dataset. Also shown is the plan view and cross-section view of the model highlighting the location of the producer well and injector well, as well as the oil-water contact.	96
Figure 4.2 An outline of the reservoir, the position of producer well, and the timeline of activity of the well relative to the multiple seismic data surveys for the gas exsolution scenarios.	99
Figure 4.3 The 4D seismic data response of the base case model time-lapse, base case model time-lapse gas saturation response, and perturbed models time-lapse gas saturation responses for the gas exsolution scenarios.	100
Figure 4.4 The binary gas 4D seismic data response of the base case model time-lapse, base case model time-lapse binary gas saturation response, and perturbed models time-lapse binary gas saturation responses for the gas exsolution scenarios.	101
Figure 4.5 The values of the misfit using the Hamming distance and <i>Current</i> measurement metric objective function for the different cases of perturbed models shown in Table 4.1 for the gas exsolution scenarios.	102
Figure 4.6 An outline of the reservoir, the position of the injector well and producer well, and the timeline of activity of the wells relative to the multiple seismic data surveys for the water evolution scenarios.	104
Figure 4.7 The 4D seismic data response of the base case model time-lapse, base case model time-lapse water saturation response, and perturbed models time-lapse water saturation responses for the water evolution scenarios.	105
Figure 4.8 The binary water 4D seismic data response of the base case model time-lapse, base case model time-lapse binary water saturation response, and perturbed models time-lapse binary water saturation responses for the water evolution scenarios.	106
Figure 4.9 The values of the misfit using the Hamming distance and <i>Current</i> measurement metric objective function for the different cases of perturbed models shown in Table 4.2 for the water evolution scenarios.	108

Figure 4.10 An outline of the reservoir, the position of the injector well and producer well, and the timeline of activity of the wells relative to the multiple seismic data surveys for the combined gas exsolution and water evolution scenarios.	110
Figure 4.11 The 4D seismic data response of the base case model time-lapse, base case model time-lapse water saturation and gas saturation responses, and perturbed models time-lapse water saturation and gas saturation responses for the combined gas exsolution and water evolution scenarios.....	112
Figure 4.12 The binary water and binary gas 4D seismic data response of the base case model time-lapse, base case model time-lapse binary water saturation and binary gas saturation responses, and perturbed models time-lapse binary water saturation and binary gas saturation responses for the combined gas exsolution and water evolution scenarios.	113
Figure 4.13 The values of the misfit using the Hamming distance and <i>Current</i> measurement metric objective function for the different cases of perturbed models shown in Table 4.3 for the combined gas exsolution and water evolution scenarios for matching to gas only, to water only, and to gas and water together.	115
Figure 5.1 Different domains for “closing the loop” highlighting the binary inversion domain	120
Figure 5.2 (a) The pressure, water saturation and gas saturation maps for the initial base case model, the chosen model (model 5), and the worst case model after upscaling (b) shows the cumulative field oil production, cumulative field gas production, cumulative field water production and field average pressure for the initial base case model, the chosen model (model 5), and the worst case model after upscaling (c) shows the total spatial misfit, total well data misfit, and the combined misfit versus simulation runtime for all the upscaled models highlighting the chosen model 5 in a light green square.....	124
Figure 5.3 The process of generating the binary (gas and water) maps from the 4D seismic data. The 4D seismic data are initially clustered and separated into ‘hardening’ and ‘softening’ signals; historical production data are then introduced to aid the interpretation and deciphering of potential gas and water signals due to the injector/producer positioning, as well as the volumes produced which are represented by the size of the bubble plots. Application of these processes leads to	

the final seismic binary gas and water maps. Inset shows the 4D seismic colour bar and the associated physical interpretation.	126
Figure 5.4 Evolution algorithm workflow (Schulze-Riegert and Ghedan, 2007).....	131
Figure 5.5 Seismic Assisted History Matching Workflow - combining the production data with the time-lapse seismic data. The blue arrows (upper part) highlight the production history match loop; the black arrows (lower part) highlight the seismic history match loop; the orange arrows (middle part) showcases their individual or combined path; while the green arrows (circular arrows) shows the direction of the loop.	133
Figure 5.6 The sensitivity analysis of the initial 104 parameters to the production data (oil, gas and water) of wells P1 and P2, and also to the binary gas and water maps. The most sensitivity parameters are shown (top seven). From these parameters, 35 are selected for the history matching exercise. Also shown are the initial geobodies, and the selected geobodies after the sensitivity analysis.	135
Figure 5.7 The binary (gas and water) maps have been generated from the 4D seismic data for all the relevant time-steps.....	139
Figure 5.8 The seismic binary (gas and water) maps compared to the simulation binary (gas and water) maps highlighting areas of mismatch. The first 4 monitors (the first four rows) will be used for the history matching exercise, while the last 2 monitors (the last 2 rows) will be used for the forecasting analysis.....	140
Figure 5.9 Normalized production profiles for wells P1 (left column) and P2 (right column) showing the initial base case model responses (black lines), the initial ensemble responses (green lines), and the historical observed data (red dots) for oil production rate, gas production rate and water production rate.	141
Figure 5.10 Normalized production profiles for wells P1 (left column) and P2 (right column) highlighting the improved model responses (dark blue lines), after history matching to production data only.	144
Figure 5.11 The updated binary simulation maps compared to the binary seismic maps highlighting areas of improvement after history matching to production data only	145

Figure 5.12 (a) Initial and updated parameters for history matching to production data only. (b) Objective function and uncertainty plot for history matching to production data only. The uncertainty is quantified as the range of response parameters in each iteration.	146
Figure 5.13 Normalized production profiles (oil production rate, gas production rate and water production rate) for well P1 (a) HM to binary seismic gas only, using Hamming distance (b) HM to binary seismic water only, using Hamming distance.	148
Figure 5.14 Normalized production profiles (oil production rate, gas production rate and water production rate) for well P1, HM to production data and binary seismic (gas and water), using Hamming distance.....	149
Figure 5.15 Normalized production profiles (oil production rate, gas production rate and water production rate) for well P2 (a) HM to binary seismic gas only, using Hamming distance (b) HM to binary seismic water only, using Hamming distance.	150
Figure 5.16 Normalized production profiles (oil production rate, gas production rate and water production rate) for well P2, HM to production data and binary seismic (gas and water), using Hamming distance.....	151
Figure 5.17 The updated binary simulation maps compared to the binary seismic maps highlighting areas of improvement after history matching to binary seismic gas only, using Hamming distance.	152
Figure 5.18(a) Histogram of selected parameters for history matching to binary seismic gas only, using Hamming distance. (b) Histogram of selected parameters for history matching to binary seismic water only, using Hamming distance. (c) Histogram of selected parameters for history matching to production data and binary seismic (gas and water).	153
Figure 5.19 (a) Objective function and uncertainty plot for history matching to binary seismic gas only, using Hamming distance. (b) Objective function and uncertainty plot for history matching to binary seismic water only, using Hamming distance. (c) Objective function and uncertainty plot for history matching to production data and binary seismic (gas and water). The uncertainty is quantified as the range of response parameters in each iteration.	154

Figure 5.20 The updated binary simulation maps compared to the binary seismic maps highlighting areas of improvement after history matching to binary seismic water only, using Hamming distance.	156
Figure 5.21 The updated binary simulation maps compared to the binary seismic maps highlighting areas of improvement after history matching to production data and binary seismic (gas and water).....	158
Figure 5.22 Normalized production profiles (oil production rate, gas production rate and water production rate) for well P1 (a) HM to binary seismic gas only, using <i>Current</i> measurement metric (b) HM to binary seismic water only, using <i>Current</i> measurement metric.....	160
Figure 5.23 Normalized production profiles (oil production rate, gas production rate and water production rate) for well P1, HM to production data and binary seismic (gas and water), using <i>Current</i> measurement metric.....	161
Figure 5.24 Normalized production profiles (oil production rate, gas production rate and water production rate) for well P2 (a) HM to binary seismic gas only, using <i>Current</i> measurement metric (b) HM to binary seismic water only, using <i>Current</i> measurement metric.....	162
Figure 5.25 Normalized production profiles (oil production rate, gas production rate and water production rate) for well P2, HM to production data and binary seismic (gas and water), using <i>Current</i> measurement metric.....	163
Figure 5.26 The updated binary simulation maps compared to the binary seismic maps highlighting areas of improvement after history matching to binary seismic gas only, using <i>Current</i> measurement metric.	164
Figure 5.27 (a) Histogram of selected parameters for history matching to binary seismic gas only, using <i>Current</i> measurement metric. (b) Histogram of selected parameters for history matching to binary seismic water only, using <i>Current</i> measurement metric. (c) Histogram of selected parameters for history matching to production data and binary seismic (gas and water).	165
Figure 5.28 (a) Objective function and uncertainty plot for history matching to binary seismic gas only, using <i>Current</i> measurement metric. (b) Objective function and uncertainty plot for history matching to binary seismic water only, using <i>Current</i> measurement metric. (c) Objective function and uncertainty plot for history	

matching to production data and binary seismic (gas and water). The uncertainty is quantified as the range of response parameters in each iteration.	166
Figure 5.29 The updated binary simulation maps compared to the binary seismic maps highlighting areas of improvement after history matching to binary seismic water only, using <i>Current</i> measurement metric.	168
Figure 5.30 The updated binary simulation maps compared to the binary seismic maps highlighting areas of improvement after history matching to production data and binary seismic (gas and water).....	170
Figure 6.1 The baseline seismic map, the change in pressure, change in water saturation, change in gas saturation, and initial 4D seismic maps for the relevant time-steps in the current analysis.	178
Figure 6.2 Conventional seismic modelling workflow.....	179
Figure 6.3 Top row shows reservoir dynamic changes, the middle row shows the initial 4D seismic data, and the last row shows generated 4D seismic maps using different coefficients derived from equation (6.1) for 2002 – 1998.....	182
Figure 6.4 Top row shows reservoir dynamic changes, the middle row shows the initial 4D seismic data, and the last row shows generated 4D seismic maps using different coefficients derived from equation (6.1) for 2004 – 1998.....	183
Figure 6.5 Top row shows reservoir dynamic changes, the middle row shows the initial 4D seismic data, and the last row shows generated 4D seismic maps using different coefficients derived from equation (6.2) for 2002 – 1998.....	187
Figure 6.6 Top row shows reservoir dynamic changes, the middle row shows the initial 4D seismic data, and the last row shows generated 4D seismic maps using different coefficients derived from equation (6.2) for 2004 – 1998.....	188
Figure 6.7 Normalized production profiles for wells P1 (left column) and P2 (right column) showing the initial base case model responses (black lines), the initial ensemble responses (green lines), and the historical observed data (red dots) for oil production rate, gas production rate and water production rate.	190
Figure 6.8 The base case 4D seismic maps, observed 4D seismic maps, and history matched (to seismic data) 4D seismic maps for all the relevant time-steps. The first	

4 monitors (the first four rows) are used for the history matching exercise, while the last 2 monitors (the last 2 rows) are used for the forecasting analysis.	191
Figure 6.9 Normalized production profiles for wells P1 (left column) and P2 (right column) highlighting the improved model responses (dark blue lines), after history matching to seismic data.....	193
Figure 6.10 (a) Initial and updated parameters for history matching to seismic data. (b) Objective function and uncertainty plot for history matching to seismic data. The uncertainty is quantified as the range of response parameters in each iteration....	194
Figure 6.11 Normalized production profiles for wells P1 (left column) and P2 (right column) highlighting the improved model responses (dark blue lines), after history matching to production data and seismic data.	196
Figure 6.12 The base case 4D seismic maps, observed 4D seismic maps, and history matched (to production data and seismic data) 4D seismic maps for all the relevant time-steps. The first 4 monitors (the first four rows) are used for the history matching exercise, while the last 2 monitors (the last 2 rows) are used for the forecasting analysis.....	197
Figure 6.13 (a) Initial and updated parameters for history matching to production data and seismic data. (b) Objective function and uncertainty plot for history matching to production data and seismic data. The uncertainty is quantified as the range of response parameters in each iteration.	198
Figure 6.14 The interpretation of the binary maps derived from 4D seismic data.	200
Figure 6.15 Comparison of the binary approach and the conventional approach.....	202
Figure 7.1 Modified binary seismic assisted history matching workflow with the dash arrows showing potential for Geological model updating.....	210
Figure 7.2 (a) The amplitude difference map of the reservoir base, where light blue represents oil replaced by water. (b) An absolute horizontal permeability map derived from 4D imaging and permeability from the DST (Johann et al., 2009)..	211
Figure 7.3 Schematic representation of simulation model grid size (75m by 75m), and seismic data bin size (12.5m by 12.5m).	212
Figure 7.4 Sum of 4D P-wave velocity ratio until oil- water contact. Left) observed data, middle up) data in prior model, right up) data in posterior model updated with	

seismic data alone, lower middle) data in posterior model updated with seismic data and production data, and lower right) data in posterior model updated with production data alone (Alerini et al., 2014). The misfit analysis is done on the simulation model scale.213

Figure 7.5 Inverted (left) and simulated (right) $V_{P \text{ monitor}} / V_{P \text{ base}}$ for a grid layer around the oil water contact. The injecting and producing wells are shown as black lines. Besides a somewhat higher noise level in the inverted ratio, the maps exhibit a similar qualitative behaviour in terms of observed 4D seismic data anomalies as well as a remarkable quantitative match which allows direct use of the inversion results in a history matching workflow (Ayzenberg et al., 2013). Showing map based analysis.214

Figure 7.6 Schematic representation of a depth averaged map and a volumetric 3D grid.215

Figure 7.7 An example of Hausdorff distance calculation. The historical points (pressure points for a given well) are depicted with black dots. The red curve corresponds to simulation data. The dark blue curve corresponds to the curve fitting the historical data. The light blue lines correspond to the different distance evaluations required for the Hausdorff distance calculation. The Hausdorff distance is the maximum of all these evaluations and is equal to 12.91 (Bouzarkouna and Nobakht, 2015). Showing the production data misfit calculated using a different method.216

Figure 7.8 The characterisation of 4D seismic data signals into softening (pressure up and gas), hardening (pressure down and water), and a region of noise and ambiguous signal.217

List of Appendix Figures

Figure B.1 An idealized model representation of the reservoir and fluid contacts for the calculation in Appendix B	223
Figure C.1 The historical gas oil ratio (WGORH) and base case model gas oil ratio (WGOR) of well P1. The vertical scale is hidden for confidentiality but is the same for the two plots.	228
Figure C.2 The historical gas oil ratio (WGORH) and base case model gas oil ratio (WGOR) of well P2. The vertical scale is hidden for confidentiality but is the same for the two plots.	228
Figure C.3 The historical gas production rate (WGPRH) and base case model gas production rate (WGPR) of well P1. The vertical scale is hidden for confidentiality but is the same for the two plots.	229
Figure C.4 The historical gas production rate (WGPRH) and base case model gas production rate (WGPR) of well P2. The vertical scale is hidden for confidentiality but is the same for the two plots.	229
Figure C.5 The historical water cut (WWCTH) and base case model water cut (WWCT) of well P1. The vertical scale is hidden for confidentiality but is the same for the two plots.....	230
Figure C.6 The historical water cut (WWCTH) and base case model water cut (WWCT) of well P2. The vertical scale is hidden for confidentiality but is the same for the two plots.....	230
Figure C.7 The historical water production rate (WWPRH) and base case model water production rate (WWPR) of well P1. The vertical scale is hidden for confidentiality but is the same for the two plots.	231
Figure C.8 The historical water production rate (WWPRH) and base case model water production rate (WWPR) of well P2. The vertical scale is hidden for confidentiality but is the same for the two plots.	231
Figure C.9 The historical water production total/cumulative (WWPTH) and base case model water production total/cumulative (WWPT) of well P1. The vertical scale is hidden for confidentiality but is the same for the two plots.	232

Figure C.10 The historical water production total/cumulative (WWPTH) and base case model water production total/cumulative (WWPT) of well P2. The vertical scale is hidden for confidentiality but is the same for the two plots.	232
Figure D.1 <i>k</i> -means clustering technique	234

List of Symbols and Acronyms

Symbols

ΔA	Time lapse seismic amplitude
ΔP	Change in pressure distribution
ΔS_g	Change in gas saturation
ΔS_w	Change in water saturation
ΔV_g	Free gas volume
a_p	Change in pressure distribution coefficient
a_{Sg}	Change in gas saturation coefficient
a_{Sw}	Change in water saturation coefficient
A_o	Baseline seismic map
b_g	Exponential/shape factor
b_{og}	Exponential/shape factor
b_{ow}	Exponential/shape factor
b_w	Exponential/shape factor
B_g	Formation volume factor
β	Seismic to well calibration factor
H_{CMM}	Current measurement metric
H_{hamm}	Hamming distance
H_{hausd}	Hausdorff distance
K_h	Horizontal permeability
k_{rg}	Gas relative permeability
k_{rog}	Relative permeability of oil in gas

k_{row}	Relative permeability of oil in water
k_{rw}	Water relative permeability
K_v	Vertical permeability
MI	Mutual information
R^2	Coefficient of determination
R_s	Solution gas oil ratio
S_{gc}	Critical gas saturation
S_{gmax}	Maximum gas saturation
S_{gr}	Residual gas saturation
S_{org}	Residual oil saturation (to gas)
S_{orw}	Residual oil saturation (to water)
S_{wc}	Critical water saturation
V_{gp}	Volume of gas produced
V_o	Initial oil volume
V_{op}	Volume of oil produced

Acronyms

4D	Time lapse
API	American petroleum institute oil gravity
AVO	Amplitude versus offset
CMA-ES	Covariance matrix adaptation evolution strategy
DST	Drill stem test

DWNE	Dynamic weighted normalized error
DWNSE	Dynamic weighted normalized square error
EnKF	Ensemble kalman filter
LHED	Latin hypercube experimental design
NE	Normalised error
NRMS	Normalised root mean square
NSE	Normalize square error
NTG	Net to gross
PVT	Pressure – volume – temperature
RMS	Root mean square
SCF	Standard cubic feet
SE	Simple error
SNA	Sum of negative amplitudes
SqE	Square error
STB	Stock tank barrel
STOIP	Stock tank oil initially in place
TVD	True vertical depth
TWT	Two way time
UKCS	United Kingdom continental shelf
WNE	Weighted normalized error
WNSE	Weighted normalized square error

List of Publications

Part of the work presented in this thesis is also presented in the following publications:

- Obidegwu, D., and MacBeth, C. 2014. Estimation of Critical and Maximum Gas Saturation Using Multiple 4D Seismic Surveys. Paper presented at the EAGE Annual Conference and Exhibition, Amsterdam, The Netherlands. 16 – 19 June, 2014.
- Obidegwu, D., and MacBeth, C. 2014. Quantitative Analysis of Gas Volumes Using Multiple 4D Seismic Surveys & Material Balance. Paper presented at the 5th SEG/EAGE International Geosciences Student Conference (IGSC), Nizhny Novgorod, Russia. July 28 – August 01, 2014.
- Falahat, R., Obidegwu, D., Shams, A. and MacBeth, C. 2014. The Interpretation of Amplitude Changes in 4D Seismic Data Arising from Gas Exsolution and Dissolution. *Petroleum Geoscience*, Volume 20, Issue 03, Pages 303-320.
- Obidegwu, D., Chassagne, R. and MacBeth, C. 2014. Using 4D Seismic Surveys and History Matching to Estimate Critical and Maximum Gas Saturation. Paper presented at the International Petroleum Technology Conference (IPTC), Kuala Lumpur, Malaysia. 10 -12 December, 2014.
- Obidegwu, D., Chassagne, R. and MacBeth, C. 2015. Seismic Assisted History Matching Using Binary Image Matching. Paper presented at the SPE Europec/ EAGE Annual Conference and Exhibition, Madrid, Spain. 1 – 4 June, 2015.
- Obidegwu, D., MacBeth, C. and Chassagne, R. 2016. Comparative Analysis of Binary and Conventional Seismic Assisted History Matching. Paper presented at the SPE Europec/ EAGE Annual Conference and Exhibition, Vienna, Austria. 30 May – 2 June, 2016.

List of Awards

Part of the work presented in this thesis won the following awards:

(Best Paper Award).

- Obidegwu, D., and MacBeth, C. 2014. Quantitative Analysis of Gas Volumes Using Multiple 4D Seismic Surveys & Material Balance. Paper presented at the 5th SEG/EAGE International Geosciences Student Conference (IGSC), Nizhny Novgorod, Russia. July 28 – August 01, 2014.

(Best Presentation Award – Runner Up).

- Obidegwu, D., 2015. Seismic Assisted History Matching Using Binary Image Matching. Presented at the BG Group Geoscience Research Forum 2015, Reading, United Kingdom. September 16 – September 18, 2015.

Chapter 1

Introduction

This chapter lays the foundation and sets the structure for this thesis. It gives an insight into past works of literature pertaining to the integration of 4D seismic data and production data in a history matching workflow in order to replicate the historical data, and improve the reservoir model's forecast ability. The different methods of integration are discussed, as well as the different seismic domains of analysis. The transition from a qualitative approach to a quantitative approach of integration is reviewed, and the numerous challenges are acknowledged. The objective of this research, its challenges and the contribution of this work to the scientific world is discussed. This chapter concludes with an outline of the subsequent chapters of this thesis.

1.1 Overview

In the exciting world of physical processes, the petroleum industry does stand shoulder high with regards to its ability to challenge an engineer's thought process and dexterity in solving complex problems. These complex problems are somewhat simplified using scenarios, models and logical interpretation. The quest to predict the flow of multiple fluids in a reservoir is a complex challenge that has been the target of much research in the petroleum industry. This is desired because it facilitates efficient reservoir monitoring, management, planning and economic evaluation (Obidegwu and MacBeth, 2014a). In order to achieve this target, different tools and techniques are employed to acquire, coordinate and interpret data obtained from the reservoir as input to the reservoir simulation model. This model has to confidently replicate the historical data for it to be considered worthy of realistic predictions, and this process of updating the reservoir model to satisfy the historical data is known as history matching. Over the past years, well production data (oil rates, water rates, gas rates, pressure) has been the main historical data available, however, time lapse (4D) seismic data is now considered a major dynamic input for history matching. The integration of all these data to improve models is a very broad and complex task that deals with many areas of expertise, and as such the aim of this thesis is not to resolve all these challenges, but to make an input into the ongoing research of outputting improved models.

The research theme of this thesis is seismic assisted history matching using a binary approach, so some topics will need to be addressed in order to set the scene. These are: time lapse seismic data analysis, objective function for quantifying misfits, history matching and uncertainty quantification, upscaling for simulation runtime reduction,

seismic response to reservoir engineering concepts, and the role of 4D seismic data in estimating some oil-gas relative permeability parameters.

1.1.1 Time Lapse Seismic Data

That a model is matched to well production data is not a sufficient condition for it to make improved predictions (Sahni and Horne, 2006), the model needs to integrate all available data as well as the geologists interpretation of the reservoir in order to provide the most representative reservoir model or models (Landa, 1997, Landa and Horne, 1997, Wang and Kovscek, 2002). The need to monitor fluid displacement is a great challenge that has been successfully overcome with the use of 4D seismic technology (Hatchell et al., 2002, Lygren et al., 2002, Staples et al., 2002, Waggoner et al., 2002, Vasco et al., 2004, Portella and Emerick, 2005, Huang and Lin, 2006, Emerick et al., 2007, Kazemi, 2011, Davolio et al., 2014), which is the process of repeating 3D seismic surveys over a producing reservoir in time-lapse mode (Kretz et al., 2004, Avansi and Schiozer, 2011). 4D seismic data has become a powerful ingredient in the history matching of reservoir models due to its spatially high coverage which complements the spatially sparse and distributed nature of well data; conversely, the rapid time sampling of well data compensates for the coarser time sampling of the seismic data (Nielsen et al., 2010, Jin et al., 2012a) (Figure 1.1).

The integration of 4D seismic data into the reservoir simulation model began on a qualitative basis to reduce uncertainties (Lumley and Behrens, 1997, Elde et al., 2000, O'Donovan et al., 2000, Pagano et al., 2000, Aggio and Burns, 2001, Fagervik et al., 2001, Hatchell et al., 2002, Pannett et al., 2004), mainly by identifying saturation fronts which resulted in improved reservoir characterisation and consequently good history

matching. Despite the success, there was still need to utilise the information available in a more efficient and quantitative manner in order to achieve improved results. This led to the birth of the integration of 4D seismic data into the reservoir model in a quantitative manner.

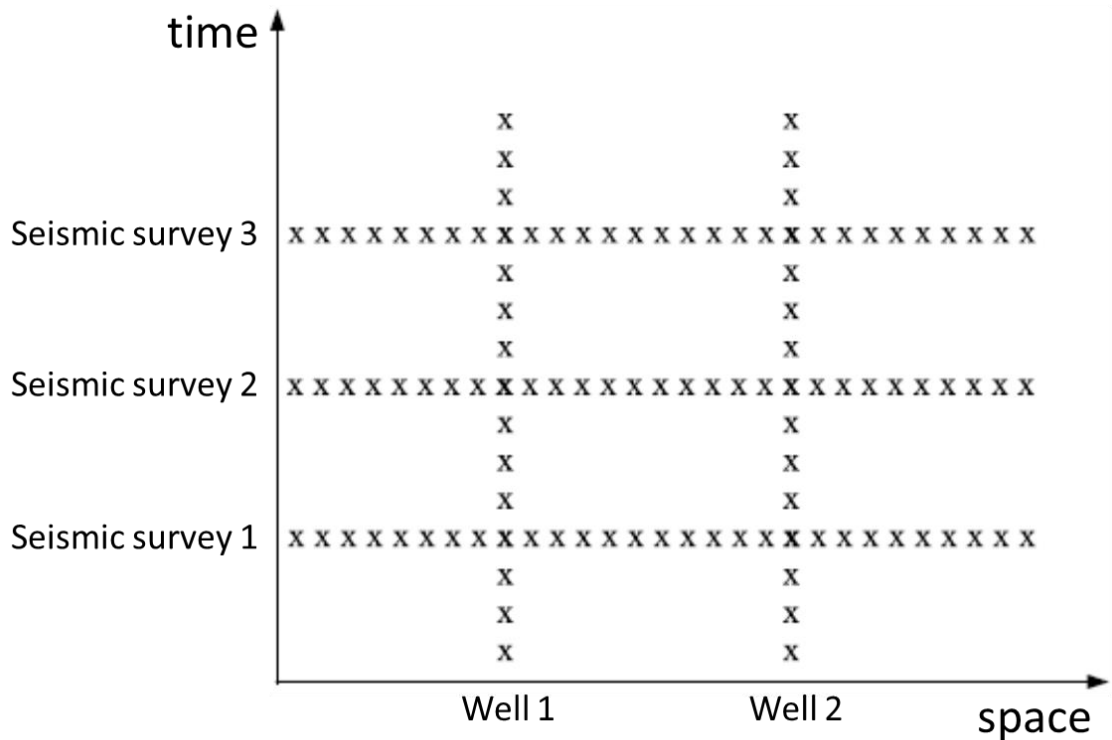


Figure 1.1 Distribution of measurements in time and space. The well data is sparsely distributed in space, while the time frequency is high. The seismic data has the opposite characterisation, with high frequency in space but a lower frequency in time. The two data sources give complimentary information in the time and space domain (Nielsen et al., 2010).

1.1.2 Quantitative Integration of 4D Seismic Data

Quantitative use of 4D seismic data in history matching is an active research topic that has been explored extensively (Arenas et al., 2001, Aanonsen et al., 2003, Clifford et al., 2003, Gosselin et al., 2003, Falcone et al., 2004, MacBeth et al., 2004, Mezghani et al.,

2004, Staples et al., 2005, Stephen and MacBeth, 2006, Avansi et al., 2010, Souza et al., 2010, Kazemi et al., 2011, Jin et al., 2012a, Joosten et al., 2014, Yan, 2014, Pazetti et al., 2015), the main challenge being quantitatively incorporating the 4D seismic into the reservoir model (Landa, 1997, Walker et al., 2006, Jin et al., 2011).

Figure 1.2 shows the different domains in which seismic data could be incorporated into the reservoir model as has been described previously (Stephen and MacBeth, 2006, Landa and Kumar, 2011, Alerini et al., 2014). The three main domains are: (1) The simulation model domain, where the observed seismic data is inverted to changes in pressure and saturation, and are then compared with the simulation output (Landrø, 2001); (2) The impedance domain, where the observed seismic data is inverted to changes in impedance, and the simulation model is forward modelled to derive impedances, and both impedances are then compared (Ayzenberg et al., 2013), or (3) The seismic domain, where the impedances derived from the simulation model are convolved with a wavelet to generate a synthetic seismic, and this is then compared with the observed seismic (Landa and Kumar, 2011).

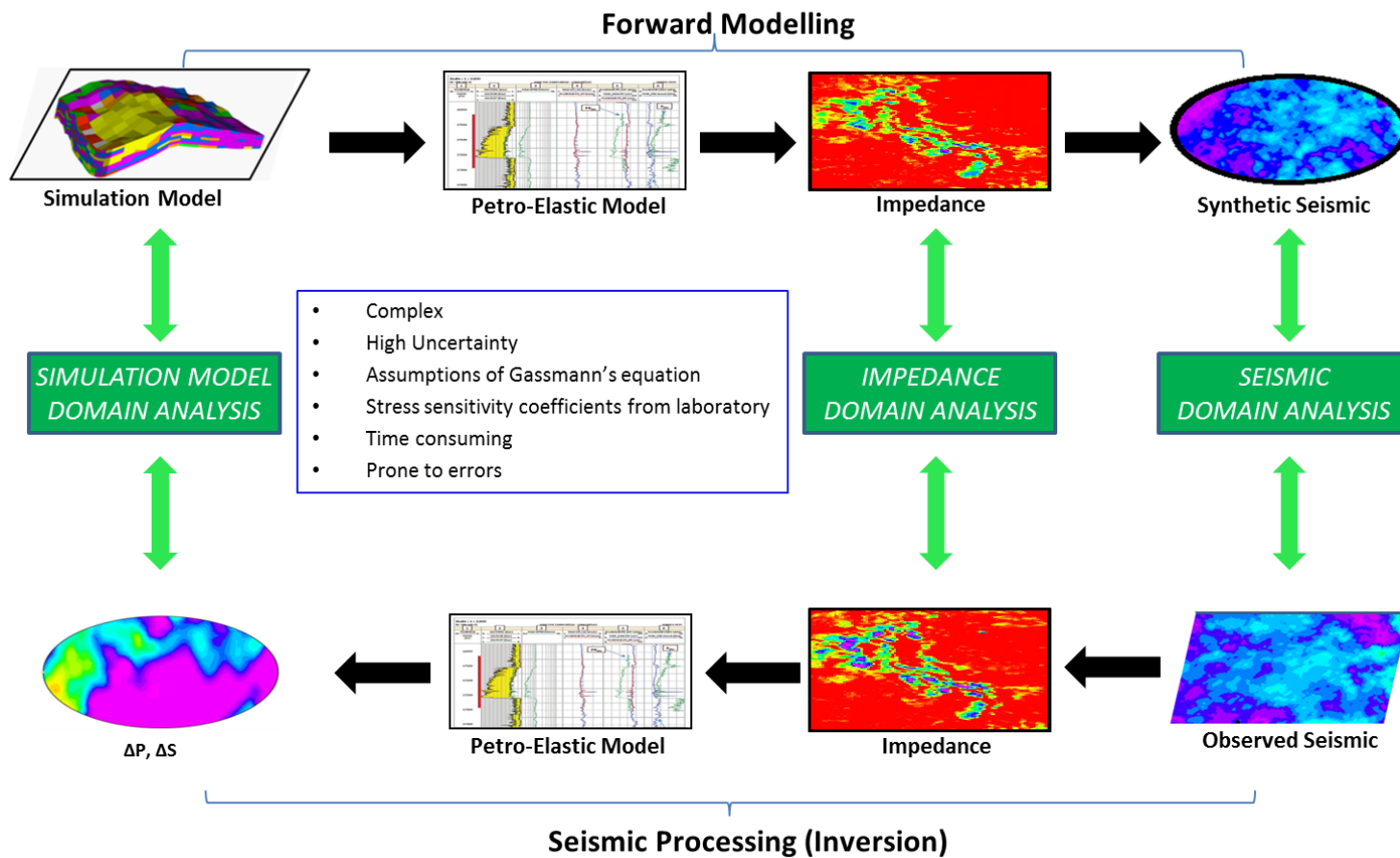


Figure 1.2 The different domains at which seismic history matching can be explored – the simulation model domain, the impedance domain, and the seismic domain

The aforementioned domains use seismic modelling, rock physics modelling or petro-elastic modelling to address this challenge, however these modelling processes are complex, time consuming, uses laboratory stress sensitivity coefficients, as well as Gassmann's equation assumptions (Landrø, 2001, Gosselin et al., 2003, Stephen et al., 2005, Floricich, 2006, Wen et al., 2006, Amini, 2014). There have been other methods that circumvent the complex seismic modelling process (Landa and Horne, 1997, Kretz et al., 2004, Wen et al., 2006, Jin et al., 2012b, Le Ravalec et al., 2012b, Rukavishnikov and Kurelenkov, 2012, Tillier et al., 2013) which employed the use of image analysis tools, binary processing, or dynamic clusters to integrate the seismic data into the reservoir model.

The use of emulator and canonical correlation to integrate 4D seismic data has also been explored (Ferreira et al., 2014, Ferreira et al., 2015). This is done by creating a stochastic representation of the model by an emulator which acts as a proxy model in order to quantify the reduction in the parameter input space, and then incorporating the 4D seismic data through canonical correlation techniques whereby water saturation maps derived from seismic data are converted into different canonical functions which represent the observable characteristics to be matched in the history matching process. The canonical correlation explores the relationship between two sets of variables, and is a multivariate statistical model that enables the study of interrelationships among set of multiple dependent variables (e.g. response parameters) and multiple independent variables (e.g. input parameters). The large number of evaluations required to identify the range of the input parameters whose output match the historical data justifies the use of an emulator, while a reduction of uncertainties with area characteristics show the successful incorporation of the 4D seismic data using canonical correlations (Ferreira et al., 2015).

1.1.3 Objective Function

In this thesis, a new approach is proposed where the seismic data and simulation data are converted to binary seismic gas/water maps and binary simulation gas/water maps respectively, such that the observed seismic data can be compared directly with the simulation output. The binary approach and seismic objective function will be analysed in subsequent chapters, while the production data objective function will be the conventional least squares method. An analysis of the influence of different objective functions in history matching was done by Bertolini and Schiozer (2011), (Table 1.1), where 8 different global objective functions are assessed. The objective functions are tested using different reservoir attributes in order to increase the reliability of the results, and reduce the influence of the optimization algorithm. The base case simulation model used for the analysis is created by varying a selection of uncertain attributes, and acts as a reference for the history matching process.

Table 1.1 shows the objective functions were index h represents the historical data, s , simulated data, b , base case model data, n , total number of data, m , total number of partial objective functions, ws , simple weight, ws_D , dynamic simple weight, wq , quadratic weight, and wq_D , dynamic quadratic weight. The results show that all the objective functions obtained improvements in the history matching, and that the simple error (SE) and square error (SqE) are the two best performers for lowest misfits, with the square error obtaining a faster misfit reduction. It is noted that the normalized and weighted functions did not present an improvement over the square error in the example, but can be further investigated in other cases (Bertolini and Schiozer, 2011).

Global objective functions.

GOF	Description	Formula
SE	Simple error	$SE = \sum_{j=1}^m \sum_{i=1}^n (h_{ji} - s_{ji})$
NE	Normalized error	$NE = \sum_{j=1}^m \frac{\sum_{i=1}^n (h_{ji} - s_{ji})}{\sum_{i=1}^n (h_{ji} - b_{ji})}$
WNE	Weighted normalized error	$WNE = \sum_{j=1}^m w_{sj} \cdot \frac{\sum_{i=1}^n (h_{ji} - s_{ji})}{\sum_{i=1}^n (h_{ji} - b_{ji})}$
DWNE	Dynamic weighted normalized error	$DWNE = \sum_{j=1}^m w_{Dj} \cdot \frac{\sum_{i=1}^n (h_{ji} - s_{ji})}{\sum_{i=1}^n (h_{ji} - b_{ji})}$
SqE	Square error	$SqE = \sum_{j=1}^m \sum_{i=1}^n (h_{ji} - s_{ji})^2$
NSE	Normalize square error	$NSE = \sum_{j=1}^m \frac{\sum_{i=1}^n (h_{ji} - s_{ji})^2}{\sum_{i=1}^n (h_{ji} - b_{ji})^2}$
WNSE	Weighted normalized square error	$WNSE = \sum_{j=1}^m w_{qj} \frac{\sum_{i=1}^n (h_{ji} - s_{ji})^2}{\sum_{i=1}^n (h_{ji} - b_{ji})^2}$
DWNSE	Dynamic weighted normalized square error	$DWNSE = \sum_{j=1}^m w_{qDj} \frac{\sum_{i=1}^n (h_{ji} - s_{ji})^2}{\sum_{i=1}^n (h_{ji} - b_{ji})^2}$

Table 1.1 Global objective functions (Bertolini and Schiozer, 2011). 8 different objective functions are analysed for history matching.

1.1.4 History Matching and Uncertainty Quantification

History matching methodologies can be classified into two major categories – the gradient based method (local optimisation method) and the derivative free method (global optimisation method) (Maschio and Schiozer, 2005). The gradient based method which can be subdivided into 3 classes – Gauss-Newton method, Conjugate Gradient method, and Quasi-Newton method uses gradient-based analysis (which can be obtained by the adjoint method) that requires the calculation of derivatives in a reservoir simulator which is a challenging task that needs access to the source code. (Arenas et al., 2001, Brun et al., 2001, Wu, 2001, Rodrigues, 2005).

The derivative free method uses the objection function value and does not require the computation of derivatives or gradient information (Romero et al., 2000, Schulze-Riegert et al., 2002). The algorithms used for the derivative free method include simulated annealing (Ouenes and Bhagavan, 1994), genetic algorithm (Sen et al., 1995), particle swarm optimisation (Mohamed et al., 2010), Ensemble Kalman Filter (Liu and Oliver, 2005), Ensemble Optimiser (Chen, 2008), covariance matrix adaptation evolution strategy (CMA-ES) (Fursov, 2015) and evolutionary algorithm (Schulze-Riegert et al., 2002) which are said to possess the potential of generating suitable solutions. The uncertainty of the history matching process is quantified through obtaining a posterior probability density function after sampling a prior probability density function through iterative processes. The final ensemble are then sampled so as to examine the dispersion of the response parameter prior to and after the uncertainty reduction (Maschio and Schiozer, 2013).

1.1.5 Upscaling

The history matching process involves running a number of simulations and is time consuming. In order to be more efficient, the dimensionality to the history matching problem can be reduced by streamline simulation (Stephen et al., 2007), proxy modelling (Risso et al., 2008) or upscaling (Christie and Blunt, 2001). Upscaling methods define equivalent or effective properties of the initial fine grid, and can be subdivided into analytical methods, numerical methods, and empirical power averaging methods (Scheibe and Yabusaki, 1998). Maschio and Schiozer (2003) propose a method of upscaling by using a Dykstra-Parsons heterogeneity coefficient which is said to be fast and efficient, and is tested using a streamline simulator. Summarily, regardless of whatever method of expediting the simulation run time is adopted, the key factor is to preserve the geological structure of the porous media, as well as replicate the flow behaviour of the reservoir simulation process (Maschio and Schiozer, 2003).

1.1.6 4D Seismic Data and Reservoir Engineering Concepts

When pore pressure falls below the bubble point of the oil in an initially undersaturated reservoir, then gas exsolution occurs (Dake, 2001) and gas migrates upwards to the top of the reservoir to form secondary gas caps or is produced. If the reservoir is initially saturated (initial pressure \leq bubble point pressure), then gas exsolution occurs immediately and may supplement pre-existing primary gas caps. This exsolution phenomenon can occur for most hydrocarbon oils but is significant for medium–light oils (medium oils are defined as having an API of between 22 and 31, light oils as between 31 and 42). For certain specific reservoirs, the drive from the gas cap that forms from this process can assist production.

Generally, gas arrives at production wells faster than oil owing to the higher gas mobility, and subsequently forms a cone-shaped accumulation around the well. Eventually, the relative permeability of the oil through the three-phase fluid mix decreases as the gas saturation increases, and this in turn lowers the oil production rate. Indeed, for oil reservoirs in which gas cap drive is not significant, gas exsolution is economically undesirable and can also lead to the practical issues of handling gas during production. Pressure drop and gas liberation are typically controlled by the injection plan, and the normal way of stopping gas from breaking out is by increasing pore pressure by injecting water. In this process, in agreement with the physics observed in the laboratory (Danesh, 1998), liberated gas is encouraged to go back into solution, in principle reversing the exsolution behaviour at the expense of additional water saturation.

To demonstrate what can be observed for this sequence of events in 4D seismic data, Figure 1.3 shows root mean square (RMS) amplitude maps for a baseline and two subsequent monitor surveys in the Foinaven field (Marsh et al., 2001, Bagley et al., 2004). This reveals a brightening due to gas exsolution at the time of the first monitor survey after 1 year of production, followed by a dimming due to dissolution and water-flooding at the time of the second monitor survey after another year of water injection and production. In this particular UKCS reservoir, knowledge of the gas distribution using 4D seismic data and knowledge of its causative reservoir engineering mechanisms contributed significantly to the understanding of reservoir connectivity, and hence field management.

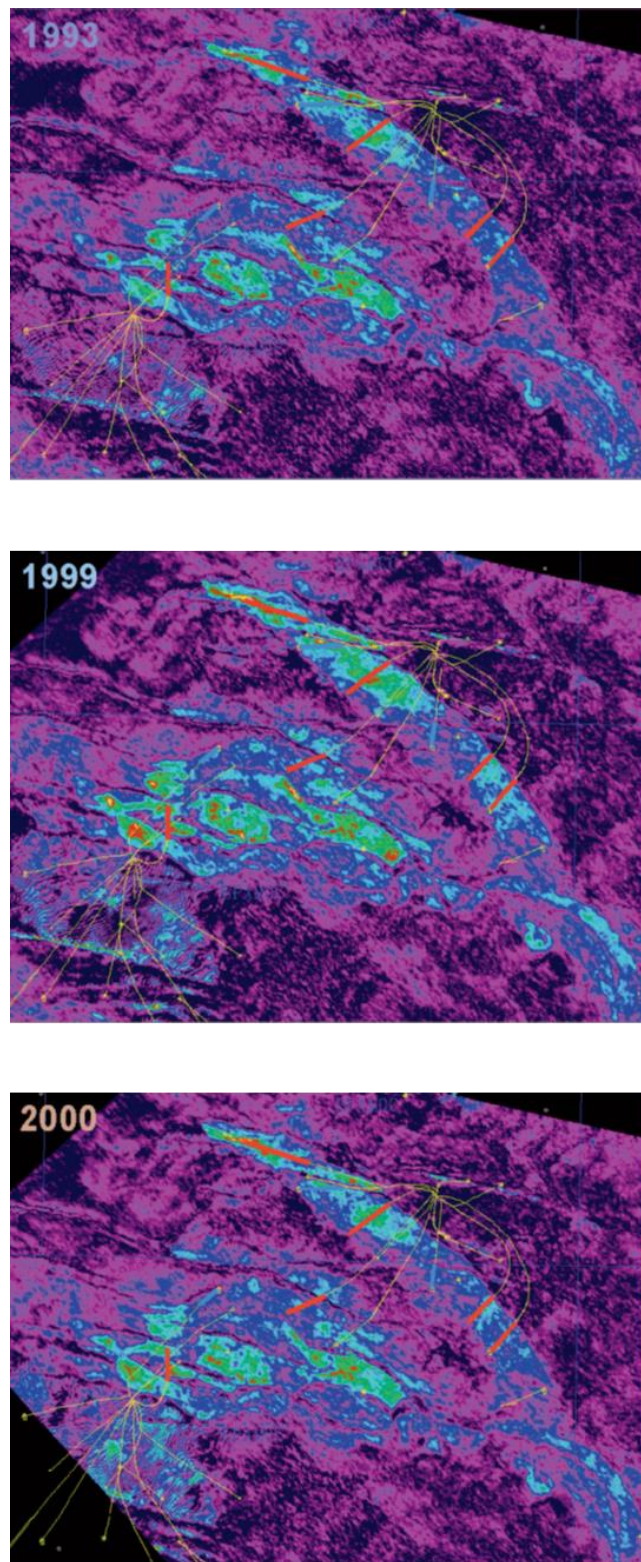


Figure 1.3 A 4D seismic data example of gas exsolution and dissolution from the Foinaven field, UKCS. Amplitude maps are generated for the 1993 baseline survey prior to production, then again in 1999 following gas exsolution after one year of production, and finally in 2000 after dissolution due to repressurization, gas migration and production. The mapped anomalies visibly expand due to the liberated gas, then contract upon pressure increase (Marsh et al., 2001).

There are several publications in which the 4D seismic response of liberated gas has been noted, both for clastic fields (Johnston et al., 2000, Alsos et al., 2009) and for carbonate fields (van Gestel et al., 2011), although typically these observations form part of a broader case study and do not focus specifically on the gas-exsolution mechanisms. Reports of gas dissolution, however, are less frequent and limited to a few select publications (Marsh et al., 2001, Gainski et al., 2010). Recently, 4D seismic detection of gas exsolution has also been demonstrated as a tool for indirectly assessing pressure connectivity (Mitchell et al., 2010, Johnston, 2013), and injected gas has been utilized to illuminate complicated top reservoir structure (Roy et al., 2011).

1.1.7 Seismic Response to Reservoir Activities

The seismic response to liberated or dissolved gas is expected to be substantial, as it is well recognized that laboratory experiments indicate that the presence of gas should lead to a strong, non-linear reduction in seismic velocity (Domenico, 1977) and impedance. Thus, for example, in reservoirs characterized by a high to low impedance contrast between the overburden and the top of the reservoir unit, very visible bright amplitudes on the 3D seismic profiles are associated with the presence of gas, typifying the classic Gulf of Mexico bright spots widely observed in seismic exploration (Johnston and Cooper, 2010). Thus, it is also expected that 4D seismic response should have a strong sensitivity to gas, generally outweighing the contributions from rock-stress sensitivity and water saturation. As a consequence, it is possible to focus almost entirely on the response due to gas out of solution and, perhaps, dissolution.

The seismic response to reservoir mechanism in general is illustrated in Figure 1.4 by Huang (2011), where the effect of gas injection, gas out of solution, water flood and gas production are analysed. Production activity in a reservoir causes more than one type of effect in the reservoir, where changes in oil/water/gas saturation and pressure are most important for a 4D seismic data analysis perspective. Interpreting 4D seismic data signals dominated by each individual type of change is usually uncomplicated, however the challenge lies in the overlapping of pressure and saturation effects when multiple simultaneously acting effects combine towards the generation of the seismic data.

For example, in a gas injection scenario, injected gas saturation increase will increase the overall compressibility of the rock, thereby reducing the velocity at which seismic wave will travel through the rock. Similarly, the injected gas volume may cause pressure increase which reduces the effective stress (difference between the confining pressure and the pore pressure), which also reduces velocity (Figure 1.4a). This may lead to a masking of the gas saturation effect by the pressure build-up effect as they both have the same polarity (Huang, 2011). Also, the interpretation of 4D seismic data signal due to a combination of pressure and saturation change with conflicting effects on seismic velocity is even more complicated, such as during water injection and gas coming out of solution due to pressure depletion below bubble point (Figures 1.4b and 1.4c).

In a gas exsolution scenario which occurs due to reservoir depressurization below bubble point pressure, the gas coming out of solution causes a reduction in velocity, while the reduction in pressure increases the effective stress, which increases the velocity; hence whichever signal is seen on the seismic data signifies whether the saturation or pressure dominates. In a water injection scenario, the water flood causes an increase in velocity, while the accompanying pressure increase due to injected water reduces the effective

stress, which reduces the velocity; hence whichever signal is seen on the seismic data signifies what effect dominates.

A quantitative classification of these conflicting effects on seismic data from a UKCS reservoir is shown in Figure 1.5 by Amini (2014) where the relative impact of different scenarios on impedance change is assessed and represented by histograms, thereby indicating what phenomena dominates. In this field, gas breakout is shown to have the highest impact as opposed to pressure build-up and waterflood.

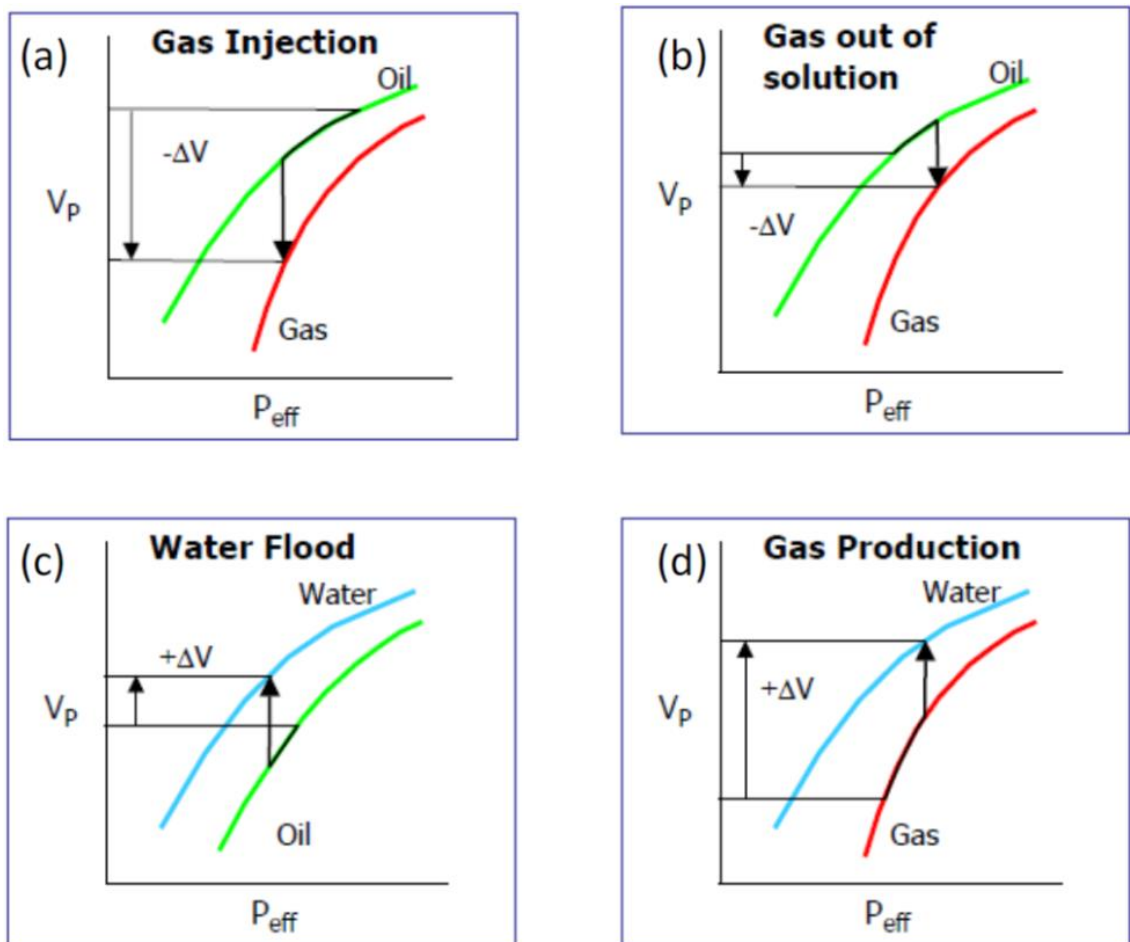


Figure 1.4 Generalised plots of P-wave velocity change in the different reservoir production scenarios, (a) gas injection, (b) gas out of solution, (c) water flood and (d) gas production (Huang, 2011).

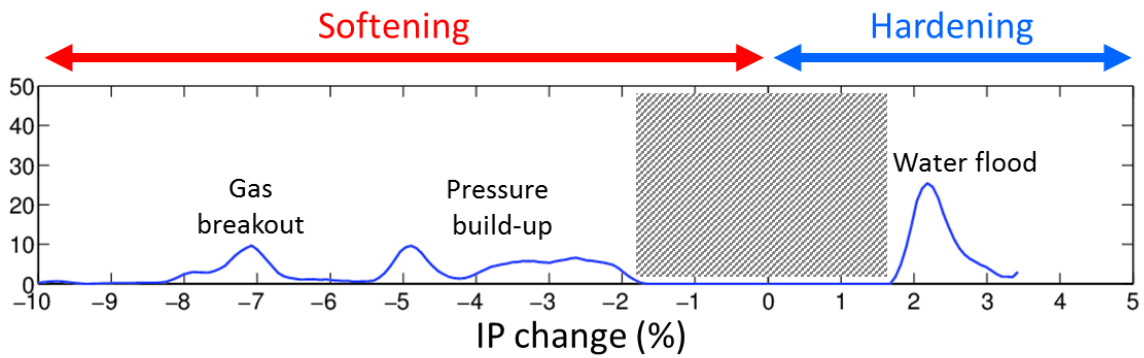


Figure 1.5 Quantitative representation of impedance response to different reservoir mechanisms (Amini, 2014).

The ability to use 4D seismic data to directly access gas distributions is an important observation, as it is known from fluid-flow simulation studies that gas exsolution and dissolution are controlled by many reservoir-dependent rock and fluid properties - the numerical values of which remain largely uncertain and require constraint. These factors relate mainly to the vertical and horizontal reservoir connectivity, and also, at the pore scale, to the relative permeability behaviour. Thus, the exact volume of gas liberated during exsolution, dissolved during dissolution, and the behaviour of the gas migration in the reservoir is typically uncertain (Danesh, 1998).

1.1.8 Gas and Oil Relative Permeability

In a reservoir with multiphase fluids, the flow of the fluids in the reservoir is determined by the relative permeability values on a relative permeability curve (Figure 1.6). The curve acknowledges the drainage process (non-wetting phase displacing wetting phase, e.g. gas displacing oil/water, or oil displacing water), and the imbibition process (wetting phase displacing non-wetting phase, e.g. water displacing oil/gas, or oil displacing gas) thus taking into account the hysteresis effects (Chassagne and Hammond, 2012). Table 1.2 shows the key parameters that are used in generating the relative permeability curves (Stone, 1970, Stone, 1973, Blunt, 2000, Li et al., 2012), and the equations are shown below.

For an oil – gas two phase flow system, the relative permeability of gas is (see Table 1.2 for definition of equation parameters):

$$k_{rg} = a_g \left(\frac{S_g - S_{gc}}{1 - S_{org} - S_{wc} - S_{gc}} \right)^{b_g} \quad (1.1)$$

End Point Parameters	Shape Factor Parameters
(1) S_{wc} – Critical water saturation	(1) b_w – exponential/shape factor
(2) S_{orw} – Residual oil saturation	(2) b_{ow} – exponential/shape factor
(3) S_{gc} – Critical gas saturation (S_{gr})	(3) b_g – exponential/shape factor
(4) S_{org} – Residual oil saturation (S_{gmax})	(4) b_{og} – exponential/shape factor

Table 1.2 The endpoint parameters and shape factor parameters used in creating relative permeability curves (Li et al., 2012).

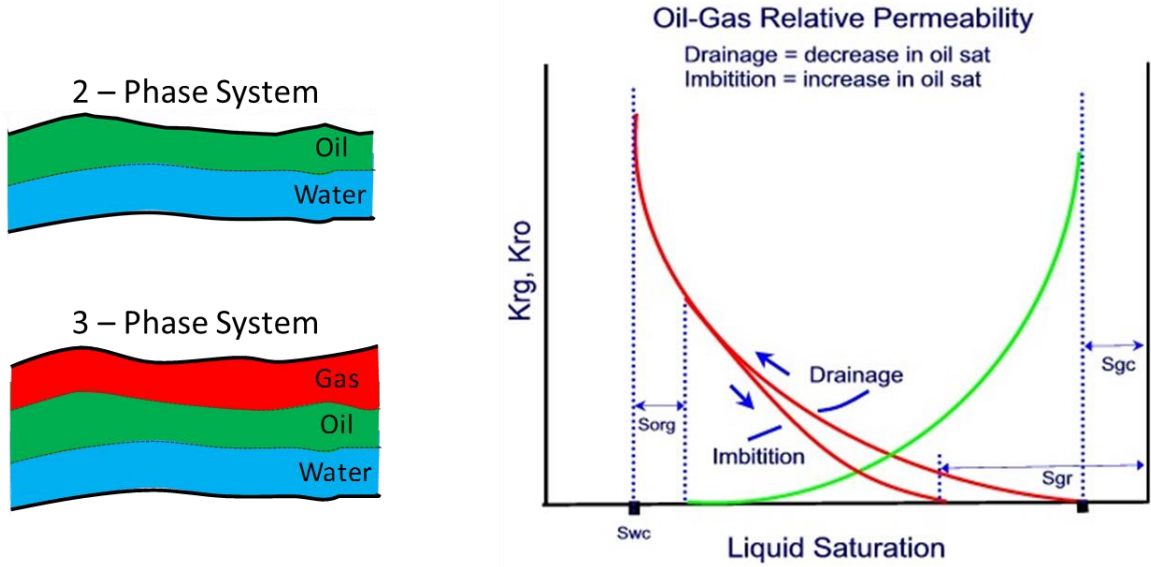


Figure 1.6 Schematic of a 2-phase and 3-phase fluid flow system, and an oil-gas relative permeability curve for a 3-phase system

For an oil – gas two phase flow system, the relative permeability of oil is:

$$k_{rog} = a_{og} \left(\frac{1 - S_{org} - S_{wc} - S_g}{1 - S_{org} - S_{wc} - S_{gc}} \right)^{b_{og}} \quad (1.2)$$

For an oil-gas-water three phase flow system, the water and gas relative permeability can be calculated using the two-phase flow system equation as they are assumed to only be in contact with one phase (schematic in Figure 1.6), however the oil relative permeability can be calculated using the Stone Model II equation which is the interpolation shown below:

$$k_{ro} = a_o \left[\left(\frac{k_{row}}{a_o} + k_{rw} \right) \left(\frac{k_{rog}}{a_{og}} + k_{rg} \right) - (k_{rw} + k_{rg}) \right] \quad (1.3)$$

Where, k_{rg} is the relative permeability of gas, k_{rog} is the relative permeability of oil at present S_g , S_g is gas saturation, S_{gc} is critical gas saturation, S_{org} is residual oil saturation, a_g is relative permeability of gas at $S_g = 1 - S_{org} - S_{wc}$, a_{og} is relative permeability of oil at $S_g = S_{gc}$, and b_g and b_{og} are exponential/shape factors that determine shape of the relative permeability curve.

The parameters to generate the relative permeability curves are sourced using different techniques as shown in Figure 1.7. These include core laboratory experiments (Closmann, 1987, Moulu, 1989, Firoozabadi et al., 1992), history matching exercises (Bansal, 1988, Goodfield and Goodyear, 2003, Faseemo and Onyema, 2013), log analysis (Kamath and Boyer, 1995), and pore network modelling (Blunt, 2001, Bondino et al., 2002). 4D seismic data is earmarked as a potential useful addition to this list, as it directly measures effects of reservoir activity, and thus would generate results that would reflect in-situ fluid movement.

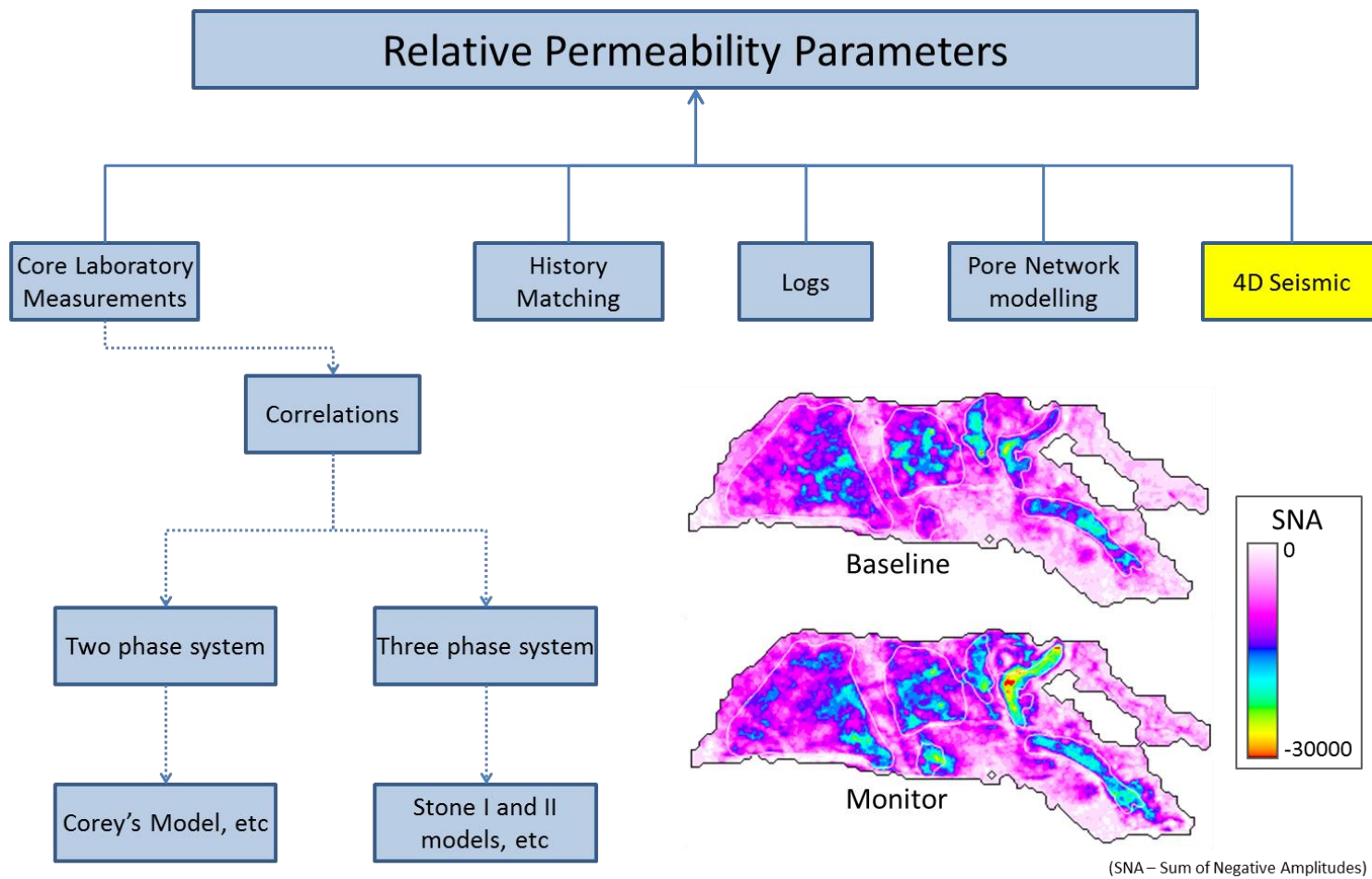


Figure 1.7 Different sources of inputs for generating relative permeability curves. 4D seismic data is highlighted as a potential addition.

1.2 Motivation of this Research

The ever present challenge of improving accurate representation of the subsurface reservoir by using cutting edge techniques and reservoir simulation analysis is of great interest to the oil and gas industry, and this encourages research in this direction and domain. Most of the reservoir parameters that are input to a reservoir simulation model are inferred from laboratory experiments and processes which do not replicate the subsurface conditions, and are hence not very reliable. The question then arises as to what suitable alternatives are available that directly measure subsurface phenomenon. An answer to that question would be to utilise 4D seismic data, as seismic data is a direct measurement of acoustic waves bearing the imprint of subsurface conditions, and 4D seismic data is a measurement of these conditions over time, hence capturing the changes within. In this research, 4D seismic data is proposed to estimate some endpoints of a relative permeability curve (critical gas saturation and maximum gas saturation), and this is made possible by proper interpretation of the 4D seismic data.

Another major issue is the integration of 4D seismic data and production data information into a reservoir simulation model using a history matching process. The main challenge lies in the nature of the different data types and how to reconcile them with the reservoir simulation model. An approach which has been commonly used is petro elastic modelling (Amini, 2014), which attempts to convert the reservoir simulation model output to synthetic seismic, and then compare the synthetic seismic with the observed seismic. This approach is quite complex, uses laboratory coefficients, time consuming and prone to errors. The motivation of this research is to circumvent this process by utilising a binary approach that would be faster to implement and generate suitable results.

1.3 Objectives of this Research

The main objective and challenge of this thesis is to quantitatively integrate 4D seismic data and production data into a history matching workflow. This a non-trivial problem which is actively being researched about around the globe. The aim of this work is to make a contribution to the already existing body of knowledge. The main task is to utilize a binary image approach as a technique to circumvent the need to use seismic modelling or petro elastic modelling, which is known to be complex, uncertain and time consuming. This will be achieved by following these main targets:

1. An extensive study of the seismic response to reservoir models exhibiting a wide range of mechanisms and distribution of properties.
2. An in-depth analysis of gas exsolution and gas dissolution processes, and being able to interpret these phenomenon on 4D seismic data in order to estimate some endpoints of a relative permeability curve (S_{gc} and S_{gmax}).
3. Developing the binary images approach, and setting up tests to justify its use as opposed to a multi-level or analogue approach. Also, determining an appropriate misfit function that will be used to correlate binary maps from different sources.
4. Validating the binary images approach by conducting tests on synthetic scenarios that replicate expected real field occurrence
5. Utilising the binary images approach for seismic assisted history matching on a real field data, and examining its potential, as well as contrasting it to the conventional approach to further underscore its usefulness.

The main value of this work arises from the ability to integrate 4D seismic data and production data into a history matching workflow in a fast, efficient and reliable manner.

1.4 Contributions of this Work

The ability to quantify gas volumes in a reservoir using 4D seismic data only is a major step towards achieving a fully quantitative application of 4D seismic data in the reservoir engineering domain. This work has shown that clear brightening and dimming of seismic amplitudes observed in 4D seismic data can be used to estimate the critical gas saturation, maximum gas saturation, and the solution gas oil ratio in a producing reservoir. It also demonstrates that monitoring of gas exsolution and dissolution can be potentially useful for comprehending the reservoir activity, and improving the reservoir simulation model.

The application of the binary approach to a seismic assisted history matching exercise of a real field data has shown the potential of integrating seismic data into the reservoir model in a timely, effective and efficient way. This heralds a unique approach of bypassing the seismic modelling or petro-elastic modelling process, and the *Current* measurement metric utilised as a misfit function has been shown to be a very useful addition to the set of binary misfit functions. This has been applied to gas exsolution scenarios and water evolution scenarios, so it has the potential for applicability on a wide range of reservoir occurrences.

1.5 Thesis Outline

The remainder of this thesis consists of six chapters.

Chapter 2 investigates the quantitative analysis of gas volumes in a United Kingdom Continental Shelf (UKCS) field. It examines the 4D seismic data signatures from multiple seismic surveys shot during gas exsolution and dissolution, and focuses in particular on what reservoir information may be extracted from their analysis. It also introduces the background of the real field data that will be used in this thesis

Chapter 3 is about the development of the binary images approach for incorporating 4D seismic data into the history matching workflow. The method of generating the binary map is discussed, and idealised models are created and used to determine the suitability of a binary approach as opposed to a multi-level or analogue approach. Also metrics for comparing binary maps are sourced and are analysed on test case scenarios so as to ascertain their effectiveness as misfit functions.

Chapter 4 validates the binary images approach using the selected misfit functions analysed in chapter 3. A synthetic simulation model is modified to generate different scenarios that replicate expected real field occurrence, and then it is demonstrated that the binary approach does provide a quick and efficient means of assessing reservoir parameters that would reproduce the required seismic data response.

Chapter 5 utilizes the binary images approach in a binary seismic assisted history matching scheme applied to a real field data. The production data is matched using the conventional least squares error, while the seismic data is matched using the binary approach and misfit functions assessed in Chapter 4.

Chapter 6 presents a comparative analysis of the binary seismic assisted history matching approach with that of a conventional seismic assisted history matching approach.

Chapter 7 summarizes the thesis with conclusions, and in addition, recommendations are put forth towards the future improvement of the proposed workflow, as well as suggestions and food for thought.

Chapter 2

Quantitative Analysis of Gas Volumes in a UKCS Field

This chapter introduces and describes the Schiehallion field which will be the main dataset used throughout this thesis. It examines the time-lapse or 4D seismic signatures from multiple seismic surveys shot during gas exsolution and dissolution, and focuses in particular on what reservoir information may be extracted from their analysis. Hydrocarbon gas properties, their behaviour, and their relationship to fluid-flow physics are studied. This knowledge is then applied to interpret the seismic response of the field which has surveys repeated at intervals of 12–24 months, to obtain an estimate of the critical gas saturation of between 0.6% and 4.0%. These low values are consistent with a range of measurements from laboratory and numerical studies in the open literature. The critical gas-saturation estimate is also in qualitative agreement with the solution gas–oil ratios estimated in a material balance exercise using the data. It is believed that the methodology and approach used may be readily generalized to other moderate to high permeability oil reservoirs, and used as input in simulation model updating.

2.1 Background to the Schiehallion Field

The Schiehallion field is located at the United Kingdom Continental Shelf (UKCS) (Figure 2.1), and it is a turbidite field (Martin and Macdonald, 2010) whose reservoir fluid is a black oil with an API gravity ranging from 22° to 28° (there is a variation with depth in the reservoir) at a temperature of 120 °F (48.89 °C). Its initial reservoir pressure is approximately 2900 psi (19.99 MPa), whilst bubble point is 2850 psi (16.65 MPa) at the top reservoir level, and the solution gas–oil ratio (R_s) is a low 354 scf/bbl (62.99 $\text{sm}^3 \text{m}^{-3}$). In this field, there is known to be gas exsolution, gas mobilization, and then repressurization with subsequent dissolution. During the course of production, poor connectivity led to a lack of support from injectors. This combines with a weak aquifer influx to give a strong pressure decrease in some areas, and a drop below bubble point with the consequent liberation of free gas. The drilling plan adjusted for this phenomenon and recovered the pressure (Govan et al., 2006). There are multiple vintages of seismic shot across this field for reservoir management purposes, and, for this work, the preproduction baseline in 1996 and six monitors shot in 1999, 2000, 2002, 2004, 2006 and 2008 are selected which have been shot at intervals of 12 – 24 months. These data have been cross-equalized by the data provider for 4D seismic interpretation purposes, and have a non-repeatability normalized root mean square (NRMS) noise metric (Kragh and Christie, 2001) of approximately 31%. The data have been transformed into relative impedance traces by coloured inversion (Lancaster and Whitcombe, 2000). Importantly, the seismic data are repeated on a timescale shorter than most offshore 4D seismic projects, and therefore offer a good opportunity to analyse the rapidly occurring phenomena of gas exsolution and dissolution. An isolated sector is identified for study that is segmented by two major east–west-trending normal faults. Figure 2.2 shows a vertical section from the baseline seismic survey.

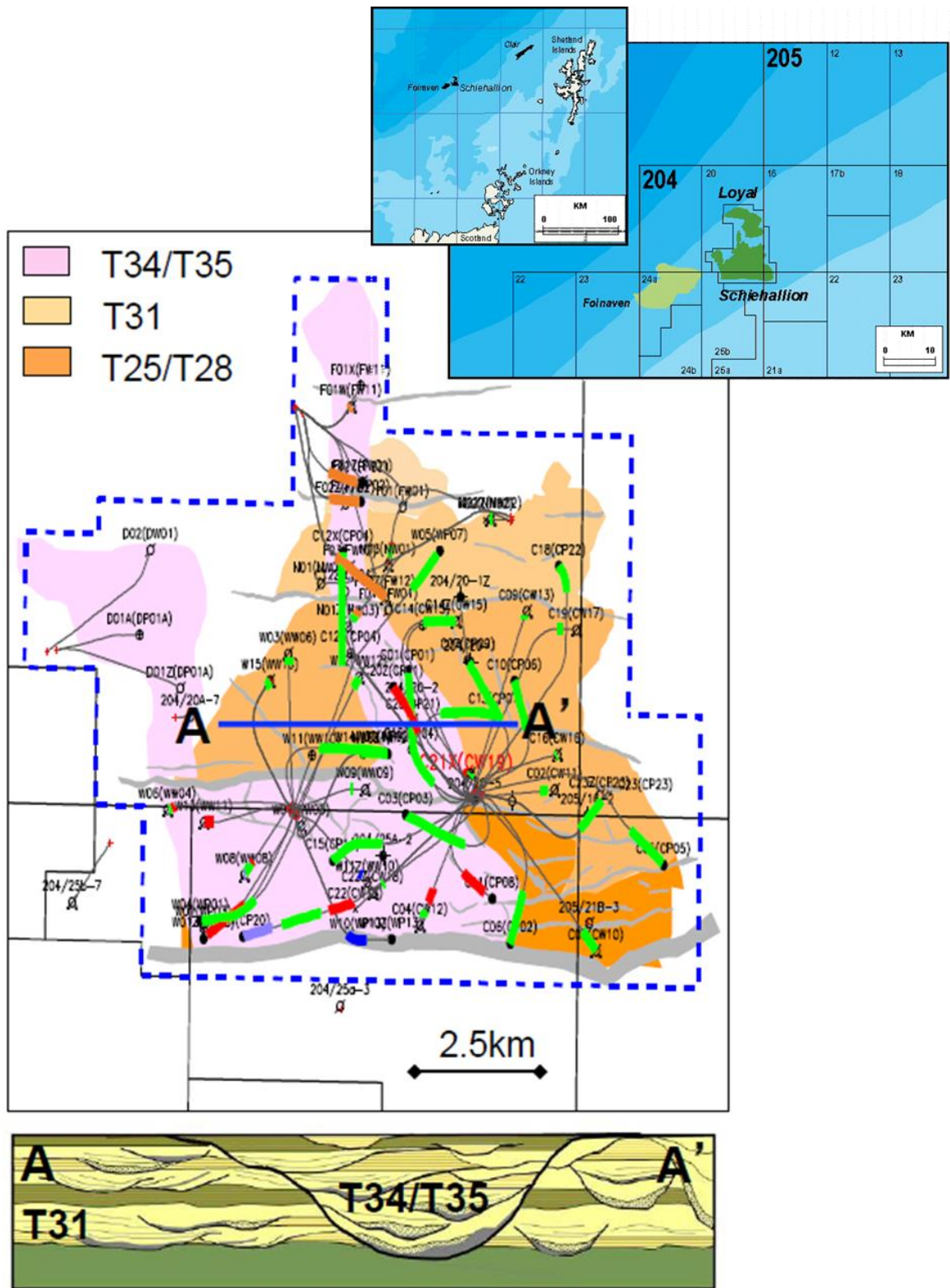


Figure 2.1 The Schiehallion oil field location in the United Kingdom Continental Shelf (UKCS) highlighting a cross-section (A to A') of segment 1 showing the T31 which is the reservoir of interest (Martin and Macdonald, 2010).

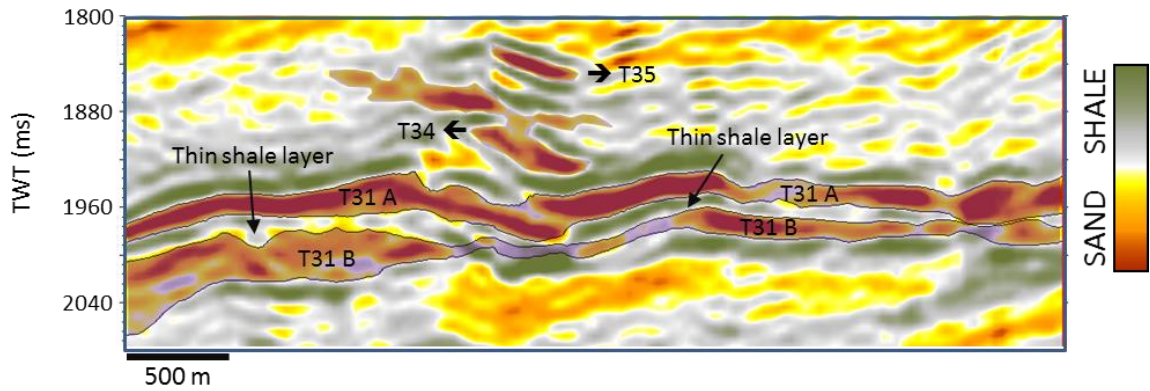


Figure 2.2 Vertical-section from the 1996 preproduction coloured inversion seismic data, showing the reservoir structure. Troughs in dark red represent the sand bodies, whilst peaks in grey represent the shales. The top and base of the sand layers are picked as zero crossings by the data provider (Amini, 2014).

The reservoirs consist of multiple-stacked, interconnected and amalgamated discrete sand bodies. The sediment system is thus expected to be highly compartmentalized, with both vertical and lateral connectivity being a major reservoir management issue. The T31 producing interval is mapped for the purposes of this study as it is the main reservoir in which gas exsolution occurs in this area. This particular reservoir interval has a variable character ranging from thin interbedded sands and shale to massive sands. The T31 is divided into two units, T31a and T31b, separated by thin shale. There are sheet-like units in this sector, typically 10–20 m thick that can be mapped on the seismic profile over a large proportion of the area (Martin and Macdonald, 2010). As the seismic data have a wavelength of 140 m (20 Hz peak frequency for the seismic wavelet and a velocity of 2800 m s^{-1}), the reservoirs in this sector are generally below tuning thickness which implies that seismic cannot vertically resolve the different sub-layers within, and thus a map-based approach may be suitable.

2.2 The Reservoir Mechanisms

In this section, an in-depth analysis of the physics of gas exsolution and dissolution in the reservoir is discussed, and the uncertainties in these processes are underscored. These would lay the foundation for tackling the complex challenge of properly analysing the 4D seismic data.

2.2.1 Gas Exsolution

The gas exsolution mechanism can be explained using a fluid-phase diagram such as that shown in Figure 2.3, calculated from state equations and the composition of the reservoir fluid determined from the laboratory. This phase envelope describes the various expected hydrocarbon fluid states at each pressure and temperature, and represents a composite physical behaviour of the many hydrocarbon constituents that make up the oil in the reservoir. At pressures above the bubble point, the hydrocarbon is a liquid, whilst, below the dew point pressure, it is a gas. Gas and liquid co-exist in the region between these two points but the exact proportion of the liquid to gas varies with pressure and temperature. Decreasing pressure from an initial condition just above the bubble point at a fixed temperature moves the fluid conditions along a vertical line A–B drawn in Figure 2.3. As the bubble point is reached, the lightest hydrocarbon molecules (usually methane - C1) leave the liquid oil to form gas bubbles and then, as the total fluid expands more, the liquid is vaporized. As pressure decreases below bubble point, the gas saturation builds progressively as gas bubbles are first nucleated, and then coalesce or grow more by the diffusion of additional free gas. Heavier gas components are also released at this stage. When a significant number of bubbles are liberated, and have grown in size, the fluid system reaches a critical gas saturation (S_{gc}) for which the gas becomes mobile.

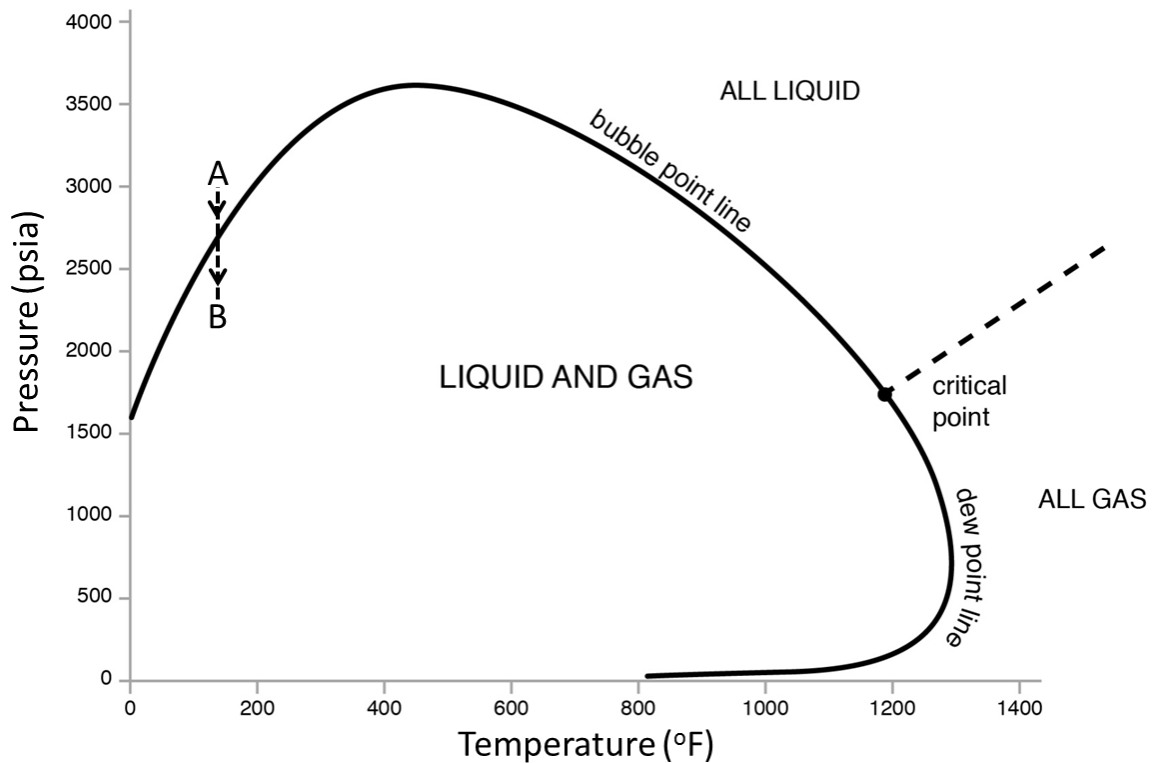


Figure 2.3 Pressure-temperature phase envelope for the field based on measured oil compositional data from the data provider. The initial reservoir pressure is 2900 psi (19.99 MPa) and the temperature is 120 °F (48.89 °C), and so the oil is already very close to bubble point.

The value of S_{gc} is usually defined as the point at which the gas first becomes mobile. However, importantly, gas bubbles in the oil that are saturated below this critical saturation still remain in the oil. The mobilized gas migrates upwards and also towards the wellbore due to the actions of the gravitational force and well pressure gradients, collecting in local highs or structural traps to form gas caps in the reservoir or being produced (Figure 2.4). Depending on the reservoir connectivity and injection-production scenario, this overall process can occur quickly in a few months or less (Falahat, 2012). In practice, trapped gas can still remain in the reservoir oil due to geological heterogeneity such as low net to gross or small-scale structure.

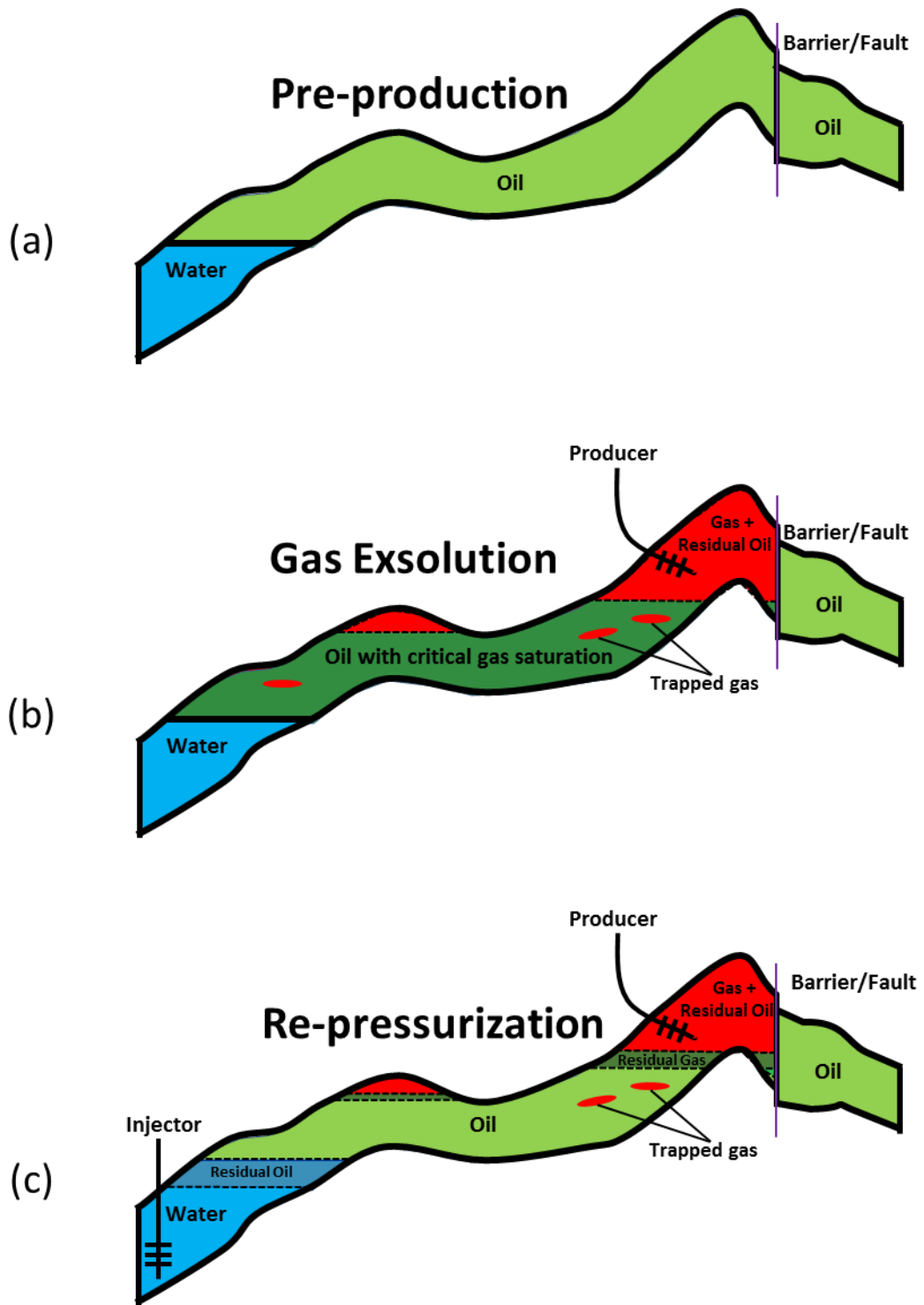


Figure 2.4 Schematic illustrating the three main stages of gas exsolution and dissolution (repressurization) that are being examined, and their consequent effect on the reservoir saturation conditions. (a) Initial preproduction state: live oil and no free gas; (b) after gas exsolution and mobilization of the free gas (note the trapped gas under low NTG pockets or structure); (c) oil production, repressurization by water injection and gas-cap shrinkage due to production. In this latter case, it is highly likely that the residual gas may be reduced to zero by the repressurization.

The exact volume of gas liberated into the reservoir formation is a function of the initial oil in place, oil type, rock properties and the overall pressure drop. The gas saturation in the secondary gas cap is $S_{gmax} = 1 - S_{wc} - S_{org}$, where S_{wc} is the initial (connate) water saturation and S_{org} is the residual oil left behind after displacement by the expanding gas cap. The various pore-scale saturation regimes generated by the process of gas exsolution described above are illustrated in Figure 2.5. Appendix A addresses the concern of the fluid property and seismic wave property changes before, during and after gas exsolution, and the impact this would have on the seismic interpretation.

2.2.2 Gas Dissolution

From Figure 2.3, the effect of a pore-pressure increase may be construed as a reversal of the gas-exsolution mechanism along the vertical trajectory and, in the ideal case (a closed container), gas does indeed dissolve back into solution. However, once the pore pressure has built up over the entire volume in the reservoir (pressure spreads quickly to equilibrate in hours/days), the gas at and above (several cells or a few metres) the gas-oil contact tends to dissolve rapidly. Simulation studies by Falahat (2012) indicate that gas remaining in the oil leg at the critical gas saturation dissolves in only a few days in response to the pressure increase. In addition, the injected water physically displaces gas from around the injection well (gravity effect permitting); however, as gas close to the injection well dissolves in the oil before the arrival of the water (due to the pressure effect), there is generally no residual gas in the area flooded by water. During this period, the gas-oil and oil-water contacts may also move upwards due to gas production or water injection, respectively.

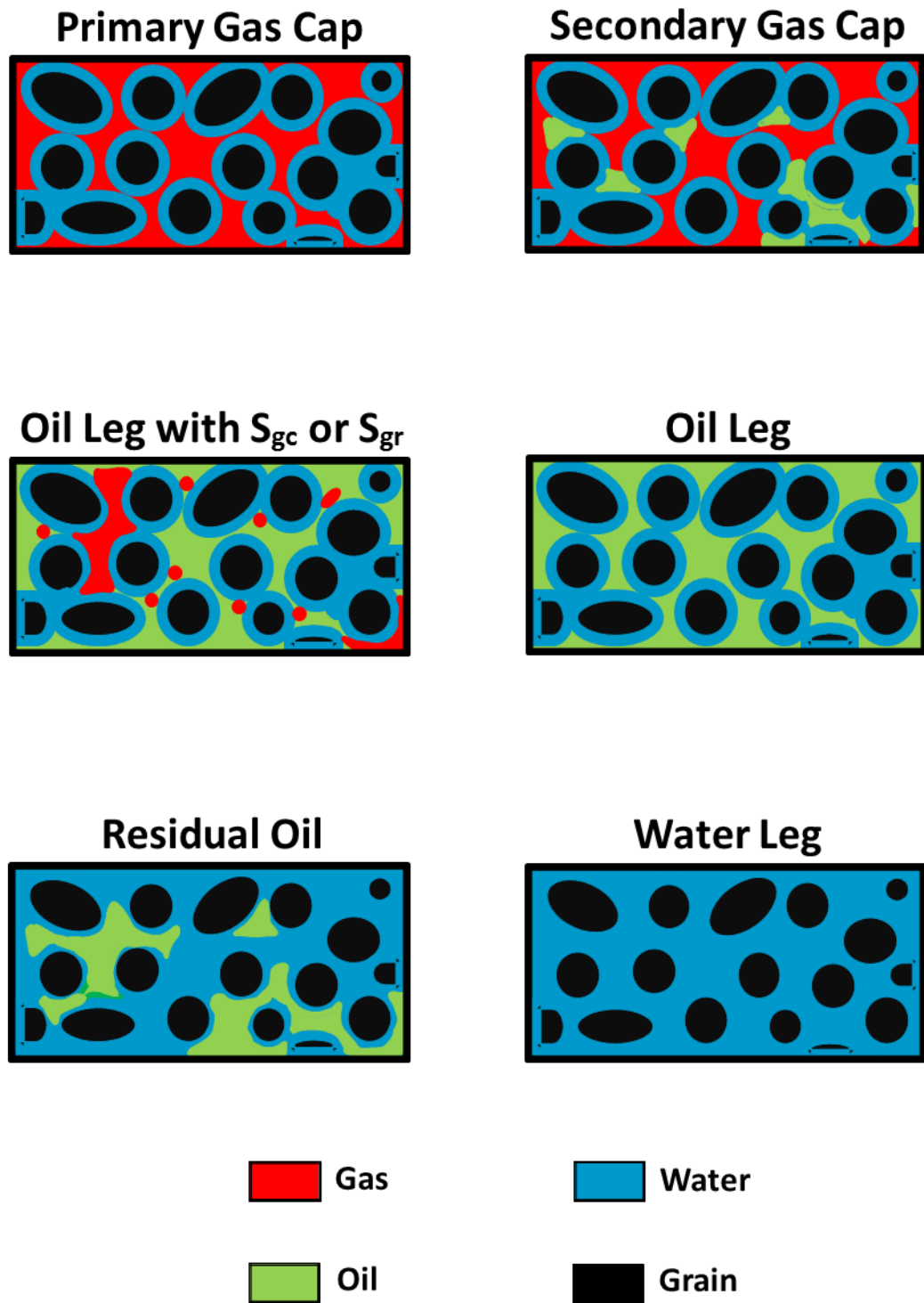


Figure 2.5 A pore-scale description of the six saturation states relevant to the calculation of the seismic response from the exsolution and dissolution scenarios shown in Figure 2.4. S_{gr} refers to the residual gas saturation after gas-cap contraction and S_{gc} to the critical gas saturation.

As the volume of oil remaining in the gas cap (S_{org}) and the residual in local traps (S_{otrap}) is insufficient to dissolve all of the gas present, this volume remains largely in place. However, a proportion of the gas migrates from its original position owing to the new pressure gradients established by the injection. Thus, it is expected that a volume of free gas still remains present in the reservoir despite the pore pressure arriving back at the initial bubble point pressure. The exact quantity of gas dissolving back into the oil depends on many factors, including the reservoir properties, gas mobility, fluid type, well-pressure behaviour, and the pressure-volume-temperature (PVT) properties (i.e. the exact shape of the phase envelope in Figure 2.3). For example, for light oils, a higher volume of the gas is liberated by pressure drop, but a smaller volume of the gas can be dissolved by pressure build-up (McCain, 1990). Conversely, for heavier oils, a smaller volume of gas is liberated by pressure drop, and a higher volume of this gas is dissolved by pressure build-up. The next section describes the monitoring of exsolution and dissolution of gas using the 4D seismic data acquired for this field.

2.3 Description of Gas Exsolution and Dissolution

For the purposes of 4D seismic analysis, the ‘sum of negatives’ attribute (SNA) is employed. This attribute sums all negative amplitudes over the T31 reservoir interval defined between the top T31a and base T31b. This is used as it has been demonstrated in past work to be sensitive to the reservoir conditions when the sands are known to be softer than the shales – giving a high to low seismic impedance contrast and a negative relative impedance (Jack et al., 2010). Figures 2.6 and 2.7 show the sequence of resultant attribute maps for each survey in the chosen segment.

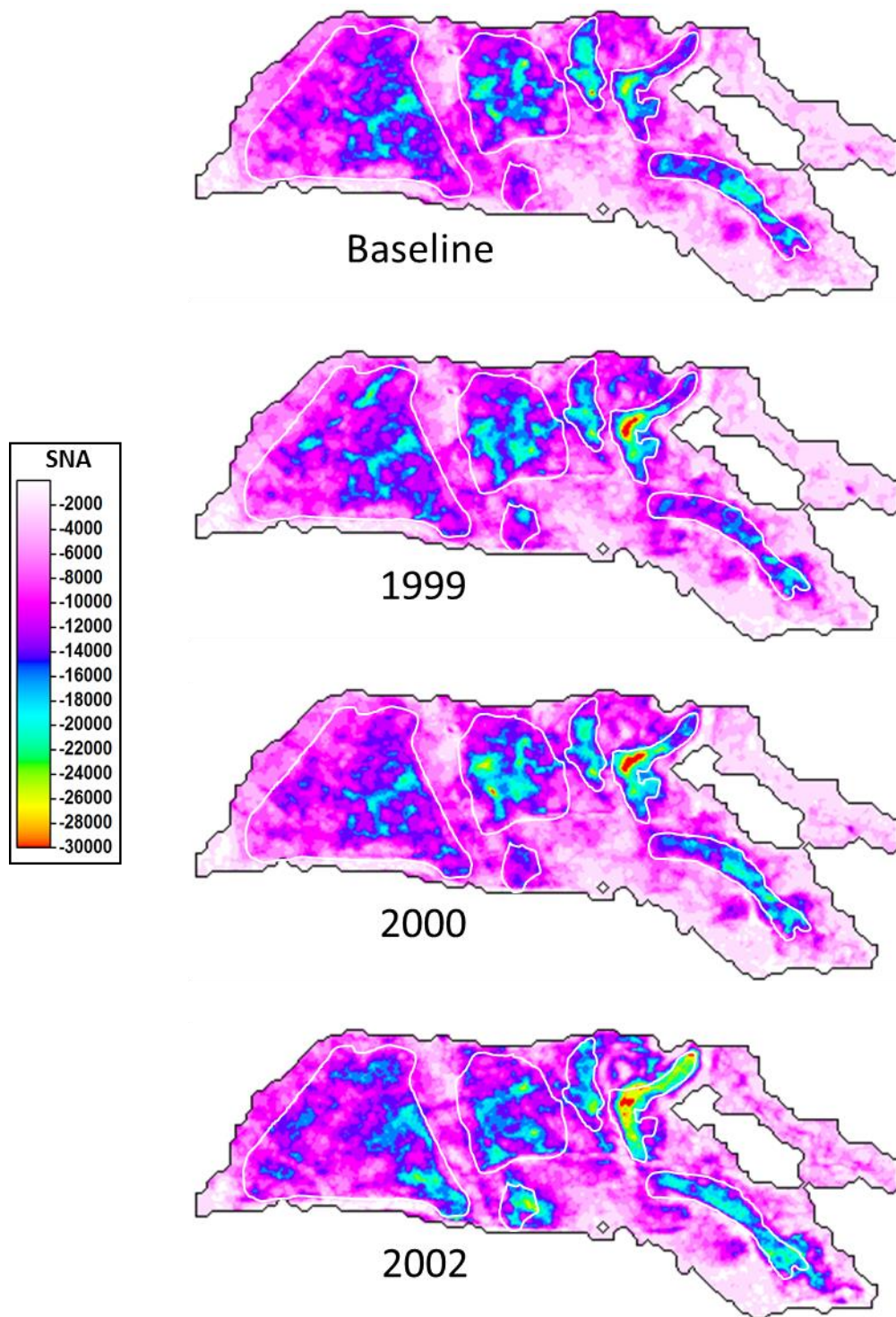


Figure 2.6 Amplitude maps (using the sum of negative amplitudes attribute) for seismic surveys at times 1996 (production was in 1998), 1999, 2000 and 2002. The anomalies are related to gas or oil accumulations in the reservoir sand deposits.

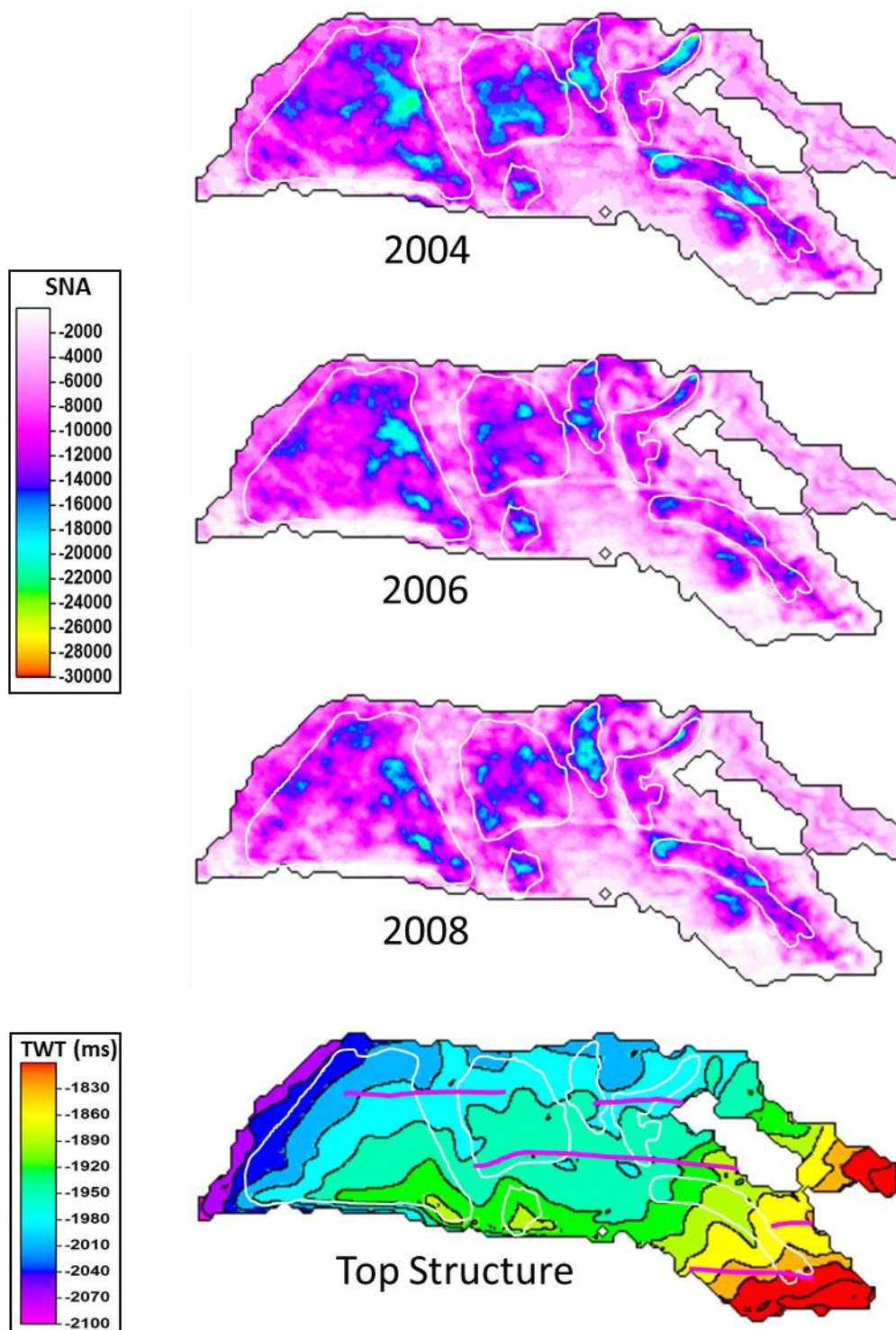


Figure 2.7 Amplitude maps (using the sum of negative amplitudes attribute) for seismic surveys at times 2004, 2006, and 2008. The anomalies are related to gas or oil accumulations in the reservoir sand deposits. Also shown is a contour map indicating the time structure of the top T31a reservoir horizon.

The maps have been cross-equalized such that difference in amplitudes across vintages can be interpreted for time-lapse effects. To achieve this, selected combinations of surveys initially cross-equalized by the data provider are taken, and then further cross-equalization of the mapped amplitudes between subsets are done by applying a single scalar evaluated from a region outside the reservoir. In these data, the existence of gas exsolution is inferred from the well production as a consequence of known pressure drops observed at the producers and excess gas production and gas oil ratio. (see production profiles in Appendix C), (Note that gas is naturally liberated from live oil upon production at surface conditions, i.e. solution gas. This observation refers to the gas produced over and above this process).

On each map, moderate to high amplitude anomalies indicate hydrocarbon-filled sand bodies with good-quality NTG. A progressive brightening of a sand body over time identifies a reservoir softening or impedance decrease (gas liberation or pore-pressure increase), whilst a dimming over time indicates a reservoir hardening or impedance increase (water saturation increase or pore-pressure decrease). By the time of the first monitor survey (1999), pressure is known to have dropped by 900 psi (6.21 MPa) in the vicinity of the production wells. Thus, gas is expected to be liberated during the first three monitor surveys in 1999, 2000 and 2002. This is evident as a general brightening of the individual reservoir sands near to producers (brightening close to injectors associated with a pore-pressure increase is not being considered). After 2002, pressure increases again due to existing and new injectors, and hence dissolution occurs. On the seismic data, these effects are masked by an increase in water saturation at the base of the reservoir interval. This is again generally evident as a dimming of the mapped sand bodies due to a gas-saturation decrease and increased water saturation, and water production at the producer wells. For reference, Figure 2.7 also shows a map of the top structure and identifies NW–

SE as the up-dip direction, where secondary gas caps may be located. Overall, the seismic observations appear to show broad consistency with the phenomena of dissolution and gas production as described previously. Interestingly, however, owing to the sequencing of producers and injectors (Figure 2.8), different sand bodies deplete at different rates, and hence the brightening and dimming events in each are not quite synchronized in time. Here, it is recognized that the effects of gas in this interpretation may also, to some extent, be combined with rock-stress sensitivity and fluid-pressure effects, especially for the large pressure increases around the injectors. However, by confining the quantitative analysis to brightening around the producers, it is assumed that this interference will be limited.

2.4 Field Regional Analysis

Six main regions (A–F) are identified on the map in Figure 2.8(a), selected based on their general seismic character and known geology. In region A, an initial injector–producer (I2–P4) pair is later supplemented by injector I4 to maintain pressure. Later, injectors I9 and I10 are activated to counteract the pressure decline due to producer P8. Exsolved gas is observed initially in 1999, and it quickly collects in a local high in the SE corner to form a secondary gas cap. Increased water saturation and dissolution reduce the amplitudes after 2000, although some gas remains. Region B sits on a local high into which exsolved gas collects. With no direct injector support initially, dissolution does not occur until 2003 when the nearby injector I8 becomes active. Region C is bounded along its south edge by a sealing fault (see the contour plot in Figure 2.7). Critical gas saturation is evident as a consequence of production in P1 and P6, and there is an upward migration of the gas influenced by possible pressure gradients from producer P1, which then traps at the fault due to buoyancy effects. Injector I5 is active after 2001 to supply pressure support.

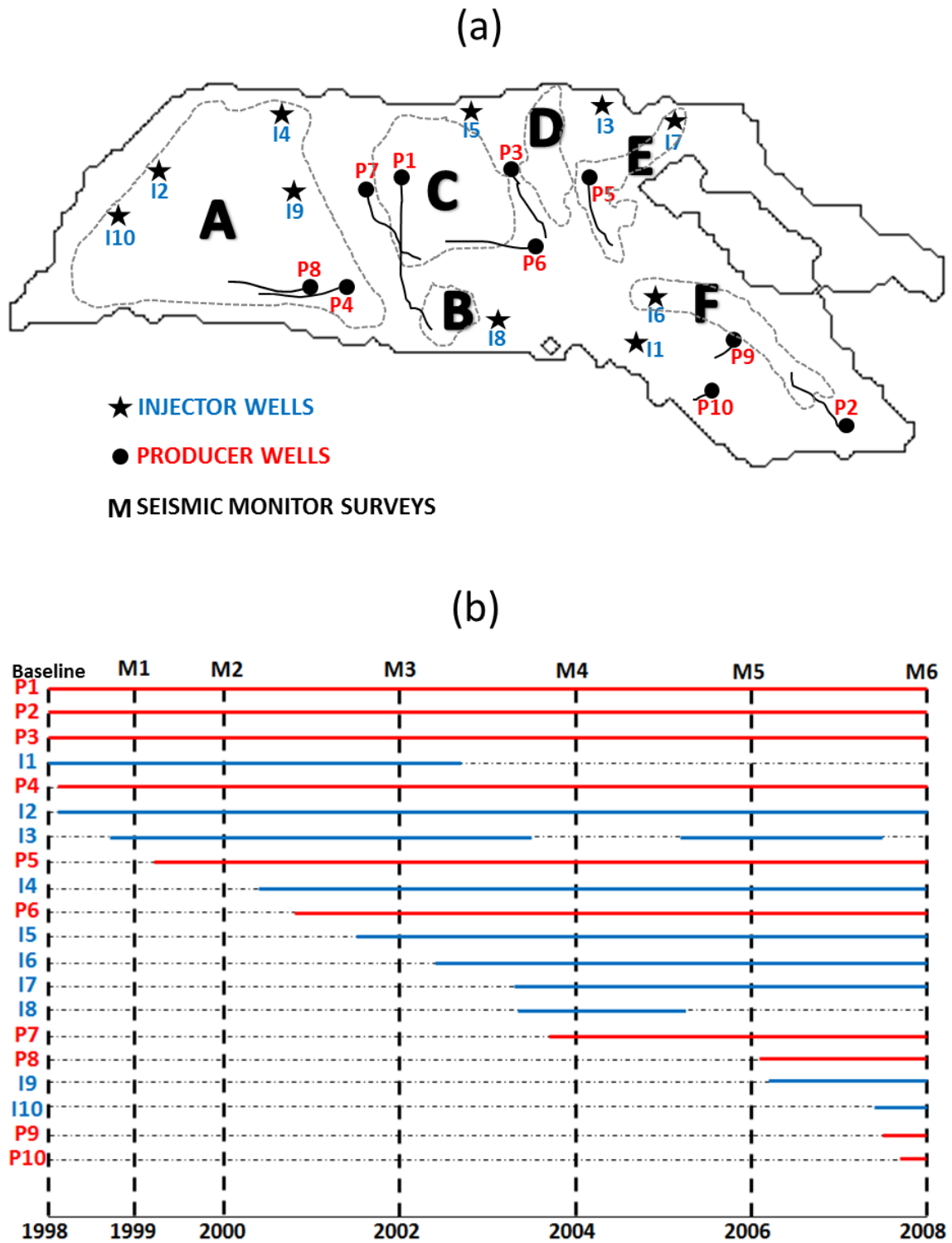


Figure 2.8 (a) Labelling of main sand bodies highlighting the position of the injector wells and producer wells. The solid stars and circles correspond to the well TD (b) Timelines of activity for the wells showing when they are put on production/injection and shut-in, relative to the seismic data baseline and monitor surveys. The red lines represent the producer wells, while the blue lines represent the injector wells.

Region D is possibly connected with region C but it is not intersected by a producing well. Earlier amplitudes in this region are fairly constant – suggesting a lack of pressure connection. Water sweep from injector I3 and I5 may play a role in decreasing the amplitude after 2002. In region E, there is a strong initial brightening that continues until 2002 due to producer P5. In 2003, injector I7 is drilled towards the northern edge, which then dims the amplitudes in subsequent years. The final region for consideration is F, which dips upwards to the SE. The initial action of injector I1 dims the amplitudes in 1999 but pressure support is not sufficient and gas exsolution occurs in 2000 due to producer P2. After 2002, injector I6 replaces I1 close to the same location, and this provides the required pressure support.

Figure 2.9(a) indicates a number of small sub-regions within A–F that are chosen for the analysis. These are selected to be of known high NTG and signal quality, and are used to determine seismic amplitude levels associated with an oil sand in preproduction state, oil sand with critical gas saturation and the secondary gas cap. The ‘sum of negative amplitudes’ (SNA) attribute for each sub-region and their combined (arithmetic) average are plotted in Figure 2.9(b) against survey time. The amplitude level of the baseline (oil-filled sand) response and the maximum are determined for each. If the amplitude level after the maximum has been reached still remains above the initial baseline, then this is interpreted as a case where a secondary gas cap has developed. This interpretation is supported by the identification of local structural highs from inspection of the top structure map in Figure 2.7. However, if the amplitude level after the maximum goes below the baseline level, this is interpreted as critical gas dissolution in addition to water-flood masking.

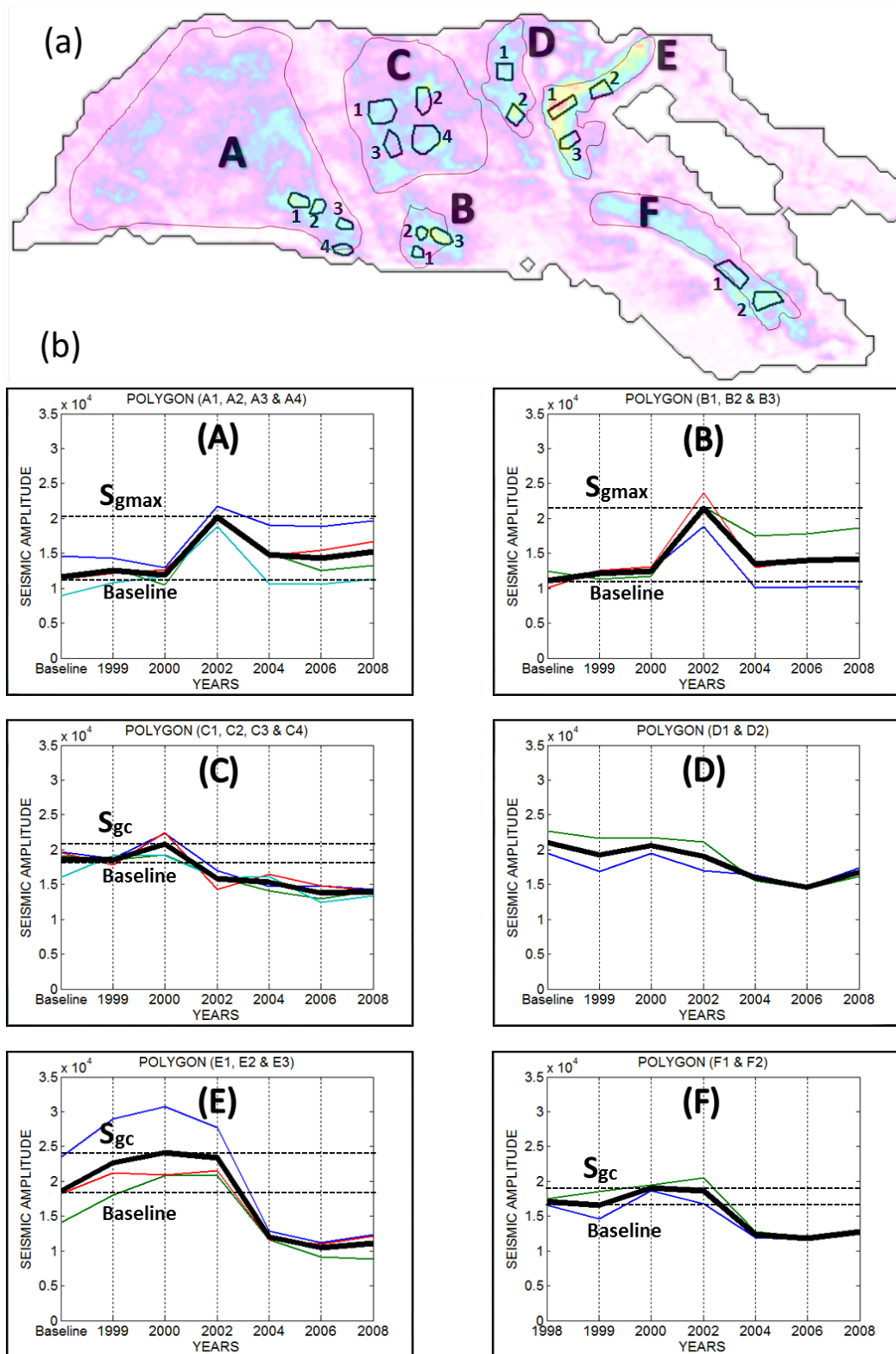


Figure 2.9 (a) Sub-regions of sand bodies used for the calculation of time-lapse amplitudes and gas-saturation analysis. (b) Seismic amplitude variations with survey time, together with inferred amplitude levels for maximum and critical gas saturations (dotted horizontal lines). Thin coloured lines correspond to the individual sub-region results, whilst the solid black line is the average of these values.

The interpretation, based on the known well activity and time-lapse seismic amplitudes, indicates that the maxima for regions A and B correspond to the maximum gas saturation, and these occur in 2002. The maxima for regions C, E and F are interpreted to correspond to the critical gas saturation, and these occur in 2000. Region D is not used in the analysis as the contributions from the injectors and producers plus neighbouring connected regions appear too complicated to fully resolve with the current understanding. The next stage is to relate these amplitude levels to the gas-saturation values. In this analysis it is acknowledged that errors may still be present due to the 31% average seismic survey non-repeatability in this field segment.

2.5 Quantitative Analysis for S_{gc} and S_{gmax}

The simulation model study by Falahat (2012) shows that if the frequency of time-lapse seismic acquisition is several months or more, then gas saturation after exsolution consists of two narrow peaks. These peaks are associated with accumulations in the gas cap at maximum gas saturation (S_{gmax}) and those in the underlying oil leg where the gas is at critical gas saturation (S_{gc}). Some intermediate gas saturations do exist in practice, but these are distributed in the very thin transition zone (typically less than one cell thick) between these two regions.

For repressurization and subsequent dissolution, only one saturation peak at S_{gmax} need be considered as the small gas saturations at S_{gc} readily dissolve back into oil by pressure increase. However, in the reservoir, dissolution is complicated by the increase in water saturation at the base of the reservoir, and hence cannot be easily used in the seismic interpretation. As the secondary gas caps in regions A and B on the seismic amplitudes visibly contract with survey time in response to gas production, residual gas saturation

(S_{gro}) due to oil displacement is evaluated as very small. At such values of saturation, free gas is expected to dissolve in the oil upon pressure increase, rendering it undetectable on the seismic.

The distinct gas saturation behaviour upon exsolution also implies that the corresponding impedance change distribution for the reservoir must also be confined to only two characteristic peaks. It follows that the seismic response (for the monitor minus preproduction baseline) is controlled by two distinct time-lapse impedance changes, one due to the presence of maximum gas saturation in the gas cap (ΔZ_{gmax}) and the other due to critical gas saturation in the oil leg (ΔZ_{gc}). To determine how this affects the seismic interpretation, it is important to first develop an understanding of how these changes occur during the gas exsolution stage. (P-wave) impedance changes are calculated using the rock and fluid properties published by Amini et al. (2011) for the same reservoir (Table 2.1).

Property	Value
Sand porosity	30%
Reservoir pressure	2900 psi (20 MPa)
Effective pressure	3336 psi (23 MPa)
Mineral bulk modulus	38.00 GPa
Dry frame bulk modulus	6.59 GPa
Dry frame shear modulus	5.35 GPa
Dry frame density	1.92 g cm ⁻³ (1920 kg m ⁻³)
Brine bulk modulus	2.58 GPa
Oil bulk modulus	1.17 GPa
Gas bulk modulus	0.04 GPa
Brine density	1.01 g cm ⁻³ (1010 kg m ⁻³)
Oil density	0.80 g cm ⁻³ (800 kg m ⁻³)
Gas density	0.14 g cm ⁻³ (140 kg m ⁻³)

Table 2.1 Rock and fluid seismic/acoustic properties for the field.

These are computed for the preproduction baseline and post-production monitor conditions (Figure 2.10) using Gassmann's equation, and are then differenced. No rock-stress or fluid-pressure sensitivity is included in the calculation as this component is assumed to be smaller than the gas-saturation response away from major pressure increases at the injectors.

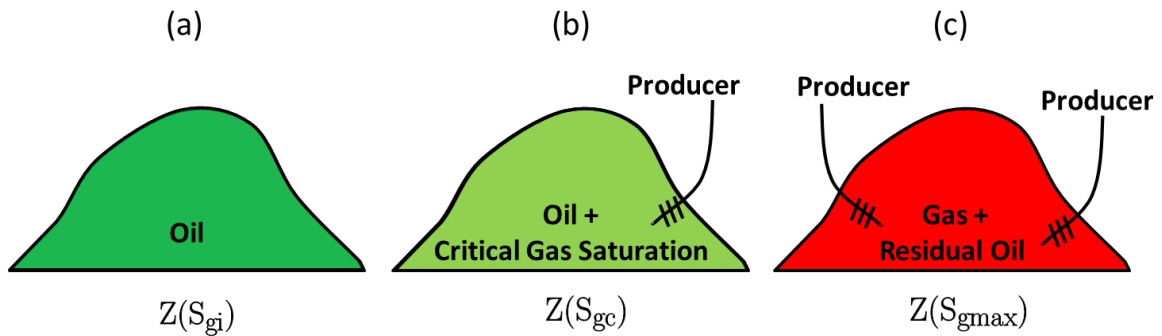


Figure 2.10 Schematic illustrating the three main reservoir states that are being examined to compute their corresponding impedances. (a) Initial preproduction state: live oil and no free gas; (b) after some oil production activity, gas exsolution to critical gas saturation; (c) Further oil production leads to just gas and residual oil, i.e. secondary gas cap.

Indeed, in this field, there are pressure increases or decreases in the inter-well reservoir area (beyond 100 m from the wells) of only 300psi (2.07 MPa) to 900 psi (6.21 MPa), and these give rise to impedance changes of, at most, only a few per cent. The quantities ΔZ_{gc} and ΔZ_{gmax} are calculated for an oil-sand with critical gas saturation and the secondary gas cap, respectively (Figure 2.10), at a known connate water saturation of 22%, residual oil of 11% and NTG of unity. It is observed that S_{gmax} values for the reservoir (in the range 50–70%) influence the impedance changes to a lesser extent than changes in the smaller S_{gc} values (in the range 0–15%) – this can be readily explained by the well-known non-linear dependence on gas saturation. This feature can be recognized in the plots of the ratio $\Delta Z_{gc} / \Delta Z_{gmax}$ for different constant maximum gas saturations in Figure 2.11, where the variation with S_{gc} is seen as the stronger dependence.

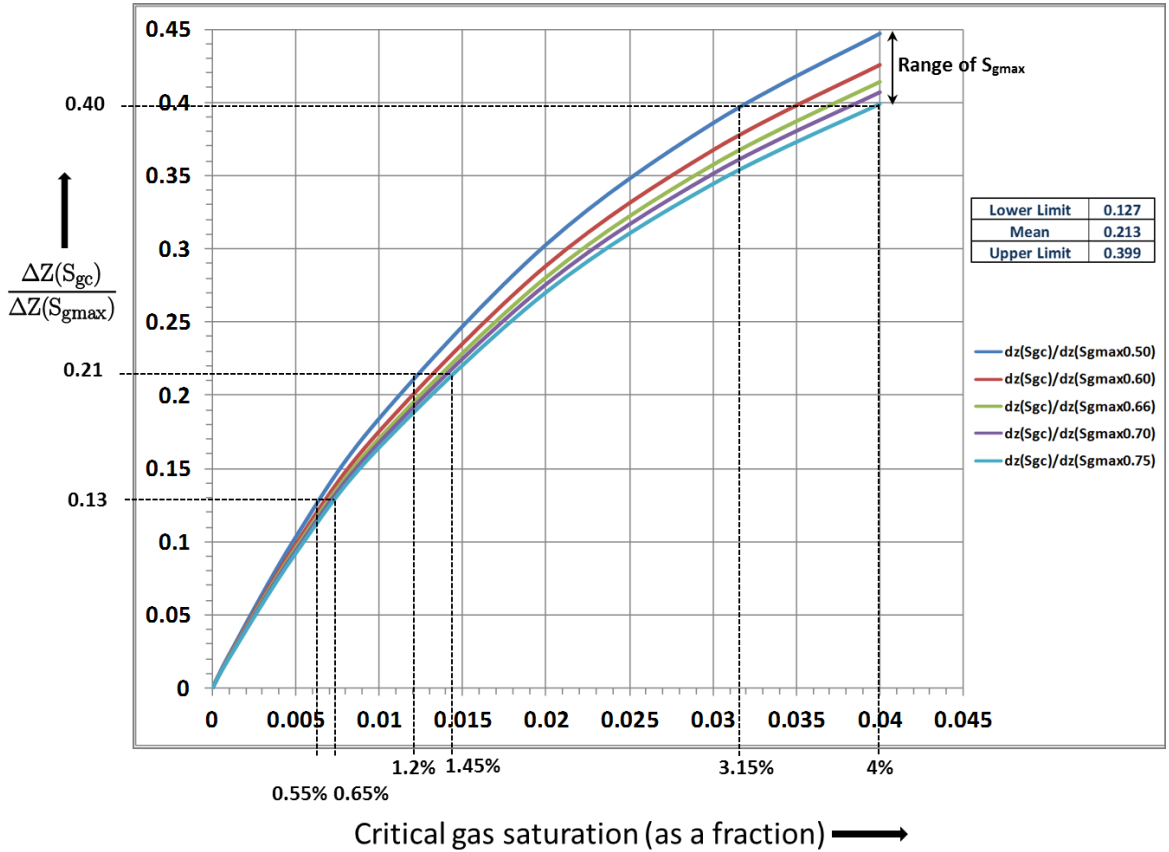


Figure 2.11 Estimate of amplitude change with critical gas saturation and no gas in the oil sands, normalized by the expected amplitude change when going from oil to maximum gas saturation in the gas cap.

Importantly, this figure gives a pathway of connecting the seismic response to gas saturations. According to the work of Falahat et al. (2011) for sub-tuning reservoirs (see also Appendix B), the time-lapse seismic amplitudes, ΔA , are proportional to the thickness of the gas accumulation and the impedance change with gas saturation (in regions where no injected water is present). This can be expressed generally as:

$$\Delta A(T) = \alpha h(T) \Delta Z_g(T) \quad (2.1)$$

where T refers to elapsed time between the surveys, h is the gas accumulation thickness, ΔZ_g is impedance change with gas saturation, and α is a constant given by the inverse of the product of reservoir velocity and the average impedance of the reservoir and the encasing shale, combined with an operator, L , representing convolution of the time derivative of the wavelet with a coloured inversion operator followed by a ‘sum of negatives’ over the reservoir interval (note that the seismic wavelets of the baseline and the monitor surveys are assumed to be identical). Thus, by normalizing time-lapse amplitudes by the baseline amplitude (A_{bl}), it is possible to relate seismic measurements (ΔA_{gc}) of critical gas saturation at location X and of maximum gas saturation at location Y (ΔA_{gmax}) back to the ratio plotted in Figure 2.11:

$$\frac{[\Delta A_{gc}(T)/A_{bl}]_X}{[\Delta A_{gmax}(T)/A_{bl}]_Y} \approx \frac{\Delta Z_{gc}}{\Delta Z_{gmax}} \quad (2.2)$$

Specifically, the ratio of seismic amplitudes:

$$D_1 = \frac{A(2002) - A(1996)}{A(1996)} \quad (2.3)$$

is computed for each part of the reservoir with maximum gas saturation, and

$$D_2 = \frac{A(2000) - A(1996)}{A(1996)} \quad (2.4)$$

for parts with critical gas saturation.

The calculation is shown in Table 2.2, and indicates D_1 values for regions A and B of 0.75 and 0.92, respectively, whilst D_2 for regions C, E and F are 0.12, 0.30 and 0.12, respectively. The time-lapse seismic ratio D_2/D_1 is now obtained. In order to evaluate possible errors in this calculation, a lower limit is formed by taking the lowest D_2 and the highest D_1 values, and then the highest D_2 and the lowest D_1 values. This yields a lower limit of 0.13 and upper limit of 0.40, with their mean being 0.21. These results are now interpolated back to the curves in Figure 2.11, and give estimates of the possible critical gas saturations in the range of 0.55–4% for the reservoir.

$A(S_{gmax})$	1996	MAX
A1, A2, A3, A4	11570	20212
B1, B2, B3	11136	21413
$A(S_{gcr})$		
C1, C2, C3, C4	18615	20805
E1, E2, E3	18593	24140
F1, F2	17050	19070
D_1		
A: 0.747		
B: 0.923		
D_2		
C: 0.118		
E: 0.298		
F: 0.119		

Table 2.2 Amplitude values for the regions of the field sector in which oil-filled sands are saturated with gas at critical gas saturation ($A(S_{gcr})$) and maximum gas saturation ($A(S_{gmax})$). D_1 and D_2 correspond to the ratios defined in equation (2.3) and equation (2.4), from which the time-lapse metric in Figure 2.11 can be formed.

Uncertainties in these estimates may also arise due to lateral variations in NTG in the selected areas, imperfect cancellation of the reservoir thickness variations and water-saturation changes. Another source of uncertainty could possibly arise from the presence of a thin layer of maximum gas saturation in the critical gas-saturation areas, and vice versa, although the behaviour of each area over time in Figure 2.9 clearly defines the predominant effect. It is also important to note that Figure 2.11 is specific to this particular reservoir, and will also change depending on rock and fluid properties.

In addition, it is known that for a low value of critical gas saturation (and, hence, mobilized gas saturation), it takes longer for the reservoir to assume the bimodal saturation conditions than higher critical gas saturation. The latter will lead to a more prominent seismic response to exsolution in the oil leg, and oil containing critical gas saturation is then likely to have a similar response to the gas cap with the maximum gas saturation. Also, for high S_{gc} values, the dissolution process would be very pronounced as both the oil leg and gas cap brighten at first but only the bright amplitudes related to the oil would dim due to dissolution, whilst those associated with the unproduced gas caps remain. Indeed, it is the absence of this effect that can also be used to confirm the small critical gas saturation in this field.

2.6 Quantitative Analysis of Gas Volumes

To further investigate the sequence of gas exsolution and dissolution, the seismic data is analysed by following the work of Falahat et al. (2011), where a linear relationship between the change in free gas volume (ΔV_g) and the 2D integral of the mapped time-lapse amplitude change (ΔA) was proposed:

$$\Delta V_g = \beta \iint_{\Sigma} \Delta A \, dx dy \quad (2.5)$$

where β is a seismic-to-well production/injection calibration factor to be determined. For this analysis, the time-lapse quantities are taken between the baseline survey and each monitor. Thus, as there is no gas at the time of the baseline survey, ΔV_g represents the volume at the time of the monitor. This equation assumes that changes in water saturation do not affect ΔA – clearly this may be a suitable approximation during the exsolution stage but may not be completely appropriate in some regions of the field sector experiencing dissolution for which the injected water clearly has a strong influence. The integral is performed over the area Σ formed by a composite of areas C, D, E and F in Figure 2.8, which is known to be hydraulically isolated. In the integration, only positive (bright and, hence, gas-related) time-lapse difference amplitudes are used and the summation extends spatially across regions known to contain oil with critical gas saturation. Although empirical in nature, equation (2.5) may be inferred from equations (2.1) and (2.2) by assuming a direct correlation between the impedance change and the product of gas accumulation thickness, effective porosity and gas-saturation change. Calculation indicates that this linearity is a good approximation for the small critical gas saturations in this field. Finally, an additional assumption made is that the pressure change

between the time-lapse surveys does not significantly affect the 4D seismic signature via the rock-stress or fluid-pressure sensitivity. This assumption has been previously tested by Amini et al. (2011) in a simulator to seismic modelling study on the same dataset and was found to be valid.

There is an exsolution stage from the start of production in 1998 until 2001, and a dissolution stage from 2001 to 2008. The behaviour thus forms a natural two-stage division for the analysis. Consider first the application of equation (2.5) to the period between the preproduction baseline and the 2000 monitor surveys during the primary exsolution stage. The left-handside of equation (2.5) can be expanded according to the well-known material balance equation (Dake, 2001) focused only on the gas component:

$$[V_o R_{sb} - (V_o - V_{op}) R_{sm} - V_{gp}] B_{gm} = \beta \iint_{\Sigma} \Delta A \, dx dy \quad (2.6)$$

where V_o is the initial (time of baseline survey) oil volume available to be produced at the wells, V_{op} is the actual oil volume produced (at the time of the monitor) and V_{gp} is the gas volume produced (i.e. free gas plus that released from the oil produced at the surface). As there are no initial gas caps in the chosen study area for this calculation, V_{gp} is also the change in the overall gas volume. For the purpose of the calculation, these gas volumes are defined at surface (stock tank oil) temperature and pressure. In equation (2.6), R_{sb} and R_{sm} are the preproduction (at the baseline time) and current (at the monitor time) solution gas–oil ratios, respectively. The solution gas–oil ratio quantifies the total amount of gas dissolved in the oil. It is defined as the ratio of the volume of gas produced at the surface under standard conditions divided by the volume of oil entering the stock tank at standard conditions, and has units of standard cubic feet per stock tank barrel (scf/stb or in SI units

$\text{sm}^3 \text{ m}^{-3}$). For the purposes of these calculations, these R_s values represent a reservoir average for areas C, D, E and F. R_s is a linear function of pressure for pressures below the bubble point (Figure 2.12(a)). Thus, $V_o R_{sb}$ gives the total amount of gas dissolved in the oil at the preproduction stage, which could potentially be liberated upon production of the volume V_o .

Similarly, $(V_o - V_{op})R_{sm}$ is the amount of gas in the oil remaining in the reservoir at the monitor time. R_{sm} is always less than R_{sb} as there is less gas dissolved in the reservoir oil at the monitor time because the free gas is either produced or remains trapped within the reservoir. Finally, by subtracting the actual gas produced, as measured by the well data, from the estimated dissolved gas contributions – assuming it is also not produced – the result must be the gas still remaining free (and structurally or capillary trapped) in the reservoir. The final parameter in this calculation is B_{gm} , the gas formation volume factor, which converts all of the gas volumes calculated under stock tank barrel conditions to their equivalent reservoir volumes (this therefore has units of reservoir barrel per stock tank barrel).

The 4D seismic signature in the integrand of equation (2.6) is the difference in the mapped sum of negative amplitudes evaluated between the monitor and baseline surveys. As mentioned previously, to isolate the gas-related response, only the positive difference between the seismic maps in Figures 2.6 and 2.7 are extracted. It was not found necessary to threshold the resultant difference amplitudes due to the obvious prominence of the gas response. For this field case, the pressure dependences of R_s and B_g are obtained directly from the PVT tables determined from the laboratory measurements that have been calibrated for the reservoir and used in the full-field flow simulator by the data provider. Calculation from the simulator shows that R_s is expected to reduce from a preproduction

of 354 ($62.99 \text{ sm}^3 \text{ m}^{-3}$) to 322 scf/ stb ($57.30 \text{ sm}^3 \text{ m}^{-3}$) after the reservoir pressure drop from 2850 psi (19.65 MPa) in 1998 to 2760 psi (19.03 MPa) in 2008. Applying equation (2.6) to the observations, two relatively known quantities are identified: the initial oil volume (extracted from the simulation model); and $R_s=R_{sb}$ prior to production and $R_s=R_{sm1}$ for the first monitor (taken from the PVT tables for the field oil and assuming a mean pressure for the sector).

There are two relatively unknown quantities, the seismic calibration factor β , and R_s at each of the subsequent monitor times. By applying equation (2.6) to the baseline 1996 seismic data together with the monitors at 1999 and 2000 (for which gas continues to come out of solution), two equations are generated and can be solved to obtain: $\beta = 0.029$ (with dimensions of m/amplitude unit) and R_s for the first monitor. By applying a similar reasoning to the preproduction and subsequent monitor surveys 2002, 2004, 2006 and 2008 acquired during the gas-dissolution stage, equation (2.6) will be adapted slightly as R'_{sm} now replaces R_{sm} , where $R'_{sm} > R_{sm}$ because the volume of gas available to go back into solution is smaller than the original as it has been produced or trapped in local highs, structure or by low NTG regions. Thus, after dissolution the oil is not now fully saturated by gas.

The gas at critical gas saturation immediately goes back into the oil upon pressure increase but the gas–oil contact remains in a continual state of dissolution. In equation (2.6), only R'_{sm} is now unknown, as β has been determined from the gas exsolution stage, and it can therefore be calculated for each of the four remaining monitor surveys. The seismic estimates of R_s versus the predictions from the simulation model are shown in Figure 2.12(b). For reference, results are also given for a 10% variation in the oil volume showing a high and low estimate of the R_s values.

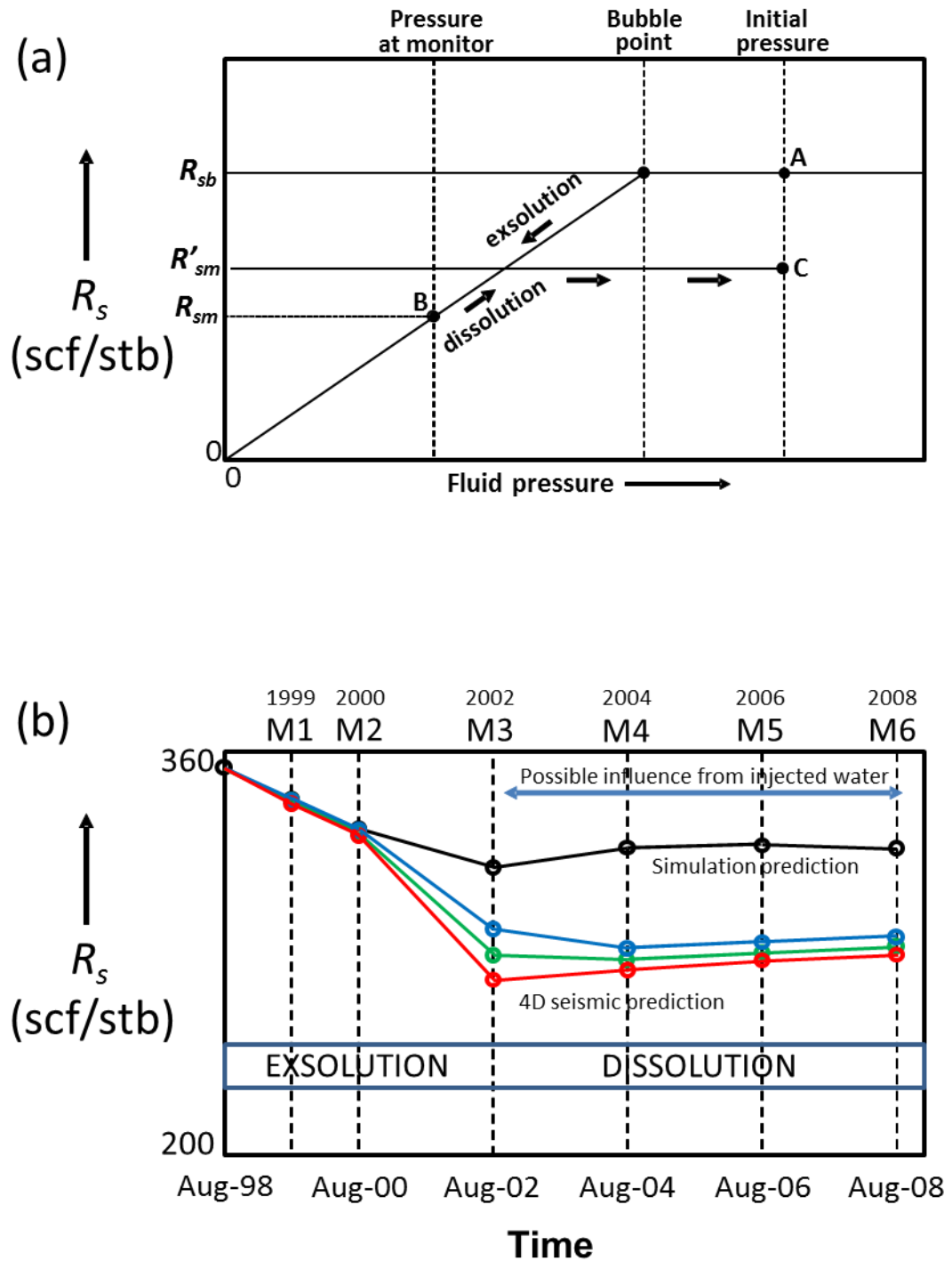


Figure 2.12 (a) Schematic illustration of the pressure dependence of the solution gas-oil ratio, R_s , for a black oil. The ratio decreases as pressure drops below bubble point until the monitor state is reached at point B. Repressurization increases R_s again but as less gas is available to dissolve in the gas, the R_s behaviour reaches a plateau at a lower constant value and point C is reached. (b) R_s values predicted for the study area from fluid-flow simulation (black line and circles) versus the variation estimated from the 4D seismic data for low (red), medium (green) and high (blue) cases derived from varied STOIP.

Fluid-flow simulation predicts that R_s in the reservoir decreases from an initial (and known) value of 352 scf/bbl ($62.63 \text{ sm}^3 \text{ m}^{-3}$) to 315 scf/bbl ($56.05 \text{ sm}^3 \text{ m}^{-3}$) in 2002 due to the pressure drop, before rising slightly to 322 scf/bbl ($57.30 \text{ sm}^3 \text{ m}^{-3}$) in 2008. This equates to approximately 4.5% of free gas under reservoir conditions. The seismic R_s estimates also show this dip followed by an increase but the R_s values are slightly lower than those predicted from the simulator (a minimum of 268 scf/bbl ($47.67 \text{ sm}^3 \text{ m}^{-3}$)). The low values of R_s above suggest that more free gas is being produced in the reservoir but a more likely cause is bias due to the masking effect of injected water in the lower part of the reservoir during the dissolution phase. However, it is not possible to quantify this phenomenon or draw further conclusions using the 4D seismic data.

2.7 Discussion

It has been shown that multiple 4D seismic surveys shot during gas exsolution and dissolution can be used to estimate critical gas saturation, and provide some understanding of the maximum gas saturation. The critical gas saturation for this UKCS field is estimated to be between 0.5 and 4.0%, which falls within the lower range values reported in the literature. A discussion of this finding and its implications for the reservoir is given in this section. Determination of this particular result has been made possible as there is sufficient time between the seismic surveys to allow gas liberated from solution to settle into either critical or maximum gas-saturation states. This point is also further discussed below. It is anticipated that this framework for seismic interpretation can be generalized to other fields and production scenarios, provided that the transition zone between the oil and gas, or the water- and gas-saturated regions of the reservoir remains smaller than seismic resolution. Thus, these results would be applicable to most reservoirs except those with a very low porosity and permeability, or strong vertical or lateral

heterogeneity. As a guide, for permeabilities of tens of mD (10^{-14} m²), the transition zone can extend over many tens of metres (Ahmed, 2006). In this case the transition zone would, therefore, be seismically significant and would support a wide range of saturation states. These results may however not be applicable to other gases. For example, it would be expected that CO₂ injection will have a more complicated saturation histogram as there is a larger transition zone, due to the smaller density differences, between the gas and water (Cairns et al., 2012). For this latter case, there are generally many gas-saturation states influencing the 4D seismic response, and the fluid system takes longer to reach the bimodal quasi-equilibrium state.

2.7.1 Values for the Critical and Maximum Gas Saturation

Knowledge of the reservoir-scale (or seismic-scale) S_{gc} is important for a number of reasons. First, it helps to assess the effective relative permeability of gas, oil and water through the reservoir. Secondly, in solution gas drive reservoirs or during depressurization, it is key to predicting the expected gas volume produced from the gas-cap expansion, and hence the oil or gas recovery. Finally, in the early years of a field it can help anticipate risks to productivity from gas exsolution. In the reservoir, S_{gc} is known to be a function of a number of interrelated factors such as the surface area of the pore space, clay content and placement, grain shape, grain arrangement, wettability, and fluid properties. However, it is understood from engineering literature that precise values of S_{gc} are difficult to obtain using laboratory experiments. This uncertainty arises because of the high fluid flow rates that are induced during experiments (relative to those in the field), the dependence of S_{gc} on the pressure decline rate and capillary end effects. This combination of effects makes extrapolation to in situ field conditions unreliable and, as a consequence, the accurate estimation of S_{gc} remains an active research topic (Beecroft et

al., 1999). Recently, alternative measurements are offered from methods such as numerical simulations enabled by pore-network modelling, which attempt to emulate realistic gas nucleation and mobilization to obtain the required understanding (McDougall and Sorbie, 1999, Bondino et al., 2002).

Another issue is that relative permeability end points measured in the laboratory do not represent properties at the scale of the reservoir production due to trapping in fine-scale heterogeneities such as cross-bedding and laminae (Honarpour and Saad, 1994), thus the S_{gc} at the reservoir scale is an effective value. Literature on the evaluation of pressure depletion due to depressurization (blow down) at the end of field life provides, perhaps, the best guide of the effective reservoir-scale S_{gc} as they combine both laboratory and history-matched simulation studies. Examples for UKCS clastic fields include Miller (Beecroft et al., 1999), 9%, South Brae (Drummond et al., 2001), 2.5%, Brent (Ligthelm et al., 1997), 9.6% and Statfjord (Boge et al., 2005), 5%. An extensive survey of the literature from laboratory, pore-scale modelling and simulation studies suggests measured values vary from as low as 0.5% to as high as 38% (Table 2.3). These values are from different sources and field types, and this just highlights the variability of S_{gc} in different scenarios. Low values in the range of this study's findings have been measured in many cases and, thus, the findings are not atypical. Although there is no definite trend in the literature, low values are common in moderate porosity reservoirs with good permeability development. Heavier oils tend to have lower S_{gc} values. Further validation is provided by communication with the operator of the field, which indicate a value of between 3.5% and 5% is appropriate in this case. The maximum gas saturation, S_{gmax} , in the gas cap is determined by the amount of residual oil, S_{org} , due to the gravity drainage of the oil by the gas-cap expansion; that is: $S_{gmax} = 1 - S_{wc} - S_{org}$.

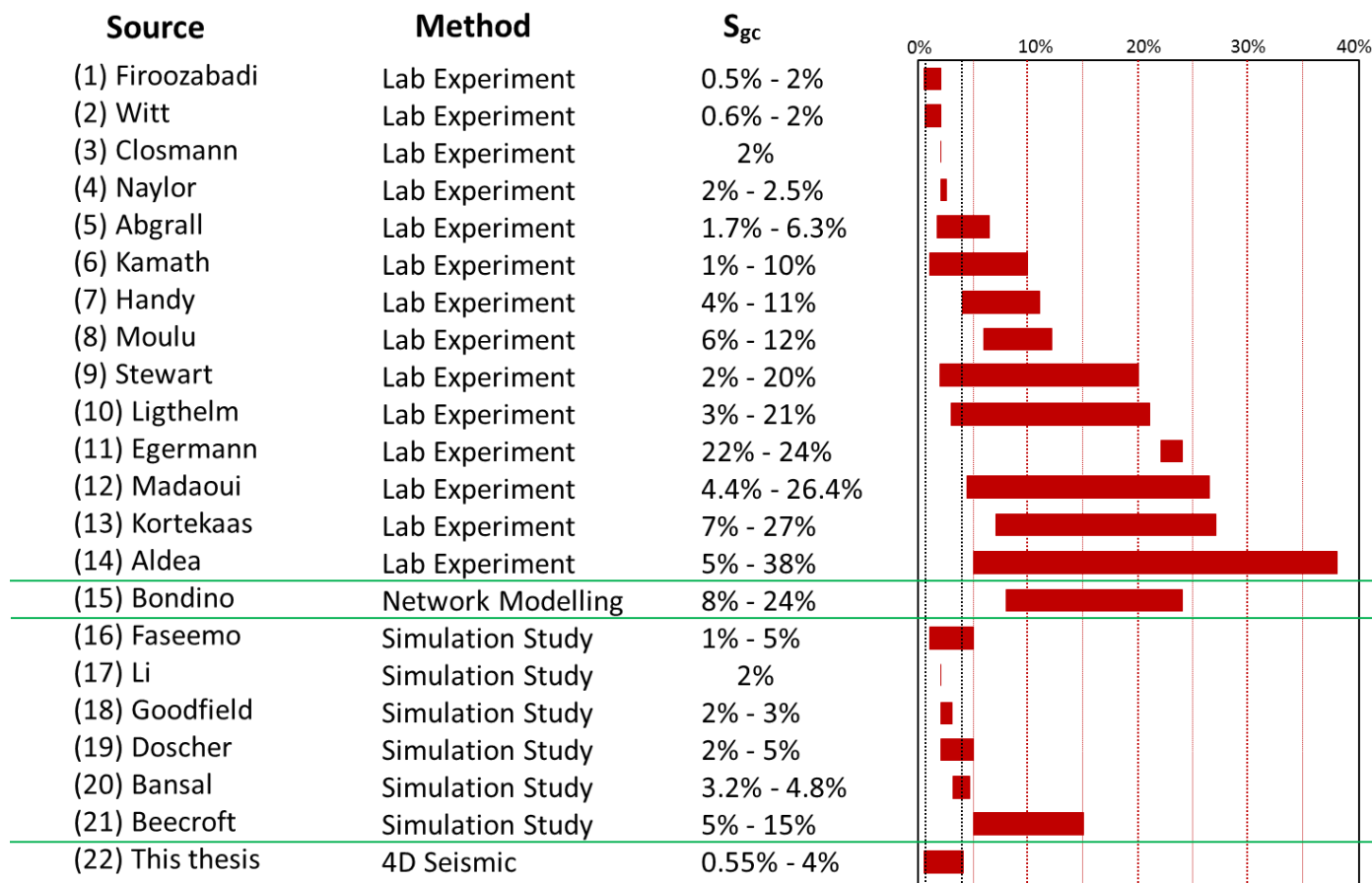


Table 2.3 Critical gas-saturation values for a range of studies (horizontal bars) compared to the results from the 4D seismic estimates (entry number 22).

The amount of oil immiscibly displaced by the exsolved gas in the presence of the initial water (S_{wc}) by this process may be gauged to some degree by gas-injection experiments on cores (despite this being a distinctly different physical process). For example, Skauge and Ottesen (2002) found a mean S_{org} of 16% for a range of fields, and possible variability with porosity, permeability and initial oil saturation. Similarly, Beecroft et al. (1999) found an S_{org} of 20% for the Miller field. According to Edwards et al. (1998), gravity drainage by gas-cap expansion is slow and efficient, and there is a remaining oil saturation of 3–10%, with gas-flood tests in the laboratory give higher values. In this case study of the UKCS field, taking an average S_{wc} of 22%, a rough estimate of S_{gmax} may realistically be greater than 58%. It is not possible to be more precise as the calculations show that the seismic response is relatively insensitive to this gas saturation.

2.7.2 Timing of the Seismic Surveys

The time period between the seismic baseline and successive monitors has an impact on the application of the findings and results. Gas exsolution and dissolution in the reservoir are relatively immediate events, taking less than 1 day or so to complete, and are dependent only on the time for the pressure change profile to diffuse and equilibrate (Figure 2.13). However, depending on the connectivity of the reservoir, it can take several weeks or months for the free gas to be finally produced and observed at the wells. For example, for the reservoir models used in this study it took less than 6 months for the saturation states to settle down to the idealized bimodal distribution under the action of buoyancy and well pressure gradients. The rate at which steady state is attained depends on the production and injection rate, although, after stabilization, the saturation states are independent of the production activities but the volume of gas present changes.

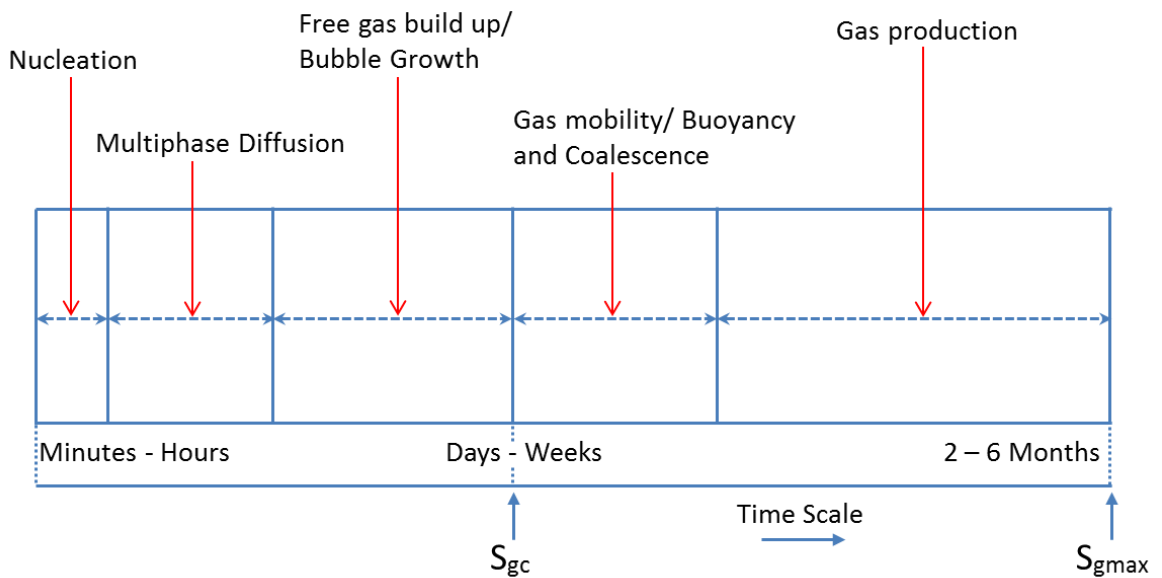


Figure 2.13 Timing of the physics of nucleation and development of gas exsolution in a hydrocarbon oil. Timings are based on simulation model studies for this field.

Thus, for oil production at a more rapid rate than that predicted from the simulation model, gas may be quickly mobilized and produced but very few gas caps form, and therefore a much smaller amount of gas is dissolved back into the oil than anticipated. A faster production rate gives rise to a more rapid approach to steady state, although the exact timing depends on the reservoir connectivity and lateral extent. In contrast, there is more gas dissolved back into the oil by increasing the injection rate, although there is a limit to this process as the liberated gas cannot be dissolved if it has already been produced.

Importantly, every time the well activity changes (as in this field example), the timescale to reach the bimodal state must again be revised in conjunction with the timing of the seismic surveys. For 4D seismic surveys with a repeat time of 1 to several years, the timescale of the physical processes discussed in this study may not be important but, for repeats with permanent sensor arrays that are 3–6 months apart (Huang et al., 2011, Watts

and Marsh, 2011), this may well present a problem for quantitative 4D seismic analysis. A key parameter to this is the ratio of vertical to horizontal permeability, K_v/K_h , which also determines the timescale to reach the bimodal gas-saturation condition. This ratio is difficult to define spatially, and can vary quite considerably in clastic reservoirs (Link, 2001).

Modelling studies show that when K_v/K_h is 0.01, the exsolved gas takes longer to migrate upwards and steady state is not attained for 6 months, and that as K_v/K_h increases to 1, the time to reach the steady state progressively reduces to less than 2 months (Falihat, 2012). Consideration of these factors suggests that choice of the optimal survey frequency for 4D analysis must be examined on a case by case basis, and tailored to the particular reservoir conditions (MacBeth et al., 2013).

2.8 Summary

This chapter introduces the dataset of interest which is the Schiehallion field. It focuses on understanding the mechanisms of gas exsolution and dissolution, and an evaluation of the ability to estimate the associated controlling parameters using 4D seismic data from multiple seismic surveys. This is motivated by the clear brightening and dimming of seismic amplitudes observed in the 4D seismic data reported from several separate publications, and the drive to provide a more quantitative interpretation of this phenomenon. By analysing data from multiple seismic surveys shot between preproduction in 1998 until 2008, it is possible to estimate the gas saturation for this UKCS clastic reservoir.

Critical gas saturation is estimated to be between 0.6% and 4.0% using seismic data analysis, and the values are consistent with previous measurements on similar fields. The seismic amplitudes are expected to be relatively insensitive to the maximum gas saturation ($1 - S_{wc} - S_{org}$) (approximately 68% in this case) as modelled through fluid substitution, while the data suggest that the residual gas saturation upon gas-cap contraction (S_{gr}) is less than a few percent. This analysis demonstrates that monitoring of gas exsolution and dissolution is potentially useful for understanding the reservoir and constraining the simulation model, although case-dependent reservoir fluid and pressure changes can cause some interference with this finding. Having analysed the field data of interest, an approach to history match and update the reservoir parameters will now be considered.

Chapter 3

SHM Using Binary Images - Development

This chapter considers the development of an approach for incorporating 4D seismic data into the history matching workflow in a quantitative manner, having previously analysed seismic data in a semi-quantitative manner in the previous chapter. In order to do this integration, a binary approach is adopted, and the focus here will be on the different metrics for quantifying the binary misfit in terms of their strengths and short comings. The manner of creating the binary maps is also discussed where *k*-means clustering algorithm is implemented. The metrics analysed for quantifying the binary misfit are the Hamming distance, Hausdorff distance, Mutual Information, and *Current* measurement metric. Test case scenarios are set up to replicate seismic scenarios and model changes so as to ascertain effectiveness of the different metrics. The results show that the *Current* measurement metric and Hamming distance seem suitable for efficiently quantifying the misfit between the predicted and actual seismic data using the binary approach.

3.1 Binary Measurement Metrics

One of the simplest kinds of images in the field of image processing, computer vision and pattern matching is the binary image. The shape of the image is considered as the most dominant feature that can be used for retrieval purposes. The ability to determine the similarity or dissimilarity between images is very valuable in many application areas (Teshome et al., 2011), and to be useful in practice, the methods should be generic, fast and robust (Pele and Werman, 2008). A number of methods, some of which are complex, have been previously proposed for matching the similarity between images. Baudrier et al. (2004) proposed an approach for comparing the binary images without feature extraction by using the windowed Hausdorff distance in a pixel adaptive way. In the reservoir engineering and reservoir geophysics field, Landa (1997) shown in (Figure 3.1) used a binary images approach to estimate permeability in the reservoir, while Jin et al. (2012b) shown in (Figure 3.2), Kretz et al. (2004), and Tillier et al. (2013) shown in (Figure 3.3) have proposed approaches for history matching using a binary concept.

The concept of converting an image into binary will be analysed in the next section. This will include an analysis of the different levels of threshold, and the means of organising the images into clusters.

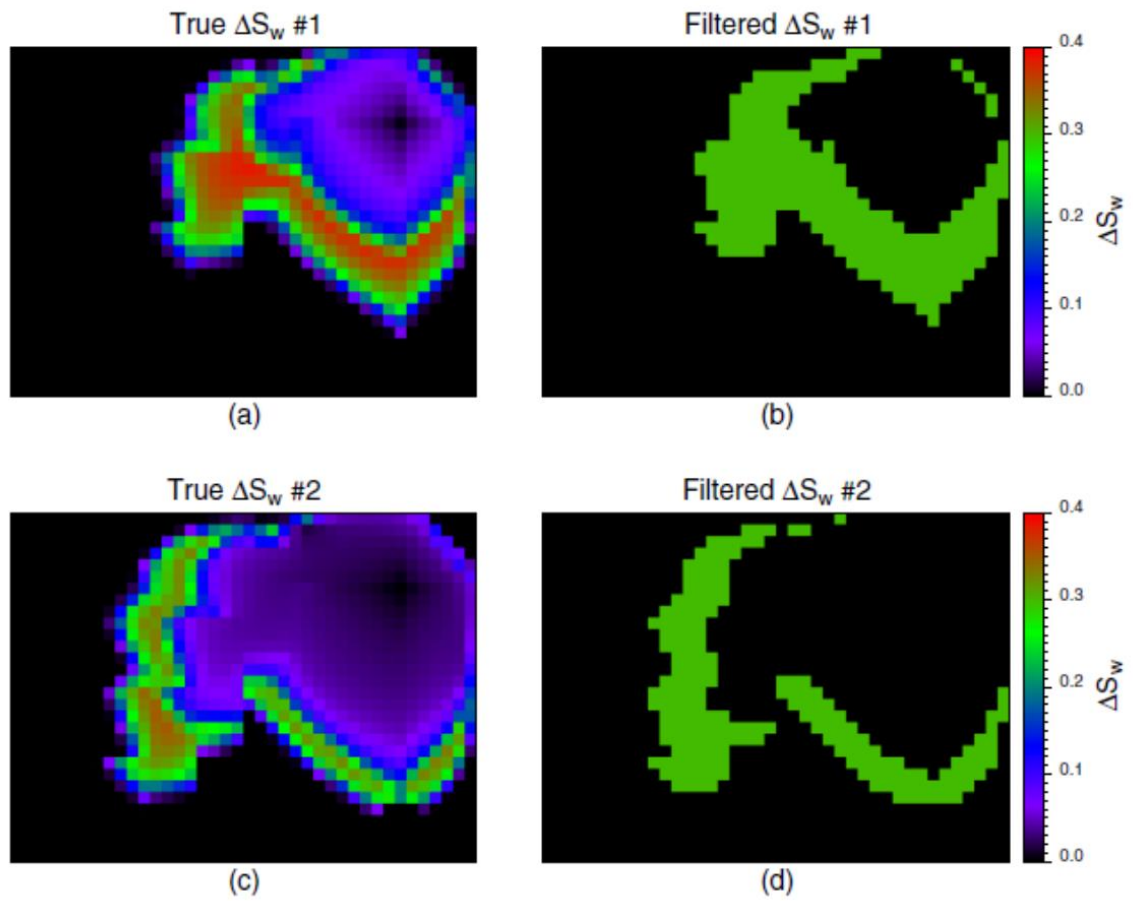


Figure 3.1 4-D seismic data in “black and white” format (Landa, 1997). Saturation representation displayed in binary format.

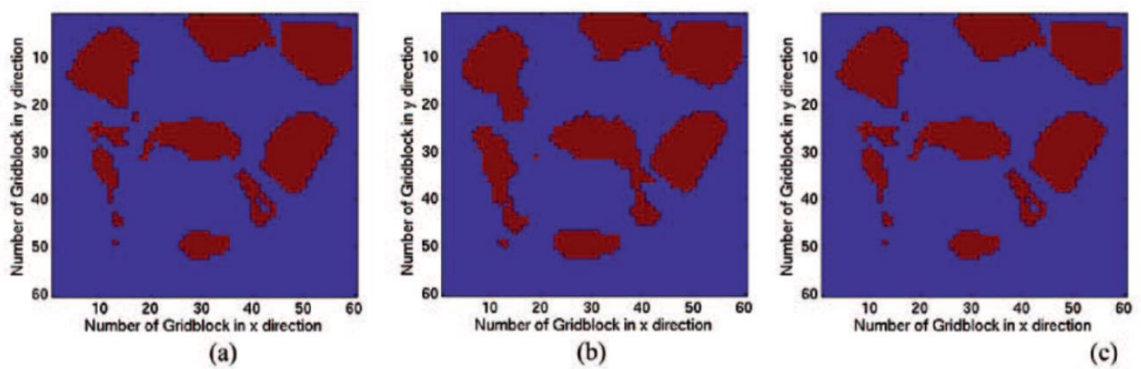


Figure 3.2 Saturation differences after binary processing from (a) the true model (b) the initial model (c) the updated model (Jin et al., 2012b).

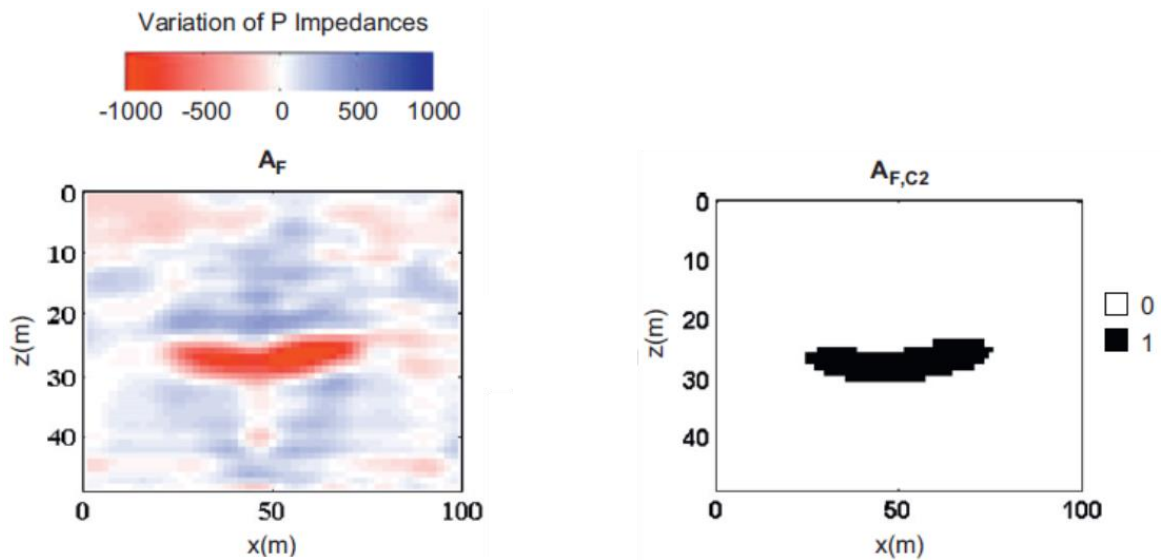


Figure 3.3 Illustration of the clustering of 4D seismic data into two classes (Tillier et al., 2013).

3.2 Clustering and Thresholding

An analysis will be conducted to characterise the effect of converting a normal continuous image into different cluster levels. The cluster levels will be represented as two level (binary), three level, four level and full level (which is the initial continuous image with no cluster). The clustering method utilised is the k -means algorithm because of its simplicity and its effectiveness. The k -means algorithm (MacQueen, 1967) can be defined as a classical method based on the concept of classifying data by clustering points close to each other, and this has been described explicitly in Appendix D. There are other methods of clustering and applying threshold, and this can even be done manually; however doing this will be time consuming and non-unique, that is why the k -means algorithm has been adopted. The aim of the analysis is to investigate the efficiency of the binary approach (two level), as well as analyse the pros and cons of having different levels of clusters (three level or four level) or the initial continuous image (full level) (Figure 3.4).

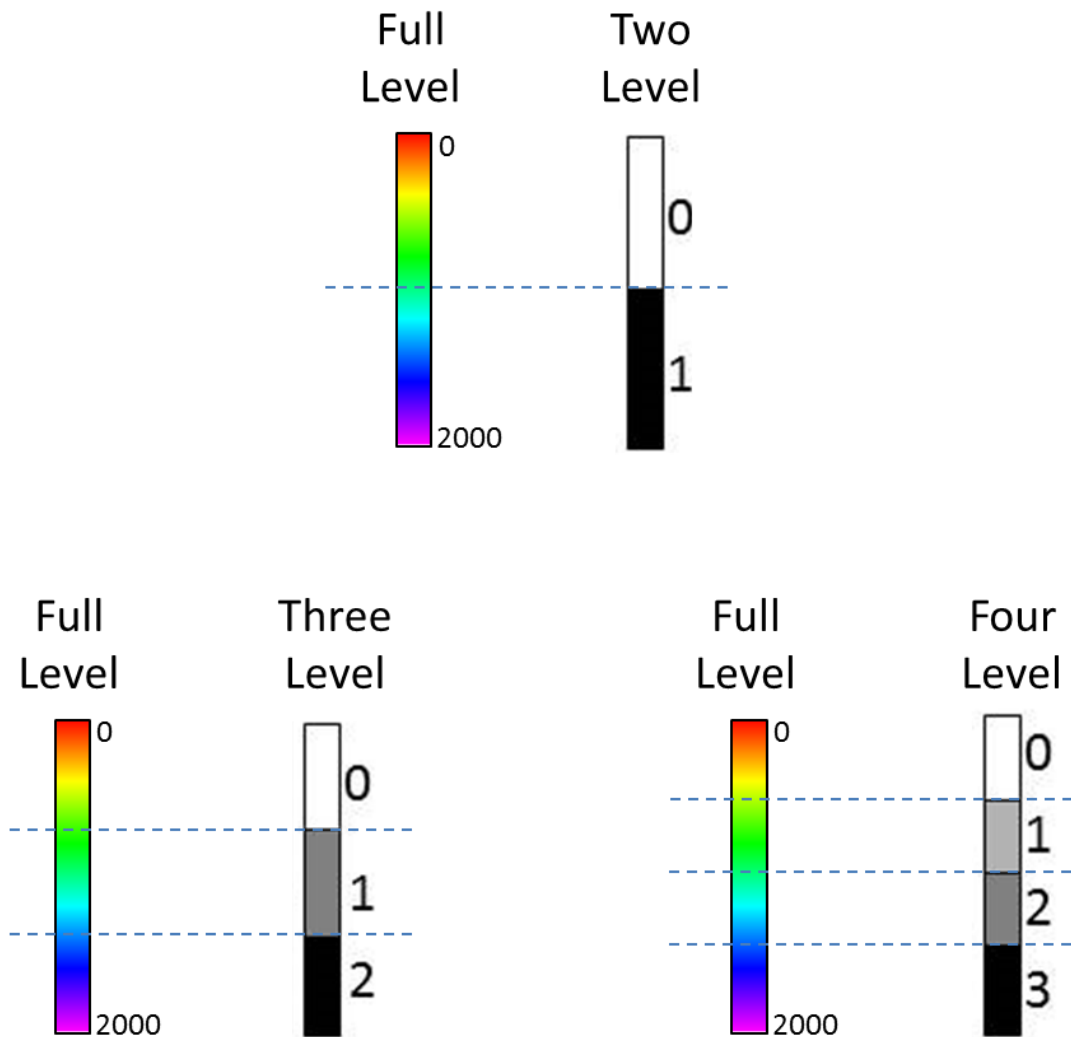


Figure 3.4 Illustration of the different levels of clustering achieved by implementing the k -means clustering algorithm.

To implement the analysis, four idealised models are set up which have been designed to capture the main characteristic of reservoir saturation maps, as well as four idealised seismic representations which would act practically as “observed seismic images”. The four idealised models are defined as Gaussian functions shown in equations (3.1), (3.2), (3.3) and (3.4). There were designed such that they have different spatial orientations and act as representation of reservoir saturation maps as shown in Figures 3.5(d) and 3.6(d), which represent Model 1, Model 2, Model 3 and Model 4 respectively.

$$F_1 = e^{(-a_0x^2 - b_0y^2 + E)} \quad (3.1)$$

$$F_2 = e^{-a_0x^2 - b_0y^2} + e^{-a_0(x-1)^2 - b_0(y-1.6+E)^2} \quad (3.2)$$

$$F_3 = e^{-a_0x^2 - b_0y^2} + e^{-8a_0(x-0.8)^2 - b_0(y-1.2+E)^2} \quad (3.3)$$

$$\begin{aligned} F_4 = & e^{-a_0(x+1)^2 - b_0(y+1.2)^2} + e^{-a_0(x+1)^2 - b_0(y+0.8)^2} \\ & + e^{-a_0(x+1)^2 - b_0(y+0.2)^2} \\ & + e^{-0.2a_0(x-1.2)^2 - 0.2b_0(y-1.6+E)^2} \end{aligned} \quad (3.4)$$

In the Gaussian functions, x and y are defined as $x, y = [-2, 2]$, a_0 and b_0 are constants defined as $a_0 = 0.9954$, $b_0 = 1.856$, and E represents an error term. The model images are generated without any error (where $E = 0$), while their corresponding seismic representations are generated with the addition of an error (where $E = 0.8xy$), so as to make the seismic image and the idealised model image different, and prevent the optimisation algorithm from easily getting a perfect match. The optimisation algorithm utilised to enforce the match of the idealised model and idealised seismic is the evolutionary algorithm (Schulze-Riegert et al., 2002). The idealised model and seismic are classified into different clusters (two, three and four level) using the k -means clustering algorithm, and these are shown in Figures 3.5, 3.6, 3.7 and 3.8.

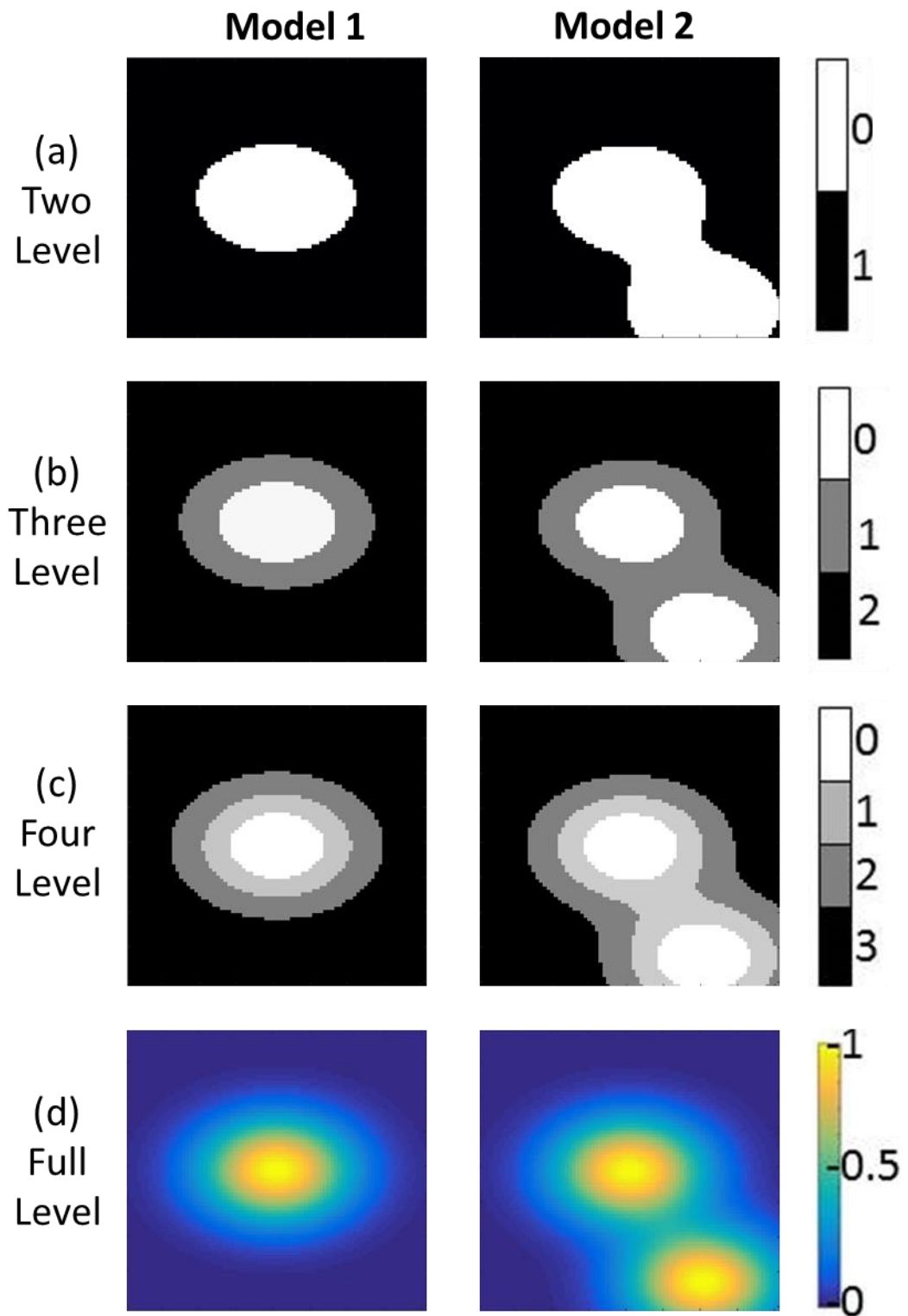


Figure 3.5 Test cases model 1 and 2 with different threshold levels to quantify the accuracy of misfit through the matching process. Three threshold levels are presented from the top to the bottom, the last one has no threshold (full level) as it is the initial continuous image.

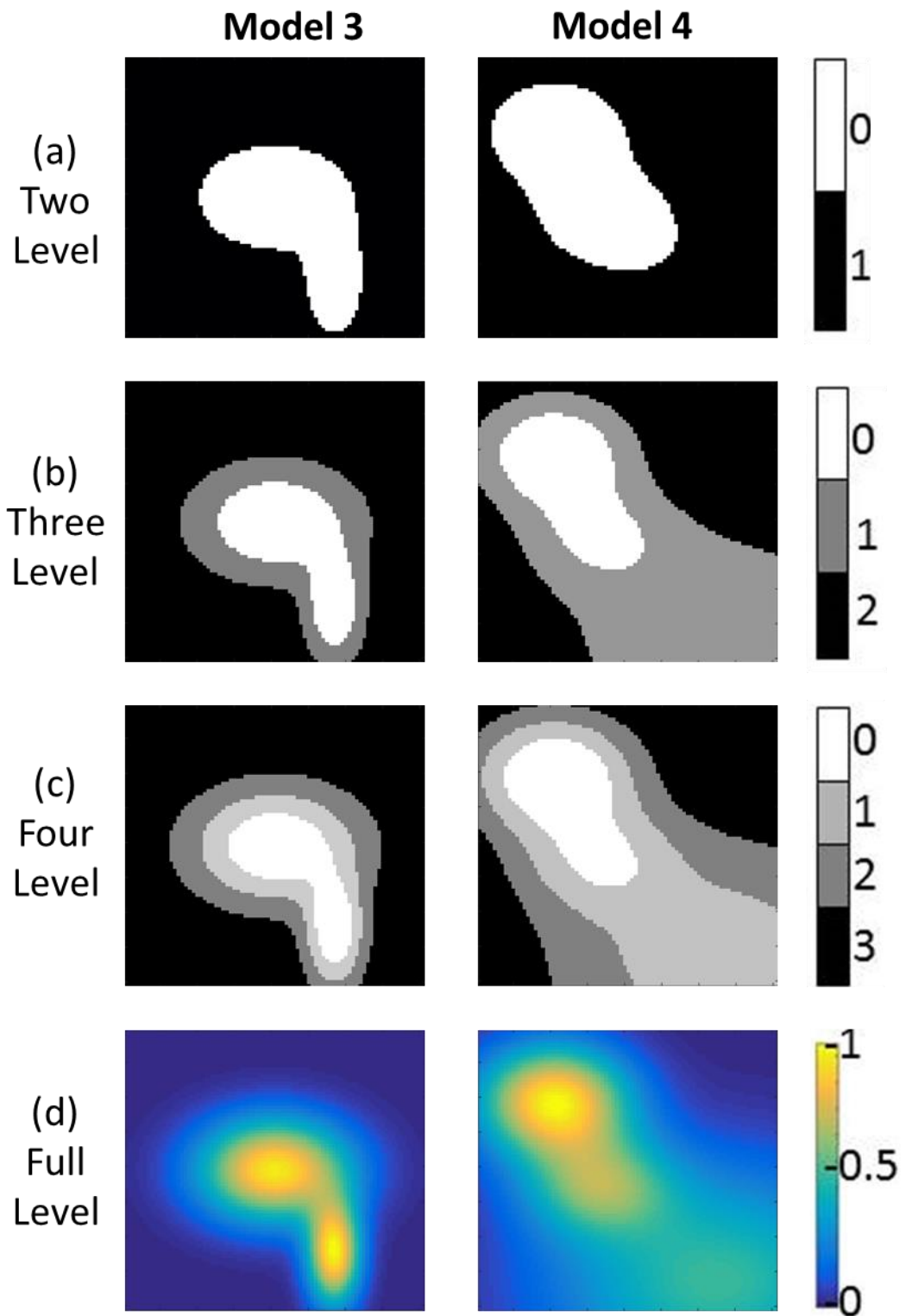


Figure 3.6 Test cases model 3 and 4 with different threshold levels to quantify the accuracy of misfit through the matching process. Three threshold levels are presented from the top to the bottom, the last one has no threshold (full level) as it is the initial continuous image.

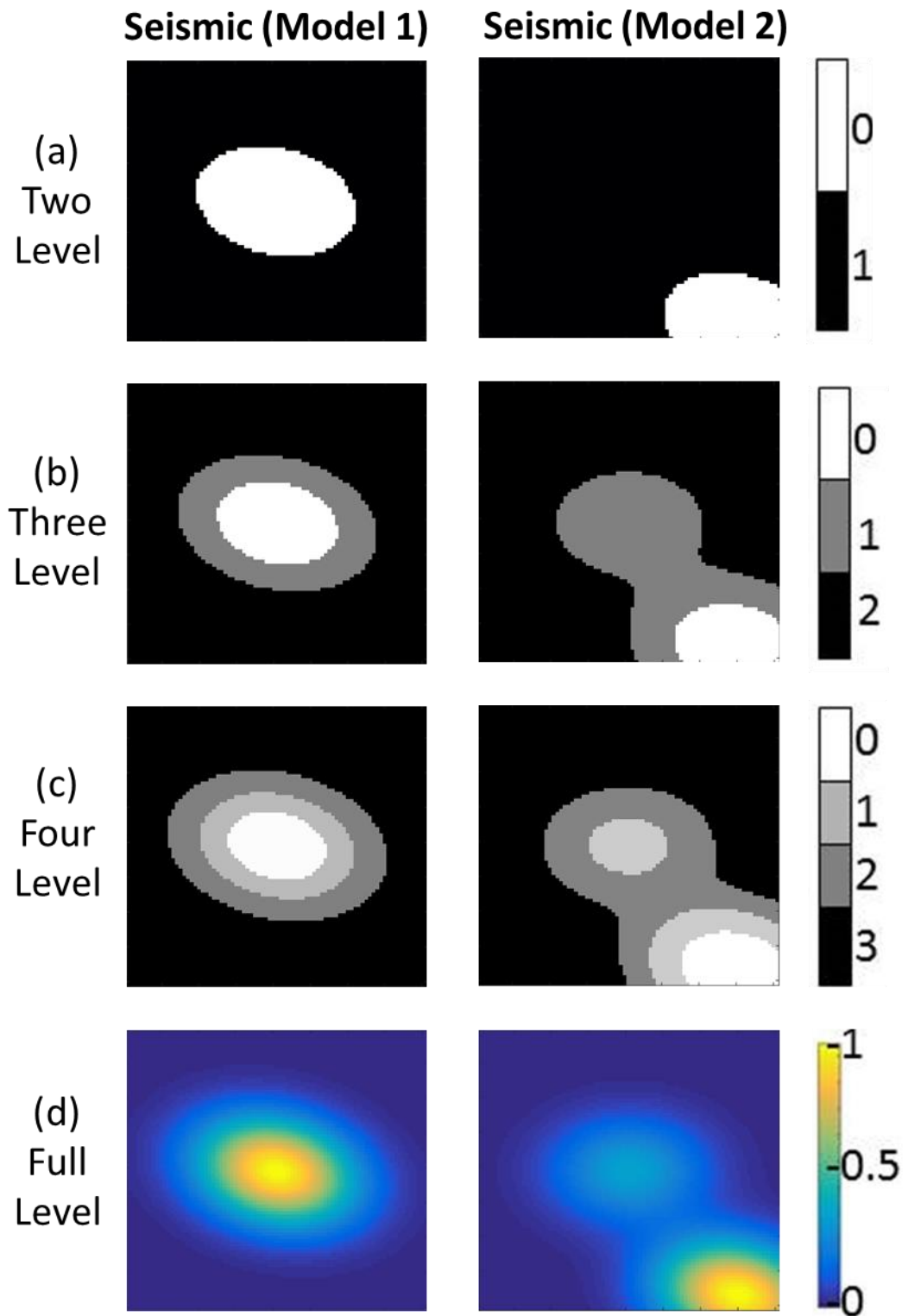


Figure 3.7 Test cases seismic model 1 and 2 with different threshold levels to quantify the accuracy of misfit through the matching process. Three threshold levels are presented from the top to the bottom, the last one has no threshold (full level) as it is the initial continuous image.

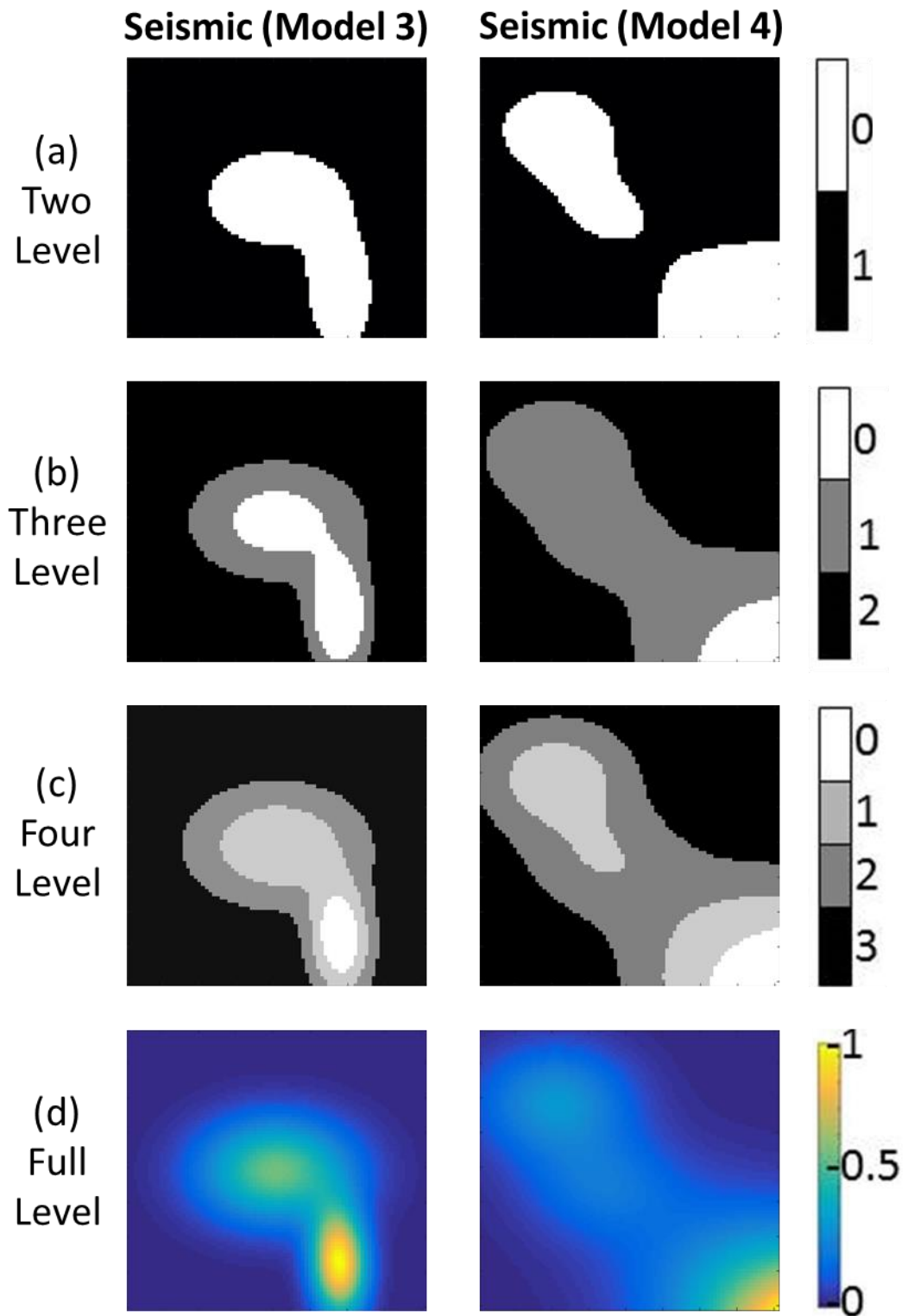
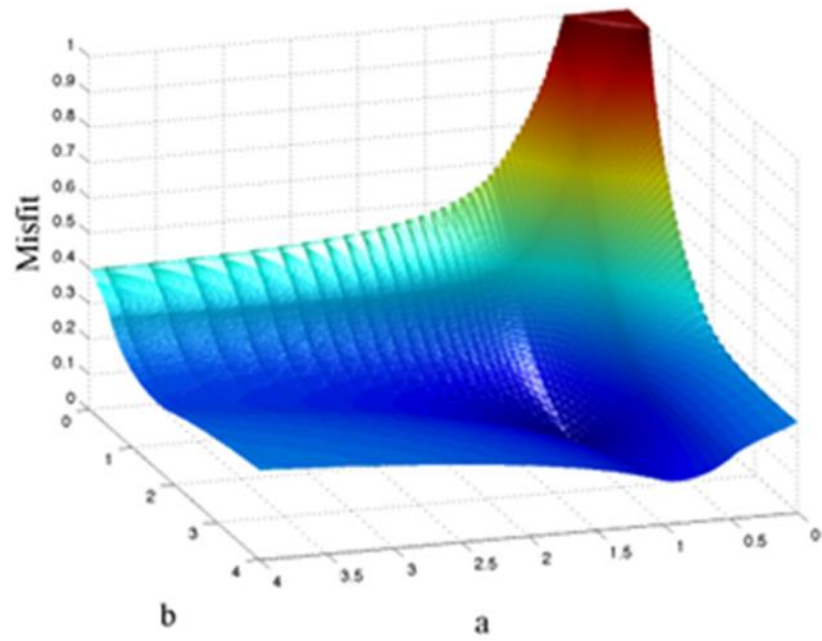


Figure 3.8 Test cases seismic model 3 and 4 with different threshold levels to quantify the accuracy of misfit through the matching process. Three threshold levels are presented from the top to the bottom, the last one has no threshold (full level) as it is the initial continuous image.

The comparison of the generated maps for the different threshold levels (two, three and four) leads to the conclusion that the features or shapes of each model has been correctly captured, and that there is no significant difference between the three different levels of threshold, in terms of capturing the main characteristics of the phenomena. Also the binary maps (two-level) seem to be as efficient as a three-level or four-level threshold considered in the chosen example. For further study, Model 1 (equation (3.1)) search space analysis is shown in the next paragraph; however the analysis is performed on all the models which leads to the final conclusion.

Figures 3.9 and 3.10 show the search space shape of the landscape that an optimisation algorithm would have to search in other to find a solution. The plots present similar landscapes, with a seemingly large plateau with a misfit value of 1, and a trough located at $(x_1 = 1, x_2 = 2)$ which is the optimum point. The plateau which corresponds to the highest misfit value reduces with an increase in the number of threshold levels, and for no threshold, the plateau becomes a well formed peak. In the rest of the landscape, there is some ruggedness propagating all over the descending landscape.

(a) Two Level



(b) Three Level

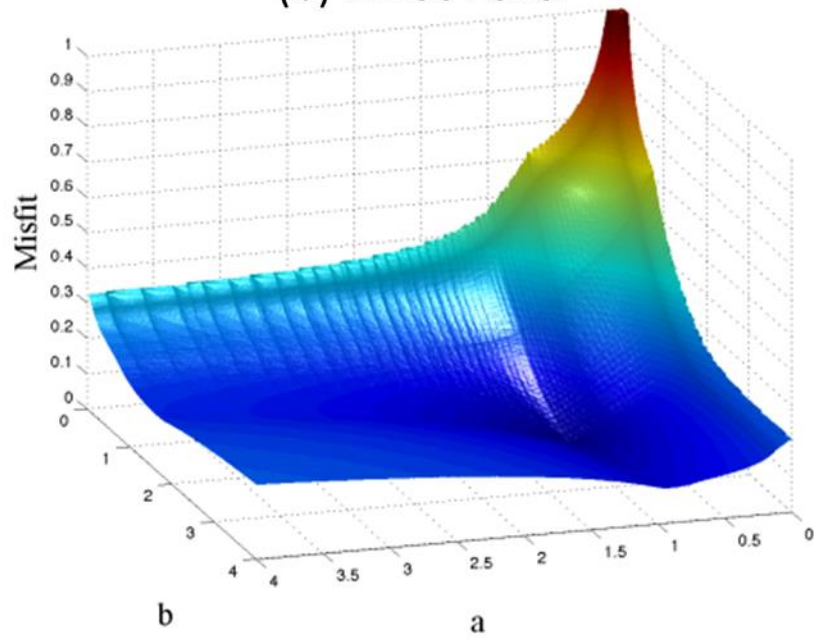
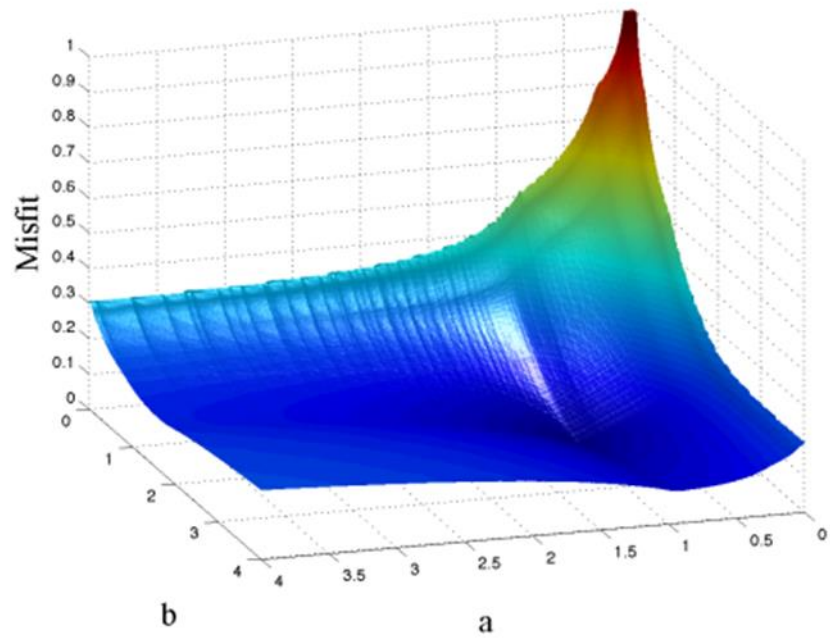


Figure 3.9 Normalised search space applied to different threshold levels

(a) Four Level



(b) Full Level

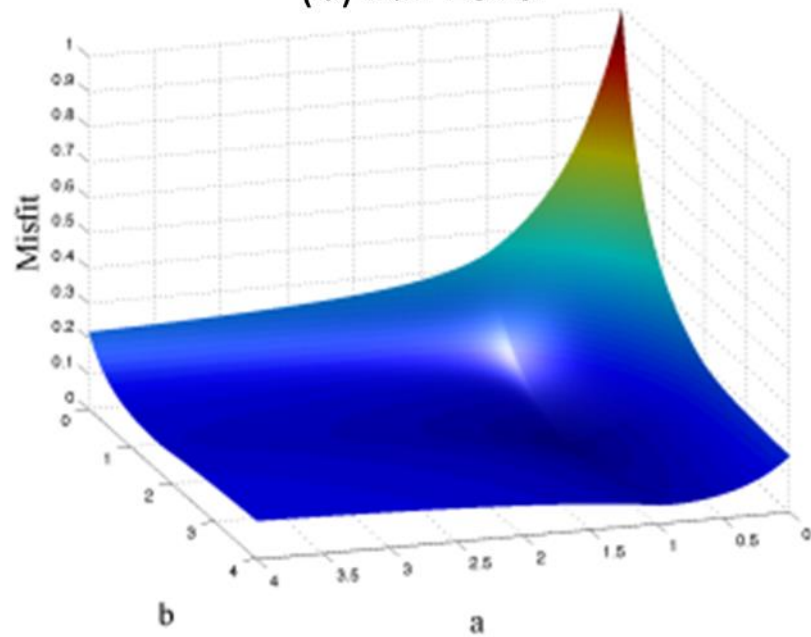


Figure 3.10 Normalised search space applied to different threshold levels

The ruggedness propagating the descending landscape is strongly defined for a two-level threshold (binary), and progressively becomes smoother with an increase in the threshold level, until the landscape becomes very smooth when no threshold level (full level). In terms of structure, the landscape has approximately the same global structure regardless of the number of threshold, but the local geometry of the search space is affected by the level of the threshold, by the emergence of the ruggedness. In the case of a finer grid, the conclusions drawn previously still stand – a finer discretisation just smoothens out the global landscape, but locally, the plateau and ruggedness are still present. Therefore, optimizing a binary map (two-level) is not necessarily simplest as compared to a more traditional image composed of several levels of threshold (three, four or full level).

Moreover, this exercise reveals that a gradient type algorithm might be unsuitable for a binary approach as it could be stuck on a local plateau or within the ruggedness; a recommendation would be to use a derivative-free optimisation algorithm in order to avoid such challenges. With respect to the context of binary seismic assisted history matching, the necessity to measure differences between images, as well as taking into account the constraints highlighted previously, it is recommended that the selected metric should be globally inclined, so as to compensate for the local ruggedness of the landscape.

A history matching process is then conducted with the four idealised models and the corresponding seismic images, with different threshold levels (two, three, four and full level). The standard deviation for each case is measured (Figure 3.11), where the uncertainty in finding the corresponding best solution for the chosen optimisation algorithm is evaluated. One key observation is that an increase in the threshold levels leads to less variability in the solution. Also there is a clear difference between the two-level threshold and the multiple-level (three, four, full level) threshold. Using the two-

level threshold (binary) is less precise in terms of finding the best solution, and adding more threshold levels increases the precision, however this leads to more complication and time consuming analysis.

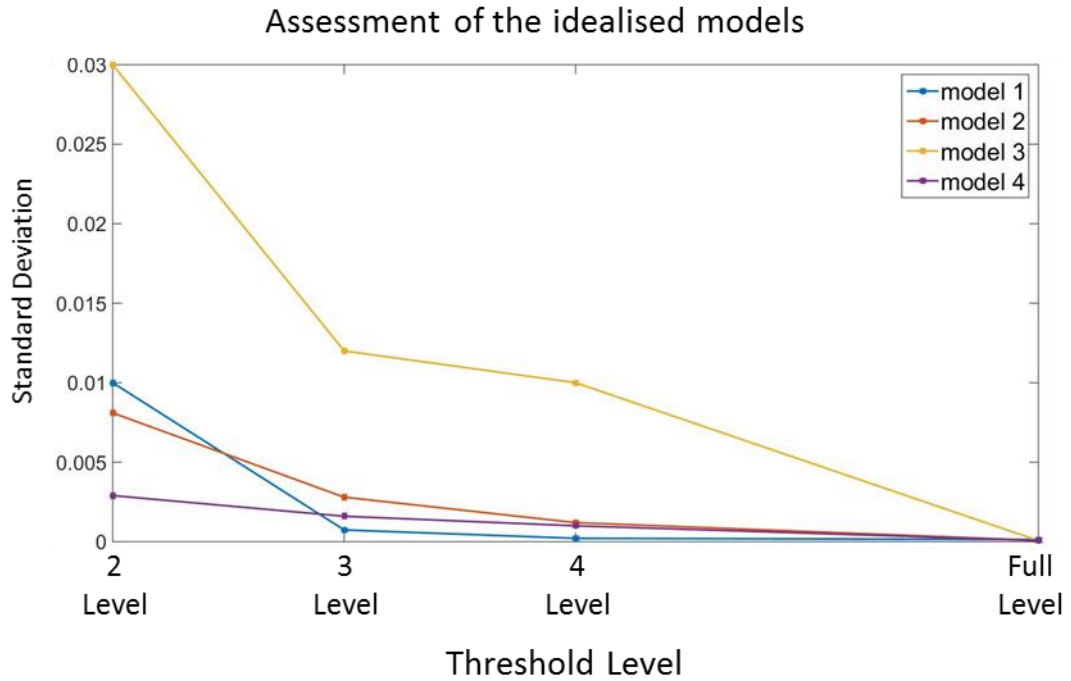


Figure 3.11 Standard deviation for Models 1, 2, 3 and 4 as a function of different threshold levels.

Four binary metrics will be analysed in the next section – the Hamming distance, the Hausdorff distance, the Mutual Information and the *Current* measurement metric. They will be generally introduced, and then tests will be conducted in order to ascertain the pros and cons of the different metrics, and which ones will be the best for a binary seismic assisted history matching exercise.

3.2.1 Hamming Distance

The Hamming distance is an algorithm that determines whether two digital images are similar or dissimilar (Hamming, 1950). This is measured by measuring the number of dissimilar corresponding elements between two images, and it is known to be invariant to light changes, small deformations, small geometrical transforms and non-rigid deformations, and has an inherent robustness to noise (Pele and Werman, 2008). Zhao et al. (2013) observed from their analysis that a Hamming distance value greater than 30 indicates that the images are non-identical and can be considered different. Figure 3.12 shows examples of the Hamming distance value “ D ” between images that were converted to binary, where one image is “original”, and the other distorted image is “forged” (Zhao et al., 2010).



















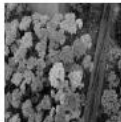
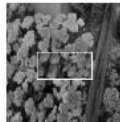
Original	Forged	Image size	D	Original	Forged	Image size	D
		512×512	26			600×399	40
		570×395	43			482×319	49
		540×319	40			600×430	54
		700×525	59			289×432	55
		128×128	51			128×128	55

Figure 3.12 Hamming Distance “ D ” between original and forged images (Zhao et al., 2010).

Mathematically, the Hamming distance can be described as the sum of the absolute differences between two binary images, and is represented by equation (3.5).

$$H_{hamm} = \sum_{i=j}^n |A_i - B_j| \quad (3.5)$$

Where H_{hamm} is the Hamming distance, and A_i and B_j are the corresponding binary images

3.2.2 Hausdorff Distance

The Hausdorff distance is the distance measured between two images or models, that show the extent to which each point in both images or models align. This distance is used to determine the degree of resemblance or disparity between the two models or images. Mathematically, the Hausdorff distance, H_{hausd} can be represented by equation (3.6) (Huttenlocher et al., 1993).

$$H_{hausd} = \max\{dist(A, B), dist(B, A)\} \quad (3.6)$$

where

$$dist(A, B) = \max\left\{\min\left(dist(A_i, B_j)\right)\right\} \quad (3.7)$$

The function $dist(A, B)$ is known as the directed Hausdorff distance from A to B, and it identifies the point i as an element of A that is farthest from any point of B, and measures the distance (using the Euclidean distance) from point i to its nearest neighbour in B. The function $dist(A, B)$ ranks each point in A with regards its distance to the nearest point of

B, and selects the largest ranked point as the distance (the farthest away point). The Hausdorff distance, H_{hausd} is then the maximum value of $dist(A, B)$ and $dist(B, A)$, and this measures the level of mismatch between two sets of data (A and B), by measuring the distance of the point A that is farthest from any point in B, and vice versa (Huttenlocher et al., 1993).

3.2.3 Mutual Information

Mutual Information aims to quantify the information shared between two sets of data (Dowson and Bowden, 2004). It is an information theory measure of the statistical dependence between two random variables, in other words, it can be qualitatively explained as a measure of how well one image matches the other (Roshni and Revathy, 2008). Mathematically, it can be said to be the reduction in the uncertainty of one random variable due to the knowledge of the other, and it is represented as equation (3.8).

$$MI = H(A) + H(B) - H(A, B) \quad (3.8)$$

Where $H(A)$, $H(B)$ are the individual entropy of images A and B respectively, while $H(A, B)$ is the joint entropy. More details on Mutual Information and types of entropy can be found in MacKay (2003).

3.2.4 Current Measurement Metric

The *Current* measurement metric was introduced by (Glaunès, 2005) for computational anatomy, and it is an alternative tool for calculating the distance between closed curves or surfaces. The main concept of the *Current* measurement metric is to identify the image shape to a mapping that returns the value of circulation of any vector field along the curve. This mapping is a measure, and for every given curve there is an associated measure. It is possible to mathematically define this measure which can be used to quantify the differences between curves. Glaunès (2005) used this method on parametric curves and 3D meshes, however, Chesseboeuf (2015) showed that this approach can work directly on images. The *Current* measurement metric between two images can be computed as the Euclidean norm of a filtered difference between the two images. This filter is similar to a smoothing kernel, and depends on a parameter p which tunes the amount of smoothing applied. Mathematically, the *Current* measurement metric for binary images is represented by equation (3.9).

$$H_{CMM} = \sum_{i,j=1}^N K_{ij} |\widehat{A}_{ij} - \widehat{B}_{ij}|^2 \quad (3.9)$$

Where \widehat{A}_{ij} and \widehat{B}_{ij} denote the (i,j) -th Fourier coefficients of A and B , and K is the aforementioned smoothing kernel. The smoothing kernel is mathematically represented as:

$$K_{ij} = (i^2 + j^2)^2 \left(1 + \sqrt{i^2 + j^2}\right)^{-p} \quad (3.10)$$

Where p is the smoothing parameter. When p is small the norm becomes more local, which means that small details are well measured but large translations are not captured; however as p becomes large, the norm becomes large small details are missed while the larger displacements are well measured. More details on *Current* measurement metric and the smoothing kernel can be found in Chesseboeuf (2015).

3.3 Analysis on Test Case Scenarios

In the context of seismic history matching, two images will be compared - a source image which is the observed seismic data and a target image which is from the simulator, constrained by the input parameters decided by the optimiser. To compare these metrics, scenarios (Figures 3.13, 3.14 and 3.15) have been designed to determine their efficiency and reliability. These scenarios have been created in the context of reservoir saturation maps, whose principal characteristics have been identified from the saturation maps given by the optimisation process of a North Sea field dataset. The scenarios have been categorised into five groups, and the expectation from a suitable metric would be its ability to “understand” these different categories.

The first scenario concerns isolated clusters. The optimizer might generate an isolated cluster of points from a new set of input parameters, so this needs to be analysed. It is expected that a suitable metric will be able to identify them as not being a part of the observed seismic data. The second scenario concerns addition of noise. A suitable metric should be able to identify noise as an artefact, and not as a good update to the model. As noise could sometimes be small and sparse, it is quite tricky for some metrics to adequately capture it. The third scenario examines a growing shape. In other words, the ability for the metric to identify a shape that is roughly the same shape as that from the

source in the target image, but with a different size. The fourth scenario examines a similar concepts as the third scenario, but focuses on the capability of identifying the displacement of a shape. The fifth scenario is not about an individual potential scenario; on the contrary, it is a combination of all the aforementioned scenarios. This is quite practical because during the optimisation process, all these scenario occurrences are combined. Indeed a metric might characterise some individual scenarios very well, but not when they are combined. Conversely, a metric that might identify a mixed scenario could potentially be badly suited to characterise them individually. So the fifth scenario has to be regarded as just another scenario as it is necessary to cover all the possible range of scenarios generated during the history matching process.

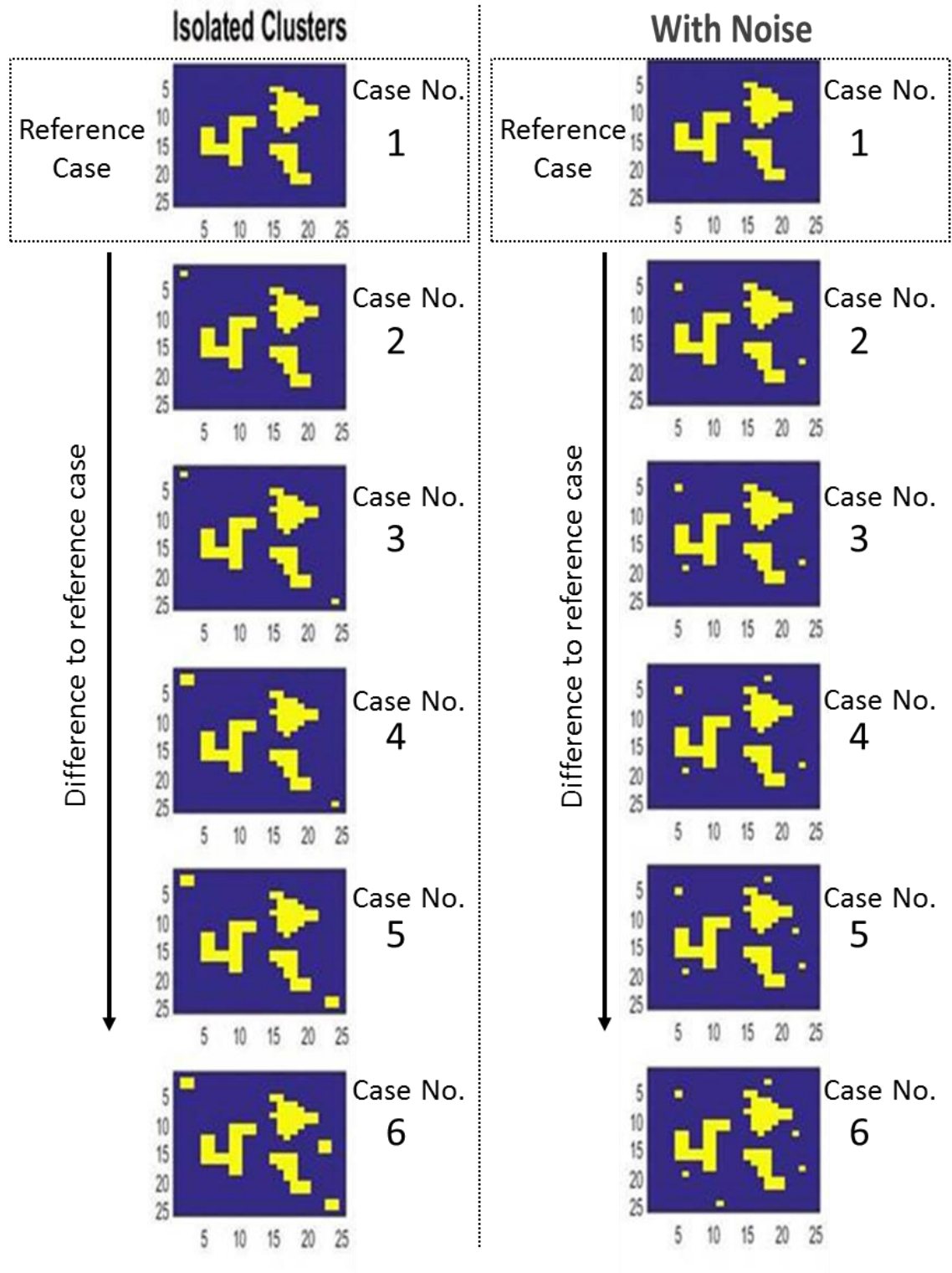


Figure 3.13 Different scenarios to test the metrics.

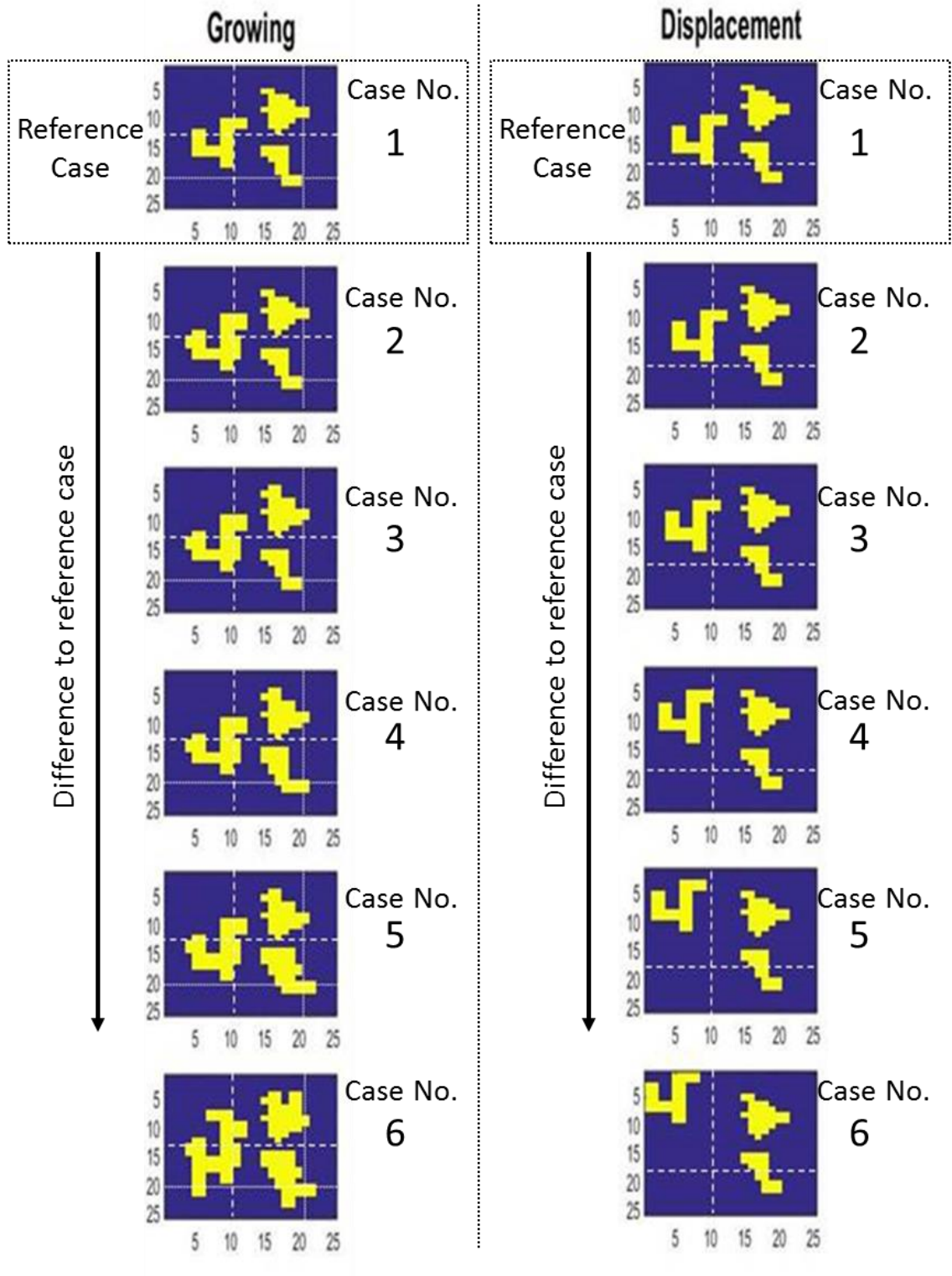


Figure 3.14 Different scenarios to test the metrics

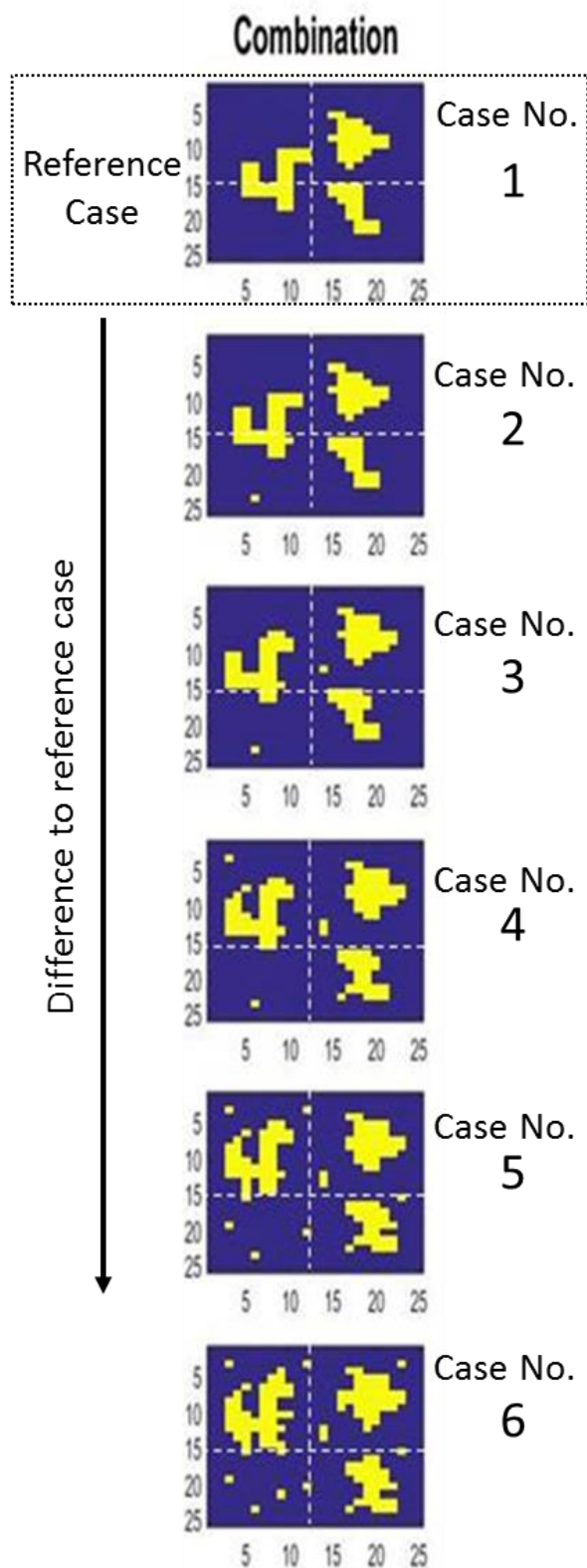


Figure 3.15 Different scenarios to test the metrics

The results for these scenarios are summarised in Figures 3.16, 3.17 and 3.18. The expectation from an ideal measurement metric is a monotonic increase of misfit with an increase in case number (as the cases become more different to the reference case). Thus a situation where the misfit flattens out or decreases and increasing intermittently signifies an unsuitable measurement metric.

In the first scenario (isolated clusters), all metrics give valuable information, except the Hausdorff distance which is not able to identify isolated points at all (remains flat from case 2 to case 6), whatever the case. The second scenario which concerns testing the sensitivity to noise, has quite a similar characteristic to the first scenario, almost the same results are obtained - implying that the Hausdorff distance is not able to identify random isolated points on a grid (remains flat from case 2 to case 6). For the third scenario (growing shape), three metrics are positively responsive except the Hausdorff distance which classifies the case number four as less different to case number three (remains flat from case 3 to case 4), and this is wrong. This is confirmed by the others metrics which have no problem with these two cases. On the test of the displacement of shape in the fourth scenario, Hamming distance and Mutual Information have trouble identifying differences after the case number four (remain flat from case 4 to case 6). Finally for the fifth scenario (the combination of scenarios), the Mutual Information fails as the metric evaluates that case number six is less different than case number five (decreases from case 5 to case 6), and the Hausdorff distance does not get satisfactory results at all (remains flat from case 2 to case 3, and from case 4 to case 6). The *Current* measurement metric also has a very slight misjudgement with case number five and six (very slight decrease from case 5 to case 6).

To summarize, the Hamming distance had some challenge with the displacement of shape scenario, the *Current* measurement metric had a very slight misjudgement of the combination scenario, the Hausdorff distance had challenges with the isolated clusters scenario, noise scenario, growing shape scenario and combination scenario, and the Mutual Information had challenges with the displacement of shape scenario and combination scenario. Each of these metrics have shown potential for capturing some features more accurately than their counterparts, but overall, the Hamming distance and the *Current* measurement metric have proven to be the most robust and effective, and therefore they will be used for further analysis in the history matching study.

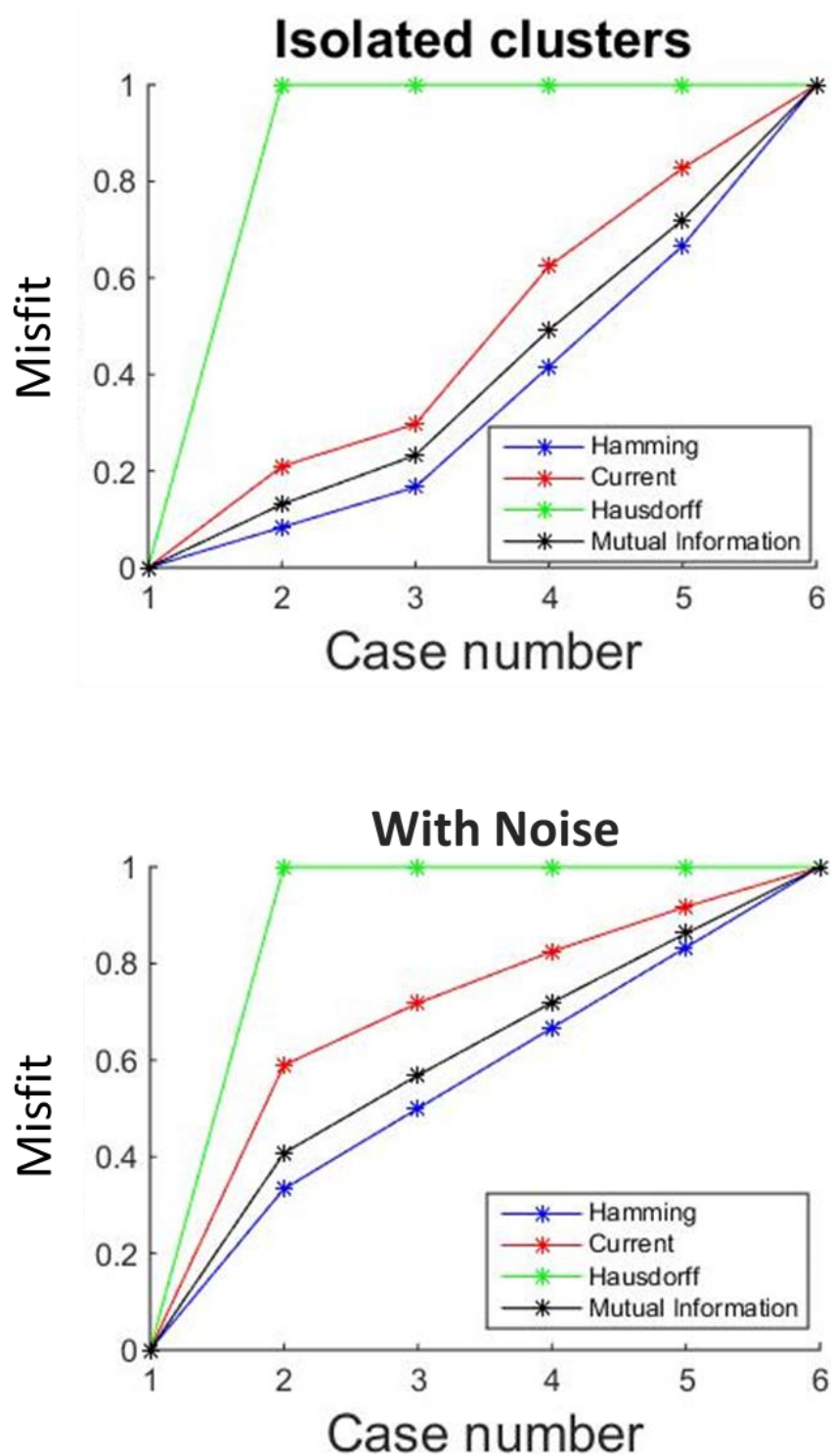


Figure 3.16 Results of the performance of the different tested metrics on the different selected scenarios

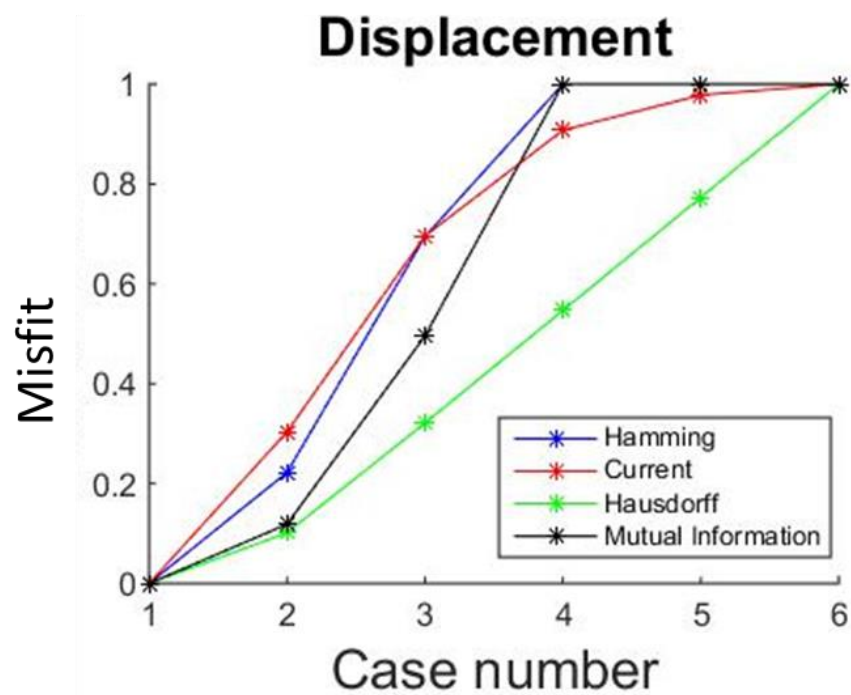
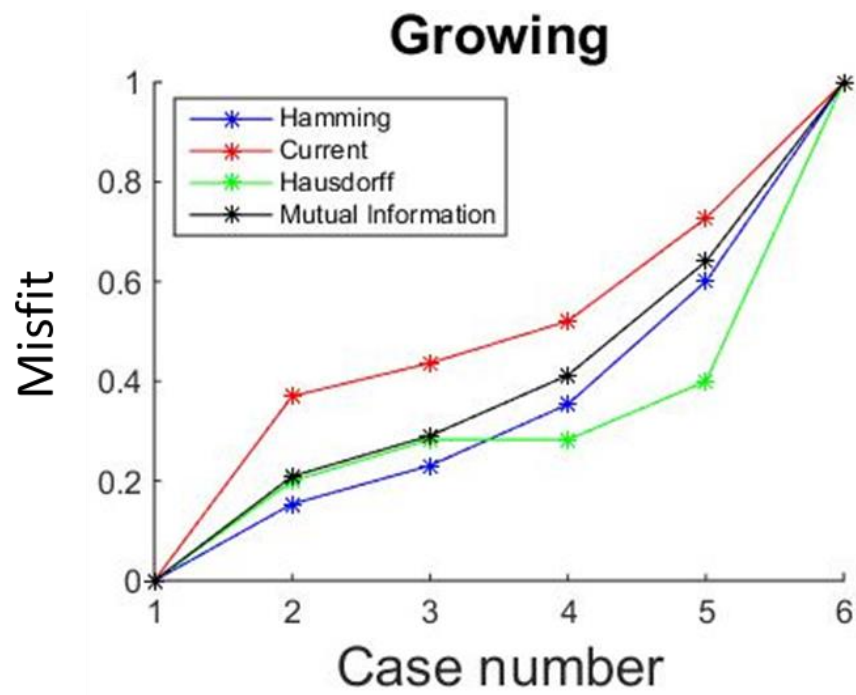


Figure 3.17 Results of the performance of the different tested metrics on the different selected scenarios

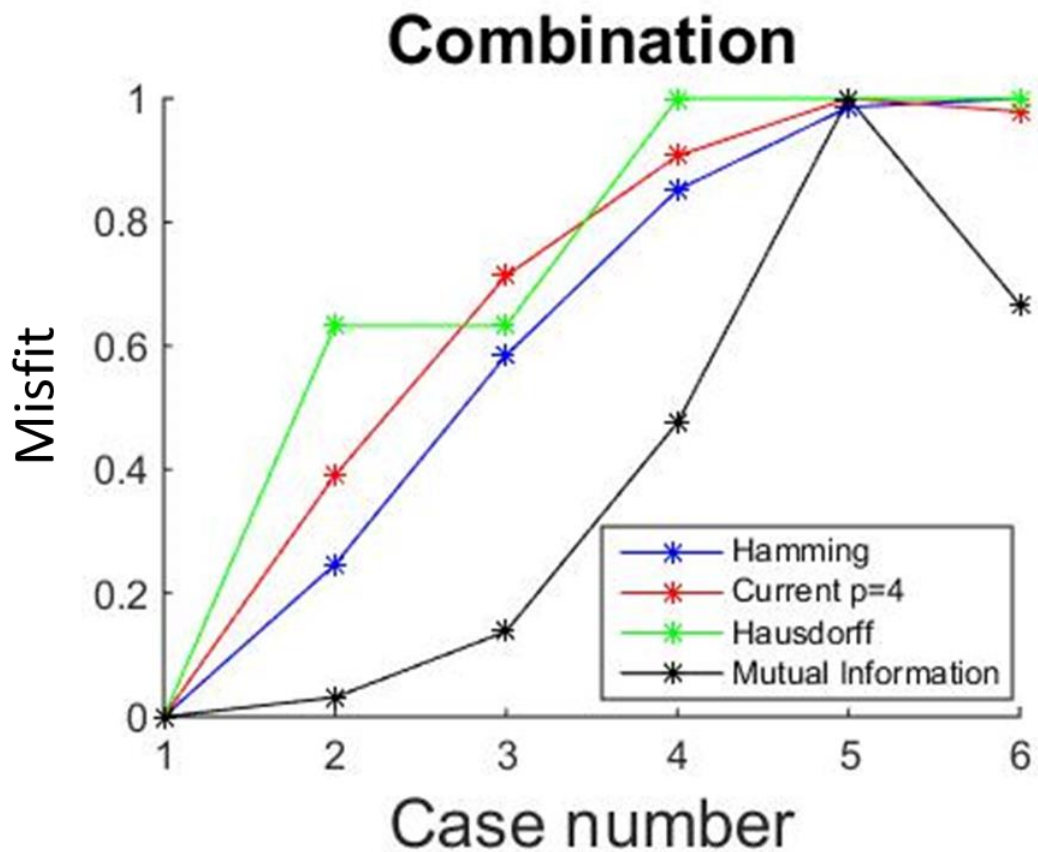


Figure 3.18 Results of the performance of the different tested metrics on the different selected scenarios

3.4 Summary

This chapter discusses the development of the binary images approach, clustering and binary threshold techniques, and analyses and testing of four measurement metrics – Hamming distance, Hausdorff distance, Mutual Information and *Current* measurement metric. This ushers in a more quantitative outlook as opposed to a qualitative or semi-quantitative manner. Idealised models are created in order to test the implementation of a two-level (binary approach), multi-level, and full-level threshold approach, and the results show that binary does capture the major data characteristics. In terms of the efficacy of the measurement metrics, case scenarios were analysed that replicate changes observed

during the history matching process, and the results show that the *Current* measurement metric and Hamming distance seem to be the most satisfactory. Having done the development analysis of the binary approach, a validation of this approach will be the next step.

Chapter 4

SHM Using Binary Images - Validation

Having analysed different metrics for comparing the misfit or correlation of binary maps in the previous chapter (where one binary map comes from seismic data and the other binary map comes from the simulation model), the Hamming distance metric and the *Current* measurement metric were shown to possess the best attributes for accurately distinguishing misfits between different binary maps. These two metrics are now further tested on a synthetic model in order to validate the use of the binary image approach, as well as show its functionality in a practical setting. In this chapter, I will give an overview of the synthetic simulation model being used, as well as the corresponding synthetic seismic generated for the relevant time-steps. Three different scenarios will be analysed with the aim of replicating expected real field occurrence. These are the gas exsolution scenarios, the water evolution scenarios, and a combination of gas exsolution and water evolution. It will be demonstrated that converting the seismic data and perturbed simulation model outputs to binary maps provides a quick and efficient method of assessing the reservoir parameters so as to arrive at a simulation model which reproduces the seismic data response. This observation will serve as a proof of validity of the efficacy of the binary images approach.

4.1 Field Description

The dataset that will be used for this analysis is a modification of ETLPmodel, which is a synthetic dataset that was recently used by Fursov (2015), and it is built from the characteristics of a turbidite field from the United Kingdom Continental Shelf (UKCS). The reservoir fluid is black oil with an API gravity of approximately 25° (medium oil) at a temperature of 120°F (48.89°C). Initial reservoir pressure is approximately 3620 psi (24.96 MPa) (at depth 1510m TVDSS) whilst bubble point is 2970 psi (20.48 MPa) at the top reservoir level, and the solution gas-oil ratio (R_s) is 385 scf/bbl (68.52 sm^3/m^3). It is a three phase reservoir penetrated by two vertical wells – a producer well and an injector well, that are controlled by bottom-hole pressure or liquid rate (depending on the production scenario). The reservoir has an average thickness of 35m (115ft), and heterogeneous properties (horizontal permeability, vertical permeability, porosity, NTG) as shown in Figure 4.1.

The figure also shows the plan view and cross sectional view of the model, the position of the injector and producer, as well as the small water saturated zone penetrated by the injector. The field operational period is 500 days, and the production/injection plan is adjusted as required to replicate the different scenarios and this will be discussed in their respective sections. There are two seismic surveys generated – a baseline seismic survey prior to production start (Day 0), and a monitor seismic survey at the end of the field operational period (Day 500). The seismic surveys were generated by seismic modelling according to the procedure specified in Amini (2014), using the petro-elastic properties, seismic wavelet and rock stress sensitivity of a typical UKCS field. The Sum of Negative Amplitudes (SNA) between the reservoir top and reservoir base horizons is used as the seismic attribute.

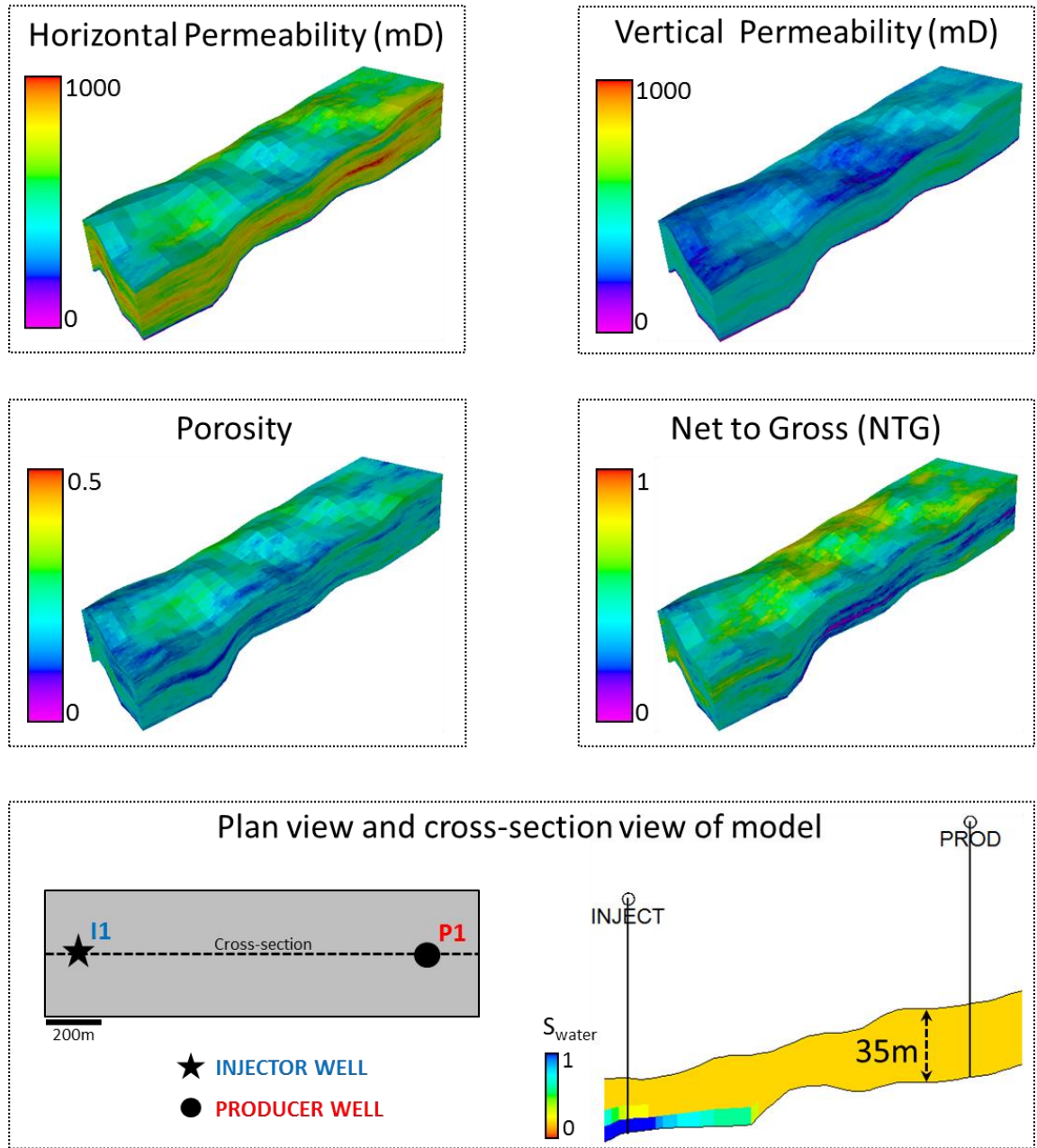


Figure 4.1 Heterogeneous properties (horizontal permeability, vertical permeability, porosity and NTG) of the dataset. Also shown is the plan view and cross-section view of the model highlighting the location of the producer well and injector well, as well as the oil-water contact.

The geological model of the dataset has 114 x 38 x 30 cells with approximate thicknesses of 10m x 10m x 1m in the X, Y and Z direction respectively, while the simulation model has 57 x 19 x 4 cells with approximate thicknesses of 20m x 20m x 8m in the X, Y and Z direction respectively. The simulation model will be used in this analysis, as this is what will be applicable in real reservoir management operations where rapid simulation run time and accuracy will be of importance. The simulation model responses will be represented as pore volume weighted 2D maps as recommended by Falahat (2012) for a reservoir below tuning thickness, while the seismic attributes will also be map-based.

Having described the dataset in detail, I will now proceed to showcase the analysis of the three different scenarios which are:

- Gas exsolution scenarios
- Water evolution scenarios
- Combination of gas exsolution and water evolution.

4.2 Gas Exsolution Scenarios

The initial reservoir pressure is above the bubble point pressure, hence there is no initial gas cap in the reservoir. In order to develop a scenario whereby sufficient gas is exsolved from the oil in the reservoir, the reservoir is depressurized by putting the producer well on stream for 500 days at a constant liquid rate of 630 stb/day (100 sm³/day), and as there is no need for pressure support, there is no injector well activity. The field production and seismic acquisition plan is illustrated in Figure 4.2.

The goal of this exercise is to validate the binary approach by mimicking a history matching process whereby the initial simulation model (base case) is perturbed. This is achieved by transforming the absolute permeability with multiplier values of 0.8, 0.6 and 0.4. The different simulation model 4D responses represented by pore-volume weighted gas saturation maps, and the base case model generated 4D synthetic seismic are shown in Figure 4.3.

In the base case 4D (monitor minus baseline) model, gas is exsolved around the producer as the reservoir goes below the bubble point pressure. Once the gas attains its critical saturation (saturation at which it becomes mobile), it accumulates at the local high due to its density property and gravity effect. The gas can then be seen gently migrating from the right side to the left side through the centre, and this is due to the nature of the reservoir structure, as well as the pressure gradient. Perturbing the base case model by incrementally reducing the permeability increases the exsolved gas swept from the right side to the left side, and these spatial gas changes will be analysed by the objective function metrics.

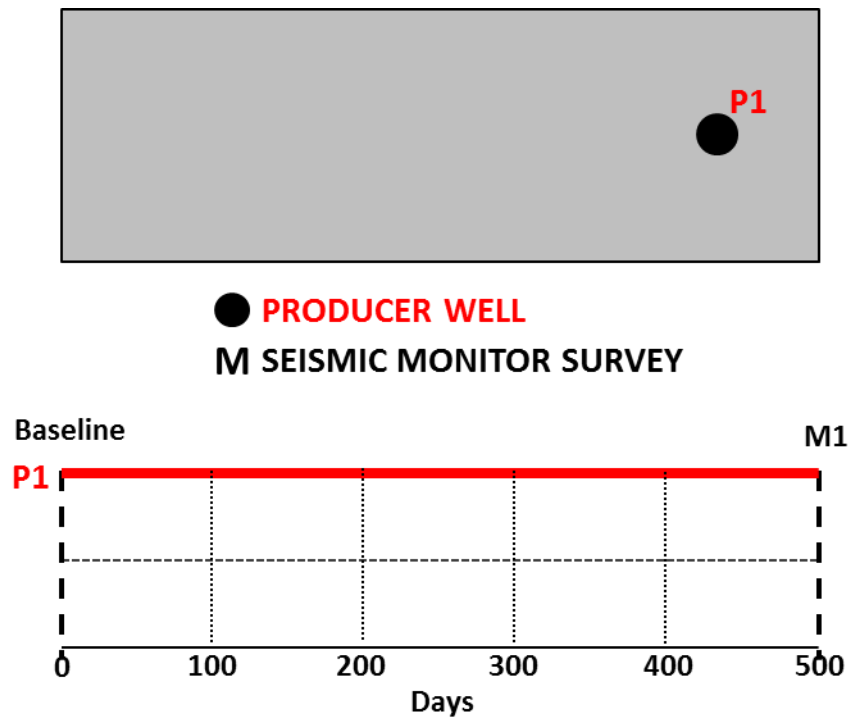


Figure 4.2 An outline of the reservoir, the position of producer well, and the timeline of activity of the well relative to the multiple seismic data surveys for the gas exsolution scenarios.

In order to analyse the spatial gas changes, the 4D seismic data response of the base case model time-lapse, base case model time-lapse gas saturation response, and perturbed models time-lapse gas saturation responses are converted into binary maps as shown in Figure 4.4.

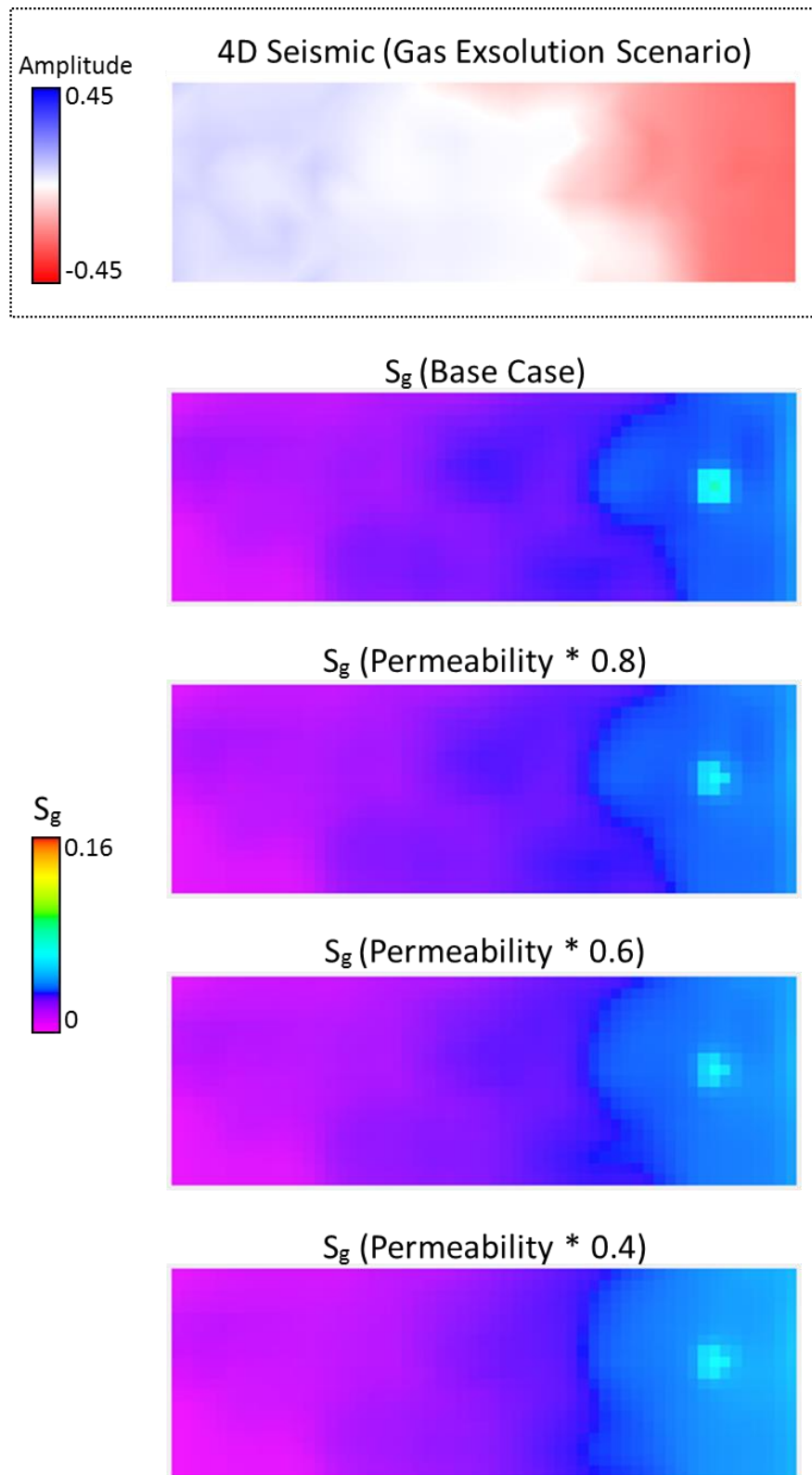


Figure 4.3 The 4D seismic data response of the base case model time-lapse, base case model time-lapse gas saturation response, and perturbed models time-lapse gas saturation responses for the gas exsolution scenarios.

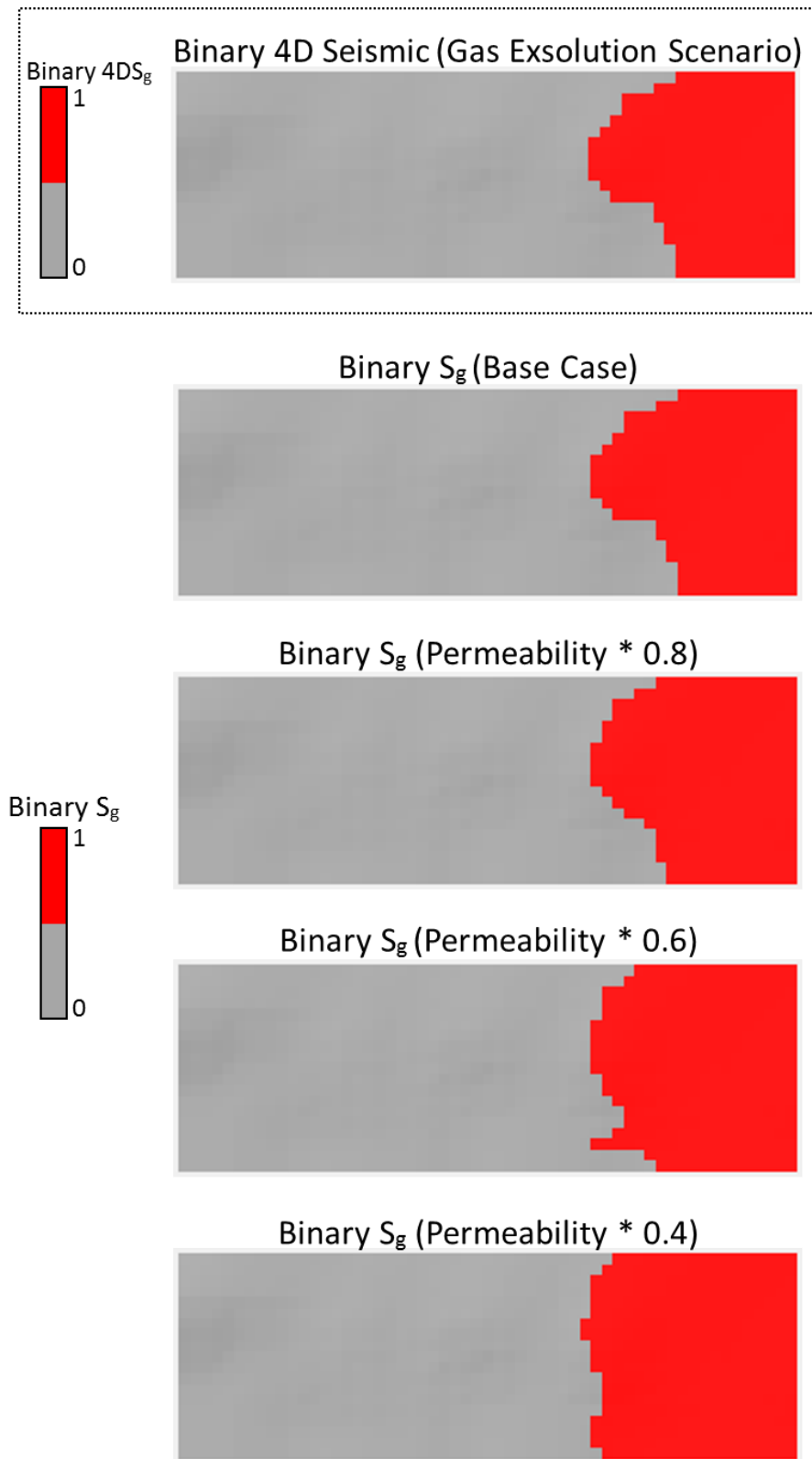


Figure 4.4 The binary gas 4D seismic data response of the base case model time-lapse, base case model time-lapse binary gas saturation response, and perturbed models time-lapse binary gas saturation responses for the gas exsolution scenarios.

The binary maps clearly represent the gas distribution in the reservoir model and are generated using *k*-means clustering as described in Chapter 3 and Appendix D. Table 4.1 and Figure 4.5 show the comparisons of the binary maps.

Perturbation	Objective Function	Hamming	Current
A	"Binary (S_g) Base Case" compared to "Binary (S_g) Seismic"	0	0
B	"Binary (S_g) Perm.*0.8" compared to "Binary (S_g) Seismic"	24.29	5.44
C	"Binary (S_g) Perm.*0.6" compared to "Binary (S_g) Seismic"	61.43	41.44
D	"Binary (S_g) Perm.*0.4" compared to "Binary (S_g) Seismic"	100	100

Table 4.1 The Hamming distance and *Current* measurement metric objective function for the different perturbations (A to D) for the gas exsolution scenarios. The values that have been normalised are plotted in Figure 4.5.

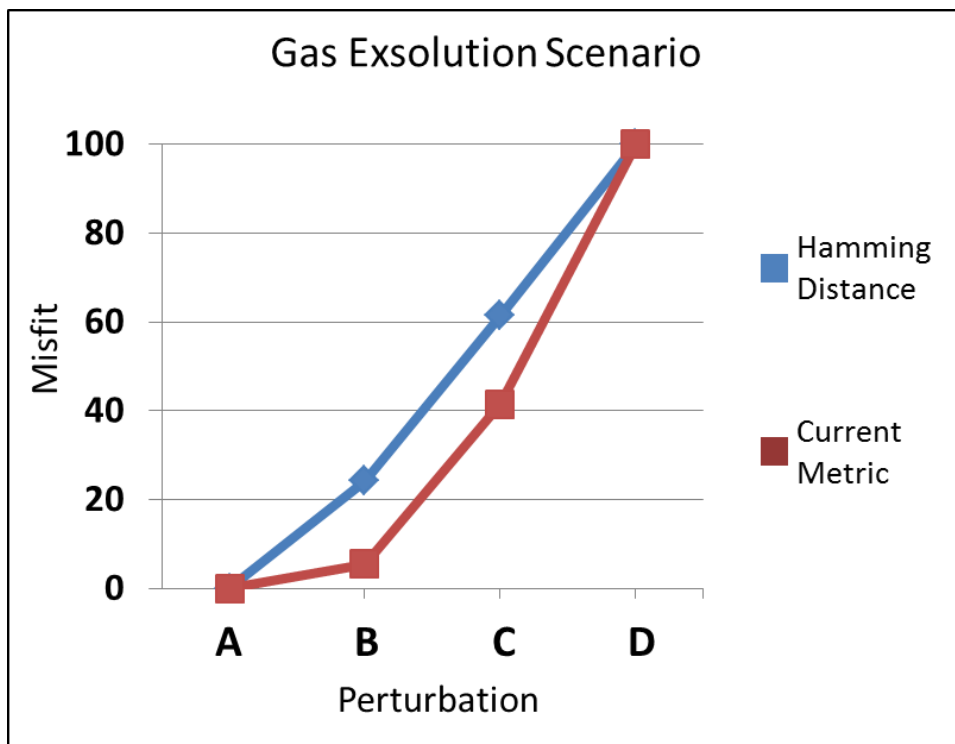


Figure 4.5 The values of the misfit using the Hamming distance and *Current* measurement metric objective function for the different cases of perturbed models shown in Table 4.1 for the gas exsolution scenarios.

The binary 4D seismic map is compared to the base case binary gas saturation 4D map, and to the perturbed binary gas saturation 4D maps using the Hamming distance metric and *Current* measurement metric. The perturbations are labelled A to D, where A is the comparison of the binary 4D seismic map to the base case binary gas saturation 4D map which gives a perfect match, all through to D which is the comparison of the binary 4D seismic map to the binary gas saturation map of the model whose permeability has been multiplied by 0.4 which gives the least perfect match.

The Hamming distance and *Current* measurement metric misfit values have been normalised so as to make them easily comparable. The plot of the misfit (Figure 4.5) shows a similar expected response from both metrics, where perturbation D has the highest misfit, and this misfit gradually reduces to a misfit of zero for perturbation A which represents the initial base case starting model. The Hamming distance has an approximately linear misfit profile, while the *Current* measurement metric has a quadratic misfit profile. This can be attributed to the way they are computed and was also observed in the previous analysis in Chapter 3, and may both be advantageous in misfit analyses of the output of the reservoir simulator. The responses from these metrics show that the binary approach is sensitive to these different scenarios. A similar analysis for water evolution scenarios will now be performed.

4.3 Water Evolution Scenarios

In these scenarios, the initial reservoir pressure is also above the bubble point pressure, hence there is no initial gas cap in the reservoir. The reservoir pressure is above the bubble point pressure and maintained that way through the field operational period. This is done to prevent gas break-out (as just water evolution effect is analysed here), and this

is achieved by assigning a well thought out operational plan for the producer well, and also installing an injector well plan. The injector and producer wells are put on stream for 500 days with a bottom hole pressure upper limit of 3760 psi (25.92 MPa) and 2970 psi (20.48 MPa) respectively so as to establish a voidage replacement scheme. The field production and seismic acquisition plan is illustrated in Figure 4.6.

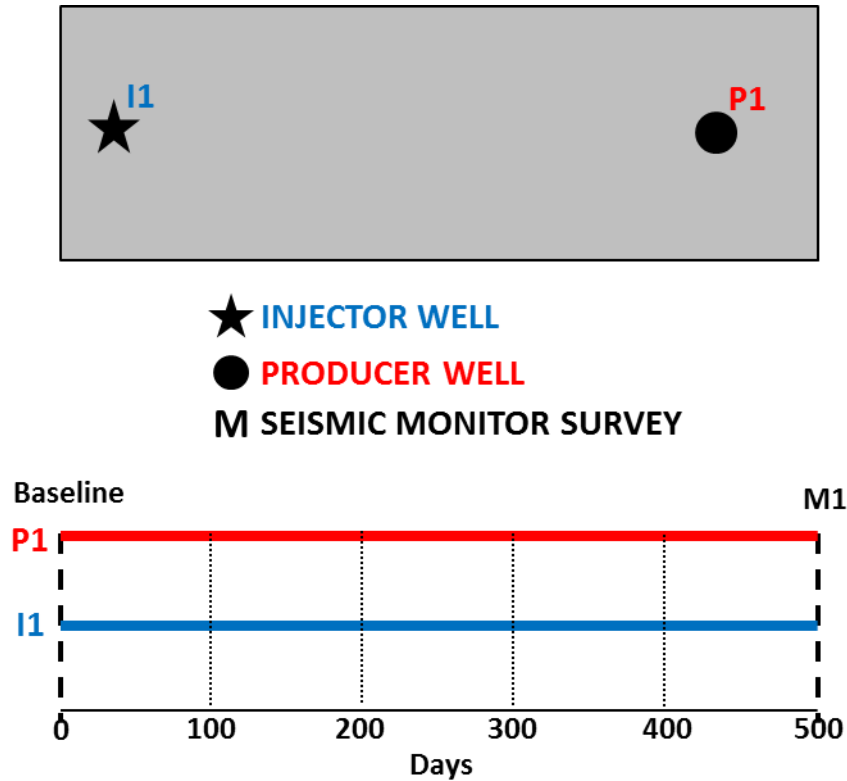


Figure 4.6 An outline of the reservoir, the position of the injector well and producer well, and the timeline of activity of the wells relative to the multiple seismic data surveys for the water evolution scenarios.

For this validation exercise, the initial simulation model (base case) is perturbed. This is achieved by perturbing the reservoir absolute permeability with multiplier values of 1.2, 1.4 and 1.6. The different simulation model 4D responses represented by pore-volume weighted water saturation maps, and the base case model generated 4D synthetic seismic are shown in Figure 4.7 and their 4D binary map representatives in Figure 4.8.

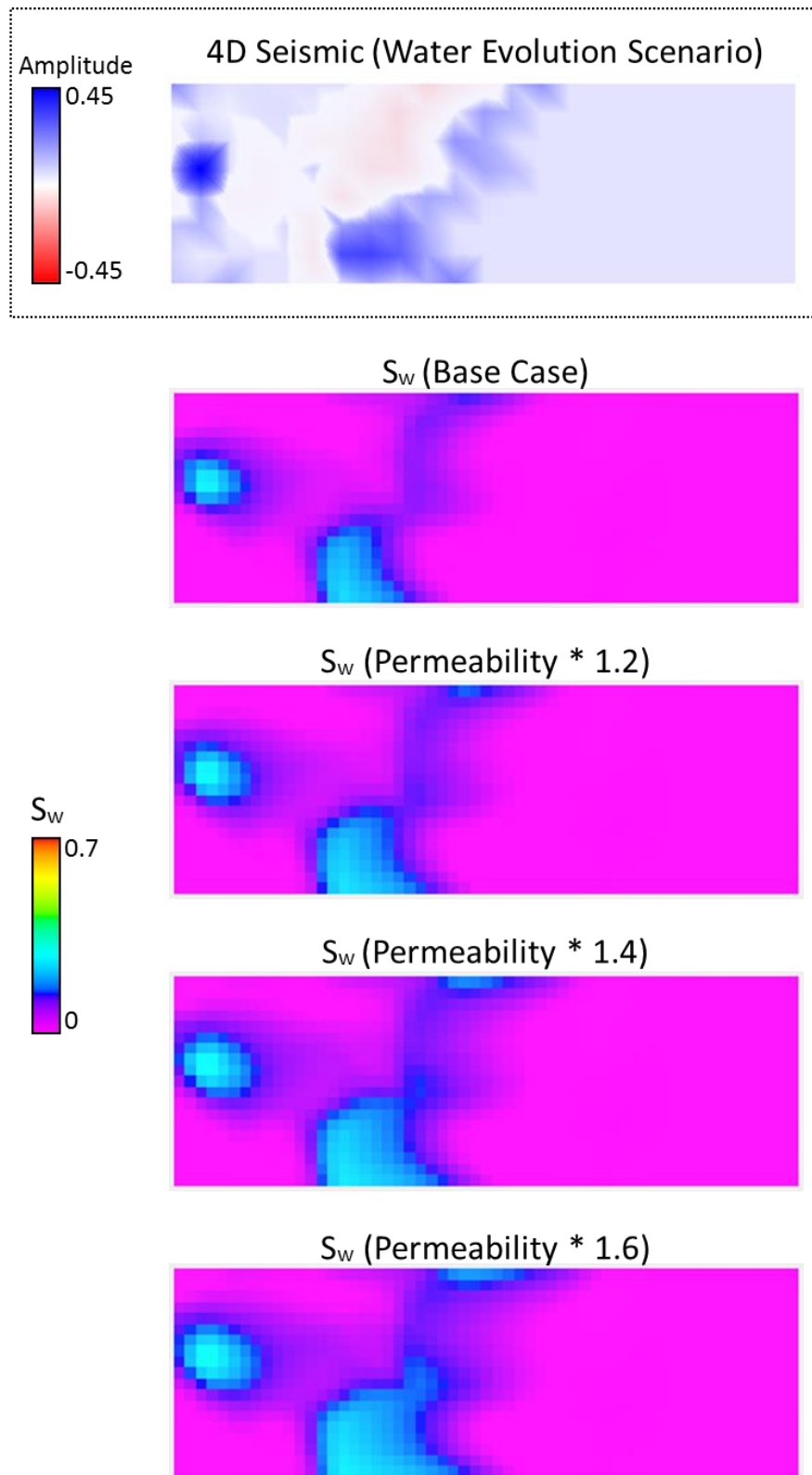


Figure 4.7 The 4D seismic data response of the base case model time-lapse, base case model time-lapse water saturation response, and perturbed models time-lapse water saturation responses for the water evolution scenarios.

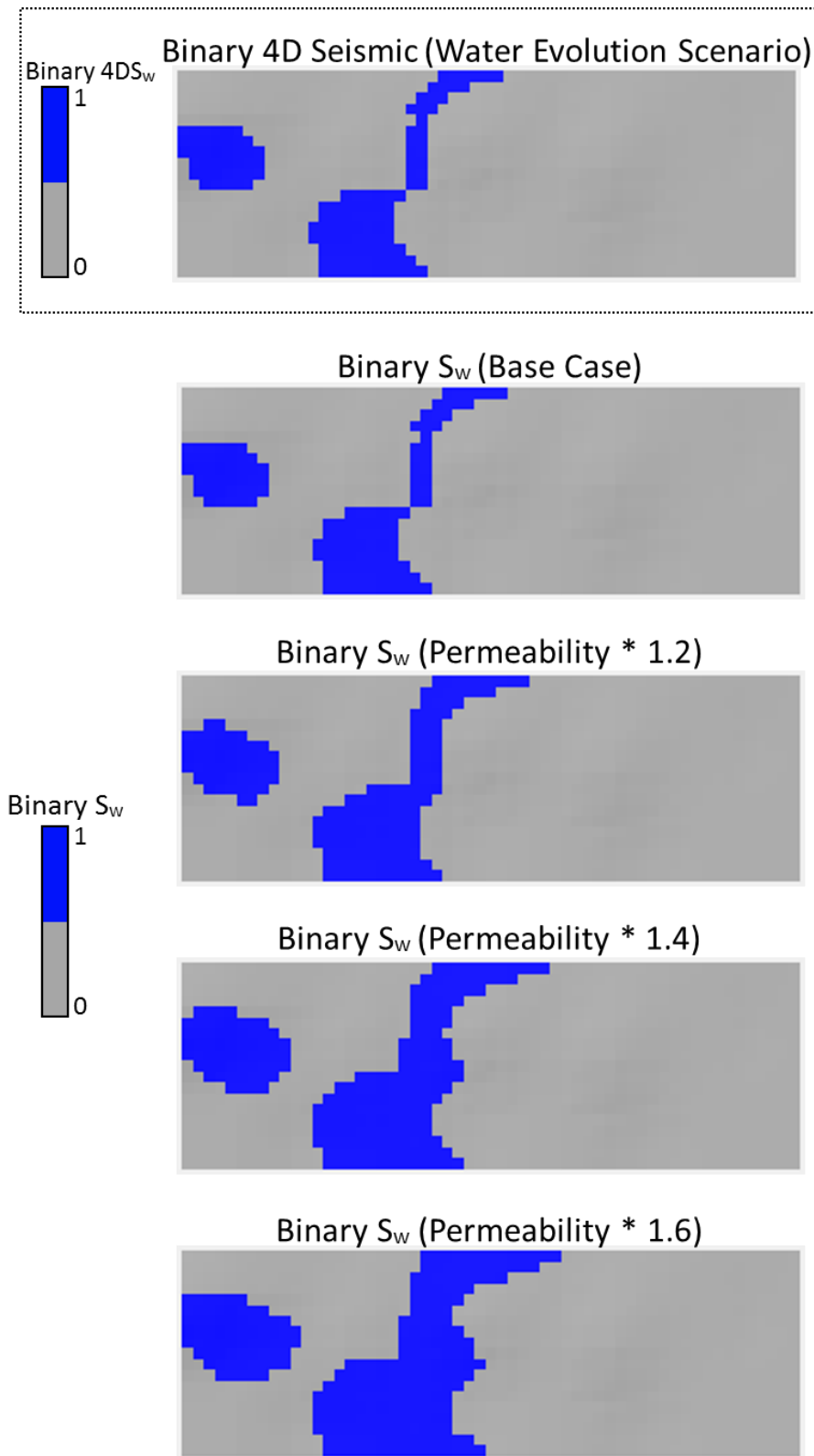


Figure 4.8 The binary water 4D seismic data response of the base case model time-lapse, base case model time-lapse binary water saturation response, and perturbed models time-lapse binary water saturation responses for the water evolution scenarios.

In the base case 4D (monitor minus baseline) model, water saturation increases around the injector well and the oil-water contact. The injector well is perforated along the whole reservoir interval which penetrates both oil and water as was shown in Figure 4.1 and this causes the signal around the injector. The signal further to the right of the injector is the water sweep which occurs due to the density property of water, gravity effect and viscous forces. Perturbing the base case model by incrementally increasing the permeability increases the width of flood front, and these spatial water saturation changes will be analysed by the objective function metrics.

In order to analyse the spatial water saturation changes, the 4D seismic data response of the base case 4D model, base case 4D model water saturation response, and perturbed 4D models (permeability perturbed) water saturation responses are converted into binary maps which are generated using *k*-means clustering. Table 4.2 and Figure 4.9 give the result of comparison of the binary maps. As before, the binary 4D seismic map is compared to the base case binary water saturation 4D map, and to the perturbed binary water saturation 4D maps using the Hamming distance metric and *Current* measurement metric. The model perturbations are labelled E to H, where E is the comparison of the binary 4D seismic map to the base case binary water saturation 4D map which gives a perfect match, through to H which is the comparison of the binary 4D seismic map to the binary water saturation map of the model whose permeability has been multiplied by 1.6 which gives the least perfect match.

The Hamming distance and *Current* measurement metric misfit values have been normalised so as to make them easily comparable, and they both show a similar approximately linear response where perturbation H has the highest misfit, and this gradually reduces to zero for perturbation E which represents the initial base case starting

model. The responses from these metrics indicate that the binary approach can be used to distinguish the scenarios when used as a misfit in the optimisation process. The next line of thought would be to analyse a combination of gas exsolution and water evolution, as this would be a common occurrence in a real reservoir management scheme, and this is what the next section analyses.

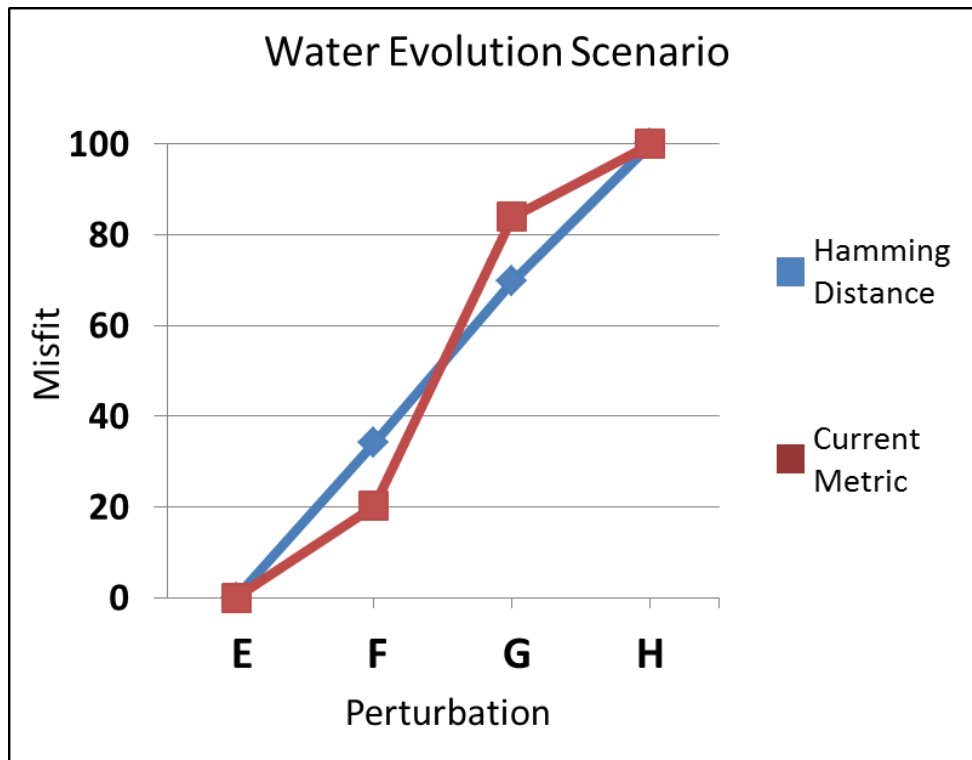


Figure 4.9 The values of the misfit using the Hamming distance and *Current* measurement metric objective function for the different cases of perturbed models shown in Table 4.2 for the water evolution scenarios.

Perturbation	Objective Function	Hamming	Current
E	"Binary (S_w) Base Case" compared to "Binary (S_w) Seismic"	0	0
F	"Binary (S_w) Perm.*1.2" compared to "Binary (S_w) Seismic"	34.11	20.16
G	"Binary (S_w) Perm.*1.4" compared to "Binary (S_w) Seismic"	69.77	83.95
H	"Binary (S_w) Perm.*1.6" compared to "Binary (S_w) Seismic"	100	100

Table 4.2 The Hamming distance and *Current* measurement metric objective function for the different perturbations (E to H) for the water evolution scenarios. The values which have been normalised are plotted in Figure 4.9.

4.4 Combined Gas Exsolution and Water Evolution Scenarios

These scenarios represent a realistic field operational experience where wells are shut-in and put on stream intermittently (probably due to well workover, intervention and testing, or just management planning), and this helps to replicate the simultaneous gas exsolution and water evolution over the time period. There is no initial gas cap as the initial reservoir pressure is above the bubble point pressure. The field operational plan is such that the injector well is put on stream for the first 250 days with a bottom hole pressure upper limit of 2970 psi (20.48 MPa) to enable water sweep, and then shut-in for the subsequent 250 days to allow depressurization of the reservoir and hence gas exsolution. On the other hand, the producer well is put on stream for the first 250 days at a constant liquid rate of 630 stb/day (100 sm^3/day), and then this is increased to a constant liquid rate of 880 stb/day (140 sm^3/day) for the subsequent 250 days in order to enhance the depressurization process and gas exsolution. The field production and seismic acquisition plan is illustrated in Figure 4.10.

For these combined scenarios, the initial simulation model (base case) is perturbed. This is achieved by perturbing the reservoir absolute permeability with multiplier values of 0.8, 0.6 and 0.4. The different simulation model 4D responses represented by pore-volume weighted water saturation maps and gas saturation maps, and the base case model generated 4D synthetic seismic are shown in Figure 4.11. In the base case model time-lapse, water saturation increases around the injector well (which is fully perforated in the reservoir interval) and oil-water contact during the functional years of the injector, and the shape of the front is dictated by gravity and viscous forces effect. Gas is exsolved around the producer as the reservoir goes below the bubble point pressure in the later years when the injector well has been shut-in.

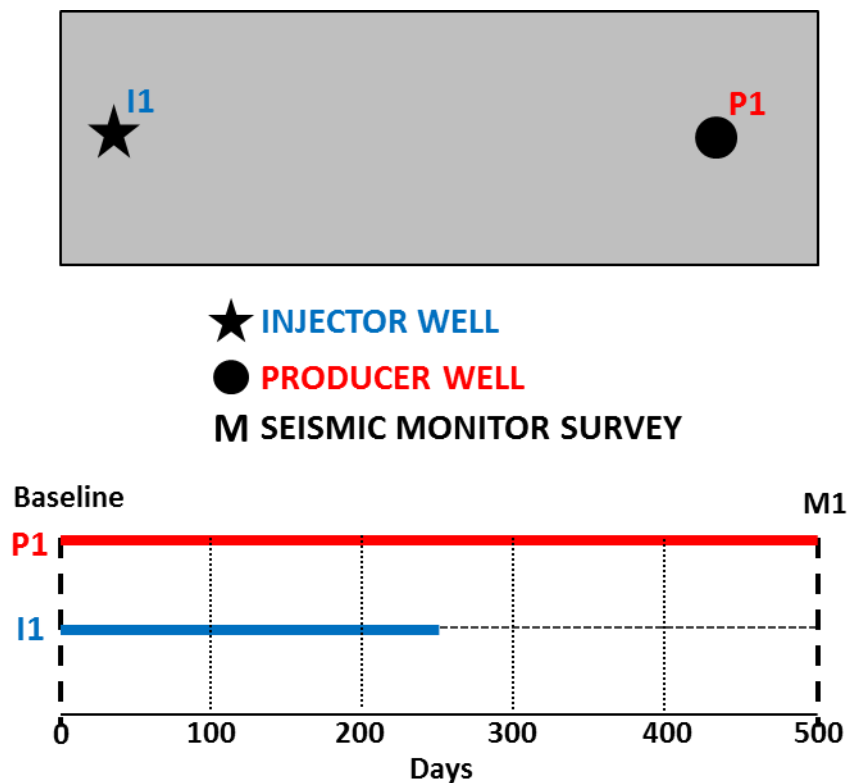


Figure 4.10 An outline of the reservoir, the position of the injector well and producer well, and the timeline of activity of the wells relative to the multiple seismic data surveys for the combined gas exsolution and water evolution scenarios.

Perturbing the base case model by incrementally reducing the overall permeability reduces the water swept from the injector well location and increases the volume of exsolved gas migrating from the producer location. These spatial water and gas changes will be analysed independently and collectively by the objective function metrics. In order to do this, the 4D seismic data response of the base case model time-lapse, base case model time-lapse water saturation and gas saturation response, and perturbed models time-lapse water saturation and gas saturation responses are converted into water binary maps and gas binary maps as shown in Figure 4.12 using *k*-means clustering as described in Chapter 3 and Appendix D.

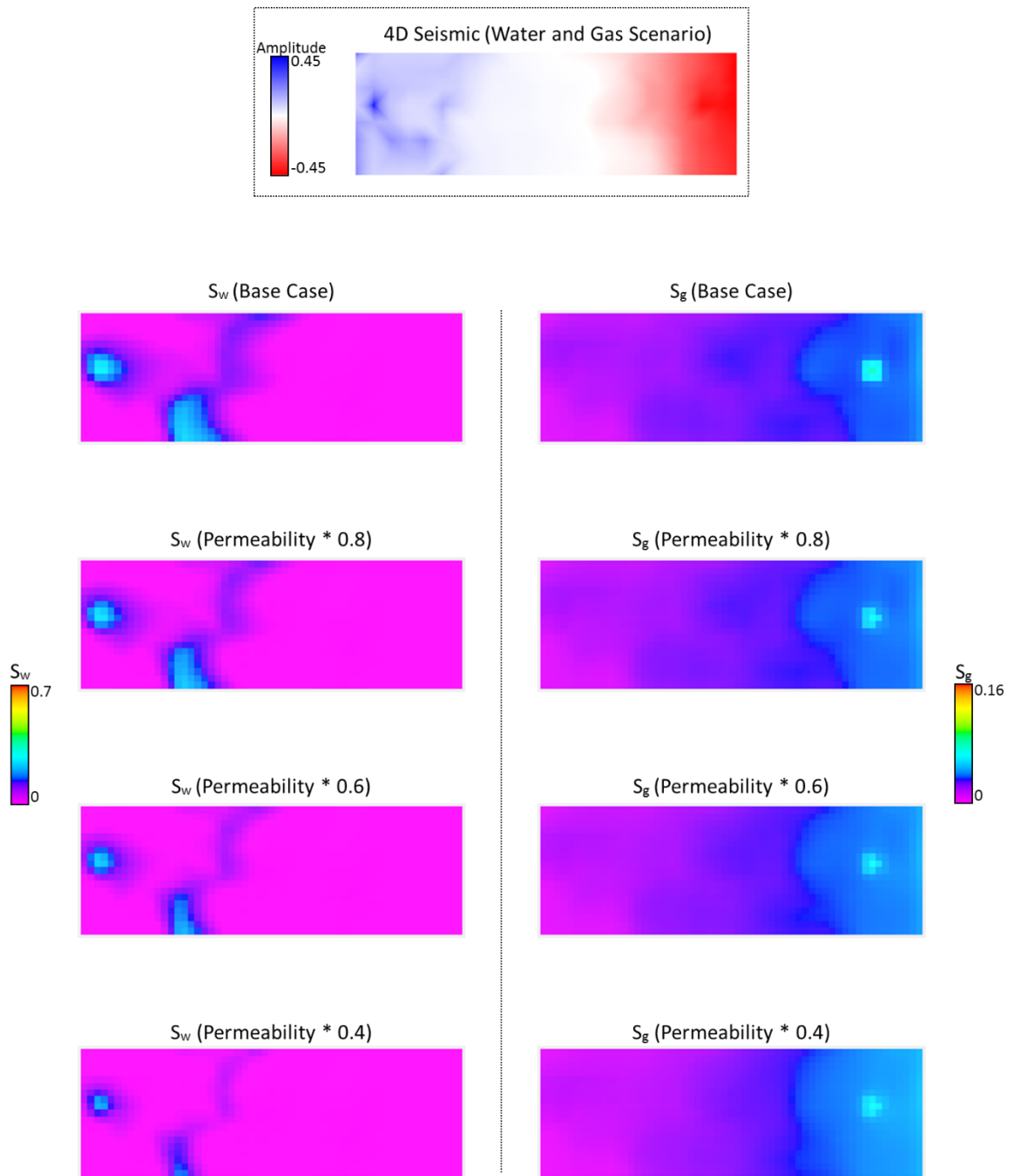


Figure 4.11 The 4D seismic data response of the base case model time-lapse, base case model time-lapse water saturation and gas saturation responses, and perturbed models time-lapse water saturation and gas saturation responses for the combined gas exsolution and water evolution scenarios.

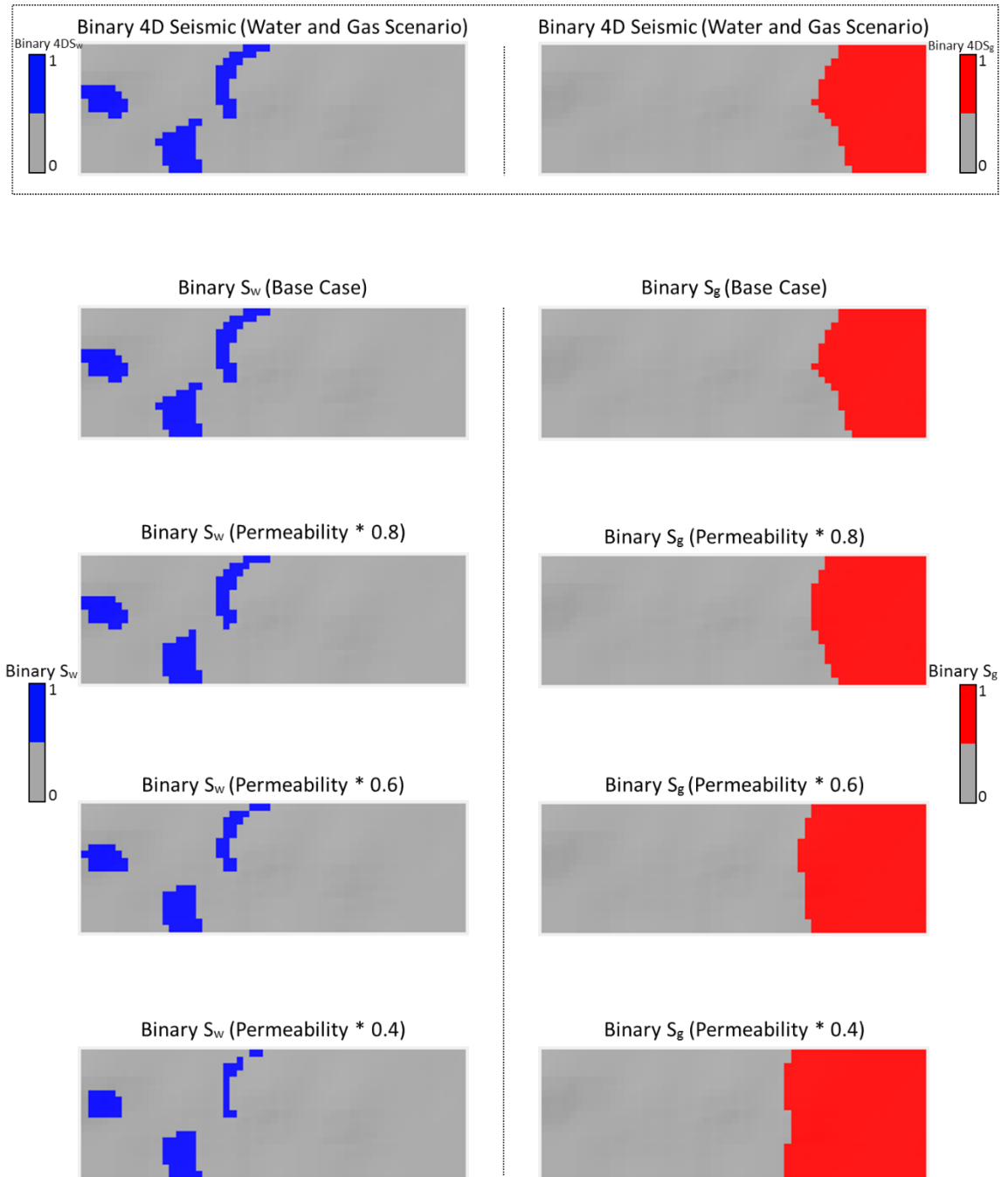


Figure 4.12 The binary water and binary gas 4D seismic data response of the base case model time-lapse, base case model time-lapse binary water saturation and binary gas saturation responses, and perturbed models time-lapse binary water saturation and binary gas saturation responses for the combined gas exsolution and water evolution scenarios.

The “observed” binary 4D seismic map is compared to those predicted from the base case binary water and gas saturation maps, and to the perturbed binary water saturation and binary gas saturation 4D maps using the Hamming distance metric and *Current* measurement metric as shown in Table 4.3 and Figure 4.13. The Hamming distance and *Current* measurement metric misfit values have been normalised so as to make them easily comparable.

Perturbation	Objective Function	H(S _g)	C(S _g)	H(S _w)	C(S _w)	H	C
I	"Binary (S _g and S _w) Base Case" compared to "Binary (S _g and S _w) Seismic"	0	0	0	0	0	0
J	"Binary (S _g and S _w) Perm.*0.8" compared to "Binary (S _g and S _w) Seismic"	26.19	8.20	15.38	4.79	24.34	7.68
K	"Binary (S _g and S _w) Perm.*0.6" compared to "Binary (S _g and S _w) Seismic"	61.11	36.19	50	21.37	59.21	33.93
L	"Binary (S _g and S _w) Perm.*0.4" compared to "Binary (S _g and S _w) Seismic"	100	100	100	100	100	100

Table 4.3 The Hamming distance and *Current* measurement metric objective function for the different perturbations (I to L) for the combined gas exsolution and water evolution scenarios. H(S_g) and C(S_g) are the Hamming distance and *Current* measurement metric for matching to gas only, H(S_w) and C(S_w) are the Hamming distance and *Current* measurement metric for matching to water only, while H and C are the Hamming distance and *Current* measurement metric for matching to gas and water together. The normalised values are plotted in Figure 4.13.

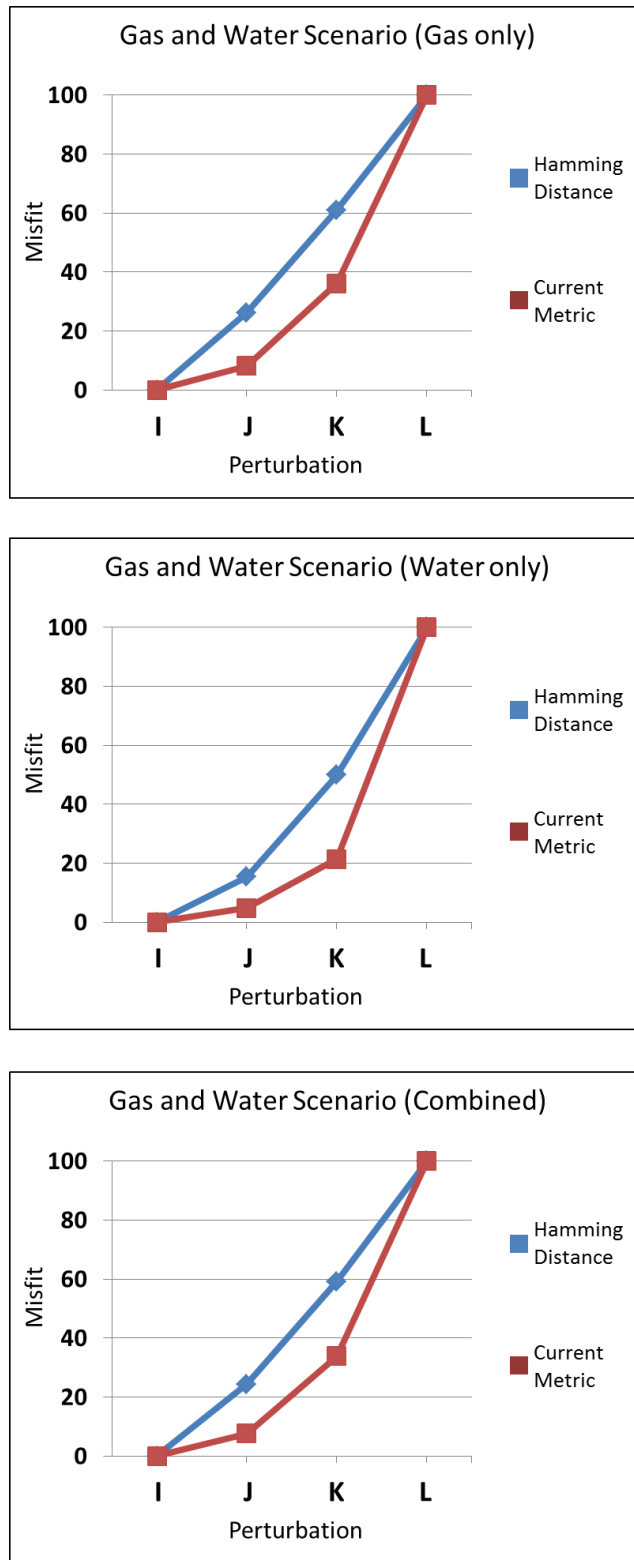


Figure 4.13 The values of the misfit using the Hamming distance and *Current* measurement metric objective function for the different cases of perturbed models shown in Table 4.3 for the combined gas exsolution and water evolution scenarios for matching to gas only, to water only, and to gas and water together.

The perturbations are labelled I to L, where I is the comparison of the binary 4D seismic map to the base case binary water and gas saturation maps which give a perfect match, through to L which is the comparison of the binary 4D seismic map to the binary water and gas saturation map of the model whose permeability has been multiplied by 0.4 which give the least perfect match. Even though this is a joint analysis of water evolution and gas exsolution, their spatial effects are also analysed independently, and the results show a similar trend all through. The Hamming distance has an approximately linear misfit profile, while the *Current* measurement metric has a quadratic misfit profile where perturbation L has the highest misfit. This gradually reduces to zero for perturbation I which represents the initial base case starting model. The responses from these metrics indicate that the binary approach can be used in an optimisation process to distinguish a water evolution and gas exsolution scenario either independently or jointly.

4.5 Summary

This chapter discusses the application of the binary map approach on a synthetic field data where scenarios have been created to mimic real field operational experience. Gas exsolution scenarios, water evolution scenarios, and a combination of gas exsolution and water evolution scenarios have been created and analysed. A mock history matching exercise was carried out by perturbing reservoir parameters that would affect the spatial distribution of the gas and water saturations which have been converted to binary maps using *k*-means clustering algorithm. Using the Hamming distance metric and *Current* measurement metric as objective functions, the similarity or disparity of the perturbed models with respect to a binary 4D synthetic seismic map which was generated from the initial model were assessed. The results using the Hamming distance metric and *Current* measurement metric were similar and promising, as they were able to correctly identify

models that were highly deviated as well as the models that had the right values. The analysis in this chapter validates the competence of the binary approach for a history matching exercise, and this binary approach would be utilised on a real field dataset where the production data will also be taken into account in the subsequent chapters.

Chapter 5

Binary SAHM of Gas and Water in a UKCS Field

This chapter presents seismic assisted history matching of gas and water distributions in a United Kingdom Continental Shelf (UKCS) Field using binary image matching. The Hamming distance and *Current* measurement metric are used to determine the mismatch between the binary seismic and the binary simulation images of saturation (gas and water) distribution predictions. The production data is also matched using the conventional least squares objective function method calculated between the historical production data and the simulation predictions. An initial ensemble of fluid flow simulation models is created where the full range of uncertain parameters are acknowledged using experimental design methods, and an evolutionary algorithm is used for optimization in the history matching process. It is found that the primary control parameters for the binary seismic gas match are the permeability and critical gas saturation, while the volumetric parameters are important for the binary seismic water match in this particular reservoir. It was also observed that to a limit, the global parameters have more effect on the match than the local parameters. The *Current* measurement metric also shows slightly better forecasting ability than the Hamming distance metric.

5.1 Introduction

Reservoir engineers desire the ability to predict the performance of an oil field in an efficient and timely manner; this is coveted as it expedites efficient reservoir monitoring, management, planning and economic evaluation (Obidegwu and MacBeth, 2014b). In order to accomplish this objective, different procedures and mechanisms are employed to acquire, coordinate and interpret data obtained from the reservoir as input to the reservoir simulation model. This model has to confidently replicate the historical data for it to be considered worthy of realistic predictions, and this process of updating the reservoir model to satisfy the historical data is known as history matching.

Over the past years, production data (oil rates, water rates, gas rates, pressure) has been the main historical data available, however, time-lapse (4D) seismic data is now considered a major dynamic input for history matching. There are three main domains (simulation model domain, impedance domain and seismic amplitudes domain) for comparing the 4D seismic data and the simulation model output as explained in chapter one. These domains were shown to use laboratory stress sensitivity coefficients, as well as Gassmann's equation assumptions for their seismic modelling, rock physics modelling or petro-elastic modelling processes, and were complex and time consuming. In order to circumvent these processes, a binary approach of this thesis is adopted, such that the 4D seismic data and simulation data output are converted to binary seismic maps and binary simulation maps respectively. These binary maps are representations of gas and water saturation distributions in the reservoir, and the binary maps from 4D seismic and simulation model are compared in the binary inversion domain as shown in Figure 5.1. The field of interest will now be described in the next section.

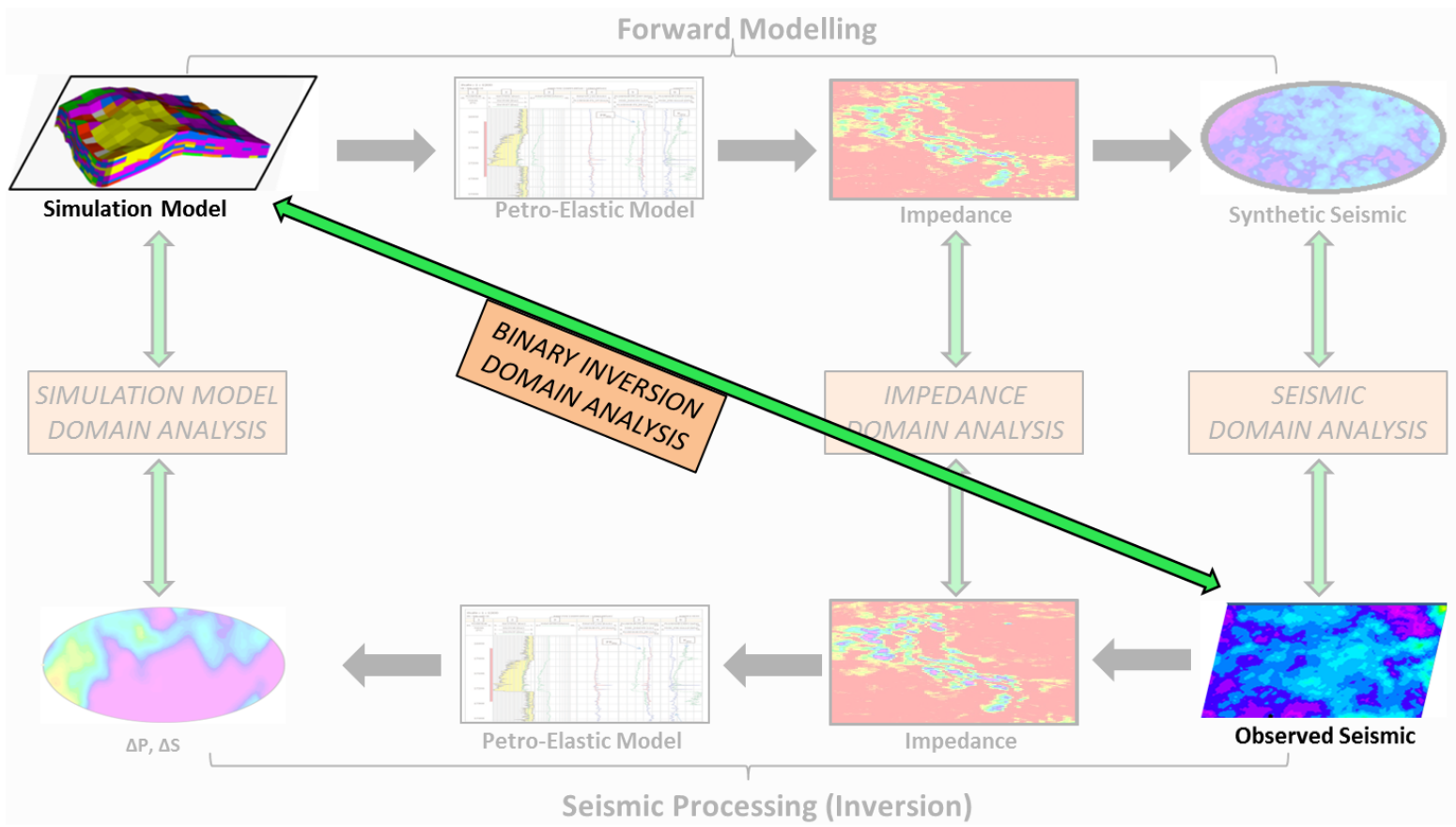


Figure 5.1 Different domains for “closing the loop” highlighting the binary inversion domain

5.2 Field Description

The binary seismic assisted history matching concepts in this thesis will now be applied to a real field data, with the aim of history matching the observed data, as well as forecasting the future production profiles and saturation distributions as a means of validating the new improved models. This history matching technique will be applied using production data only, binary seismic data (gas and water independently) only, and a combination of production data and binary seismic data (gas and water). The field data are located in the UKCS and have been introduced in Chapter 2.

The main features of the data are that the reservoir pressure is close to its bubble point pressure, such that the commencement of production activities will lead to depressurization and gas exsolution, and that there is a subsequent pressure maintenance scheme in place by the use of water injector wells, so there will be water sweep distributions expected in the reservoir. The reservoir permeability is in the range of 200 mD to 2000 mD, with a reservoir porosity ranging from 25% to 30%. The pore compressibility is $7 \times 10^{-6} \text{ psi}^{-1}$, oil viscosity is 3.5 cp at reservoir temperature, water viscosity is 0.5 cp at reservoir temperature, and the oil formation volume factor is 1.16 rb/stb. There are 10 years of production activity from 1998 to 2008, and it should be noted that the history matching will be implemented for the first 7 years, while the remaining 3 years will be used to validate the history matching process and forecasting ability. It should be noted that the 3 years used for the forecasting analysis is not really forecast per se, but observed historical data which is just used to validate the conducted history matching exercise. The simulation model was provided by the data provider, and its dynamic properties will be discussed in the next section.

5.3 Simulation Model Conditioning

The simulation model has dimensions of approximately 9600 metres by 4900 metres by 700 metres, and has 128 cells by 53 cells by 35 cells in the X, Y and Z direction respectively. The simulation model runtime on a standard computer workstation (Intel CPU E5-1650 @ 3.20GHz) with 6 processors is approximately 5 hours. This computer specification will be used all through this analysis. In order to efficiently generate multiple runs of the model which is required in a history matching process, the runtime has to be reduced to an appreciable level; however this has to be achieved without distorting the output results, as the simulation model may give non-physical results if too coarse a grid is used (Carlson, 2003). The initial model is modified and upscaled to different levels of coarseness shown in Table 5.1 and Figure 5.2, and the output results are validated against the initial model output. The upscaling process involves rebuilding the grid structure to a coarser mesh, and using pore volume weighted averaging for the volumetric parameters, and flow based upscaling for the transmissibility parameters.

Table 5.1 shows the different models (model 1 to 7) that were created, their cell dimensions, their simulation runtime, and their least squares error misfits relative to the initial model. The total spatial misfit was calculated for pressure distribution, water saturation distribution and gas saturation distribution in the field (Figure 5.2(a)), while the total well data misfit was calculated for oil production, gas production, water production and field pressure (Figure 5.2(b)). All these outputs were combined equally to generate the combined misfit. The measurement analysis of the different misfit is shown in Appendix E. Figure 5.2(c) shows the total spatial misfit, total well data misfit and the combined misfit for the model outputs plotted against simulation model runtime.

	Cell Dimensions	Runtime (Mins)	Spatial Misfit	Well Data Misfit	Combined Misfit
Base case	128*53*35	295.24	0	0	0
Model 1	32*53*07	1.03	0.5066	0.5539	0.3073
Model 2	64*27*17	7.01	0.4372	0.6084	0.2978
Model 3	32*53*35	8.27	0.4942	0.6484	0.3268
Model 4	128*53*07	9.21	0.4150	0.6234	0.2942
Model 5	64*27*35	9.45	0.3919	0.5239	0.2616
Model 6	64*53*35	28.34	0.3597	0.4995	0.2448
Model 7	128*27*35	40.94	0.3953	0.5424	0.2674

Table 5.1 The parameters of the different upscaled models as compared to the initial model. Model 5 was selected as the most suitable model for the history matching exercise in terms of run time efficiency and simulation accuracy. The measurement analysis of the different misfit is in Appendix E.

Model 5 was selected as the most suitable model for the history matching exercise in terms of runtime efficiency and simulation accuracy. It was upscaled laterally by a factor of 4, such that its vertical heterogeneity is preserved and the material balance in the model is conserved so as to maintain the characteristics of the field geology and reservoir quality (King, 2007). Inasmuch as model 5 does not have the lowest misfit or the fastest runtime, its selection makes the point that there often needs to be a trade-off between simulation model output accuracy and simulation model runtime in every upscaling exercise as highlighted by Maschio and Schiozer (2003), who state that the loss of information is inevitable using any upscaling technique, and that the two key aspects that must be taken into account are the agreement of the results obtained from the upscaled model when compared to the initial model, and the upscaling computational performance. Having conditioned the simulation model to an acceptable runtime for history matching, the 4D seismic data is now conditioned to be an input in the history matching process.

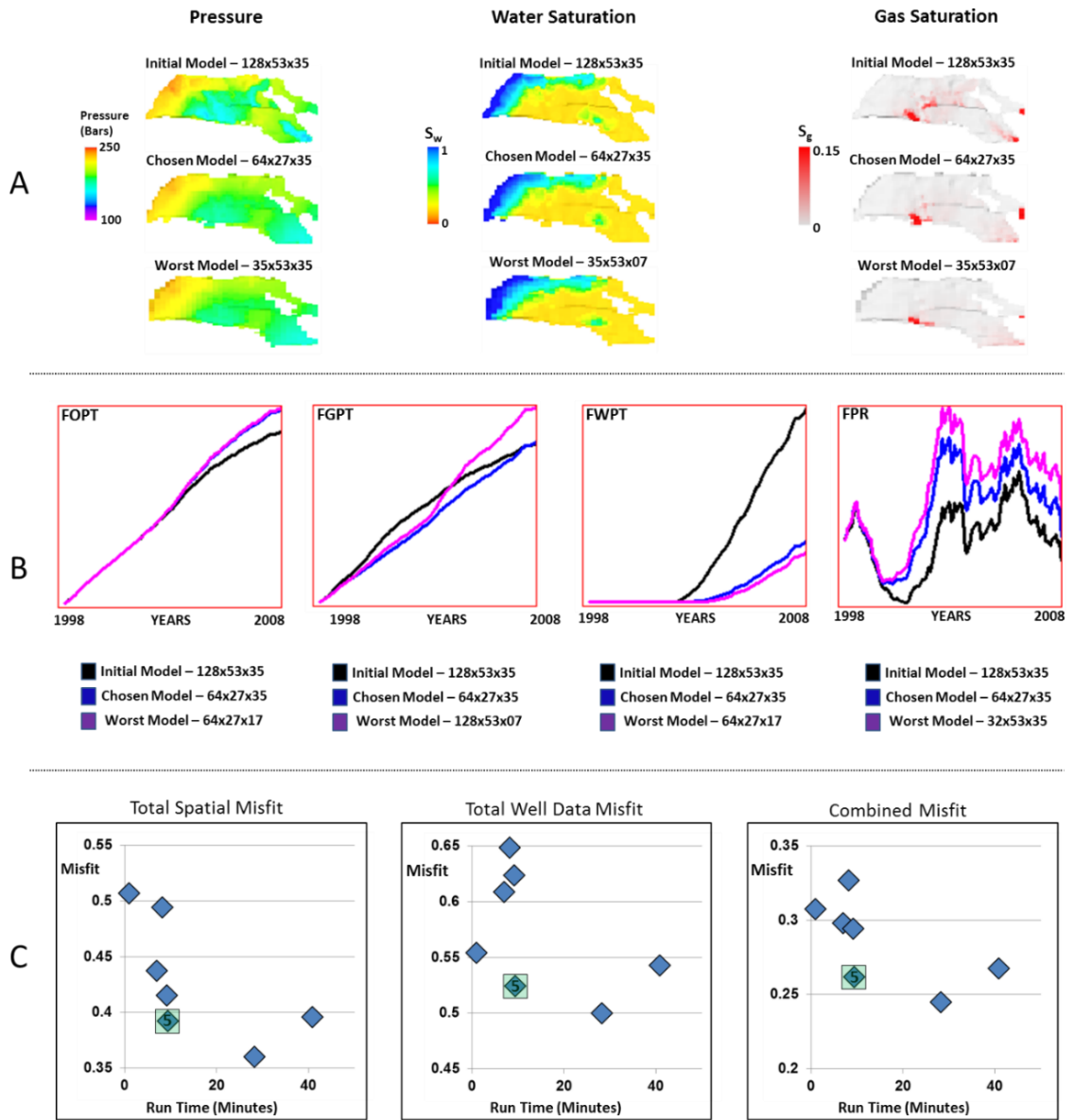


Figure 5.2 (a) The pressure, water saturation and gas saturation maps for the initial base case model, the chosen model (model 5), and the worst case model after upscaling (b) shows the cumulative field oil production, cumulative field gas production, cumulative field water production and field average pressure for the initial base case model, the chosen model (model 5), and the worst case model after upscaling (c) shows the total spatial misfit, total well data misfit, and the combined misfit versus simulation runtime for all the upscaled models highlighting the chosen model 5 in a light green square.

5.4 4D Seismic Data Conditioning

The notion of 4D seismic data integration is to complement production data. This is because 4D seismic data has high spatial and low temporal frequency while production data has low spatial and high temporal frequency (Jin et al., 2012b). In order to integrate the 4D seismic data into the history matching workflow, a binary approach has been proposed. This is because the use of conventional least squares formulation for computing production data objective function and misfit has been shown to be suitable and efficient (Bertolini and Schiozer, 2011, Oliver and Chen, 2011), such that it can be significantly reduced during the history matching process, and properly characterizes the error between the simulated data and the real data (Tillier et al., 2013); however, applying the least squares formulation to compute the seismic objective function and mismatch has been shown to be unsuitable because of the nature of seismic data (Aanonsen et al., 2003, Le Ravalec et al., 2012a, Roggero et al., 2012, Tillier et al., 2013).

5.4.1 Clustering and Thresholding

The proposed approach is such that the observed 4D seismic data is converted to binary seismic gas and water maps. The observed 4D seismic data is initially clustered and separated into ‘softening’ and ‘hardening’ signals; historical production data are then superimposed on the maps to aid the interpretation and deciphering of potential gas and water signals due to the injector/producer positioning, as well as the volumes produced which are represented by the size of the bubble plots. Application of these processes leads to the final binary seismic gas and water maps as shown in Figure 5.3.

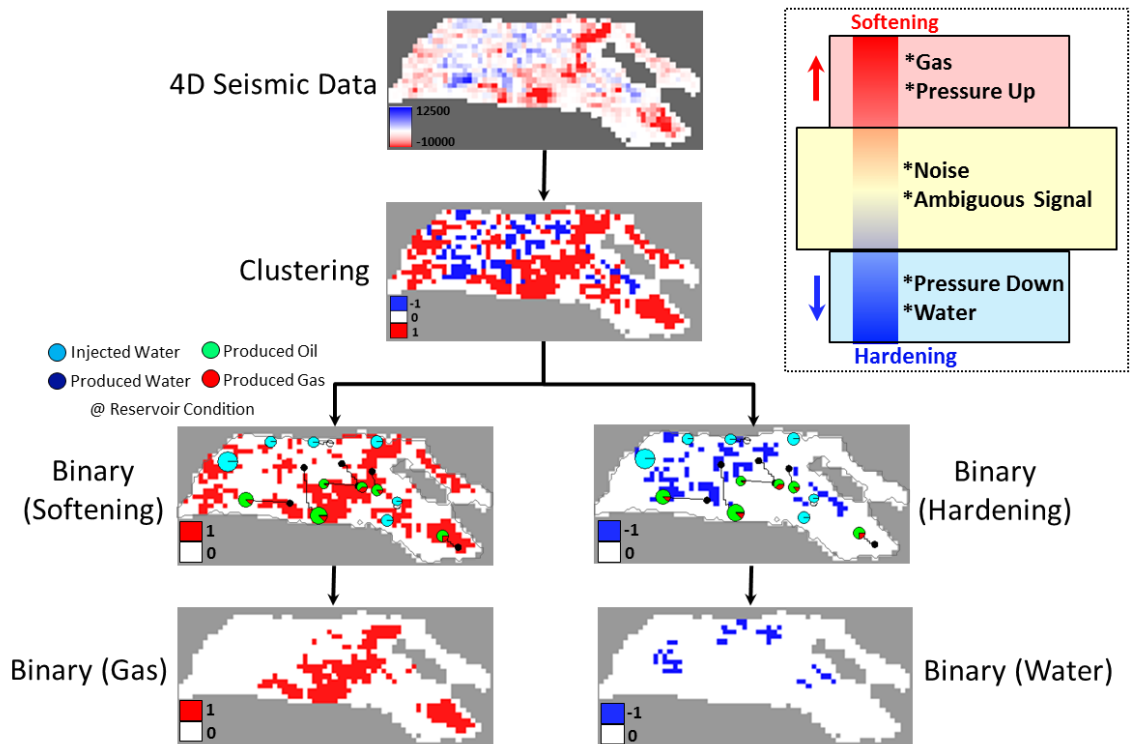


Figure 5.3 The process of generating the binary (gas and water) maps from the 4D seismic data. The 4D seismic data are initially clustered and separated into ‘hardening’ and ‘softening’ signals; historical production data are then introduced to aid the interpretation and deciphering of potential gas and water signals due to the injector/producer positioning, as well as the volumes produced which are represented by the size of the bubble plots. Application of these processes leads to the final seismic binary gas and water maps. Inset shows the 4D seismic colour bar and the associated physical interpretation.

The softening and hardening signals on seismic are represented by red and blue colours respectively. The softening signal is as a consequence of pressure increase or gas saturation increase. In broad terms, a drainage process will give rise to a softening signal due to the different elastic properties of the fluids, as a non-wetting phase fluid displaces a wetting phase fluid, i.e. gas displacing oil or water, or oil displacing water. Conversely, a hardening signal is as a consequence of pressure decrease or an imbibition process, where a wetting phase fluid displaces a non-wetting phase fluid, i.e. water displacing oil or gas, or oil displacing gas. Figure 5.3 highlights an example of generating the binary maps from

4D seismic data, by clustering the 4D seismic data into “hardening” and “softening” signals (e.g. using *k*-means clustering), and then interpreting the binary gas and water signals with a validation from the activities of the injection and producer wells. The cross-effect of water saturation, gas saturation and pressure signals in the 4D seismic data will likely be characterised in the “ambiguous signal” region (shown on the colour bar in Figure 5.3), and will therefore not be captured by the binary approach.

For binary seismic gas and water maps, a change in the saturation values are represented by a value of one, while no change is represented by a value of zero. A region exists that is characterised as ambiguous signal or noise, and this is not captured by this binary approach. The pore volume weighted gas and pore volume weighted water saturation difference maps (monitor year minus baseline year) are also generated from the simulation model and then converted to binary simulation gas and water maps, where a value of one represents presence of gas or water respectively, and zero represents an absence of gas and water respectively. The binary seismic maps (gas and water) are then compared to those predicted from the simulation maps using a binary seismic objective function. The objective function is calculated on the simulation model scale, so the 4D seismic data is arithmetically upscaled to the simulation model scale.

In order to convert the pore-volume weighted gas and water saturation from the simulation model and the 4D seismic data to binary maps, cut-off values representing thresholds need to be obtained. These can be derived from a calibration exercise using seismic forward modelling, or by interactive interpretation which requires a clear understanding of the 4D seismic response in terms of the dynamic behaviour of the reservoir (Jin et al., 2012b). A combination of both methods is utilised, where seismic forward modelling is used to determine the initial threshold values in collaboration with *k*-

means clustering (Appendix D); then integration of reservoir engineering knowledge, injector and producer well activities, reservoir geology and structural contour, as well as 4D seismic concepts are applied to generate the binary seismic maps (Figure 5.3).

The procedure for interpreting a suitable threshold is shown below:

- a. To interpret as exsolved gas, the reservoir pressure should be below bubble point pressure, or at least should have previously been below bubble point pressure, so that there will be gas (exsolved gas) present in the reservoir.
- b. The presence of gas signal around a producer well is validated from gas production profile of the well.
- c. The gas may be present at expected locations, for example at local structural highs.
- d. The presence of water is expected around water injector wells
- e. Being aware that amplitude decrease (softening) in the 4D seismic data is as a consequence of gas, as well as pressure increase (Calvert et al., 2014), the amplitude decrease caused by an increase in pressure around a water injection well is removed from the analysis; however in the case of a gas injector well (where an increase in pressure and the presence of gas cause the same softening effect on seismic data), the magnitude of the pressure and gas saturation will need to be determined in order to ascertain which has a more dominant effect on the seismic data. It should be noted that there are no gas injector wells in the data provided for this reservoir of interest.
- f. The same as above applies to an amplitude increase (hardening) in the 4D seismic data, which can be as a consequence of water saturation or

pressure decrease, as it is unlikely for injected water to coincide with a pressure decrease; hence any hardening signal that is not around an injector well is ignored.

5.5 Binary Objective Function

The Hamming distance and the *Current* measurement metric are used as the binary seismic objective function independently to quantify the dissimilarity between the binary simulated pore-volume weighted saturation difference map and the binary 4D seismic data difference map. Some of the advantages of this approach are that it eliminates the magnitude of the difference in values of the simulator output and the seismic data (i.e. the gas saturation difference maximum range value is 100, while that of the 4D seismic difference amplitudes can be more than 10000), it bypasses the complex petro-elastic model procedure, it provides a means of comparing the observed seismic data to the simulation model output, and that it is fast and effective.

The selection of appropriate weight coefficient values for obtaining the objective function is usually driven by reservoir engineering experience and can be case dependent (Tillier et al., 2012). For the production data, the practice of boosting the effects of the ill-fitted production data is adopted, and this is done by selecting the weights as being proportional to the square of the difference between the data computed for the base case model and the observed data (Kretz et al., 2004); while the binary seismic data are equally weighted. The combined production data and 4D seismic data objective function is normalized (Kretz et al., 2004) such that at the beginning of the history match, the combined misfit is a value of one.

5.6 Setting the Scene

To perform the history match, an initial ensemble of models is created using the Latin Hypercube Experimental Design (LHED) method (Roggero et al., 2007), as multiple models have extensive coverage of the search space and deliver robust results. The initial input parameter sampling is important, and is usually carried out using experimental design methods, such as Plackett-Burman, LHED or Factorial Design (Schulze-Riegert and Ghedan, 2007, Zubarev, 2009). The LHED is a statistical method for generating a sample of plausible collections of parameter values from a multidimensional distribution, and it is useful for exploring the uncertainty range (Schulze-Riegert and Ghedan, 2007, Risso et al., 2011, Maschio and Schiozer, 2014).

An optimisation algorithm is required for the optimization process in order to calibrate the uncertain values in the reservoir. The optimisation algorithm has to be transparent, robust with suitable performance, deliver reproducible results and solutions within the uncertainty framework, and be simple to understand and implement (Schulze-Riegert and Ghedan, 2007). The evolutionary algorithm satisfies these conditions, and covers a broad application area, and has been used extensively for reservoir history matching (Bäck, 1996, Soleng, 1999, Romero et al., 2000, Williams et al., 2004, Schulze-Riegert and Ghedan, 2007, Maschio et al., 2008, Aranha et al., 2015). It is a derivative-free optimisation method, as it does not require the computation of the gradient in the optimisation problem (which will require access to the simulator source code), and utilises only the objective function value to determine new search steps. The basic outline of the evolutionary algorithm is based on the notion of Darwinian evolution where natural selection inspires “survival of the fittest” which leads to an increase in population fitness. The selection of new search steps are generated by applying recombination and mutation

operators which generate new set of outputs. Based on their fitness, some of the outputs from the previous generation are considered for the next generation, and this process continues until outputs with sufficient fitness are found (Schulze-Riegert and Ghedan, 2007) (Figure 5.4).

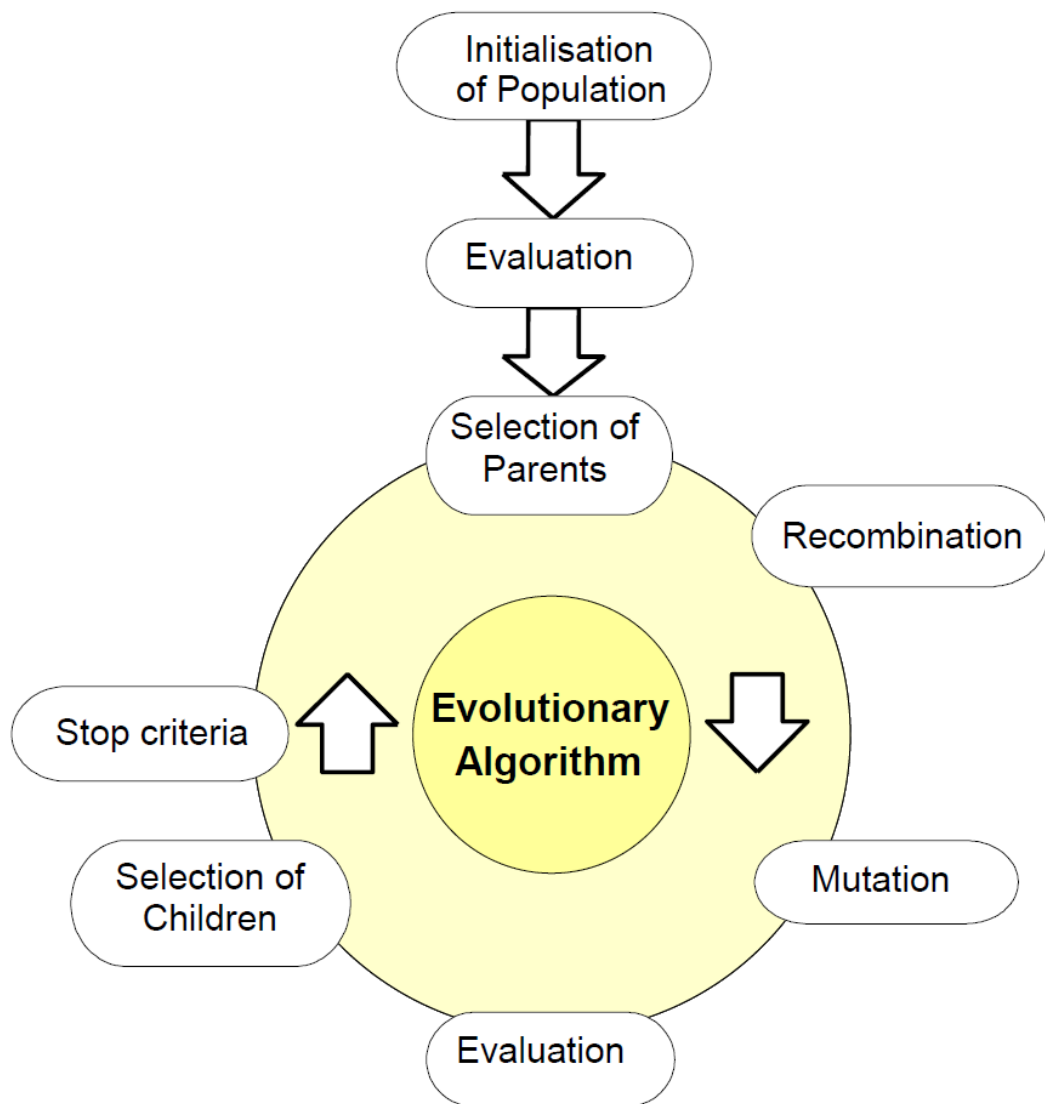


Figure 5.4 Evolution algorithm workflow (Schulze-Riegert and Ghedan, 2007).

In history matching, the termination criteria which signifies the completion of the exercise is usually until the objective function is small enough, convergence is obtained, or the number of iterations exceeds a maximum value (Tillier et al., 2012). The termination criteria used in this work is the convergence criteria. When convergence of the objective function is achieved, an improved set of models and their accompanying uncertainty is generated. The uncertainty is generated as a function of the variation in the response parameters. The probability redistribution of the a priori uncertain parameters reduces the spread of the a posteriori distribution, and as a direct consequence, reduces the dispersion of the reservoir response parameters, hence mitigating risk and uncertainty (Maschio and Schiozer, 2014).

One of the advantages of using this approach is that multiple initial realizations can be updated to match the same dynamic data to assess uncertainty reduction in the reservoir characterization due to the integration of dynamic data, and this is similar to the randomized maximum likelihood method (Liu et al., 2001, Wen et al., 2006). As has been mentioned, the history matching exercise will be applied using production data only, binary seismic data (gas and water independently) only, and a combination of production data and binary seismic data (gas and water). Figure 5.5 shows the workflow for the binary seismic assisted history matching which has been developed using Python programming language (Appendix F) and MEPO software.

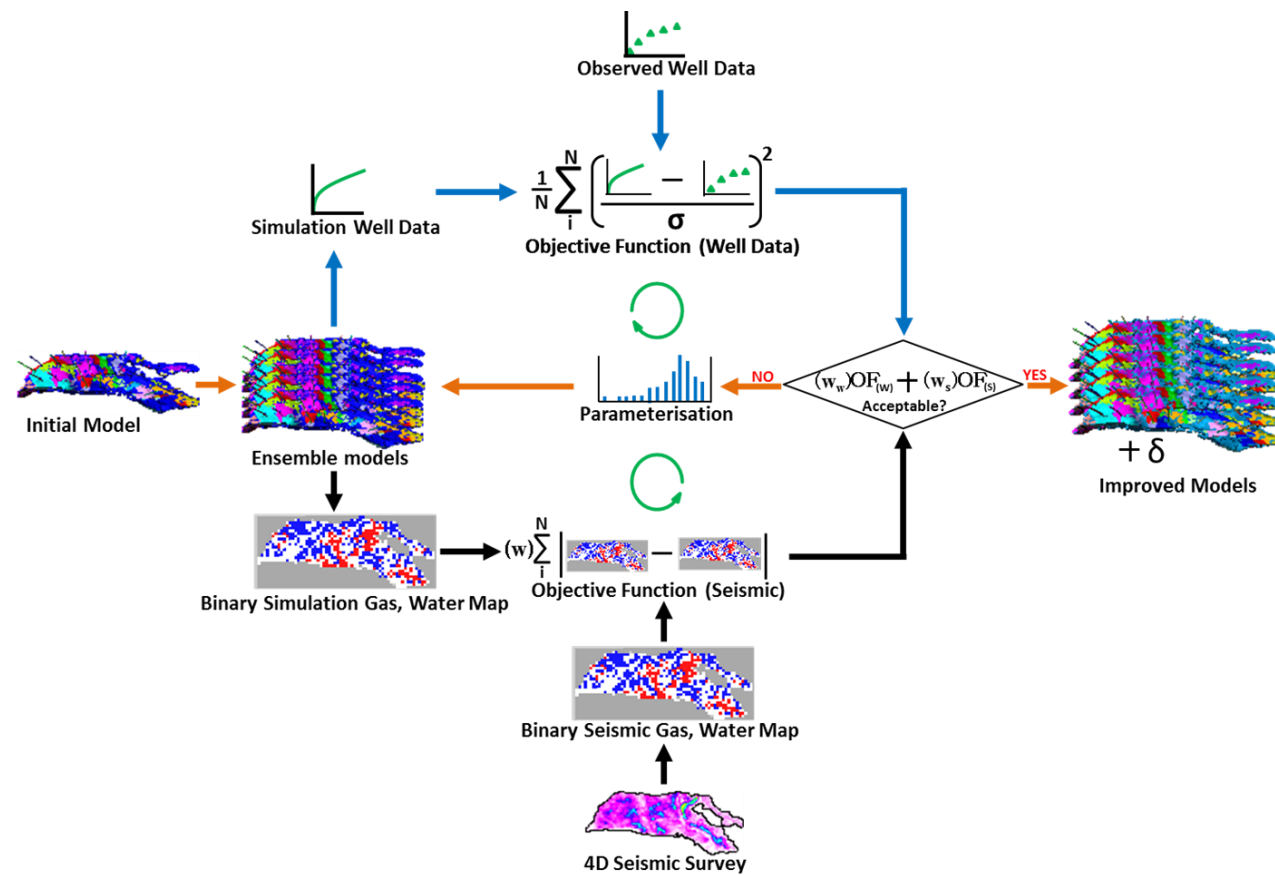


Figure 5.5 Seismic Assisted History Matching Workflow - combining the production data with the time-lapse seismic data. The blue arrows (upper part) highlight the production history match loop; the black arrows (lower part) highlight the seismic history match loop; the orange arrows (middle part) showcases their individual or combined path; while the green arrows (circular arrows) shows the direction of the loop.

5.7 Model Parameterisation

In order to proceed in a history matching exercise, pertinent reservoir parameters have to be perturbed. Over the years of production in this reservoir, it has been observed that the major challenges to the field development and management plan are the field connectivity and the representation of its numerous geobodies. These geobodies were derived from the 3D seismic interpretation and used for geological model construction. A sensitivity study starting with 104 parameters was carried out to determine which parameters and geobodies were most significant to the seismic assisted history matching objective function.

Figure 5.6 shows the top 7 most significant parameters of the sensitivity analysis for gas production, oil production and water production for wells P1 and P2 which would be used for the history matching study, as well as the binary gas and water maps. Combining the geobody regions and global parameters, 35 parameters were identified for the history matching exercise. These include the permeability multipliers, porosity multipliers, net-to-gross multipliers, pore volume multipliers, geobody transmissibility multipliers, connate water saturation and critical gas saturation. Table 5.2 shows all the parameters and the ranges used. The starting values of the parameters are the initial values, while the ranges are selected generally based on engineering judgement, and such that the perturbed model remains physically and geologically meaningful and consistent with the initial understanding of the field.

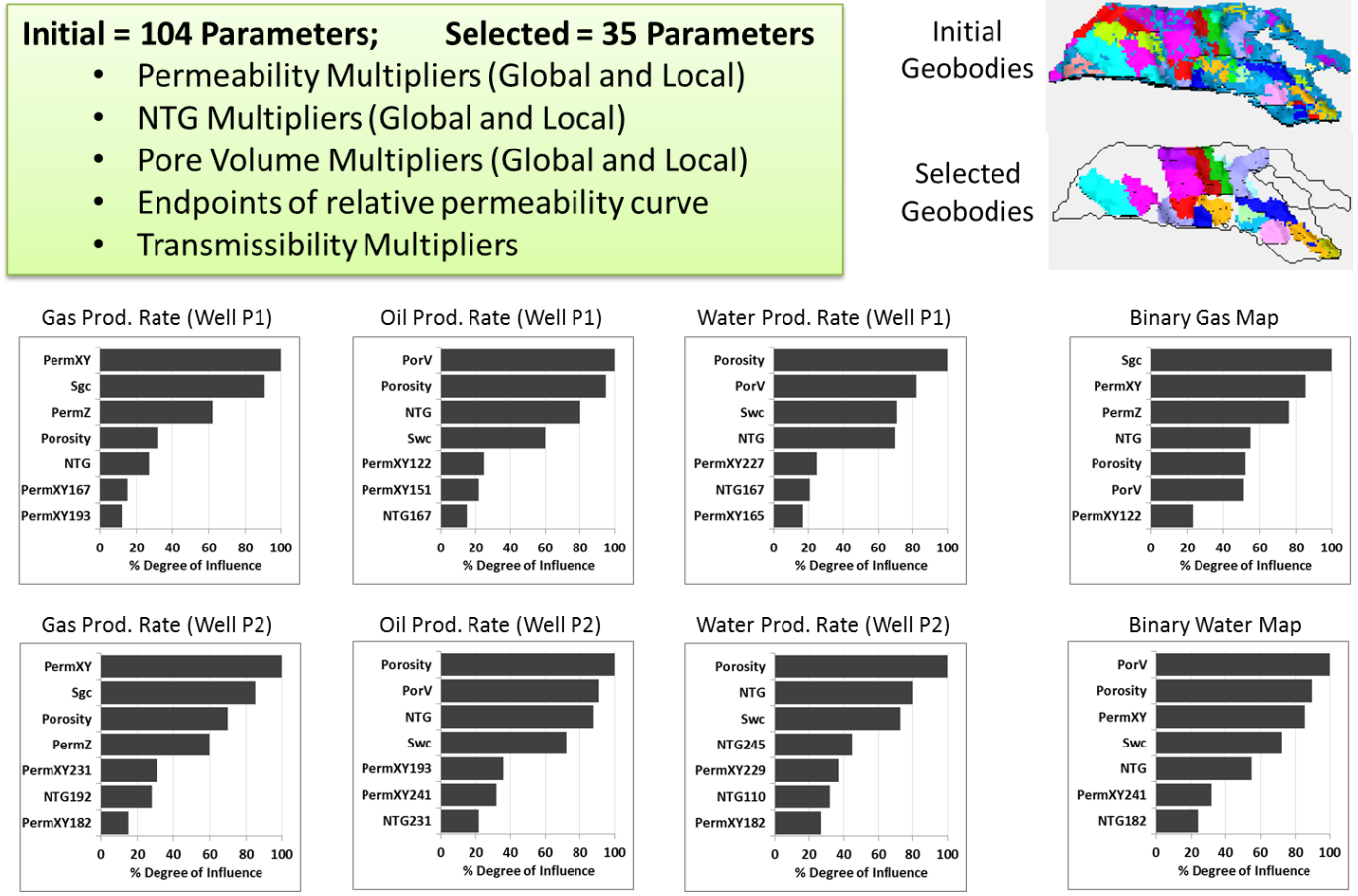


Figure 5.6 The sensitivity analysis of the initial 104 parameters to the production data (oil, gas and water) of wells P1 and P2, and also to the binary gas and water maps. The most sensitivity parameters are shown (top seven). From these parameters, 35 are selected for the history matching exercise. Also shown are the initial geobodies, and the selected geobodies after the sensitivity analysis.

Parameters	Number	Lower Limit	Start Value	Upper Limit
Global NTG Multiplier	1	0.35	1	2
Global Perm. Multiplier	3	0.35	1	5
Global Poro. Multiplier	1	0.35	1	2
Global Pore Vol. Multiplier	1	0.35	1	2
Transmissibility Multiplier	3	0	1	3
Regional NTG Multiplier	7	0.35	1	2
Regional Perm. Multiplier	14	0.35	1	5
Regional Pore Vol. Multiplier	3	0.35	1	2
Critical Water Saturation	1	0.4	0.428	0.5
Critical Gas Saturation	1	0	0.001	0.05
Total Number of Parameters	35			

Table 5.2 Model Parameterization for history matching the reservoir. The global parameters are parameters that are perturbed over the entire reservoir, while the regional parameters are parameters that are perturbed over selected regions/geobodies.

The upper limit of the volumetric parameter multipliers (NTG, porosity, pore volume) is twice their initial value, which is quite high but explores such possibilities, while the lower limit is 0.35, such that the reservoir cells are not de-activated. The upper limit of the transmissibility multiplier is three times the initial value, while the lower limit is zero, thus preventing any flow or communication across the transmissible boundary. The upper limit of the permeability multiplier is 5, while the lower limit is 0.35. The upper limit of the critical water saturation, which is the saturation at which the water would gain mobility is 0.5, while the lower limit is 0.4. The upper limit of the critical gas saturation, which is the saturation at which the gas would gain mobility is 0.05, while the lower limit is 0, which implies that at the point of gas exsolution, the gas becomes mobile immediately.

5.8 Application of Binary SAHM

The initial state of the reservoir and base case conditions of the history matching process are shown in Figures 5.7, 5.8 and 5.9. Figure 5.9 shows the observed data, the base case model and the initial ensemble of the response parameters (oil production rate, gas production rate and water production rate) of wells P1 and P2 which have been selected for this history matching exercise due to the location and availability of historical data. The observed data represents data measured at the wells, the base case represents the initial model's production profile, while the initial ensemble represents profiles for the models generated using the Latin Hypercube Experimental Design which encompasses the effects of the defined uncertain parameters.

The observed oil production rate and gas production rate of producer well P1 drops continuously for the first 3 years until an improved oil recovery plan is put in place by introducing an injector well to provide pressure support as well as water to sweep the oil. This action stabilizes the production rate for the subsequent years. The same trend is observed for producer well P2, however the oil production rate drops continuously for the first 4 years until an inefficient injector well is replaced. The introduction of the new injector well boosts and maintains the oil production rate for the subsequent years until it gently declines.

The gas production rate of producer well P2 is high for the first 4 years as there is gas exsolution in the reservoir due to poor pressure maintenance; when this is curbed by introducing an injector well, the gas production rate drops and declines in the subsequent years. There is also uncertainty on some sporadic high values of gas production rate on

producer well P2 which can potentially be attributed to noise errors (e.g. faulty gauge or just inaccurate readings) The water production in wells P1 and P2 occurs significantly in the later years due to a rise in water cut from the water swept from the injector wells.

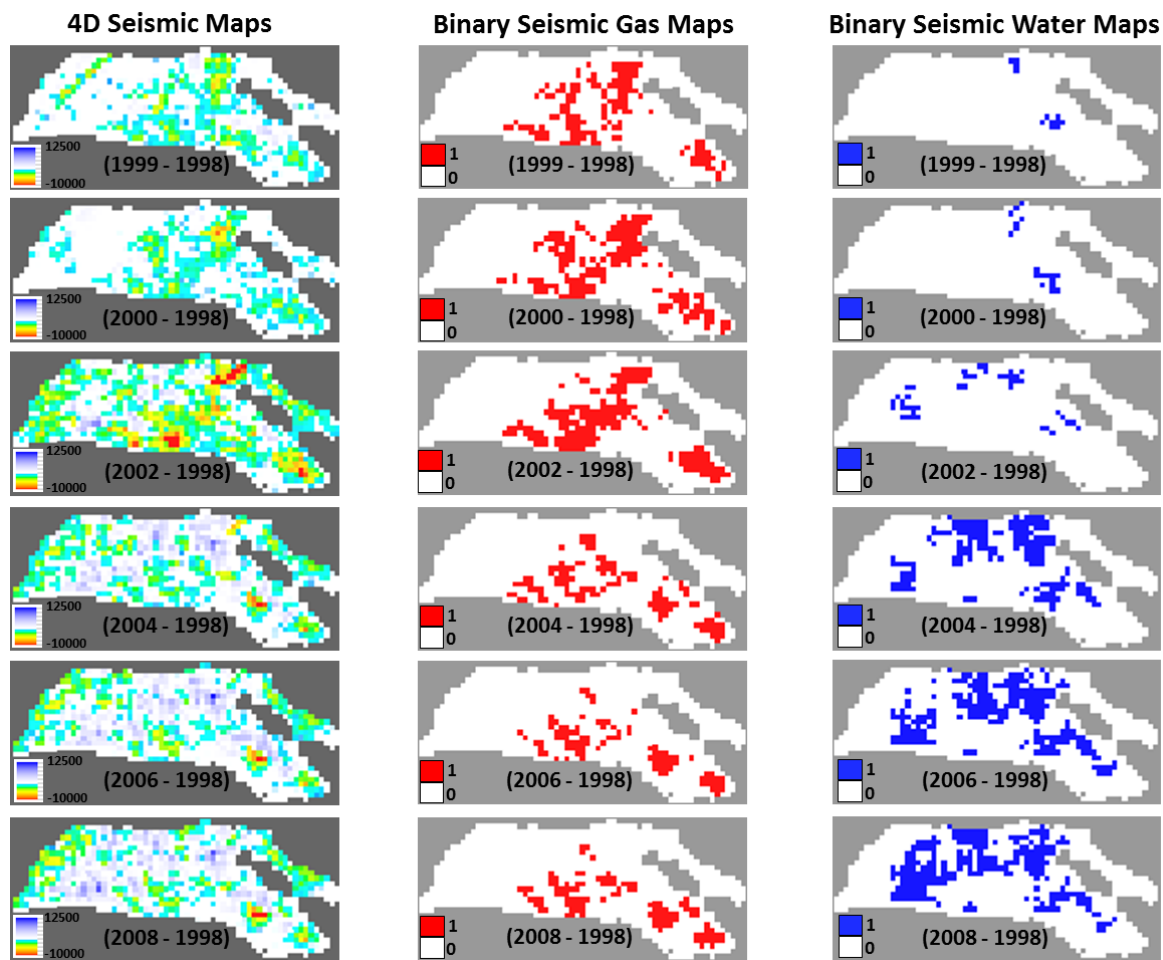


Figure 5.7 The binary (gas and water) maps have been generated from the 4D seismic data for all the relevant time-steps.

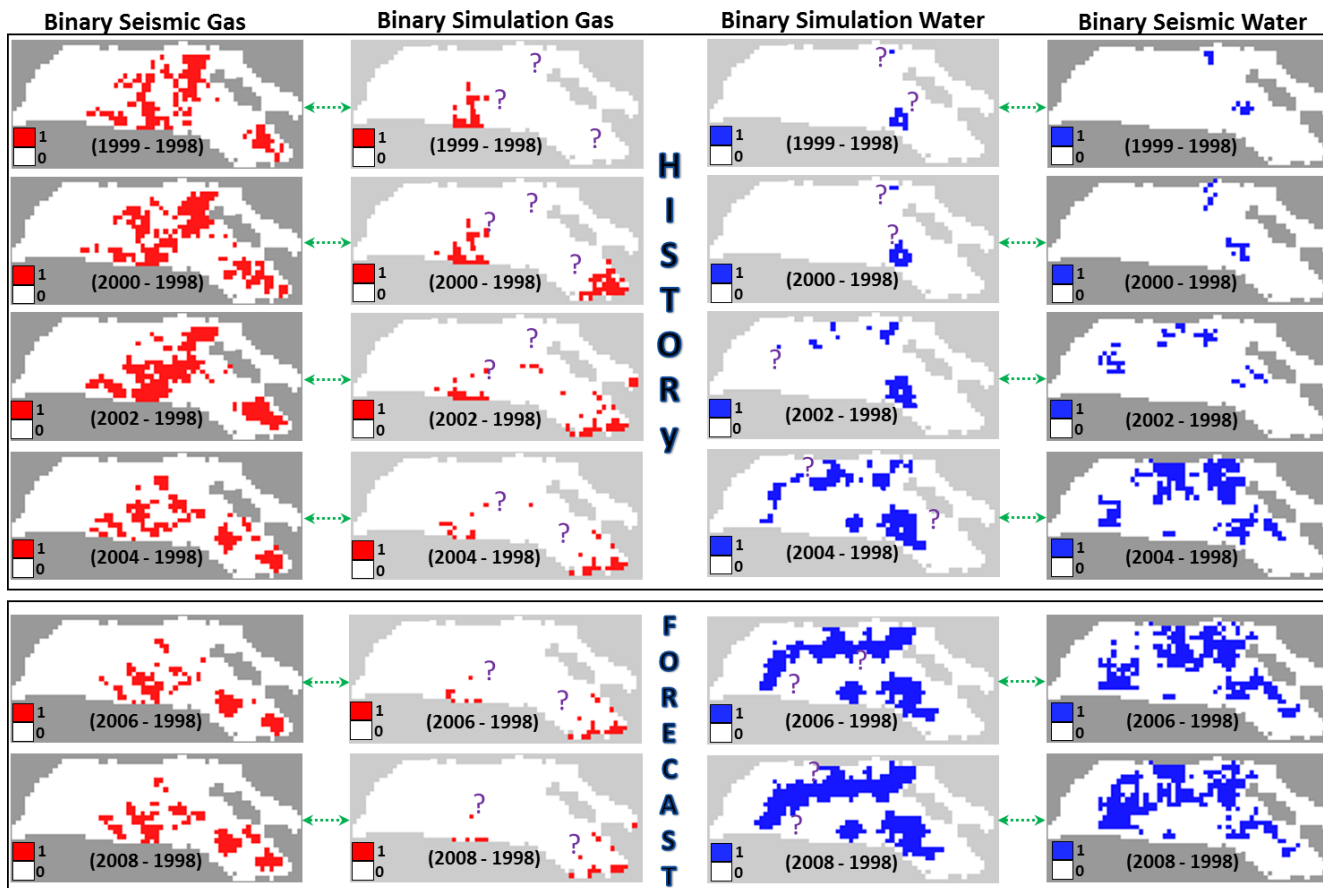


Figure 5.8 The seismic binary (gas and water) maps compared to the simulation binary (gas and water) maps highlighting areas of mismatch. The first 4 monitors (the first four rows) will be used for the history matching exercise, while the last 2 monitors (the last 2 rows) will be used for the forecasting analysis.

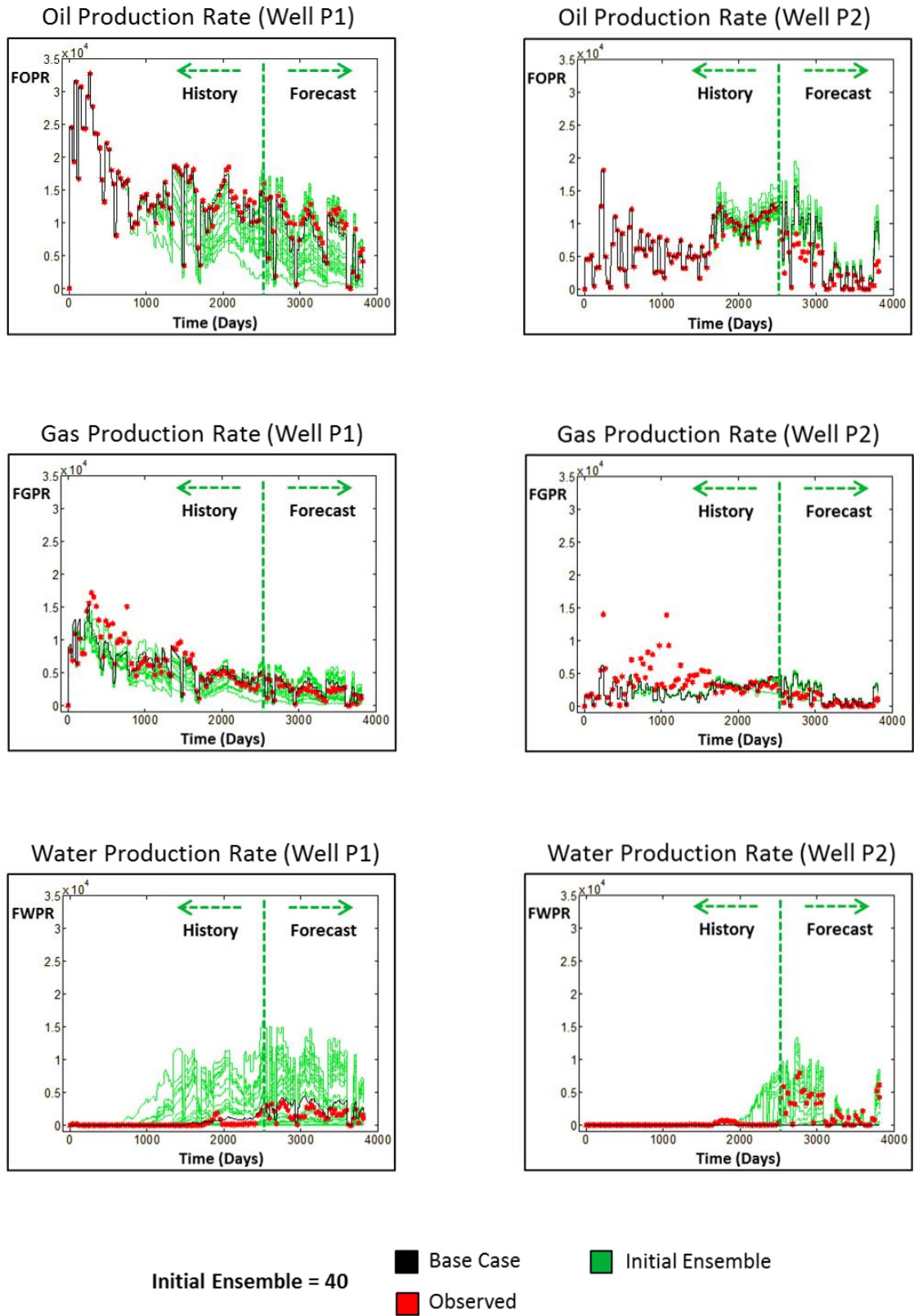


Figure 5.9 Normalized production profiles for wells P1 (left column) and P2 (right column) showing the initial base case model responses (black lines), the initial ensemble responses (green lines), and the historical observed data (red dots) for oil production rate, gas production rate and water production rate.

The binary seismic gas and water maps generated from the data are all shown for the relevant time-steps in Figure 5.7. Figure 5.8 shows the comparison of the binary seismic gas maps versus the binary simulation gas maps, and the binary seismic water maps versus the binary simulation water maps. The gas maps show evidence of exsolved gas in the early years, and declining gas volumes in the later years; while the water maps show little amount of water in the early years but the water comes into full effect in the later years. The first 4 monitor surveys corresponding to the first 7 years will be used for the history match, while the last 2 monitor surveys corresponding to the remaining 3 years will be used to analyse the forecast. The areas of mismatch are highlighted on the binary simulation gas and binary simulation water maps as compared to the binary seismic gas and binary seismic water maps respectively, and getting these maps to match is the aim of the seismic assisted history matching exercise.

5.8.1 HM to Production Data only

To history match to production data only, the seismic data term in the combined objective function is assigned a value of zero, such that the reservoir models are constrained to only the historical production data. After history matching to production data only, the updated production profiles (oil production rate, gas production rate and water production rate) and saturation distribution are shown in Figures 5.10 and 5.11. Figure 5.10 shows the production profiles of wells P1 and P2 for the updated models (in dark blue colour), and indeed there is an improved match to the observed data as compared to the initial ensemble (in green colour). Figure 5.11 shows the updated binary simulation maps compared to the binary seismic maps highlighting areas of minimal improvement on the updated maps even though the model is not constrained to the seismic data. This improvement is as a result of a combination of the uncertain parameters perturbed.

Figure 5.12(a) shows the histograms of selected converging parameters, where the horizontal permeability multiplier is about 1.6, the critical gas saturation value tends towards a low value of 1.5%, , and the pore volume multiplier is approximately 1.2. The low value of the critical gas saturation creates early gas mobility, hence the minimal presence of gas in the reservoir model, while the permeability multipliers improve fluid flow. Figure 5.12(b) shows the plot of objective function and uncertainty for history matching to production data only, which have been normalized to a maximum value of 100 and 1 respectively for easy comparison.

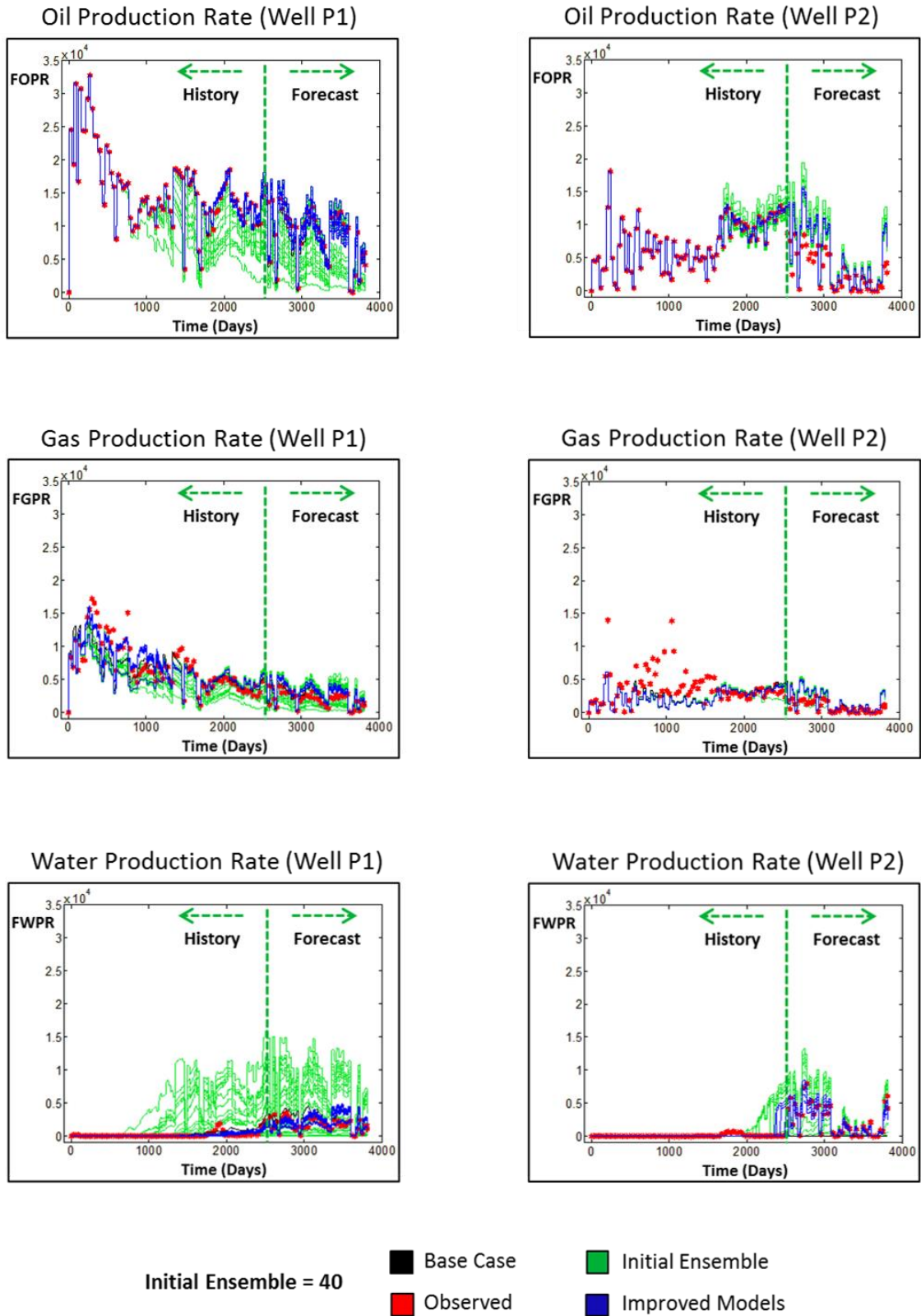


Figure 5.10 Normalized production profiles for wells P1 (left column) and P2 (right column) highlighting the improved model responses (dark blue lines), after history matching to production data only.

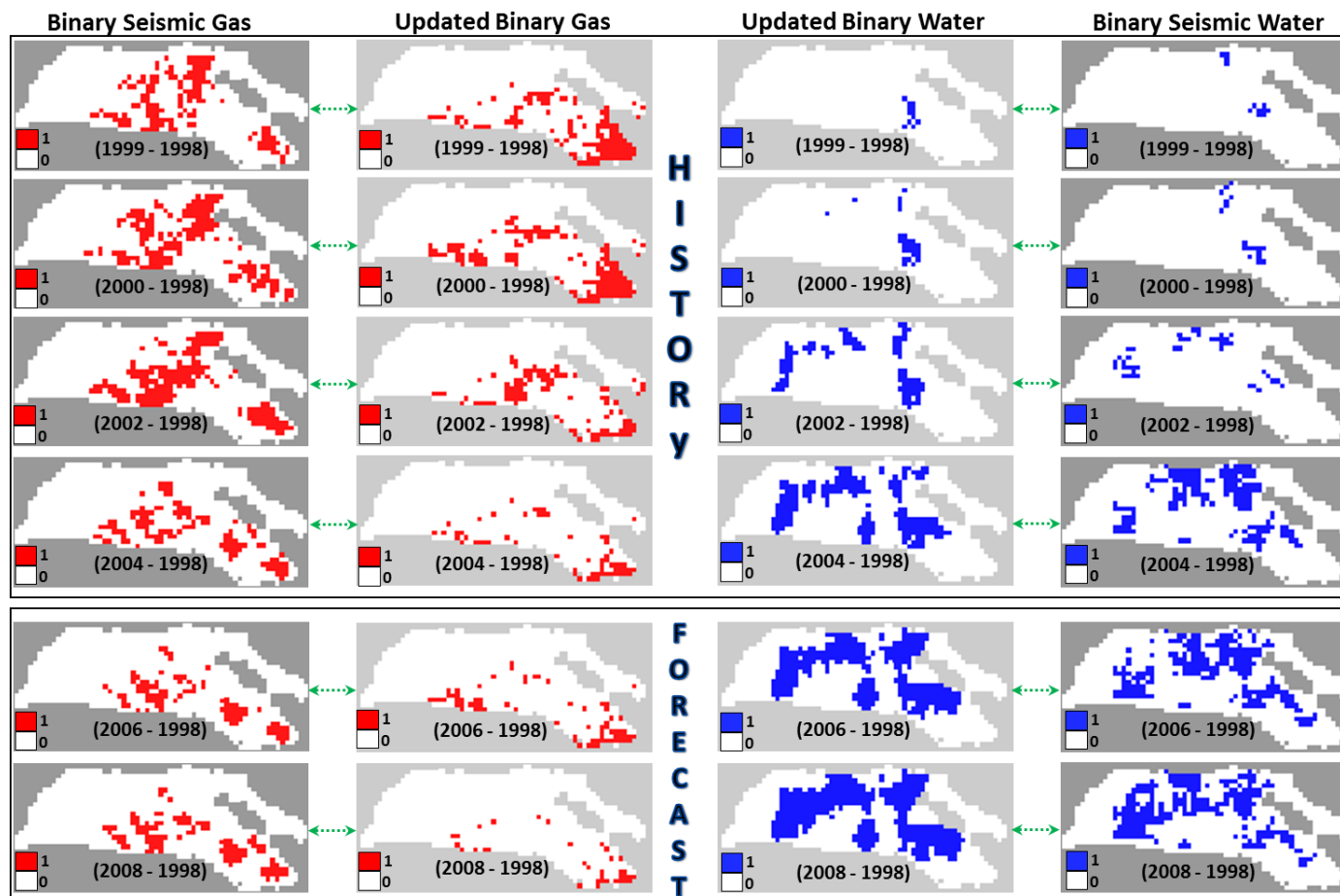


Figure 5.11 The updated binary simulation maps compared to the binary seismic maps highlighting areas of improvement after history matching to production data only

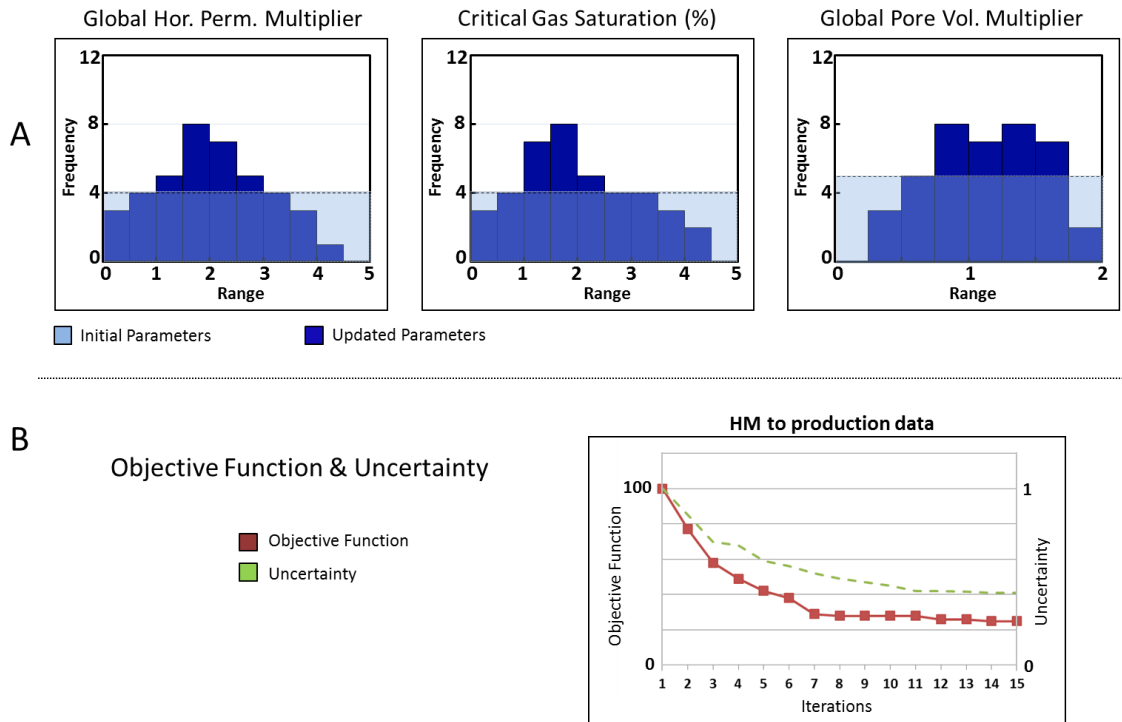


Figure 5.12 (a) Initial and updated parameters for history matching to production data only. (b) Objective function and uncertainty plot for history matching to production data only. The uncertainty is quantified as the range of response parameters in each iteration.

5.8.2 Binary SAHM Using Hamming Distance

Binary seismic assisted history matching is conducted using the Hamming distance as the binary seismic objective function. The history matching is done using binary seismic gas data only, binary seismic water data only, and a combination of both production data and binary seismic data (gas and water).

5.8.2.1 HM to Binary Seismic Gas only

In order to history match to observed binary seismic gas data only, the production data term and binary seismic water term in the combined objective function are assigned a value of zero. The reservoir models are therefore constrained to only the observed binary seismic gas data. After history matching using the Hamming distance to observed binary seismic gas data only, the updated production profile and saturation distribution are shown in Figures 5.13(a), 5.15(a) and 5.17.

Figures 5.13(a) and 5.15(a) show the production profiles (oil production rate, gas production rate and water production rate) of the updated models (in dark blue colour) of well P1 and well P2 respectively, and as the history matching is not constrained to production data the match is not perfect. Figure 5.17 shows the updated binary simulation maps compared to the binary seismic maps highlighting areas of significant improvement on the updated gas maps. Figure 5.18(a) shows the histograms of selected converging parameters, where the horizontal permeability multiplier is about 2.8, the critical gas saturation value tends towards a value of 3.8%, and the pore volume multiplier is approximately 1.0. The high value of the critical gas saturation prevents early gas mobility, hence the presence of more gas in the reservoir model. Figure 5.19(a) shows the plot of objective function and uncertainty for history matching to binary seismic gas only.

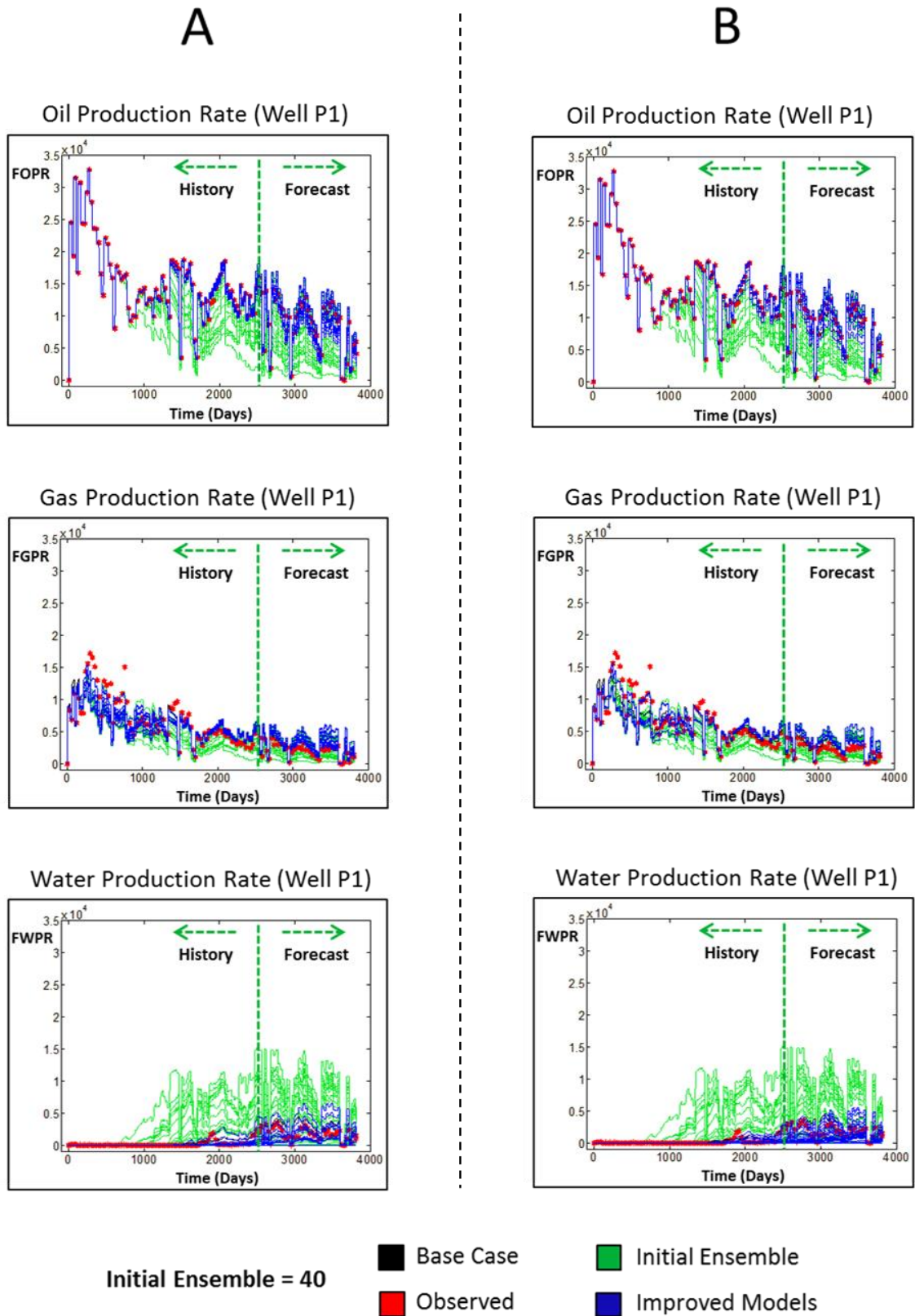
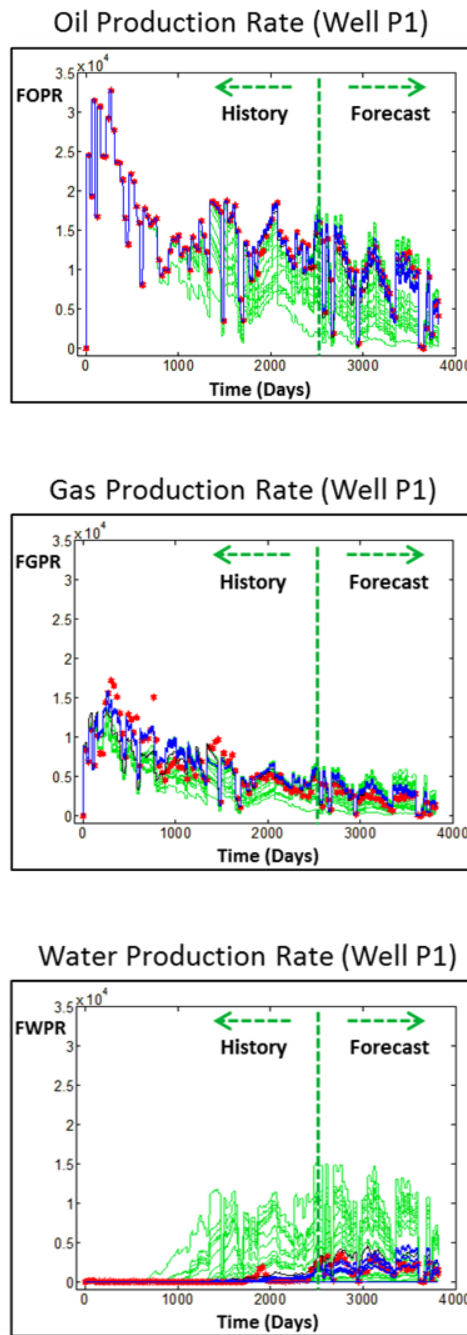


Figure 5.13 Normalized production profiles (oil production rate, gas production rate and water production rate) for well P1 (a) HM to binary seismic gas only, using Hamming distance (b) HM to binary seismic water only, using Hamming distance.



Initial Ensemble = 40

■ Base Case	■ Initial Ensemble
■ Observed	■ Improved Models

Figure 5.14 Normalized production profiles (oil production rate, gas production rate and water production rate) for well P1, HM to production data and binary seismic (gas and water), using Hamming distance.

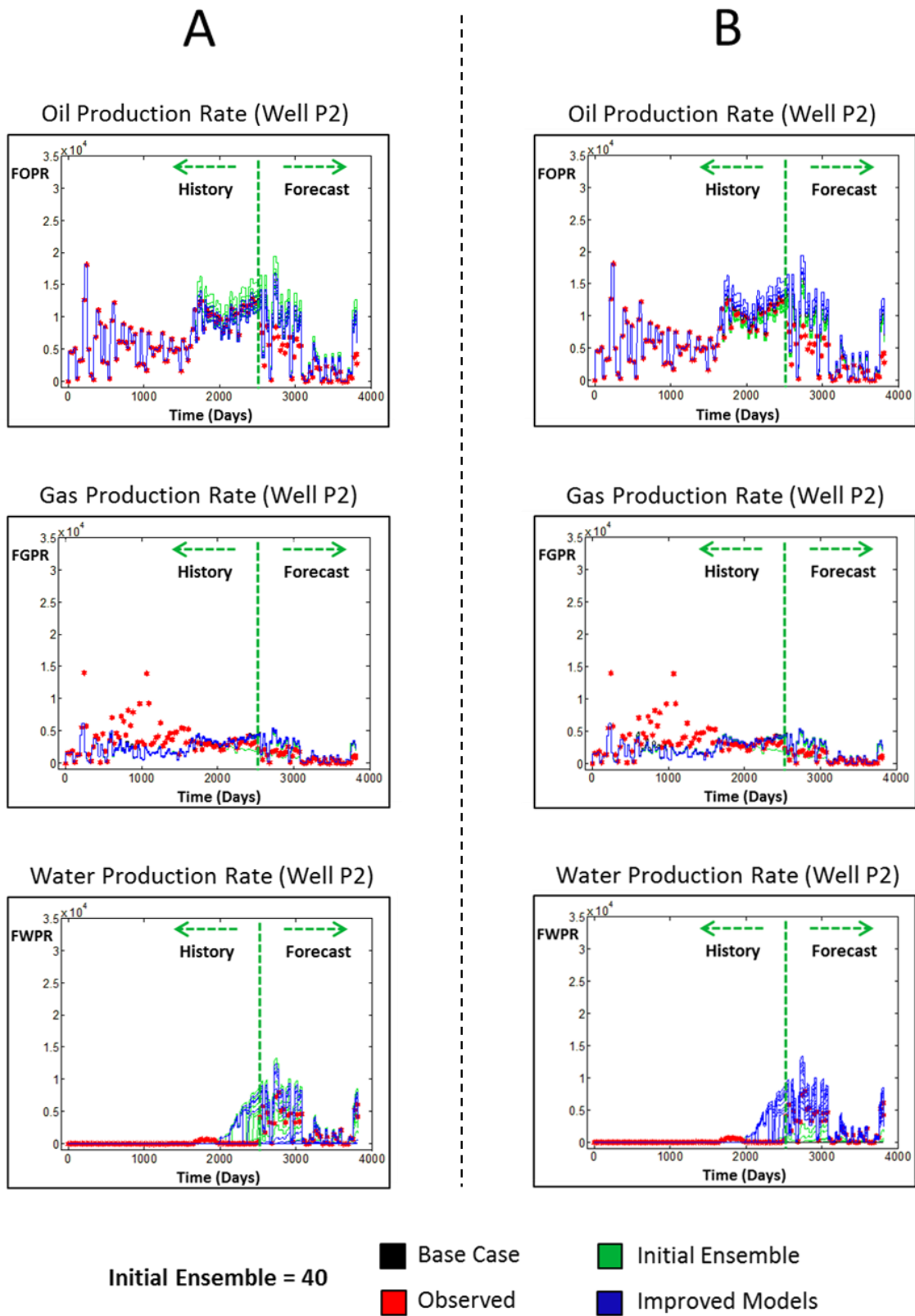


Figure 5.15 Normalized production profiles (oil production rate, gas production rate and water production rate) for well P2 (a) HM to binary seismic gas only, using Hamming distance (b) HM to binary seismic water only, using Hamming distance.

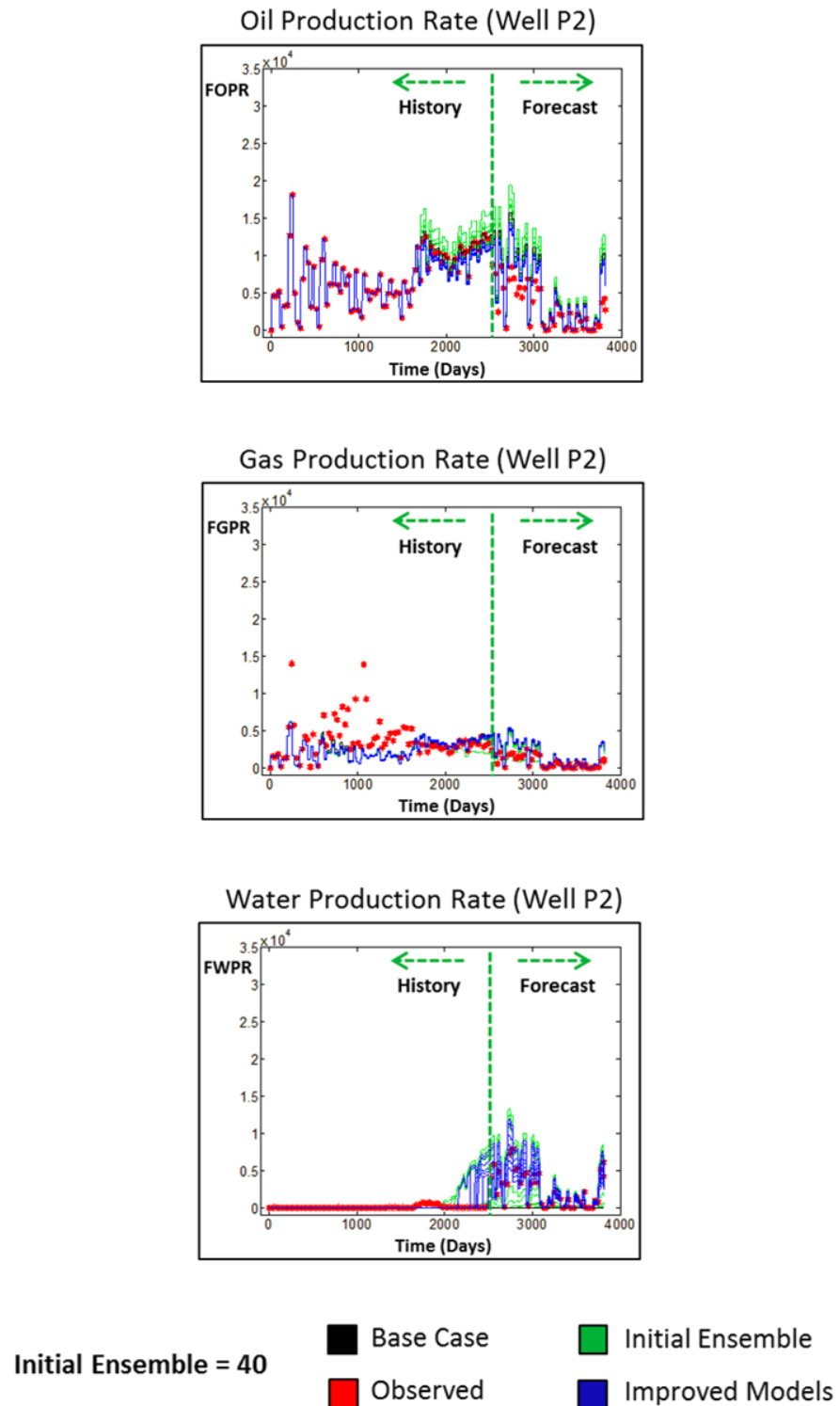


Figure 5.16 Normalized production profiles (oil production rate, gas production rate and water production rate) for well P2, HM to production data and binary seismic (gas and water), using Hamming distance.

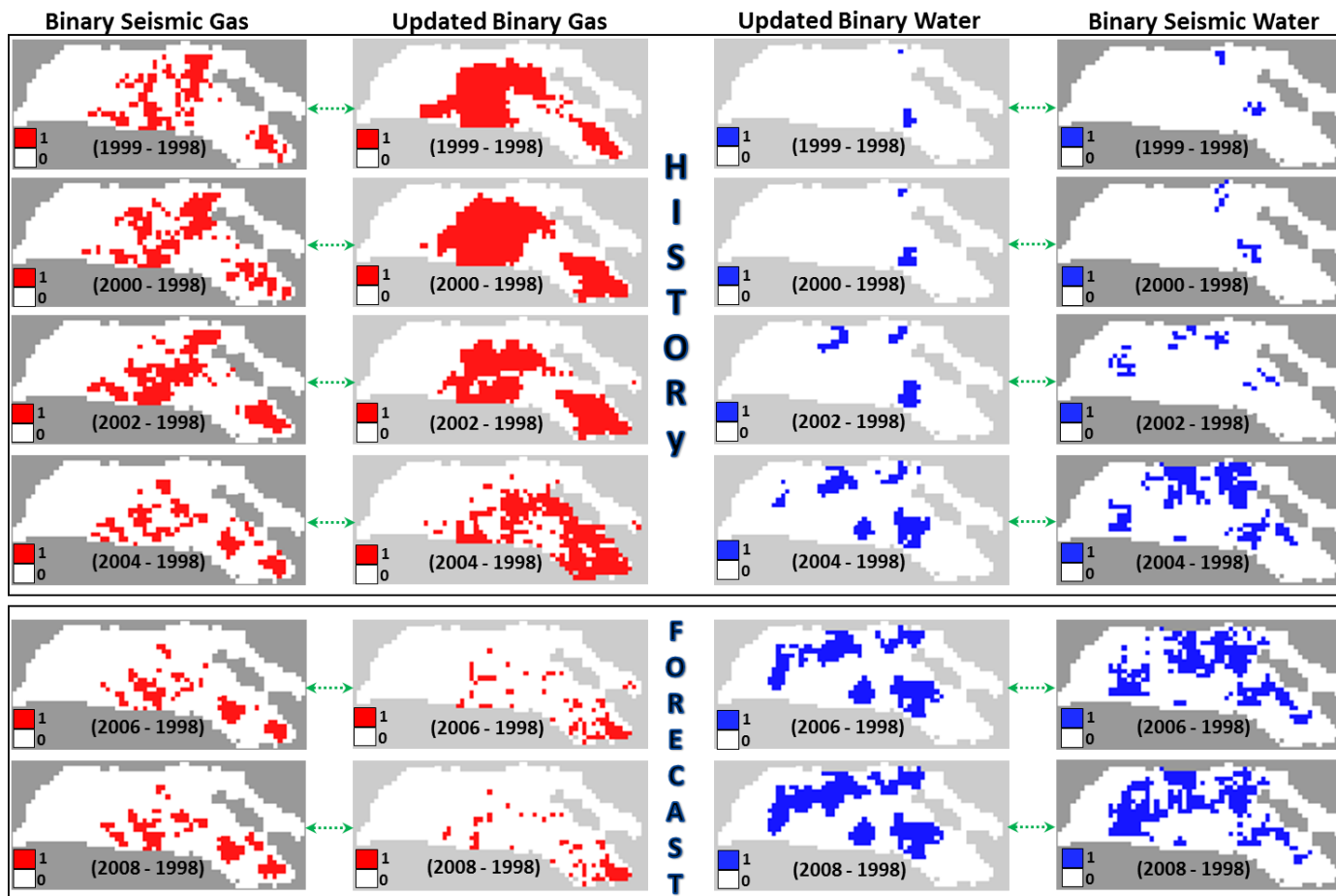


Figure 5.17 The updated binary simulation maps compared to the binary seismic maps highlighting areas of improvement after history matching to binary seismic gas only, using Hamming distance.

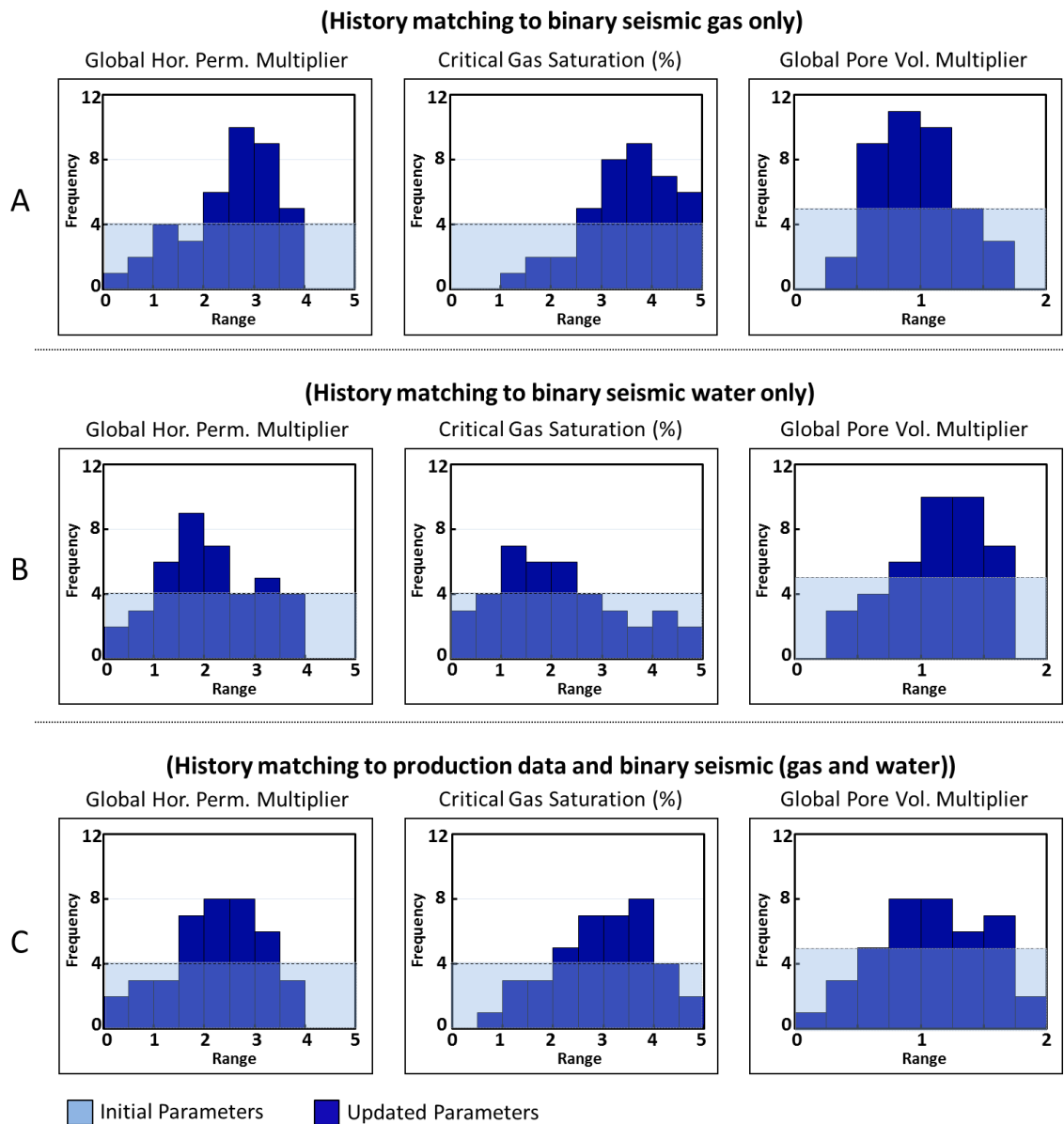


Figure 5.18(a) Histogram of selected parameters for history matching to binary seismic gas only, using Hamming distance. (b) Histogram of selected parameters for history matching to binary seismic water only, using Hamming distance. (c) Histogram of selected parameters for history matching to production data and binary seismic (gas and water).

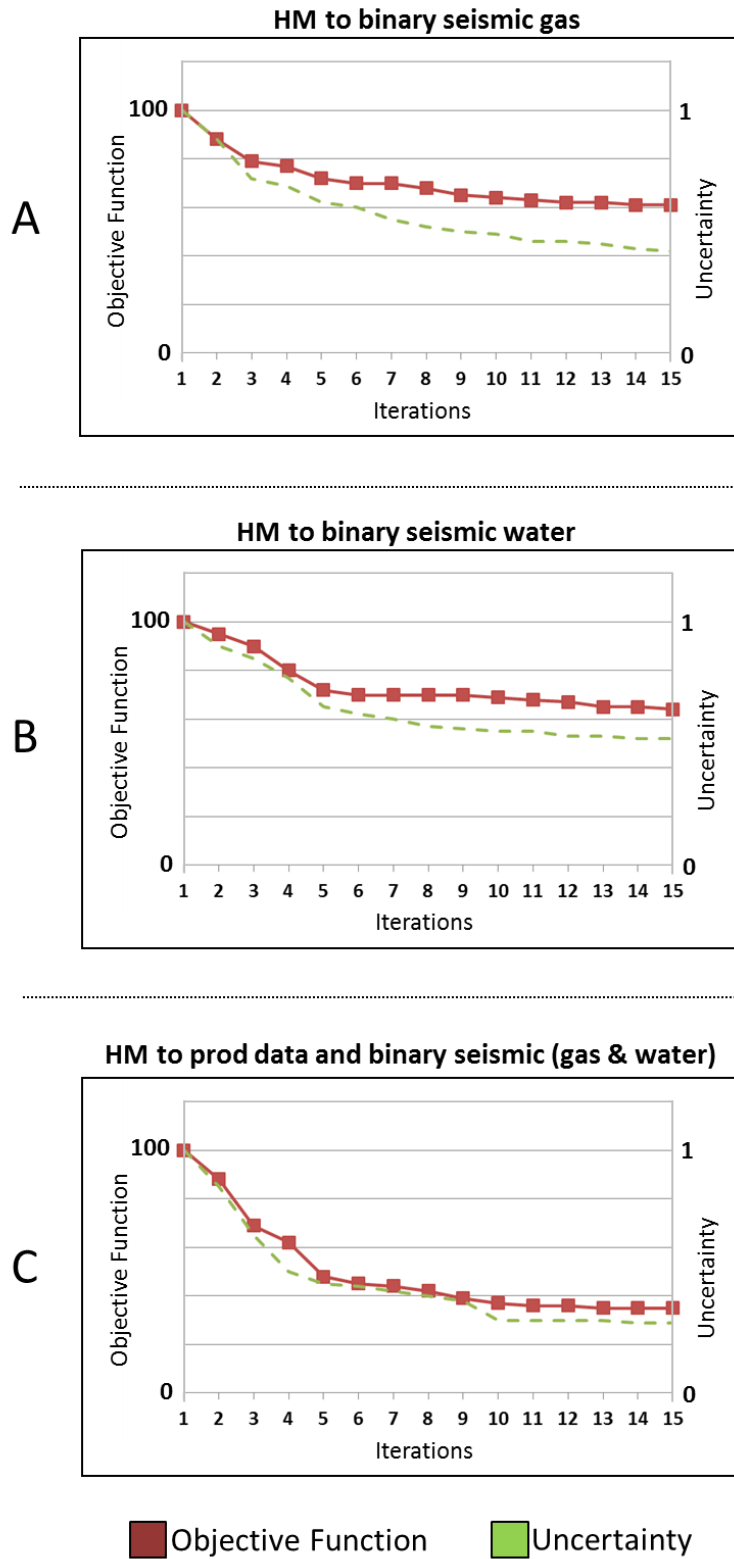


Figure 5.19 (a) Objective function and uncertainty plot for history matching to binary seismic gas only, using Hamming distance. (b) Objective function and uncertainty plot for history matching to binary seismic water only, using Hamming distance. (c) Objective function and uncertainty plot for history matching to production data and binary seismic (gas and water). The uncertainty is quantified as the range of response parameters in each iteration.

5.8.2.2 HM to Binary Seismic Water only

History matching to observed binary seismic gas water only requires the production data term and binary seismic gas term in the combined objective function are assigned a value of zero, such that the reservoir models are constrained to only the observed binary seismic water data. Hamming distance to observed binary seismic water data only is used for history matching, and the updated production profile and saturation distribution are shown in Figures 5.13(b), 5.15(b) and 5.20.

Production profiles (oil production rate, gas production rate and water production rate) of the updated models (in dark blue colour) of well P1 and well P2 are shown in Figures 5.13(b) and 5.15(b) respectively. The match is not ideal as the history matching is not constrained to production data. Figure 5.20 shows the updated binary simulation maps compared to the binary seismic maps highlighting areas of improvement on the updated water maps. Figure 5.18(b) shows the histograms of selected converging parameters, where the horizontal permeability multiplier is about 1.9, the critical gas saturation value tends towards a value of 1.8%, , and the pore volume multiplier is approximately 1.4. The increase in pore volume enhances the presence of more water volume in the reservoir model. The plot of objective function and uncertainty for history matching to binary seismic water only is shown in Figure 5.19(b).

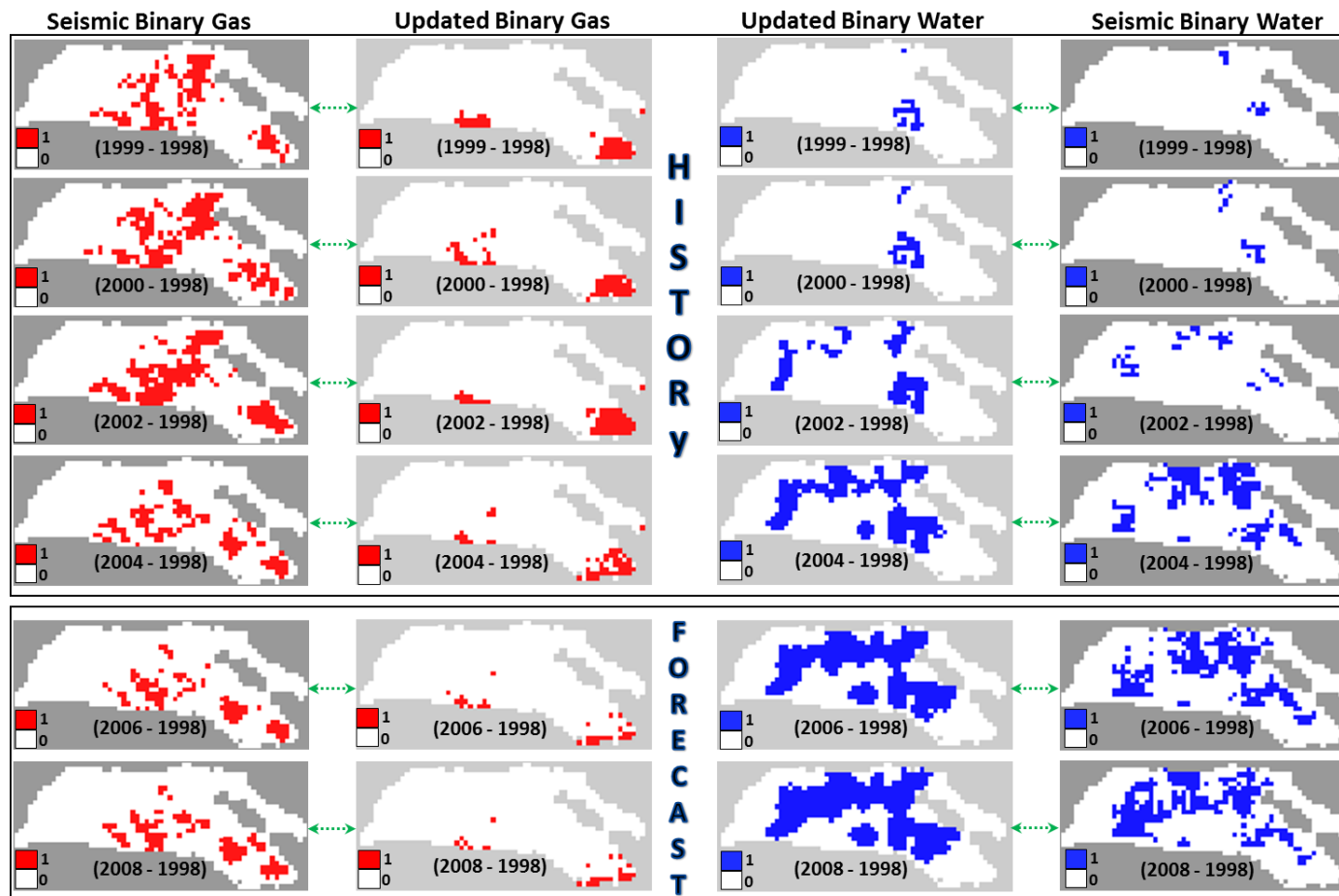


Figure 5.20 The updated binary simulation maps compared to the binary seismic maps highlighting areas of improvement after history matching to binary seismic water only, using Hamming distance.

5.8.2.3 HM to Production Data and Binary Seismic (Gas and Water)

For a joint history match to production data and binary seismic data (gas and water), the combined objective function is normalized such that the effect of the production data and binary seismic data (gas and water) are equal, and that at the beginning of the history match, the combined misfit is a value of unity. After history matching to both production data and binary seismic data (gas and water), Figures 5.14, 5.16 and 5.21 show the updated production profile and saturation distribution.

The production profiles (oil production rate, gas production rate and water production rate) of the updated models (in dark blue colour) of well P1 and well P2 are displayed in Figures 5.14 and 5.16 respectively, and there is an improvement. Figure 5.21 shows the updated binary simulation maps compared to the binary seismic maps highlighting areas of improvement on both the updated gas maps and updated water maps. The histograms of selected converging parameters are shown in Figure 5.18(c), where the horizontal permeability multiplier is about 2.5, the critical gas saturation value tends towards a value of 3.8%, and the pore volume multiplier is approximately 1.2. Figure 5.19(c) displays the plot of objective function and uncertainty for history matching to production data and binary seismic (gas and water).

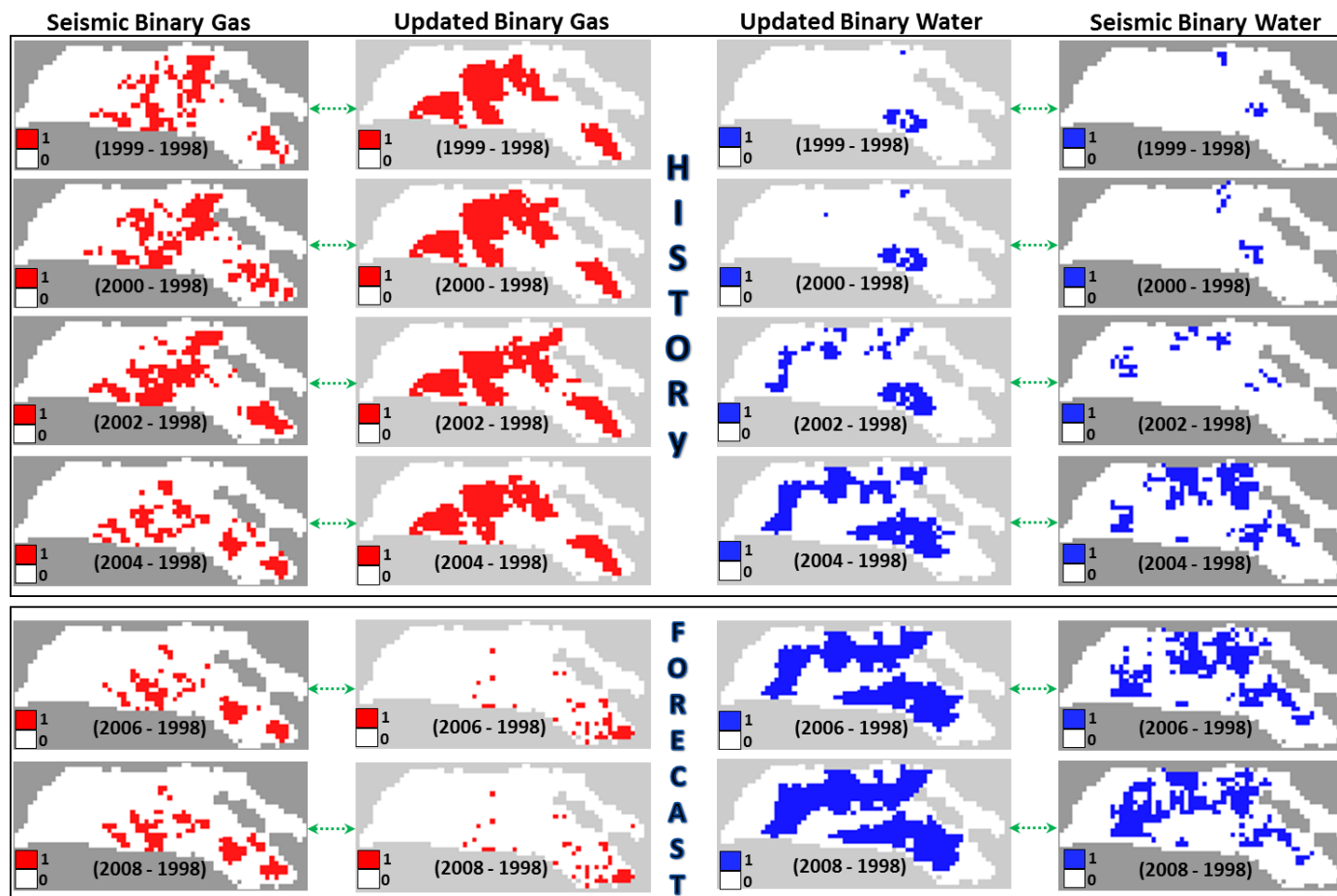


Figure 5.21 The updated binary simulation maps compared to the binary seismic maps highlighting areas of improvement after history matching to production data and binary seismic (gas and water).

5.8.3 Binary SAHM Using Current Measurement Metric

Binary seismic assisted history matching is conducted using the *Current* measurement metric as the binary seismic objective function. The history matching is done using binary seismic gas data only, binary seismic water data only, and a combination of both production data and binary seismic data (gas and water).

5.8.3.1 HM to Binary Seismic Gas only

When history matching to observed binary seismic gas data only, the production data term and binary seismic water term in the combined objective function are assigned a zero value, this implies that the reservoir models are constrained to only the observed binary seismic gas data. After history matching using the *Current* measurement metric to observed binary seismic gas data only, the updated production profile and saturation distribution are shown in Figures 5.22(a), 5.24(a) and 5.26.

Figures 5.22(a) and 5.24(a) show the production profiles (oil production rate, gas production rate and water production rate) of the updated models (in dark blue colour) of well P1 and well P2 respectively. Figure 5.26 shows the updated binary simulation maps compared to the binary seismic maps highlighting areas of significant improvement on the updated gas maps. The histograms of selected converging parameters are displayed in Figure 5.27(a), where the horizontal permeability multiplier is about 3.0, the critical gas saturation value tends towards a value of 4.0%, and the pore volume multiplier is approximately 1.0. The objective function and uncertainty plot for history matching to binary seismic gas only is shown in Figure 5.28(a).

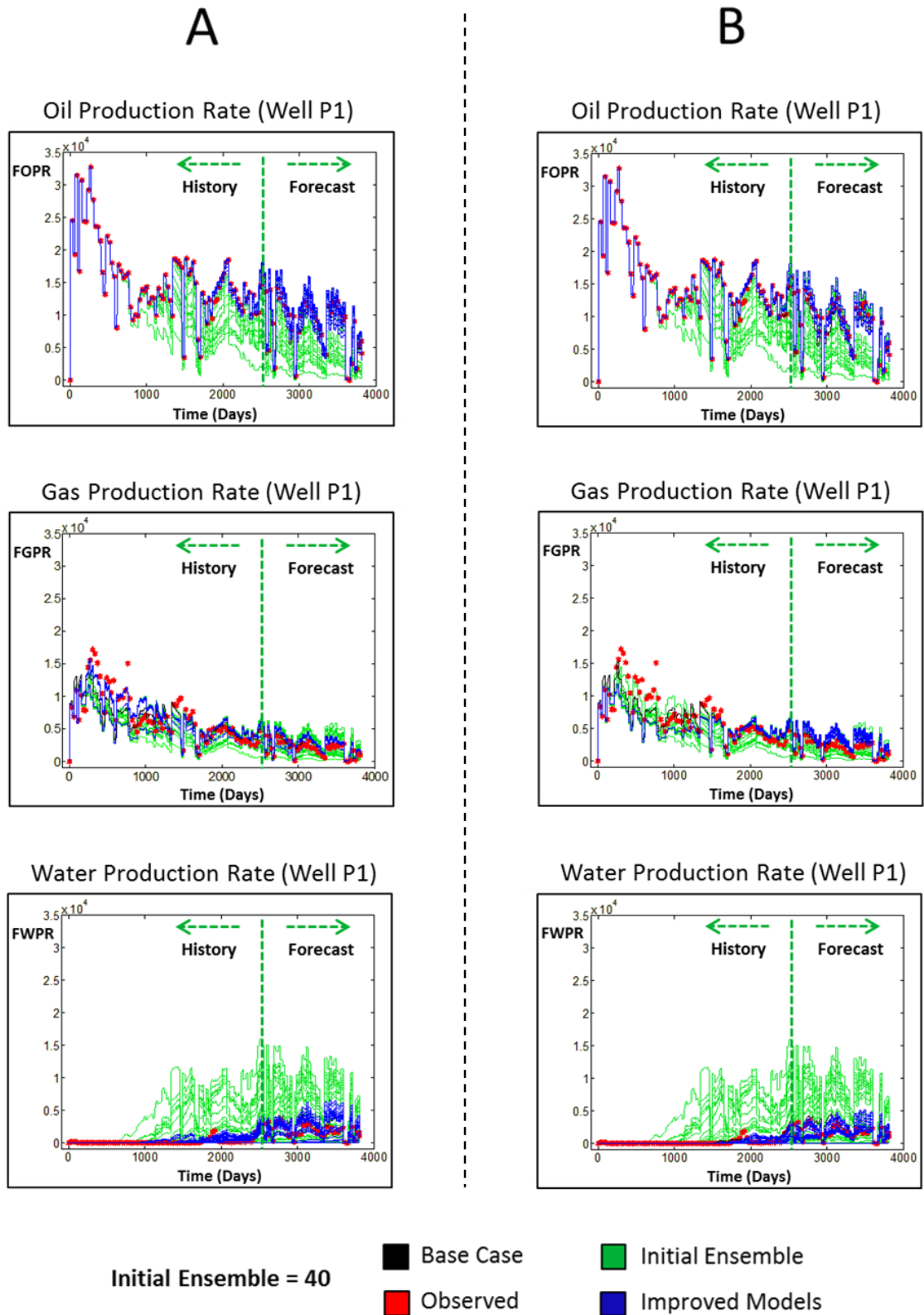


Figure 5.22 Normalized production profiles (oil production rate, gas production rate and water production rate) for well P1 (a) HM to binary seismic gas only, using *Current* measurement metric (b) HM to binary seismic water only, using *Current* measurement metric.

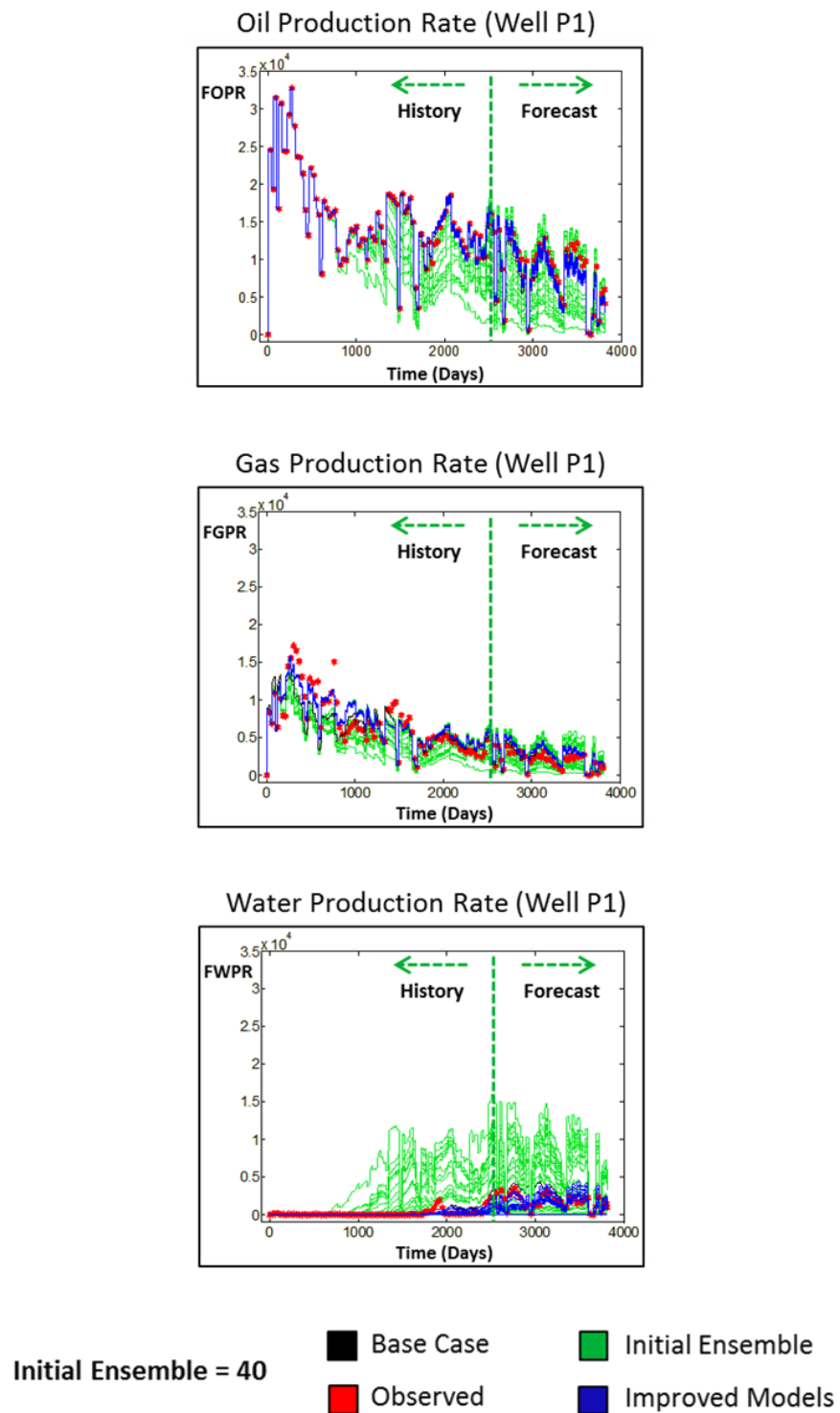


Figure 5.23 Normalized production profiles (oil production rate, gas production rate and water production rate) for well P1, HM to production data and binary seismic (gas and water), using *Current* measurement metric.

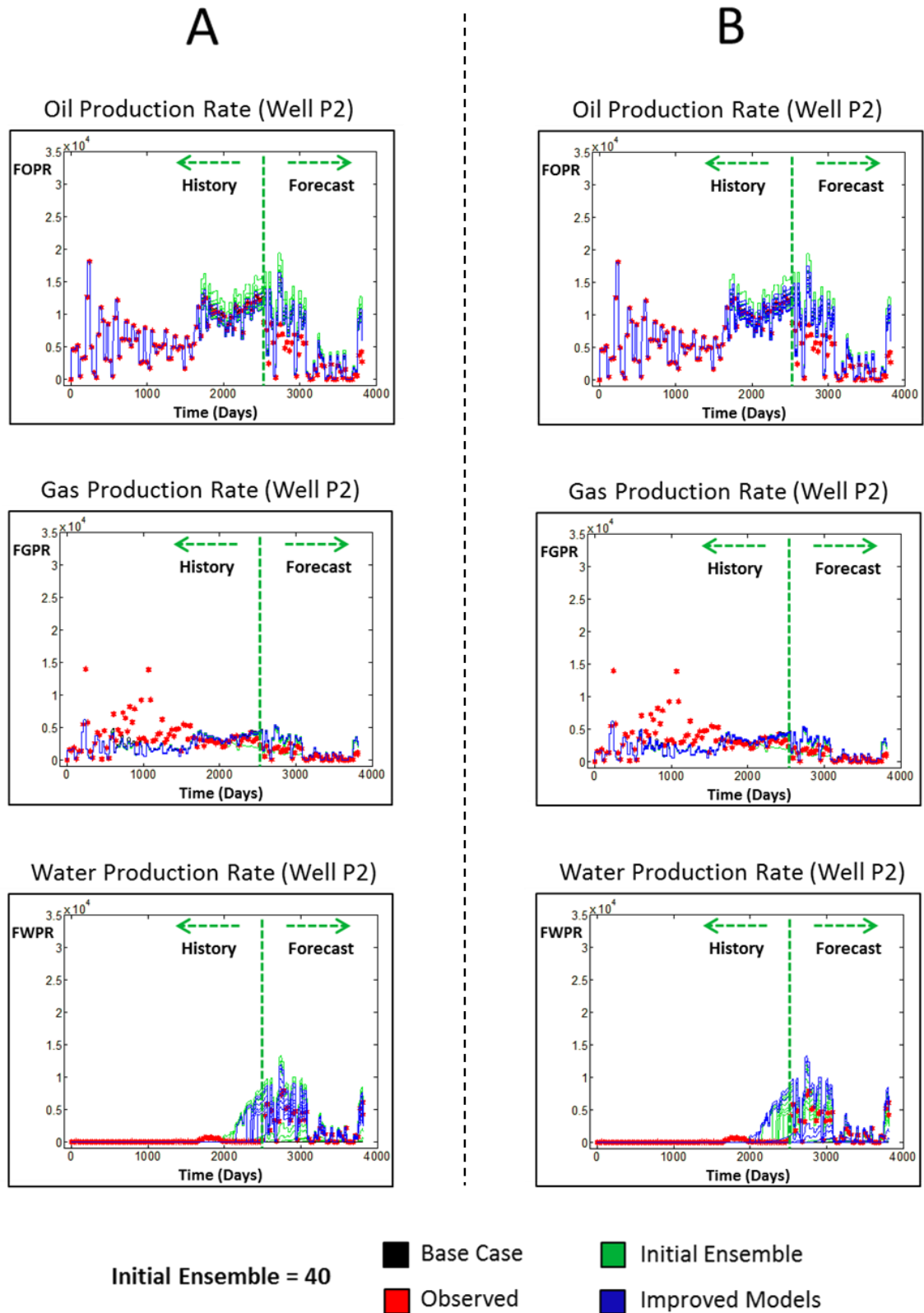


Figure 5.24 Normalized production profiles (oil production rate, gas production rate and water production rate) for well P2 (a) HM to binary seismic gas only, using *Current* measurement metric (b) HM to binary seismic water only, using *Current* measurement metric.

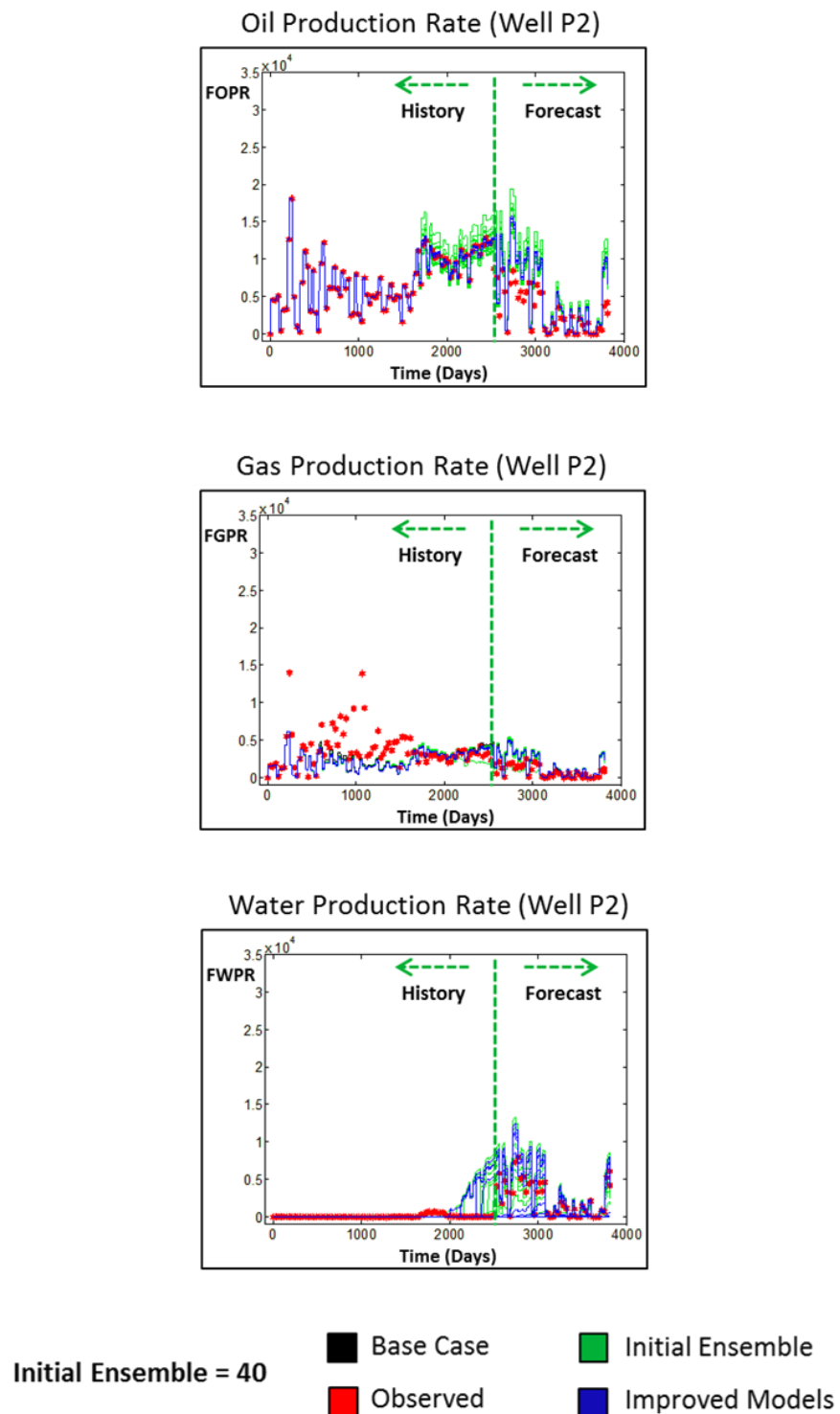


Figure 5.25 Normalized production profiles (oil production rate, gas production rate and water production rate) for well P2, HM to production data and binary seismic (gas and water), using *Current* measurement metric.

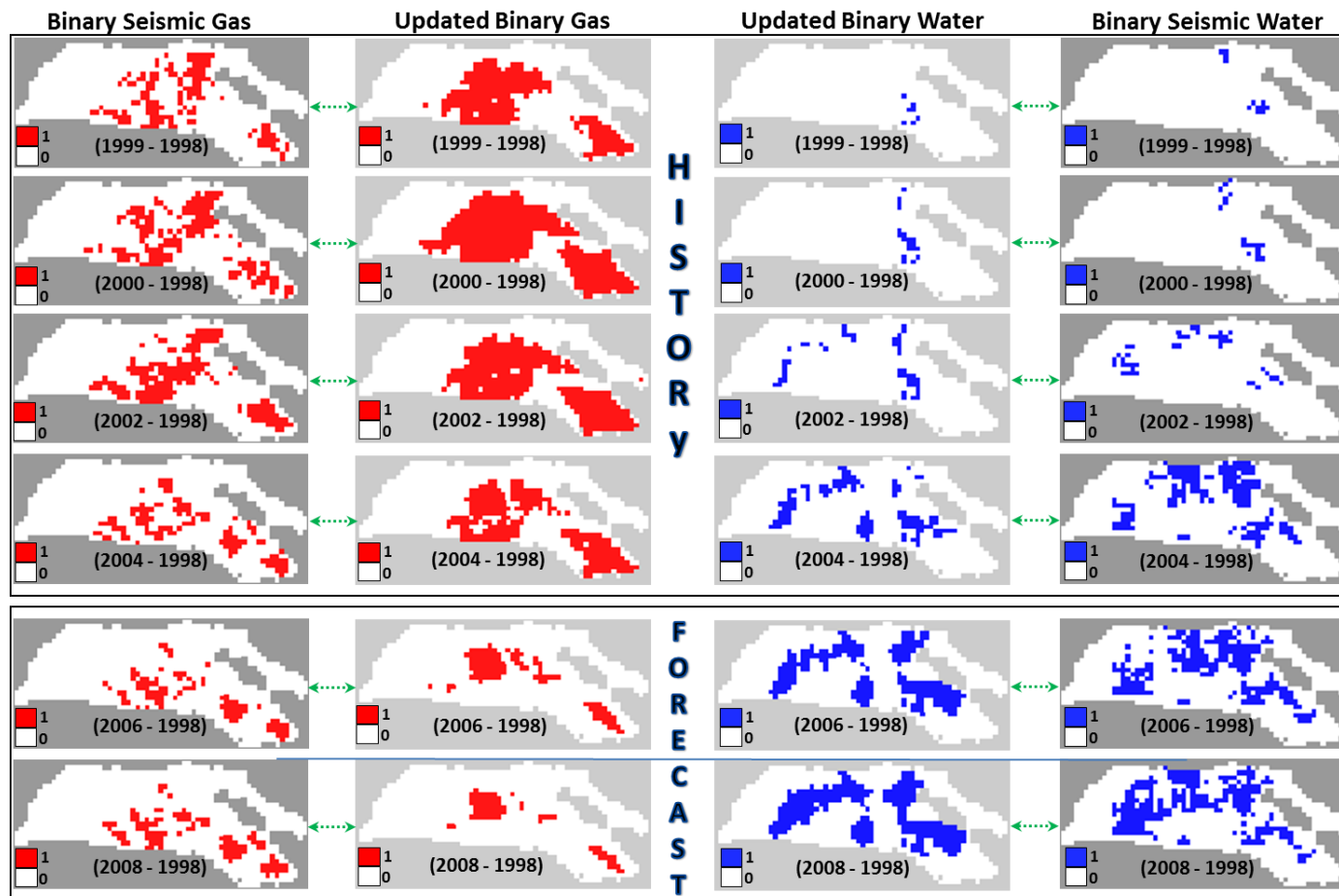


Figure 5.26 The updated binary simulation maps compared to the binary seismic maps highlighting areas of improvement after history matching to binary seismic gas only, using *Current* measurement metric.

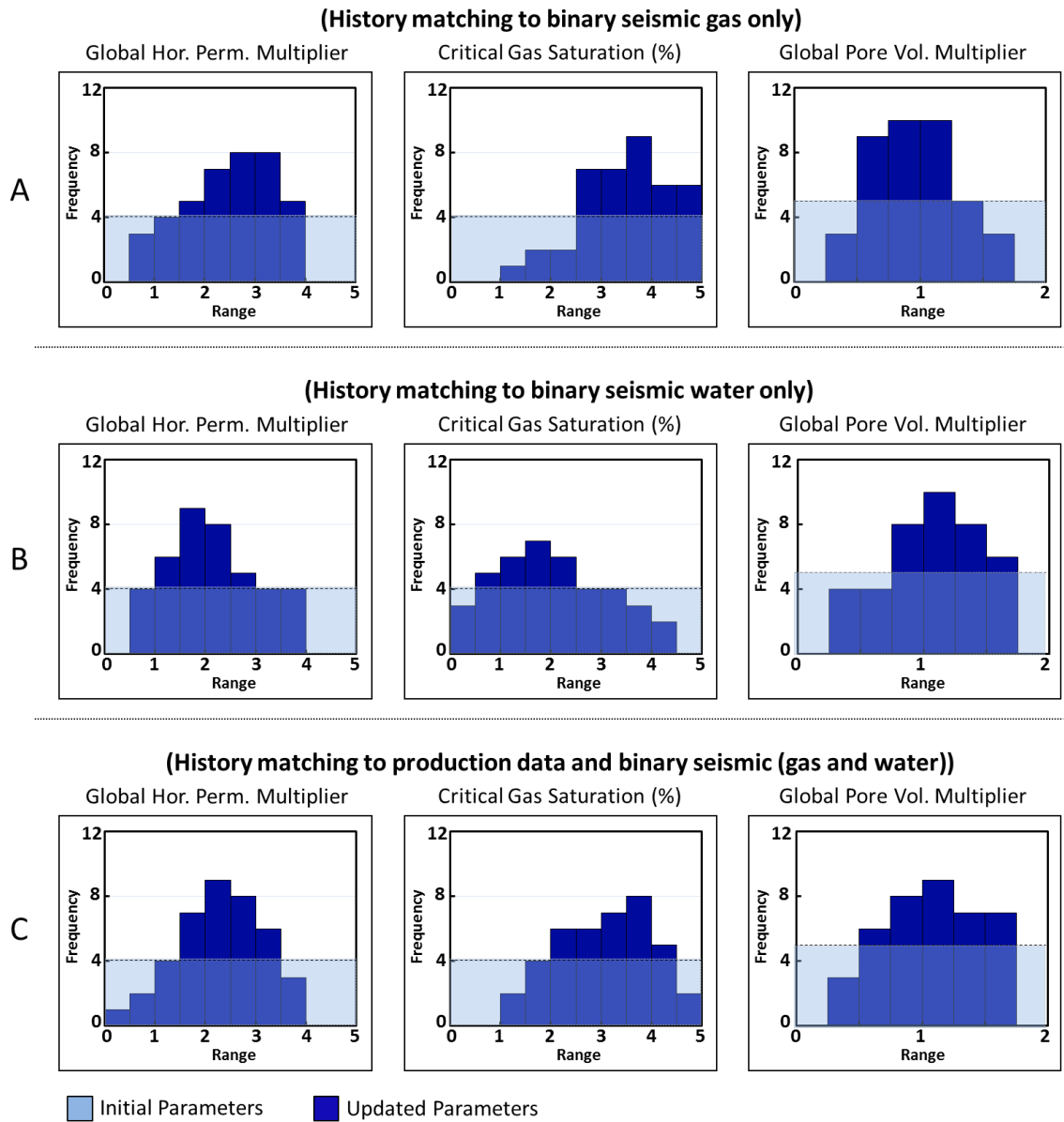


Figure 5.27 (a) Histogram of selected parameters for history matching to binary seismic gas only, using *Current* measurement metric. (b) Histogram of selected parameters for history matching to binary seismic water only, using *Current* measurement metric. (c) Histogram of selected parameters for history matching to production data and binary seismic (gas and water).

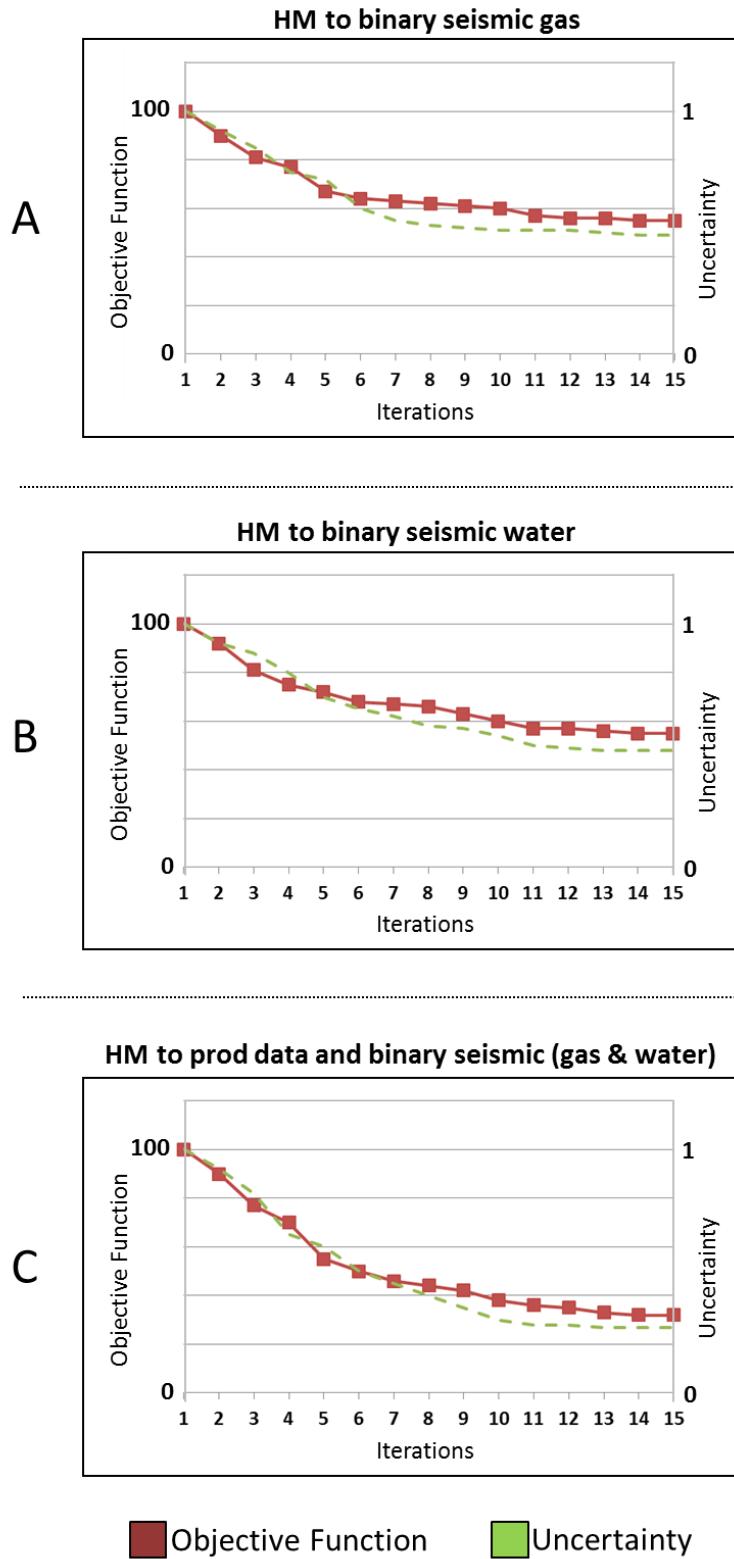


Figure 5.28 (a) Objective function and uncertainty plot for history matching to binary seismic gas only, using *Current* measurement metric. (b) Objective function and uncertainty plot for history matching to binary seismic water only, using *Current* measurement metric. (c) Objective function and uncertainty plot for history matching to production data and binary seismic (gas and water). The uncertainty is quantified as the range of response parameters in each iteration.

5.8.3.2 HM to Binary Seismic Water only

To history match to observed binary seismic gas water only, the production data term and binary seismic gas term in the combined objective function will be assigned a value of zero, such that the reservoir models will be constrained to only the observed binary seismic water data. After history matching using the *Current* measurement metric to observed binary seismic water data only, the updated production profile and saturation distribution are shown in Figures 5.22(b), 5.24(b) and 5.29.

The production profiles (oil production rate, gas production rate and water production rate) of the updated models (in dark blue colour) of well P1 and well P2 are shown in Figures 5.22(b) and 5.24(b) respectively. Figure 5.29 shows the updated binary simulation maps compared to the binary seismic maps highlighting areas of improvement on the updated water maps. Figure 5.27(b) shows the histograms of selected converging parameters, where the horizontal permeability multiplier is about 1.8, the critical gas saturation value tends towards a value of 2.0%, , and the pore volume multiplier is approximately 1.4. The plot of objective function and uncertainty for history matching to binary seismic water only is displayed in Figure 5.28(b).

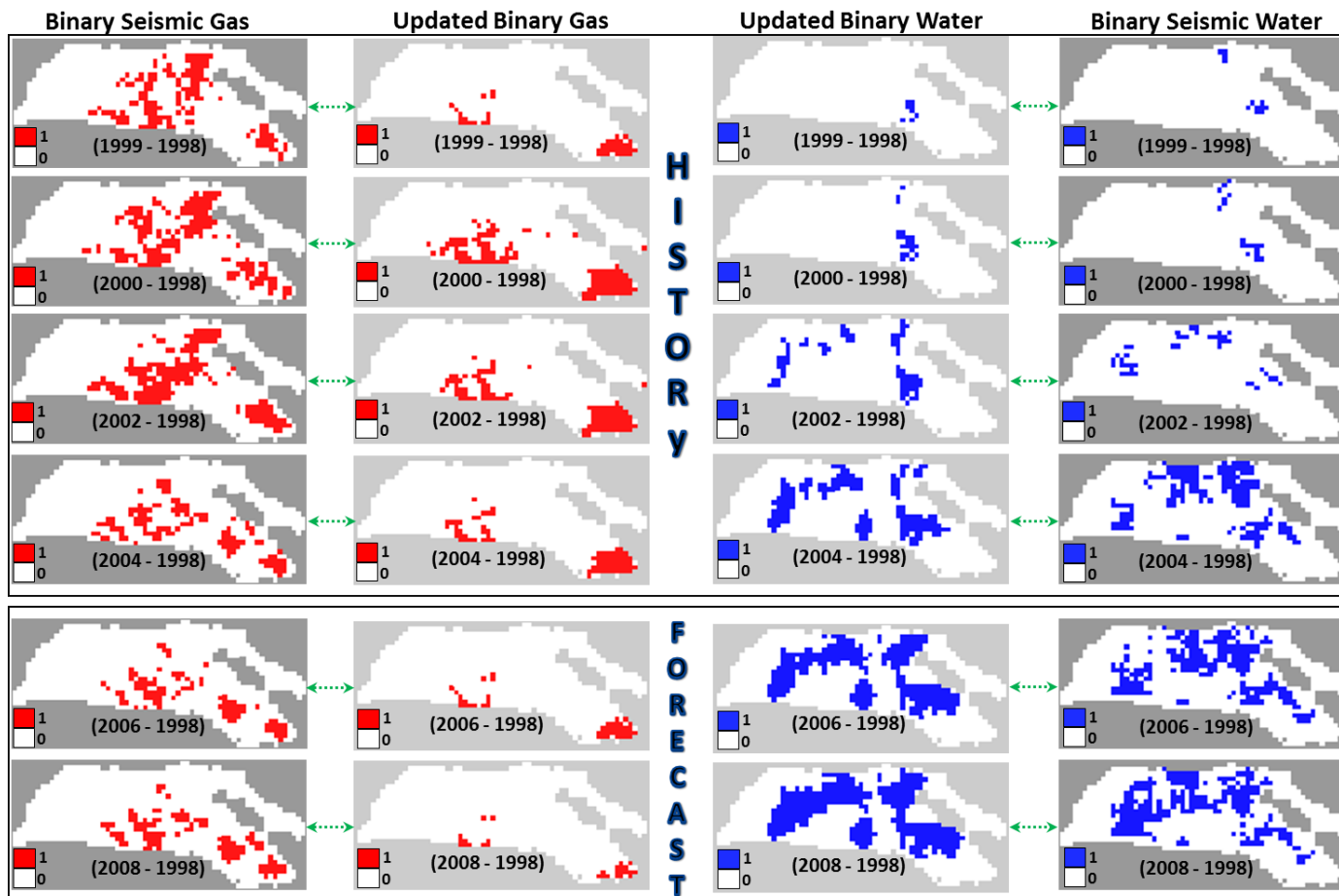


Figure 5.29 The updated binary simulation maps compared to the binary seismic maps highlighting areas of improvement after history matching to binary seismic water only, using *Current* measurement metric.

5.8.3.3 HM to Production Data and Binary Seismic (Gas and Water)

Production data and binary seismic data (gas and water) are history matched, and the combined objective function is normalized such that the effect of the production data and binary seismic data (gas and water) are equal, and that at the beginning of the history match, the combined misfit is a value of unity. After history matching to both production data and binary seismic data (gas and water), Figures 5.23, 5.25 and 5.30 display the updated production profile and saturation distribution.

Figures 5.23 and 5.25 show the production profiles (oil production rate, gas production rate and water production rate) of the updated models (in dark blue colour) of well P1 and well P2 respectively, and there is an improvement; while Figure 5.30 shows the updated binary simulation maps compared to the binary seismic maps highlighting areas of significant improvement on both the updated gas maps and updated water maps. Figure 5.27(c) shows the histograms of selected converging parameters, where the horizontal permeability multiplier is about 2.0, the critical gas saturation value tends towards a value of 3.5%, , and the pore volume multiplier is approximately 1.1. Figure 5.28(c) shows the plot of objective function and uncertainty for history matching to production data and binary seismic (gas and water).

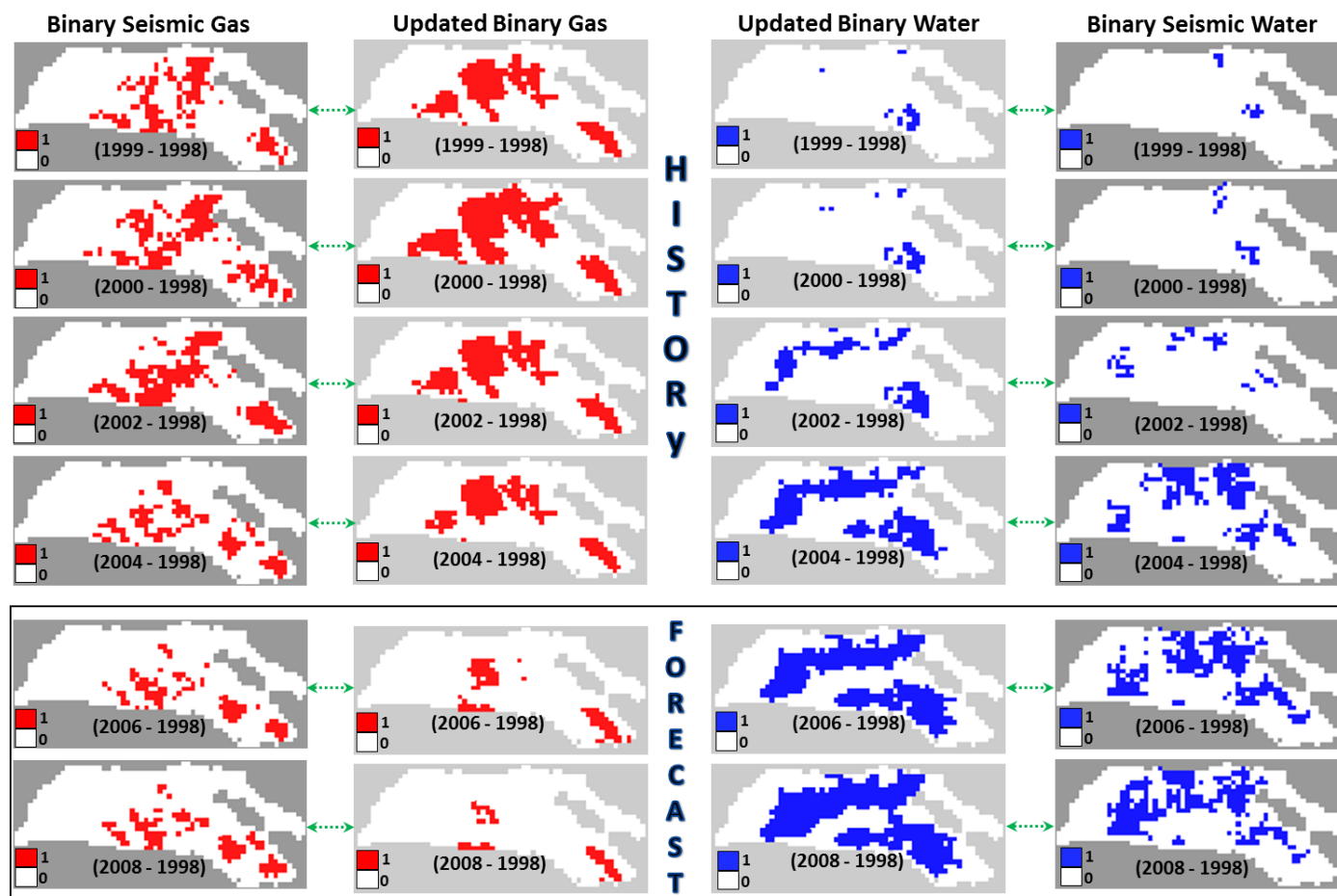


Figure 5.30 The updated binary simulation maps compared to the binary seismic maps highlighting areas of improvement after history matching to production data and binary seismic (gas and water).

5.8.4 Forecast Analysis

In order to have proper appreciation of the history matching results using the Hamming distance and the *Current* measurement metric, an analysis of the forecasting capability of the improved is carried out, as it well known that the strength of a history matched model is in predictability.

Table 5.3 shows the forecast misfit for the average of the improved models, where the well data misfit is calculated using the least squares error, and the seismic misfit (gas and water) is calculated using the Hamming distance. The results are shown for the initial base case model, matching to seismic gas only, matching to seismic water only, and matching to a combination of well data and seismic (gas and water). A percentage improvement to the initial base case model is calculated individually and combined as shown in Table 5.4. Overall, matching to seismic gas only yields a 21.60% improvement to the initial base case model, matching to seismic water only yields a 20.80% improvement to the initial base case model, and matching to well data and seismic (gas and water) yields a 42.60% improvement to the initial base case model using the Hamming distance binary seismic objective function.

	Well Data	Seismic (Gas)	Seismic (Water)
Basecase	14285	272	342
Seismic Gas only	10945	182	313
Seismic Water only	11482	261	209
Well & Seismic (G &W)	6146	177	219

Table 5.3 Forecast misfit for the average of the improved models. The well data misfit is calculated using the least squares error, and the seismic misfit (gas and water) is calculated using the Hamming distance.

	Well Data	Seismic (Gas)	Seismic (Water)	Combined
Seismic Gas only	23.40%	33.10%	8.40%	21.60%
Seismic Water only	19.60%	4.10%	38.80%	20.80%
Well & Seismic (G &W)	56.90%	34.90%	35.90%	42.60%

Table 5.4 Percentage improvement to the initial base case model using the Hamming distance as the binary seismic objective function.

Table 5.5 shows the forecast misfit for the average of the improved models, where the well data misfit is calculated using the least squares error, and the seismic misfit (gas and water) is calculated using the *Current* measurement metric. The results are shown for the initial base case model, matching to seismic gas only, matching to seismic water only, and matching to a combination of well data and seismic (gas and water). A percentage improvement to the initial base case model is calculated individually and combined as shown in Table 5.6. Overall, matching to seismic gas only yields a 25.84% improvement to the initial base case model, matching to seismic water only yields a 24.89% improvement to the initial base case model, and matching to well data and seismic (gas and water) yields a 45.58% improvement to the initial base case model using the Hamming distance binary seismic objective function.

	Well Data	Seismic (Gas)	Seismic (Water)
Basecase	14285	4792	9254
Seismic Gas only	10225	2901	8361
Seismic Water only	11251	4125	5595
Well & Seismic (G &W)	6054	2835	5711

Table 5.5 Forecast misfit for the average of the improved models. The well data misfit is calculated using the least squares error, and the seismic misfit (gas and water) is calculated using the Hamming distance.

	Well Data	Seismic (Gas)	Seismic (Water)		Combined
Seismic Gas only	28.40%	39.50%	9.60%		25.80%
Seismic Water only	21.20%	13.90%	39.50%		24.90%
Well & Seismic (G &W)	57.60%	40.80%	38.30%		45.60%

Table 5.6 Percentage improvement to the initial base case model using the Hamming distance as the binary seismic objective function.

Based on the analysis above, it is observed that using the *Current* measurement metric as the binary seismic objective function as opposed to the Hamming distance has the potential to produce improved models with better predictive capabilities, and might be regarded as a more effective metric. This result also concurs with the previous analysis in Chapter 3 about the effectiveness and efficiency of the *Current* measurement metric.

5.9 Summary

This chapter discusses the application of the binary seismic assisted history matching of gas and water to a UKCS field. It tackles the challenges of integrating the 4D seismic data into the history matching workflow by using a binary approach, and addresses how the binary maps are created. The Hamming distance and *Current* measurement metric were used as the binary seismic objective function, while the least squares error method was used as the production data objective function. 104 parameters which consist of global and local parameters, flow based multipliers (permeability, transmissibility), volume based multipliers (net-to-gross, pore volume), as well as the end points of the relative permeability curves (critical saturation points) were initial screened, and reduced to 35 parameter after a sensitivity analysis study. After history matching, it is found that the primary control parameters for the seismic binary gas match are the permeability and

critical gas saturation, while the volumetric parameters are important for the seismic binary water match in this particular reservoir. It was also observed that to a limit, the global parameters have more effect on the match than the local parameters, and that the local parameters might be useful to further reduce the misfit. The forecast analysis showed that the *Current* measurement metric produced slightly improved models with better predictive capabilities than the Hamming distance, however, both showed positive improvement. The analysis in this chapter highlights the potential of the binary approach for a seismic assisted history matching exercise, and its applicability to real field scenario. It should be noted that the success of the binary approach is dependent on the ability to correctly interpret the 4D seismic data, as inaccurate interpretation of the 4D seismic data may lead to erroneous results. The next step will then be to compare this approach to a conventional seismic modelling history matching approach as will be done in the next chapter.

Chapter 6

Comparative Analysis of Binary and Conventional SAHM

This chapter presents a comparative analysis of the binary seismic assisted history matching approach using *Current* measurement metric utilised in Chapter 5, and the conventional seismic assisted history matching approach which involves using seismic modelling. The analysis is done using the same field data (UKCS field) and model parameters. The initial ensemble of fluid flow simulation models is created where the full range of uncertain parameters are acknowledged using experimental design methods, and an evolutionary algorithm is used for optimization in the history matching process. The results show that the binary approach gives a good match to gas saturation distribution and water saturation distribution, and the parameters converge towards a solution. The conventional approach captures some signals of hardening and softening in the seismic data, however most parameters do not fully converge towards a solution. The objective function and uncertainty has a better reduction using the binary approach as opposed to the conventional approach, as well as a better forecast analysis. In summary, the binary approach seems more suitable as a quick look reservoir management tool.

6.1 Introduction

In order to implement a seismic assisted history matching scheme, the 4D seismic data has to be integrated into the history matching loop. A procedure previously proposed and used by MacBeth et al. (2004), Floricich et al. (2006) and Fursov (2015) which enables quantitative estimation of the similarity between the seismic data and the simulation model output will be adopted as the conventional method. A relationship between the seismic data and the average maps of the reservoir simulation output dynamic properties (pressure distribution, water saturation and gas saturation) is proposed and analysed. Coefficients are derived which determine the impact of the individual dynamic properties on the generated seismic data, and a scalar map (ideally the baseline seismic) is applied to the dynamic properties so as to capture the effects of the reservoir geology, porosity, net-to-gross and general static properties. These relationships will be used to generate the seismic response, thus avoiding a full physics seismic modelling which is time consuming.

6.2 Conventional SAHM

The conventional seismic assisted history matching procedure is analysed using a seismic modelling approximation (MacBeth et al., 2015) which improves the reservoir and seismic characterisation. The initial 4D seismic data is generated using a seismic forward modelling approach using the petro-elastic properties, seismic wavelet and rock stress sensitivity as proposed by Amini (2014). Figure 6.1 shows the baseline seismic map, change in pressure, change in water saturation, change in gas saturation, and initial 4D seismic maps for the relevant time-steps which were selected because of the occurrence of all the expected physical reservoir phenomena, i.e. gas exsolution and dissolution, water evolution, pressure increase and depressurisation.

A linear regression is performed between the generated seismic and the dynamic properties in order to determine proxy coefficients that will be used in equations (6.1) and (6.2). A good quality regression can be regarded as a sign of good agreement and the coefficient of determination, R^2 can be used as a quantitative measure of it. An R^2 value close to one is regarded as a high quality regression, and a value close to zero or even negative is regarded as a poor quality regression. After calibrating the coefficients to the initial 4D seismic data, subsequent 4D seismic data are then generated using the seismic modelling approximation. Thus, the generated seismic data is then compared to the observed seismic data, and this whole process is shown in Figure 6.2.

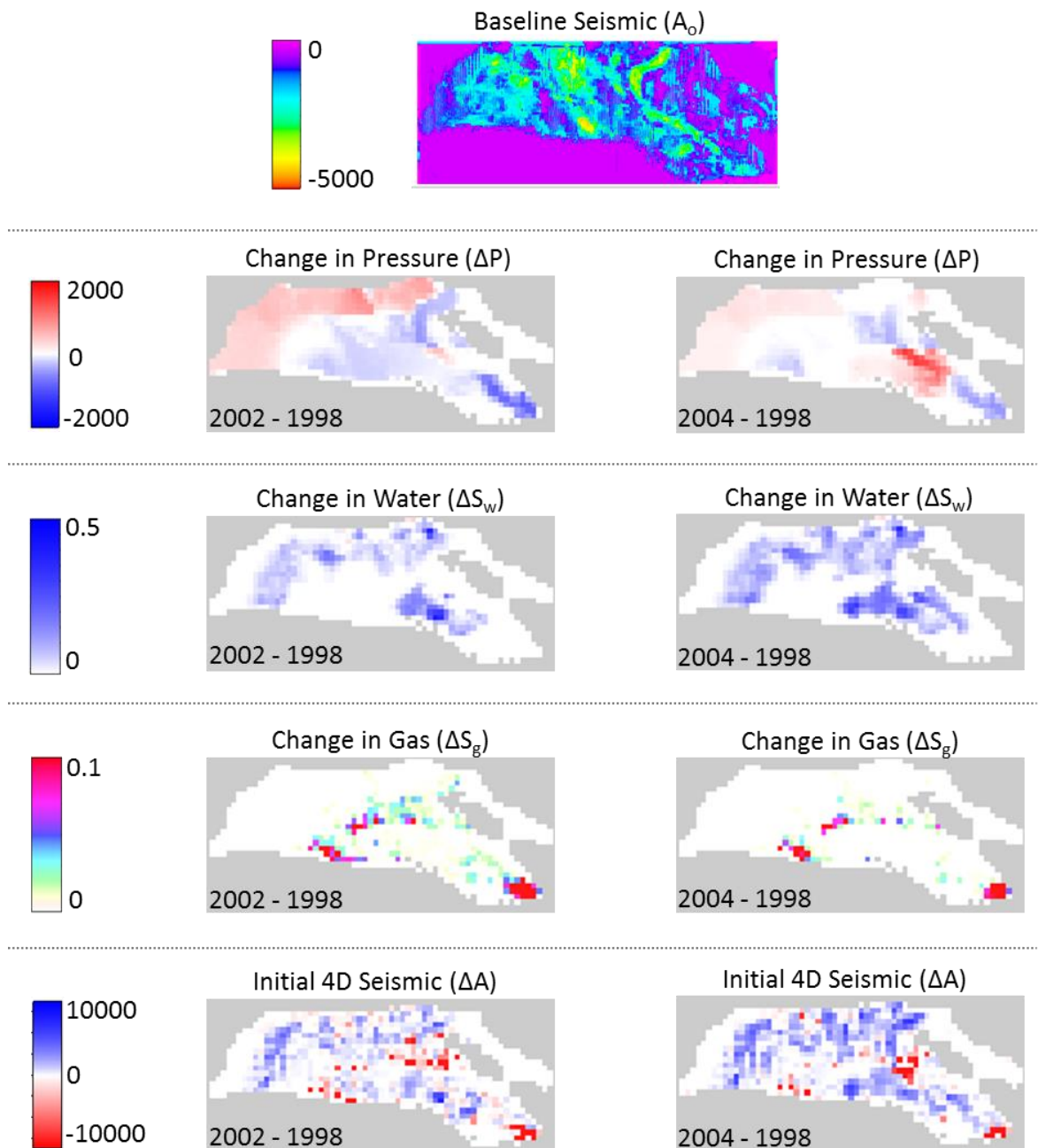


Figure 6.1 The baseline seismic map, the change in pressure, change in water saturation, change in gas saturation, and initial 4D seismic maps for the relevant time-steps in the current analysis.

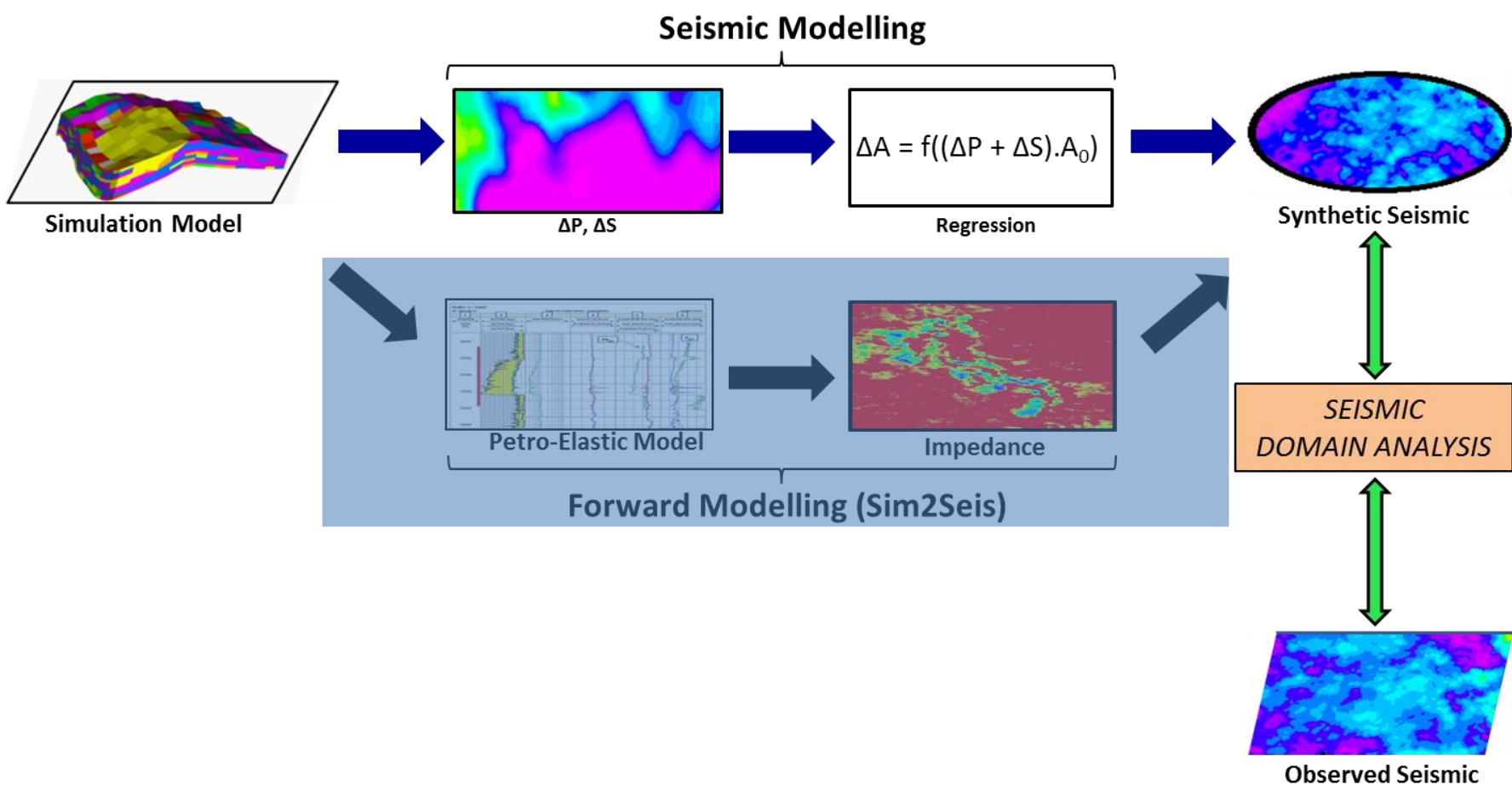


Figure 6.2 Conventional seismic modelling workflow.

6.2.1 Seismic Modelling Approximation

An expression that indicates the relationship between seismic data and average maps of reservoir dynamic properties (pressure distribution, water saturation and gas saturation) is shown in equation (6.1) (MacBeth et al., 2015).

$$\Delta A = (a_p \Delta P + a_{Sw} \Delta Sw + a_{Sg} \Delta Sg). A_o \quad (6.1)$$

where, ΔA is the time lapse map, ΔP is the change in pressure distribution, ΔSw is the change in water saturation, ΔSg is the change in gas saturation, and A_o is the baseline seismic map which captures the effects of the reservoir geology, porosity, net-to-gross and general static properties. The coefficient, a_p is for the change in pressure distribution which takes into account the rock stress sensitivities and fluids response to pressure change, a_{Sw} is the coefficient for the change in water saturation which takes into account the difference in bulk modulus and density between the water and other reservoir fluids, and a_{Sg} is the coefficient for the change in gas saturation which takes into account the difference in bulk modulus and density between the gas and other reservoir fluids. For the linear regression, the points from ΔA and A_o are the dependent variables, the corresponding points from ΔP , ΔSw and ΔSg are the independent variables, while the constants a_p , a_{Sw} and a_{Sg} are the regression coefficients.

Table 6.1 shows the resultant regression coefficients for the expression when constraining the model to period 2002 – 1998 data, period 2004 – 1998 data, and a combination of period 2002 – 1998 and 2004 – 1998 data. The coefficient of determination, R^2 is 0.43 for period 2002 – 1998, 0.57 for period 2004 – 1998, and 0.51 for a combination of period 2002 – 1998 and 2004 – 1998. The 4D seismic maps generated with the expression and

coefficients are shown in Figure 6.3 and Figure 6.4 for time lapse 2002 – 1998 and time lapse 2004 – 1998 respectively.

These analysis will also be done with a more detailed expression, and then a suitable set of coefficients will be estimated for the conventional seismic assisted history matching approach.

	Coeff. 1	Coeff. 2	Coeff. 3
	2002-1998	2004-1998	2002-1998 and 2004-1998
P	3.77E-07	6.70E-05	2.06E-05
S_w	-0.49522	-0.54326	-0.50162
S_g	1.00919	1.13849	1.06806
R²	0.43	0.57	0.51

Table 6.1 The coefficients for equation (6.1) for different time steps, as well as the corresponding coefficient of determination, R^2 .

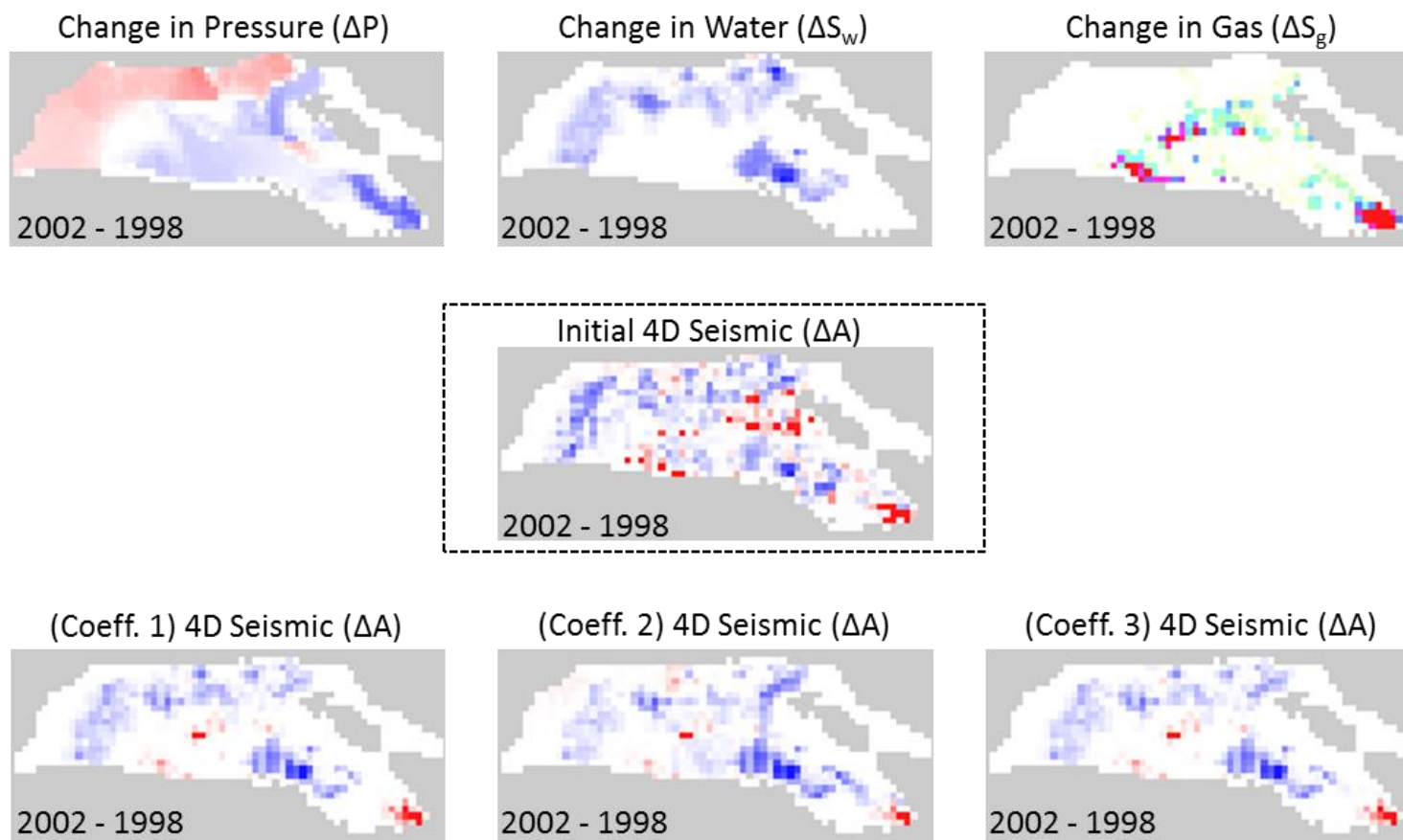


Figure 6.3 Top row shows reservoir dynamic changes, the middle row shows the initial 4D seismic data, and the last row shows generated 4D seismic maps using different coefficients derived from equation (6.1) for 2002 – 1998.

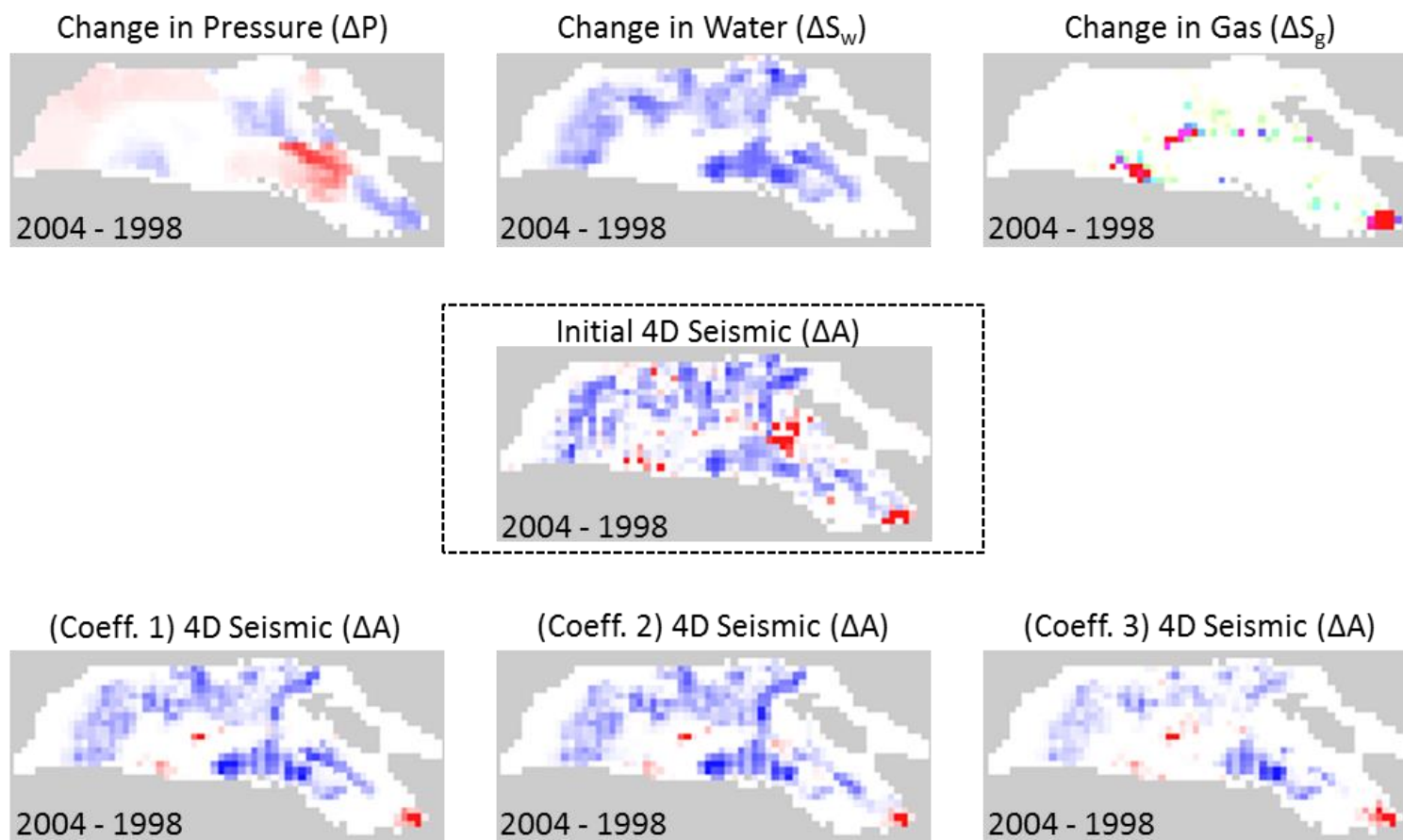


Figure 6.4 Top row shows reservoir dynamic changes, the middle row shows the initial 4D seismic data, and the last row shows generated 4D seismic maps using different coefficients derived from equation (6.1) for 2004 – 1998.

A more detailed expression that indicates the relationship between seismic data and average maps of reservoir dynamic properties (pressure distribution, water saturation and gas saturation) is shown in equation (6.2) (MacBeth et al., 2015).

$$\Delta A = (a_p \Delta P + a_{Sw} \Delta Sw + a_{Sg} \Delta Sg + a_{PSw} \Delta P \Delta Sw + a_{PSg} \Delta P \Delta Sg + a_{PP} \Delta P \Delta P + a_{SwSw} \Delta Sw \Delta Sw + a_{SgSg} \Delta Sg \Delta Sg) \cdot A_o \quad (6.2)$$

where, ΔA is the time lapse map, ΔP is the change in pressure distribution, ΔSw is the change in water saturation, ΔSg is the change in gas saturation, A_o is the baseline seismic map which captures the effects of the reservoir geology, porosity, net-to-gross and general static properties, and the double terms represent the quadratic terms. The coefficient, a_p is for the change in pressure distribution which takes into account the rock stress sensitivities and fluids response to pressure change, a_{Sw} is the coefficient for the change in water saturation which takes into account the difference in bulk modulus and density between the water and other reservoir fluids, a_{Sg} is the coefficient for the change in gas saturation which takes into account the difference in bulk modulus and density between the gas and other reservoir fluids, and a_{PSw} , a_{PSg} , a_{PP} , a_{SwSw} and a_{SgSg} are double term coefficients. For the linear regression, the points from ΔA and A_o are the dependent variables, the corresponding points from ΔP , ΔSw , ΔSg , $\Delta P \Delta Sw$, $\Delta P \Delta Sg$, $\Delta P \Delta P$, $\Delta Sw \Delta Sw$ and $\Delta Sg \Delta Sg$ are the independent variables, while the constants a_p , a_{Sw} , a_{Sg} , a_{PSw} , a_{PSg} , a_{PP} , a_{SwSw} and a_{SgSg} are the regression coefficients.

Table 6.2 shows the resultant regression coefficients for this expression when constraining the model to period 2002 – 1998 data, period 2004 – 1998 data, and a combination of period 2002 – 1998 and 2004 – 1998 data. The coefficient of

determination, R^2 is 0.45 for period 2002 – 1998, 0.61 for period 2004 – 1998, and 0.53 for a combination of period 2002 – 1998 and 2004 – 1998. The 4D seismic maps generated with the expression and coefficients are shown in Figure 6.5 and Figure 6.6 for time lapse 2002 – 1998 and time lapse 2004 – 1998 respectively.

From the comparison of the results of equations (6.1) and (6.2), it is observed from the maps (Figures 6.3, 6.4, 6.5 and 6.6) that equation (6.2) produces maps that better replicate the initial 4D seismic data. The coefficients generated for period 2004-1998 (Coeff. 5) for equation (6.2) is selected for the conventional seismic assisted history matching exercise, as its results best matches the initial 4D seismic data, and its coefficient of determination, R^2 indicates that it is the best fit.

	Coeff. 4	Coeff. 5	Coeff. 6
	2002-1998	2004-1998	2002-1998 and 2004-1998
P	7.86E-06	6.43E-05	3.12E-05
S_w	-0.68357	-0.78418	-0.70846
S_g	1.42943	1.03913	1.33533
P²	2.43E-09	3.22E-08	1.04E-08
S_w²	0.668523	0.857184	0.695681
S_g²	-1.69925	0.108977	-1.01183
P.S_w	-1.39E-05	-6.50E-05	3.81E-06
P.S_g	-2.72E-06	-5.34E-06	-2.43E-07
S_w.S_g	1.56502	1.39446	1.372
R²	0.45	0.61	0.53

Table 6.2 The coefficients for equation (6.2) for different time steps, as well as the corresponding coefficient of determination, R^2 .

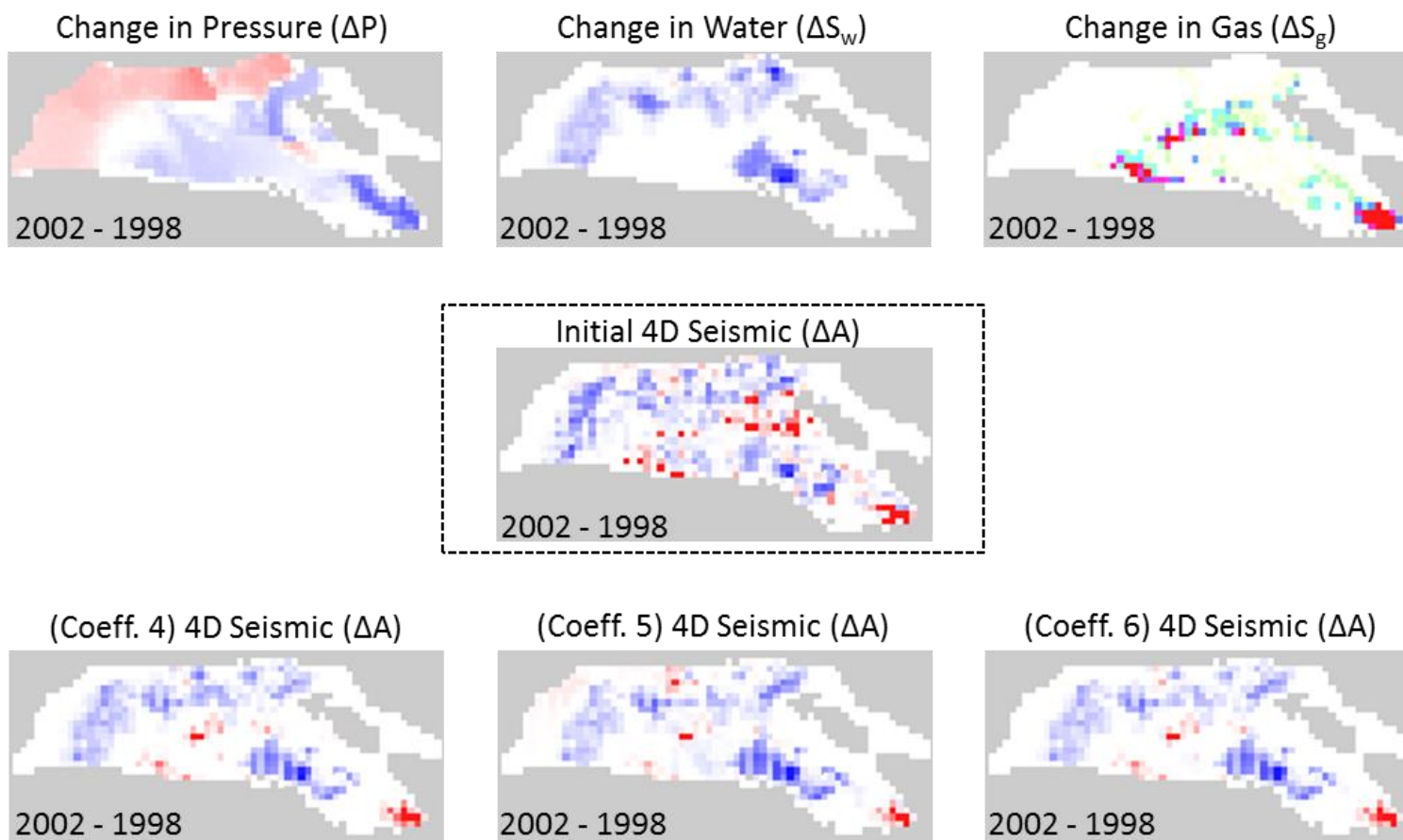


Figure 6.5 Top row shows reservoir dynamic changes, the middle row shows the initial 4D seismic data, and the last row shows generated 4D seismic maps using different coefficients derived from equation (6.2) for 2002 – 1998.

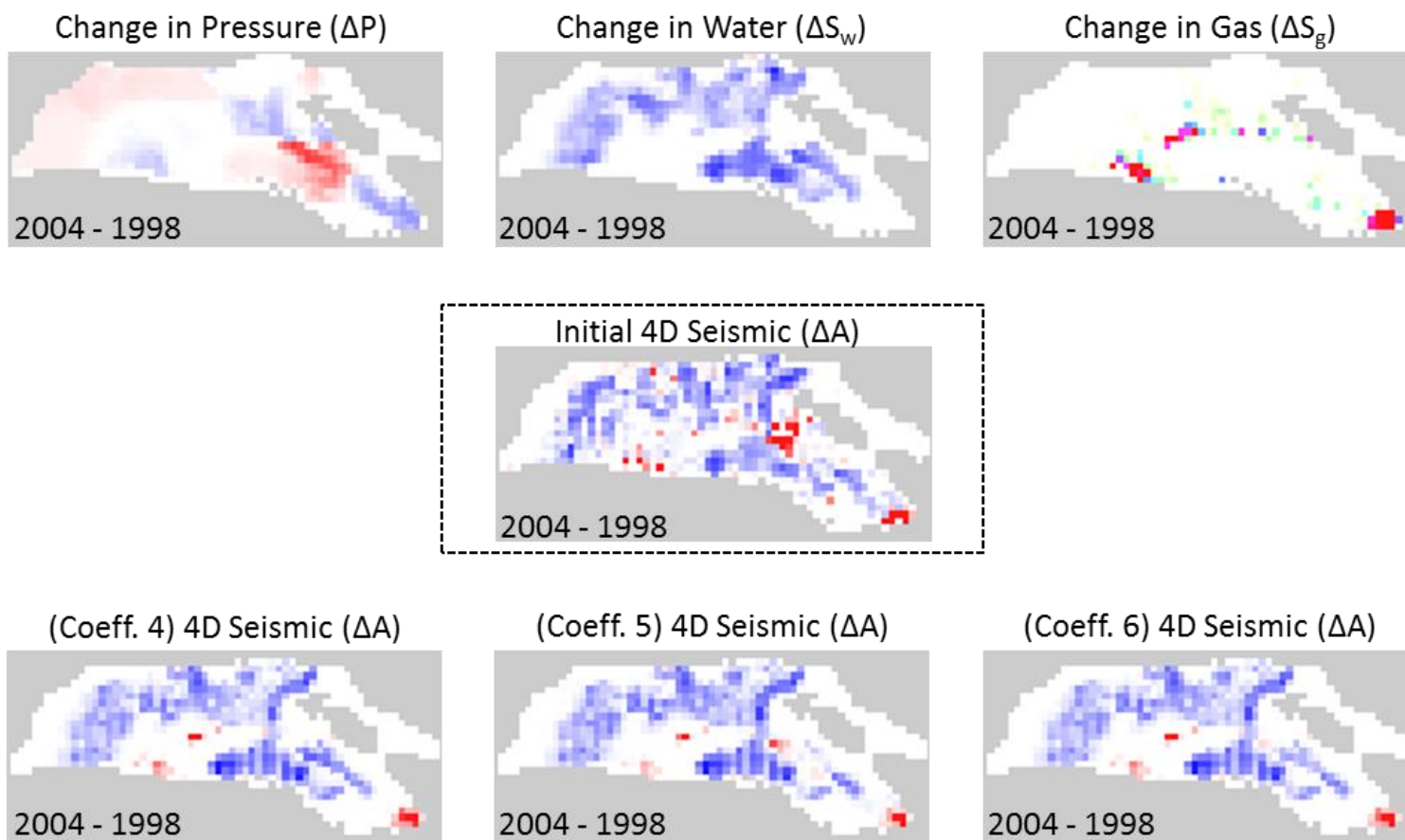


Figure 6.6 Top row shows reservoir dynamic changes, the middle row shows the initial 4D seismic data, and the last row shows generated 4D seismic maps using different coefficients derived from equation (6.2) for 2004 – 1998.

6.3 Application of Conventional SAHM

The initial state of the reservoir and base case conditions of the history matching process are shown in Figures 6.7 and 6.8. Figure 6.7 shows the observed data, the base case model and the initial ensemble of the response parameters (oil production rate, gas production rate and water production rate) of wells P1 and P2 respectively. The observed data represents data measured at the wells, the base case represents the initial model's production profile, while the initial ensemble represents profiles for the models generated using the Latin Hypercube Experimental Design which encompasses the effects of the uncertain parameters.

The base case model 4D seismic data and the observed 4D seismic data are shown for all the relevant time-steps in the first and second column respectively in Figure 6.8. The observed 4D seismic map shows a progressive brightening in the early years (softening, red colour), and subsequent dimming in the later years (hardening, blue colour). The base case 4D seismic maps do not replicate most of these signals, and improving this match is the aim of this exercise. The first 4 monitor surveys corresponding to the first 7 years will be used for the history match, while the last 2 monitor surveys corresponding to the remaining 3 years will be used to analyse the forecast.

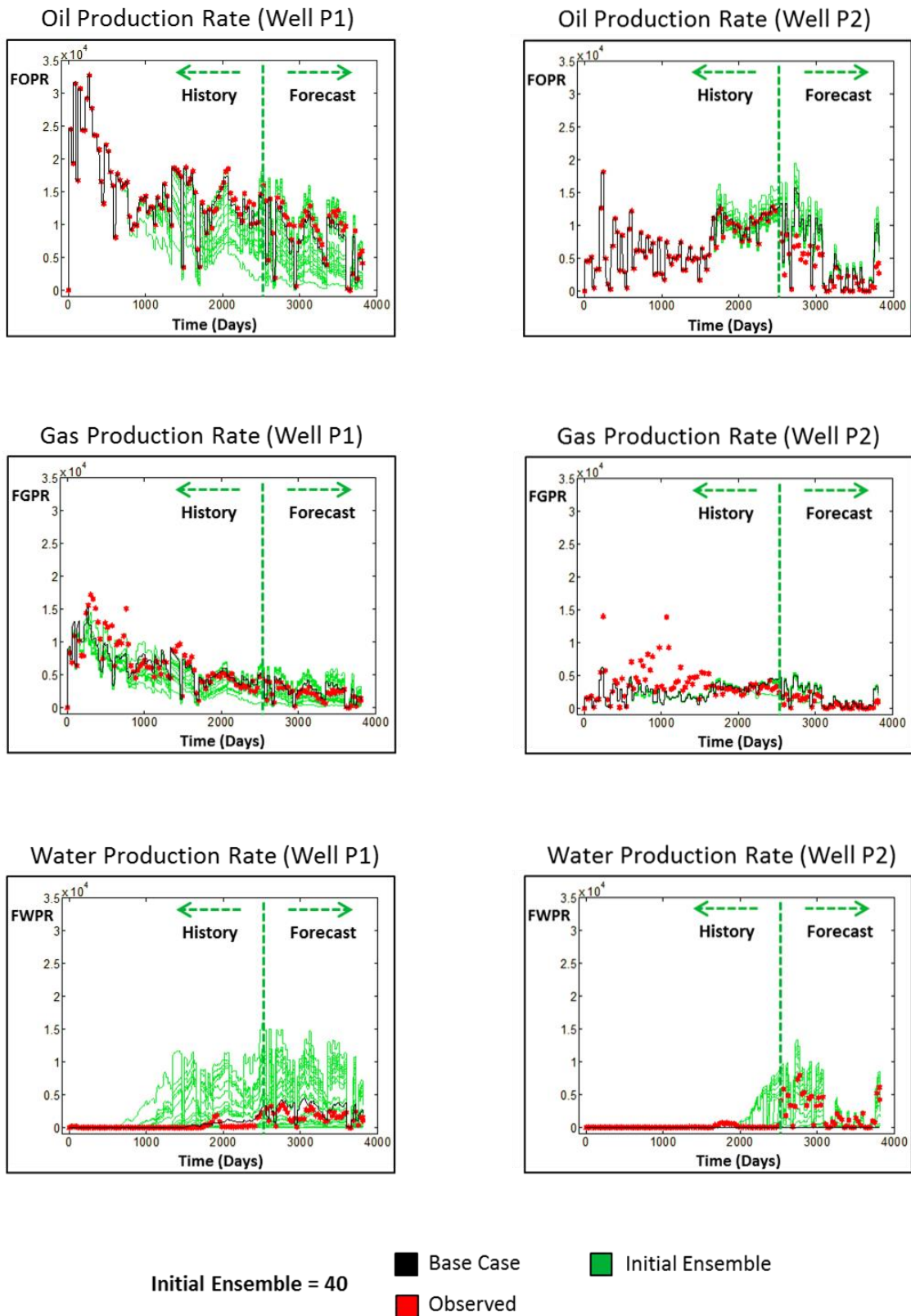


Figure 6.7 Normalized production profiles for wells P1 (left column) and P2 (right column) showing the initial base case model responses (black lines), the initial ensemble responses (green lines), and the historical observed data (red dots) for oil production rate, gas production rate and water production rate.

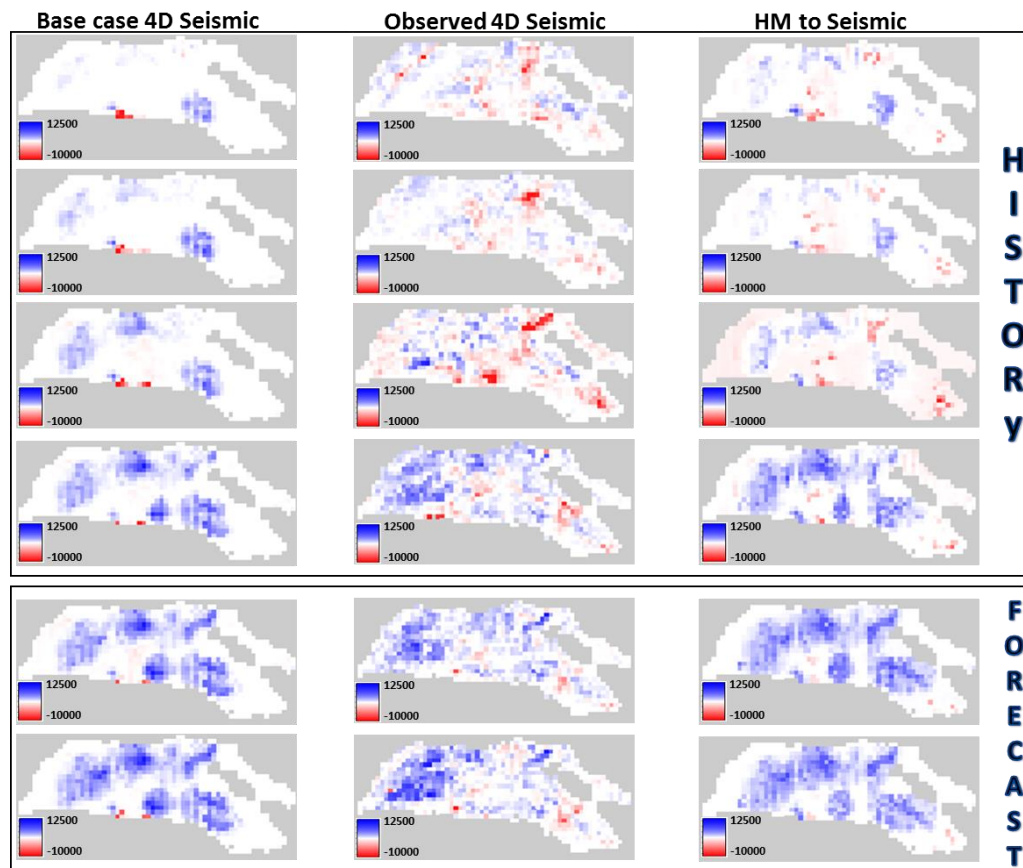


Figure 6.8 The base case 4D seismic maps, observed 4D seismic maps, and history matched (to seismic data) 4D seismic maps for all the relevant time-steps. The first 4 monitors (the first four rows) are used for the history matching exercise, while the last 2 monitors (the last 2 rows) are used for the forecasting analysis.

6.3.1 HM to Seismic

To history match to observed seismic data only, the production data term in the combined objective function will be assigned a value of zero, such that the reservoir models will be constrained to only the observed seismic data. After history matching to observed seismic data only, the updated production profiles are shown in Figure 6.9, and the updated 4D seismic data is shown in the third column in Figure 6.8.

Figure 6.9 shows the production profiles (oil production rate, gas production rate and water production rate) of the updated models (in dark blue colour) of well P1 and well P2. Figure 6.8 shows the updated 4D seismic data maps compared to the observed 4D seismic data maps and base case model 4D seismic data maps highlighting areas of improvement of the hardening and softening signals on the updated 4D seismic data maps. Figure 6.10(a) shows the histograms of selected parameters, where the horizontal permeability multiplier is about 1.5, the critical gas saturation value tends towards a value of 3.0%, and the pore volume multiplier is approximately 1.3. Figure 6.10(b) shows the plot of objective function and uncertainty for history matching to seismic data only.

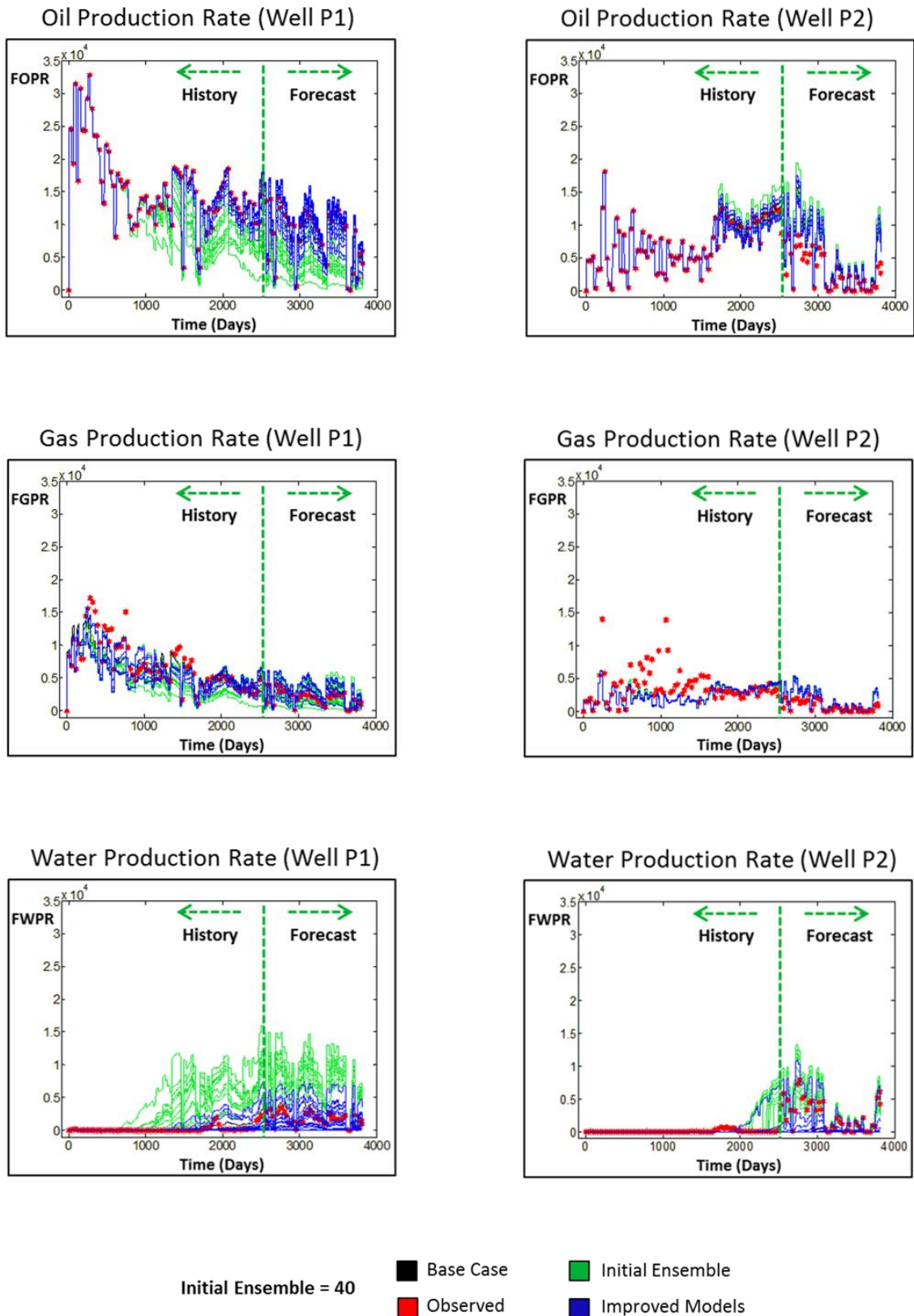


Figure 6.9 Normalized production profiles for wells P1 (left column) and P2 (right column) highlighting the improved model responses (dark blue lines), after history matching to seismic data.

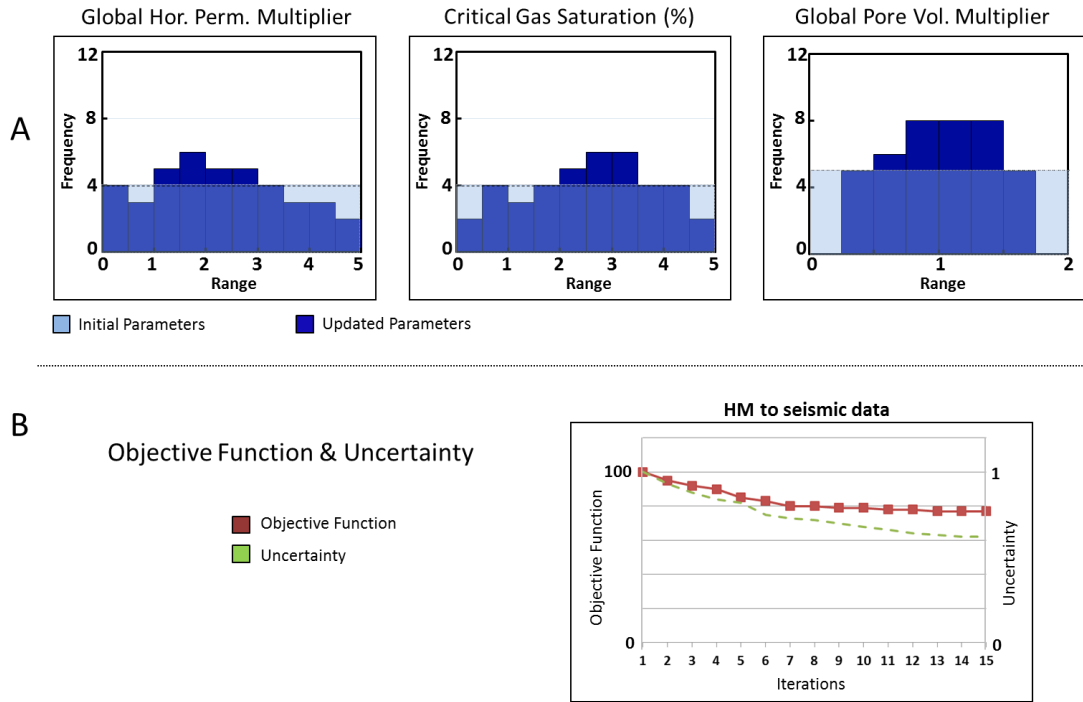


Figure 6.10 (a) Initial and updated parameters for history matching to seismic data. (b) Objective function and uncertainty plot for history matching to seismic data. The uncertainty is quantified as the range of response parameters in each iteration.

6.3.2 HM to Production Data and Seismic

For a joint history match to production data and observed seismic data, the combined objective function is normalized such that the effect of the production data and observed seismic data are equal, and that at the beginning of the history match, the combined misfit is a value of unity. After history matching to production data and observed seismic data, the updated production profiles are shown in Figure 6.11, and the updated 4D seismic data is shown in the third column in Figure 6.12.

The production profiles (oil production rate, gas production rate and water production rate) of the updated models (in dark blue colour) of well P1 and well P2 are displayed in

Figure 6.11. Figure 6.12 shows the updated 4D seismic data maps compared to the observed 4D seismic data maps and base case model 4D seismic data maps highlighting areas of improvement of the hardening and softening signals on the updated 4D seismic data maps. The histograms of selected parameters are displayed in Figure 6.13(a), where the horizontal permeability multiplier is about 2.5, the critical gas saturation value tends towards a value of 2.5%, and the pore volume multiplier is approximately 1.2. The plot of objective function and uncertainty for history matching to production data and observed seismic data is displayed in Figure 6.13(b).

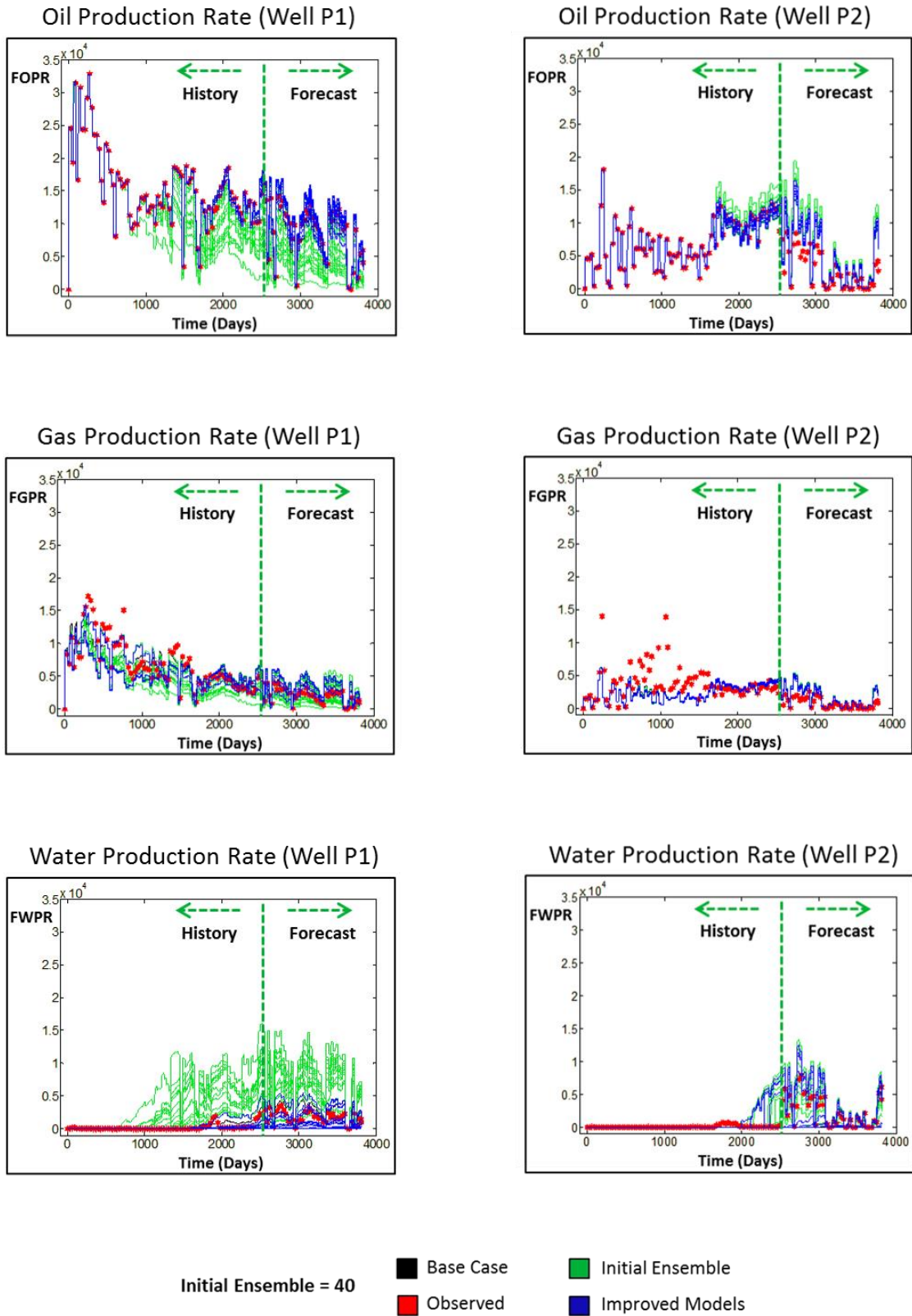


Figure 6.11 Normalized production profiles for wells P1 (left column) and P2 (right column) highlighting the improved model responses (dark blue lines), after history matching to production data and seismic data.

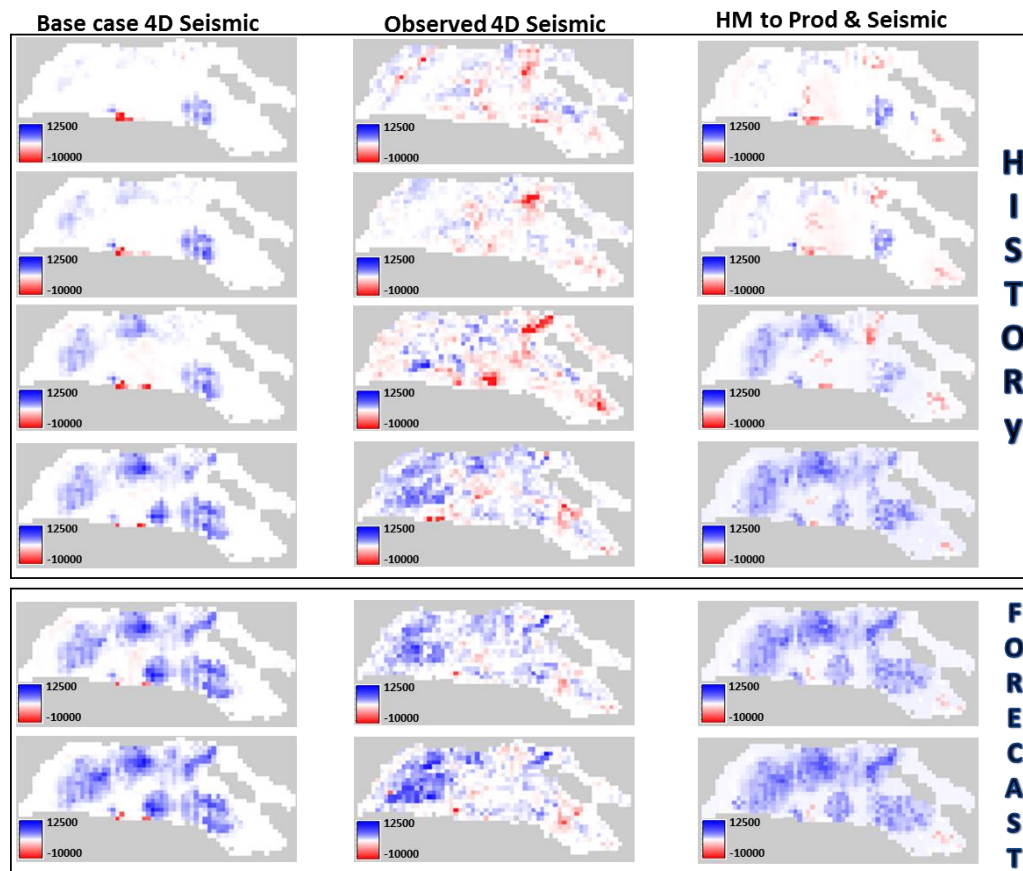


Figure 6.12 The base case 4D seismic maps, observed 4D seismic maps, and history matched (to production data and seismic data) 4D seismic maps for all the relevant time-steps. The first 4 monitors (the first four rows) are used for the history matching exercise, while the last 2 monitors (the last 2 rows) are used for the forecasting analysis.

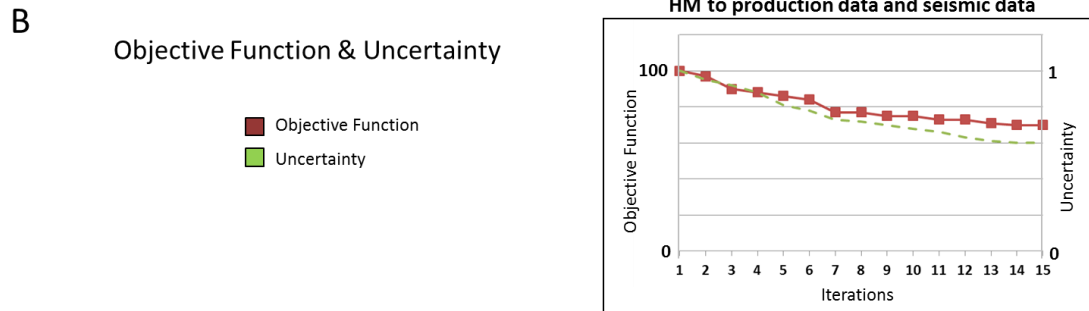
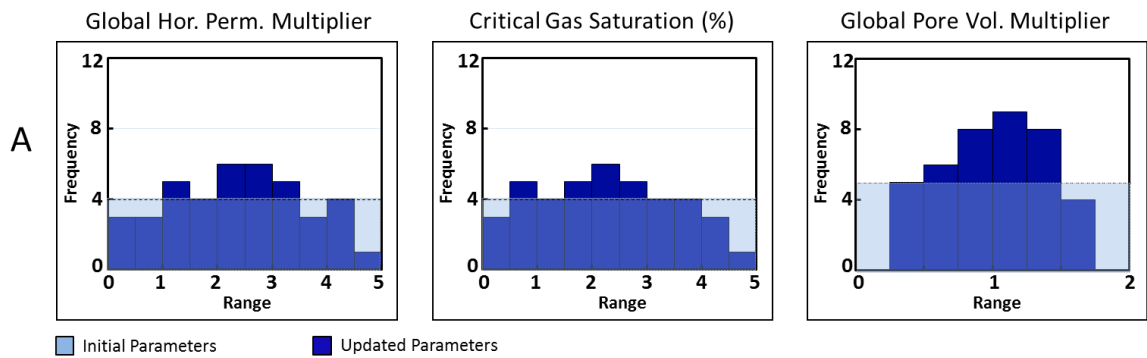


Figure 6.13 (a) Initial and updated parameters for history matching to production data and seismic data. (b) Objective function and uncertainty plot for history matching to production data and seismic data. The uncertainty is quantified as the range of response parameters in each iteration.

6.4 Forecast Analysis

An analysis of the forecasting capabilities of the history match to seismic data, and history match to production data and observed seismic data is implemented. Table 6.3 shows the forecast misfit for the average of the improved models, where the well data misfit is calculated using the least squares error, and the seismic misfit is from seismic modelling. The results are shown for the initial base case model, matching to seismic only, and matching to a combination of well data and seismic. A percentage improvement to the initial base case model is calculated individually and combined as shown in Table 6.4. Overall, matching to seismic only yields a 31.15% improvement to the initial base case model, while matching to well data and seismic yields a 37.38% improvement to the initial base case model.

	Well Data	Seismic Data
Basecase	14285	271108
Seismic only	10525	173548
Well & Seismic	7945	188745

Table 6.3 Forecast misfit for the average of the improved models. The well data misfit is calculated using the least squares error, and the seismic misfit is from seismic modelling.

	Well Data	Seismic Data		Combined
Seismic only	26.32%	35.98%		31.15%
Well & Seismic	44.38%	30.38%		37.38%

Table 6.4 Percentage improvement to the initial base case model.

Based on the analysis, it is observed that integrating the 4D seismic data and well data produces improved models with better forecast capabilities. These results will be compared with the binary approach results (from Chapter 5) in the next section.

6.5 Comparative Analysis

The procedure, workflow and results of the binary seismic assisted history matching and conventional seismic assisted history matching are analysed in this section.

The binary seismic assisted history matching approach has been shown to be an effective quick look reservoir management tool. It takes much less time to compute and circumvents the use of a complex petro elastic modelling approach (for example, the PEM approach by Amini, 2014). However, the challenge of the masking effect of water on gas,

masking effect of gas on water, masking effect of pressure, and the ambiguous signal regions still exists (Figure 6.14).

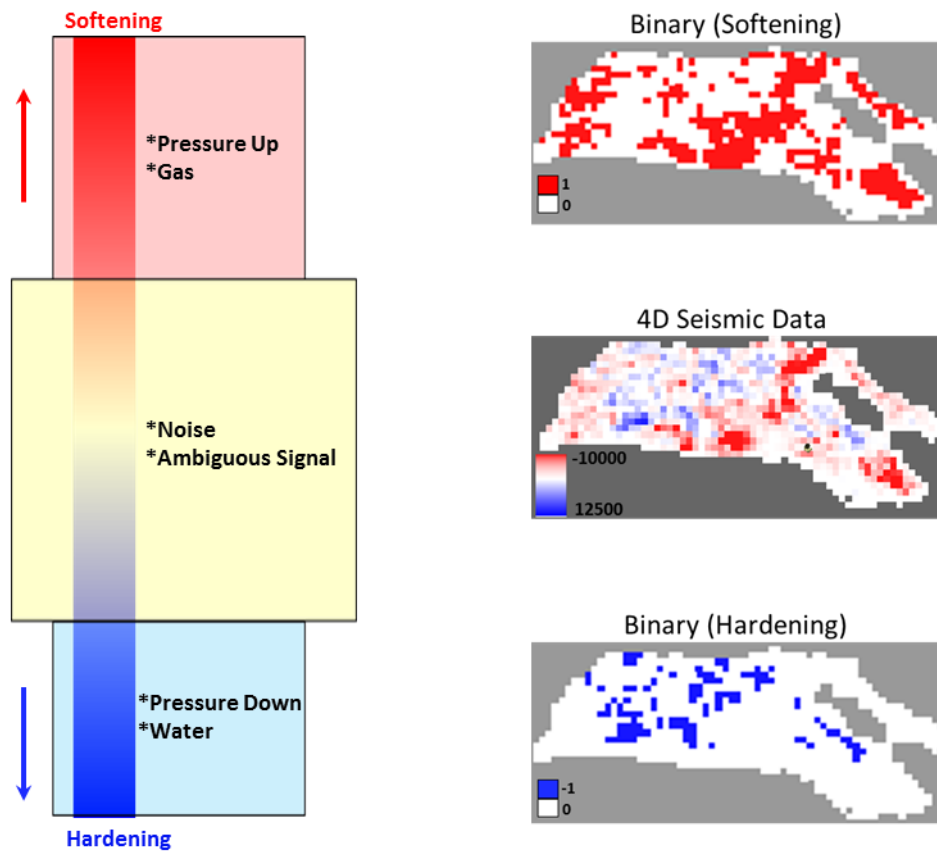


Figure 6.14 The interpretation of the binary maps derived from 4D seismic data.

The conventional seismic assisted history matching approach has shown potential as a reservoir management tool. The seismic modelling process has been fast tracked in order to be useful for history matching. However, the results show there is still room for improvement. A comparison of the results of the binary seismic assisted history matching approach and conventional seismic assisted history matching approach is shown in Figure 6.15. The figure shows the convergence of selected parameters, the objective function and uncertainty, and the forecast capabilities. The parameters converge to a solution when using the binary approach, but do not fully converge to a solution when using the conventional approach. Also, the binary approach shows a better reduction in the

objective function and uncertainty, as opposed to the fair reduction when using the conventional approach. The overall forecast percentage improvement for the binary approach is 46%, while that for the conventional approach is 38%. The well data forecast improvement for the binary approach is 58%, in contrast with the well data forecast improvement for the conventional approach which is 44%. The binary approach gives a good match to the gas saturation distribution and water saturation distribution, and the conventional approach captures the hardening and softening signals in some areas in the seismic data.

Based on the analysis, it is concluded that the binary approach for seismic assisted history matching is the preferred method, and seems more suitable as a quick look reservoir management tool, as it circumvents the use of the complex seismic modelling approach, however, the conventional approach explored here has shown some positive potential.

Binary Approach versus Conventional Approach

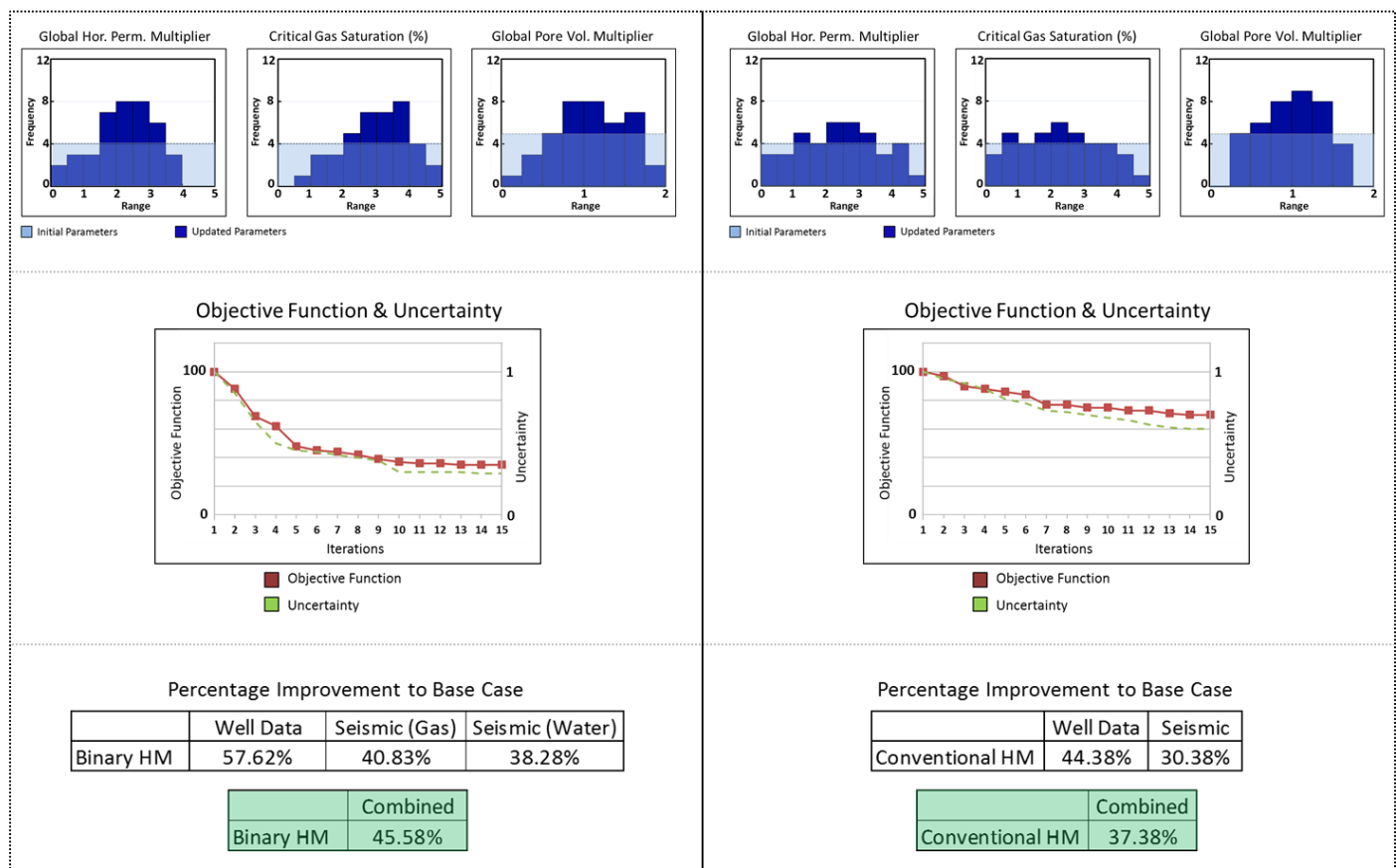


Figure 6.15 Comparison of the binary approach and the conventional approach

6.6 Summary

This chapter explores the comparative analysis of the binary seismic assisted history matching approach and the conventional seismic assisted history matching approach. It showcases the workflow for the conventional approach through seismic modelling approximation. The preliminary results show that the detailed expression produces a better fit to the 4D seismic data, and hence it is used for the conventional seismic assisted history matching exercise. After history matching, it is observed that integrating the 4D seismic data and well data produces improved models with better forecast capabilities. The comparison of the binary approach and conventional approach highlights the potential of both methods. The binary approach shows a better reduction in the objective function and uncertainty, a better model forecast capability, parameters that converge towards a solution, and good matches to gas saturation distribution and water saturation distribution. The conventional approach shows a fair reduction in the objective function and uncertainty as well as model forecast capability, parameters that do not fully converge to a solution, and good matches of the 4D seismic hardening and softening signals in some areas.

The analysis in this chapter highlights the pros and cons of both methods, and the conclusion is that the binary approach is the preferred method for seismic assisted history matching as it circumvents the use of the complex seismic modelling approach, however, the conventional approach has shown its applicability, and MacBeth et al. (2015) have shown in their paper that the misfit surface is not affected by this approach.

Chapter 7

Conclusions and Recommendations

This chapter summarizes all the work that has been done in this thesis, and then provides recommendations for future work that will enhance the efficiency and effectiveness of the workflow. The key objective of this thesis which is the progression of analysing 4D seismic data from a qualitative approach to a quantitative approach using binary images is examined, and the perceived limitations are prescribed as future recommendations.

7.1 Conclusions

Qualitative interpretation of 4D seismic data is an important first step to understanding the characteristics of the signals seen on the 4D seismic maps. This entails superimposing the production data details on the 4D seismic maps. The production data details are not limited to the well locations and trajectory, but also and especially, the volumes of injected or produced fluids are of great importance. This interpretation technique was fully utilized for the analysis in Chapter 2 by delineating the seismic data signals of hardening and softening in order to implement a quantitative analysis of gas volumes in a UKCS field.

This was an interesting study due to the nature of the field and the reservoir activities whereby injection wells and production wells were shut-in and put on stream intermittently due to the reservoir management planning of the field operator. After the quantitative analysis, it was shown that multiple 4D seismic surveys shot during gas exsolution and dissolution proved useful in estimating critical gas saturation, and providing some understanding of the maximum gas saturation.

Also, estimates of the solution gas oil ratio were derived using multiple 4D seismic surveys, and these values had a similar trend, but lower values than that which the reservoir simulator predicted, and this was attributed to the possible influence of injected water on the seismic data. These analyses were really interesting and termed to be semi-quantitative, so a more quantitative approach was sought, whereby the reservoir model could be updated using production data and seismic data. The key challenge being integrating the seismic data in the history matching workflow, and the potential solution being using a binary images approach.

In a quest to integrate the production data and seismic data, a binary images approach is developed in Chapter 3. The binary images approach is such that a change in gas or water saturation in the seismic data or simulation data is assigned a value of one, and no change in gas or water saturation in the seismic data or simulation data is assigned a value of zero. This approach simplifies the challenges that are abound when using a petro elastic modelling or seismic modelling approach. However, before settling for the binary approach, idealised models are created to test the implementation of a two-level (binary approach), multi-level, and full-level threshold approach, and the results shows that the binary approach captures the major data characteristics. The next step is to analyse suitable metrics as objective function for computing the misfit between the binary seismic maps and binary simulation model maps. Four measurement metrics – Hamming distance, Hausdorff distance, Mutual Information and *Current* measurement metric were examined using test case scenarios that replicate changes observed during the history matching process, and the results show that the *Current* measurement metric and Hamming distance seem to be the most satisfactory. Having done the development analysis of the binary approach, a validation of this approach will be the next step.

Chapter 4 deals with the validation of the binary images approach for integrating seismic data and production data in a history matching exercise. The Hamming distance metric and the *Current* measurement metric which have been shown to possess the best ability of accurately distinguishing misfits between binary maps of different dispositions are now tested on a representative synthetic model in order to validate the use of the binary image approach, as well as show its functionality in a practical setting. Three different scenarios are analysed with the aim of replicating expected real field occurrence, and these are the gas exsolution scenarios, the water evolution scenarios, and a combination of gas exsolution and water evolution.

It is demonstrated that converting the seismic data and perturbed simulation model outputs to binary maps provides a quick and efficient method of assessing the reservoir parameters so as to arrive at a simulation model which reproduces the seismic data response. The analysis in this chapter validates the competence of the binary approach for a history matching exercise, and this binary approach would be utilised on a real field dataset were the production data will also be taken into cognisance in the next chapter.

Seismic assisted history matching of gas and water distributions in a real field using binary image matching is analysed in Chapter 5. The production data is matched using the conventional least squares objective function method calculated between the historical production data and the simulation predictions, while the Hamming distance and *Current* measurement metric are independently used to ascertain the mismatch between the binary seismic and the binary simulation images of saturation (gas and water) distribution predictions.

An initial ensemble of fluid flow simulation models is created where the full range of uncertain parameters are acknowledged using experimental design methods, and an evolutionary algorithm is used for optimization in the history matching process. 104 parameters which consist of global and local parameters, flow based multipliers (permeability, transmissibility), volume based multipliers (net-to-gross, pore volume), as well as the end points of the relative permeability curves (critical saturation points) are initial screened, and reduced to 35 parameter after a sensitivity analysis study. It is found that the primary control parameters for the binary seismic gas match are the permeability and critical gas saturation, while the volumetric parameters are important for the binary seismic water match in this particular reservoir. It is also observed that the global parameters have more effect on the match than the local parameters, and that the *Current*

measurement metric also shows better forecasting ability than the Hamming distance metric. The next step will then be to compare this approach to a conventional seismic modelling history matching approach.

Chapter 6 covers the comparative analysis of the binary seismic assisted history matching approach using the *Current* measurement metric and the conventional seismic assisted history matching approach which involves using seismic modelling approximation, and this is implemented on the field data and reservoir parameters examined in Chapter 5. The comparative history matching results show that the binary approach gives a good match to gas saturation distribution and water saturation distribution, and the parameters converge towards a solution. The conventional approach captures some signals of hardening and softening in the seismic data, however most parameters do not fully converge towards a solution. The objective function and uncertainty has a better reduction using the binary approach as opposed to the conventional approach, as well as a better forecast analysis. Having fully examined the different approaches, it can be concluded that the binary approach is a more viable technique to be used as a quick look reservoir management tool. It is important to also discuss the challenges and limitations of the methods used in this thesis, and offer some suggestions and potential solutions to be considered for future research, and this will be addressed in the next section.

7.2 Recommendations for Future Research

This section is about possible ways to expand the boundaries of the work in this thesis, it addresses some of the concepts, questions and decision-making that were thought about and considered but were not fully implemented. These include the potential of updating the geological model in the workflow, as the work implemented thus far in this thesis has been on the simulation model, with the assumption that the geological model is suitable, which is usually not the case. Also the question about scale suitability for comparing the seismic data and simulation data predictions – should this be on the seismic data scale or on the simulation model scale? Should it be map-based or volumetric? Also can the production data objective function and seismic data objective function be of the same scale or nature? Other food for thought are the issue of ambiguous signals that exist in the region not captured by the binary approach. Does this region need to be captured, or is it all noise? Would a simulation to seismic exercise be necessary to capture this, or perhaps a proxy seismic expression might be suitable? All these thoughts and more will be examined in the following sub-sections.

7.2.1 Workflow Modification for Geological Model Updating

The introduction of the geological model into the binary seismic assisted history matching workflow is shown in Figure 7.1, and will indeed get the nod of approval of most geologists. This is mainly because as more information about the reservoir is obtained, the initial assumptions about the geological model will need to be updated and acknowledged.

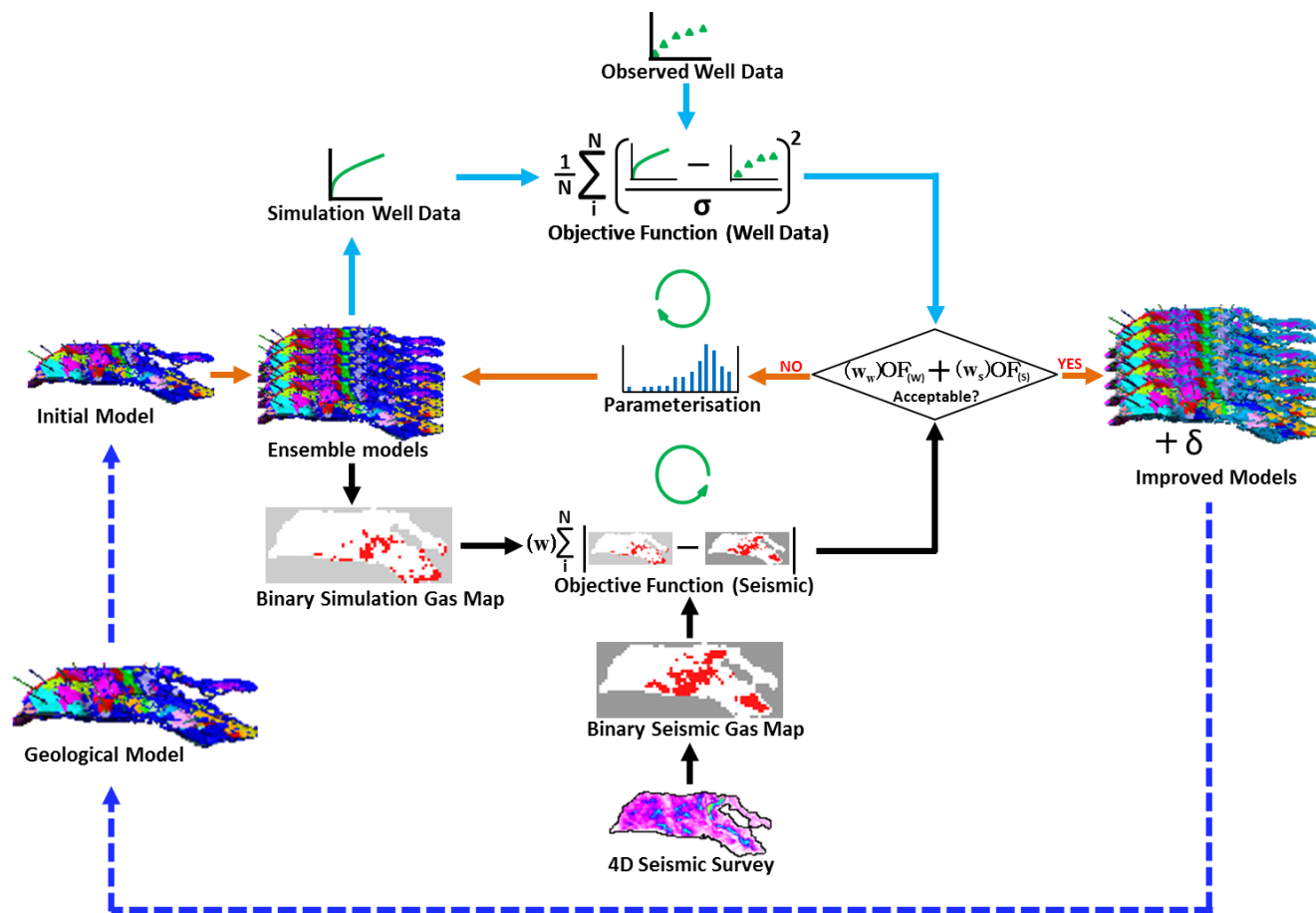


Figure 7.1 Modified binary seismic assisted history matching workflow with the dash arrows showing potential for Geological model updating

The geological model update loop is with dashed lines as it is expected that this loop will not be as frequently updated as the simulation model loop. An example of the potential of updating the geological model is shown in Figure 7.2 from Johann et al. (2009), where the absolute horizontal permeability trends for a geological model is updated with 4D seismic data interpretation constrained by sedimentary and petrophysical facies distribution. This was said to improve the history matching of the field by introducing more realistic geological permeability maps.

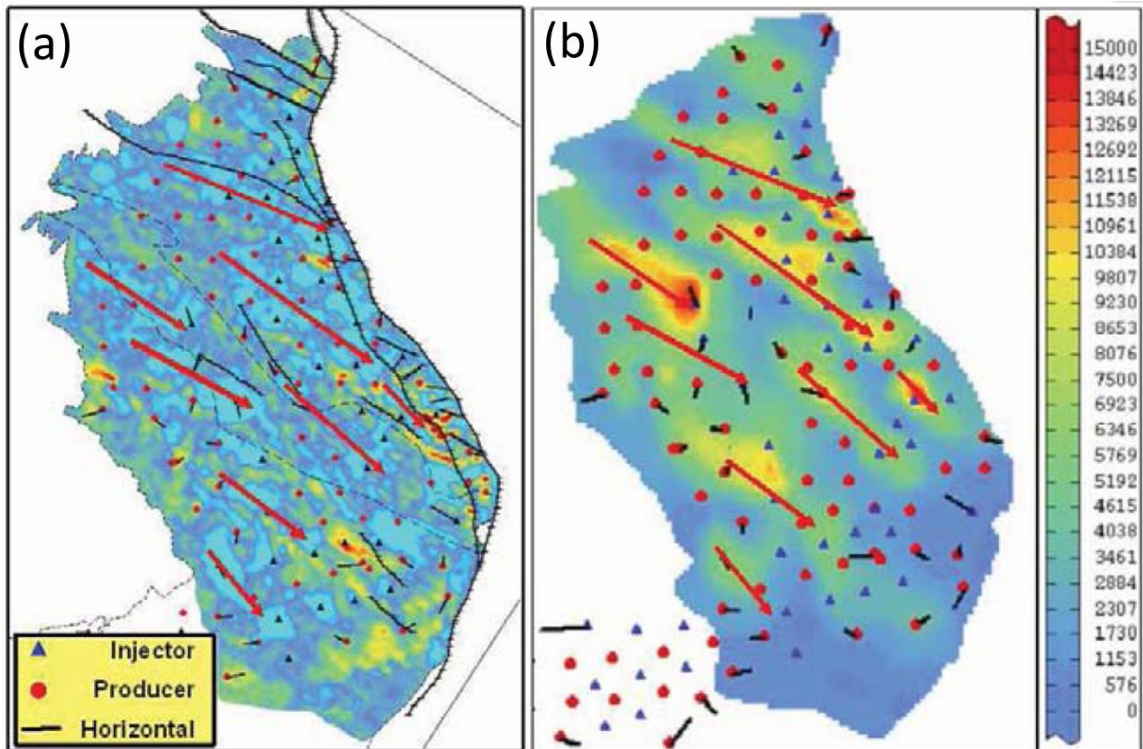


Figure 7.2 (a) The amplitude difference map of the reservoir base, where light blue represents oil replaced by water. (b) An absolute horizontal permeability map derived from 4D imaging and permeability from the DST (Johann et al., 2009).

7.2.2 Different Scales of Analysis

7.2.2.1 Simulation Scale and Seismic Scale

The average reservoir model grid size is about 75m by 75m, while the average seismic data bin size is 12.5m by 12.5m (Figure 7.3). The differences in scale of these different sets of data pose a challenge as to what scale should the misfit analyses be implemented on. Choosing either of these scales will require some element of upscaling or downscaling of the other set of data to fit the chosen scale. The studies of Kretz et al. (2004), Jin et al. (2011), and Alerini et al. (2014) (Figure 7.4) show that the simulation model scale is the preferred option. The work in this thesis also adopted that approach due to its simplicity, straight forward upscaling procedure, and bypassing all the complexity and non-uniqueness involved in downscaling. The downscaling methods are not very successful in capturing the fine-scale heterogeneities (Johnston, 2013), although new methods have been proposed with different levels of sophistication (Sengupta and Mavko, 2003, Castro, 2007, Enchery et al., 2007, Le Ravalec et al., 2012a).

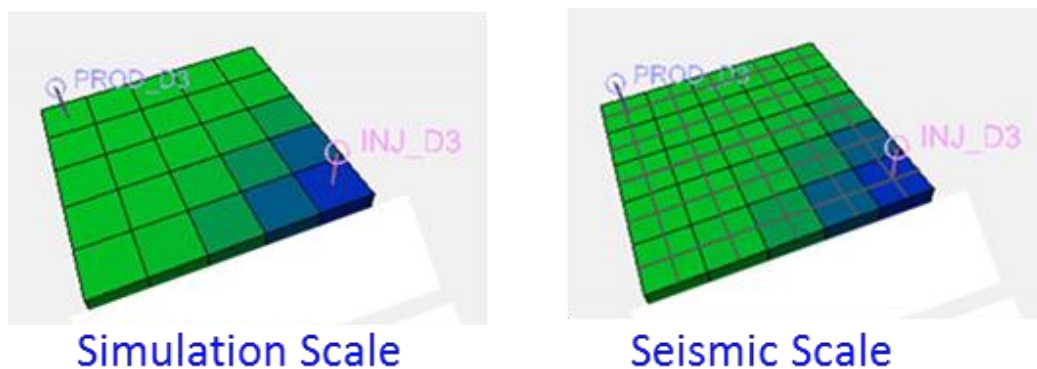


Figure 7.3 Schematic representation of simulation model grid size (75m by 75m), and seismic data bin size (12.5m by 12.5m).

In this regard, the fine seismic scale does present an opportunity to preserve the fine details of pressure and saturation sweep, and thus might have potential for capturing some important information. The winning solution here might be to have the reservoir simulation model grid size at the same scale as the seismic data bin size. The obvious challenge will be the increased simulation runtime, but with the constant improvement in computing capability and capacity, this challenge might be offset in the near future.

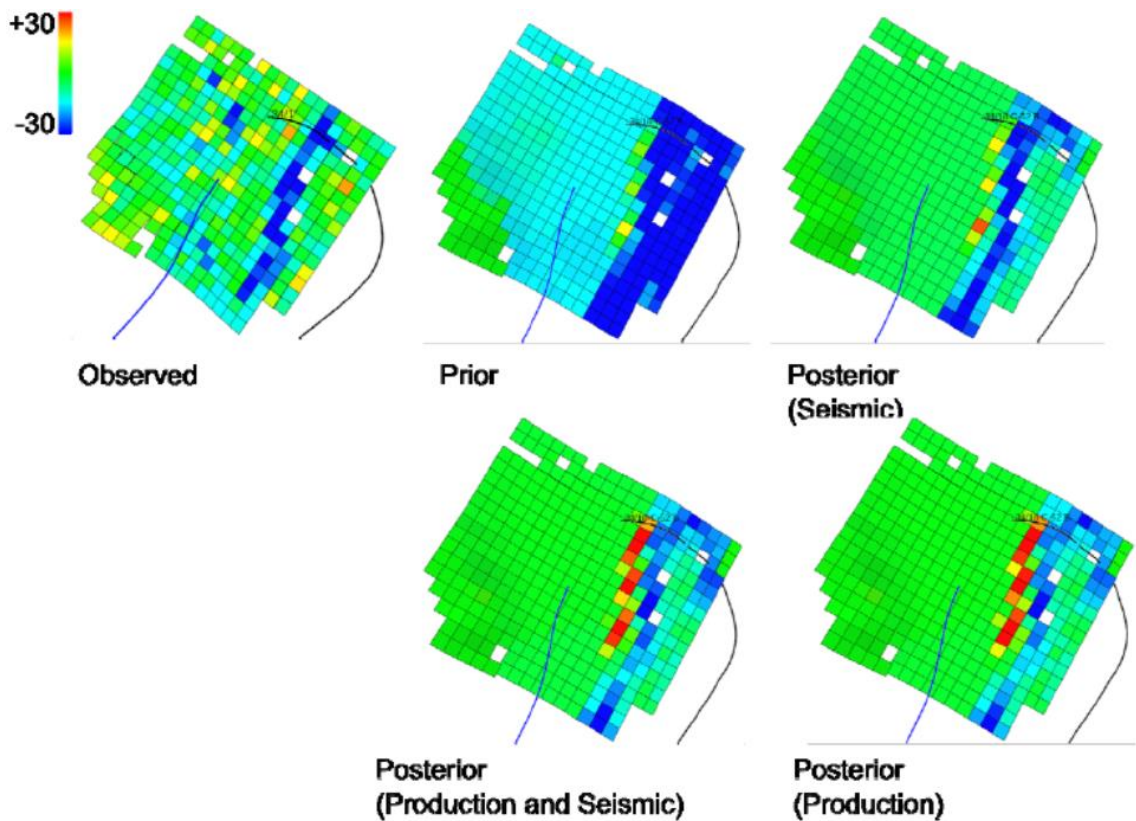


Figure 7.4 Sum of 4D P-wave velocity ratio until oil- water contact. Left) observed data, middle up) data in prior model, right up) data in posterior model updated with seismic data alone, lower middle) data in posterior model updated with seismic data and production data, and lower right) data in posterior model updated with production data alone (Alerini et al., 2014). The misfit analysis is done on the simulation model scale.

7.2.2.2 Depth Averaged Maps and Volumetric

In the advent of qualitative interpretation of seismic data, visual and manual confirmation of the seismic signals on the output from the simulation model has been map based. Map seismic attributes have been generated such as the root mean square and sum of negative amplitudes, while simulation model outputs have been depth averaged to generate maps of pressure and saturation. This approach has steadily been adopted in the quantitative integration of seismic data into the reservoir model as shown in Figure 7.5 by Ayzenberg et al. (2013).

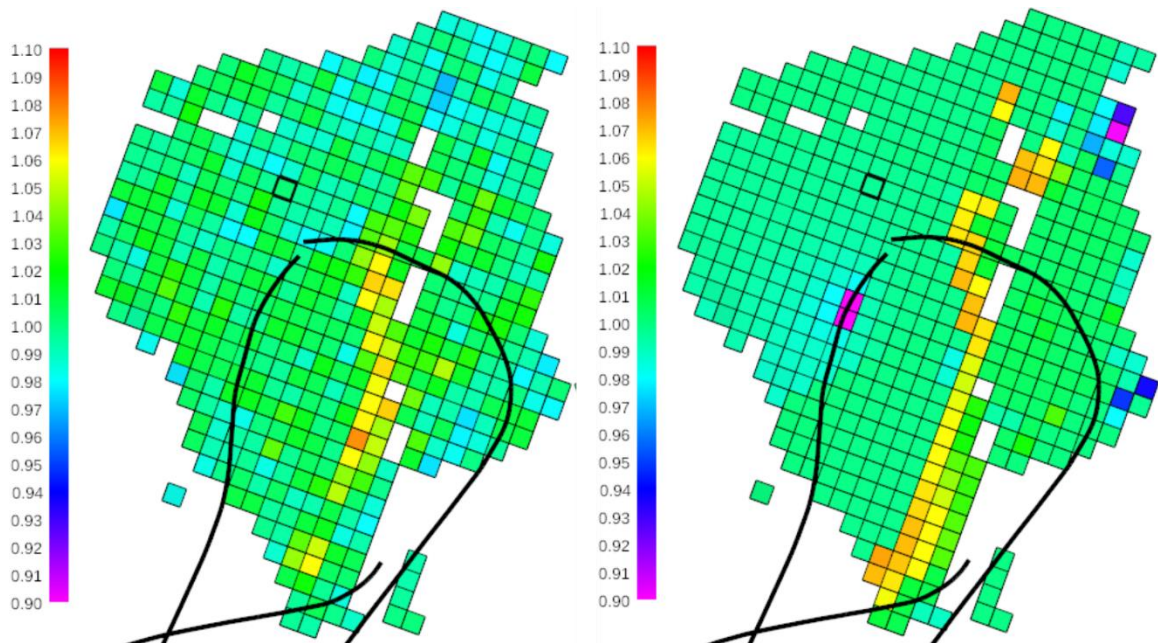


Figure 7.5 Inverted (left) and simulated (right) $V_{P \text{ monitor}} / V_{P \text{ base}}$ for a grid layer around the oil water contact. The injecting and producing wells are shown as black lines. Besides a somewhat higher noise level in the inverted ratio, the maps exhibit a similar qualitative behaviour in terms of observed 4D seismic data anomalies as well as a remarkable quantitative match which allows direct use of the inversion results in a history matching workflow (Ayzenberg et al., 2013). Showing map based analysis.

The map based approach as opposed to a volumetric approach (Figure 7.6) has been widely used due to its simplicity, and having to deal with less data. This approach is acceptable for fairly thin reservoirs that are below tuning thickness, however reservoirs with great thickness might result in specious maps of seismic data and simulation model outputs. The potential of extracting information from every grid cell in the vertical direction exists, as this will help in nullifying the smoothening effect of averaging to create maps, especially when a case of water sweep in the lower cells and gas presence in the upper cells exist. Reservoir heterogeneity might also be better defined and preserved.

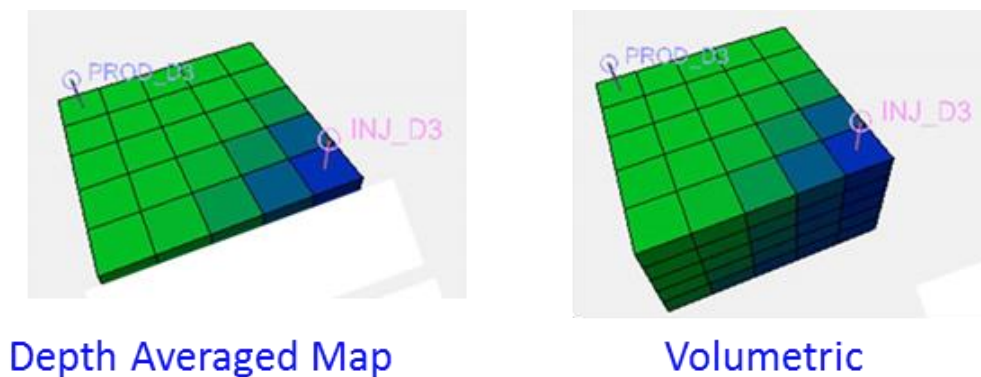


Figure 7.6 Schematic representation of a depth averaged map and a volumetric 3D grid.

7.2.2.3 Similar Objective Function

The production data objective function that is commonly used for comparing the historical production data and simulation model production profile output is the conventional least squares method. The seismic data objective function used in this work is the binary approach where the Hamming distance, Hausdorff distance, Mutual Information and *Current* measurement metric are considered as misfit metrics for comparing the observed 4D seismic data and the simulation model output. The least

squares method and the binary approach are very different metrics and the misfit values they generate and of a different order of magnitude, hence requiring a normalization process to equate them. An approach such as that used by Bouzarkouna and Nobakht (2015) shown in Figure 7.7, where the Hausdorff distance is used as the metric for calculating the production data misfit can be embraced, and perhaps extended to other available metrics such that the production data misfit and the seismic data misfit will be similar and of the same order.

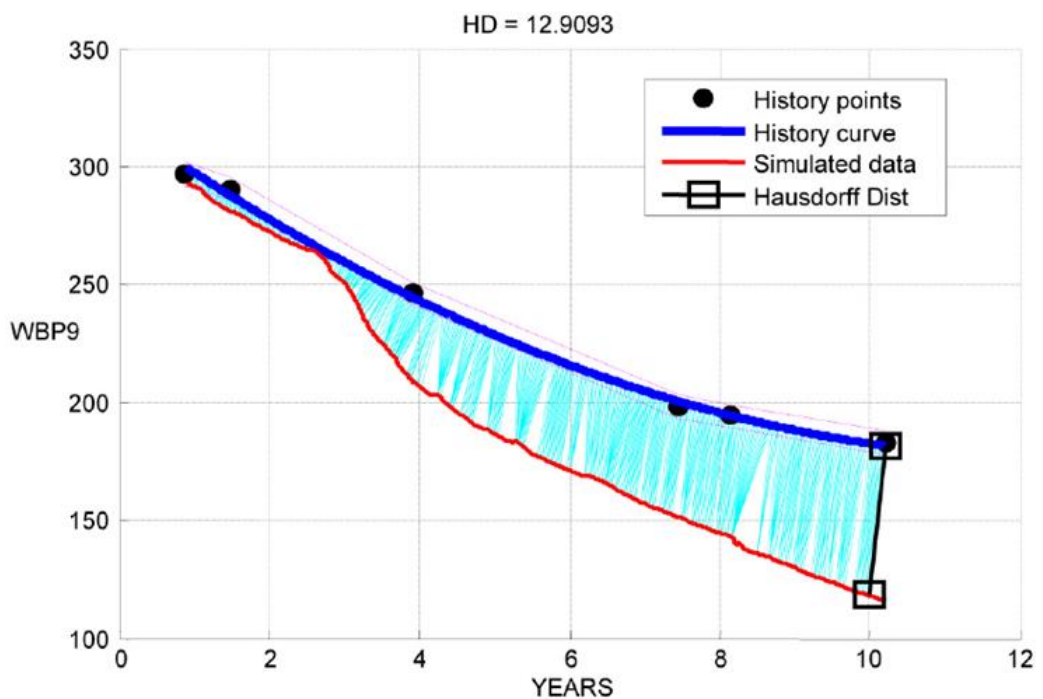


Figure 7.7 An example of Hausdorff distance calculation. The historical points (pressure points for a given well) are depicted with black dots. The red curve corresponds to simulation data. The dark blue curve corresponds to the curve fitting the historical data. The light blue lines correspond to the different distance evaluations required for the Hausdorff distance calculation. The Hausdorff distance is the maximum of all these evaluations and is equal to 12.91 (Bouzarkouna and Nobakht, 2015). Showing the production data misfit calculated using a different method.

7.2.3 Utilization of Ambiguous Signal

In the implementation of the binary approach, the most dominant signals of softening and hardening of the seismic data are assigned as gas and water effects respectively (Figure 7.8). That leaves a region unaccounted for in between which has been characterised as noise or ambiguous signal. The results of this approach shown in this thesis look promising, however there is still potential to analyse the region that is unaccounted for as there might be valid gas or water signals there, as well as the effect of pressure which might mask the signals selected.

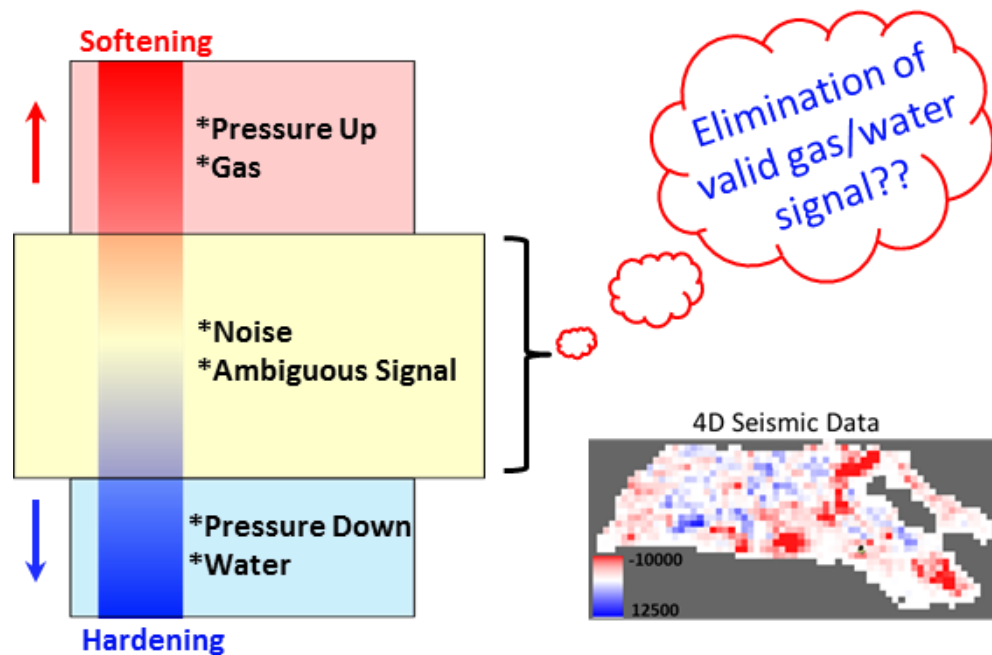


Figure 7.8 The characterisation of 4D seismic data signals into softening (pressure up and gas), hardening (pressure down and water), and a region of noise and ambiguous signal.

There are some options that can be explored such as slowly changing the cut-off values and analysing the resulting matched result, slowly evolving from binary to analogue and analysing the results, or using a proxy seismic or Simulation to Seismic based approach to compensate for the ambiguous region and characterise the effect of the noise present. This would however also present additional challenges due to the complexity of the seismic modelling process.

There is also the possibility of using a ternary approach as opposed to a binary approach, where the ternary approach would imply that a positive change in gas or water saturation is assigned a value of one, no change in gas or water saturation is assigned a value of zero, and a negative change in gas or water saturation is assigned a value of minus one. This will help to further capture the reservoir mechanisms in play, and will be suitable for a case scenario where for instance, an initial gas cap exists pre-production. This would mean that a region where the initial gas cap is produced or displaced by another fluid (e.g. oil or water) would be assigned a value of minus one, as gas was initially there and is no longer there, while a region which exhibits gas exsolution will be assigned a value of one, as gas was not there initially but is there presently.

7.3 Final Remarks

The aim of the research output of this thesis is to ask pertinent scientific questions, and attempt to proffer solutions to them, as well as raise further inquiries and food for thought. The subject of quantitatively integrating 4D seismic data and production data is indeed broad, interesting and fascinating, and I have but attempted to address some modest challenges. Even though some progress has been made, I am fully aware of the fact that this is the tip of the iceberg, however my hope is that this research will play some role towards quantifying the exact size, shape and location of the iceberg.

Appendix A

A.1 Fluid Property Changes at, and near to, Critical Gas Saturation

The seismic wave properties (density and bulk modulus) of live oil before, during and after gas exsolution is analysed here. This is important, as it provides an understanding of exactly what fluid effects are visible in the seismic data and how they should be treated. As described in the main body, if fluid pressure is dropped in a porous rock saturated with live oil then small-scale bubbles are nucleated, which start to grow, coalesce and then collect as free gas until critical saturation is reached. Laboratory measurement concludes that the seismic wave properties are not significantly impacted by the pore-scale mechanisms at play during the time leading up to the development of free gas as a separate phase in the pore space. That is, the very tiny bubbles developing in the oil do not affect the seismic wave properties (Han and Batzle, 2000a, Han and Batzle, 2000b).

However, after the development of free gas (i.e. a mobilised gas phase) this is not the case. Indeed, free gas is known to have a substantial effect on the wave properties particularly at appropriate reservoir depths (Han and Batzle, 2000a, Han and Batzle, 2000b). However the impact of the gaseous phase may be counteracted by the oil now becoming less “lively” due to the loss of the lighter gas components. To understand whether this contribution is significant, the density and bulk modulus is calculated for an oil with the same composition as in the case study (an API of 25 and initial R_s of 354 scf/bbl ($62.99 \text{ m}^3 \text{ m}^{-3}$)), at the reservoir pressure and temperature. Density and bulk modulus of the hydrocarbon fluid are calculated at an initial pressure of 2850 psi (19.65

MPa) with no gas saturation, and then after at a pressure drop of 900 psi (6.21 MPa) with free gas. Based on the pressure dependence of R_s for the reservoir oil, it is calculated that the pressure drop releases 1.2% of free gas and the oil now has an API of 23.7 and R_s of 342 scf/bbl ($60.85 \text{ sm}^3 \text{ m}^{-3}$).

Application of the FLAG software (Han and Batzle, 2000a, Han and Batzle, 2000b) gives an initial oil fluid density and bulk modulus of 0.816 g cm^{-3} (816 kg m^{-3}) and 1.36 GPa respectively, which changes to 0.822 g cm^{-3} (822 kg m^{-3}) and 1.33 GPa after the pressure drop. The change in the oil properties is not large. Mixing the final oil with the gas component (fluid density and bulk modulus of 0.096 g cm^{-3} (96 kg m^{-3}) and 0.0178 GPa respectively) according to Wood's equation, determines that the oil and gas mixture has a combined density and bulk modulus of 0.813 g cm^{-3} (813 kg m^{-3}) and 0.830 GPa respectively.

Thus, the outcome is a familiar, exaggerated (beyond its volumetric proportion), non-linear decrease of the bulk modulus after the bubble point and free gas development, and the consequent brightening of the seismic amplitudes. Amplitudes would therefore continue to brighten as free gas saturation increased in the pore space. Importantly, if the API and R_s in the oil are (incorrectly) assumed to be identical for the initial and final states in this calculation, then the final oil and gas mixture now has density and bulk modulus of 0.806 g cm^{-3} (806 kg m^{-3}) and 0.817 GPa respectively. The difference between these values and those from the previous calculation is not significant, and thus fluid substitution calculations and resultant interpretations in the main text can ignore the oil phase changes to first order. The addition of connate water saturation in practice will not alter the above conclusion.

Appendix B

B.1 Prediction of the 4D Seismic Amplitude Response to Gas Exsolution and Dissolution

The time-lapse amplitude response of a thin reservoir below tuning is considered, such that the time thickness $2H/V$ (where H is the physical reservoir thickness and V is the P-wave velocity of the reservoir rocks) is much less than the seismic period $1/f$ (where f is the peak frequency of the seismic wave). In this case, the top and base of the reservoir cannot be independently distinguished on the seismic data. In practice, the amplitude is evaluated within a time window defined around a peak and/or trough that represents the composite reservoir package (which includes any fluid contacts). It is therefore assumed that despite the appearance of gas in the reservoir, the relative spacing of the top, base and intra-reservoir events is below tuning thickness.

In comparison to the seismic period of 40 ms, the time thickness of the reservoir is 15 ms without gas, and 15.5 ms in the presence of gas (with a maximum gas thickness of 10 m, and a saturation of between 10% and 67%). As such, there is no breakdown in the linearity predicted from the following equations. The impact of underlying water saturation in the reservoir would be to reduce the magnitude of the time-lapse change in equation (B.8) and to enhance that in equation (B.9) by an amount proportional to the water saturation thickness.] Further, only the zero offset response is calculated here in order to simulate a stacked response. It is acknowledged that for reservoirs with significant 3D amplitude versus offset (AVO) behaviour that the calculations should

include an offset variation for each reflection coefficient (Aki and Richards, 1980), and the event timing should be adjusted to allow for the offset raypaths (e.g. $2H/V$ becomes $2H/V \cos\vartheta$, where ϑ is the incidence angle).

Error! Reference source not found. shows the three situations for which the reservoir amplitude is to be calculated: these correspond to the preproduction baseline seismic and an oil-filled reservoir; a monitor survey after gas exsolution and the formation of a secondary gas cap plus gas at the critical gas saturation in the oil; and, finally, a monitor after repressurization and dissolution with the remaining gas cap and the original oil. There is assumed to be no injected water below the gas for the purposes of this particular calculation.

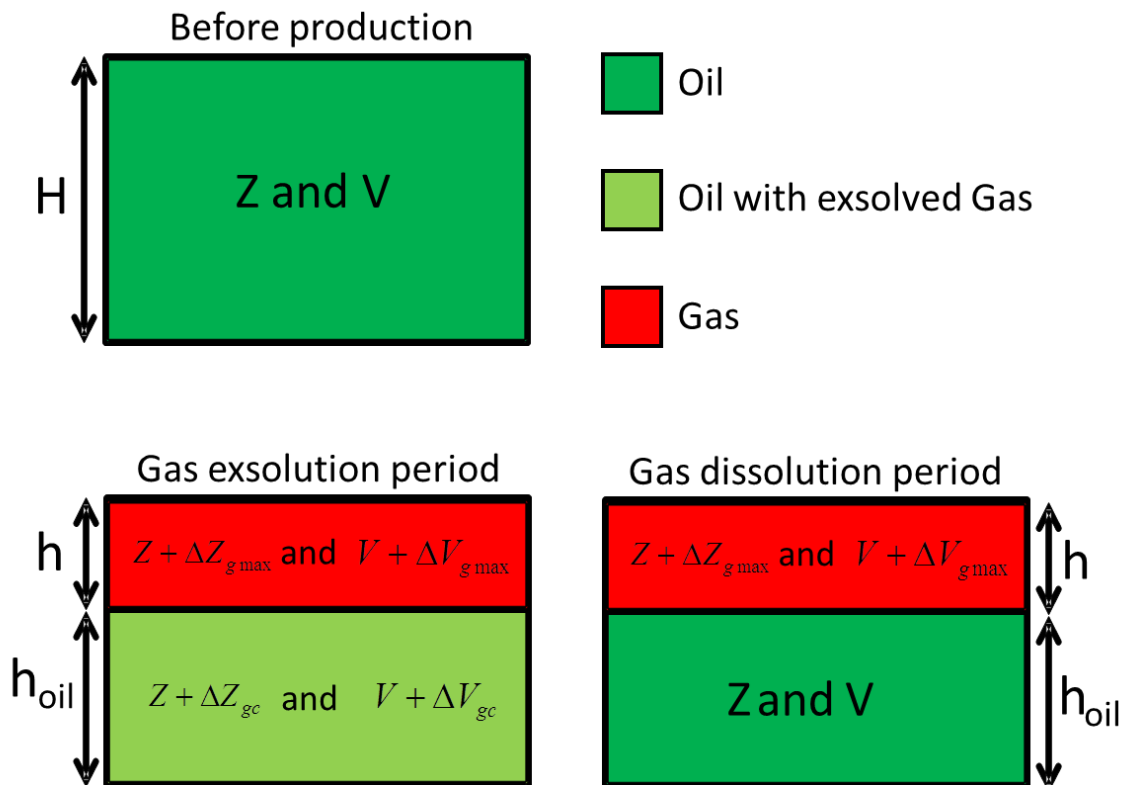


Figure B.1 An idealized model representation of the reservoir and fluid contacts for the calculation in Appendix B

B.2 Preproduction

Assuming that the reservoir is completely surrounded by shale with identical properties above and below, the composite reflectivity sequence, R_{res} , for the baseline seismic can be written in the frequency domain as:

$$R_{res} = R_{top} + R_{base} e^{-i\omega\left(\frac{2H}{V}\right)} \quad (\text{B.1})$$

where R_{top} and R_{base} are the individual frequency-independent reflection coefficients for the top and base of the reservoir, and V is the P-wave velocity for the preproduction reservoir condition. For the assumption of a thin reservoir, the approximation is valid, giving:

$$R_{res} \approx R_{top} + \left\{1 - i\omega\left(\frac{2H}{V}\right)\right\} R_{base} \quad (\text{B.2})$$

The composite reflection response is converted to the seismic attribute used in the interpretation in the main text by, first, convolving the time-domain reflectivity with the seismic wavelet $s(t)$ (in the frequency domain this is multiplication of equation (B.2) by $S(\omega)$), convolving with a coloured inversion operator (Lancaster and Whitcombe, 2000) and then applying a ‘sum of negatives’ to the resultant relative impedance trace - a compound operator defined here by L . The resultant time-domain amplitude is now:

$$\{R_{top} + R_{base}\}L\{s(t)\} - \left\{R_{base}\left(\frac{2H}{V}\right)\right\}L\{s'(t)\} \quad (\text{B.3})$$

where $s'(t)$ is the time derivative of the seismic wavelet. The assumption of identical shale above and below the reservoir gives the condition $R_{top} = -R_{base}$, and thus equation (B.3) leads to the small contrast approximation between the reservoir and the surrounding shales:

$$A_{res} = -\left(\frac{\Delta Z}{\bar{Z}}\right) \frac{H}{V} L\{s'(t)\} \quad (B.4)$$

where $\Delta Z = Z_{sh} - Z$ is the difference between the shale impedance Z_{sh} and the impedance Z , and \bar{Z} represents the average of the two impedances.

B.3 After Gas Exsolution

In this case, there is a gas-oil contact to complicate the reflectivity. The impedance of the reservoir rock within the gas cap is now $Z + \Delta Z_{gmax}$ and the P-wave velocity is $V + \Delta V_{gmax}$. For the oil leg, the impedance and velocity are now $Z + \Delta Z_{gcr}$ and $V + \Delta V_{gcr}$, respectively (see Figure B.1). Applying similar logic and assumptions as in the previous calculation leads to an expression for the new reservoir amplitude A_{gs} :

$$A_{gs} \approx \frac{1}{2} \left\{ \left(\frac{Z + \Delta Z_{gmax} - Z_{sh}}{\bar{Z}} \right) + \left(\frac{Z + \Delta Z_{gcr} - Z - \Delta Z_{gmax}}{\bar{Z}} \right) + \left(\frac{Z_{sh} - Z - \Delta Z_{gcr}}{\bar{Z}} \right) \right\} L\{s(t)\} - \left\{ \left(\frac{Z + \Delta Z_{gcr} - Z - \Delta Z_{gmax}}{\bar{Z}} \right) \left(\frac{h}{V + \Delta V_{gmax}} \right) + \left(\frac{Z_{sh} - Z - \Delta Z_{gcr}}{\bar{Z}} \right) \left[\left(\frac{h}{V + \Delta V_{gmax}} + \frac{h_{oil}}{V + \Delta V_{gcr}} \right) \right] \right\} L\{s'(t)\} \quad (B.5)$$

where h and h_{oil} are the thicknesses of the gas cap and oil leg, respectively. After some clarification, equation (B.5) can be simplified to:

$$A_{gs} = - \left\{ h \left(\frac{\Delta Z - \Delta Z_{gmax}}{\bar{Z}(V + \Delta V_{gmax})} \right) + h_{oil} \left(\frac{\Delta Z - \Delta Z_{gcr}}{\bar{Z}(V + \Delta V_{gcr})} \right) \right\} L\{s'(t)\} \quad (B.6)$$

In this field, $\bar{Z}\Delta V_{gmax}$ and $\bar{Z}\Delta V_{gcr}$ are less than 5% of $\bar{Z}V$. Thus, it can be further assumed that these two quantities are negligible, which yields:

$$A_{gs} = - \left\{ h \left(\frac{\Delta Z - \Delta Z_{gmax}}{\bar{Z}V} \right) + h_{oil} \left(\frac{\Delta Z - \Delta Z_{gcr}}{\bar{Z}V} \right) \right\} L\{s'(t)\} \quad (B.7)$$

The time-lapse amplitudes $\Delta A_{gs} = A_{gs} - A_{res}$, which in the data are expressed as a map of the gas exsolution formed between the monitor and baseline, can now be obtained:

$$A_{gs} = \left\{ h \left(\frac{\Delta Z_{gmax}}{\bar{Z}V} \right) + h_{oil} \left(\frac{\Delta Z_{gcr}}{\bar{Z}V} \right) \right\} L\{s'(t)\} \quad (B.8)$$

For this specific field, regions are found that are predominantly controlled by critical gas saturation ($\Delta Z_{gmax}=0$) or maximum gas saturation ($\Delta Z_{gcr}=0$).

B.4 After Gas Dissolution

During the gas dissolution period, the same equations as in equation (B.8) apply except that ΔZ_{gr} is now zero. Thus, the time-lapse amplitudes ΔA_{diss} for this case are:

$$\Delta A_{\text{diss}} = h \left(\frac{\Delta Z_{\text{gmax}}}{\bar{Z}V} \right) L\{s'(t)\} \quad (\text{B.9})$$

Note that, in the main body, attention is given to h and H (hence $V = H/T$ in the denominator) in the above equations as this predicts that the time-lapse amplitudes are controlled by the thickness of the gas accumulation and the reservoir thickness. The remaining parameters are lumped together into a single reservoir-related constant, α , where:

$$\alpha = \left(\frac{1}{\bar{Z}V} \right) L\{s'(t)\} \quad (\text{B.10})$$

Appendix C

C.1 Production Profiles

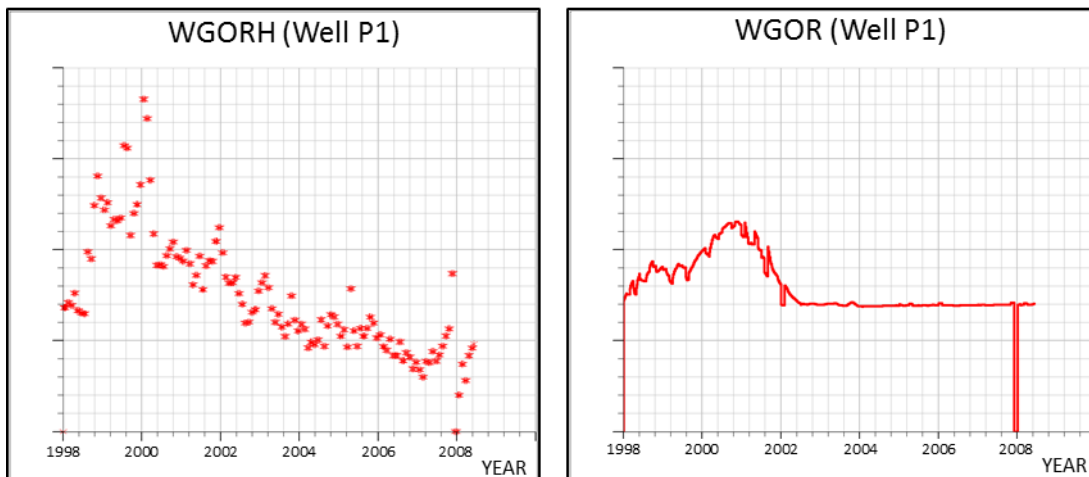


Figure C.1 The historical gas oil ratio (WGORH) and base case model gas oil ratio (WGOR) of well P1. The vertical scale is hidden for confidentiality but is the same for the two plots.

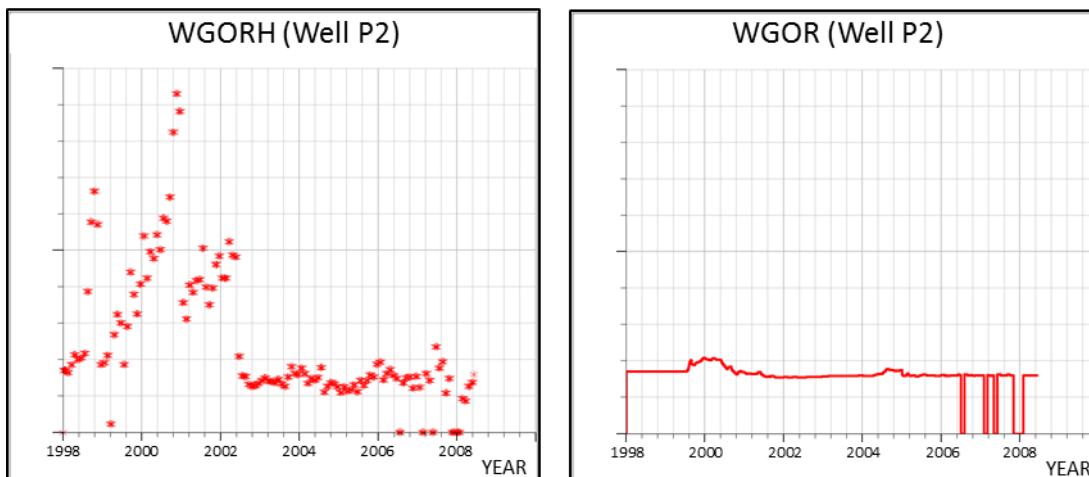


Figure C.2 The historical gas oil ratio (WGORH) and base case model gas oil ratio (WGOR) of well P2. The vertical scale is hidden for confidentiality but is the same for the two plots.

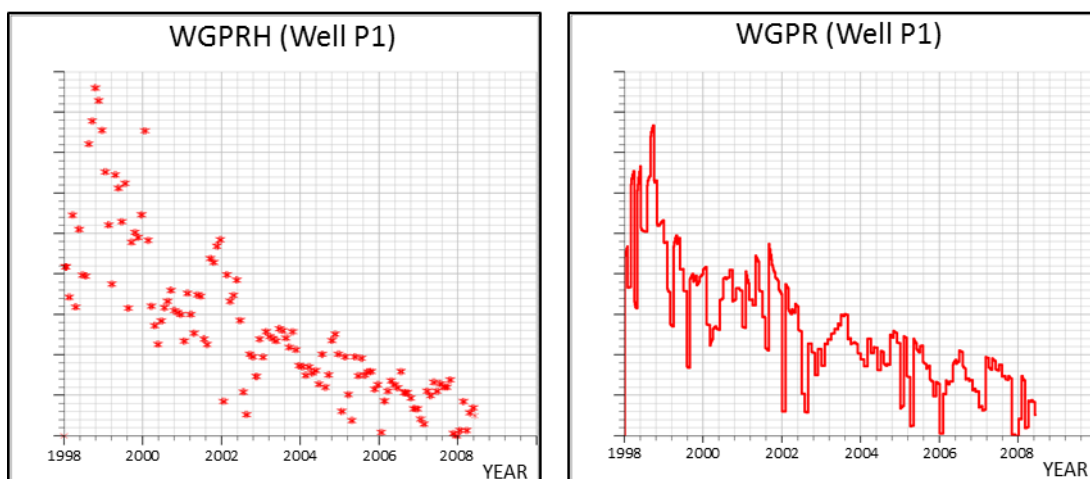


Figure C.3 The historical gas production rate (WGPRH) and base case model gas production rate (WGPR) of well P1. The vertical scale is hidden for confidentiality but is the same for the two plots.

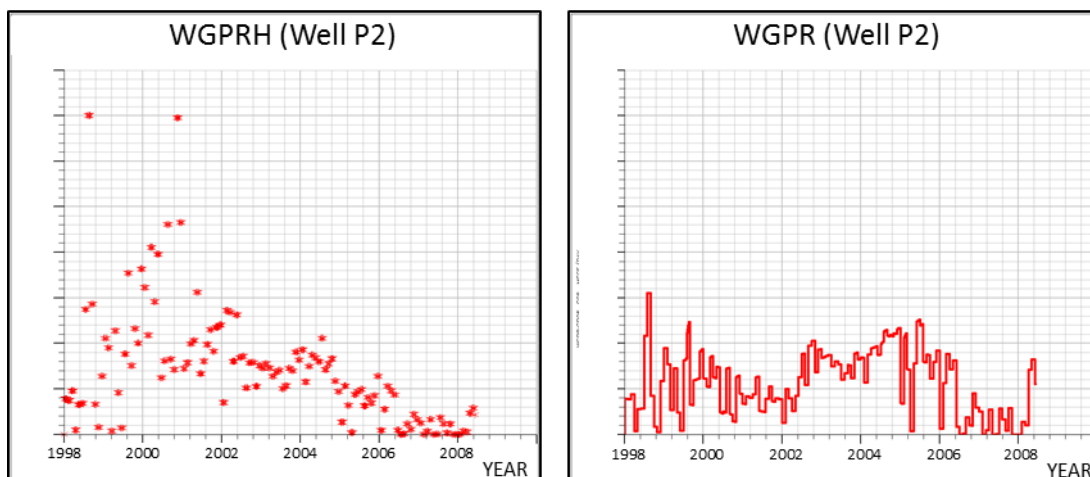


Figure C.4 The historical gas production rate (WGPRH) and base case model gas production rate (WGPR) of well P2. The vertical scale is hidden for confidentiality but is the same for the two plots.

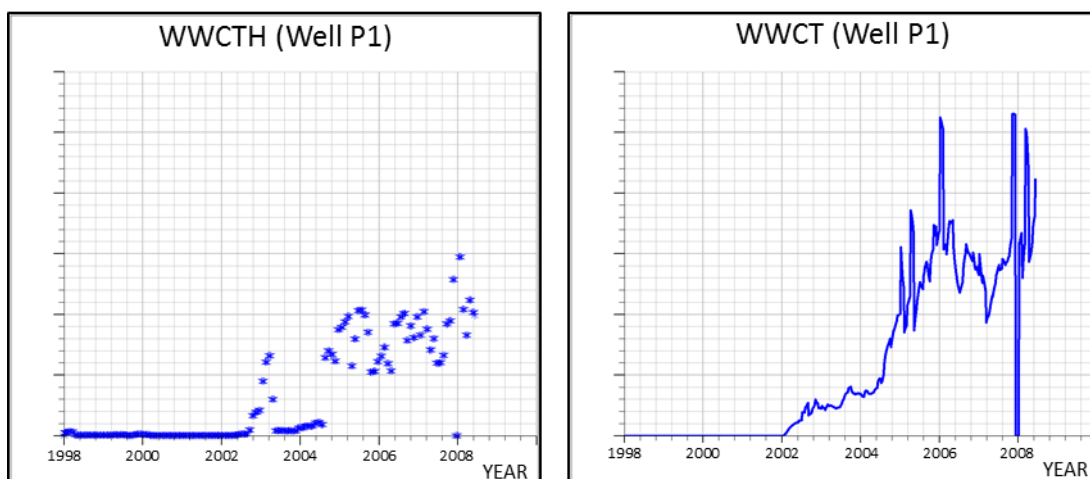


Figure C.5 The historical water cut (WWCTH) and base case model water cut (WWCT) of well P1. The vertical scale is hidden for confidentiality but is the same for the two plots.

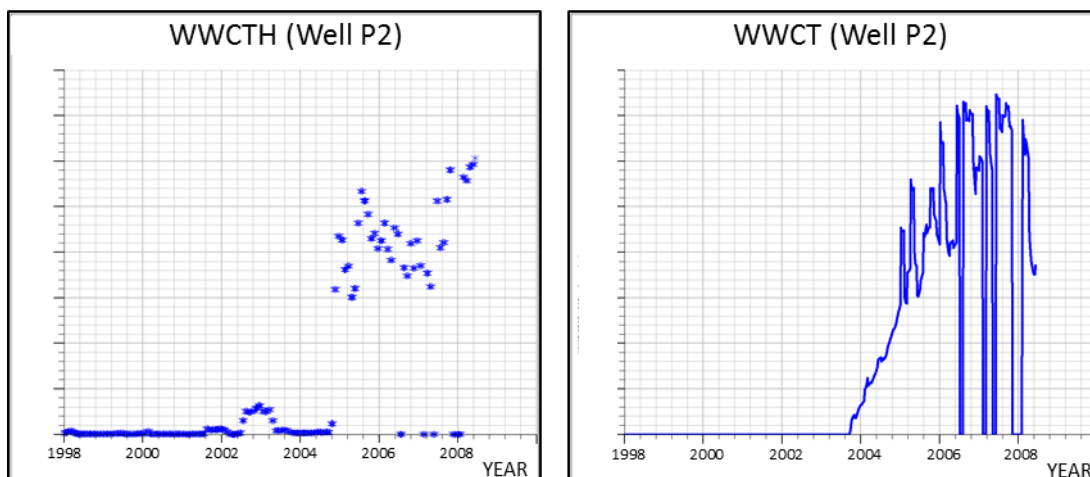


Figure C.6 The historical water cut (WWCTH) and base case model water cut (WWCT) of well P2. The vertical scale is hidden for confidentiality but is the same for the two plots.

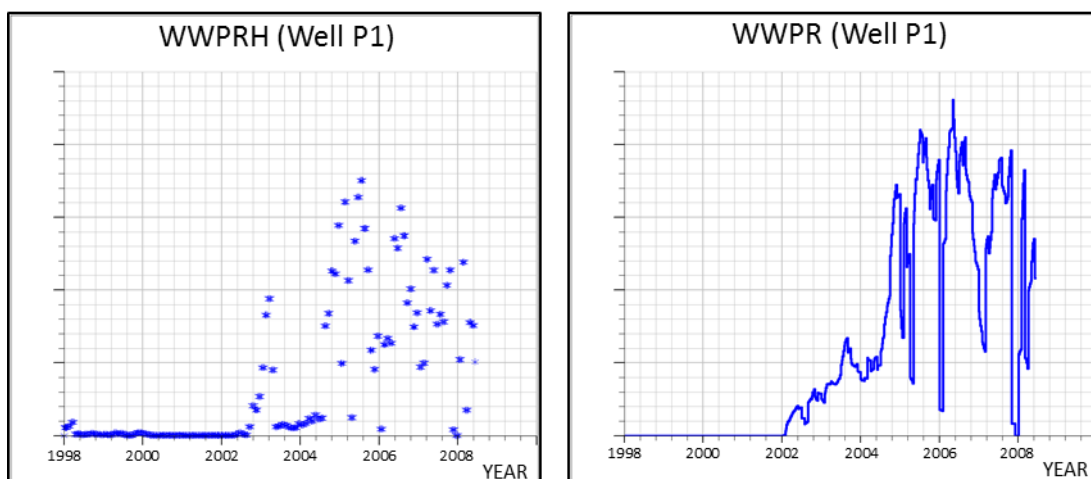


Figure C.7 The historical water production rate (WWPRH) and base case model water production rate (WWPR) of well P1. The vertical scale is hidden for confidentiality but is the same for the two plots.

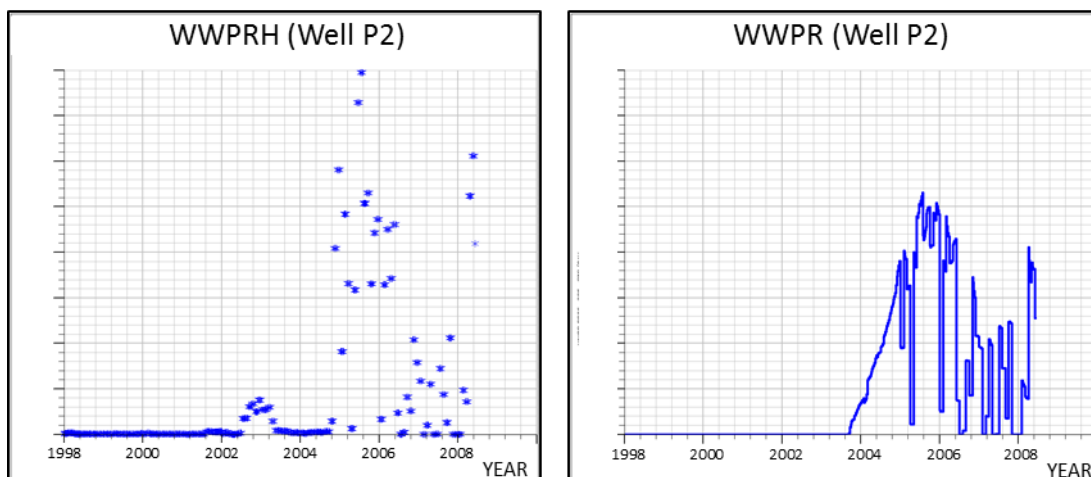


Figure C.8 The historical water production rate (WWPRH) and base case model water production rate (WWPR) of well P2. The vertical scale is hidden for confidentiality but is the same for the two plots.

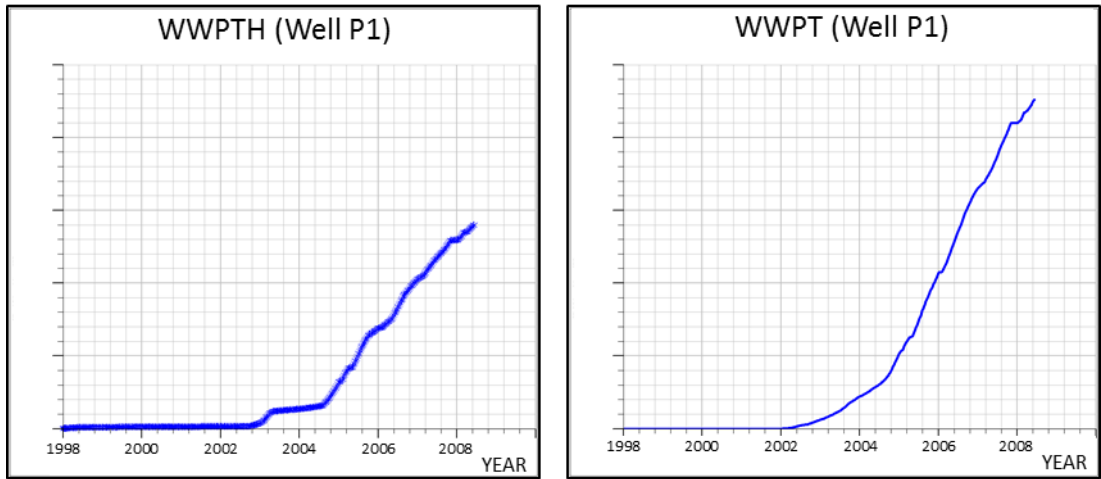


Figure C.9 The historical water production total/cumulative (WWPTH) and base case model water production total/cumulative (WWPT) of well P1. The vertical scale is hidden for confidentiality but is the same for the two plots.

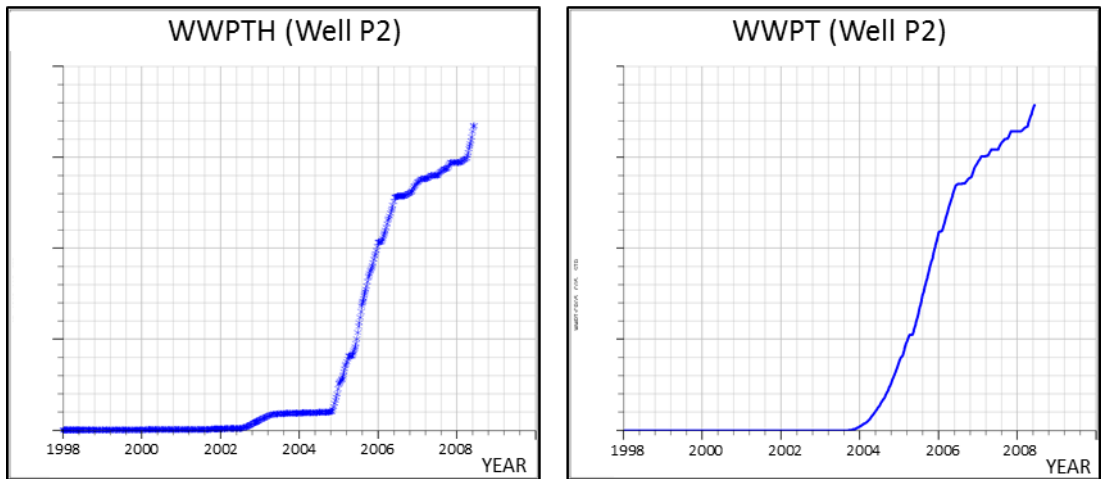


Figure C.10 The historical water production total/cumulative (WWPTH) and base case model water production total/cumulative (WWPT) of well P2. The vertical scale is hidden for confidentiality but is the same for the two plots.

Appendix D

D.1 *k*-means Clustering

This appendix describes the *k*-means clustering technique (MacQueen, 1967) with a diagrammatic illustration shown in Figure D.1. The diagrams are labelled “a” to “n”, and the manifestation is shown below:

“a” – K points (here $K = 2$, i.e red and blue) are placed into the space represented by the objects that are being clustered. The K points represent the initial group centroids.

“b and c” – Assign each object to the group that is closest to a particular centroid.

“d and e” – When all the objects have been assigned, recalculate the position of the K centroids.

“f to n” – Repeat the above steps until the centroids no longer move (diagram n). This produces a separation of the objects into groups with similarities.

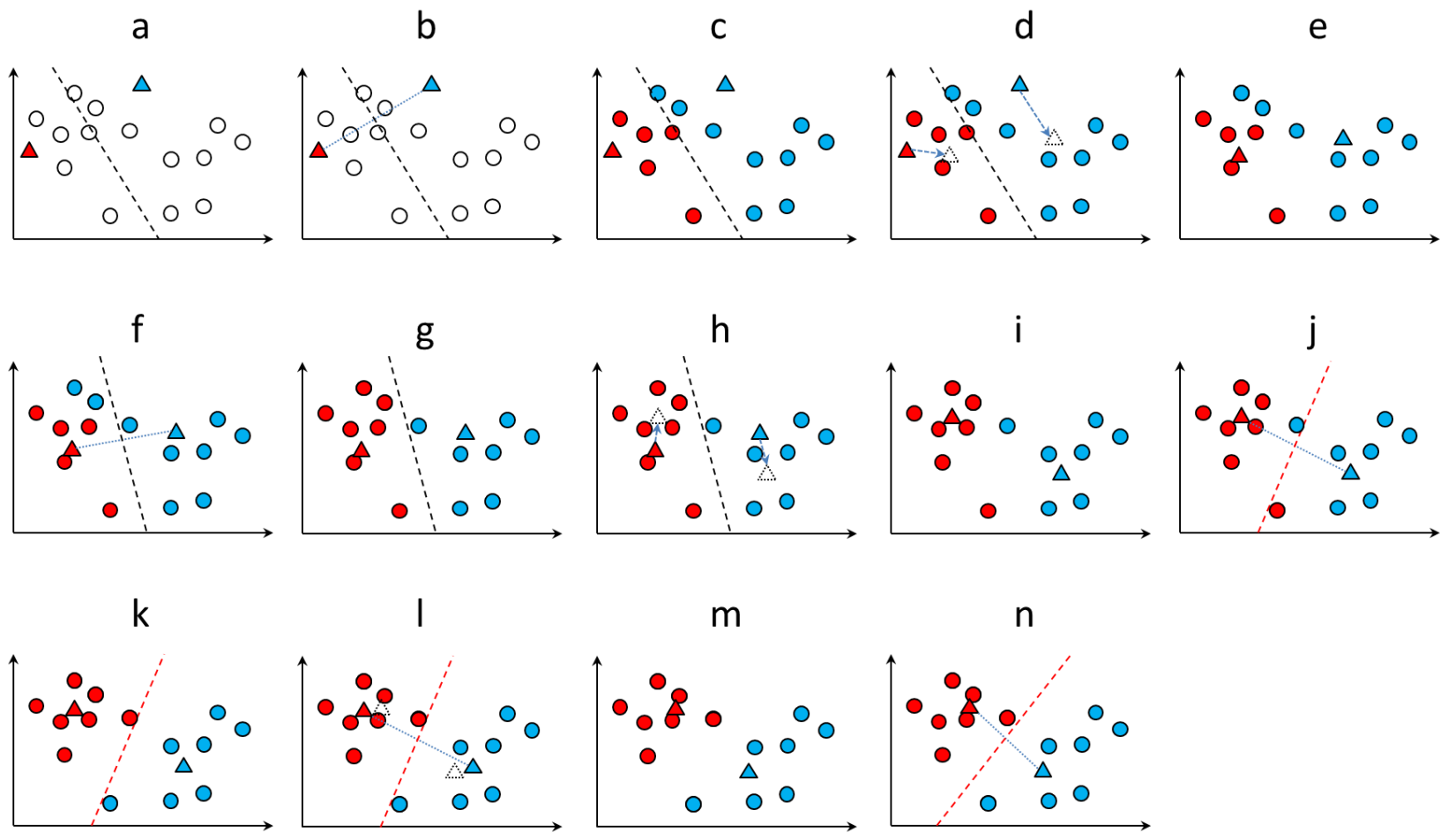


Figure D.1 *k*-means clustering technique

Appendix E

E.1 Misfit Analysis

In the analysis, $Misfit (M1)$ is misfit of a particular model (i.e. model 1), $Misfit (M1, t)$ is misfit of model 1 at time, t (where t is the seismic baseline/monitor time), i represents all the models being analysed, and $Mfit (M1)|_{Response}$ represents the misfit of a particular response (e.g. pressure, gas, water) after the analysis for Model 1.

The analysis for Spatial misfit is shown below. Spatial pressure misfit (equation (E.1)), spatial gas saturation misfit (equation (E.2)), spatial water saturation misfit (equation (E.3)), and total spatial misfit (equation (E.4)).

$$Mfit (M1)|_{Pressure} = \sum_{t=1998}^{2008} \left[\frac{Misfit (M1, t)|_{Pressure}}{\sum_i Misfit (M_i, t)|_{Pressure}} \right] \quad (E.1)$$

$$Mfit (M1)|_{Gas} = \sum_{t=1998}^{2008} \left[\frac{Misfit (M1, t)|_{Gas}}{\sum_i Misfit (M_i, t)|_{Gas}} \right] \quad (E.2)$$

$$Mfit (M1)|_{Water} = \sum_{t=1998}^{2008} \left[\frac{Misfit (M1, t)|_{Water}}{\sum_i Misfit (M_i, t)|_{Water}} \right] \quad (E.3)$$

$$Mfit (M1)|_{Spatial} = Mfit (M1)|_{Pressure} + Mfit (M1)|_{Gas} + Mfit (M1)|_{Water} \quad (E.4)$$

The analysis for well data misfit is shown below. Field oil production total (FOPT) misfit (equation (E.5)), field gas production total (FGPT) misfit (equation (E.6)), field water production total (FWPT) misfit (equation (E.7)), field average pressure (FPR) misfit (equation (E.8)), and total well data misfit (equation (E.9)).

$$Mfit (M1)|_{FOPT} = \sum_{t=1998}^{2008} \left[\frac{Misfit (M1, t)|_{FOPT}}{\sum_i Misfit (M_i, t)|_{FOPT}} \right] \quad (E.5)$$

$$Mfit (M1)|_{FGPT} = \sum_{t=1998}^{2008} \left[\frac{Misfit (M1, t)|_{FGPT}}{\sum_i Misfit (M_i, t)|_{FGPT}} \right] \quad (E.6)$$

$$Mfit (M1)|_{FWPT} = \sum_{t=1998}^{2008} \left[\frac{Misfit (M1, t)|_{FWPT}}{\sum_i Misfit (M_i, t)|_{FWPT}} \right] \quad (E.7)$$

$$Mfit (M1)|_{FPR} = \sum_{t=1998}^{2008} \left[\frac{Misfit (M1, t)|_{FPR}}{\sum_i Misfit (M_i, t)|_{FPR}} \right] \quad (E.8)$$

$$Mfit(M1)|_{well} = Mfit (M1)|_{FOPT} + Mfit (M1)|_{FGPT} + Mfit (M1)|_{FWPT} + Mfit(M1)|_{FPR} \quad (E.9)$$

The total combined misfit for spatial misfit and well data misfit is shown in (equation (E.10)).

$$Mfit(M1)|_{Combined} = \left[\frac{Mfit (M1)|_{spatial}}{\sum_i Mfit (M_i)|_{spatial}} \right] + \left[\frac{Mfit (M1)|_{well}}{\sum_i Mfit (M_i)|_{well}} \right] \quad (E.10)$$

The equations have been shown for “Model 1”, and will be substituted for other models.

The combined misfit will be used as a comparative means of selecting a suitable model.

Appendix F

F.1 Python Program Script

This appendix provides the script in Python programming language that was written to implement the seismic assisted history matching workflow. The code script shown here is for one time-step (year 1998 to year 1999), and can be easily expanded for multiple time steps. Comments have been included in the code script for easy comprehension.

```

1  #import time
2  #start_time = time.time()
3
4  import numpy as np
5  import os
6
7  #ASSIGNMENT OF INPUT DATA AND VARIABLES
8  PORVa = "PORV    AT      0.00 DAYS" #message
9  initPORV = 'initporv.txt'
10
11 #####
12 Sgas1998a = "SGAS    AT      31.00 DAYS" #welspecs
13 Sgas1998 = '1998Sg.txt'
14
15 Sgas1999a = "SGAS    AT      365.00 DAYS" #message
16 Sgas1999 = '1999Sg.txt'
17
18 #####
19 welspecs = "READING WELSPEDS"
20 message = "MESSAGE"
21 ijk = "(I, J, K)"
22
23 copypv = False; copya = False; copyb = False; copyc = False;
24 copyd = False; copye = False; copyf = False; copyg = False;
25 copypv1 = False; copya1 = False; copyb1 = False; copyc1 = False;
26 copyd1 = False; copye1 = False; copyf1 = False; copyg1 = False;
27
28 infile = open('NSCH_SIM_COARSEN642635.PRT', 'r');
29 tmp = infile.readlines()
30
31 outfilea = open(Sgas1998, 'w'); outfileb = open(Sgas1999, 'w');
32 outfilepv = open(initPORV, 'w');
33
34 execfile('part1_basemonitors_sgas.py')
35
36 #####
37 #'part1_basemonitors_sgas.py' code details - start
38 for line in tmp:
39     if PORVa in line:        copypv = True
40     elif message in line:   copypv = False
41     elif copypv:
42         youpv = line.replace('-----', '0.00000')
43         ourpv = youpv.replace('-', ' ')
44         wepv = ourpv.replace('*', '.')
45         thempv = wepv.replace('C', '.')
46         if thempv.rstrip():
47             if ijk in thempv: copypv1 = True
48             elif copypv1:    outfilepv.write(thempv[14:])
49
50     if Sgas1998a in line:    copya = True
51     elif welspecs in line:  copya = False
52     elif copya:
53         youa = line.replace('-----', '0.00000')
54         oura = youa.replace('-', ' ')
55         wea = oura.replace('*', '.')
56         thema = wea.replace('C', '.')
57         if thema.rstrip():
58             if ijk in thema: copya1 = True
59             elif copya1:    outfilea.write(thema[14:])
60
61     if Sgas1999a in line:    copyb = True
62     elif message in line:  copyb = False
63     elif copyb:
64         youb = line.replace('-----', '0.00000')
65         ourb = youb.replace('-', ' ')
66         web = ourb.replace('*', '.')
67         themb = web.replace('C', '.')
68         if themb.rstrip():
69             if ijk in themb: copyb1 = True
70             elif copyb1:    outfileb.write(themb[14:])
71
72 outfilepv.close(); outfilea.close(); outfileb.close()
73
74 #'part1_basemonitors_sgas.py' code details - end
75 #####
76
77 #####
78 ##### WATER
79 #PORVa = "PORV    AT      0.00 DAYS" #message
80 #initPORV = 'initporv.txt'
81
82 Swat1998a = "SWAT    AT      31.00 DAYS" #wahala
83 Swat1998 = '1998Sw.txt'
84
85 Swat1999a = "SWAT    AT      365.00 DAYS" #wahala
86 Swat1999 = '1999Sw.txt'

```

```

87
88 #####
89 welspecs = "READING WELSPEDS"
90 message = "MESSAGE"
91 ijk = "(I, J, K)"
92 wahala = "1          *****"
93
94 copypv = False; copya = False; copyb = False; copyc = False;
95 copyd = False; copye = False; copyf = False; copyg = False;
96 copypv1 = False; copya1 = False; copyb1 = False; copyc1 = False;
97 copyd1 = False; copye1 = False; copyf1 = False; copyg1 = False;
98
99 del tmp
100
101 infile = open('NSCH_SIM_COARSEN642635.PRT', 'r');
102 tmp = infile.readlines()
103
104 outfilea = open(Swat1998, 'w'); outfileb = open(Swat1999, 'w');
105 #outfilepv = open(initPORV, 'w');
106
107 execfile('part1_basemonitors_swat.py')
108
109 #####
110 # 'part1_basemonitors_swat.py' code details
111 # Similar to 'part1_basemonitors_sgas.py'
112 #####
113
114 #####
115 ##### PORV
116 initialfile='initporv.txt'
117 execfile('part2_reservoir.py')
118 os.rename ('reserv.txt','PORV.txt')
119 # Delete some files
120 os.remove("initporv.txt");
121
122 #####
123 # 'part2_reservoir.py' code details - start
124 from collections import deque
125
126 first1=0; first2=1855; second1=1855; second2=3710; third1=3710;
127 third2=5565; fourth1=5565; fourth2=7420; fifth1=7420; fifth2=9275;
128 sixth1=9275; sixth2=11130; seventh1=11130; seventh2=12985;
129 eighth1=12985; eighth2=14840; ninth1=14840; ninth2=16695;

```

```

130
131 trans1='firsttrans.txt';trans2='secondtrans.txt';
132 trans3='thirdtrans.txt';trans4='fourthtrans.txt';
133 trans5='fifthtrans.txt';trans6='sixthtrans.txt';
134 trans7='seventhtrans.txt';trans8='eighthtrans.txt';
135 trans9='ninthtrans.txt';
136
137 ##### for the 1st set of lines
138 with open(initialfile) as infile:
139     outfile = open('first.txt', 'w')
140     keep = list(range(first1,first2))
141     for i, line in enumerate(infile):
142         if i in keep:
143             outfile.write(line)
144     outfile.close()
145
146 with open('first.txt') as infile:
147     outfile = open(trans1, 'w')
148     lines = (line.split() for line in infile)
149     for row in zip(*lines):
150         q = (" ".join(row))
151         outfile.write(q+'\n')
152     outfile.close()
153
154 ##### for the 2nd set of lines
155 with open(initialfile) as infile:
156     outfile = open('second.txt', 'w')
157     keep = list(range(second1,second2))
158     for i, line in enumerate(infile):
159         if i in keep:
160             outfile.write(line)
161     outfile.close()
162
163 with open('second.txt') as infile:
164     outfile = open(trans2, 'w')
165     lines = (line.split() for line in infile)
166     for row in zip(*lines):
167         q = (" ".join(row))
168         outfile.write(q+'\n')
169     outfile.close()
170
171 ##### for the 3rd set of lines
172 with open(initialfile) as infile:

```

```

173 outfile = open('third.txt', 'w')
174 keep = list(range(third1,third2))
175 for i, line in enumerate(infile):
176     if i in keep:
177         outfile.write(line)
178 outfile.close()
179
180 with open('third.txt') as infile:
181     outfile = open(trans3, 'w')
182     lines = (line.split() for line in infile)
183     for row in zip(*lines):
184         q = (" ".join(row))
185         outfile.write(q+'\n')
186 outfile.close()
187
188 ##### for the 4th set of lines
189 with open(initialfile) as infile:
190     outfile = open('fourth.txt', 'w')
191     keep = list(range(fourth1,fourth2))
192     for i, line in enumerate(infile):
193         if i in keep:
194             outfile.write(line)
195 outfile.close()
196
197 with open('fourth.txt') as infile:
198     outfile = open(trans4, 'w')
199     lines = (line.split() for line in infile)
200     for row in zip(*lines):
201         q = (" ".join(row))
202         outfile.write(q+'\n')
203 outfile.close()
204
205 ##### for the 5th set of lines
206 with open(initialfile) as infile:
207     outfile = open('fifth.txt', 'w')
208     keep = list(range(fifth1,fifth2))
209     for i, line in enumerate(infile):
210         if i in keep:
211             outfile.write(line)
212 outfile.close()
213
214 with open('fifth.txt') as infile:
215     outfile = open(trans5, 'w')

```

```

216     lines = (line.split() for line in infile)
217     for row in zip(*lines):
218         q = (" ".join(row))
219         outfile.write(q+'\n')
220 outfile.close()
221
222 ##### for the 6th set of lines
223 with open(initialfile) as infile:
224     outfile = open('sixth.txt', 'w')
225     keep = list(range(sixth1,sixth2))
226     for i, line in enumerate(infile):
227         if i in keep:
228             outfile.write(line)
229 outfile.close()
230
231 with open('sixth.txt') as infile:
232     outfile = open(trans6, 'w')
233     lines = (line.split() for line in infile)
234     for row in zip(*lines):
235         q = (" ".join(row))
236         outfile.write(q+'\n')
237 outfile.close()
238
239 ##### for the 7th set of lines
240 with open(initialfile) as infile:
241     outfile = open('seventh.txt', 'w')
242     keep = list(range(seventh1,seventh2))
243     for i, line in enumerate(infile):
244         if i in keep:
245             outfile.write(line)
246 outfile.close()
247
248 with open('seventh.txt') as infile:
249     outfile = open(trans7, 'w')
250     lines = (line.split() for line in infile)
251     for row in zip(*lines):
252         q = (" ".join(row))
253         outfile.write(q+'\n')
254 outfile.close()
255
256 ##### for the 8th set of lines
257 with open(initialfile) as infile:
258     outfile = open('eight.txt', 'w')

```



```

259     keep = list(range(eight1,eight2))
260     for i, line in enumerate(infile):
261         if i in keep:
262             outfile.write(line)
263 outfile.close()
264
265 with open('eight.txt') as infile:
266     outfile = open(trans8, 'w')
267     lines = (line.split() for line in infile)
268     for row in zip(*lines):
269         q = (" ".join(row))
270         outfile.write(q+'\n')
271 outfile.close()
272
273 ##### for the 9th set of lines
274 with open(initialfile) as infile:
275     outfile = open('ninth.txt', 'w')
276     keep = list(range(ninth1,ninth2))
277     for i, line in enumerate(infile):
278         if i in keep:
279             outfile.write(line)
280 outfile.close()
281
282 with open('ninth.txt') as infile:
283     outfile = open(trans9, 'w')
284     lines = (line.split() for line in infile)
285     for row in zip(*lines):
286         q = (" ".join(row))
287         outfile.write(q+'\n')
288 outfile.close()
289
290 ##### Combine all the transposed files
291 read_files=[trans1,trans2,trans3,trans4,trans5,trans6,\
292 trans7,trans8,trans9]
293
294 with open('fulltrans.txt','w') as outfile:
295     for f in read_files:
296         with open(f, 'r') as infile:
297             for line in infile:
298                 outfile.write(line)
299 outfile.close()
300
301 ##### transpose the transposed file back
302 with open('fulltrans.txt') as infile:
303     outfile = open('fullfinal.txt', 'w')
304     lines = (line.split() for line in infile)
305     for row in zip(*lines):
306         q = (" ".join(row))
307         outfile.write(q+'\n')
308 outfile.close()
309
310 ##### Select Reservoir Area (Rows 17 to 35) - 128x53x19
311 with open('fullfinal.txt') as infile:
312     outfile = open('reserv.txt', 'w')
313     outfile.writelines(deque(infile, 1007))
314 outfile.close()
315
316 #####
317 os.remove("first.txt"); os.remove("firsttrans.txt")
318 os.remove("second.txt"); os.remove("secondtrans.txt")
319 os.remove("third.txt"); os.remove("thirdtrans.txt")
320 os.remove("fourth.txt"); os.remove("fourthtrans.txt")
321 os.remove("fifth.txt"); os.remove("fifthtrans.txt")
322 os.remove("sixth.txt"); os.remove("sixthtrans.txt")
323 os.remove("seventh.txt"); os.remove("seventhtrans.txt")
324 os.remove("eight.txt"); os.remove("eighttrans.txt")
325 os.remove("ninth.txt"); os.remove("ninthtrans.txt")
326 os.remove("fulltrans.txt"); os.remove("fullfinal.txt")
327
328 # 'part2_reservoir.py' code details - end
329 #####
330
331 #####
332 ##### 1998
333 ##### GAS 1998
334 initialfile='1998Sg.txt'
335 execfile('part2_reservoir.py')
336
337 # Multiply the reservoir property (Sgas) by Pore Volume
338 execfile('part3_multporv.py')
339
340 #####
341 # 'part3_multporv.py' code details - start
342 porevolume = np.loadtxt('PORV.txt')
343 reser = np.loadtxt('reserv.txt')
344 resrvoir = (porevolume*reser)

```

```

345 np.savetxt('reservoir.txt', resrvoir, delimiter = ' ', fmt='%0.5f')
346
347 os.remove("reserv.txt");
348
349 # 'part3_multporv.py' code details - end
350 #*****
351
352 #Creates the Property*PV weighted Map (Sum of layers 17 to 35)
353 outfinalfinalPV = '1998Sg128x53PV.txt'
354 execfile('part4_propertymap.py')
355
356 #*****
357 # 'part4_propertymap.py' code details - start
358 infile = np.loadtxt('reservoir.txt')
359 data = np.array(infile)
360
361 l1 = [sum(x) for x in zip(*data[0:1007:53])]
362 l2 = [sum(x) for x in zip(*data[1:1007:53])]
363 l3 = [sum(x) for x in zip(*data[2:1007:53])]
364 l4 = [sum(x) for x in zip(*data[3:1007:53])]
365 l5 = [sum(x) for x in zip(*data[4:1007:53])]
366 l6 = [sum(x) for x in zip(*data[5:1007:53])]
367 l7 = [sum(x) for x in zip(*data[6:1007:53])]
368 l8 = [sum(x) for x in zip(*data[7:1007:53])]
369 l9 = [sum(x) for x in zip(*data[8:1007:53])]
370 l10 = [sum(x) for x in zip(*data[9:1007:53])]
371
372 l11 = [sum(x) for x in zip(*data[10:1007:53])]
373 l12 = [sum(x) for x in zip(*data[11:1007:53])]
374 l13 = [sum(x) for x in zip(*data[12:1007:53])]
375 l14 = [sum(x) for x in zip(*data[13:1007:53])]
376 l15 = [sum(x) for x in zip(*data[14:1007:53])]
377 l16 = [sum(x) for x in zip(*data[15:1007:53])]
378 l17 = [sum(x) for x in zip(*data[16:1007:53])]
379 l18 = [sum(x) for x in zip(*data[17:1007:53])]
380 l19 = [sum(x) for x in zip(*data[18:1007:53])]
381 l20 = [sum(x) for x in zip(*data[19:1007:53])]
382
383 l21 = [sum(x) for x in zip(*data[20:1007:53])]
384 l22 = [sum(x) for x in zip(*data[21:1007:53])]
385 l23 = [sum(x) for x in zip(*data[22:1007:53])]
386 l24 = [sum(x) for x in zip(*data[23:1007:53])]
387 l25 = [sum(x) for x in zip(*data[24:1007:53])]
388 l26 = [sum(x) for x in zip(*data[25:1007:53])]
389 l27 = [sum(x) for x in zip(*data[26:1007:53])]
390 l28 = [sum(x) for x in zip(*data[27:1007:53])]
391 l29 = [sum(x) for x in zip(*data[28:1007:53])]
392 l30 = [sum(x) for x in zip(*data[29:1007:53])]
393
394 l31 = [sum(x) for x in zip(*data[30:1007:53])]
395 l32 = [sum(x) for x in zip(*data[31:1007:53])]
396 l33 = [sum(x) for x in zip(*data[32:1007:53])]
397 l34 = [sum(x) for x in zip(*data[33:1007:53])]
398 l35 = [sum(x) for x in zip(*data[34:1007:53])]
399 l36 = [sum(x) for x in zip(*data[35:1007:53])]
400 l37 = [sum(x) for x in zip(*data[36:1007:53])]
401 l38 = [sum(x) for x in zip(*data[37:1007:53])]
402 l39 = [sum(x) for x in zip(*data[38:1007:53])]
403 l40 = [sum(x) for x in zip(*data[39:1007:53])]
404
405 l41 = [sum(x) for x in zip(*data[40:1007:53])]
406 l42 = [sum(x) for x in zip(*data[41:1007:53])]
407 l43 = [sum(x) for x in zip(*data[42:1007:53])]
408 l44 = [sum(x) for x in zip(*data[43:1007:53])]
409 l45 = [sum(x) for x in zip(*data[44:1007:53])]
410 l46 = [sum(x) for x in zip(*data[45:1007:53])]
411 l47 = [sum(x) for x in zip(*data[46:1007:53])]
412 l48 = [sum(x) for x in zip(*data[47:1007:53])]
413 l49 = [sum(x) for x in zip(*data[48:1007:53])]
414 l50 = [sum(x) for x in zip(*data[49:1007:53])]
415
416 l51 = [sum(x) for x in zip(*data[50:1007:53])]
417 l52 = [sum(x) for x in zip(*data[51:1007:53])]
418 l53 = [sum(x) for x in zip(*data[52:1007:53])]
419
420 np.savetxt(outfinalfinalPV, (l1,l2,l3,l4,l5,l6,l7,l8,l9,\
421 l10,l11,l12,l13,l14,l15,l16,l17,l18,l19,l20,l21,l22,l23,\
422 l24,l25,l26,l27,l28,l29,l30,l31,l32,l33,l34,l35,l36,l37,\
423 l38,l39,l40,l41,l42,l43,l44,l45,l46,l47,l48,l49,\
424 l50,l51,l52,l53), delimiter = ' ', fmt='%0.5f')
425
426 os.remove("reservoir.txt");
427
428 # 'part4_propertymap.py' code details - end
429 #*****
430

```

```

431 #Creates the PV weighted Map (Sum of layers 17 to 35)
432 PV1 = 'PV1.txt'
433 execfile('part4a_propertymap.py')
434
435 #*****
436 # 'part4a_propertymap.py' code details
437 # Similar to 'part4_propertymap.py'
438 #*****
439
440 PV1 = np.loadtxt('PV1.txt')
441 foo = np.array(PV1)
442 foo[foo == 0.00000] = 1.00000
443 np.savetxt('PV.txt', foo, delimiter = ' ', fmt='%5f')
444 os.remove("PV1.txt");
445
446 #Creates the Property PV weighted Map (Sum of layers 17 to 35)
447 numerator = np.loadtxt('1998Sg128x53PV.txt')
448 denominator = np.loadtxt('PV.txt')
449 zdiv = numerator/denominator
450 np.savetxt('1998Sg128x53.txt', zdiv, delimiter = ' ', fmt='%5f')
451
452 #Upscale to 64x27
453 outfinalfinal = '1998Sg128x53.txt'
454 outerfinal = '1998Sg64x27.txt'
455 execfile('part5_upscale.py')
456
457 # Delete some files
458 os.remove("1998Sg.txt"); os.remove("1998Sg128x53PV.txt");
459
460 ##### WATER 1998
461 initialfile='1998Sw.txt'
462 execfile('part2_reservoir.py')
463
464 # Multiply the reservoir property (Swat) by Pore Volume
465 execfile('part3_multporv.py')
466
467 #Creates the Property*PV weighted Map (Sum of layers 17 to 35)
468 outfinalfinalPV = '1998Sw128x53PV.txt'
469 execfile('part4_propertymap.py')
470
471 #Creates the Property PV weighted Map (Sum of layers 17 to 35)
472 numerator = np.loadtxt('1998Sw128x53PV.txt')
473 denominator = np.loadtxt('PV.txt')
474
475 zdiv = numerator/denominator
476 np.savetxt('1998Sw128x53.txt', zdiv, delimiter = ' ', fmt='%5f')
477
478 #Upscale to 64x27
479 outfinalfinal = '1998Sw128x53.txt'
480 outerfinal = '1998Sw64x27.txt'
481 execfile('part5_upscale.py')
482
483 # 'part5_upscale.py' code details - start
484 infile = np.loadtxt(outfinalfinal)
485 data = np.array(infile)
486
487 r1 = [sum(x) for x in zip(*data[0:1])]
488 r2 = [sum(x)/(2) for x in zip(*data[1:3])]
489 r3 = [sum(x)/(2) for x in zip(*data[3:5])]
490 r4 = [sum(x)/(2) for x in zip(*data[5:7])]
491 r5 = [sum(x)/(2) for x in zip(*data[7:9])]
492 r6 = [sum(x)/(2) for x in zip(*data[9:11])]
493 r7 = [sum(x)/(2) for x in zip(*data[11:13])]
494 r8 = [sum(x)/(2) for x in zip(*data[13:15])]
495 r9 = [sum(x)/(2) for x in zip(*data[15:17])]
496 r10 = [sum(x)/(2) for x in zip(*data[17:19])]
497
498 r11 = [sum(x)/(2) for x in zip(*data[19:21])]
499 r12 = [sum(x)/(2) for x in zip(*data[21:23])]
500 r13 = [sum(x)/(2) for x in zip(*data[23:25])]
501 r14 = [sum(x)/(2) for x in zip(*data[25:27])]
502 r15 = [sum(x)/(2) for x in zip(*data[27:29])]
503 r16 = [sum(x)/(2) for x in zip(*data[29:31])]
504 r17 = [sum(x)/(2) for x in zip(*data[31:33])]
505 r18 = [sum(x)/(2) for x in zip(*data[33:35])]
506 r19 = [sum(x)/(2) for x in zip(*data[35:37])]
507 r20 = [sum(x)/(2) for x in zip(*data[37:39])]
508
509 r21 = [sum(x)/(2) for x in zip(*data[39:41])]
510 r22 = [sum(x)/(2) for x in zip(*data[41:43])]
511 r23 = [sum(x)/(2) for x in zip(*data[43:45])]
512 r24 = [sum(x)/(2) for x in zip(*data[45:47])]
513 r25 = [sum(x)/(2) for x in zip(*data[47:49])]
514 r26 = [sum(x)/(2) for x in zip(*data[49:51])]
515 r27 = [sum(x)/(2) for x in zip(*data[51:53])]
516

```

```

517 np.savetxt('rowupscale.txt', (r1,r2,r3,r4,r5,r6,r7,r8,r9,r10,r11,\
518 r12,r13,r14,r15,r16,r17,r18,r19,r20,r21,r22,r23,r24,r25,r26,\
519 r27), delimiter = ' ', fmt='%0.5f')
520
521 # Transpose in order to do column upscale to 64x27
522 with open('rowupscale.txt') as infile:
523     outfile = open('rowtrans.txt', 'w')
524     lines = (line.split() for line in infile)
525     for row in zip(*lines):
526         q = " ".join(row)
527         outfile.write(q+'\n')
528 outfile.close()
529
530 #column upscale to 64x27
531 infile = np.loadtxt('rowtrans.txt')
532 data = np.array(infile)
533
534 c1 = [sum(x)/(2) for x in zip(*data[0:2])]
535 c2 = [sum(x)/(2) for x in zip(*data[2:4])]
536 c3 = [sum(x)/(2) for x in zip(*data[4:6])]
537 c4 = [sum(x)/(2) for x in zip(*data[6:8])]
538 c5 = [sum(x)/(2) for x in zip(*data[8:10])]
539 c6 = [sum(x)/(2) for x in zip(*data[10:12])]
540 c7 = [sum(x)/(2) for x in zip(*data[12:14])]
541 c8 = [sum(x)/(2) for x in zip(*data[14:16])]
542 c9 = [sum(x)/(2) for x in zip(*data[16:18])]
543 c10 = [sum(x)/(2) for x in zip(*data[18:20])]
544
545 c11 = [sum(x)/(2) for x in zip(*data[20:22])]
546 c12 = [sum(x)/(2) for x in zip(*data[22:24])]
547 c13 = [sum(x)/(2) for x in zip(*data[24:26])]
548 c14 = [sum(x)/(2) for x in zip(*data[26:28])]
549 c15 = [sum(x)/(2) for x in zip(*data[28:30])]
550 c16 = [sum(x)/(2) for x in zip(*data[30:32])]
551 c17 = [sum(x)/(2) for x in zip(*data[32:34])]
552 c18 = [sum(x)/(2) for x in zip(*data[34:36])]
553 c19 = [sum(x)/(2) for x in zip(*data[36:38])]
554 c20 = [sum(x)/(2) for x in zip(*data[38:40])]
555
556 c21 = [sum(x)/(2) for x in zip(*data[40:42])]
557 c22 = [sum(x)/(2) for x in zip(*data[42:44])]
558 c23 = [sum(x)/(2) for x in zip(*data[44:46])]
559 c24 = [sum(x)/(2) for x in zip(*data[46:48])]
560 c25 = [sum(x)/(2) for x in zip(*data[48:50])]
561 c26 = [sum(x)/(2) for x in zip(*data[50:52])]
562 c27 = [sum(x)/(2) for x in zip(*data[52:54])]
563 c28 = [sum(x)/(2) for x in zip(*data[54:56])]
564 c29 = [sum(x)/(2) for x in zip(*data[56:58])]
565 c30 = [sum(x)/(2) for x in zip(*data[58:60])]
566
567 c31 = [sum(x)/(2) for x in zip(*data[60:62])]
568 c32 = [sum(x)/(2) for x in zip(*data[62:64])]
569 c33 = [sum(x)/(2) for x in zip(*data[64:66])]
570 c34 = [sum(x)/(2) for x in zip(*data[66:68])]
571 c35 = [sum(x)/(2) for x in zip(*data[68:70])]
572 c36 = [sum(x)/(2) for x in zip(*data[70:72])]
573 c37 = [sum(x)/(2) for x in zip(*data[72:74])]
574 c38 = [sum(x)/(2) for x in zip(*data[74:76])]
575 c39 = [sum(x)/(2) for x in zip(*data[76:78])]
576 c40 = [sum(x)/(2) for x in zip(*data[78:80])]
577
578 c41 = [sum(x)/(2) for x in zip(*data[80:82])]
579 c42 = [sum(x)/(2) for x in zip(*data[82:84])]
580 c43 = [sum(x)/(2) for x in zip(*data[84:86])]
581 c44 = [sum(x)/(2) for x in zip(*data[86:88])]
582 c45 = [sum(x)/(2) for x in zip(*data[88:90])]
583 c46 = [sum(x)/(2) for x in zip(*data[90:92])]
584 c47 = [sum(x)/(2) for x in zip(*data[92:94])]
585 c48 = [sum(x)/(2) for x in zip(*data[94:96])]
586 c49 = [sum(x)/(2) for x in zip(*data[96:98])]
587 c50 = [sum(x)/(2) for x in zip(*data[98:100])]
588
589 c51 = [sum(x)/(2) for x in zip(*data[100:102])]
590 c52 = [sum(x)/(2) for x in zip(*data[102:104])]
591 c53 = [sum(x)/(2) for x in zip(*data[104:106])]
592 c54 = [sum(x)/(2) for x in zip(*data[106:108])]
593 c55 = [sum(x)/(2) for x in zip(*data[108:110])]
594 c56 = [sum(x)/(2) for x in zip(*data[110:112])]
595 c57 = [sum(x)/(2) for x in zip(*data[112:114])]
596 c58 = [sum(x)/(2) for x in zip(*data[114:116])]
597 c59 = [sum(x)/(2) for x in zip(*data[116:118])]
598 c60 = [sum(x)/(2) for x in zip(*data[118:120])]
599
600 c61 = [sum(x)/(2) for x in zip(*data[120:122])]
601 c62 = [sum(x)/(2) for x in zip(*data[122:124])]
602 c63 = [sum(x)/(2) for x in zip(*data[124:126])]

```

```

603 c64 = [sum(x)/(2) for x in zip(*data[126:128])]
604
605 np.savetxt('colupscale.txt', (c1,c2,c3,c4,c5,c6,c7,c8,c9,\
606 c10,c11,c12,c13,c14,c15,c16,c17,c18,c19,c20,c21,c22,c23,\
607 c24,c25,c26,c27,c28,c29,c30,c31,c32,c33,c34,c35,c36,c37,\
608 c38,c39,c40,c41,c42,c43,c44,c45,c46,c47,c48,c49,c50,c51,\
609 c52,c53,c54,c55,c56,c57,c58,c59,c60,c61,c62,c63,\
610 c64), delimiter = ' ', fmt='%.5f')
611
612 #Transpose back to 64x27
613 with open('colupscale.txt') as infile:
614     outfile = open(outerfinal, 'w')
615     lines = (line.split() for line in infile)
616     for row in zip(*lines):
617         q = (" ".join(row))
618         outfile.write(q+'\n')
619 outfile.close()
620
621 os.remove("rowtrans.txt"); os.remove("rowupscale.txt");
622 os.remove("colupscale.txt");
623
624 # 'part5_upscale.py' code details - end
625 #*****
626
627 # Delete some files
628 os.remove("1998Sw.txt"); os.remove("1998Sw128x53PV.txt");
629
630
631 ##### 1999
632 ##### GAS 1999
633 initialfile='1999Sg.txt'
634 execfile('part2_reservoir.py')
635
636 # Multiply the reservoir property (Sgas) by Pore Volume
637 execfile('part3_multporv.py')
638
639 #Creates the Property*PV weighted Map (Sum of layers 17 to 35)
640 outfinalfinalPV = '1999Sg128x53PV.txt'
641 execfile('part4_propertymap.py')
642
643 #Creates the Property PV weighted Map (Sum of layers 17 to 35)
644 numerator = np.loadtxt('1999Sg128x53PV.txt')
645 denominator = np.loadtxt('PV.txt')
646
646 zdiv = numerator/denominator
647 np.savetxt('1999Sg128x53.txt', zdiv, delimiter = ' ', fmt='%.5f')
648
649 #Upscale to 64x27
650 outfinalfinal = '1999Sg128x53.txt'
651 outerfinal = '1999Sg64x27.txt'
652 execfile('part5_upscale.py')
653
654 #Calculate diff. btw. Baseline and Monitor (1999 - 1998) for 128x53
655 Sg1998_128x53up = np.loadtxt('1998Sg128x53.txt')
656 Sg1999_128x53up = np.loadtxt('1999Sg128x53.txt')
657 Sg9998_128x53 = (Sg1999_128x53up-Sg1998_128x53up)
658 np.savetxt('Sg9998_128x53.txt',Sg9998_128x53,delimiter=' ',fmt='%.5f')
659
660 #Calculate the diff. btw. Baseline and Monitor (1999 - 1998) for 64x27
661 Sg1998_64x27up = np.loadtxt('1998Sg64x27.txt')
662 Sg1999_64x27up = np.loadtxt('1999Sg64x27.txt')
663 Sg9998_64x27 = (Sg1999_64x27up-Sg1998_64x27up)
664 np.savetxt('Sg9998_64x27.txt',Sg9998_64x27,delimiter = ' ',fmt='%.5f')
665
666 #Convert to Binary - 1999-1998 for 64x27
667 Binaryinfile = 'Sg9998_64x27.txt'
668 Binaryoutfile= 'binarySg9998_64x27.txt'
669 execfile('part9_binary64x27_sgas.py')
670
671 #*****
672 # 'part9_binary64x27_sgas.py' code details - start
673
674 infile = np.loadtxt(Binaryinfile)
675 data = np.array(infile)
676
677 d1 = [(1 if num>threshold else 0) for num in data[0]]
678 d2 = [(1 if num>threshold else 0) for num in data[1]]
679 d3 = [(1 if num>threshold else 0) for num in data[2]]
680 d4 = [(1 if num>threshold else 0) for num in data[3]]
681 d5 = [(1 if num>threshold else 0) for num in data[4]]
682 d6 = [(1 if num>threshold else 0) for num in data[5]]
683 d7 = [(1 if num>threshold else 0) for num in data[6]]
684 d8 = [(1 if num>threshold else 0) for num in data[7]]
685 d9 = [(1 if num>threshold else 0) for num in data[8]]
686 d10 = [(1 if num>threshold else 0) for num in data[9]]
687
688 d11 = [(1 if num>threshold else 0) for num in data[10]]

```

```

689 d12 = [(1 if num>threshold else 0) for num in data[11]]
690 d13 = [(1 if num>threshold else 0) for num in data[12]]
691 d14 = [(1 if num>threshold else 0) for num in data[13]]
692 d15 = [(1 if num>threshold else 0) for num in data[14]]
693 d16 = [(1 if num>threshold else 0) for num in data[15]]
694 d17 = [(1 if num>threshold else 0) for num in data[16]]
695 d18 = [(1 if num>threshold else 0) for num in data[17]]
696 d19 = [(1 if num>threshold else 0) for num in data[18]]
697 d20 = [(1 if num>threshold else 0) for num in data[19]]
698
699 d21 = [(1 if num>threshold else 0) for num in data[20]]
700 d22 = [(1 if num>threshold else 0) for num in data[21]]
701 d23 = [(1 if num>threshold else 0) for num in data[22]]
702 d24 = [(1 if num>threshold else 0) for num in data[23]]
703 d25 = [(1 if num>threshold else 0) for num in data[24]]
704 d26 = [(1 if num>threshold else 0) for num in data[25]]
705 d27 = [(1 if num>threshold else 0) for num in data[26]]
706
707 np.savetxt(Binaryoutfile, (d1,d2,d3,d4,d5,d6,d7,d8,d9,d10,\
708 d11,d12,d13,d14,d15,d16,d17,d18,d19,d20,d21,d22,d23,d24,d25,\
709 d26,d27), delimiter = ' ', fmt='%s')
710
711 # 'part9_binary64x27_sgas.py' code details - end
712 #*****
713
714 #Reverse for PETREL Format, as PETREL writes/reads from bottom to top
715 infile = open('Sg9998_128x53.txt');
716 execfile('part6_reversePetrel.py')
717
718 #*****
719 # 'part6_reversePetrel.py' code details - start
720
721 outfile = open('reverse.txt', 'w');
722
723 rev = infile.readlines()
724 rev.reverse()
725 for line in rev:
726     outfile.write(line)
727 outfile.close()
728
729 # 'part6_reversePetrel.py' code details - end
730 #*****
731
732 #Convert 4D_9998Sg128x53 to PETREL Format
733 yes = 'PETREL: Properties\n1\nSg4D9998_code128'
734 petrelformat = 'PETRELSg4D9998_128x53.txt'
735 execfile('part7_PetrelFormat128x53.py')
736
737 #*****
738 # 'part7_PetrelFormat128x53.py' code details - start
739
740 infile = np.loadtxt('reverse.txt')
741 data = np.array(infile)
742
743 n1 = [(x) for x in zip(*data[0:1])]
744 n2 = [(x) for x in zip(*data[1:2])]
745 n3 = [(x) for x in zip(*data[2:3])]
746 n4 = [(x) for x in zip(*data[3:4])]
747 n5 = [(x) for x in zip(*data[4:5])]
748 n6 = [(x) for x in zip(*data[5:6])]
749 n7 = [(x) for x in zip(*data[6:7])]
750 n8 = [(x) for x in zip(*data[7:8])]
751 n9 = [(x) for x in zip(*data[8:9])]
752 n10 = [(x) for x in zip(*data[9:10])]
753
754 n11 = [(x) for x in zip(*data[10:11])]
755 n12 = [(x) for x in zip(*data[11:12])]
756 n13 = [(x) for x in zip(*data[12:13])]
757 n14 = [(x) for x in zip(*data[13:14])]
758 n15 = [(x) for x in zip(*data[14:15])]
759 n16 = [(x) for x in zip(*data[15:16])]
760 n17 = [(x) for x in zip(*data[16:17])]
761 n18 = [(x) for x in zip(*data[17:18])]
762 n19 = [(x) for x in zip(*data[18:19])]
763 n20 = [(x) for x in zip(*data[19:20])]
764
765 n21 = [(x) for x in zip(*data[20:21])]
766 n22 = [(x) for x in zip(*data[21:22])]
767 n23 = [(x) for x in zip(*data[22:23])]
768 n24 = [(x) for x in zip(*data[23:24])]
769 n25 = [(x) for x in zip(*data[24:25])]
770 n26 = [(x) for x in zip(*data[25:26])]
771 n27 = [(x) for x in zip(*data[26:27])]
772 n28 = [(x) for x in zip(*data[27:28])]
773 n29 = [(x) for x in zip(*data[28:29])]
774 n30 = [(x) for x in zip(*data[29:30])]

```

```
775
776 n31 = [(x) for x in zip(*data[30:31])]
777 n32 = [(x) for x in zip(*data[31:32])]
778 n33 = [(x) for x in zip(*data[32:33])]
779 n34 = [(x) for x in zip(*data[33:34])]
780 n35 = [(x) for x in zip(*data[34:35])]
781 n36 = [(x) for x in zip(*data[35:36])]
782 n37 = [(x) for x in zip(*data[36:37])]
783 n38 = [(x) for x in zip(*data[37:38])]
784 n39 = [(x) for x in zip(*data[38:39])]
785 n40 = [(x) for x in zip(*data[39:40])]
786
787 n41 = [(x) for x in zip(*data[40:41])]
788 n42 = [(x) for x in zip(*data[41:42])]
789 n43 = [(x) for x in zip(*data[42:43])]
790 n44 = [(x) for x in zip(*data[43:44])]
791 n45 = [(x) for x in zip(*data[44:45])]
792 n46 = [(x) for x in zip(*data[45:46])]
793 n47 = [(x) for x in zip(*data[46:47])]
794 n48 = [(x) for x in zip(*data[47:48])]
795 n49 = [(x) for x in zip(*data[48:49])]
796 n50 = [(x) for x in zip(*data[49:50])]
797
798 n51 = [(x) for x in zip(*data[50:51])]
799 n52 = [(x) for x in zip(*data[51:52])]
800 n53 = [(x) for x in zip(*data[52:53])]
801 n54 = [(x) for x in zip(*data[53:54])]
802 n55 = [(x) for x in zip(*data[54:55])]
803 n56 = [(x) for x in zip(*data[55:56])]
804 n57 = [(x) for x in zip(*data[56:57])]
805 n58 = [(x) for x in zip(*data[57:58])]
806 n59 = [(x) for x in zip(*data[58:59])]
807 n60 = [(x) for x in zip(*data[59:60])]
808
809 n61 = [(x) for x in zip(*data[60:61])]
810 n62 = [(x) for x in zip(*data[61:62])]
811 n63 = [(x) for x in zip(*data[62:63])]
812 n64 = [(x) for x in zip(*data[63:64])]
813 n65 = [(x) for x in zip(*data[64:65])]
814 n66 = [(x) for x in zip(*data[65:66])]
815 n67 = [(x) for x in zip(*data[66:67])]
816 n68 = [(x) for x in zip(*data[67:68])]
817 n69 = [(x) for x in zip(*data[68:69])]
```

```
818 n70 = [(x) for x in zip(*data[69:70])]
819
820 n71 = [(x) for x in zip(*data[70:71])]
821 n72 = [(x) for x in zip(*data[71:72])]
822 n73 = [(x) for x in zip(*data[72:73])]
823 n74 = [(x) for x in zip(*data[73:74])]
824 n75 = [(x) for x in zip(*data[74:75])]
825 n76 = [(x) for x in zip(*data[75:76])]
826 n77 = [(x) for x in zip(*data[76:77])]
827 n78 = [(x) for x in zip(*data[77:78])]
828 n79 = [(x) for x in zip(*data[78:79])]
829 n80 = [(x) for x in zip(*data[79:80])]
830
831 n81 = [(x) for x in zip(*data[80:81])]
832 n82 = [(x) for x in zip(*data[81:82])]
833 n83 = [(x) for x in zip(*data[82:83])]
834 n84 = [(x) for x in zip(*data[83:84])]
835 n85 = [(x) for x in zip(*data[84:85])]
836 n86 = [(x) for x in zip(*data[85:86])]
837 n87 = [(x) for x in zip(*data[86:87])]
838 n88 = [(x) for x in zip(*data[87:88])]
839 n89 = [(x) for x in zip(*data[88:89])]
840 n90 = [(x) for x in zip(*data[89:90])]
841
842 n91 = [(x) for x in zip(*data[90:91])]
843 n92 = [(x) for x in zip(*data[91:92])]
844 n93 = [(x) for x in zip(*data[92:93])]
845 n94 = [(x) for x in zip(*data[93:94])]
846 n95 = [(x) for x in zip(*data[94:95])]
847 n96 = [(x) for x in zip(*data[95:96])]
848 n97 = [(x) for x in zip(*data[96:97])]
849 n98 = [(x) for x in zip(*data[97:98])]
850 n99 = [(x) for x in zip(*data[98:99])]
851 n100 = [(x) for x in zip(*data[99:100])]
852
853 n101 = [(x) for x in zip(*data[100:101])]
854 n102 = [(x) for x in zip(*data[101:102])]
855 n103 = [(x) for x in zip(*data[102:103])]
856 n104 = [(x) for x in zip(*data[103:104])]
857 n105 = [(x) for x in zip(*data[104:105])]
858 n106 = [(x) for x in zip(*data[105:106])]
859 n107 = [(x) for x in zip(*data[106:107])]
860 n108 = [(x) for x in zip(*data[107:108])]
```

```

861 n109 = [(x) for x in zip(*data[108:109])]
862 n110 = [(x) for x in zip(*data[109:110])]
863
864 n111 = [(x) for x in zip(*data[110:111])]
865 n112 = [(x) for x in zip(*data[111:112])]
866 n113 = [(x) for x in zip(*data[112:113])]
867 n114 = [(x) for x in zip(*data[113:114])]
868 n115 = [(x) for x in zip(*data[114:115])]
869 n116 = [(x) for x in zip(*data[115:116])]
870 n117 = [(x) for x in zip(*data[116:117])]
871 n118 = [(x) for x in zip(*data[117:118])]
872 n119 = [(x) for x in zip(*data[118:119])]
873 n120 = [(x) for x in zip(*data[119:120])]
874
875 n121 = [(x) for x in zip(*data[120:121])]
876 n122 = [(x) for x in zip(*data[121:122])]
877 n123 = [(x) for x in zip(*data[122:123])]
878 n124 = [(x) for x in zip(*data[123:124])]
879 n125 = [(x) for x in zip(*data[124:125])]
880 n126 = [(x) for x in zip(*data[125:126])]
881 n127 = [(x) for x in zip(*data[126:127])]
882 n128 = [(x) for x in zip(*data[127:128])]
883
884 np.savetxt(petrelformat, (list(n1)+list(n2)+list(n3)+\
885 list(n4)+list(n5)+list(n6)+list(n7)+list(n8)+list(n9)+\
886 list(n10)+list(n11)+list(n12)+list(n13)+list(n14)+\
887 list(n15)+list(n16)+list(n17)+list(n18)+list(n19)+\
888 list(n20)+list(n21)+list(n22)+list(n23)+list(n24)+\
889 list(n25)+list(n26)+list(n27)+list(n28)+list(n29)+\
890 list(n30)+list(n31)+list(n32)+list(n33)+list(n34)+\
891 list(n35)+list(n36)+list(n37)+list(n38)+list(n39)+\
892 list(n40)+list(n41)+list(n42)+list(n43)+list(n44)+\
893 list(n45)+list(n46)+list(n47)+list(n48)+list(n49)+\
894 list(n50)+list(n51)+list(n52)+list(n53)+list(n54)+\
895 list(n55)+list(n56)+list(n57)+list(n58)+list(n59)+\
896 list(n60)+list(n61)+list(n62)+list(n63)+list(n64)+\
897 list(n65)+list(n66)+list(n67)+list(n68)+list(n69)+\
898 list(n70)+list(n71)+list(n72)+list(n73)+list(n74)+\
899 list(n75)+list(n76)+list(n77)+list(n78)+list(n79)+\
900 list(n80)+list(n81)+list(n82)+list(n83)+list(n84)+\
901 list(n85)+list(n86)+list(n87)+list(n88)+list(n89)+\
902 list(n90)+list(n91)+list(n92)+list(n93)+list(n94)+\
903 list(n95)+list(n96)+list(n97)+list(n98)+list(n99)+\
904 list(n100)+list(n101)+list(n102)+list(n103)+list(n104)+\
905 list(n105)+list(n106)+list(n107)+list(n108)+list(n109)+\
906 list(n110)+list(n111)+list(n112)+list(n113)+list(n114)+\
907 list(n115)+list(n116)+list(n117)+list(n118)+list(n119)+\
908 list(n120)+list(n121)+list(n122)+list(n123)+list(n124)+\
909 list(n125)+list(n126)+list(n127)+list(n128)),\
910 delimiter = ' ', fmt='%s', newline='\n', header=yes, comments='')
911
912 os.remove("reverse.txt");
913
914 # 'part7_PetrelFormat128x53.py' code details - end
915 #*****
916
917 #Reverse for PETREL Format, as PETREL writes/reads from bottom to top
918 infile = open('Sg9998_64x27.txt');
919 execfile('part6_reversePetrel.py')
920
921 #Convert 4D_9998Sg64x27 to PETREL Format
922 yes = 'PETREL: Properties\n1\nSg4D9998code64'
923 petrelformat = 'PETRELSg4D9998_64x27.txt'
924 execfile('part8_PetrelFormat64x27.py')
925
926 #*****
927 # 'part8_PetrelFormat64x27.py' code details
928 # Similar to 'part7_PetrelFormat128x53.py'
929 #*****
930
931 #Reverse for PETREL Format, as PETREL writes/reads from bottom to top
932 infile = open('binarySg9998_64x27.txt');
933 execfile('part6_reversePetrel.py')
934
935 #Convert 4D_9998BinarySg64x27 to PETREL Format
936 yes = 'PETREL: Properties\n1\nBinSg4D9998code64'
937 petrelformat = 'PETRELBinSg4D9998_64x27.txt'
938 execfile('part8_PetrelFormat64x27.py')
939
940 # Delete some files
941 os.remove("1999Sg.txt"); os.remove("1999Sg128x53.txt");
942 os.remove("1999Sg64x27.txt"); os.remove("Sg9998_128x53.txt");
943 os.remove("Sg9998_64x27.txt"); os.remove("1999Sg128x53PV.txt");
944 os.remove("1998Sg128x53.txt"); os.remove("1998Sg64x27.txt");
945
946 ##### WATER 1999

```



```

947 initialfile='1999Sw.txt'
948 execfile('part2_reservoir.py')
949
950 # Multiply the reservoir property (Swat) by Pore Volume
951 execfile('part3_multporv.py')
952
953 #Creates the Property*PV weighted Map (Sum of layers 17 to 35)
954 outfinalfinalPV = '1999Sw128x53PV.txt'
955 execfile('part4_propertymap.py')
956
957 #Creates the Property PV weighted Map (Sum of layers 17 to 35)
958 numerator = np.loadtxt('1999Sw128x53PV.txt')
959 denominator = np.loadtxt('PV.txt')
960 zdiv = numerator/denominator
961 np.savetxt('1999Sw128x53.txt', zdiv, delimiter = ' ', fmt='%.5f')
962
963 #Upscale to 64x27
964 outfinalfinal = '1999Sw128x53.txt'
965 outerfinal = '1999Sw64x27.txt'
966 execfile('part5_upscale.py')
967
968 #Calculate diff. btw. Baseline and Monitor (1999 - 1998) for 128x53
969 Sw1998_128x53up = np.loadtxt('1998Sw128x53.txt')
970 Sw1999_128x53up = np.loadtxt('1999Sw128x53.txt')
971 Sw9998_128x53 = (Sw1999_128x53up-Sw1998_128x53up)
972 np.savetxt('Sw9998_128x53.txt',Sw9998_128x53,delimiter=' ',fmt='%.5f')
973
974 #Calculate diff. btw. Baseline and Monitor (1999 - 1998) for 64x27
975 Sw1998_64x27up = np.loadtxt('1998Sw64x27.txt')
976 Sw1999_64x27up = np.loadtxt('1999Sw64x27.txt')
977 Sw9998_64x27 = (Sw1999_64x27up-Sw1998_64x27up)
978 np.savetxt('Sw9998_64x27.txt',Sw9998_64x27,delimiter=' ',fmt='%.5f')
979
980 #Convert to Binary - 1999-1998 for 64x27
981 Binaryinfile = 'Sw9998_64x27.txt'
982 Binaryoutfile= 'binarySw9998_64x27.txt'
983 execfile('part9_binary64x27_swat.py')
984
985 #Reverse for PETREL Format, as PETREL writes/reads from bottom to top
986 infile = open('Sw9998_128x53.txt');
987 execfile('part6_reversePetrel.py')
988
989 #Convert 4D_9998Sw128x53 to PETREL Format
990 yes = 'PETREL: Properties\n1\nSw4D9998_code128'
991 petrelformat = 'PETRELSw4D9998_128x53.txt'
992 execfile('part7_PetrelFormat128x53.py')
993
994 #Reverse for PETREL Format, as PETREL writes/reads from bottom to top
995 infile = open('Sw9998_64x27.txt');
996 execfile('part6_reversePetrel.py')
997
998 #Convert 4D_9998Sw64x27 to PETREL Format
999 yes = 'PETREL: Properties\n1\nSw4D9998code64'
1000 petrelformat = 'PETRELSw4D9998_64x27.txt'
1001 execfile('part8_PetrelFormat64x27.py')
1002
1003 #Reverse for PETREL Format, as PETREL writes/reads from bottom to top
1004 infile = open('binarySw9998_64x27.txt');
1005 execfile('part6_reversePetrel.py')
1006
1007 #Convert 4D_9998BinarySw64x27 to PETREL Format
1008 yes = 'PETREL: Properties\n1\nBinSw4D9998code64'
1009 petrelformat = 'PETRELBinSw4D9998_64x27.txt'
1010 execfile('part8_PetrelFormat64x27.py')
1011
1012 # Delete some files
1013 os.remove("1999Sw.txt"); os.remove("1999Sw128x53.txt");
1014 os.remove("1999Sw64x27.txt"); os.remove("Sw9998_128x53.txt");
1015 os.remove("Sw9998_64x27.txt"); os.remove("1999Sw128x53PV.txt");
1016 os.remove("1998Sw128x53.txt"); os.remove("1998Sw64x27.txt");
1017 os.remove("PORV.txt"); os.remove("PV.txt");
1018
1019
1020 #####
1021 #####
1022 # TO CALCULATE THE CURRENT OR HAMMING MISFIT
1023 outfile = open('ObjFxn_SgNSw.txt', 'w');
1024 outfile2 = open('NSCH_SIM_COARSEN642635.infc', 'w');
1025 execfile('part10_Currentmisfit_sgasNswat.py')
1026 execfile('part10_Hammingmisfit_sgasNswat.py')
1027
1028
1029 #####
1030 # 'part10_Currentmisfit_sgasNswat.py' code details - start
1031 import currents
1032

```

```

1033 ##### GAS misfit
1034 BinSNA9998Sg = np.loadtxt('BINARYSNA9998_64x27Sg.txt')
1035 binSg9998 = np.loadtxt('binarySg9998_64x27.txt')
1036
1037 mfitsum9998Sg=(currents.currentDistSobolev(BinSNA9998Sg,binSg9998,2))
1038 seismfitSg = (mfitsum9998Sg)
1039
1040 ##### WATER misfit
1041 BinSNA9998Sw = np.loadtxt('BINARYSNA9998_64x27Sw.txt')
1042 binSw9998 = np.loadtxt('binarySw9998_64x27.txt')
1043
1044 mfitsum9998Sw=(currents.currentDistSobolev(BinSNA9998Sw,binSw9998,2))
1045 seismfitSw = (mfitsum9998Sw)
1046
1047 ##### GAS AND WATER misfit
1048 seismfitSgSw = (seismfitSg + seismfitSw)
1049
1050 ##### GAS for MEPO
1051 mfitsum9998Sgsqrt = ((mfitsum9998Sg*1)**(.5))
1052
1053 ##### WATER for MEPO
1054 mfitsum9998Swsqrt = ((mfitsum9998Sw*1)**(.5))
1055
1056 ##### Objective function document for gas and water
1057 outfile.write('Seis mfit sum 99-98Sg = '+str(mfitsum9998Sg)+'\n')
1058 outfile.write('Sum of Seis mfit for Sg = '+str(seismfitSg))
1059 outfile.write('\n')
1060 outfile.write('Seis mfit sum 99-98Sw = '+str(mfitsum9998Sw)+'\n')
1061 outfile.write('Sum of Seis mfit for Sw = '+str(seismfitSw))
1062 outfile.write('\n')
1063 outfile.write('Total Sum Seis mfit SgNSw = '+str(seismfitSgSw))
1064 outfile.close()
1065
1066 #Output individual misfits for each monitor, the output...
1067 #will be squared by the objective function
1068 outfile2.write('VECTOR Year1999Sg'+'\n')
1069 outfile2.write('1999'+'\n')
1070 outfile2.write('VECTOR Mfit1999Sg'+'\n')
1071 outfile2.write(str(mfitsum9998Sgsqrt)+'\n')
1072 outfile2.write('\n')
1073 outfile2.write('VECTOR Year1999Sw'+'\n')
1074 outfile2.write('1999'+'\n')
1075 outfile2.write('VECTOR Mfit1999Sw'+'\n')
1076 outfile2.write(str(mfitsum9998Swsqrt)+'\n')
1077 outfile2.close()
1078
1079 # 'part10_Currentmisfit_sgasNswat.py' code details - end
1080 #####
1081
1082 #####
1083 # 'part10_Hammingmisfit_sgasNswat.py' code details - start
1084
1085 ##### GAS misfit
1086 BinSNA9998Sg = np.loadtxt('BINARYSNA9998_64x27.txt')
1087 binSg9998 = np.loadtxt('binarySg9998_64x27.txt')
1088
1089 mfit9998Sg = (BinSNA9998Sg!=binSg9998)
1090 mfitsum9998Sg = sum(sum(mfit9998Sg.astype(int)))
1091 seismfitSg = (mfitsum9998Sg)
1092
1093 ##### WATER misfit
1094 BinSNA9998Sw = np.loadtxt('BINARYSNA9998_64x27.txt')
1095 binSw9998 = np.loadtxt('binarySw9998_64x27.txt')
1096
1097 mfit9998Sw = (BinSNA9998Sw!=binSw9998)
1098 mfitsum9998Sw = sum(sum(mfit9998Sw.astype(int)))
1099 seismfitSw = (mfitsum9998Sw)
1100
1101 ##### GAS AND WATER misfit
1102 seismfitSgSw = (seismfitSg + seismfitSw)
1103
1104 ##### GAS for MEPO
1105 mfitsum9998Sgsqrt = ((mfitsum9998Sg*1)**(.5))
1106
1107 ##### WATER for MEPO
1108 mfitsum9998Swsqrt = ((mfitsum9998Sw*1)**(.5))
1109
1110 ##### Objective function document for gas and water
1111 outfile.write('Seis mfit sum 99-98Sg = '+str(mfitsum9998Sg)+'\n')
1112 outfile.write('Sum of Seis mfit for Sg = '+str(seismfitSg))
1113 outfile.write('\n')
1114 outfile.write('Seis mfit sum 99-98Sw = '+str(mfitsum9998Sw)+'\n')
1115 outfile.write('Sum of Seis mfit for Sw = '+str(seismfitSw))
1116 outfile.write('\n')
1117 outfile.write('Total Sum Seis mfit SgNSw = '+str(seismfitSgSw))
1118

```

```

1119 outfile.close()
1120
1121 ##### Objective function for gas and water (MEPO)
1122 outfile2.write('VECTOR YEARSG'+'\n')
1123 outfile2.write('BINARY GAS'+'\n')
1124 outfile2.write('1999'+'\n')
1125 outfile2.write('\n')
1126 outfile2.write('VECTOR Misfitg'+'\n')
1127 outfile2.write('BINARY GAS'+'\n')
1128 outfile2.write(str(mfitsum9998Sgsqrt)+'\n')
1129 outfile2.write('\n')
1130 outfile2.write('\n')
1131 outfile2.write('VECTOR YEARSW'+'\n')
1132 outfile2.write('BINARY WATER'+'\n')
1133 outfile2.write('1999'+'\n')
1134 outfile2.write('\n')
1135 outfile2.write('VECTOR MISFITw'+'\n')
1136 outfile2.write('BINARY WATER'+'\n')
1137 outfile2.write(str(mfitsum9998Swsqrt)+'\n')
1138 outfile2.close()
1139
1140 # 'part10_Hammingmisfit_sgasNswat.py' code details - end
1141 *****
1142
1143
1144 # TO CALCULATE THE NUMERICAL SYNTHETIC 4D SEISMIC
1145 execfile('part9_NumS2S.py')
1146
1147 *****
1148 # 'part9_NumS2S.py' code details - start
1149
1150 ##### 1999 - 1998
1151 dP9998 = np.loadtxt('P9998_64x27.txt')
1152 dSw9998 = np.loadtxt('Sw9998_64x27.txt')
1153 dSg9998 = np.loadtxt('Sg9998_64x27.txt')
1154 static9998 = np.loadtxt('staticmap64x27.txt')
1155
1156 dA9998=((dP9998*0.0000414668)+(-0.739295*dSw9998)\
1157         +(5.61548*dSg9998)\
1158         +(dP9998*dSw9998*0.0000395671)\
1159         +(0.0119935*dP9998*dSg9998)\
1160         +(7.12809*dSw9998*dSg9998)\
1161         +(dP9998*dP9998*0.00000182363)\
1162         +(0.208531*dSw9998*dSw9998)\
1163         +(121.982*dSg9998*dSg9998)\
1164         *static9998
1165
1166 np.savetxt('dA9998.txt', dA9998, delimiter = ' ', fmt='%.5f')
1167
1168 #Reverse for PETREL Format, as PETREL writes/reads bottom to top
1169 infile = open('dA9998.txt');
1170 execfile('part6_reversePetrel.py')
1171
1172 #Convert dA999864x27 to PETREL Format
1173 yes = 'PETREL: Properties\n1\ndA9998code64'
1174 petrelformat = 'PETRELdA9998_64x27.txt'
1175 execfile('part8_PetrelFormat64x27.py')
1176
1177 os.remove("staticmap64x27.txt"); os.remove("Sg9998_64x27.txt");
1178 os.remove("Sw9998_64x27.txt"); os.remove("P9998_64x27.txt");
1179
1180 # 'part9_NumS2S.py' code details - end
1181 *****
1182
1183 # TO CALCULATE THE NUMS2S MISFIT
1184 outfile = open('ObjFxn_LSMfitSeisTotal.txt', 'w');
1185 outfile2 = open('NSCH_SIM_COARSEN642635.infc', 'w');
1186 execfile('part10_misfit_NumS2S.py')
1187
1188 *****
1189 # 'part10_misfit_NumS2S.py' code details - start
1190
1191 ##### 1999 - 1998
1192 dA9998 = np.loadtxt('dA9998.txt')
1193 dSNA9998 = np.loadtxt('dSNA9998_64x27.txt')
1194
1195 LSM9998=((dA9998-dSNA9998)*(dA9998-dSNA9998))
1196 LSMfit9998 = sum(sum(LSM9998))
1197
1198 ##### Combining all surveys
1199 LSMfitTotal = (LSMfit9998)
1200
1201 ##### LSMfitTotal for MEPO
1202 LSMfit9998sqrt = ((LSMfit9998*1)**(.5))
1203
1204 ##### Objective function document for gas and water

```

```

1205 outfile.write('Seismic misfit sum 1999-1998 = '+str(LSMfit9998)+'\n')
1206     outfile.write('The Sum of Seismic Misfit = '+str(LSMfitTotal))
1207     outfile.close()
1208
1209     ##### Objective function (MEPO)
1210     outfile2.write('VECTOR YEARS'+'\n')
1211     outfile2.write('SEISMIC'+'\n')
1212     outfile2.write('1999'+'\n')
1213     outfile2.write('\n')
1214     outfile2.write('VECTOR Misfit'+'\n')
1215     outfile2.write('SEISMIC'+'\n')
1216     outfile2.write(str(LSMfit9998sqrt))
1217     outfile2.close()
1218
1219     os.remove("dA9998.txt");
1220
1221     # 'part10_misfit_NumS2S.py' code details - end
1222     #####
1223
1224     # Delete some files
1225     ##### GAS
1226     os.remove("binarySg9998_64x27.txt");
1227     ##### WATER
1228     os.remove("binarySw9998_64x27.txt");
1229
1230     print(time.time() - start_time, 'seconds')

```

Appendix G

G.1 Publications

- Obidegwu, D., and MacBeth, C. 2014. Estimation of Critical and Maximum Gas Saturation Using Multiple 4D Seismic Surveys. Paper presented at the EAGE Annual Conference and Exhibition, Amsterdam, The Netherlands. 16 – 19 June, 2014.
- Obidegwu, D., and MacBeth, C. 2014. Quantitative Analysis of Gas Volumes Using Multiple 4D Seismic Surveys & Material Balance. Paper presented at the 5th SEG/EAGE International Geosciences Student Conference (IGSC), Nizhny Novgorod, Russia. July 28 – August 01, 2014.
- Falahat, R., Obidegwu, D., Shams, A. and MacBeth, C. 2014. The Interpretation of Amplitude Changes in 4D Seismic Data Arising from Gas Exsolution and Dissolution. *Petroleum Geoscience*, Volume 20, Issue 03, Pages 303-320.
- Obidegwu, D., Chassagne, R. and MacBeth, C. 2014. Using 4D Seismic Surveys and History Matching to Estimate Critical and Maximum Gas Saturation. Paper presented at the International Petroleum Technology Conference (IPTC), Kuala Lumpur, Malaysia. 10 -12 December, 2014.
- Obidegwu, D., Chassagne, R. and MacBeth, C. 2015. Seismic Assisted History Matching Using Binary Image Matching. Paper presented at the SPE Europec/ EAGE Annual Conference and Exhibition, Madrid, Spain. 1 – 4 June, 2015.
- Obidegwu, D., MacBeth, C. and Chassagne, R. 2016. Comparative Analysis of Binary and Conventional Seismic Assisted History Matching. Paper presented at the SPE Europec/ EAGE Annual Conference and Exhibition, Vienna, Austria. 30 May – 2 June, 2016.

Tu G102 05

Estimation of Critical and Maximum Gas Saturation Using Multiple 4D Seismic Surveys

D. Obidegwu* (Heriot-Watt University) & C. MacBeth (Heriot Watt University)

SUMMARY

Estimates for critical and maximum gas saturation are obtained using time-lapse seismic signatures from multiple surveys shot during gas liberation and dissolution in a producing hydrocarbon reservoir. To aid this process, hydrocarbon gas properties and behaviour are studied, and their relation to the fluid-flow physics is understood using numerical simulation and seismic modelling. It is concluded that for seismic surveys repeated at time intervals of six months or more, the gas saturation distribution during either liberation or dissolution exists in two fixed saturation conditions defined by the critical and the maximum gas saturation. This understanding is then used to interpret seismic data from a turbidite field in the North Sea, which has surveys repeated every 12 to 24 months. We find a critical gas saturation of between 0.6 and 4%, but that the maximum gas saturation is relatively unconstrained. These low critical gas saturation values are consistent with the range of measurements from other similar fields in the open literature.

Introduction

The need to predict the flow of multiple fluids in a reservoir has been the subject of much research in the oil and gas industry. This is highly sought after because it enables efficient reservoir monitoring, management, planning and economic evaluation. In the reservoir engineering domain such understanding has so far been driven by research in laboratory measurements, log analysis, history matching as well as pore network modelling; however many parameters in multiphase flow remain unconstrained (Di Pierro et al. 2003), especially at the reservoir scale. In particular, for drainage and imbibition involving gas, the critical (S_{gc}) and maximum (S_{gmax}) gas saturation values need to be better determined. The S_{gc} is the saturation at which gas first becomes mobile and occurs during the drainage process such as gas out of solution. S_{gmax} is the highest gas saturation obtainable in the presence of only connate water saturation and residual oil saturation to gas, and is important in situations such as when a secondary gas cap is formed due to migrating free gas. Pore pressure drop in producing oil reservoirs that have poor or misunderstood connectivity, followed by re-pressurisation with water injection, can create both of these scenarios (Dake, 2002). Therefore, seismic monitoring of gas liberation or dissolution may provide a way of estimating key fluid-flow parameters. This appears initially possible as the seismic response to the presence of free gas generally leads to a strong, non-linear reduction in seismic velocity and impedance (Han & Batzle 2000). Previously, Falahat et al. (2013) showed how access to reservoir-scale versions of S_{gc} and S_{gmax} can be obtained using 4D seismic. Here, we extend this study by developing a quantitative analysis method suitable for multiple seismic surveys.

Interpretation of the 4D seismic data

The field of interest is a North Sea field that comprises of turbidite sands containing multiple stacked reservoirs which are compartmentalized. It has an aquifer and the reservoirs which are typically 30m thick or less are thought to be fully oil filled. The depletion mechanisms are solution gas drive and water drive, and the field is close to its bubble point pressure. Production activities as well as insufficient pressure support in its early years have led to gas exsolution. The baseline seismic for the field was acquired preproduction (1998), and six monitors – 1999, 2000, 2002, 2004, 2006 and 2008 (Martin and MacDonald 2010) are analyzed in this paper.

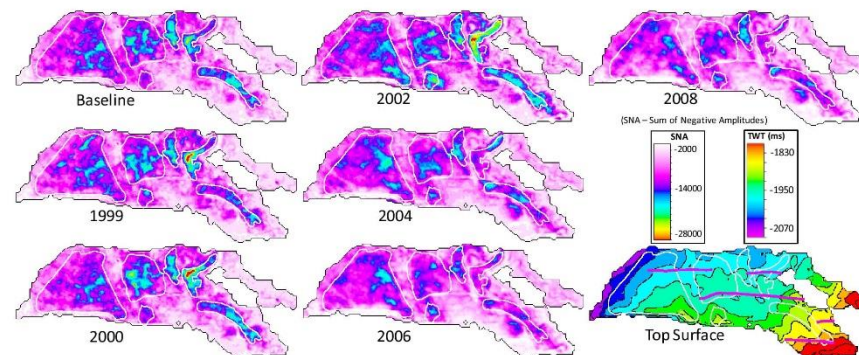


Figure 1 Amplitude maps from individual seismic surveys. The attribute used is the sum of negative amplitudes (SNA) over the reservoir interval. The top surface map is shown, highlighting the position of faults, geometry and structural highs where gas is likely to migrate towards due to gravity effects.

The area of interest is divided into six regions (regions A to F) for our analysis as shown in Figures 1 and 2. These six regions are selected based on the quality of the reservoir and seismic signals. In each region, high amplitude anomalies indicate hydrocarbon-filled sand bodies with good quality net-to-gross. A progressive brightening of a sand body identifies a reservoir softening or impedance

decrease, whilst a dimming indicates a reservoir hardening or impedance increase. By year 2000, pressure is known to have dropped by 900psi in the vicinity of the production wells. Thus, gas is expected to be liberated during the first three monitor surveys in years 1999, 2000 and 2002. This is obvious as a general brightening of the individual reservoir sands. After year 2002, pressure increases again and gas dissolution occurs due to an increase in water saturation (from below) from existing and new injectors. This is again generally evident as a dimming of the mapped sand bodies. Interestingly, however, based on the production and injection wells' start-up and shut-in history (Figure 2), different sand bodies deplete at different rates and hence the brightening and dimming events in each are not quite synchronised in time.

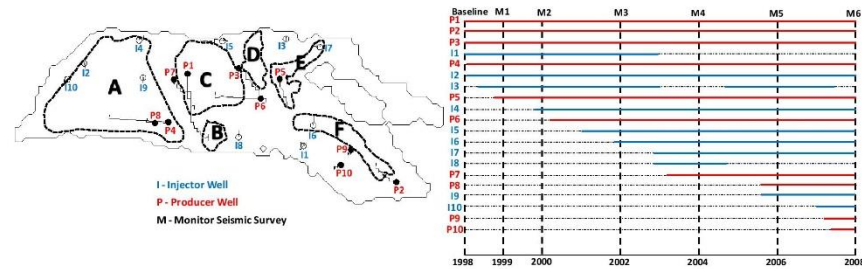


Figure 2 Reservoir outline showing the six selected regions A-F highlighting the position of the injector wells and producer wells. Also shown is the sequence at which the wells are put on production/injection and shut-in, relative to the timing of the seismic baseline and monitor surveys. The red lines represent producer wells, while the blue lines represent injector wells.

- In region A, an initial injector-producer (I2-P4) pair is supplemented by injector I4 to maintain pressure. Later, injectors I9 and I10 come on stream to counteract the pressure decline due to producer P8. Exsolved gas is observed initially in 1999, and it collects in a local high in the south-eastern corner to form a secondary gas cap in 2002. Increased water saturation and gas dissolution reduce the amplitudes after 2002, although some gas remains.
- Region B sits on a local high into which exsolved gas collects. With no direct injector support initially, gas dissolution does not occur until after 2002 when the nearby injector I8 becomes active.
- Region C is bounded along its south edge by a sealing fault (Figure 1). Critical gas saturation is evident as a consequence of production in P1 and P6, and there is an upward migration of the gas influenced by possible pressure gradients from producer P1. Injector I5 is active after 2001 to provide pressure support.
- Region D is possibly connected with region C, but it is not intersected by a producing well. Earlier amplitudes in this region D are fairly constant – suggesting a lack of pressure connection. Water sweep from injectors I3 and I5 may play a role in decreasing the amplitude after 2002.
- In region E, there is a strong and evident initial brightening until 2002 due to the producer P5. In 2003 injector I7 is drilled towards the northern edge, which then dims the amplitudes in subsequent years.
- The final region for consideration is F, which dips upwards to the south-east. The initial action of injector I1 dims the amplitudes in 1999, but pressure support is not sufficient and gas exsolution occurs in 2000 due to producer P2. Around year 2002, injector I6 replaces I1 close to the same location, and this provides the required pressure support.

Figure 3 shows the amplitudes of a number of small sub-regions within A to F and their combined averages plotted against survey time. These sub-regions are selected to be of known high net-to-gross and signal quality, and are used to determine the seismic amplitude levels associated with an oil sand (pre-production state), oil sand with critical gas saturation, and the secondary gas cap. The amplitude level of the baseline response and the maximum value of the amplitude as a function of time are determined for each. If the amplitude level after the maximum has been reached still remains above

the initial baseline, this is interpreted as a case where a secondary gas cap has developed; however, if the amplitude level after the maximum goes below the baseline line level, this is interpreted as critical gas saturation dissolution, as well as potential water saturation sweep. Our interpretation based on the known well activity, reservoir geometry and time-lapse seismic amplitudes indicates that the maxima for regions A and B correspond to the maximum gas saturation, and these occur in 2002. The maxima for regions C, E and F are interpreted to correspond to the critical gas saturation, and these occur in 2000. Region D is not used in the analysis as the effect of the contributions from the injectors and producers plus neighbouring connected regions is not yet fully understood. The next stage is to quantitatively relate these 4D seismic amplitude levels to the gas saturation values.

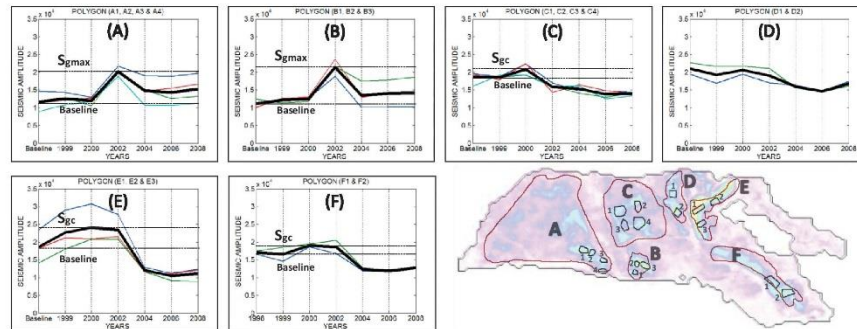


Figure 3 Quantitative representation of sub-regions selected from the six regions (A to F) to show the occurrence of the maximum gas saturation and the critical gas saturation on the 4D seismic data.

Seismic estimation of gas saturations

By normalising time-lapse amplitudes (maxima) by the baseline amplitude A_{bl} , it is possible to relate seismic (ΔA) or impedance (ΔZ) measurements of critical gas saturation at location X to the maximum gas saturation at location Y in the following way

$$\frac{\left[\frac{\Delta A_{gc}(T)}{A_{bl}} \right]_X}{\left[\frac{\Delta A_{gmax}(T)}{A_{bl}} \right]_Y} \approx \frac{\Delta Z_{gc}}{\Delta Z_{gmax}} \quad (1)$$

The numerator in (1) is calculated for the years 1998 (baseline) and 2000 combination, and the denominator in (1) is calculated for the years 1998 (baseline) and 2002 combination. The numerator values for regions C, E and F are 0.12, 0.30 and 0.12 respectively, whilst the denominator values for regions A and B are 0.75 and 0.92 respectively. In order to evaluate possible errors in the resultant calculation, a lower limit is formed by taking the lowest numerator value and highest denominator value; and then for the upper limit, the highest numerator value and lowest denominator value. This yields a lower limit of 0.127, and upper limit of 0.399, with their mean being 0.213. These results are now interpolated back to the curves in Figure 4 to produce estimates of the possible critical gas saturations in the range 0.55 to 4% for our reservoir. The curves in Figure 4 have been generated using a range of maximum gas saturation values. As the value of the maximum gas saturation is not known, a range of likely values of 50% to 75% is used to generate the curves. These curves are closely spaced and indicate an insensitivity of our seismic metric to this saturation value due to the anticipated non-linear behaviour of gas saturation.

Discussion and conclusions

Estimates of critical gas saturation (S_{gc}) of a turbidite reservoir using 4D seismic data are determined to be in the range of 0.55% to 4.00%, and this is comparable with results from other studies in the literature (for example Kamath et al., 1995). After analysis, it is not found possible to quantify the maximum gas saturation using the 4D seismic alone, despite the multiple surveys, due to the insensitivity of the seismic to this magnitude of gas saturation (see Figure 4). As an addition, the effect of the residual gas saturation (S_{gr}) signal on our 4D seismic data is also found to be masked with pressure and water saturation effects as this occurs during water injection for pressure maintenance in the reservoir. Uncertainties in the saturation estimates may also arise due to lateral variations in net-to-gross in the selected areas, and imperfect cancellation of the reservoir thickness variations. The areas of high quality reservoir that were chosen for the regions gave a very good gas response on the seismic. The identification of critical and maximum gas saturation on the 4D seismic data is key to this technique.

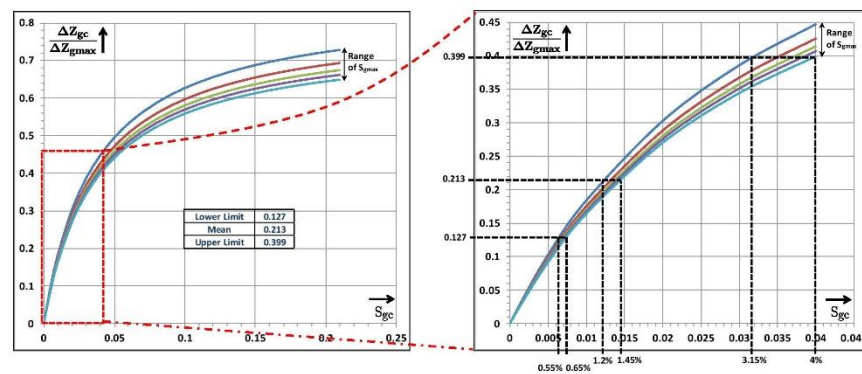


Figure 4 Plot of seismic amplitudes ratios versus critical gas saturation for a range of maximum gas saturation. The plot is further zoomed out to the area of interest so as to estimate the critical gas saturation value.

Acknowledgements

We thank the sponsors of the Edinburgh Time-Lapse Project (BG, BP, CGG, Chevron, ConocoPhillips, ENI, ExxonMobil, Hess, Ikon Science, Landmark, Maersk, Nexen, Norsar, Petro, Petrobras, RSI, Shell, Statoil, Suncor, Taqa, TGS and Total) for supporting this research. Also, special thanks to BP for providing the data set.

References

- Dake L. P., 2002. Fundamental of Reservoir Engineering, Nineteenth impression, Elsevier Science B. V., Amsterdam, The Netherlands.
- Di Piero E., Stephen K., McDougall S. and Pickup G., 2003. Sensitivity Analysis on the Two-Phase Flow Properties in a Turbidite Reservoir. SPE81020, SPE Latin and American and Caribbean Petroleum Engineering Conference held in Port-of-Spain, Trinidad, West Indies, 27 -30 April 2003.
- Falahat, R., Shams, A. and MacBeth, C., 2013. An interpretation of the 4D seismic response to gas exsolution and dissolution. 75th EAGE Conference & Exhibition incorporating SPE EUROPEC 2013, London
- Han D., and Batzle M., 2000. Velocity, Density and Modulus of Hydrocarbon Fluids – Empirical Modeling, SEG 2000 Expanded Abstracts.
- Kamath J. and Boyer, R., 1995. Critical gas saturation and supersaturation in low permeability rocks. December 1995 SPE Formation Evaluation, 247-253.
- Martin K. and MacDonald C., 2010. Schiehallion Field: Applying a geobody modelling approach to piece together a complex turbidite reservoir. 7th European Production and Development Conference, Aberdeen, UK.

QUANTITATIVE ANALYSIS OF GAS VOLUMES USING MULTIPLE 4D SEISMIC SURVEYS AND MATERIAL BALANCE

D. Obidegwu¹, C. MacBeth²

¹ Heriot-Watt Institute of Pet. Engr., Edinburgh, PhD Student, Dennis.Obidegwu@pet.hw.ac.uk

² Heriot-Watt Institute of Pet. Engineering, Edinburgh, Professor, Colin.MacBeth@pet.hw.ac.uk

Summary. Multiple time-lapse seismic surveys offer the opportunity to quantitatively analyse the changing fluid and rock properties in the reservoir over time. Combining this analysis with conservation of mass in the reservoir through material balance equations provide a gateway to estimating gas volumes in the reservoir. For reservoirs close to bubble point pressure, further pressure decrease leads to gas out of solution which reduces the solution gas oil ratio. Therefore, knowledge of the solution gas oil ratio is very important in order to understand the state of the reservoir. The determination of the solution gas oil ratio is explored through the use of the multiple 4D seismic surveys and material balance, the advantage being the determination of in situ values, as opposed to laboratory experiment values.

Key words. Quantitative 4D seismic interpretation, Material balance, Solution gas-oil ratio, Gas exsolution, Gas dissolution

INTRODUCTION

The reservoir pore pressure in oil reservoirs currently on production can typically vary by several megapascals, and often by much more in the neighbourhood of the producing or injecting wells. It is not generally in the best interests of operators to allow this to happen, however if reservoir connectivity is poor or not fully understood, injectors or active aquifers cannot adequately support the pressure drops that may occur in certain areas of the field. If pore pressure falls below the bubble point of the oil in an initially undersaturated reservoir, then gas exsolution occurs (Dake 2002), and gas migrates upwards to the top of the reservoir to form secondary gas caps or is produced. If the reservoir is initially saturated (initial pressure \leq bubble point pressure) then gas exsolution occurs immediately and may supplement pre-existing primary gas caps. The exact volume of gas liberated into the reservoir formation is a function of the initial oil in place, oil type, rock properties and the overall pressure drop, while the exact quantity of gas dissolving back into the oil depends on many factors, including the reservoir properties, gas mobility, fluid type, well pressure behaviour, and the PVT properties. The seismic response to liberated or dissolved gas is expected to be dramatic, as it is well recognised that laboratory experiments indicate that the presence of gas should lead to a strong, non-linear reduction in seismic velocity (Domenico 1974) and impedance. Thus, it is also our expectation that the 4D seismic response should have a strong sensitivity to gas, generally outweighing the contributions from rock stress sensitivity and water saturation. As a consequence, it is possible to focus almost entirely on the response due to gas out of solution and, perhaps, dissolution. In continuation of the work of Falahat et al (2012) where he showed how reservoir-scale gas volumes can be obtained using 4D seismic, we extend this study by combining 4D seismic with a material balance approach to analyse solution gas oil ratio values.

4D SEISMIC DATA INTERPRETATION

The observed data is from a UKCS field that comprises of turbidite sands containing multiple stacked reservoirs which are compartmentalized. It has an aquifer and the reservoirs which are typically 30m thick or less are thought to be fully oil filled. The depletion mechanisms are solution gas drive and water drive, and the field is close to its bubble point pressure. Production activities as well as insufficient pressure support in its early years have led to gas exsolution. The baseline seismic for the field was acquired preproduction (1996), and six monitors – 1999, 2000, 2002, 2004, 2006 and 2008 (Martin and MacDonald 2010) are analyzed in this paper.

5th International Geosciences Student Conference

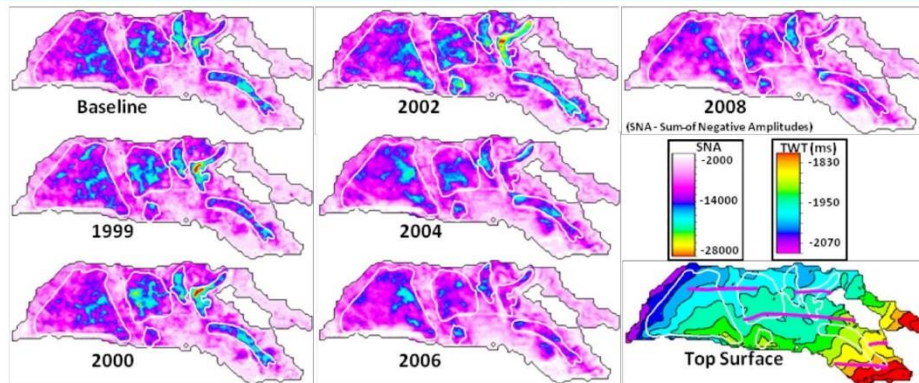


Fig. 1. Amplitude maps from individual seismic surveys. The attribute used is the sum of negative amplitudes (SNA) over the reservoir interval. Also shown is a contour map indicating the time structure of the reservoir horizon.

Six main regions (A to F) are identified on the maps in Fig.1 and 2, selected based on their general seismic character and known geology. A progressive brightening of a sand body identifies a reservoir softening or impedance decrease, whilst a dimming indicates a reservoir hardening or impedance increase. By year 2000, pressure is known to have dropped by 900psi in the vicinity of the production wells. Thus, gas is expected to be liberated during the first three monitor surveys in years 1999, 2000 and 2002, hence decreasing the solution gas-oil ratio. This is obvious as a general brightening of the individual reservoirs sands. After year 2002, pressure increases again and gas dissolution occurs due to an increase in water saturation (from below) from existing and new injectors, hence potentially increasing the solution gas-oil ratio. This is again generally evident as a dimming of the mapped sand bodies.

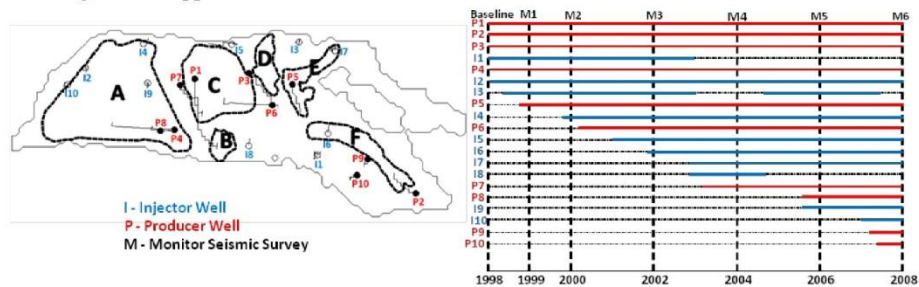


Fig. 2. Reservoir outline showing the six selected regions A- F highlighting the position of the injector wells and producer wells. Also shown is the sequence at which the wells are put on production/injection and shut-in, relative to the timing of the seismic baseline and monitor surveys. The red lines represent producer wells, while the blue lines represent injector wells.

QUANTITATIVE ANALYSIS OF GAS VOLUMES

In order to investigate the sequence of gas exsolution and dissolution in our field sector, we analyse the seismic data by following the work of Falahat et al. (2012), who proposed a linear relationship between the change in free gas volume ΔV_g and the 2D integral of the mapped time-lapsed amplitude change ΔA

$$\Delta V_g = \beta \iint_{\Sigma} \Delta A dx dy \tag{1}$$

5th International Geosciences Student Conference

where β is a seismic-to-well production/injection calibration factor to be determined. For the purposes of our work, the time-lapsed quantities are taken between the baseline survey and each monitor. Thus, as there is no gas at the time of the baseline survey, ΔV_g represents the volume at the time of the monitor. This equation assumes that changes in water saturation do not affect ΔA – clearly this may be a suitable approximation during the exsolution stage, but may not be completely appropriate in some regions of the sector experiencing dissolution for which the injected water clearly has a strong influence. The integral is performed over the area Σ formed by a composite of areas C, D, E and F in Fig. 2, which is known to be hydraulically isolated. There is an exsolution stage from the start of production in 1998 until 2001, and a dissolution stage from 2001 to 2008. The behaviour thus forms a natural two-stage division for the analysis. Consider first the application of (1) to the period between the pre-production baseline and the 2000 monitor surveys during the primary exsolution stage. The left-hand side of (1) can be expanded according to the well-known material balance equation (Dake 2002) focussed only on the gas component

$$[V_o R_{sb} - (V_o - V_{op})R_{sm} - V_{gp}]B_{gm} = \beta \iint_{\Sigma} \Delta A dx dy \quad (2)$$

In (2), R_{sb} and R_{sm} are the pre-production (at the baseline time) and current (at the monitor time) solution gas-oil ratios respectively. The solution gas-oil ratio quantifies the total amount of gas dissolved in the oil. For the purposes of our calculations these R_s values represent a reservoir average for areas C, D, E and F. R_s is a linear function of pressure for pressures below the bubble point (Fig.3(a)). Thus, $V_o R_{sb}$ gives the total amount of gas dissolved in the oil at the pre-production stage, which could potentially be liberated upon production of the initial oil volume V_o . Similarly, $(V_o - V_{op})R_{sm}$ is the amount of gas in the oil remaining in the reservoir at the monitor time, while V_{gp} is the gas volume produced. R_{sm} is always less than R_{sb} , as there is less gas dissolved in the reservoir oil at the monitor time because the free gas is either produced or remains trapped within the reservoir. The final parameter in this calculation is B_{gm} , the gas formation volume factor, which converts all of the gas volumes calculated under stock tank barrel conditions to their equivalent reservoir volumes. The 4D seismic signature in the integrand of (2) is the difference in the mapped sum of negative amplitudes evaluated between the monitor and baseline surveys.

For our field case, the pressure dependences of R_s and B_g are obtained directly from the PVT tables determined from the laboratory measurements, that have been calibrated for the reservoir and used in the full field flow simulator by the operator. Calculation from the simulator shows that R_s is expected to reduce from a pre-production of 354 scf/stb to 322 scf/stb after the reservoir pressure drop from 2850 psi (in 1998) to 2760 psi (in 2008). Applying (2) to our observations, we identify two relatively known quantities – the initial oil volume (extracted from the simulation model), and $R_s = R_{sb}$ prior to production and $R_s = R_{sm1}$ for the first monitor (taken from the PVT tables for the field oil and assuming a mean pressure for our sector). There are two relatively unknown quantities, the seismic calibration factor β , and R_s at each of the subsequent monitor times. By applying (2) to the baseline 1996 seismic data together with the monitors at 1999 and 2000 (for which gas continues to come out of solution), we have two equations and can solve to obtain: $\beta = 0.029$ and R_s for the first monitor. By applying a similar reasoning to the pre-production and subsequent monitor surveys 2002, 2004, 2006 and 2008 acquired during the gas dissolution stage, equation (2) must be adapted slightly as R'_{sm} now replaces R_{sm} , where $R'_{sm} > R_{sm}$ because the volume of gas available to go back into solution is smaller than the original as it has been produced or trapped in local highs, structure or by low NTG regions. Thus after dissolution the oil is not now fully saturated by gas. The gas at critical gas saturation immediately goes back into the oil upon pressure increase, but the gas-oil contact remains in a continual state of dissolution. In (2), only R'_{sm} is now unknown, as β has been determined from the gas exsolution stage, and it can therefore be calculated for each of the four remaining monitor surveys.

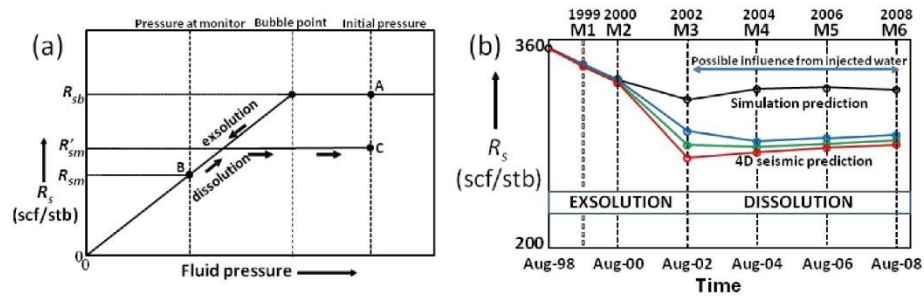
5th International Geosciences Student Conference

Fig. 3. (a) Schematic illustration of the pressure dependence of the solution gas-oil ratio, R_s for a black oil such as that in this study. The ratio decreases as pressure drops below bubble point until the monitor state is reached at point B. Re-pressurisation increases R_s again, but as less gas is available to dissolve in the gas the R_s behaviour reaches a plateau at a lower constant value and point C is reached (b) R_s values predicted for our study area from fluid-flow simulation (black lines and circles) versus the variation estimated from the 4D seismic data for low (red), medium (green) and high (blue) cases.

DISCUSSION AND CONCLUSIONS

The seismic estimates of R_s versus the predictions from the simulation model are shown in Fig. 3(b). For reference, results are also given for a 10% variation in the oil volume showing a high and low estimate of the R_s values. Fluid flow simulation predicts that R_s in the reservoir decreases from an initial (and known) value of 352 scf/bbl to 315 scf/bbl in 2002 due to the pressure drop, before rising slightly to 322 scf/bbl in 2008. This equates to approximately 4.5% of free gas under reservoir conditions. The seismic R_s estimates also show this dip followed by an increase, but the R_s values are slightly lower than those predicted from the simulator (a minimum of 268 scf/bbl). The low values of R_s above suggest more free gas being produced in the reservoir, but a more likely cause is bias due to the masking effect of injected water in the lower part of the reservoir during the dissolution phase. However, it has not been possible to quantify this phenomenon or draw further conclusions using the 4D seismic data.

ACKNOWLEDGEMENTS

We thank the sponsors of the Edinburgh Time-Lapse Project (BG, BP, CGG, Chevron, ConocoPhillips, ENI, ExxonMobil, Hess, Ikon Science, Landmark, Maersk, Nexen, Norsar, Petoro, Petrobras, RSI, Shell, Statoil, Suncor, Taqa, TGS and Total) for supporting this research. Also, special thanks to BP for providing the data set.

REFERENCES

- DAKE L. P., 2002. *Fundamental of Reservoir Engineering*, Nineteenth impression, Elsevier Science B. V., Amsterdam, The Netherlands.
- DOMENICO, S. N., 1974. Effect of water saturation on seismic reflectivity of sand reservoirs encased in shale, *Geophysics*, 39, 759 - 769.
- FALAHAT, R., 2012. *Quantitative monitoring of gas injection, exsolution and dissolution using 4D seismic*. PhD thesis, Heriot-Watt University.
- MARTIN K., MACDONALD C., 2010. Schiehallion Field: Applying a Geobody Modelling Approach to Piece Together a Complex Turbidite Reservoir, 7th European Production & Development Conference, Aberdeen, UK.

Downloaded from <http://pg.lyellcollection.org/> at Heriot-Watt University on September 7, 2014

Petroleum Geoscience

The interpretation of amplitude changes in 4D seismic data arising from gas exsolution and dissolution

Reza Falahat, Dennis Obidegwu, Asghar Shams and Colin MacBeth

Petroleum Geoscience 2014, v.20; p303-320.
doi: 10.1144/petgeo2014-008

Email alerting service	click here to receive free e-mail alerts when new articles cite this article
Permission request	click here to seek permission to re-use all or part of this article
Subscribe	click here to subscribe to Petroleum Geoscience or the Lyell Collection

Notes

© The Geological Society of London 2014



The interpretation of amplitude changes in 4D seismic data arising from gas exsolution and dissolution

Reza Falahat^{1,2}, Dennis Obidegwu¹, Asghar Shams¹ and Colin MacBeth^{1*}

¹*Institute of Petroleum Engineering, Heriot-Watt University, Edinburgh EH14 4AS, UK*

²*Present address: ERC Equipoise, 2 Cherry Orchard Road, Croydon CR0 6BA, London, UK*

**Corresponding author (e-mail: colin.macbeth@pet.hw.ac.uk)*

ABSTRACT: This study examines the four-dimensional (4D) seismic signatures from multiple seismic surveys shot during gas exsolution and dissolution in a producing hydrocarbon reservoir, and focuses in particular on what reservoir information may be extracted from their analysis. To aid in this process, hydrocarbon gas properties and behaviour are studied, and their relationship to the fluid-flow physics is understood using numerical simulation. This knowledge is then applied to interpret the seismic response of a turbidite field in the UK Continental Shelf (UKCS). It is concluded that for a repeat seismic survey shot 6 months or more after a pressure change above or below bubble point (as in our field case), the gas-saturation distribution during either exsolution or dissolution exists in two fixed saturation conditions defined by the critical and the maximum possible gas saturation. Awareness of this condition facilitates an interpretation of the data from our field example, which has surveys repeated at intervals of 12–24 months, to obtain an estimate of the critical gas saturation of between 0.6 and 4.0%. These low values are consistent with a range of measurements from laboratory and numerical studies in the open literature. Our critical gas-saturation estimate is also in qualitative agreement with the solution gas–oil ratios estimated in a material balance exercise using our data. It is not found possible to quantify the maximum gas saturation using the 4D seismic data alone, despite the advantage of having multiple surveys, owing to the insensitivity of the seismic amplitudes to the magnitude of this gas saturation. Assessment of the residual gas saturation left behind after secondary gas-cap contraction during the dissolution phase suggests that small values of less than a few per cent may be appropriate. The results are masked to some extent by an underlying water flood. It is believed that the methodology and approach used in this study may be readily generalized to other moderate- to high-permeability oil reservoirs, and used as input in simulation model updating.

INTRODUCTION

In oil reservoirs currently in production, reservoir pore pressure can typically vary by several megapascals (MPa), and often by much more in the neighbourhood of the producing or injecting wells. It is not generally in the best interests of operators to allow this to happen; however, if reservoir connectivity is poor or not fully understood, injectors or active aquifers cannot adequately support the pressure drops that may occur in certain areas of the field. If pore pressure falls below the bubble point of the oil in an initially undersaturated reservoir, then gas exsolution occurs (Dake 2002) and gas migrates upwards to the top of the reservoir to form secondary gas caps or is produced. If the reservoir is initially saturated (initial pressure \leq bubble point pressure), then gas exsolution occurs immediately and may supplement pre-existing primary gas caps. This exsolution phenomenon can occur for most hydrocarbon oils but is significant for medium–light oils (medium oils are defined as having an API of between 22 and 31, light oils as between 31 and 42). For certain specific reservoirs, the drive from the gas cap that forms from this process can assist production.

Generally, gas arrives at production wells faster than oil owing to the higher gas mobility, and subsequently forms a cone-shaped accumulation around the well. Eventually, the relative permeability of the oil through the three-phase fluid mix decreases as the gas saturation increases, and this in turn lowers the oil production rate. Indeed, for oil reservoirs in which gas cap drive is not significant, gas exsolution is economically undesirable and can also lead to the practical issues of handling gas during production. Pressure drop and gas liberation are typically controlled by the injection plan, and the normal way of stopping gas from breaking out is by increasing pore pressure by injecting water. In this process, in agreement with the physics observed in the laboratory (e.g. Danesh 1998), liberated gas is encouraged to go back into solution, in principle reversing the exsolution behaviour at the expense of additional water saturation. To demonstrate what can be observed for this sequence of events in four-dimensional (4D) seismic data, Figure 1 shows root mean square (RMS) amplitude maps for a baseline and two subsequent monitor surveys in the Foinaven field (Marsh *et al.* 2001; Bagley *et al.* 2004). This reveals a brightening due to gas exsolution at the time of the first

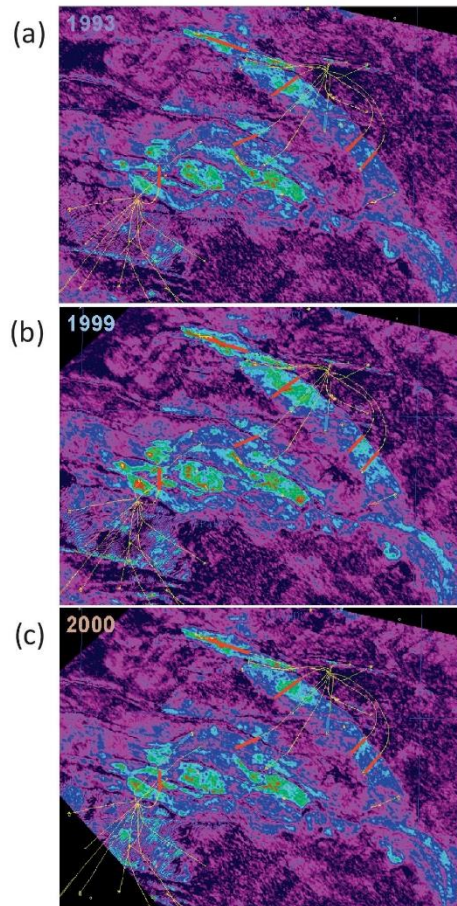


Fig. 1. A 4D seismic data example of gas exsolution and dissolution from the Foinaven field, UKCS. Amplitude maps are generated for the 1993 baseline survey prior to production (a), then again in 1999 following gas exsolution after one year of production (b), and finally in 2000 after dissolution due to repressurization from water injectors, gas migration and production (c). The mapped anomalies visibly expand due to the liberated gas, then contract upon pressure increase. After Marsh *et al.* 2001.

monitor survey after 1 year of production, followed by a dimming due to dissolution and water-flooding at the time of the second monitor survey after another year of water injection and production. In this particular UKCS reservoir, knowledge of the gas distribution using 4D seismic data and knowledge of its causative mechanisms contributed significantly to the understanding of reservoir connectivity, and, hence, field management.

There are several publications in which the 4D seismic response of liberated gas has been noted, both for clastic (e.g. Johnston *et al.* 2000, and Alsos *et al.* 2009) and for carbonate (e.g. van Gestel *et al.* 2011) fields, although typically these

observations form part of a broader case study and do not focus specifically on the gas-exsolution mechanisms. Reports of gas dissolution, however, are less frequent and limited to a few select publications (Marsh *et al.* 2001, 2003; Gainski *et al.* 2010). Recently, 4D seismic detection of gas exsolution has also been demonstrated as a tool for indirectly assessing pressure connectivity (Mitchell *et al.* 2009, Johnston 2013), and injected gas has been utilized to illuminate complicated top reservoir structure (Roy *et al.* 2011).

The seismic response to liberated or dissolved gas is expected to be substantial, as it is well recognized that laboratory experiments indicate that the presence of gas should lead to a strong, non-linear reduction in seismic velocity (Domenico 1974) and impedance. Thus, for example, in reservoirs characterized by a high to low impedance contrast between the overburden and the top of the reservoir unit, very visible bright amplitudes on the 3D seismic profiles are associated with the presence of gas, typifying the classic Gulf of Mexico bright spots widely observed in seismic exploration (e.g. Johnston 2010). Thus, it is also our expectation that the 4D seismic response should have a strong sensitivity to gas, generally outweighing the contributions from rock-stress sensitivity and water saturation. As a consequence, it is possible to focus almost entirely on the response due to gas out of solution and, perhaps, dissolution. The ability to use 4D seismic data to directly access gas distributions in this way is an important observation, as it is known from fluid-flow simulation studies that gas exsolution and dissolution are controlled by many reservoir-dependent rock and fluid properties – the numerical values of which remain largely uncertain and require constraint. These factors relate mainly to the vertical and horizontal reservoir connectivity, and also, at the pore scale, to the relative permeability behaviour. Thus, the exact volume of gas liberated during exsolution, dissolved during dissolution, and the behaviour of the gas migration in the reservoir is typically uncertain (Danesh 1998). To address this, the current study assesses whether monitoring of gas-saturation distributions with 4D seismic data could supplement well data when evaluating fluid behaviour in simulation studies and understanding the key reservoir controls. Specifically, the quantitative link between 4D seismic amplitudes, and the gas exsolution and dissolution is investigated. This requires knowledge of how gas is distributed and saturates the rocks within the reservoir, and the impact of varying gas saturation on the seismic amplitudes. The context for our study is set by a UKCS dataset, in which six monitor surveys have been shot at intervals of 12–24 months.

THE RESERVOIR MECHANISMS

Here, the physics of gas exsolution and dissolution in the reservoir is discussed in more depth, and the uncertainties in these processes are highlighted. As we shall see, these in turn lay down the challenges for 4D seismic data analysis.

Gas exsolution

This mechanism can be explained using a fluid-phase diagram such as that in Figure 2, calculated from state equations and the composition of the reservoir fluid determined from the laboratory. This phase envelope describes the various expected hydrocarbon fluid states at each pressure and temperature, and represents a composite physical behaviour of the many hydrocarbon constituents that make up the oil in the reservoir. At pressures above the bubble point, the hydrocarbon is a liquid, whilst, below the dew point pressure, it is a gas. Gas and liquid co-exist in the region between these two points but the exact proportion of the liquid to gas varies with pressure and

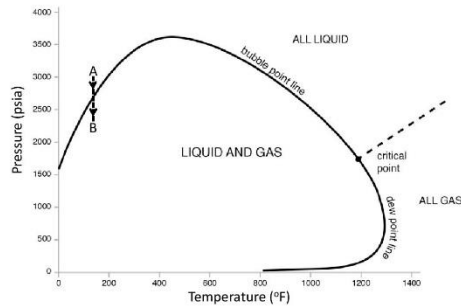


Fig. 2 Pressure-temperature phase envelope similar to that for our case study based on measured oil compositional data (BP pers. comm.). The initial reservoir pressure is 2900 psi (19.99 MPa) and the temperature is 120°F (48.89°C), and so the oil is already very close to bubble point.

temperature. Decreasing pressure from an initial condition just above the bubble point at a fixed temperature moves the fluid conditions along a vertical line A–B drawn in Figure 2. As the bubble point is reached, the lightest hydrocarbon molecules (usually methane – C1) leave the liquid oil to form gas bubbles and then, as the total fluid expands more, the liquid is vaporized. As pressure decreases below bubble point, the gas saturation builds progressively as gas bubbles are first nucleated, and then coalesce or grow more by the diffusion of additional free gas. Heavier gas components are also released at this stage. When a significant number of bubbles are liberated, and have grown in size, the fluid system reaches a critical gas saturation (S_{gc}) for which the gas becomes mobile. The value of S_{gc} is usually defined as the point at which the gas first becomes mobile. However, importantly, gas bubbles in the oil that are saturated below this critical saturation still remain in the oil. The mobilized gas migrates upwards and also towards the wellbore due to the actions of the gravitational force and well pressure gradients, collecting in local highs or structural traps to form gas caps in the reservoir or being produced (Fig. 3). Depending on the reservoir connectivity and injection–production scenario, this overall process can occur quickly in a few months or less (this is observed in simulation model studies of North Sea clastic reservoirs: e.g. Falahat 2012). In practice, trapped gas can still remain in the reservoir oil due to geological heterogeneity such as low net to gross or small-scale structure – this particular gas saturation is highly reservoir dependent and is not considered in our current study. The exact volume of gas liberated into the reservoir formation is a function of the initial oil in place, oil type, rock properties and the overall pressure drop. The gas saturation in the secondary gas cap is $S_{gmax} = 1 - S_{wc} - S_{org}$, where S_{wc} is the initial (connate) water saturation and S_{org} is the residual oil left behind after displacement by the expanding gas cap (the controls on these values are described later). The various pore-scale saturation regimes generated by the process of gas exsolution described above are illustrated in Figure 4.

Gas dissolution

From Figure 2, the effect of a pore-pressure increase may be construed as a reversal of the gas-exsolution mechanism along the vertical trajectory and, in the ideal case (a closed container), gas does indeed dissolve back into solution. However, once the pore pressure has built up over the entire volume in the reservoir (pressure spreads quickly to equilibrate in hours/days), the

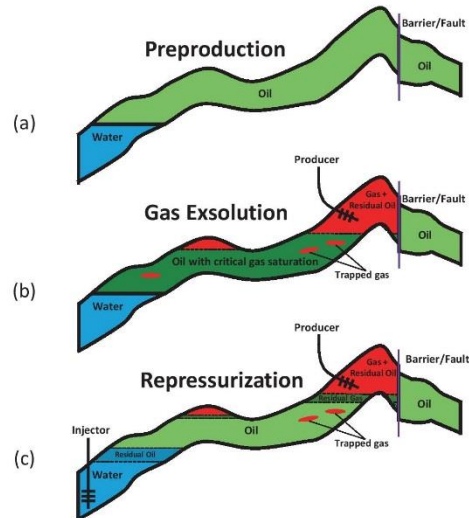


Fig. 3 Schematic illustrating the three main stages of gas exsolution and dissolution (repressurization) that are being examined in this paper, and their consequent effect on the reservoir saturation conditions.

(a) Initial preproduction state: live oil and no free gas; (b) after gas exsolution and mobilization of the free gas (note the trapped gas under low NTG pockets or structure); (c) oil production, repressurization by water injection and gas-cap shrinkage due to production. In this latter case, it is highly likely that the residual gas may be reduced to zero by the repressurization.

gas at and above (several cells or a few metres) the gas–oil contact tends to dissolve rapidly. Our simulation studies indicate that gas remaining in the oil leg at the critical gas saturation dissolves in only a few days in response to the pressure increase. In addition, the injected water physically displaces gas from around the injection well (gravity effect permitting); however, as gas close to the injection well dissolves in the oil before the arrival of the water (due to the pressure effect), there is generally no residual gas in the area flooded by water. During this period, the gas–oil and oil–water contacts may also move upwards due to gas production or water injection, respectively. As the volume of oil remaining in the gas cap (S_{org}) and the residual in local traps ($S_{trapped}$) is insufficient to dissolve all of the gas present, this volume remains largely in place. However, a proportion of the gas migrates from its original position owing to the new pressure gradients established by the injection. Thus, it is expected that a volume of free gas still remains present in the reservoir despite the pore pressure arriving back at the initial bubble point pressure. The exact quantity of gas dissolving back into the oil depends on many factors, including the reservoir properties, gas mobility, fluid type, well-pressure behaviour, and the pressure–volume–temperature (*PVT*) properties (i.e. the exact shape of the phase envelope in Fig. 2). For example, for light oils, a higher volume of the gas is liberated by pressure drop, but a smaller volume of the gas can be dissolved by pressure build-up (MacCain 1990). Conversely, for heavier oils, a smaller volume of gas is liberated by pressure drop, and a higher volume of this gas is dissolved by pressure build-up. Given the uncertainty on the factors controlling the amount of gas that suc-

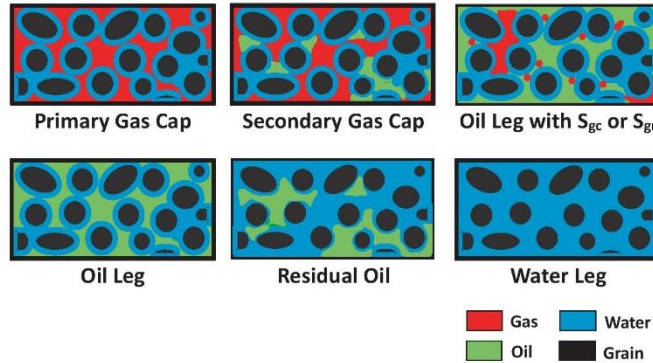


Fig. 4. A pore-scale description of the six saturation states relevant to the calculation of the seismic response from the exsolution and dissolution scenarios in Figure 3. S_{gr} refers to the residual gas saturation after gas-cap contraction and S_{gc} to the critical gas saturation.

cessfully dissolves back into the oil, this remains an important unknown to be determined in reservoir studies.

Calibration of saturation distributions using numerical simulation

To understand how the various gas saturations detailed in the previous subsection might distribute in the reservoir and the particular timescales involved, fluid-flow simulations are performed for a homogenous and heterogeneous reservoir model, with rock and fluid properties and relative permeability curves based on a full-field simulation model from a producing UKCS turbidite reservoir. Both models are built with a cell size of $20 \times 20 \times 0.2$ m – a finer horizontal and vertical dimension than is normal for simulation model studies by a factor of 4 horizontally and 10 vertically. This particular cell size is selected to compute a physically realistic gas distribution within a reasonable computational run time. The properties of the two models used are given in Table 1. The homogeneous model has a critical gas saturation of 3.5%, maximum gas saturation of 67%, and residual oil saturation to gas displacement of 11%. The heterogeneous model is built to provide similar characteristics to the field data we will analyse in the next section. Thus, net-to-gross (NTG), permeability and porosity distributions are assigned to geostatistically resemble the field model values. For simulation purposes, a single well produces for 2 years before being shut down. A second well injects water for a further 2 years beyond the time at which the producer shuts down. During the production period, pore pressure drops to around 1000 psi (6.89 MPa), whilst, during the injection stage, pressure builds back up to the initial value of 2900 psi (19.99 MPa).

Figure 5(a) and (b) shows the histograms recording the evolution of the gas saturations in the reservoir with time. These document a 2 year period of production followed by a pressure increase via water injection recovery, and hence evolution through the exsolution and dissolution stages. It is observed from these simulation studies that the gas saturation appears to settle down into a bimodal distribution after significant gas mobilization has occurred, with only a smaller amount of gas in the range of intermediate values. It should be noted that the tendency towards this bimodal condition can be seen even at an early stage of the flow simulation. The conclusion is that for gas exsolution, the gas saturation in the reservoir is fixed mainly at the critical gas saturation (S_{gc}) everywhere within the oil leg or lies at a maximum (S_{gmax}) within the gas cap. Indeed, the two peaks do correspond quite closely to the critical gas saturation and the

Table 1. Rock and fluid properties for the two idealized reservoir models used in this work to simulate gas exsolution and dissolution. For both models, the bubble point is 2900 psi (19.99 MPa), as is the case for the full-field model of our dataset

Property	Homogeneous model	Heterogeneous model
Model shape	Anisotropic anticline	Anisotropic anticline
Cell size (m)	$20 \times 20 \times 0.2$	$20 \times 20 \times 0.2$
Sand porosity (%)	30	29–31
Permeability (mD) ($\times 10^{-14} \text{m}^2$)	1000	200–1900
K_r/K_h	0.10	0.10
NTG	1	0.40 – 1
Critical gas saturation (S_{gc}) (%)	3.50	3.50
Connate water saturation (S_{wc}) (%)	22	22
Residual oil saturation in gas cap (S_{org}) (%)	11	11
Maximum gas saturation in gas cap ($S_{gmax} = 1 - S_{wc} - S_{org}$) (%)	67	67
Oil API	25	25

maximum gas saturation. This is consistent with our understanding that, owing to the large density difference between water and hydrocarbon gas, capillary pressure curves for our reservoir show a sharp behaviour in the transition zone (Morrow & Melrose 1991). Therefore the transition zone is abrupt and the vertical thickness over which gas-saturation variation occurs is typically less than a few metres, and may be neglected in our seismic analysis. During exsolution, the peak at the critical gas saturation is particularly strong, whilst, during dissolution, the maximum gas saturation becomes quickly dominant. Interestingly, as the rapid mobilization phase subsides (6 months for these models), the saturation peaks become more prominent, narrower and there are very few cells with an intermediate state of saturation. Simulations are also performed for a heterogeneous model with the same structure but variable porosity, permeability and net-to-gross (NTG) (see Table 1). The widths of the saturation peaks appear quite narrow (only a few per cent), even in the case of model heterogeneity (see Fig. 6a–d). Intermediate saturations are confined to lie within the thin (less than two cells thick) transition zone layer in the model, formed owing to capillary effects between the gas cap and the oil leg. There may also be small values of gas saturation corresponding to residual gas saturation from oil replacing gas. This behaviour is an important feature of reservoirs that have moderate–high vertical permeability.

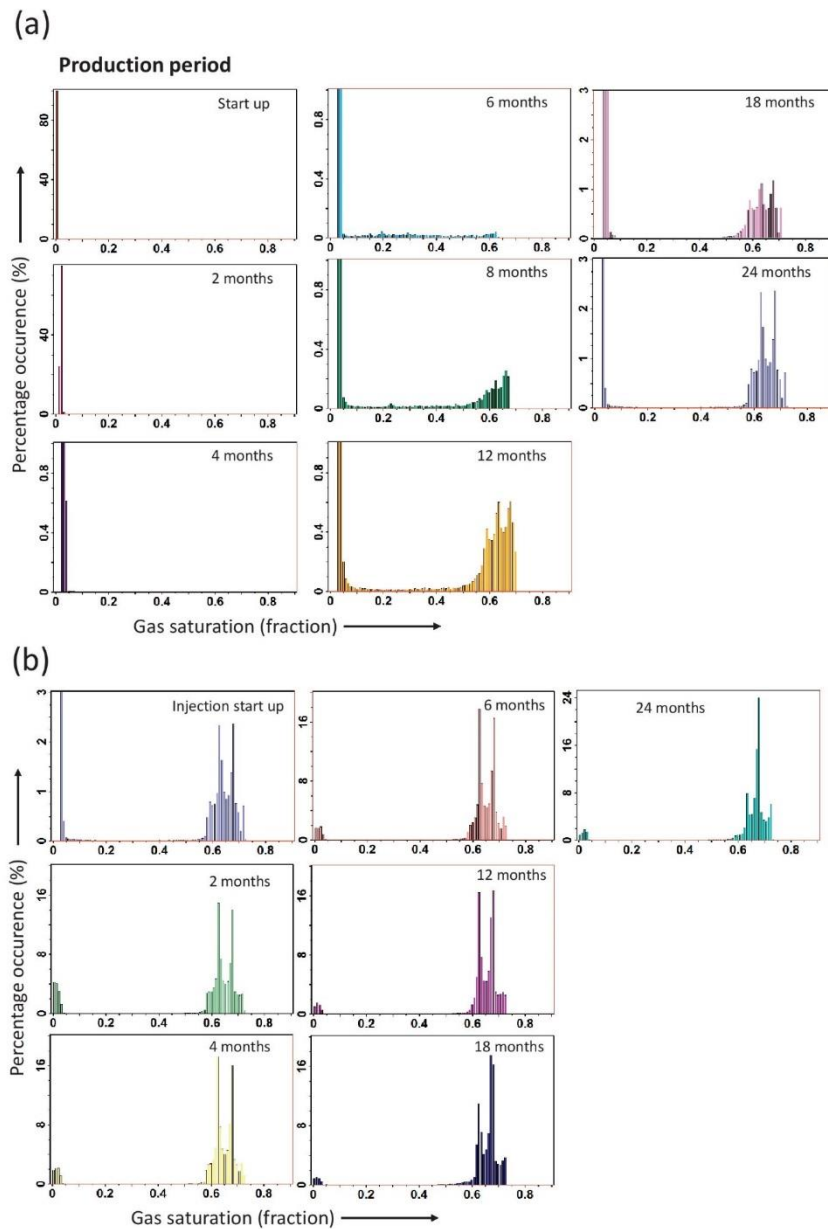


Fig. 5. (a) Gas-saturation histograms for the homogeneous simulation model detailed in Table 1 for the period of gas exsolution. (b) Gas-saturation histograms for the same model but over the period of subsequent dissolution. The vertical axis is the percentage of gas-filled cells with a particular saturation range. For (a), the high-magnitude (over 90%) critical gas-saturation peak is truncated in the plots so that the lower-magnitude maximum gas-saturation peak can be seen. The simulation model has a critical gas saturation of 3.5% and a maximum gas saturation of 67%, and a bimodal structure (two major modes or accumulations) can be clearly observed. Fine-scale variations inside the individual modes are not considered in our analysis.

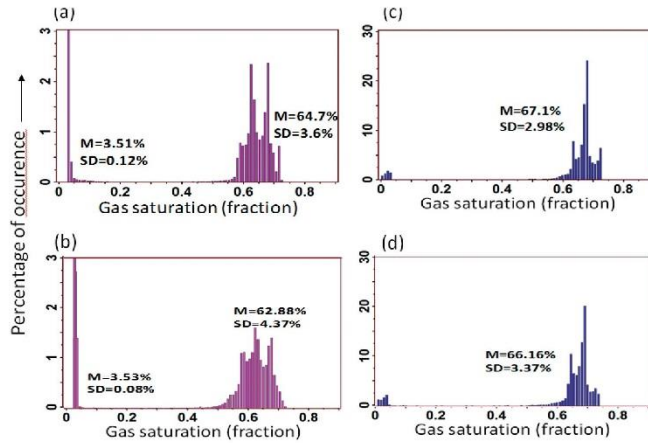


Fig. 6 Gas-saturation histograms for gas exsolution obtained after the bimodal behaviour has been attained at 24 months, for: (a) the homogeneous model; and (b) heterogeneous model defined in Table 1. In addition, gas-saturation histograms for gas dissolution, obtained after the critical gas saturation has dissipated, for: (c) the homogeneous model; and (d) heterogeneous model defined in Table 1. The percentage of occurrence refers only to the gas-filled cells in the simulation model. For exsolution, the low gas-saturation peak (at over 90%) is truncated to enable the higher maximum gas-saturation peak to be seen clearly. For dissolution, the low gas-saturation peak is now smaller than the higher maximum gas-saturation peak. Model heterogeneity does not impact the observed saturation distribution significantly. The mean (M) and standard deviation (SD) of each histogram are indicated for reference.

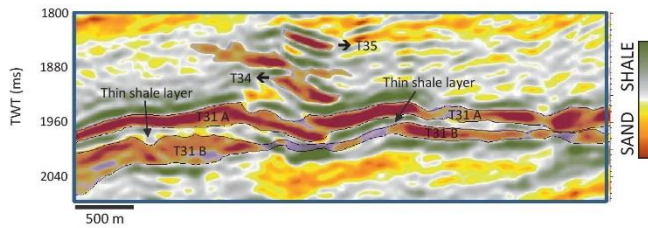


Fig. 7 Vertical section from the 1996 preproduction coloured inversion seismic data, showing the reservoir structure. Troughs in dark red represent the sand bodies, whilst peaks in grey represent the shales. The top and base of the sand layers are picked as zero crossings by the data provider (Amini 2014).

4D SEISMIC ANALYSES

Background to the field of study

The analysis of the previous section is now applied to observed data from a UKCS turbidite field (Martin & MacDonald 2010). In this field, the reservoir fluid is a black oil with an API gravity ranging from 22° to 28° (there is a variation with depth in the reservoir) at a temperature of 120 °F (48.89 °C). Initial reservoir pressure is approximately 2900 psi (19.99 MPa), whilst bubble point is 2850 psi (16.65 MPa) at the top reservoir level, and the solution gas–oil ratio (GOR) is a low 354 scf/bbl (62.99 sm³ m⁻³). In this particular field, there is known to be gas exsolution, gas mobilization, and then repressurization with subsequent dissolution. During the course of production, poor connectivity led to a lack of support from injectors. This combines with a weak aquifer influx to give a strong pressure decrease in some areas, and a drop below bubble point with the consequent liberation of free gas. The drilling plan adjusted for this phenomenon and recovered the pressure (Govan *et al.* 2005). There are multiple vintages of seismic shot across this field for reservoir management purposes, and, for our current work, the pre-production baseline in 1996 and six monitors shot in 1999, 2000, 2002, 2004, 2006 and 2008 are selected. These data have been cross-equalized by the operator for 4D seismic interpretation purposes, and have a non-repeatability normalized root mean square (NRMS) noise metric (Kragh & Christie 2002) of approximately 31%. The data have been transformed into relative impedance traces by coloured inversion (Lancaster & Whitcombe 2000). Importantly, the seismic data are repeated on a timescale shorter than most offshore 4D seismic projects, and

therefore offer a good opportunity to analyse the rapidly occurring phenomena under consideration. An isolated sector is identified for study that is segmented by two major east–west-trending normal faults. Figure 7 shows a vertical section from the baseline seismic survey. The reservoirs consist of multiple-stacked, interconnected and amalgamated discrete sand bodies. The sediment system is thus expected to be highly compartmentalized, with both vertical and lateral connectivity being a major reservoir management issue. The T31 producing interval is mapped for the purposes of our study as it is the main reservoir in which gas exsolution occurs in this area. This particular reservoir interval has a variable character ranging from thin interbedded sands and shale to massive sands. The T31 is divided into two units, T31a and T31b, separated by thin shale. There are sheet-like units in this sector, typically 10–20 m thick, that can be mapped on the seismic profile over a large proportion of the area (Martin & MacDonald 2010). As the seismic data have a wavelength of 140 m (20 Hz peak frequency for the seismic wavelet and a velocity of 2800 m s⁻¹), the reservoirs in this sector are generally below tuning thickness.

Description of gas exsolution and dissolution

For the purposes of our 4D seismic analysis, the ‘sum of negatives’ attribute is employed. This attribute sums all negative amplitudes over the T31 reservoir interval defined between the top T31a and base T31b. This is used as it has been demonstrated in past work to be sensitive to the reservoir conditions when the sands are known to be softer than the shales – giving a high to low seismic impedance contrast and a negative relative

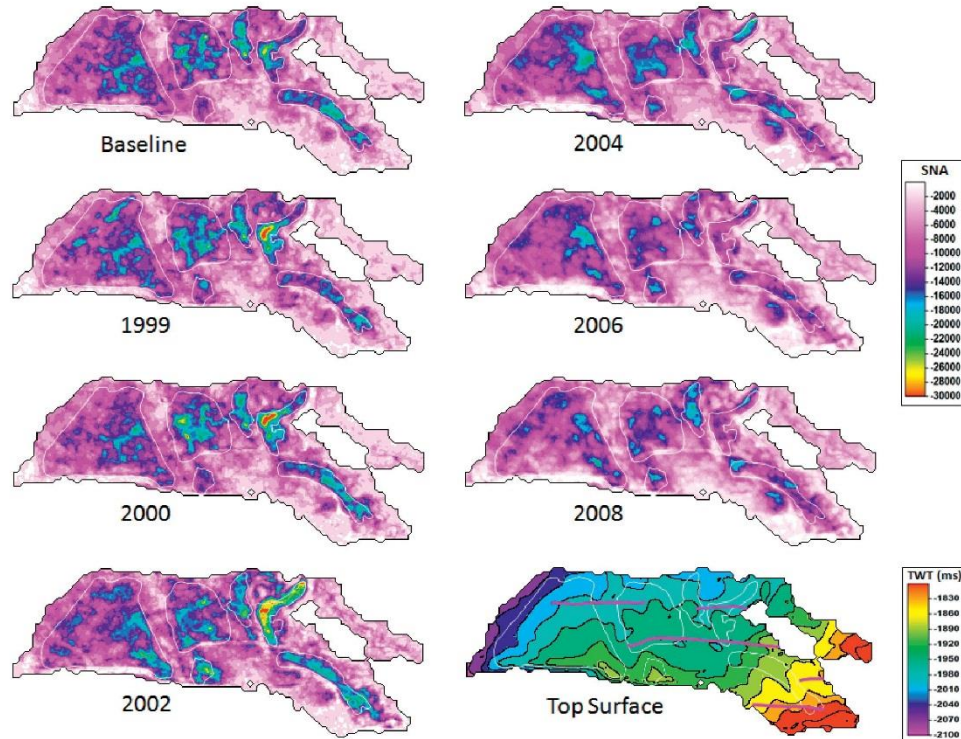


Fig. 8. Amplitude maps (using the sum of negative amplitudes attribute) for seismic surveys at times 1996 (production was in 1998), 1999, 2000, 2002, 2004, 2006, and 2008. Also shown is a contour map indicating the time structure of the top T31a reservoir horizon. The anomalies are related to gas or oil accumulations in the reservoir sand deposits.

impedance (Jack *et al.* 2010). Figure 8 shows the sequence of resultant attribute maps for each survey in our chosen segment. The maps have been cross-equalized such that difference in amplitudes across vintages can be interpreted for time-lapse effects. To achieve this, we take selected combinations of surveys initially cross-equalized by the contractor, and then further cross-equalize the mapped amplitudes between subsets by applying a single scalar evaluated from a region outside the reservoir. In these data, the existence of gas exsolution is inferred from the well production as a consequence of known pressure drops observed at the producers and excess gas production. (Note that gas is naturally liberated from live oil upon production at surface conditions. This observation refers to the gas produced over and above this process.) On each map, moderate- to high-amplitude anomalies indicate hydrocarbon-filled sand bodies with good-quality NTG. A progressive brightening of a sand body over time identifies a reservoir softening or impedance decrease (gas liberation or pore-pressure increase), whilst a dimming over time indicates a reservoir hardening or impedance increase (water saturation increase or pore-pressure decrease). By the time of the first monitor survey (1999), pressure is known to have dropped by 900psi (6.21 MPa) in the vicinity of the production wells. Thus, gas is expected to be liberated during the first three monitor surveys in 1999, 2000 and 2002. This is

evident as a general brightening of the individual reservoir sands near to producers (brightening close to injectors associated with a pore-pressure increase is not considered in our study). After 2002, pressure increases again due to existing and new injectors, and hence dissolution occurs. On the seismic data, these effects are masked by an increase in water saturation at the base of the reservoir interval. This is again generally evident as a dimming of the mapped sand bodies due to a gas-saturation decrease and increased water saturation, and water production at the producer wells. For reference, Figure 8 also shows a map of the top structure and identifies NW–SE as the up-dip direction, where secondary gas caps may be located. Overall, the seismic observations appear to show broad consistency with the phenomena of dissolution and gas production as described in the previous section. Interestingly, however, owing to the sequencing of producers and injectors (Fig. 9), different sand bodies deplete at different rates, and hence the brightening and dimming events in each are not quite synchronized in time. Here, it is recognized that the effects of gas in this interpretation may also, to some extent, be combined with rock-stress sensitivity and fluid-pressure effects, especially for the large pressure increases around the injectors. However, by confining our quantitative analysis below to brightening around the producers, we hope to limit this interference.

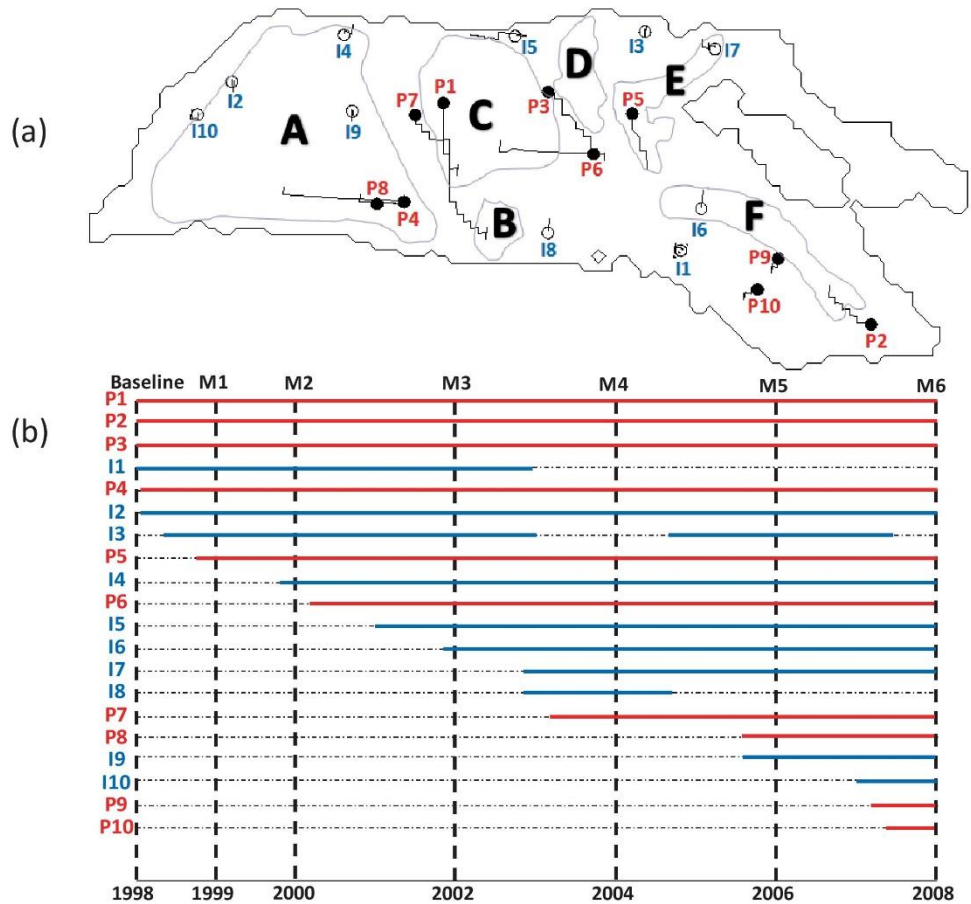


Fig. 9. (a) Labelling of main sand bodies used in our study relative to the producer and injector wells. (b) Timelines of activity for the wells in our chosen sector relative to our monitor seismic data (M1–M6) surveys. Well trajectories drawn are those that intersect the T31 regions of interest, with the exception of P7 which intersects the overlying T34 reservoir. In (a), solid circles correspond to the well TD.

Six main regions (A–F) are identified on the maps in Figure 9, selected based on their general seismic character and known geology. In region A, an initial injector–producer (I2–P4) pair is later supplemented by injector I4 to maintain pressure. Later, injectors I9 and I10 are activated to counteract the pressure decline due to producer P8. Exsolved gas is observed initially in 1999, and it quickly collects in a local high in the SE corner to form a secondary gas cap. Increased water saturation and dissolution reduce the amplitudes after 2000, although some gas remains. Region B sits on a local high into which exsolved gas collects. With no direct injector support initially, dissolution does not occur until 2003 when the nearby injector I8 becomes active. Region C is bounded along its south edge by a sealing fault (see the contour plot in Fig. 8). Critical gas saturation is evident as a consequence of production in P1 and P6, and there is an upward migration of the gas influenced by possible pressure gradients

from producer P1, which then traps at the fault due to buoyancy effects. Injector I5 is active after 2001 to supply pressure support. Region D is possibly connected with region C but it is not intersected by a producing well. Earlier amplitudes in this region are fairly constant – suggesting a lack of pressure connection. Water sweep from injector I3 and I5 may play a role in decreasing the amplitude after 2002. In region E, there is a strong initial brightening that continues until 2002 due to producer P5. In 2003, injector I7 is drilled towards the northern edge, which then dims the amplitudes in subsequent years. The final region for consideration is F, which dips upwards to the SE. The initial action of injector I1 dims the amplitudes in 1999 but pressure support is not sufficient and gas exsolution occurs in 2000 due to producer P2. After 2002, injector I6 replaces I1 close to the same location, and this provides the required pressure support.

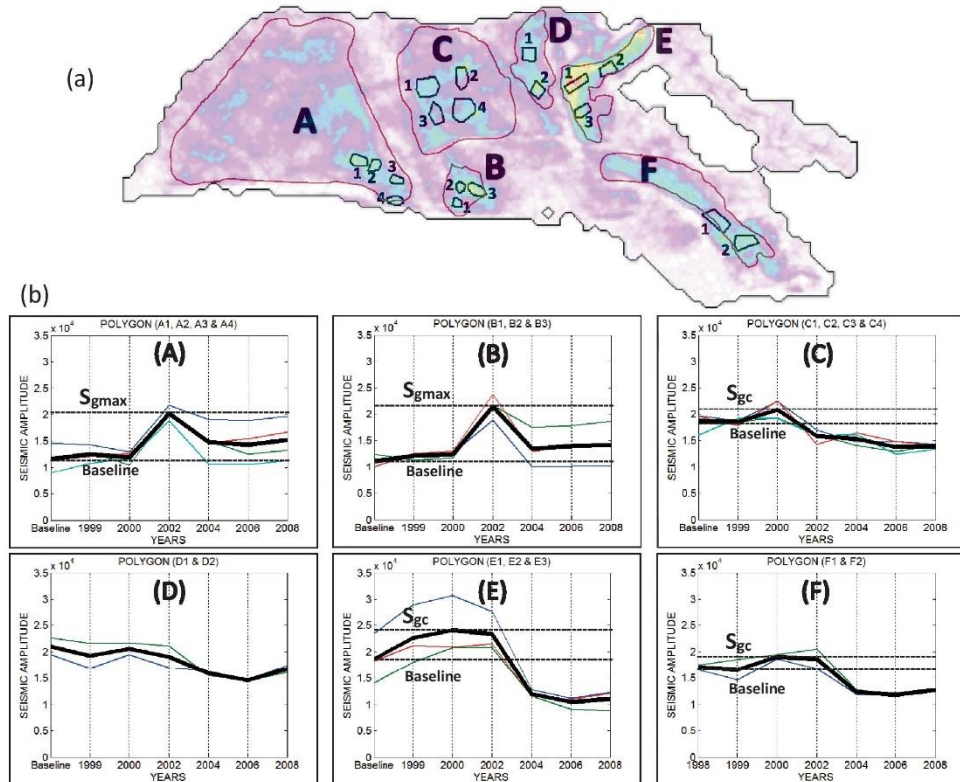


Fig. 10. (a) Subregions of our sand bodies used for the calculation of time-lapse amplitudes and gas-saturation analysis. (b) Seismic amplitude variations with survey time, together with inferred amplitude levels for maximum and critical gas saturations (dotted horizontal lines). Thin coloured lines correspond to the individual subregion results, whilst the solid black line is the average of these values.

Figure 10(a) indicates a number of small subregions within A–F that are chosen for our analysis. These are selected to be of known high NTG and signal quality, and are used to determine seismic amplitude levels associated with an oil sand in preproduction state, oil sand with critical gas saturation and the secondary gas cap. The ‘sum of negative amplitudes’ attribute for each subregion and their combined (arithmetic) average are plotted in Figure 10(b) against survey time. The amplitude level of the baseline (oil-filled sand) response and the maximum are determined for each. If the amplitude level after the maximum has been reached still remains above the initial baseline, then this is interpreted as a case where a secondary gas cap has developed. This interpretation is supported by the identification of local structural highs from inspection of the top structure map in Figure 8. However, if the amplitude level after the maximum goes below the baseline level, this is interpreted as critical gas dissolution in addition to water-flood masking. Our interpretation, based on the known well activity and time-lapse seismic amplitudes, indicates that the maxima for regions A and B correspond to the maximum gas saturation, and these occur in 2002. The maxima for regions C, E and F are interpreted to

correspond to the critical gas saturation, and these occur in 2000. Region D is not used in the analysis as the contributions from the injectors and producers plus neighbouring connected regions appear too complicated to fully resolve with our current understanding. The next stage is to relate these amplitude levels to the gas-saturation values. In this analysis we acknowledge that errors may still be present due to the 31% survey non-repeatability.

Quantitative analysis for S_{gc} and S_{gmax}

It has been concluded from the simulation model study above that if the frequency of time-lapse seismic acquisition is several months or more, then gas saturation after exsolution consists of two narrow peaks. These peaks are associated with accumulations in the gas cap at maximum gas saturation (S_{gmax}) and those in the underlying oil leg where the gas is at critical gas saturation (S_{gc}). Some intermediate gas saturations do exist in practice, but these are distributed in the very thin transition zone (typically less than one cell thick) between these two regions. For repressurization and subsequent dissolution, only one saturation peak at S_{gmax} need

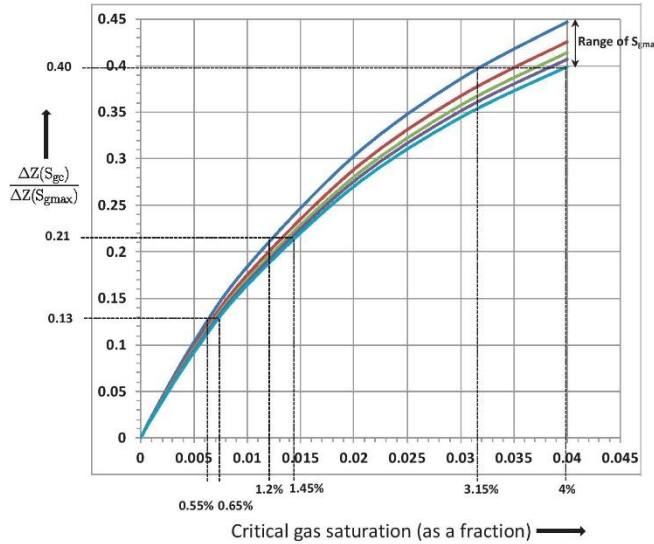


Fig. 11. Estimate of amplitude change with critical gas saturation and no gas in the oil sands, normalized by the expected amplitude change when going from oil to maximum gas saturation in the gas cap.

be considered as the small gas saturations at S_{gc} readily dissolve back into oil by pressure increase. However, in the reservoir, dissolution is complicated by the increase in water saturation at the base of the reservoir, and hence cannot be easily used in the seismic interpretation. As the secondary gas caps in regions A and B on the seismic amplitudes visibly contract with survey time in response to gas production, residual gas saturation (S_{gpc}) due to oil displacement is evaluated as very small. At such values of saturation, free gas is expected to dissolve in the oil upon pressure increase, rendering it undetectable on the seismic. The distinct gas-saturation behaviour upon exsolution also implies that the corresponding impedance change distribution for the reservoir must also be confined to only two characteristic peaks. It follows that the seismic response (for the monitor minus preproduction baseline) is controlled by two distinct time-lapse impedance changes, one due to the presence of maximum gas saturation in the gas cap (ΔZ_{gmax}) and the other due to critical gas saturation in the oil leg (ΔZ_{gc}). To determine how this affects the seismic interpretation, we must first develop an understanding of how these changes occur during the gas exsolution stage.

(P-wave) impedance changes are calculated for our UKCS field example using the rock and fluid properties published by Amini *et al.* (2011) for the same reservoir (Table 2). These are computed for the preproduction baseline and post-production monitor conditions using Gassmann's equation, and are then differenced. No rock-stress or fluid-pressure sensitivity is included in the calculation as this component is assumed to be smaller than the gas-saturation response away from major pressure increases at the injectors. Indeed, in the field under consideration in this work, there are pressure increases or decreases in the interwell reservoir area (beyond 100m from the wells) of only 300 (2.07MPa) to 900psi (6.21MPa), and these give rise to impedance changes of, at most, only a few per cent. The quantities ΔZ_{gc} and ΔZ_{gmax} are calculated for an oil-sand with critical gas saturation and the secondary gas cap, respectively, at a known connate water saturation of 22%, residual oil of 11% and NTG of unity. It is observed that S_{gmax} values for the reservoir (in the range 50–70%) influence the

Table 2. Rock and fluid seismic/acoustic properties for the calculations in the text and Figure 11

Property	Value
Sand porosity	30%
Reservoir pressure	2900psi (20 MPa)
Effective pressure	3336psi (23 MPa)
Mineral bulk modulus	38.00GPa
Dry frame bulk modulus	6.59GPa
Dry frame shear modulus	5.35GPa
Dry frame density	1.92 g cm ⁻³ (1920 kg m ⁻³)
Brine bulk modulus	2.58 GPa
Oil bulk modulus	1.17 GPa
Gas bulk modulus	0.04 GPa
Brine density	1.01 g cm ⁻³ (1010 kg m ⁻³)
Oil density	0.80 g cm ⁻³ (800 kg m ⁻³)
Gas density	0.14 g cm ⁻³ (140 kg m ⁻³)

impedance changes to a lesser extent than changes in the smaller S_{gc} values (in the range 0–15%) – this can be readily explained by the well-known non-linear dependence on gas saturation. This feature can be recognized in the plots of the ratio $\Delta Z_{gc}/\Delta Z_{gmax}$ for different constant maximum gas saturations in Figure 11, where the variation with S_{gc} is seen as the stronger dependence. Importantly, this figure gives us a way of connecting the seismic response to gas saturations. According to the work of Falahat *et al.* (2011) for sub-tuning reservoirs (see also Appendix B), the time-lapse seismic amplitudes, ΔA , are proportional to the thickness of the gas accumulation and the impedance change with gas saturation (in regions where no injected water is present). This can be expressed generally as:

$$\Delta A(T) = \alpha h(T) \Delta Z_g(T) \quad (1)$$

where T refers to elapsed time between the surveys, h is the gas accumulation thickness, ΔZ_g is impedance change with gas saturation, and α is a constant given by the inverse of the product of reservoir velocity and the average impedance of the reservoir and the encasing shale, combined with an operator, L , representing convolution of the time derivative of the wavelet with a coloured inversion operator followed by a 'sum of negatives' over the reservoir interval (equation B10: note that the seismic wavelets of the baseline and the monitor surveys are assumed to be identical). Thus, by normalizing time-lapse amplitudes by the baseline amplitude (A_{bl}), it is possible to relate seismic measurements (ΔA_{gc}) of critical gas saturation at location A and of maximum gas saturation at location B (ΔA_{gmax}) back to the ratio plotted in Figure 11:

$$\frac{\left[\frac{\Delta A_{gc}(T)/A_{bl}}{A} \right]_A}{\left[\frac{\Delta A_{gmax}(T)/A_{bl}}{B} \right]_B} \approx \frac{\Delta Z_{gc}}{\Delta Z_{gmax}} \quad (2)$$

Specifically, the ratio of seismic amplitudes:

$$R_1 = \frac{A(2002) - A(1996)}{A(1996)} \quad (3)$$

is computed for each part of the reservoir with maximum gas saturation, and

$$R_2 = \frac{A(2000) - A(1996)}{A(1996)} \quad (4)$$

for parts with critical gas saturation. Our calculation is shown in Table 3, and indicates R_1 values for regions A and B of 0.75 and 0.92, respectively, whilst R_2 for regions C, E and F are 0.12, 0.30 and 0.12, respectively. The time-lapse seismic ratio R_2/R_1 is now obtained. In order to evaluate possible errors in this calculation, a lower limit is formed by taking the lowest R_2 and the highest R_1 values, and then the highest R_2 and the lowest R_1 values. This yields a lower limit of 0.13 and upper limit of 0.40, with their mean being 0.21. These results are now interpolated back to the curves in Figure 11, and give estimates of the possible critical gas saturations in the range of 0.55–4% for our reservoir. Uncertainties in these estimates may also arise due to lateral variations in NTG in the selected areas, imperfect cancellation of the reservoir thickness variations and water-saturation changes. Another source of uncertainty could possibly arise from the presence of a thin layer of maximum gas saturation in the critical gas-saturation areas, and vice versa (see equation B8), although the behaviour of each area over time in Figure 10 clearly defines the predominant effect. It is also important to note that Figure 11 is specific to our particular reservoir, and will also change depending on rock and fluid properties. In addition, it is known that for a low value of critical gas saturation (and, hence, mobilized gas saturation), it takes longer for the reservoir to assume the bimodal saturation conditions than higher critical gas saturation. The latter will lead to a more prominent seismic response to exsolution in the oil leg, and oil containing critical gas saturation is then likely to have a similar response to the gas cap with the maximum gas saturation. Also, for high S_{gc} values, the dissolution process would be very pronounced as both the oil leg and gas cap brighten at first but only the bright amplitudes related to the oil would dim due to dissolution, whilst those associated with the unproduced gas caps remain. Indeed, it is the absence of this

Table 3. Amplitude values for the regions of our sector in which oil-filled sands are saturated with gas at critical gas saturation ($A(S_{gc})$) and maximum gas saturation ($A(S_{gmax})$). R_1 and R_2 correspond to the ratios defined in equations (3) and (4), from which the time-lapse metric in Figure 11 can be formed

$A(S_{gmax})$	1996	Maximum
A1, A2, A3, A4	11 570	20 212
B1, B2, B3	11 136	21 413
$A(S_{gc})$		
C1, C2, C3, C4	18 615	20 805
E1, E2, E3	18 593	24 140
F1, F2	17 050	19 070
R_1		
A: 0.747		
B: 0.923		
R_2		
C: 0.118		
E: 0.298		
F: 0.119		

effect that can also be used to confirm the small critical gas saturation in our case study.

Quantitative analysis of gas volumes

To further investigate the sequence of gas exsolution and dissolution in our field sector, we analyse the seismic data by following the work of Falahat *et al.* (2011), who proposed a linear relationship between the change in free gas volume (ΔV_g) and the 2D integral of the mapped time-lapse amplitude change (ΔA):

$$\Delta V_g = \beta \iint_{\Sigma} \Delta A dx dy \quad (5)$$

where β is a seismic-to-well production/injection calibration factor to be determined. For the purposes of our work, the time-lapse quantities are taken between the baseline survey and each monitor. Thus, as there is no gas at the time of the baseline survey, ΔV_g represents the volume at the time of the monitor. This equation assumes that changes in water saturation do not affect ΔA – clearly this may be a suitable approximation during the exsolution stage but may not be completely appropriate in some regions of the sector experiencing dissolution for which the injected water clearly has a strong influence. The integral is performed over the area Σ formed by a composite of areas C, D, E and F in Figure 9, which is known to be hydraulically isolated. In the integration, only positive (bright and, hence, gas-related) time-lapse difference amplitudes are used and the summation extends spatially across regions known to contain oil with critical gas saturation. Although empirical in nature, equation (5) may be inferred from equations (1) and (2) by assuming a direct correlation between the impedance change and the product of gas accumulation thickness, effective porosity and gas-saturation change. Calculation indicates that this linearity is a good approximation for the small critical gas saturations in this current study. Finally, an additional assumption made is (as in the previous section) that the pressure change between the time-lapse surveys does not significantly affect the 4D seismic signature via the rock-stress or fluid-pressure sensitivity. This assumption was tested in an earlier simulator to seismic modelling study on the same dataset (Amini *et al.* 2011) and found to be valid.

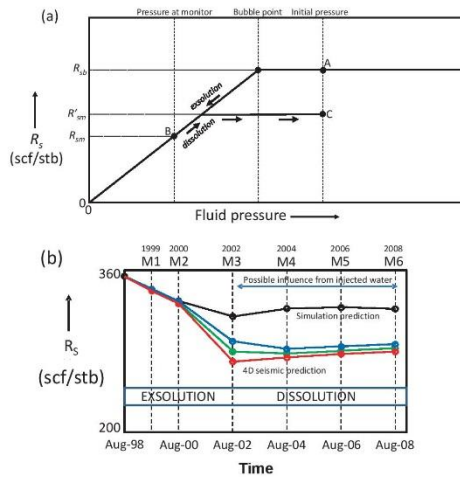


Fig. 12. (a) Schematic illustration of the pressure dependence of the solution gas-oil ratio, R_s , for a black oil such as that in this study. The ratio decreases as pressure drops below bubble point until the monitor state is reached at point B. Re-pressurization increases R_s again but as less gas is available to dissolve in the gas, the R_s behaviour reaches a plateau at a lower constant value and point C is reached. Simulation studies have shown that different volumes in the reservoir will experience different plateaus. (b) R_s values predicted for our study area from fluid-flow simulation (black line and circles) v. the variation estimated from the 4D seismic data for low (red), medium (green) and high (blue) cases.

There is an exsolution stage from the start of production in 1998 until 2001, and a dissolution stage from 2001 to 2008. The behaviour thus forms a natural two-stage division for the analysis. Consider first the application of equation (5) to the period between the preproduction baseline and the 2000 monitor surveys during the primary exsolution stage. The left-hand side of equation (5) can be expanded according to the well-known material balance equation (Dake 2002) focused only on the gas component:

$$[V_o R_{sb} - (V_o - V_{op})R_{sm} - V_{gp}]B_{gm} = \beta \iint \Delta d \, dx \, dy \quad (6)$$

where V_o is the initial (time of baseline survey) oil volume available to be produced at the wells, V_{op} is the actual oil volume produced (at the time of the monitor) and V_{gp} is the gas volume produced (i.e. free gas plus that released from the oil produced at the surface). As there are no initial gas caps in our chosen study area for this calculation, V_{gp} is also the change in the overall gas volume. For the purpose of our calculation, these gas volumes are defined at surface (stock tank oil) temperature and pressure. In equation (6), R_{sb} and R_{sm} are the preproduction (at the baseline time) and current (at the monitor time) solution gas-oil ratios, respectively. The solution gas-oil ratio quantifies the total amount of gas dissolved in the oil. It is defined as the ratio of the volume of gas produced at the surface under standard conditions divided by the volume of oil entering the stock tank at standard conditions, and has units of standard cubic feet per stock tank barrel (scf/stb or in SI units $\text{sm}^3 \text{m}^{-3}$). For the purposes of our calculations these R_s values represent a reservoir average for areas C, D,

E and F. R_s is a linear function of pressure for pressures below the bubble point (Fig. 12a). Thus, $V_o R_{sb}$ gives the total amount of gas dissolved in the oil at the preproduction stage, which could potentially be liberated upon production of the volume V_o . Similarly, $(V_o - V_{op})R_{sm}$ is the amount of gas in the oil remaining in the reservoir at the monitor time. R_{sm} is always less than R_{sb} as there is less gas dissolved in the reservoir oil at the monitor time because the free gas is either produced or remains trapped within the reservoir. Finally, by subtracting the actual gas produced, as measured by the well data, from the estimated dissolved gas contributions – assuming it is also not produced – the result must be the gas still remaining free (and structurally or capillary trapped) in the reservoir. The final parameter in this calculation is B_{gm} , the gas formation volume factor, which converts all of the gas volumes calculated under stock tank barrel conditions to their equivalent reservoir volumes (this therefore has units of reservoir barrel per stock tank barrel).

The 4D seismic signature in the integrand of equation (6) is the difference in the mapped sum of negative amplitudes evaluated between the monitor and baseline surveys. As mentioned previously, to isolate the gas-related response, only the positive difference between the maps in Figure 8 is extracted. In our work it was not found necessary to threshold the resultant difference amplitudes due to the obvious prominence of the gas response. For our field case, the pressure dependences of R_s and B_g are obtained directly from the *PVT* tables determined from the laboratory measurements that have been calibrated for the reservoir and used in the full-field flow simulator by the operator. Calculation from the simulator shows that R_s is expected to reduce from a preproduction of 354 ($62.99 \text{ sm}^3 \text{m}^{-3}$) to 322 scf/stb ($57.30 \text{ sm}^3 \text{m}^{-3}$) after the reservoir pressure drop from 2850 psi (19.65 MPa) in 1998 to 2760 psi (19.03 MPa) in 2008. Applying equation (6) to our observations, we identify two relatively known quantities: the initial oil volume (extracted from the simulation model); and $R_s = R_{sb}$ prior to production and $R_s = R_{sm}$ for the first monitor (taken from the *PVT* tables for the field oil and assuming a mean pressure for our sector). There are two relatively unknown quantities, the seismic calibration factor β , and R_s at each of the subsequent monitor times. By applying equation (6) to the baseline 1996 seismic data together with the monitors at 1999 and 2000 (for which gas continues to come out of solution), we have two equations and can solve to obtain: $\beta = 0.029$ (with dimensions of m/amplitude unit) and R_s for the first monitor. By applying a similar reasoning to the preproduction and subsequent monitor surveys 2002, 2004, 2006 and 2008 acquired during the gas-dissolution stage, equation (6) must be adapted slightly as R_{sm} now replaces R_{sm} , where $R'_{sm} > R_{sm}$ because the volume of gas available to go back into solution is smaller than the original as it has been produced or trapped in local highs, structure or by low NTG regions. Thus, after dissolution the oil is not now fully saturated by gas. The gas at critical gas saturation immediately goes back into the oil upon pressure increase but the gas-oil contact remains in a continual state of dissolution. In equation (6), only R'_{sm} is now unknown, as β has been determined from the gas exsolution stage, and it can therefore be calculated for each of the four remaining monitor surveys. The seismic estimates of R_s v. the predictions from the simulation model are shown in Figure 12(b). For reference, results are also given for a 10% variation in the oil volume showing a high and low estimate of the R_s values. Fluid-flow simulation predicts that R_s in the reservoir decreases from an initial (and known) value of 352 ($62.63 \text{ sm}^3 \text{m}^{-3}$) to 315 scf/bbl ($56.05 \text{ sm}^3 \text{m}^{-3}$) in 2002 due to the pressure drop, before rising slightly to 322 scf/bbl ($57.30 \text{ sm}^3 \text{m}^{-3}$) in 2008. This equates to approximately 4.5% of free gas under reservoir conditions. The seismic R_s estimates also show this dip followed by an increase

but the R_g values are slightly lower than those predicted from the simulator (a minimum of 268 scf/bbl (47.67 m^3m^{-3}). The low values of R_g above suggest that more free gas is being produced in the reservoir but a more likely cause is bias due to the masking effect of injected water in the lower part of the reservoir during the dissolution phase. Unfortunately, it is not possible to quantify this phenomenon or draw further conclusions using the 4D seismic data.

DISCUSSION

Our work has shown that multiple 4D seismic surveys shot during gas exsolution and dissolution can be used to estimate critical gas saturation, and provide some understanding of the maximum gas saturation. The critical gas saturation for the UKCS field in our case study is estimated to be between 0.5 and 4.0%, which falls within the lower range values reported in the literature. A discussion of this finding and its implications for the reservoir is given in the next section. Determination of this particular result has been made possible as there is sufficient time between the seismic surveys to allow gas liberated from solution to settle into either critical or maximum gas-saturation states. This point is also further discussed below. We would anticipate that our framework for seismic interpretation can be generalized to other fields and production scenarios, provided that the transition zone between the oil and gas, or the water- and gas-saturated regions of the reservoir remains smaller than seismic resolution. Thus, our results would be applicable to most reservoirs except those with a very low porosity and permeability, or strong vertical or lateral heterogeneity. As a guide, for permeabilities of tens of mD (10^{-14}m^2), the transition zone can extend over many tens of metres (Ahmed 2006). In this case the transition zone would, therefore, be seismically significant and would support a wide range of saturation states. Our results may not be applicable to other gases. For example, we would expect CO_2 injection to have a more complicated saturation histogram as there is a larger transition zone, due to the smaller density differences, between the gas and water (Cairns *et al.* 2012). For this latter case, there are generally many gas-saturation states influencing the 4D seismic response, and the fluid system takes longer to reach the bimodal quasi-equilibrium state.

Values for the critical and maximum gas saturation

Knowledge of the reservoir-scale (or seismic-scale) S_{gc} is important for a number of reasons. First, it helps to assess the effective relative permeability of gas, oil and water through the reservoir. Secondly, in solution gas drive reservoirs or during depressurization, it is key to predicting the expected gas volume produced from the gas-cap expansion, and hence the oil or gas recovery. Finally, in the early years of a field it can help anticipate risks to productivity from gas exsolution. In the reservoir, S_{gc} is known to be a function of a number of interrelated factors such as the surface area of the pore space, clay content and placement, grain shape, grain arrangement, wettability, and fluid properties. However, it is understood from engineering literature that precise values of S_{gc} are difficult to obtain using laboratory experiments. This uncertainty arises because of the high fluid-flow rates that are induced during experiments (relative to those in the field), the dependence of S_{gc} on the pressure decline rate and capillary end effects. This combination of effects makes extrapolation to *in situ* field conditions unreliable and, as a consequence, the accurate estimation of S_{gc} remains an active research topic (Beecroft *et al.* 1999). Recently, alternative measurements are offered from methods such as numerical simulations enabled by pore-network modelling, which attempt to

emulate realistic gas nucleation and mobilization to obtain the required understanding (McDougall & Sorbie 1999; Bondino *et al.* 2002). Another issue is that relative permeability end points measured in the laboratory do not represent properties at the scale of the reservoir production due to trapping in fine-scale heterogeneities such as cross-bedding and laminae (e.g. Honarpour *et al.* 1994), thus the S_{gc} at the reservoir scale is an effective value. Literature on the evaluation of pressure depletion due to depressurization (blow down) at the end of field life provides, perhaps, the best guide of the effective reservoir-scale S_{gc} as they combine both laboratory and history-matched simulation studies. Examples for UKCS clastic fields include Miller (Beecroft *et al.* 1999: 9%), South Brae (Drummond *et al.* 2001: 2.5% from laboratory), Brent (Ligthelm *et al.* 1997: 9.6%) and Statfjord (Boge *et al.* 2005: 5%). An extensive survey of the literature from laboratory, pore-scale modelling and simulation studies suggests measured values vary from as low as 0.5% to as high as 38% (Fig. 13). Low values in the range of our findings have been measured in many cases and, thus, our findings are not atypical. Although there is no definite trend in the literature, low values are common in moderate porosity reservoirs with good permeability development. Heavier oils tend to have lower S_{gc} values. Further validation is provided by communications with the operator of our field, which indicate a value of between 3.5 and 5% is appropriate in our case.

The maximum gas saturation, S_{gmax} , in the gas cap is determined by the amount of residual oil, S_{org} , due to the gravity drainage of the oil by the gas-cap expansion; that is: $S_{gmax} = 1 - S_{wc} - S_{org}$. The amount of oil immiscibly displaced by the exsolved gas in the presence of the initial water (S_{wc}) by this process may be gauged to some degree by gas-injection experiments on cores (despite this being a distinctly different physical process). For example, Skauge & Ottesen (2002) found a mean S_{org} of 16% for a range of fields, and possible variability with porosity, permeability and initial oil saturation. Similarly, Beecroft *et al.* (1999) found an S_{org} of 20% for the Miller field. According to Edwards *et al.* (1998), gravity drainage by gas-cap expansion is slow and efficient, and there is a remaining oil saturation of 3–10%, with gas-flood tests in the laboratory give higher values. This range was also confirmed in a combined field and laboratory experiment validated by reservoir simulation study. In our case study, taking an average S_{wc} of 22%, a rough estimate of S_{gmax} may realistically be greater than 58%. It is not possible to be more precise as our calculations show that the seismic response is relatively insensitive to this gas saturation.

Timing of the seismic surveys

The time period between the seismic baseline and successive monitors has an impact on the application of our findings. Gas exsolution and dissolution in the reservoir are relatively immediate events, taking less than 1 day or so to complete, and are dependent only on the time for the pressure change profile to diffuse and equilibrate (Fig. 14). However, depending on the connectivity of the reservoir, it can take several weeks or months for the free gas to be finally produced and observed at the wells. For example, for the reservoir models used in this paper it took less than 6 months for the saturation states to settle down to the idealized bimodal distribution under the action of buoyancy and well pressure gradients. The rate at which steady state is attained depends on the production and injection rate, although, after stabilization, the saturation states are independent of the production activities but the volume of gas present changes. Thus, for oil production at a more rapid rate than that predicted from the simulation model, gas may be quickly mobilized and produced but very few gas caps form, and therefore a much smaller amount of

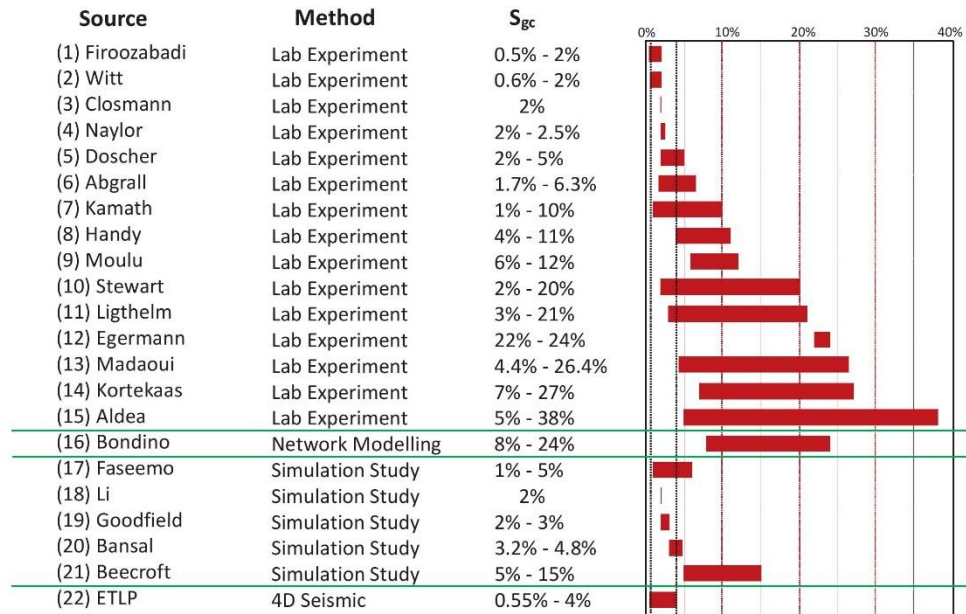


Fig. 13. Critical gas-saturation values for a range of studies (horizontal bars) compared to the results from our 4D seismic estimates (entry number 22).

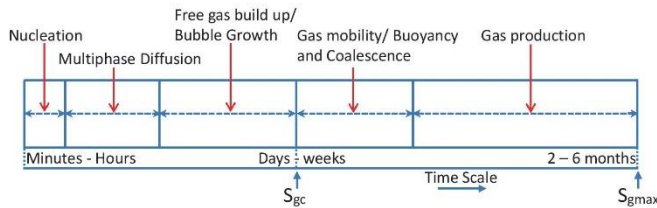


Fig. 14. Timing of the physics of nucleation and development of gas exsolution in a hydrocarbon oil. Timings are based on simulation model studies for the field in this particular publication.

gas is dissolved back into the oil than anticipated. A faster production rate gives rise to a more rapid approach to steady state, although the exact timing depends on the reservoir connectivity and lateral extent. In contrast, there is more gas dissolved back into the oil by increasing the injection rate, although there is a limit to this process as the liberated gas cannot be dissolved if it has already been produced. Importantly, every time the well activity changes (as in our field example), the timescale to reach the bimodal state must again be revised in conjunction with the timing of the seismic surveys. For 4D seismic surveys with a repeat time of 1 to several years, the timescale of the physical processes discussed in this study may not be important but, for repeats with permanent sensor arrays that are 3–6 months apart (Huang *et al.* 2011; Watts & Marsh 2011), this may well present a problem for quantitative 4D seismic analysis. A key parameter in the above is the ratio of vertical to horizontal permeability, K_v/K_h , which also determines the timescale to reach the bimodal gas-saturation condition. This ratio is difficult to define spatially, and can vary quite considerably in clastic reservoirs (Link 2001). We have performed modelling studies that show that when

K_v/K_h is 0.01, the exsolved gas takes longer to migrate upwards and steady state is not attained for 6 months (Falahat 2012). As K_v/K_h increases to 1, the time to reach the steady state progressively reduces to less than 2 months, as in the model examples in this current publication. Consideration of these factors suggests that choice of the optimal survey frequency for 4D analysis must be examined on a case by case basis, and tailored to the particular reservoir conditions (MacBeth *et al.* 2013).

CONCLUSIONS

This study contributes to an understanding of the mechanisms of gas exsolution and dissolution, and an evaluation of the ability to estimate the associated controlling parameters using 4D seismic data from multiple seismic surveys. It is motivated by the clear brightening and dimming of seismic amplitudes observed in the 4D seismic data reported from several separate publications, and the requirement to provide a more quantitative interpretation of this phenomenon. Preliminary study using simulation modelling shows that exsolution and dissolution give rise to gas distributions

that peak around the critical and maximum gas saturations. These fixed saturation states are expected after the period of rapid gas mobilization during exsolution 6–12 months after pressure drop in the reservoir. By using this result together with data from multiple seismic surveys shot between preproduction in 1998 until 2008, it is possible to estimate the gas saturation for our UKCS elastic reservoir. Critical gas saturation is estimated to be between 0.6 and 4.0%, consistent with previous measurements on similar fields. The magnitude of S_{gc} is confirmed by a separate material balance exercise (Falahat *et al.* 2011) and values used in the simulation model by the operator of the field. The seismic amplitudes are expected to be relatively insensitive to the maximum gas saturation ($1 - S_{wc} - S_{org}$) (approximately 68% in our case) as modelled through fluid substitution. Finally, the data suggest that the residual gas saturation upon gas-cap contraction (S_{gr}) is less than a few per cent. Unfortunately, estimation of the latter two values is not possible with any degree of certainty due to the masking influence of the injected water during the dissolution phase. It is believed that the results above represent the limit of what can be achieved with 4D seismic data from multiple surveys in isolation from other reservoir studies. In broad terms, our study demonstrates that monitoring of gas exsolution and dissolution is potentially useful for understanding the reservoir and constraining the simulation model, although case-dependent fluid and pressure changes can cause some interference with this finding.

APPENDIX A: FLUID PROPERTY CHANGES AT, AND NEAR TO, CRITICAL GAS SATURATION

Here we consider the seismic wave properties (density and bulk modulus) of live oil before, during and after gas exsolution. This is important, as it provides an understanding of exactly what fluid effects are visible in the seismic data and how we should treat them. As described in the main text, if fluid pressure is dropped in a porous rock saturated with live oil then small-scale bubbles are nucleated, which start to grow, coalesce and then collect as free gas until critical saturation is reached. Laboratory measurement concludes that the seismic wave properties are not significantly impacted by the pore-scale mechanisms at play during the time leading up to the development of free gas as a separate phase in the pore space: that is, the very tiny bubbles developing in the oil do not affect the seismic wave properties (Han & Batzle 2000a). However, after the development of free gas (i.e. a mobilized gas phase) this is not the case. Indeed, free gas is known to have a substantial effect on the wave properties, particularly at appropriate reservoir depths (Han & Batzle 2000a). However the impact of the gaseous phase may be counteracted by the oil now becoming less 'lively' due to the loss of the lighter gas components. To understand whether this contribution is significant, we calculate the density and bulk modulus for an oil with the same composition as in our case study (an API of 25 and an initial R_i of 354 scf/bbl (62.99 $\text{sm}^3 \text{m}^{-3}$)), at the reservoir pressure and temperature. Density and bulk modulus of the hydrocarbon fluid are calculated at an initial pressure of 2850 psi (19.65 MPa) with no gas saturation, and then after at a pressure drop of 900 psi (6.21 MPa) with free gas. Based on the pressure dependence of R_i for our reservoir oil, it is calculated that the pressure drop releases 1.2% of free gas, and the oil now has an API of 23.7 and an R_i of 342 scf/bbl (60.85 $\text{sm}^3 \text{m}^{-3}$). Application of the FLAG software (Han & Batzle 2000b) gives an initial oil fluid density and bulk modulus of 0.816 gcm^{-3} (816 kgm^{-3}) and 1.36 GPa, respectively, which changes to 0.822 gcm^{-3} (822 kgm^{-3}) and 1.33 GPa after the pressure drop. The change in the oil properties is not large. Mixing the final oil with the gas component (fluid density and bulk modulus of 0.096 gcm^{-3} (96 kgm^{-3}) and 0.0178 GPa, respectively) according

to Wood's equation, determines that the oil and gas mixture has a combined density and bulk modulus of 0.813 gcm^{-3} (813 kgm^{-3}) and 0.830 GPa, respectively. Thus, the outcome is a familiar, exaggerated (beyond its volumetric proportion), non-linear decrease of the bulk modulus after the bubble point and free gas development, and the consequent brightening of the seismic amplitudes, as observed in Figure 8. Amplitudes would therefore continue to brighten as free-gas saturation increased in the pore space. Importantly, if the API and R_i in the oil are (incorrectly) assumed to be identical for the initial and final states in this calculation, then the final oil and gas mixture now has density and bulk modulus of 0.806 gcm^{-3} (806 kgm^{-3}) and 0.817 GPa, respectively. The difference between these values and those from the previous calculation is not significant, and thus fluid substitution calculations and resultant interpretations in the main text can ignore the oil-phase changes to first order. The addition of connate water saturation in practice will not alter the above conclusion.

APPENDIX B: PREDICTION OF THE 4D SEISMIC AMPLITUDE RESPONSE TO GAS EXSOLUTION AND DISSOLUTION

We consider the time-lapse amplitude response of a thin reservoir below tuning, such that the time thickness $2H/V$ (where H is the physical reservoir thickness and V is the P-wave velocity of the reservoir rocks) is much less than the seismic period $1/f$ (where f is the peak frequency of the seismic wave). In this case, the top and base of the reservoir cannot be independently distinguished on the seismic data. In practice, the amplitude is evaluated within a time window defined around a peak and/or trough that represents the composite reservoir package (which includes any fluid contacts). It is therefore assumed that despite the appearance of gas in the reservoir, the relative spacing of the top, base and intra-reservoir events is below tuning thickness. [The assumption of all thicknesses or contact movements being below tuning thickness for our field example has been tested by numerical modelling. In comparison to the seismic period of 40 ms, the time thickness of the reservoir is 15 ms without gas, and 15.5 ms in the presence of gas (with a maximum gas thickness of 10 m, and a saturation of between 10 and 67%). As such, there is no breakdown in the linearity predicted from the following equations. The impact of underlying water saturation in the reservoir would be to reduce the magnitude of the time-lapse change in equation (B8) and to enhance that in equation (B9) by an amount proportional to the water saturation thickness.] Further, only the zero offset response is calculated here in order to simulate a stacked response. It is acknowledged that for reservoirs with significant 3D amplitude v. offset (AVO) behaviour that the calculations should include an offset variation for each reflection coefficient (e.g. see Aki & Richards 1980), and the event timing should be adjusted to allow for the offset raypaths (e.g. $2H/V$ becomes $2H/V \cos \theta$, where θ is the incidence angle). Figure B1 shows the three situations for which the reservoir amplitude is to be calculated: these correspond to the preproduction baseline seismic and an oil-filled reservoir; a monitor survey after gas exsolution and the formation of a secondary gas cap plus gas at the critical gas saturation in the oil; and, finally, a monitor after repressurization and dissolution with the remaining gas cap and the original oil. There is assumed to be no injected water below the gas for the purposes of this particular calculation.

Preproduction

Assuming that the reservoir is completely surrounded by shale with identical properties above and below, the composite reflect-

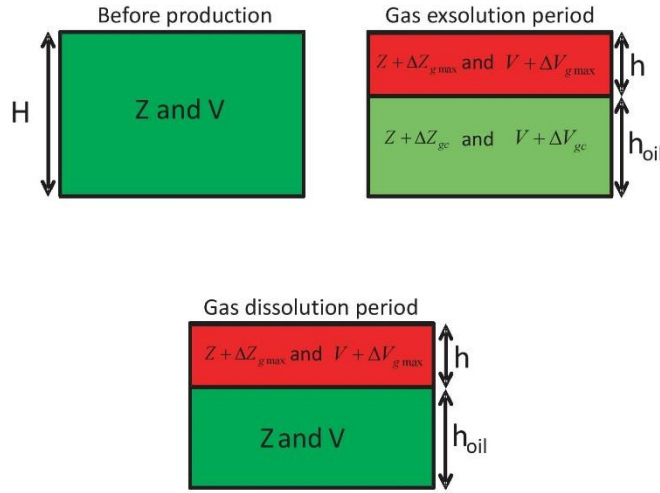


Fig. B1 An idealized model representation of the reservoir and fluid contacts for the calculation in Appendix B.

tivity sequence, R_{res} , for the baseline seismic can be written in the frequency domain as:

$$R_{res} = R_{top} + R_{base} e^{-i\omega(\frac{2H}{V})} \quad (B1)$$

where R_{top} and R_{base} are the individual frequency-independent reflection coefficients for the top and base of the reservoir, and V is the P-wave velocity for the preproduction reservoir condition. For the assumption of a thin reservoir, the approximation is valid, giving:

$$R_{res} \approx R_{top} + \{1 - i\omega(\frac{2H}{V})\} R_{base}. \quad (B2)$$

The composite reflection response is converted to the seismic attribute used in our interpretation in the main text by, first, convolving the time-domain reflectivity with the seismic wavelet $s(t)$ (in the frequency domain this is multiplication of equation (B2) by $S(\omega)$), convolving with a coloured inversion operator (Lancaster & Whitcombe 2000) and then applying a ‘sum of negatives’ to the resultant relative impedance trace – a compound operator defined here by L . The resultant time-domain amplitude is now:

$$\{R_{top} + R_{base}\}L\{s(t)\} - \{R_{base}(\frac{2H}{V})\}L\{s'(t)\} \quad (B3)$$

where $s'(t)$ is the time derivative of the seismic wavelet. The assumption of identical shale above and below the reservoir gives the condition $R_{top} = -R_{base}$, and thus equation (B3) leads to the small contrast approximation between the reservoir and the surrounding shales:

$$A_{res} = -\left(\frac{\Delta Z}{Z}\right)\frac{H}{V}L\{s'(t)\} \quad (B4)$$

where $\Delta Z = Z_{sh} - Z$ is the difference between the shale impedance Z_{sh} and the impedance Z , and \bar{Z} represents the average of the two impedances.

AFTER GAS EXSOLUTION

In this case, there is a gas–oil contact to complicate the reflectivity. The impedance of the reservoir rock within the gas cap is now $Z + \Delta Z_{gmax}$ and the P-wave velocity is $V + \Delta V_{gmax}$. For the oil leg, the impedance and velocity are now $Z + \Delta Z_{gcr}$ and $V + \Delta V_{gcr}$, respectively (see Fig. B1). Applying similar logic and assumptions as in the previous calculation leads to an expression for the new reservoir amplitude A_{gs} :

$$A_{gs} = \frac{1}{2} \left\{ \left(\frac{Z + \Delta Z_{gmax} - Z_{sh}}{\bar{Z}} \right) + \left(\frac{Z + \Delta Z_{gcr} - Z - \Delta Z_{gmax}}{\bar{Z}} \right) + \left(\frac{Z_{sh} - Z - \Delta Z_{gcr}}{\bar{Z}} \right) \right\} L\{s(t)\} - \left\{ \left(\frac{Z + \Delta Z_{gcr} - Z - \Delta Z_{gmax}}{\bar{Z}} \right) \left(\frac{h}{V + \Delta V_{gmax}} \right) + \left(\frac{Z_{sh} - Z - \Delta Z_{gcr}}{\bar{Z}} \right) \left[\left(\frac{h}{V + \Delta V_{gmax}} \right) + \left(\frac{h_{oil}}{V + \Delta V_{gcr}} \right) \right] \right\} L\{s'(t)\} \quad (B5)$$

where h and h_{oil} are the thicknesses of the gas cap and oil leg, respectively. After some manipulation, equation (B5) can be simplified to:

$$A_{gs} = -\left\{ h \left(\frac{\Delta Z - \Delta Z_{gmax}}{\bar{Z}(V + \Delta V_{gmax})} \right) + h_{oil} \left(\frac{\Delta Z - \Delta Z_{gcr}}{\bar{Z}(V + \Delta V_{gcr})} \right) \right\} L\{s'(t)\}. \quad (B6)$$

In the field and modelling examples shown in this paper, $\bar{Z} \Delta V_{gmax}$ and $\bar{Z} \Delta V_{gcr}$ are always less than 5% of $\bar{Z}V$. Thus, it can be further assumed that these two quantities are negligible, which yields:

$$A_{gs} = -\left\{ h \left(\frac{\Delta Z - \Delta Z_{gmax}}{\bar{Z}V} \right) + h_{oil} \left(\frac{\Delta Z - \Delta Z_{gcr}}{\bar{Z}V} \right) \right\} L\{s'(t)\}. \quad (B7)$$

The time-lapse amplitudes $\Delta A_{gs} = A_{gs} - A_{res}$, which in the data are expressed as a map of the gas exsolution formed between the monitor and baseline, can now be obtained:

$$\Delta A_{gs} = \left\{ h \left(\frac{\Delta Z_{gmax}}{\bar{Z}V} \right) + h_{oil} \left(\frac{\Delta Z_{gcr}}{\bar{Z}V} \right) \right\} L\{s'(t)\}. \quad (B8)$$

For the specific field example in the main text we find regions predominantly controlled by critical gas saturation ($\Delta Z_{\text{gmax}}=0$) or maximum gas saturation ($\Delta Z_{\text{gcr}}=0$).

After gas dissolution

During the gas dissolution period, the same equations as in equation (B8) apply except that ΔZ_{gcr} is now zero. Thus, the time-lapse amplitudes ΔA_{diss} for this case are:

$$\Delta A_{\text{diss}} = h \left(\frac{\Delta Z_{\text{gmax}}}{ZV} \right) L\{s^*(t)\}. \quad (\text{B9})$$

Note that, in the main text, attention is given to \tilde{h} and H (hence $V = H/T$ in the denominator) in the above equations as this predicts that the time-lapse amplitudes are controlled by the thickness of the gas accumulation and the reservoir thickness. The remaining parameters are lumped together into a single reservoir-related constant, α , where:

$$\alpha = \left(\frac{1}{ZV} \right) L\{s^*(t)\}. \quad (\text{B10})$$

We thank sponsors of the Edinburgh Time Lapse Project, Phase III, IV and V (BG, BP, CGG, Chevron, ConocoPhillips, EnCana, ENI, ExxonMobil, Hess, Ikon Science, Landmark, Maersk, Marathon, Nexen, Norsar, RSI, Petrobras, Petoro, Shell, Statoil, Suncor, Taqa, TGS, Total and Woodside) for supporting this research. The authors thank B. Tohidi, S. McDougall and E. McKay of the Institute of Petroleum Engineering, Heriot-Watt University for useful discussions on the technical aspects of this work. We thank Schlumberger for the use of their Petrel, Eclipse and PVTi software.

REFERENCES

- Ahmed, T. 2006. *Reservoir Engineering Handbook*, 3rd edn. Elsevier, Amsterdam.
- Aki, K.T. & Richards, P.G. 1980. *Quantitative Seismology: Theory and Methods*. W.H. Freeman, New York.
- Alsos, T., Osdal, B. & Høiås, A. 2009. The many faces of pressure changes in 4D seismic at the Svale Field and its implication on reservoir management. Paper Y004, presented at the 71st EAGE Conference & Exhibition incorporating SPE EUROPEC 2009, 8–11 June 2009, Amsterdam, The Netherlands.
- Amini, H. 2014. A pragmatic approach to simulator to seismic modelling for 4D seismic interpretation. PhD thesis, Heriot-Watt University.
- Amini, H., MacBeth, C. & Shams, A. 2011. Calibration of simulator to seismic modelling for quantitative 4D seismic interpretation. Paper P063, presented at the 73rd EAGE Conference & Exhibition incorporating SPE EUROPEC 2011, 23–26 May 2011, Vienna, Austria.
- Bagley, G., Saxby, I., Megarthy, J., Pearce, C. & Slater, C. 2004. 4D/time lapse seismic: Examples from the Foinhaven, Schiehallion and Loyal Fields, UKCS, West of Shetland. In: Davies, R.J., Cartwright, J.A., Stewart, S.A., Lappin, M. & Underhill, J.R. (eds) *3D Seismic Technology: Application to the Exploration of Sedimentary Basins*. Geological Society, London, *Memoirs*, **29**, 297–302.
- Beecroft, W.J., Mani, V., Wood, A.R.O. & Rusinek, I. 1999. Evaluation of depressurisation, Miller Field, North Sea. Paper SPE 56692, presented at the SPE Annual Technical Conference and Exhibition, 3–6 October 1999, Houston, Texas.
- Boge, R., Lien, S.K., Gjesdal, A. & Hansen, A.G. 2005. Turning a North Sea oil giant into a gas field – depressurisation of the statfjord field. Paper SPE 96403, presented at the SPE Offshore Europe, 6–9 September 2005, Aberdeen, Scotland, UK.
- Bondino, I., McDougall, S.R. & Hamon, G. 2002. Pore network modelling of heavy oil depressurisation: A parametric study of factors affecting critical gas saturation and three-phase relative permeabilities. Paper SPE 78976, presented at the SPE International Thermal Operations and Heavy Oil Symposium and International Horizontal Well Technology Conference, 4–7 November 2002, Calgary, Alberta, Canada.
- Cairns, G., Jakubowicz, H., Lonergan, L. & Muggeridge, A. 2012. Using time-lapse seismic monitoring to identify trapping mechanisms during CO₂ sequestration. *International Journal of Greenhouse Gas Control*, **11**, 316–325.
- Dake, L.P. 2002. *Fundamental of Reservoir Engineering, Nineteenth impression*. Elsevier Science, Amsterdam.
- Danesh, A. 1998. *PVT and Phase Behaviour of Petroleum Reservoir Fluids*. Elsevier Science, Amsterdam.
- Domenico, S.N. 1974. Effect of water saturation on seismic reflectivity of sand reservoirs encased in shale. *Geophysics*, **39**, 759–769.
- Drummond, A., Fishlock, T., Naylor, P. & Rothkopf, B. 2001. An evaluation of post-waterflood depressurisation of the south Brae field, North Sea. Paper SPE 71487, presented at the SPE Annual Technical Conference and Exhibition, 30 September–3 October 2001, New Orleans, Louisiana.
- Edwards, J.T., Honarpour, M.M., Hazlett, R.D. *et al.* 1998. Validation of gravity-dominated relative permeability and residual oil saturation in a giant oil reservoir. Paper SCA-9903, presented at the 1998 SPE Annual Technical Conference and Exhibition, 27–30 September 1998, New Orleans, Louisiana.
- Falahat, R. 2012. Quantitative monitoring of gas injection, exsolution and dissolution using 4D seismic. PhD thesis, Heriot-Watt University.
- Falahat, R., Shams, A. & MacBeth, C. 2011. Towards quantitative evaluation of gas injection using time-lapse seismic data. *Geophysical Prospecting*, **59**, 310–322.
- Gainski, M., MacGregor, A.G., Freeman, P.J. & Nieuwland, H.F. 2010. Turbidite reservoir compartmentalisation and well targeting with 4D seismic and production data: Schiehallion field, UK. In: Jolley, S.J., Fisher, Q.J.J., Ainsworth, R.B., Vrolijk, P.J. & Delisle, S.D. (eds) *Reservoir Compartmentalisation*. Geological Society, London, Special Publications, **347**, 89–102.
- Govan, A., Primmer, T., Douglas, C., Moodie, N., Davis, M. & Nieuwland, 2005. Reservoir management in a deepwater subsea field – the Schiehallion experience. Paper SPE 96610, presented at the SPE Offshore Europe, 6–9 September 2005, Aberdeen, Scotland, UK.
- Han, D. & Batzle, M. 2000a. Velocity, density and modulus of hydrocarbon fluids – data measurement. In: *SEG Technical Program Expanded Abstracts 2000*. Society of Exploration Geophysicists, Tulsa, OK, 1892–1866.
- Han, D. & Batzle, M. 2000b. Velocity, density and modulus of hydrocarbon fluids – empirical modeling. In: *SEG Technical Program Expanded Abstracts 2000*. Society of Exploration Geophysicists, Tulsa, OK, 1867–1870.
- Honarpour, M.M., Cullick, A.S. & Saad, N. 1994. Influence of small scale rock laminations on core-plug measured oil/water relative permeabilities. Paper SPE 27968, presented at the University of Tulsa Centennial Petroleum Engineering Symposium, 29–31 August 1994, Tulsa, Oklahoma.
- Huang, Y., MacBeth, C., Barkved, O. & van Gestel, J.-P. 2011. Enhancing dynamic interpretation at the Valhall Field by correlating well activity to 4D seismic signatures. *First Break*, **29**, 37–44.
- Jack, I., Barkved, O.I. & Kommedal, J.H. 2010. The life-of-field seismic system at Valhall, Norwegian Sea. In Chapter 6: The Road Ahead. In: Johnston, D.H. (ed.) *Methods and Applications in Reservoir Geophysics*. SEG Investigations in Geophysics, **15**. Society of Exploration Geophysicists, Tulsa, OK, 483–625.
- Johnston, D.H. (ed.). 2010. *Methods and Applications in Reservoir Geophysics*. SEG Investigations in Geophysics, **15**. Society of Exploration Geophysicists, Tulsa, OK.
- Johnston, D.H. 2013. *Making a Difference with 4D: Practical Applications of Time-lapse Seismic Data*. SEG Distinguished Instructor Short Course 2013.
- Johnston, D.H., Eastwood, J.E., Shych, J.J., Vauthrin, R., Khan, M. & Stanley, L.R. 2000. Using legacy seismic data in an integrated time-lapse study: Lena field, Gulf of Mexico. *The Leading Edge*, **19**, 294–302.
- Kragh, E. & Christie, P. 2002. Seismic repeatability, normalized RMS, and predictability. *Geophysics*. *The Leading Edge*, **21**, 640–647.
- Lancaster, S. & Whitcombe, D. 2000. Fast-track ‘coloured’ inversion. *SEG Expanded Abstracts*, **19**, 1298–1301.
- Lighthelm, D.J., Reijnen, G.C.A.M., Wit, K., Weisenborn, A.J. & Scherpenisse, W. 1997. Critical gas saturation during depressurisation and its importance in the Brent field. Paper SPE 38475, presented at the SPE Offshore Europe, 9–12 September 1997, Aberdeen, Scotland, UK.
- Link, P.K. 2001. *Basic Petroleum Geology*, 3rd ed. OGC Publications, Tulsa, OK.
- MacBeth, C., Huang, Y. & HajNasser, Y. 2013. 4D seismic interpretation with frequently acquired, multiple time-lapsed surveys. Paper presented at

- the 2nd EAGE Workshop on Permanent Reservoir Monitoring, 2–5 July 2013, Stavanger, Norway.
- MacCain, W.D., Jr. 1990. *The Properties of Petroleum Fluids*. PennWell Publishing, Tulsa, OK.
- Marsh, J.M., Whitcombe, D.N., Raikes, S.A., Parr, R.S. & Nash, T. 2003. BP's increasing systematic use of time-lapse seismic technology. *Petroleum Geoscience*, **9**, 7–13.
- Marsh, M., Bagley, G., Lewis, A. et al. 2001. The use of 4D seismic in reservoir management. Paper presented at the EAGE 63rd Conference and Technical Exhibition, 11–15 June 2001, Amsterdam, The Netherlands.
- Martin, K. & MacDonald, C. 2010. Schiehallion Field: applying a geobody modelling approach to piece together a complex turbidite reservoir. Paper presented at DEVEX 2010, the 7th European Production & Development Conference, 12–13 May 2010, Aberdeen, Scotland, UK.
- McDougall, S.R. & Sorbie, K. 1999. Estimation of critical gas saturation during pressure depletion in virgin and waterflooded reservoirs. *Petroleum Geoscience*, **5**, 229–233.
- Mitchell, P., Paez, R., Johnston, D., Mohler, G. & Neto, C. 2009. 4D seismic in deep water at the Dikanza field, offshore Angola, West Africa. *SEG Expanded Abstracts*, **28**, 3924–3929.
- Morrow, N.R. & Melrose, J.C. 1991. Application of capillary pressure measurements to the determination of connate water saturation. In: Morrow, N.R. (ed.) *Interfacial Phenomena in Petroleum Recovery*. Marcel Dekker, New York, 257–287.
- Roy, S.S., Boen, F., Saebo, A. & Aanonsen, S.I. 2011. 4D seismic monitoring – a case study on the Grane field, North Sea. In: *73rd EAGE Conference & Exhibition incorporating SPE EUROPEC 2011*, 23–26 May 2011, Vienna, Austria Expanded Abstracts. EAGE, Houten, The Netherlands, G026.
- Skauge, A. & Ottesen, B. 2002. A summary of experimentally derived relative permeability and residual saturation on North Sea reservoir cores. Paper SCA 2002-12, presented at the International Symposium of the Society of Core Analysts, September 22–25, 2002, Monterey, California, USA.
- van Gestel, J.-P., Best, K.D., Barkved, O.I. & Kommedal, K.H. 2011. Integration of the life of field seismic data with the reservoir model at the Valhall Field. *Geophysical Prospecting*, **59**, 673–681.
- Watts, G.F.T. & Marsh, M. [2011] How often should you acquire 4D seismic surveys to optimize value? Paper presented at the EAGE Workshop on Permanent Reservoir Monitoring (PRM) – Using Seismic, 28 February–3 March 2011, Trondheim, Norway.

Received 7 February 2014; revised typescript accepted 3 June 2014.



IPTC-18027-MS

Using 4D Seismic Surveys and History Matching to Estimate Critical and Maximum Gas Saturation

D.C. Obidegwu, R.L. Chassagne, and C. MacBeth, Heriot Watt University, IPE

Copyright 2014, International Petroleum Technology Conference

This paper was prepared for presentation at the International Petroleum Technology Conference held in Kuala Lumpur, Malaysia, 10–12 December 2014.

This paper was selected for presentation by an IPTC Programme Committee following review of information contained in an abstract submitted by the author(s). Contents of the paper, as presented, have not been reviewed by the International Petroleum Technology Conference and are subject to correction by the author(s). The material, as presented, does not necessarily reflect any position of the International Petroleum Technology Conference, its officers, or members. Papers presented at IPTC are subject to publication review by Sponsor Society Committees of IPTC. Electronic reproduction, distribution, or storage of any part of this paper for commercial purposes without the written consent of the International Petroleum Technology Conference is prohibited. Permission to reproduce in print is restricted to an abstract of not more than 300 words; illustrations may not be copied. The abstract must contain conspicuous acknowledgment of where and by whom the paper was presented. Write Librarian, IPTC, P.O. Box 833836, Richardson, TX 75083-3836, U.S.A., fax +1-972-952-9435

Abstract

An approach is explored for estimating critical and maximum gas saturation using 4D seismic data from multiple surveys shot during gas exsolution and dissolution in a producing hydrocarbon reservoir. To guide this process, hydrocarbon gas properties and behaviour are studied, and their relation to the fluid-flow physics is understood using numerical simulation and seismic modelling. This understanding is then used to interpret observed seismic data, which has surveys repeated every 12 to 24 months, from a turbidite field in the United Kingdom Continental Shelf (UKCS). Furthermore, the field reservoir simulation model is then history matched to the production data and the gas saturation effects observed on the 4D seismic data. The 4D seismic response is a function of pressure changes, fluid (oil/water/gas) changes and noise. The effects of the gas mechanism are extracted from the seismic data based on its unique relationship to the seismic amplitudes. It is found that these changes can be represented by a binary model (presence or absence of gas) which enables the use of a logical objective function to compute the misfit between the observed data and simulated data, and thus guide the parameterisation process of the history matching exercise. This approach circumvents full physics modelling in a joint history matching workflow that includes conditioning to both production data and multiple time lapse seismic data. It is concluded that for seismic surveys repeated at intervals of six months or more, the gas saturation distribution during either liberation or dissolution exists at two fixed saturations defined by the critical and the maximum gas saturation. From analysing only the 4D seismic data, we find a low critical gas saturation and a maximum gas saturation that is relatively unconstrained. The history matching exercise also gives us similar low values for the critical gas saturation, and highlights the importance of the vertical permeability in getting an extensively corroborated model. This paper explores a direct link between 4D seismic and the fluid flow parameters, a link between the gas saturation distribution and seismic response, as well as a quantitative analysis using multiple 4D seismic surveys for history matching.

Introduction

In the exciting world of physical processes, the petroleum industry does stand shoulder high with regards to its ability to challenge an engineer's thought process and dexterity in solving complex problems. These

complex problems are somewhat simplified using scenarios, models and logical interpretation. The quest to predict the flow of multiple fluids in a reservoir is a complex challenge that has been the target of much research in the petroleum industry. This is desired because it facilitates efficient reservoir monitoring, management, planning and economic evaluation (Obidegwu and MacBeth 2014). Different research themes and areas have been set up to tackle this problem; these include research in laboratory measurements, log analysis, conventional history matching, pore network modelling, etc. Notwithstanding all these efforts, many parameters in multiphase flow remain unconstrained (Di Pierro et al. 2003), especially at the reservoir scale, and in particular for drainage and imbibition processes that involve gas; for these, the critical (S_{gc}) and maximum (S_{gmax}) gas saturation values need to be better determined. The S_{gc} value is usually defined as the point at which the gas first becomes mobile. However, importantly, gas bubbles in the oil that are saturated below this critical saturation will still remain in direct contact with the oil. The mobilised gas migrates upwards, and due to the gravitational force and well pressure gradients, the gas will head towards the wellbore, collecting in local highs or structural traps to form secondary gas caps in the reservoir or being produced (Falahat et al. 2014). The saturation at the secondary gas cap which is also known as S_{gmax} is the highest gas saturation obtainable in the presence of only connate water saturation and residual oil saturation to gas. The importance of the critical gas saturation (S_{gc}) is due to the fact that it helps assess the effective relative permeability of gas, oil and water through the reservoir, it is key to predicting the expected gas volume produced from gas cap expansion, and hence oil or gas recovery, and it can also be used in early field life to anticipate risks to productivity from gas exsolution. In the reservoir, S_{gc} is known to be a function of a number of interrelated factors such as the surface area of the pore space, clay content and placement, grain shape, grain arrangement, wettability, and fluid properties. However, it is understood from engineering literature that precise values of S_{gc} are difficult to obtain using laboratory experiment. This uncertainty arises because of the high fluid flow rates that are induced during experiments (relative to those in the field), the dependence of S_{gc} on the pressure decline rate and capillary end effects. This combination of effects makes extrapolation to in situ field conditions unreliable, and as a consequence accurate estimation of S_{gc} remains an active research topic (Beecroft et al. 1999). In an oil producing reservoir that has poor or misunderstood connectivity, depressurisation by oil production and re-pressurisation with water injection can create scenarios of gas exsolution and dissolution respectively (Dake 2002). Therefore, we believe that monitoring of gas liberation or dissolution using time lapse seismic data may provide a gateway to estimating key fluid flow parameters. This is made possible by utilising multiple seismic surveys that capture the different fluid and pressure changes in the reservoir. In addition to using solely the time lapse seismic data for estimating the reservoir parameters, we embrace a seismic assisted history matching approach where we constrain the reservoir parameters to production data as well as multiple time lapse seismic data; the main challenge being quantitatively incorporating the 4D seismic into the reservoir model. Studies from (Gosellin et al. 2001, 2003; Stephen et al. 2005; Roggero et al. 2007; Landa and Kumar 2011) have used seismic modelling, rock physics modelling or petroelastic modelling to address this challenge, however this modelling process is complex, time consuming, uses laboratory stress sensitivity coefficients, as well as Gassmann's equation assumptions (Landrø 2001; Stephen et al. 2005; Floricich 2006; Amini 2014). There have been other methods that circumvent the complex seismic modelling process such as (Landa and Horne 1997; Kretz et al. 2004; Jin et al. 2012; Rukavishnikov and Kurelenkov 2012; Tillier et al. 2013) which have employed the use of image analysis tools, binary processing, or dynamic clusters to integrate the seismic data into the reservoir model. With this paper we propose a method where our seismic data and simulation data will be converted to binary seismic gas maps and binary simulation gas maps respectively. Our objective function for calculating the misfit of our production data will be the least square method, while our seismic objective function will be the summation of the absolute values of the difference between the binary seismic gas maps and binary simulation gas maps (Figure 6). The context of our study is set by a UKCS dataset which has six monitor surveys that have been shot at intervals of 12-24 months. The remainder of this paper is

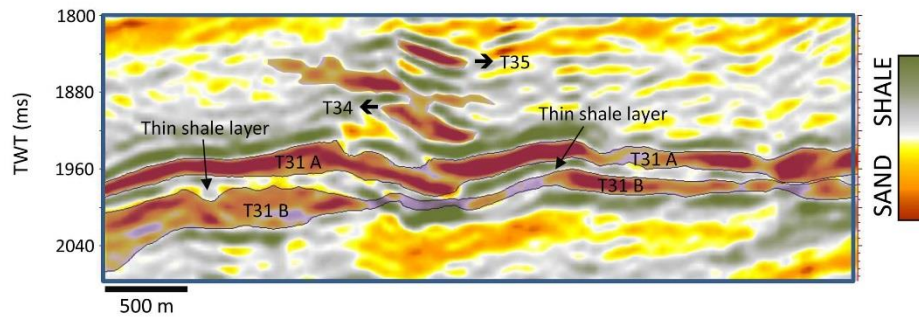


Figure 1—Vertical section from the 1996 pre-production coloured inversion seismic data, showing the reservoir structure. Troughs in dark red represent the sand bodies, whilst peaks in grey represent the shales. The top and base of the sand layers are picked as zero crossings by the data provider (Amini 2014).

organized as follows – the description of the dataset and interpretation of the 4D seismic data; estimation of S_{gc} and S_{gmax} using only 4D seismic, and then using seismic assisted history matching (SAHM); this is then summarized with a discussion and some conclusions.

Description of Dataset

The dataset is from a field in the UKCS, the complex reservoir comprises a sequence of multiple stacked deep marine silicilate turbidites with porosity of 25-30% and permeability of 200-1000mD. Each reservoir is composed of channels, amalgamated channels and sheet-like sands. The field is heavily compartmentalised with faults cross-cutting turbidite sand depositional axes. It contains black oil accumulations close to bubble point, and its drainage strategy is by water injection using down-dip injectors and up-dip producers (Martin and Macdonald, 2010). In this field there is known to be gas liberation, mobilisation, and then repressurization with subsequent dissolution. During the course of production, poor connectivity led to a lack of pressure support from injectors; this combines with a weak aquifer influx to give a strong pressure decrease in some areas, and a drop below bubble point with the consequent liberation of free gas. The drilling plan was adjusted for this reason and the reservoir recovered the pressure (Govan et al. 2005). There are multiple vintages of seismic shot across this field for reservoir management purposes, and for our current work the preproduction baseline in 1996 and six monitors shot in 1999, 2000, 2002, 2004, 2006 and 2008 have been selected. These data have been cross-equalised by the operator for 4D seismic interpretation purposes, and have a non-repeatability NRMS noise metric (Kragh and Christie 2001) of approximately 31% (Falihat et al. 2014). An isolated sector is identified for study that is segmented by two major EW trending normal faults. Figure 1 shows a vertical section from the baseline seismic survey, and our reservoir of interest is T31A and T31B.

Interpretation of 4D Seismic Data

Figure 2 shows the sequence of attribute maps calculated over the T31 reservoir interval for each survey in our chosen segment. The attribute employed is the “sum of negative amplitudes” as it has been demonstrated in past work to be sensitive to the reservoir conditions when the sands are known to be softer than the shales – giving a high to low seismic impedance contrast and a negative relative impedance (Jack et al. 2010). The maps have been cross-equalised such that difference in amplitudes across vintages can be interpreted for timelapse effects. On each map, moderate to high amplitude anomalies indicate hydrocarbon-filled sand bodies with good quality net-to-gross. A progressive brightening of a sand body over time identifies a reservoir softening or impedance decrease (gas liberation or pore pressure increase),

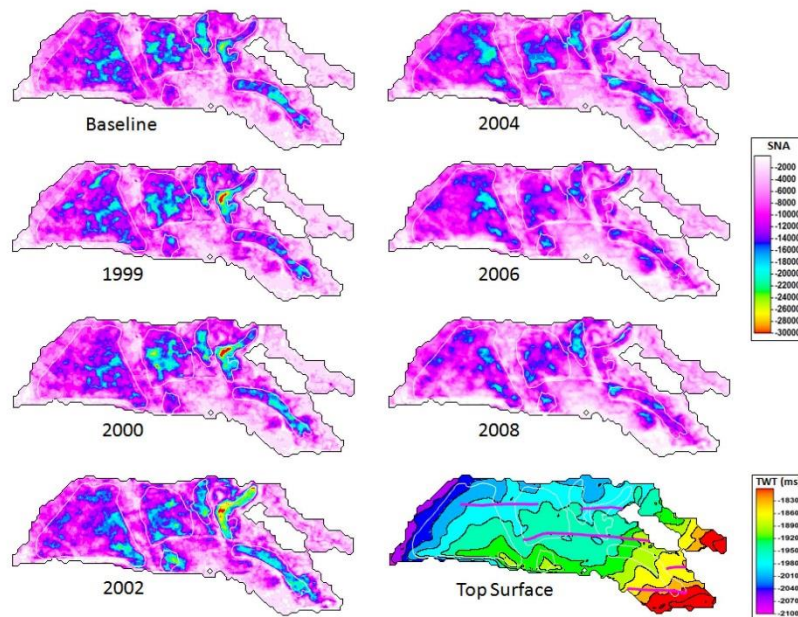


Figure 2—Amplitude maps (using the sum of negative amplitudes attribute) for seismic surveys at times 1996 (production was in 1998), 1999, 2000, 2002, 2004, 2006, and 2008. Also shown is a contour map indicating the time structure of the top T31a reservoir horizon. The anomalies are related to gas or oil accumulations in the reservoir sand deposits.

whilst a dimming over time indicates a reservoir hardening or impedance increase (water saturation increase or pore pressure decrease).

The area of interest is divided into six main regions (Figure 3) based on their general seismic character and known geology, and are used for our analysis. Figure 3a shows the divisions of the regions as well as the location of the producer and injector wells, while Figure 3b highlights the sequence at which the wells are put on production/injection and shut-in, relative to the timing of the baseline and monitor seismic surveys. In region A, an initial injector-producer (I2-P4) pair is later supplemented by injector I4 to maintain pressure. Later injectors I9 and I10 are activated to counteract the pressure decline due to producer P8. Exsolved gas is observed initially in 1999, and it quickly collects in a local high in the south-eastern corner to form a secondary gas cap. Increased water saturation and dissolution reduce the amplitudes after 2002, although some gas remains. Region B sits on a local high into which exsolved gas collects. With no direct injector support initially, dissolution does not occur until 2002 when the nearby injector I8 becomes active. Region C is bounded along its south edge by a sealing fault (see top surface contour plot in Figure 2). Critical gas saturation is evident as a consequence of production in P1 and P6, and there is an upward migration of the gas influenced by possible pressure gradients from producer P1. Injector I5 is active after 2001 to supply pressure support. Region D is possibly connected with region C, but it is not intersected by a producing well. Earlier amplitudes in this region D are fairly constant (Figures 2 and 4) – suggesting a lack of pressure connection. Water sweep from injector I3 and I5 may play a role in decreasing the amplitude after 2002. In region E, there is a strong initial brightening that continues until 2002 due to the producer P5. In 2003 injector I7 is drilled towards the northern edge, which then dims the

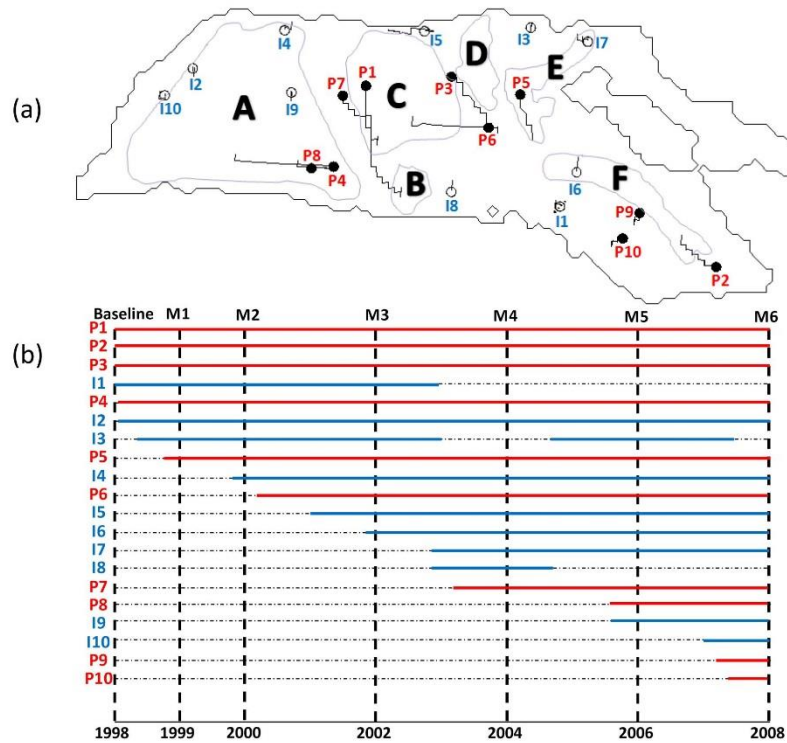


Figure 3—(a) Labelling of main sand bodies used in our study relative to the producer and injector wells. The solid circles correspond to the well TD (b) Timelines of activity for the wells in our chosen sector relative to our monitor seismic data (M1 to M6) surveys. Well trajectories drawn are those that intersect the T31 regions of interest, with the exception of P7 which intersects the overlying T34 reservoir. The red lines represent producers wells, while the blue lines represent injector wells.

amplitudes in subsequent years. The final region for consideration is F, which dips upwards to the south-east. The initial action of injector I1 dims the amplitudes in 1999, but pressure support is not sufficient and gas exsolution occurs in 2000 due to producer P2. After 2002, injector I6 replaces I1 close to the same location, and this provides the required pressure support.

Figure 4(a) indicates a number of small sub-regions within A to F that are chosen for our analysis. These are selected to be of known high net-to-gross and signal quality, and are used to determine seismic amplitude levels associated with an oil sand in pre-production state, oil sand with critical gas saturation, and the secondary gas cap. The ‘sum of negative amplitudes’ attribute for each sub-region and their combined (arithmetic) average are plotted in Figure 4(b) against survey time. The amplitude level of the baseline (oil-filled sand) response and the maximum are determined for each. If the amplitude level after the maximum has been reached still remains above the initial baseline, this is interpreted as a case where a secondary gas cap has developed. This interpretation is supported by the identification of local structural highs. However, if the amplitude level after the maximum goes below the baseline level, this is interpreted as critical gas dissolution in addition to water-flood masking. Our interpretation, based on the known well activity and time-lapse seismic amplitudes, indicates that the maxima for regions A and B correspond to

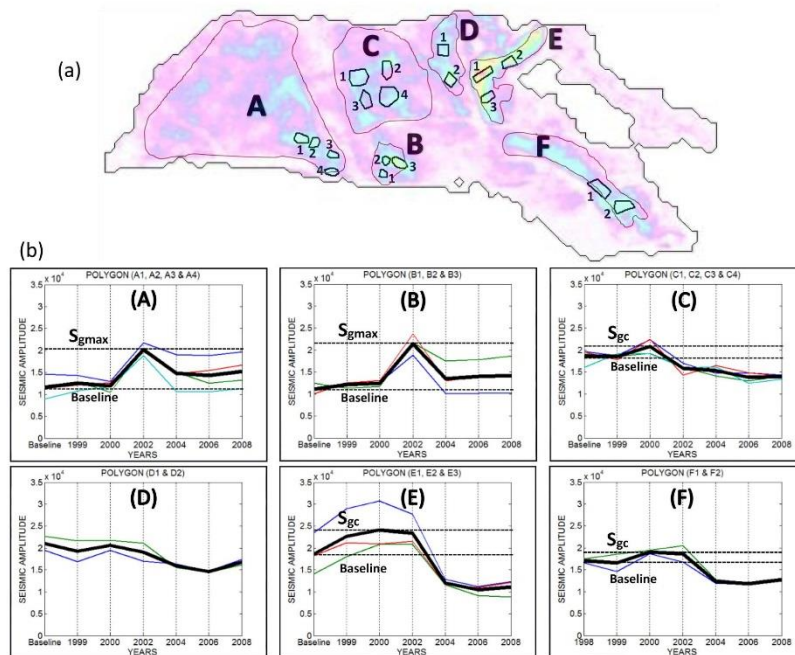


Figure 4—(a) Sub-regions of our sand bodies used for the calculation of time-lapse amplitudes, and gas saturation analysis. (b) Seismic amplitude variations with survey time, together with inferred amplitude levels for maximum and critical gas saturations (dotted horizontal lines). Thin coloured lines correspond to the individual sub-region results, whilst the solid black line is the average of these values.

the maximum gas saturation, and these occur in 2002. The maxima for regions C, E and F are interpreted to correspond to the critical gas saturation, and these occur in 2000. Region D is not used in the analysis as the contributions from the injectors and producers plus neighbouring connected regions appear too complicated to fully resolve with our current understanding. The next stage is to relate these amplitude levels to the gas saturation values.

Estimation of S_{gc} and S_{gmax} using only 4D Seismic

P-wave impedance changes are calculated for our UKCS field using the rock and fluid properties published by Amini et al. (2011) for the same reservoir. These are computed for the pre-production baseline and post-production monitor conditions using Gassmann's equation, and are then differenced. No rock stress sensitivity or fluid pressure sensitivity is included in the calculation as this component is assumed to be smaller than the gas saturation response away from major pressure increases at the injectors. The quantities ΔZ_{gc} and ΔZ_{gmax} are calculated, for an oil-sand with critical gas saturation and secondary gas cap respectively, at a known connate water saturation of 22%, residual oil of 11%, and net-to-gross of unity. It is observed that S_{gmax} values for the reservoir (in the range 50 to 70%) influence the impedance changes to a lesser extent than changes in the smaller S_{gc} values (in the range 0 to 15%) – this can be readily explained by the well-known non-linear dependence of seismic velocity to gas saturation (Domenico 1974). This feature can be recognised in the plots of the ratio $\Delta Z_{gc} / \Delta Z_{gmax}$ for

different constant maximum gas saturations in Figure 5, where the variation with S_{gc} is seen as the stronger dependence. Importantly, this Figure gives us a way of connecting the seismic response to gas saturations as shall be explained in detail. According to the work of Falahat et al. (2011) for sub-tuned reservoirs, the time-lapsed seismic amplitudes, ΔA , are proportional to the thickness of the gas accumulation and the impedance change with gas saturation (provided there is constant water saturation thickness).

This can be expressed generally as

$$\Delta A(T) = -\alpha h(T) \Delta Z_g(T) \quad (1)$$

where T refers to elapsed time between the surveys, h is the gas accumulation thickness, and α is a constant given by the inverse of the product of the reservoir velocity and the average impedance of the reservoir and the encasing shale, combined with an operator, L , representing convolution of the time derivative of the wavelet with a coloured inversion operator followed by a ‘sum of negatives’ over the reservoir interval. Thus, by normalising time-lapse amplitudes by the baseline amplitude (A_{bl}), it is possible to relate seismic measurements (ΔA_{gc}) of critical gas saturation at location A, and (ΔA_{gmax}) of maximum gas saturation at location B back to the ratio plotted in Figure 5:

$$\frac{\left[\frac{\Delta A_{gc}(T)}{A_{bl}} \right]_A}{\left[\frac{\Delta A_{gmax}(T)}{A_{bl}} \right]_B} \approx \frac{\Delta Z_{gc}}{\Delta Z_{gmax}} \quad (2)$$

Specifically, the ratio of seismic amplitudes

$$R_1 = \frac{A(2002) - A(1996)}{A(1996)} \quad (3)$$

is computed for each part of the reservoir with maximum gas saturation, and

$$R_2 = \frac{A(2000) - A(1996)}{A(1996)} \quad (4)$$

for parts with critical gas saturation. From the calculation, R1 values for regions A and B are 0.75 and 0.92 respectively, whilst R2 for regions C, E and F are 0.12, 0.30 and 0.12 respectively. The time-lapse seismic ratio R2/R1 is now obtained. In order to evaluate possible errors in this calculation, a lower limit is formed by taking the lowest R2 and highest R1 values, and then highest R2 and lowest R1 values. This yields a lower limit of 0.13, and upper limit of 0.40, with their mean being 0.21. These results are now interpolated back to the curves in Figure 5, and give estimates of the possible critical gas saturations in the range 0.55 to 4% for our reservoir. Uncertainties in these estimates may also arise due to lateral variations in net-to-gross in the selected areas, imperfect cancellation of the reservoir thickness variations and water saturation changes. Another source of uncertainty could possibly arise from the presence of a thin layer of maximum gas saturation in the critical gas saturation areas, and vice-versa, although the behaviour of each area over time in Figure 4 clearly defines the predominant effect, i.e. either critical gas saturation or maximum gas saturation. It is also important to note that Figure 5 is specific to our particular reservoir, and will also change depending on rock and fluid properties.

Estimation of S_{gc} using Seismic Assisted History Matching

Figure 6 shows the workflow for the seismic assisted history matching. This workflow comprises of the production history matching loop and the seismic history matching loop, and they are combined using weighting factors. The rationale of the values of the weighting factors are usually determined by how much confidence the engineer has on either set of data, there has been some analysis on how this can be

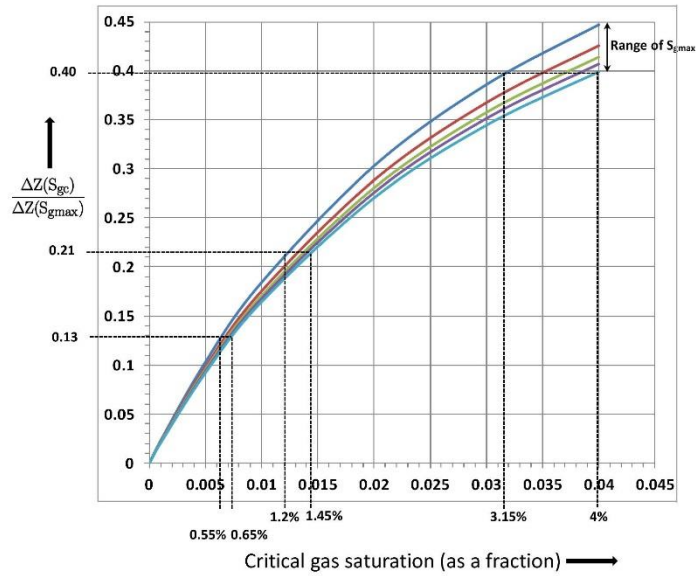


Figure 5—Estimate of amplitude change with critical gas saturation and no gas in the oil sands, normalised by the expected amplitude change when going from oil to maximum gas saturation in the gas cap.

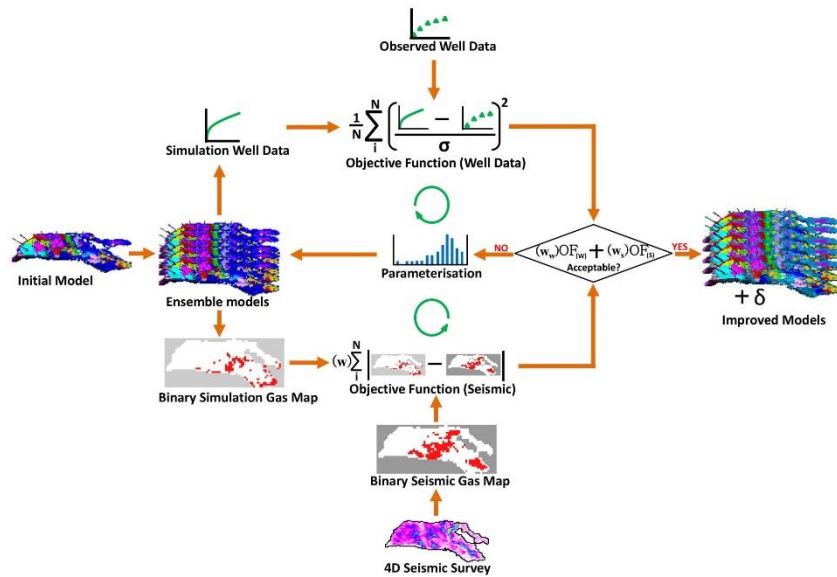


Figure 6—Seismic Assisted History Matching Workflow - combining the production data with the time-lapse seismic data

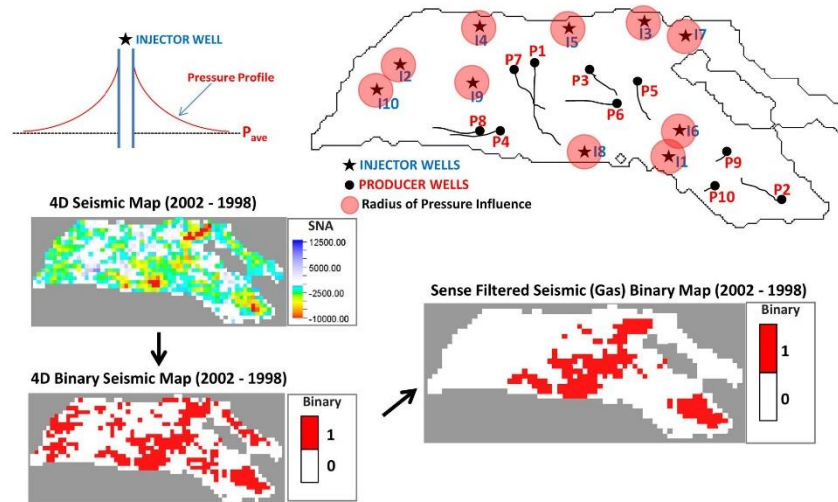


Figure 7—"Sense Filtering" of Seismic Binary Maps

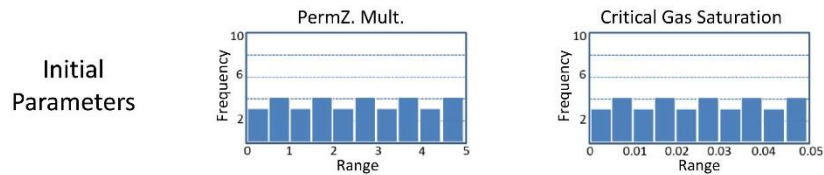


Figure 8—Initial parameter uncertainty ranges for vertical permeability multiplier and critical gas saturation

derived (for example Kjelstadli et al. 2005; Jack et al. 2010), however it still remains quite subjective. With regards to this project, we have an initial simulation model provided by the operator. In order to reduce the cost of multiple simulation runs, the initial simulation model is upscaled laterally by a factor of 4; however, the vertical layering is preserved so as to maintain the characteristics of the field geology. An initial ensemble of models is created using the Latin Hypercube Experimental Design (LHED) method (Roggero et al. 2007). The LHED is a statistical method for generating a sample of plausible collections of parameter values from a multidimensional distribution, and it is useful for exploring the uncertainty range (Schulze-Riegert and Ghedan, 2007). The response parameters (production profiles) of the initial ensemble are generated; while the pore volume weighted gas saturation difference maps (monitor year minus baseline year) are also generated and then converted to binary simulation gas maps, whereby a value of one represents presence of gas, and a value of zero represents absence of gas. The observed 4D seismic data is upscaled to the upscaled model grid size, and then converted to a binary seismic gas map by filtering out the low amplitudes (gas representations) and assigning them a value of one, while everything else is zero. We are aware that the low amplitudes (softening) is a consequence of gas, as well as pressure increase (Calvert et al. 2014), so we apply a "sense filter" such that we estimate a radius of significant pressure influence around the injectors that are likely to affect the signal. This "sense filtering" process is shown in Figure 7, where the pressure profile is defined by the diffusivity equation. After

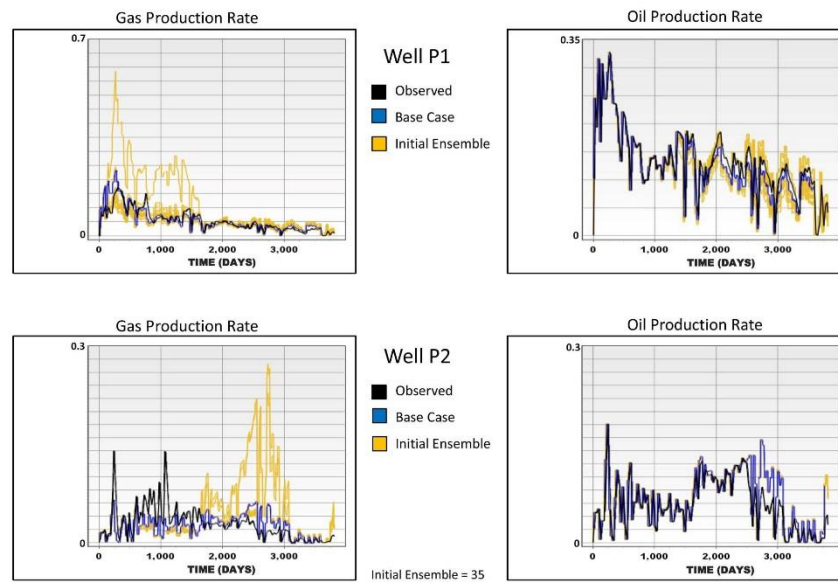


Figure 9—Production profiles (gas production rate and oil production rate) of wells P1 and P2

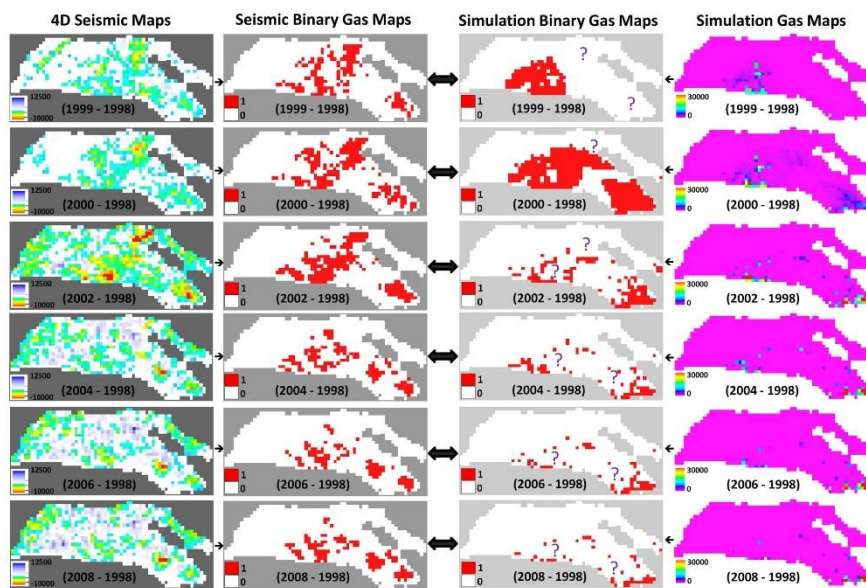


Figure 10—Shows the initial simulation binary maps compared to the seismic binary maps highlighting areas of mismatch

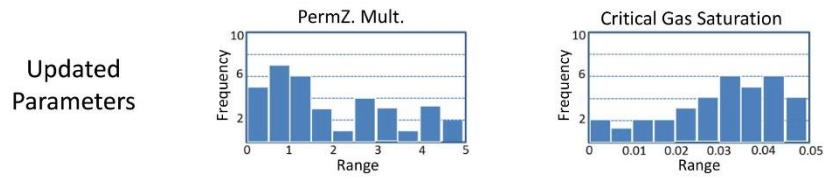


Figure 11—Updated parameter uncertainty range convergence for vertical permeability multiplier and critical gas saturation

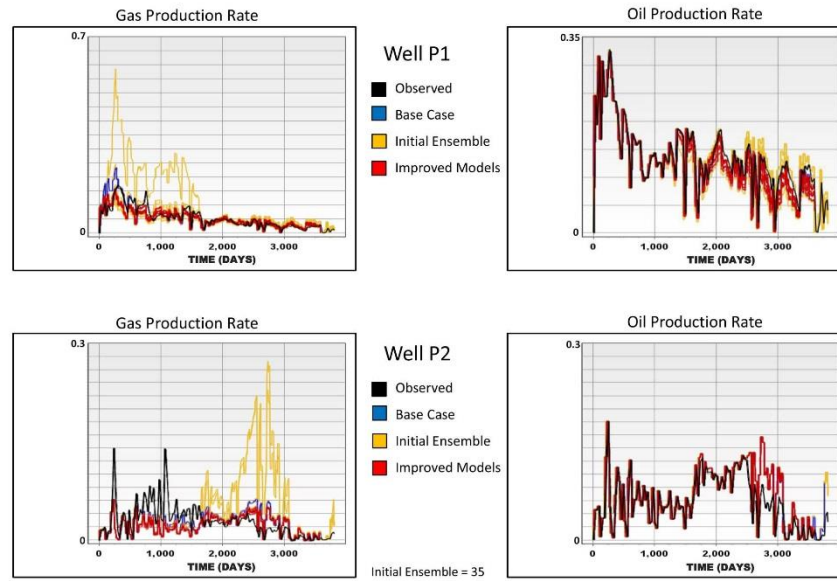


Figure 12—Updated Production profiles (gas production rate and oil production rate) of wells P1 and P2

applying this filter, the signal that is shown is a representation of the gas saturation from seismic in a binary format. The response parameters (production profiles) of the initial ensemble are then compared with the observed well data using the least square method as the objective function, while the binary maps from seismic and simulation are compared using a logical seismic objective function which is the summation of the absolute values of the difference between the binary seismic gas maps and binary simulation gas maps. The misfits generated from the production loop and seismic loop are then combined using the weight factors to obtain a final misfit value. This misfit value is then minimized by an optimisation process using the evolution strategy algorithm to parameterise the uncertain values in the reservoir. The evolutionary algorithm is based on the notion of Darwinian evolution, it deals with concepts such as selection, recombination and mutation, and it is quite popularly used for reservoir history matching (B ck 1996; Soleng 1999; Romero et al. 2000; Williams et al. 2004; Schulze-Riegert and Ghedan, 2007). When the misfit generated gets to a global minimum, an improved set of models and their accompanying uncertainty are generated.

Two uncertain parameters are analysed in this history matching exercise – the critical gas saturation (S_{gc}) and the vertical permeability, and their initial uncertainty range is shown in Figure 8. The vertical

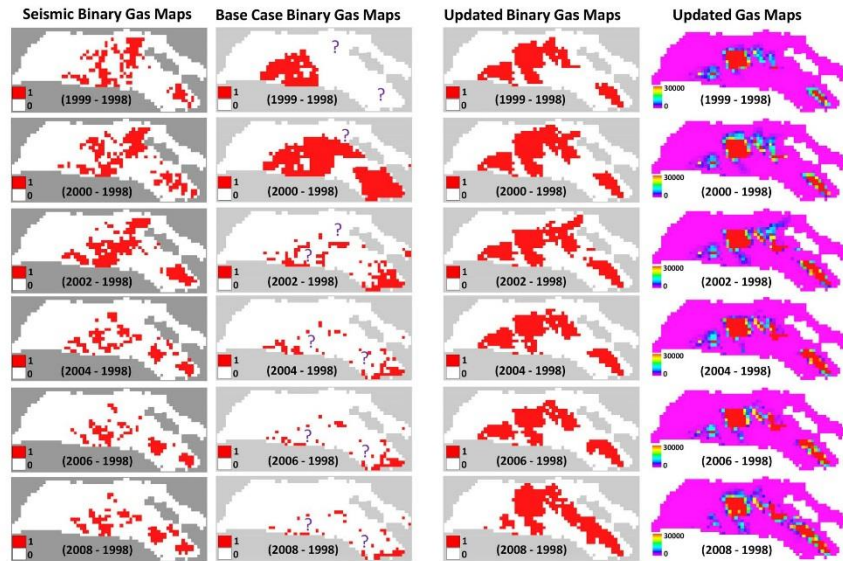


Figure 13—Shows the updated simulation binary maps compared to the seismic binary maps highlighting areas of improvement

Objective Function & Uncertainty

- Seismic O.F.
- Seismic Uncertainty
- Well Data O.F.
- Well Data Uncertainty

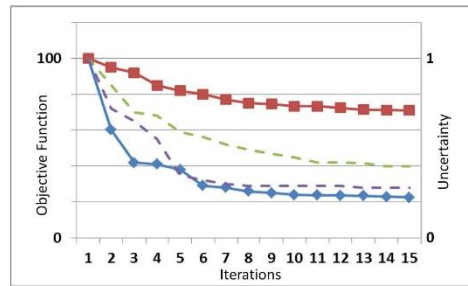


Figure 14—Objective Function and Uncertainty - The dotted lines represent the uncertainty and have their scale at the right hand side, while the continuous lines represent the objective function. The blue line represents the production data objective function, while the red line represents the seismic objective function. The purple dotted line represents the production data uncertainty, while the green dotted line represents the seismic uncertainty.

permeability is perturbed using multipliers ranging from 0 to 5, where a value less than one reduces the vertical permeability effect, and a value greater than one increases it. The S_{gc} which is the onset of gas mobility has an uncertainty range of 0% to 5% as this covers the expected value from other analysis. The starting point of the history matching process is shown in Figures 9 and 10. Figure 9 shows the observed data, the base case model and the initial ensemble of the response parameters (gas production rate and oil production rate) of wells P1 and P2. The observed data represents “hard data” measured at the wells, the base case represents our initial model’s production profile, while the initial ensemble represents profiles for the models generated using the Latin Hypercube Experimental Design which encompasses the effects

of the defined uncertain parameters. The observed oil production rate and gas production rate of well P1 drops continuously for the first 3 years until an improved oil recovery plan is put in place by introducing injector well I5 to provide pressure support as well as water to sweep the oil. This action stabilizes the production rate for the subsequent years. The same trend is observed for well P2, however the oil production rate drops continuously for the first 4 years until injector well I6 replaces the inefficient injector well I1. The introduction of injector well I6 boosts and maintains the oil production rate for the subsequent years until it gently declines. The gas production rate of well P2 is high for the first 4 years as there is gas exsolution in the reservoir due to poor pressure maintenance, when this is curbed by introducing injector well I6, the gas production rate drops and declines in the subsequent years. The initial 4D seismic maps, seismic binary gas maps, simulation gas maps and simulation binary gas maps are shown in Figure 10. The areas of mismatch are highlighted using question marks on the simulation binary gas maps as compared to the seismic binary gas maps, and getting both maps to match is the aim of the seismic assisted history matching exercise. After history matching, we get updated values shown in Figure 11, where the vertical permeability multiplier values converge towards a low value of approximately less than one, hence preventing easy migration of gas due to gravity; we also see the critical gas saturation converging towards a range of 3 – 5 %. These updated values give us a better understanding of our reservoir conditions in terms of the onset of gas mobility and migration, as well as its flow path ability. We now have a look at how these updated parameters affect the production profile (Figure 12) and gas distribution (Figure 13) in the reservoir. Figure 12 shows the production profiles (in red colour) of the updated models, and indeed we do see an improved match to the observed data as compared to the initial ensemble (in yellow colour) we started with. Figure 13 shows the updated simulation binary maps compared to the seismic binary maps with the question marks highlighting areas of improvement. We observe that by changing the vertical permeability and critical gas saturation, we have been able to get a good match of the binary gas distribution in the model. In order to quantify these improvements and the accompanying uncertainty, we create an objective function and uncertainty plot shown in Figure 14. We observe that the production data objective function minimizes quite fast after a few iterations, and then becomes steady as would be expected; we observe a similar trend for the seismic objective function but not of the same degree due to the different nature of the data. We also notice that the uncertainty reduces quite significantly for both, hence endorsing the reliability of the match.

Discussion and Conclusions

It has been shown that multiple 4D seismic surveys shot during gas exsolution and dissolution can be used to estimate critical gas saturation, and provide some understanding of the maximum gas saturation. The critical gas saturation for the UKCS field in our case study is estimated using only 4D seismic data to be between 0.5 and 4.0%, while the seismic assisted history matching approach gave values of between 3 – 5 %, which all fall within the lower range values reported in the literature (for example Boge et al., 2005). From the “seismic only” estimation view point, determination of this particular result has been made possible as there is sufficient time between the seismic surveys to allow gas liberated from solution to settle into either critical or maximum gas saturation states. We would expect our technique to be applicable to most reservoirs except those with a very low porosity and permeability, or strong vertical or lateral heterogeneity. With regards to the seismic assisted history matching estimation, we see that the critical gas saturation and vertical permeability multiplier are quite sensitive and important parameters when matching to the binary gas maps, and that matching to seismic and production data reduces the uncertainties (Walker and Lane 2007). Matching to these parameters improve the production history match and gas saturation representation in the reservoir; hence, improving the predictability of the model.

This study contributes to an understanding of the mechanisms of gas exsolution and dissolution, and an evaluation of the ability to estimate the associated controlling parameters using 4D seismic data from multiple seismic surveys. It is motivated by the clear brightening and dimming of seismic amplitudes

observed in the 4D seismic data reported from several separate publications, and the requirement to provide a more quantitative interpretation of this phenomenon. Critical gas saturation is estimated to be between 0.5 and 4.0%, consistent with previous measurements on similar fields. The magnitude of S_{gc} is confirmed by a separate history matching exercise (3 - 5%) and values used in the simulation model by the operator of the field. The seismic amplitudes are expected to be relatively insensitive to the maximum gas saturation ($1 - S_{vc} - S_{org}$) (approximately 68% in our case) as modelled through fluid substitution. In broad terms, our study demonstrates that monitoring of gas exsolution and dissolution is potentially useful for understanding the reservoir and constraining the simulation model, although case-dependent fluid and pressure changes can cause some interference with this finding. The seismic assisted history matching approach highlights the potential of updating two key reservoir parameters; notwithstanding, it is also important to note that the results are non-unique, and other reservoir parameters settings also have the potential to affect these values.

Acknowledgements

We thank the sponsors of the Edinburgh Time-Lapse Project (BG, BP, CGG, Chevron, ConocoPhillips, ENI, ExxonMobil, Hess, Ikon Science, Landmark, Maersk, Nexen, Norsar, Petoro, Petrobras, RSI, Shell, Statoil, Suncor, Taqa, TGS and Total) for supporting this research. Also, special thanks to BP for providing the data set. We thank Schlumberger for the use of their Petrel, Eclipse and Mepo software.

References

- Amini, H. 2014. *A Pragmatic Approach to Simulator to Seismic Modelling for 4D Seismic Interpretation*. PhD Thesis, Institute of Petroleum Engineering, Heriot Watt University.
- Amini, H., MacBeth, C., and Shams, A. 2011. Calibration of Simulator to Seismic Modelling for Quantitative 4D Seismic Interpretation. Paper P063 presented at the 73rd EAGE Conference and Exhibition incorporating SPE EUROPEC 2011, Vienna, Austria. 23-26 May 2011
- Bäck, T. 1996. *Evolutionary Algorithms in Theory and Practice: Evolution Strategies, Evolutionary Programming*, Genetic Algorithms Oxford University Press, Oxford (1996).
- Beecroft, W.J., Mani, V., Wood, A.R.O., and Rusinek, I., 1999. Evaluation of Depressurisation, Miller Field, North Sea, Paper SPE 56692 Presented at the SPE Annual Technical Conference and Exhibition, Houston, Texas, U.S.A., 3-6 October 1999
- Boge, R., Lien, S.K., Gjesdal, A., and Hansen, A.G. 2005. Turning a North Sea Oil Giant into a Gas Field – Depressurisation of the Statfjord Field. Paper SPE 96403 Presented at the SPE Offshore Europe, Aberdeen, Scotland, UK. 6 – 9 September, 2005
- Calvert, M.A., Roende, H.H., Herbert, I.H., Zaska, J., Hickman P. and Micksch, U. 2014. The Impact of a Quick 4D Seismic Survey and Processing over the Halfdan Field, Danish North Sea. *First Break* volume 32 (April 2014) 43–50
- Dake L. P. 2002. *Fundamental of Reservoir Engineering, Nineteenth impression*, Elsevier Science B. V., Amsterdam, The Netherlands.
- Di Pierro E., Stephen K., McDougall S. and Pickup G. 2003. Sensitivity Analysis on the Two-Phase Flow Properties in a Turbidite Reservoir. SPE81020, SPE Latin and American and Caribbean Petroleum Engineering Conference held in Port-of-Spain, Trinidad, West Indies, 27 -30 April 2003.
- Domenico, S.N. 1974. Effect of water saturation on seismic reflectivity of sand reservoirs encased in shale. *Geophysics*, 39, 759–769.
- Falahat, R., Obidegwu D., Shams, A. and MacBeth, C. 2014. The Interpretation of Amplitude Changes in 4D Seismic Data Arising from Gas Exsolution and Dissolution. *Petroleum Geoscience*, doi: 10.2118/71599-MS, XXXX

- Falahat, R., Shams, A. and MacBeth, C. 2011. Towards Quantitative Evaluation of Gas Injection using Time-lapse Seismic Data. *Geophysical Prospecting*, **59**, 310–322
- Floricich, M. 2006. *An Engineering-Consistent Approach for Pressure and Saturation Estimation from Time-lapse Seismic Data*, PhD Thesis. Institute of Petroleum Engineering, Heriot Watt University.
- Gosselin, O., Aanonsen, S. I., Aavatsmark, I., Cominelli, A., Gonard, R., Kolasinski, M., Ferdinandi, F., Kovacic, L., and Neylon, K. 2003. History Matching Using Time-lapse Seismic (HUTS). Paper SPE 84464 presented at the SPE Annual Technical Conference and Exhibition, Denver, Colorado, U.S.A., 5-8 October doi: 10.2118/84464-MS
- Gosselin, O., van den Berg, S., and Cominelli, A. 2001. Integrated History-Matching of Production and 4D Seismic Data. Paper 71599 presented at the SPE Annual Technical Conference and Exhibition, New Orleans, Louisiana, U.S.A., 30 September – 3 October doi: 10.2118/71599-MS
- Govan A., Primmer T., Douglas C., Moodie N., Davis M. and Nieuwland, 2005. Reservoir Management in a Deepwater Subsea Field – The Schiehallion Experience. Paper SPE 96610 presented at the SPE, Offshore Europe, Aberdeen, Scotland, UK. 6-9 September 2005
- Jack, I., Barkved, O. I., and Kommedal, J. H. 2010. The Life-of-Field Seismic System at Valhall, Norwegian Sea. In Chapter 6: The Road Ahead. In Johnston, D. H. (ed.) *Methods and Applications in Reservoir Geophysics. SEG Investigations in Geophysics*, **15**. Society of Exploration Geophysicists, Tulsa, OK, 483–625
- Jin, L., Weber, D., van den Hoek, P., Alpak, F. O., and Pirmez, C. 2012. 4D Seismic History Matching using Information from the Flooded Zone. *First Break* volume **30** (July 2012) 55–60
- Kjelstadli, R. M., Lane H. S., Johnson, D. T., Barkved, O. I., Buer, K. and Kristiansen, T. G. 2005. Quantitative History Match of 4D Seismic Response and Production Data in the Valhall Field. Paper SPE 96317 presented at the SPE, Offshore Europe, Aberdeen, Scotland, UK. 6-9 September 2005
- Kragh, E., and Christie, P. 2002. Seismic repeatability, normalized RMS, and predictability, Geophysics: *The Leading Edge*, **21**, 640–647.
- Kretz, V., Le Ravalec-Dupin, M., and Roggero, F. 2004. An Integrated Reservoir Characterization Study Matching Production Data and 4D Seismic Data. *SPE Reservoir Evaluation and Engineering* (April 2004) 116–122
- Landa, J., and Horne, R. 1997. A Procedure to Integrate Well Test Data, Reservoir Performance History and 4D Seismic Information into a Reservoir Description. Paper SPE 38653 presented at the 1997 SPE Annual Technical Conference and Exhibition, San Antonio, Texas, U.S.A., 5-8 October
- Landa, J. L., and Kumar, D. 2011. Joint Inversion of 4D Seismic and Production Data. Paper SPE 146771 presented at the SPE Annual Technical Conference and Exhibition, Denver, Colorado, U.S.A., 30 October – 2 November 2011
- Landrø, M. 2001. Discrimination Between Pressure and Fluid Saturation Changes from Time-lapse Seismic Data. *Geophysics* **66**, 836–844
- Martin K. and MacDonald C., 2010. Schiehallion Field: Applying a geobody modelling approach to piece together a complex turbidite reservoir. 7th European Production and Development Conference, Aberdeen, UK
- Obidegwu D., and MacBeth C. 2014. Estimation of Critical and Maximum Gas Saturation Using Multiple 4D Seismic Surveys. 76th EAGE meeting, Amsterdam, The Netherlands, Expanded Abstracts.

- Roggero, F., Ding, D. Y., Berthet, P., Lerat, O., Cap, J., and Schreiber, P. E. 2007. Matching of Production History and 4D Seismic Data – Application to the Girassol Field, Offshore Angola. Paper SPE 109929 presented at the SPE Annual Technical Conference and Exhibition, Anaheim, California, U.S.A., 11 – 14 November doi: 10.2118/109929-MS
- Romero, C.E., Carter, J.N., Zimmermann, R.W., and Gringarten, A.C. 2000. Improved Reservoir Characterization through Evolutionary Computation. Paper SPE 62942 prepared for Annual Technical Conference and Exhibition, Dallas, 1-4 October, 2000
- Rukavishnikov, V., and Kurelenkov, S. 2012. Dynamic Cluster Analysis for Updating Simulation Model using Time-lapse Seismic. 74th Conference and Exhibition, EAGE, Expanded Abstracts, Y046
- Schulze-Riegert, R., and Ghedan, S. 2007. Modern Techniques for History Matching. 9th International Forum on Reservoir Simulation. Abu Dhabi, United Arab Emirates. 9-13 December 2007
- Soleng, H.H. 1999. Oil Reservoir Production Forecasting with Uncertainty Estimation using Genetic Algorithms. Proceedings of the 1999 Congress of Evolutionary Computing, 1999
- Stephen, K. D., Soldo, J., MacBeth, C., and Christie, M. 2005. Multiple Model Seismic and Production History Matching: A Case Study. Paper SPE 94173 presented at the SPE Europe/EAGE Annual Conference, Madrid, Spain, 13 – 16 June doi: 10.2118/94173-MS
- Tillier, E., Da Veiga, S., and Derfoul, R. 2013. Appropriate Formulation of the Objective Function for the History Matching of Seismic Attributes. *Computer and Geosciences* **51** (2013) 64–73
- Walker, G. and Lane, S. 2007. “Assessing the accuracy of history-match predictions and the impact of time-lapse seismic data. A case study for the harding reservoir” Paper SPE 106019 presented at the SPE Reservoir Simulation Symposium, Houston, Texas, 26 – 28 February 2007.
- Williams, G.J.J., Mansfield, M., MacDonald, D., and Bush, M.D. 2004. Top-Down Reservoir Modelling. Paper SPE89974 presented at the Annual Technical Conference and Exhibition, Houston, Texas, 26-29. September 2004.



SPE-174310-MS

Seismic Assisted History Matching Using Binary Image Matching

Dennis Obidegwu, Romain Chassagne, and Colin MacBeth, Heriot Watt University

Copyright 2015, Society of Petroleum Engineers

This paper was prepared for presentation at the EUROPEC 2015 held in Madrid, Spain, 1–4 June 2015.

This paper was selected for presentation by an SPE program committee following review of information contained in an abstract submitted by the author(s). Contents of the paper have not been reviewed by the Society of Petroleum Engineers and are subject to correction by the author(s). The material does not necessarily reflect any position of the Society of Petroleum Engineers, its officers, or members. Electronic reproduction, distribution, or storage of any part of this paper without the written consent of the Society of Petroleum Engineers is prohibited. Permission to reproduce in print is restricted to an abstract of not more than 300 words; illustrations may not be copied. The abstract must contain conspicuous acknowledgment of SPE copyright.

Abstract

This paper presents a history matching scheme that has been applied to production data and time lapse seismic data. The production data objective function is calculated using the conventional least squares method between the historical production data and simulation predictions, while the seismic objective function uses the Hamming distance between two binary images of the gas distribution (presence of gas (1) or absence of gas (0)) sequenced over the different acquisition times. The technique is applied to a UKCS (United Kingdom Continental Shelf) field that has deep-water tertiary turbidite sands and multiple stacked reservoirs defining some degree of compartmentalisation. Thirty five parameters are perturbed in this history match, they can be classified as volumetric parameters (net-to-gross, pore volume), transmissibility parameters (permeability, transmissibility), and end points of the relative permeability curves (critical saturation points). An initial ensemble of fluid flow simulation models is created where the full range of uncertain parameters are acknowledged using experimental design methods, and an evolutionary algorithm is used for optimization in the history matching process. It is found that permeability and critical gas saturation are key parameters for achieving a good history match, and that the volumetric parameters are not significant for this match in this particular reservoir. We also observe that matching only to production data marginally improves the seismic match, whilst matching to only seismic data improves the fit to production data. Combining both sets of data delivers an improvement for the production data and seismic data, as well as an overall reduction in the uncertainties. A unique feature of this technique is the use of the Hamming distance metric for seismic data history matching analysis, as this circumvents the use of the uncertain petroelastic model. This approach is easy to implement, and also helps achieve an effective global history match.

Introduction

The ability to predict the performance of an oil field in an efficient and timely manner is the desire of every reservoir engineer. This is coveted as it expedites efficient reservoir monitoring, management, planning and economic evaluation (Obidegwu et al., 2014). In order to achieve this target, different tools and techniques are employed to acquire, coordinate and interpret data obtained from the reservoir as input to the reservoir simulation model. This model has to confidently replicate the historical data for it to be considered worthy of realistic predictions, and this process of updating the reservoir model to satisfy the historical data is known as history matching. Over the past years, production data (oil rates, water rates,

gas rates, pressure) has been the main historical data available, however, four dimensional (4D) seismic data is now considered a major dynamic input for history matching. That a model is matched to production data is not a sufficient condition for it to make improved predictions (Sahni and Horne, 2006), the model needs to integrate all available data as well as the geologists interpretation of the reservoir in order to provide the most representative reservoir model or models (Landa, 1997, Landa and Horne, 1997, Wang and Kovscek, 2002). The need to monitor fluid displacement is a great challenge that has been successfully overcome with the use of 4D seismic technology (Hatchell et al., 2002, Lygren et al., 2002, Waggoner et al., 2002, Staples et al., 2002, Vasco et al., 2004, Portella and Emerick, 2005, Huang and Lin, 2006, Emerick et al., 2007, Kazemi et al., 2011), which is the process of repeating 3D seismic surveys over a producing reservoir in time-lapse mode (Kretz et al., 2004, Avansi and Schiozer, 2011). Quantitative use of 4D seismic data in history matching is an active research topic that has been explored extensively (Arenas et al., 2001, Aanonsen et al., 2003, Clifford et al., 2003, Gosselin et al., 2003, MacBeth et al., 2004, Staples et al., 2005, Stephen and MacBeth, 2006, Kazemi et al., 2011, Jin et al., 2012), the main challenge being quantitatively incorporating the 4D seismic into the reservoir model (Landa, 1997, Walker et al., 2006, Jin et al., 2011).

Figure 1 shows the different domains in which seismic data could be incorporated into the reservoir model as has been described previously (Stephen and MacBeth, 2006, Landa and Kumar, 2011, Alerini et al., 2014). The three main domains are: (1) The simulation model domain, where the observed seismic data is inverted to changes in pressure and saturation, and are then compared with the simulation output (Landrø, 2001); (2) The impedance domain, where the observed seismic data is inverted to changes in impedance, and the simulation model is forward modelled to derive impedances, and both impedances are then compared (Ayzenberg et al., 2013), or (3) The seismic domain, where the impedances derived from the simulation model are convolved with a wavelet to generate a synthetic seismic, and this is then compared with the observed seismic (Landa and Kumar, 2011). The aforementioned domains use seismic modelling, rock physics modelling or petro-elastic modelling to address this challenge, however these modelling processes are complex, time consuming, uses laboratory stress sensitivity coefficients, as well as Gassmann's equation assumptions (Landrø, 2001, Gosselin et al., 2003, Stephen et al., 2005, Floricich, 2006, Wen et al., 2006, Amini, 2014). There have been other methods that circumvent the complex seismic modelling process (Landa and Horne, 1997, Kretz et al., 2004, Wen et al., 2006, Jin et al., 2012, Rukavishnikov and Kurelenkov, 2012, Le Ravalec et al., 2012, Tillier et al., 2013) which employed the use of image analysis tools, binary processing, or dynamic clusters to integrate the seismic data into the reservoir model. In this paper we propose a method where our seismic data and simulation data are converted to binary seismic gas maps and binary simulation gas maps respectively, such that we can compare the observed seismic data directly with the simulation output in the binary inversion domain (Figure 1). Our objective function for calculating the misfit of our production data will be the conventional least squares method, while our seismic objective function will be the Hamming distance method. The context of our study is set by a UKCS dataset which has six monitor surveys that have been shot at intervals of 12-24 months. The early years of the data will be history matched, while the later years will be used to validate the improved final models (Kretz et al., 2004, Landa et al., 2005).

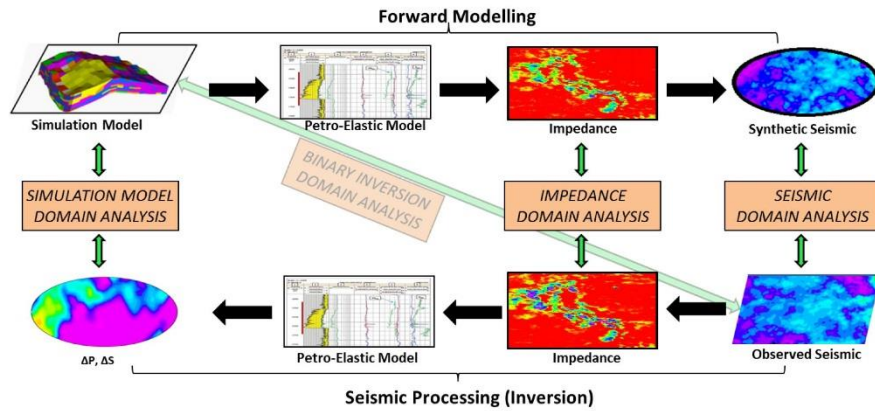


Figure 1—The different domains at which seismic history matching can be explored – the simulation model domain, the impedance domain, and the seismic domain. We propose the binary inversion domain as a quicklook reservoir management tool.

Methodology

The concept of 4D seismic data integration is to complement production data. This is because 4D seismic data has high spatial and low temporal frequency while production data has low spatial and high temporal frequency (Jin et al., 2012). The corresponding characteristics of these data aid in obtaining realistic models of the reservoir through a seismic assisted history matching scheme. History matching is considered an inverse problem (Kretz et al., 2004, Tillier et al., 2012), it is a process of simultaneously perturbing reservoir parameters such that it can be represented as a minimization problem where observed dynamic data are used to condition reservoir models by reducing the misfit between the observed data and model predicted data through an objective function. The use of the conventional least squares formulation for computing production data objective function and misfit has been shown to be suitable and efficient (Oliver and Chen, 2011), such that it can be significantly reduced during the history matching process, and properly characterizes the error between the simulated data and the real data (Tillier et al., 2013); hence this approach is used in this work. However, applying the least squares formulation to compute the seismic objective function and mismatch has been shown to be unsuitable because of the nature of seismic data (Aanonsen et al., 2003, Roggero et al., 2012, Le Ravalec et al., 2012, Tillier et al., 2013), hence the need to search for a suitable alternative.

We propose an approach where observed 4D seismic data is converted to a binary seismic gas map by filtering out the low amplitudes (gas representations) and assigning them a value of one, while everything else is zero; and pore volume weighted gas saturation difference maps (monitor year minus baseline year) are also generated and then converted to binary simulation gas maps, whereby a value of one represents presence of gas, and a value of zero represents absence of gas. The generated binary maps are then compared using a seismic binary objective function. A definitive tool for matching binary images, pattern detection and pattern matching is the Hamming distance metric (Pele and Werman, 2008, Zhao et al., 2010, Bostanci, 2014). The Hamming distance (Hamming, 1950) is a metric measuring the distance between two binary objects by the number of mismatches among their pair of variables. Mathematically, it can be expressed as the sum of the absolute difference between two binary objects (Equation 1), where $Bin(X)$ and $Bin(Y)$ represent the binary models.

$$\text{Hamming Distance} = \sum |Bin(X) - Bin(Y)| \quad (1)$$

The Hamming distance is said to have an inherent robustness to noise, can be invariant to light changes and small deformations, has a high recognition rate of input patterns, and the algorithm is simple and easy to implement (Pele and Werman, 2008). The Hamming distance will be used as the seismic binary objective function to quantify the dissimilarity between the pore volume weighted gas saturation difference and the 4D seismic data difference. Some of the advantages of this approach are that it eliminates the magnitude of the difference in values of the simulator output and the seismic data (i.e. the gas saturation difference maximum range value is 100, while that of the 4D seismic difference amplitudes can be more than 10000), it bypasses the complex petro-elastic model procedure, and that it is fast and effective. The dexterity of the Hamming distance objective function is such that algorithms which are specifically designed for minimization of a function defined as a sum of least squares (Tillier et al., 2013) can also employ Hamming distance as an objective function, as squaring the Hamming distance values i.e. ones and zeros, leaves them unchanged. The selection of appropriate weight coefficient values is usually driven by reservoir engineering experience and can be case dependent (Tillier et al., 2012). For the production data, the practice of boosting the effects of the ill-fitted production data was adopted, and this is done by selecting the weights as being proportional to the square of the difference between the data computed for the base case model and the observed data (Kretz et al., 2004); while the binary seismic data are equally weighted. The combined production data and 4D seismic data objective function is normalized (Kretz et al., 2004) such that at the beginning of the history match, the combined misfit is a value of one. In order to convert the gas saturation from the simulation model and the 4D seismic data to binary maps, cut-off values representing thresholds need to be obtained. These can be derived from a calibration exercise using seismic forward modelling, or by interactive interpretation which requires a clear understanding of the 4D seismic response in terms of the dynamic behaviour of the reservoir (Jin et al., 2012). A combination of both methods is utilised in this work, where seismic forward modelling is used to determine the initial threshold values. Then, integration of reservoir engineering knowledge, injector and producer well activities, reservoir geology and structural contour, as well as 4D seismic concepts are then applied to generate the seismic binary maps.

Below are some tips on interpreting a suitable threshold:

- a. The reservoir pressure should be below bubble point pressure, or at least should have previously been below bubble point pressure, so that there will be gas (exsolved gas) present in the reservoir.
- b. The presence of gas signal around a producer well is validated from gas production profile of the well.
- c. The gas may be present at expected locations, for example at local structural highs.
- d. As we are aware that amplitude decrease (softening) in the 4D seismic data is a consequence of gas, as well as pressure increase (Calvert et al., 2014), the amplitude decrease caused by an increase in pressure around a water injection well is removed from the analysis; however in the case of a gas injector well (where an increase in pressure and the presence of gas cause the same softening effect on seismic), the magnitude of the pressure and gas saturation will need to be determined in order to ascertain which has a more dominant effect on the seismic.

To perform the history match, an initial ensemble of models is created using the Latin Hypercube Experimental Design (LHED) method (Roggero et al., 2007), as multiple models have extensive coverage of the search space and deliver robust results. The initial input parameter sampling is important, and is usually carried out using experimental design methods, such as Plackett-Burman, LHED or Factorial Design (Schulze-Riegert and Ghedan, 2007, Zubarev, 2009). The LHED is a statistical method for generating a sample of plausible collections of parameter values from a multidimensional distribution, and it is useful for exploring the uncertainty range (Schulze-Riegert and Ghedan, 2007). Evolution strategy

algorithm is used for the optimization process to calibrate the uncertain values in the reservoir. The evolutionary algorithm is based on the notion of Darwinian evolution, it deals with concepts such as selection, recombination and mutation, and it is often used for reservoir history matching (Bick, 1996, Soleng, 1999, Romero et al., 2000, Williams et al., 2004, Schulze-Riegert and Ghedan, 2007). In history matching, the termination criteria is usually until the objective function is small enough, convergence is obtained, or the number of iterations exceeds a maximum value (Tillier et al., 2012). The termination criteria used in this work is the convergence criteria. When convergence of the objective function is achieved, an improved set of models and their accompanying uncertainty is generated. One of the advantages of using this approach is that we can update multiple initial realizations to match the same dynamic data to assess uncertainty reduction in the reservoir characterization due to the integration of dynamic data, and this is similar to the randomized maximum likelihood method (Liu et al., 2001, Wen et al., 2006).

Application

So far we have introduced a method of seismic assisted history matching using production data and binary maps of gas saturation. We now apply this concept to field data, with the aim of history matching the observed data, as well as forecasting the future production profiles and gas saturation distribution as a means of validating our new improved models. This history matching technique will be applied using production data only, seismic data only, and a combination of production data and seismic data. The seismic assisted history matching workflow is shown in Figure 2.

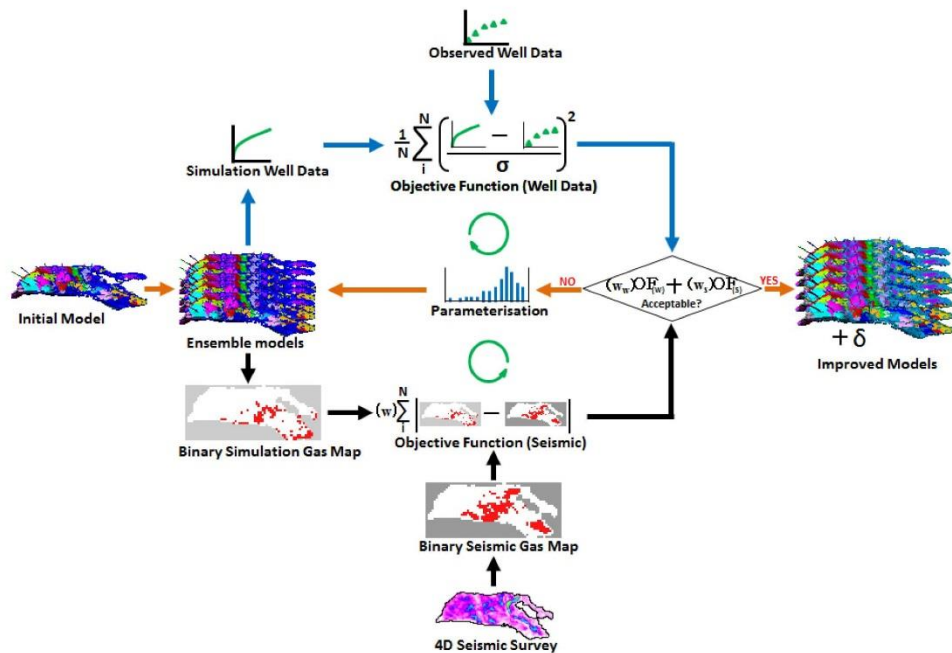


Figure 2—Seismic Assisted History Matching Workflow - combining the production data with the time-lapse seismic data. The blue arrows (upper part) highlight the production history match loop; the black arrows (lower part) highlight the seismic history match loop; the orange arrows (middle part) showcases their individual or combined path; while the green arrows (circular arrows) shows the direction of the loop.

The dataset is from a UKCS turbidite field (Martin and Macdonald, 2010). In this field, the reservoir fluid is black oil with an API gravity ranging from 22° to 28° at a temperature of 120°F (48.89°C). Initial reservoir pressure is approximately 2900 psi (19.99 MPa) (at depth 1940m TVDSS) whilst bubble point is 2850 psi (19.65 MPa) at the top reservoir level, and the solution gas-oil ratio (GOR) is 354 scf/bbl (62.99 sm^3/m^3) (Falahat et al., 2014). In this particular field, there is known to be gas exsolution, gas mobilisation, and then re-pressurisation with subsequent dissolution. During the course of production, poor connectivity led to lack of support from injectors. This combines with a weak aquifer influx to give a strong pressure decrease in some areas, and a drop below bubble point with the consequent liberation of free gas. The drilling plan was adjusted for this phenomenon and recovered the pressure (Govan et al., 2006).

There are multiple vintages of seismic shot across this field for reservoir management purposes, and for our current work the preproduction baseline in 1996 and six monitors shot in 1999, 2000, 2002, 2004, 2006 and 2008 are selected. These data have been cross-equalised by the operator for 4D seismic data interpretation purposes, and have a non-repeatability NRMS noise metric (Kragh and Christie, 2001) of approximately 31% (Falahat et al., 2014). The data have been transformed into relative impedance traces by coloured inversion (Lancaster and Whitcombe, 2000). An isolated sector is identified for study that is segmented by two major EW trending normal faults. The reservoirs consist of multiple stacked, interconnected and amalgamated discrete sand bodies. The sediment system is thus expected to be highly

compartmentalised, with both vertical and lateral connectivity being a major reservoir management issue. The T31 producing interval is mapped for the purpose of our study as it is the main reservoir in which gas exsolution occurs. This particular reservoir interval has a variable character ranging from thin inter-bedded sands and shale to massive sands. The T31 is divided into two units, T31a and T31b, separated by a thin shale layer. There are sheet-like units in this sector typically of 10m to 20m thick that can be mapped on the seismic over a large proportion of the area (Martin and Macdonald, 2010). The 'sum of negatives' attribute is employed for our 4D seismic analysis, this attribute sums all negative amplitudes over the T31 reservoir interval defined between the top T31a and base T31b. This is used as it has been demonstrated in past work to be sensitive to the reservoir conditions when the sands are known to be softer than the shales - giving a high to low seismic impedance contrast and a negative relative impedance (Jack et al. 2010). Figure 3 shows an outline of the reservoir, the position of the injectors and producers, and the timeline of activity of the wells relative to the multiple seismic data surveys. There are 10 years of production activity, it should be noted that the history matching will be implemented for the first 5 years, while the remaining 5 years will be used to validate our history matching process and forecasting ability.

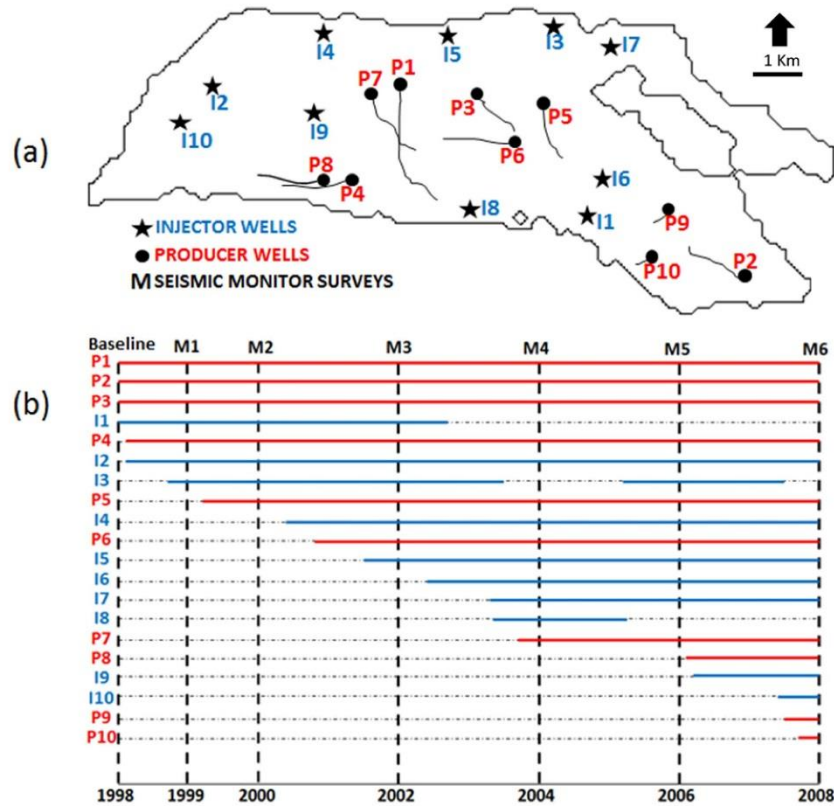


Figure 3—(a) Outline of the reservoir and the position of the producers and injectors. The solid stars and circles correspond to the well TD for the injector wells and producer wells respectively. (b) Timelines of activity for the wells in our chosen sector relative to our monitor seismic data (M1 to M6) surveys (Obidegwu and MacBeth 2014).

Over the years of production, it has been observed that the major challenges to the field development and management plan are the field connectivity and the representation of its numerous geobodies. These geobodies were derived from the 3D seismic interpretation and used for geological model construction. A sensitivity study was carried out to determine which geobodies were most significant to our seismic assisted history matching objective function and this is shown in Figure 4. Combining the geobody regions and global parameters, we were able to identify 35 parameters, which include the permeability, porosity, net-to-gross, pore volume, geobody transmissibility, connate water saturation and critical gas saturation to be used in the history matching process (Table 1). In order to reduce the reservoir flow simulation CPU run time, the initial model is upscaled laterally by a factor of 4, such that its vertical heterogeneity is preserved and the material balance in the model is conserved so as to maintain the characteristics of the field geology. Also, the binary seismic objective function is calculated on the simulation model scale, so the 4D seismic data is arithmetically upscaled to the simulation model scale.

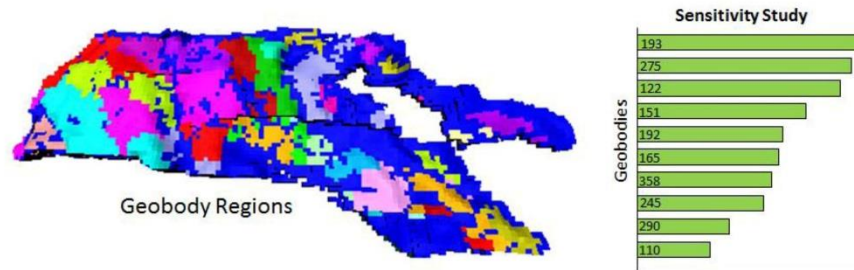


Figure 4—The image on the right shows the different geobody regions, while the figure on the left shows the relative sensitivity of the numbered geobodies to the combined seismic data and production data objective function.

Table 1—Model Parameterization for history matching the reservoir. The global parameters are parameters that are perturbed over the entire reservoir, while the regional parameters are parameters that are perturbed over selected regions/geobodies.

PARAMETERS	NUMBER	LOWER LIMIT	START VALUE	UPPER LIMIT
Global NTG Multiplier	1	0.35	1	2
Global Perm. Multiplier	3	0.35	1	5
Global Poro Multiplier	1	0.35	1	2
Global Pore Vol. Multiplier	1	0.35	1	2
Transmissibility Multiplier	3	0	1	3
Regional NTG Multiplier	7	0.35	1	2
Regional Perm. Multiplier	14	0.35	1	5
Regional Pore Vol. Multiplier	3	0.35	1	2
Critical Water Saturation	1	0.4	0.428	0.5
Critical Gas Saturation	1	0	0.001	0.05
TOTAL NO. OF PARAMETERS	35			

Setting the scene

The initial state of the reservoir and base case conditions of the history matching process are shown in Figures 5 and 6. Figure 5 shows the observed data, the base case model and the initial ensemble of the response parameters (gas production rate and oil production rate) of wells P1 and P2 which have been selected for this history matching exercise due to their location and availability of historical data. The observed data represents “hard data” measured at the wells, the base case represents our initial model’s production profile, while the initial ensemble represents profiles for the models generated using the Latin Hypercube Experimental Design which encompasses the effects of the defined uncertain parameters. The observed oil production rate and gas production rate of producer well P1 drops continuously for the first 3 years until an improved oil recovery plan is put in place by introducing injector well I5 to provide pressure support as well as water to sweep the oil. This action stabilizes the production rate for the subsequent years. The same trend is observed for producer well P2, however the oil production rate drops continuously for the first 4 years until injector well I6 replaces the inefficient injector well I1. The introduction of injector well I6 boosts and maintains the oil production rate for the subsequent years until it gently declines. The gas production rate of producer well P2 is high for the first 4 years as there is gas exsolution in the reservoir due to poor pressure maintenance, when this is curbed by introducing injector well I6, the gas production rate drops and declines in the subsequent years. The initial 4D seismic data maps, seismic binary gas maps, simulation pore volume weighted gas maps and simulation binary gas maps are shown in Figure 6. The first 3 monitor surveys corresponding to the first 5 years will be used

for the history match, while the last three monitor surveys corresponding to the remaining 5 years will be used to analyse the forecast. The areas of mismatch are highlighted using question marks on the simulation binary gas maps, and getting both maps to match is the aim of the seismic assisted history matching exercise.

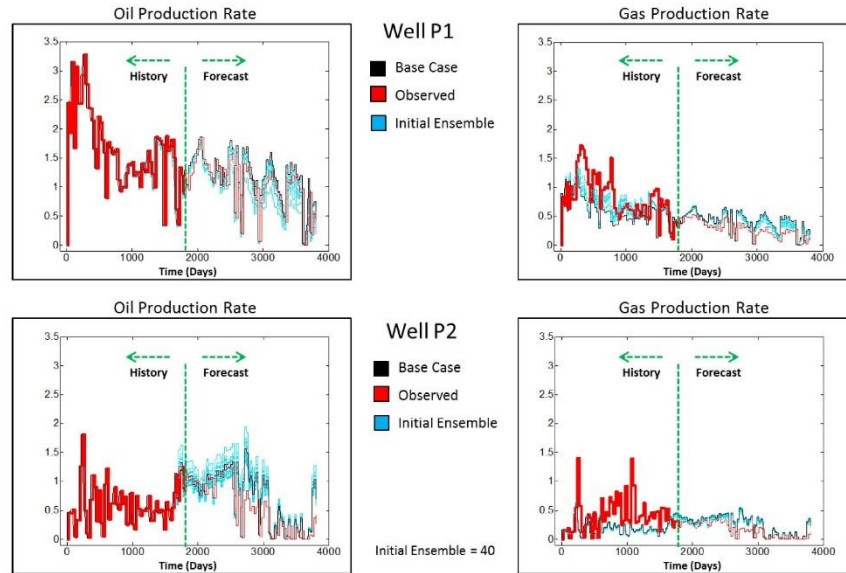


Figure 5—Normalised production profiles (gas production rate and oil production rate) of wells P1 and P2.

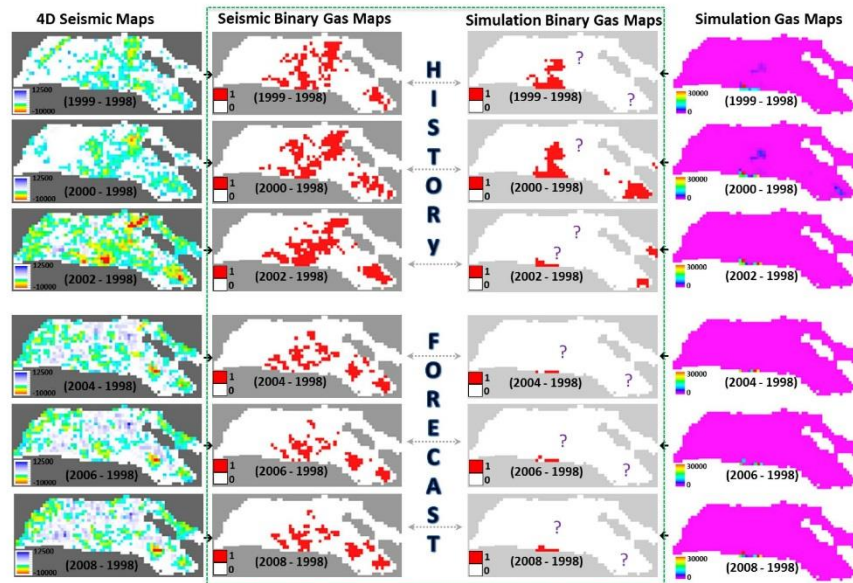


Figure 6—The initial simulation binary gas maps compared to the seismic binary maps highlighting areas of mismatch. The first 3 monitor surveys (the first 3 rows) will be used for the history matching exercise, while the last 3 monitors (last 3 rows) will be used for the forecasting analysis.

History matching and predictions

To history match to production data only, the seismic data term in the combined objective function will be assigned a value of zero, such that the reservoir models will be constrained to only the historical production data. Nonetheless, the seismic objective function will still be generated and analysed. After history matching to production data only, the updated production profile and gas distribution are shown in Figure 7 and Figure 8 respectively. Figure 7 shows the production profiles of the updated models (in dark blue colour), and indeed we see an improved match to the observed data as compared to the initial ensemble (in light blue colour). Figure 8 shows the updated simulation binary maps compared to the seismic binary maps with the question marks highlighting areas of minimal improvement on the updated maps even though the model was not constrained to the seismic data. Figure 9 shows the histograms of selected converging parameters, where the critical gas saturation value tends towards a low value of 1.5%, the horizontal permeability multiplier is about 1.2, and the vertical permeability multiplier is marginally less than 1.0. The low value of the critical gas saturation enables gas mobility quite early, hence the minimal presence of gas in the reservoir model, while the permeability multipliers improve fluid flow.

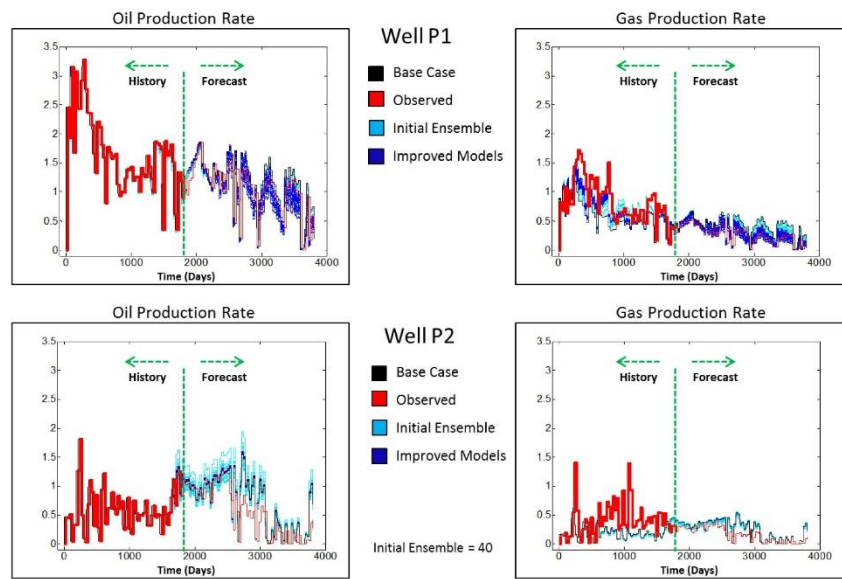


Figure 7—Normalized production profiles (gas production rate and oil production rate) of wells P1 and P2 (History matched to production data only).

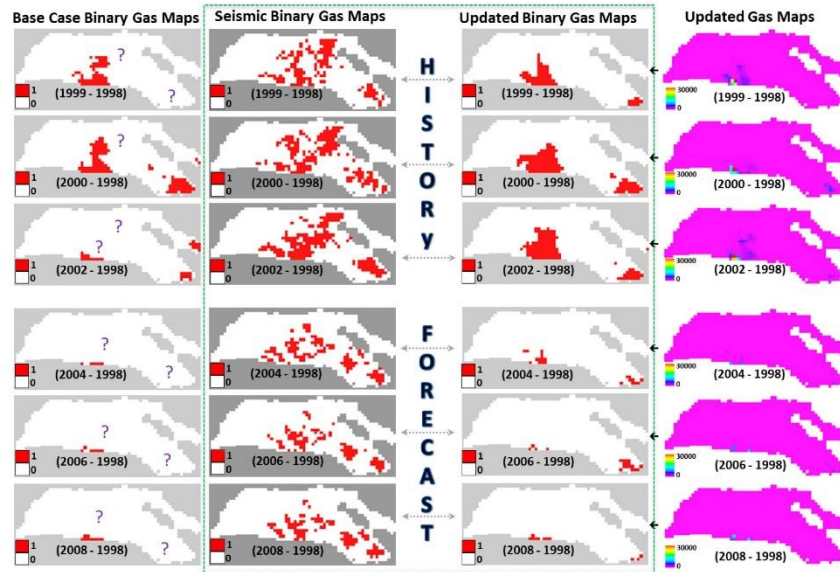


Figure 8—The updated simulation binary maps compared to the seismic binary maps highlighting areas of improvement (History matched to production data only).

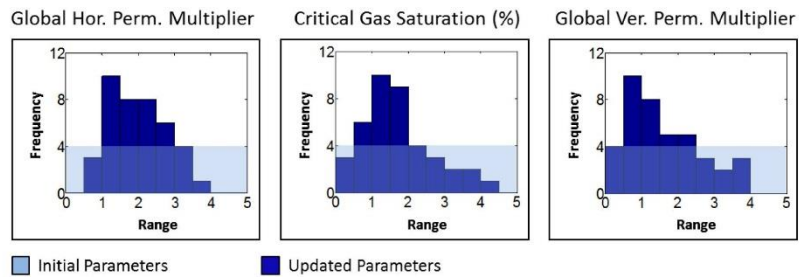


Figure 9—Initial and updated parameters (History matched to production data only).

To history match to seismic data only, the production data term in the combined objective function will be assigned a value of zero, such that the reservoir models will be constrained to only the observed seismic data. Nonetheless, the production data objective function will still be generated and analysed.

After history matching to 4D seismic data only, the updated production profile and gas distribution are shown in Figure 10 and Figure 11 respectively. Figure 10 shows the production profiles of the updated models (in dark blue colour), and since it was not constrained to production data the match is not ideal. Figure 11 shows the updated simulation binary gas maps compared to the seismic binary maps with the question marks highlighting areas of positive improvement; indeed the model predicts more gas as expected. Figure 12 shows the histogram of the parameters, where the critical gas saturation value tends towards a value of 4.5%, the horizontal permeability multiplier is about 2.0, and the vertical permeability

multiplier is less than 1.0. The high value of the critical gas saturation prevents early gas mobility, hence the presence of more gas in the reservoir model.

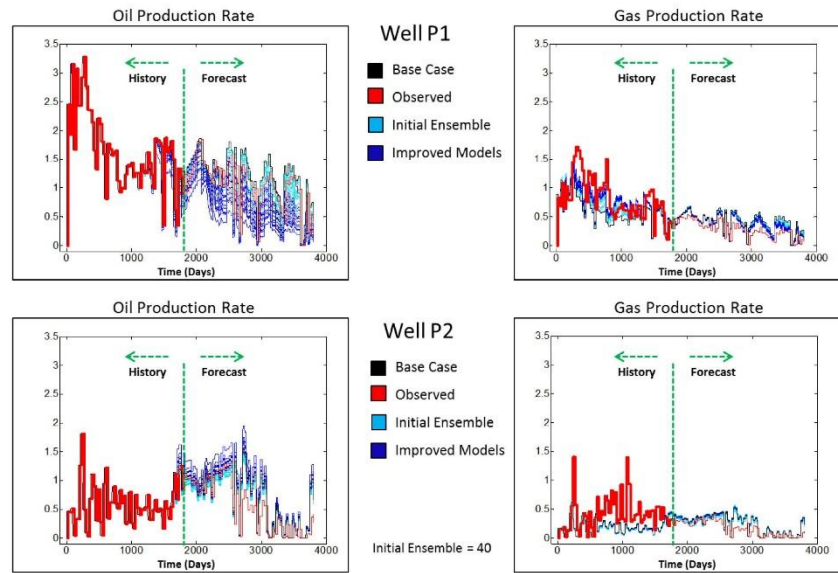


Figure 10—Normalised production profiles (gas production rate and oil production rate) of wells P1 and P2 (History matched to seismic data only).

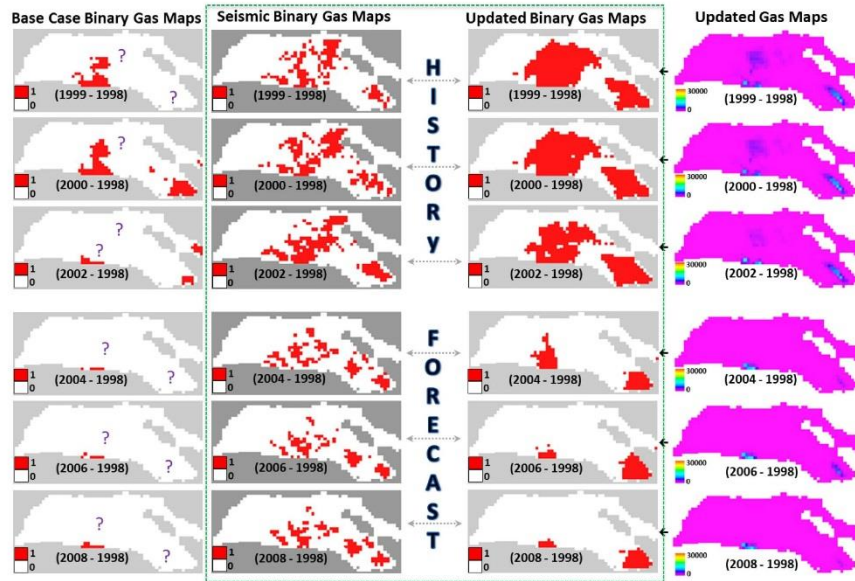


Figure 11—The updated simulation binary maps compared to the seismic binary maps highlighting areas of improvement (History matched to seismic data only).

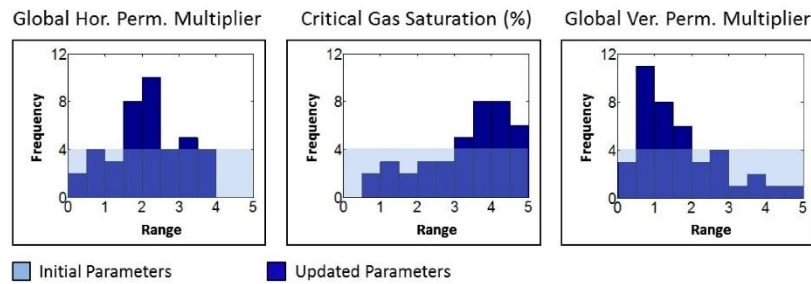


Figure 12—Initial and updated parameters (History matched to seismic data only).

To history match to both production data and seismic data, their combined objective function is normalized such that the effect of the production data and seismic data are equal, and that at the beginning of the history match, the combined misfit is a value of one. After history matching to both production data and 4D seismic data, the updated production profile and gas distribution are shown in Figure 13 and Figure 14 respectively. Figure 13 shows the production profiles of the updated models (in dark blue colour) and there is an improvement, while Figure 14 shows the updated simulation binary maps compared to the seismic binary maps with the question marks highlighting areas of improvement. Figure 15 shows the histogram of the parameters, where the critical gas saturation value tends towards a value of 3.5%, the horizontal permeability multiplier is about 1.4, and the vertical permeability multiplier is less

than 1.0.

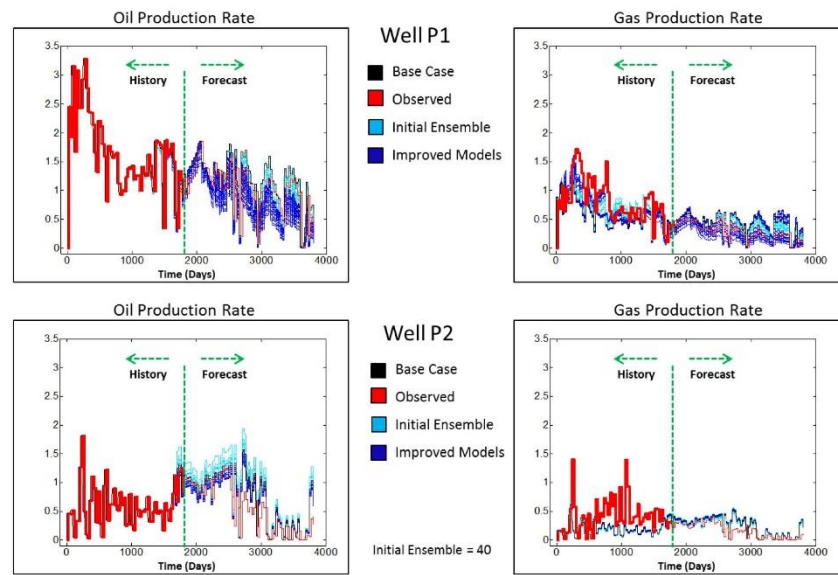


Figure 13—Normalised production profiles (gas production rate and oil production rate) of wells P1 and P2 (History matched to production data and seismic data).

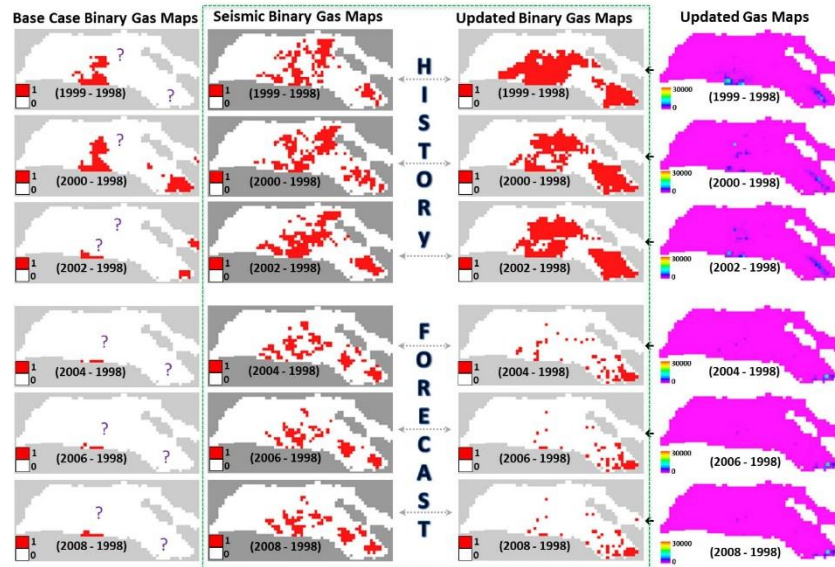


Figure 14—The updated simulation binary maps compared to the seismic binary maps highlighting areas of improvement (History matched to production data and seismic).

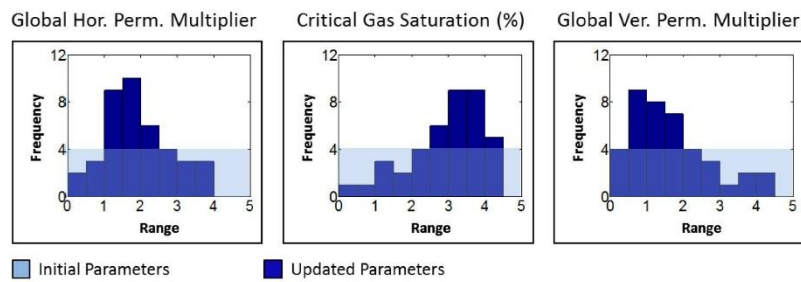


Figure 15—Initial and updated parameters (History matched to production data and seismic data).

Discussion and Conclusions

It has been demonstrated that constraining the reservoir simulation model to a variety of data (4D seismic data, production data, both) affect the updated parameters differently. The permeability multipliers and critical gas saturation reasonably converged in all scenarios, while the volumetric parameters (porosity, net to gross) remained relatively unconstrained. In order to have a better grasp on this analysis, we plot the objective function and uncertainty for the scenarios as shown in Figure 16. These have been normalized to a value of 100 and 1 for easy comparison. It is observed that when matching to well production data only, the production data objective function and uncertainties are low, but the seismic data objective function and uncertainties are high; and that when matching to seismic data only, the seismic

data objective function and uncertainties are lower, but the production data objective function and uncertainties are higher; however when matching to both the production data and seismic data, the production data and seismic data objective function and uncertainties reduces (Walker and Lane, 2007). We go further to analyse the forecasting capabilities of these scenarios and models, by comparing the updated models prediction with the initial model predictions using the combined objective function (Table 2). It is found that matching to production data only gives a 35% percent improvement, matching to 4D seismic only gives a 17% improvement, while matching to both production data and 4D seismic data gives a 42% improvement.

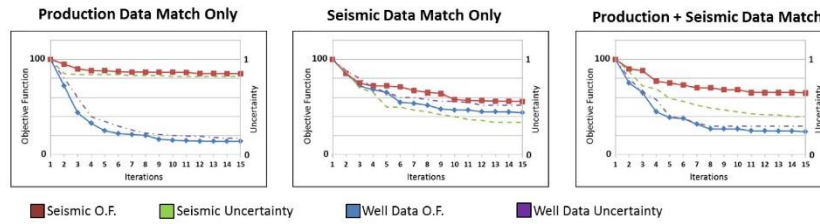


Figure 16—Objective Function and Uncertainty - The dotted lines represent the uncertainty and have their scale at the right hand side, while the continuous lines represent the objective function. The blue line represents the production data objective function, while the red line represents the seismic objective function. The purple dotted line represents the production data uncertainty, while the green dotted line represents the seismic uncertainty.

Table 2—Forecast improvement using the combined objective function, with respect to the initial model predictions.

Forecast Improvement	
Production Data Only	34.60%
Seismic Data Only	17.31%
Production & Seismic	41.65%

This study proposes a quick look reservoir management approach, where 4D seismic data and production data are used to update the reservoir simulation model without having to apply a complex full physics seismic modelling workflow. The Hamming distance metric which is invariant to small deformations and has an inherent robustness to noise is used to integrate the 4D seismic data with the production data, and has shown its potential of being a useful tool.

Acknowledgements

We thank the sponsors of the Edinburgh Time-Lapse Project (BG, BP, CGG, Chevron, ConocoPhillips, ENI, ExxonMobil, Hess, Ikon Science, Landmark, Maersk, Nexen, Norsar, Petoro, Petrobras, RSI, Shell, Statoil, Suncor, Taqa, TGS and Total) for supporting this research. Also, special thanks to BP for providing the data set. We thank Schlumberger for the use of their Petrel, Eclipse and Mepo software.

References

Aanonsen, S. I., Aavatsmark, I., Barkve, T., Cominelli, A., Gonard, R., Gosselin, O., Kolasinski, M. and Reme, H. 2003. Effect of Scale Dependent Data Correlations in an Integrated History Matching Loop Combining Production Data and 4D Seismic Data. Paper presented at the SPE Reservoir Simulation Symposium, Houston, Texas, U.S.A. 3 - 5 February 2003

- Alerini, M., Ayzenberg, M., Ek, T., Feng, T., Hustoft, L., Lie, E., Liu, S., Skjei, N. and Skjervheim, J. A. 2014. Utilization of time-lapse seismic for reservoir model conditioning. Paper presented at the SPE Europec/EAGE Annual Conference and Exhibition, Amsterdam, Netherlands. 16-19 June 2014
- Amini, H. 2014. *A pragmatic approach to simulator to seismic modelling for 4D seismic interpretation*. PhD thesis, Heriot Watt University.
- Arenas, E., van Kruijsdijk, C. and Oldenziel, T. 2001. Semi-Automatic History Matching Using the Pilot Point Method Including Time-Lapse Seismic Data. Paper presented at the SPE Annual Technical Conference and Exhibition, New Orleans, Louisiana. 30 September - 3 October 2001
- Avansi, G. D. and Schiozer, D. J. 2011. Quantitative Analysis Involving Scaling Procedures for Integration Between History Matching and 4D Seismic. Paper presented at the SPE Europec/EAGE Annual Conference and Exhibition, Vienna, Austria. 23-26 May 2011
- Ayzenberg, M., Hustoft, L., Skjei, N. and Feng, T. 2013. Seismic 4D Inversion for Quantitative Use in Automated History Matching. Paper presented at the SPE Europec/EAGE Annual Conference and Exhibition, London, UK. 10 - 13 June, 2013
- B ck, T. 1996. *Evolutionary algorithms in theory and practice: Evolution strategies, evolution programming, genetic algorithms*, Oxford University Press, Oxford.
- Bostanci, E. 2014. Is Hamming distance only way for matching binary image feature descriptors? *Electronics Letters*, **50**(11), 806–808.
- Calvert, M., Roende, H., Herbert, I., Za, J., Hickman, P. and Micksch, U. 2014. The impact of a quick 4D seismic survey and processing over the Halfdan Field, Danish North Sea. *First Break*, **32**(4), 43–50.
- Clifford, P. J., Trythall, R., Parr, R. S., Moulds, T. P., Cook, T. and Allan, P. M. 2003. Integration of 4D Seismic Data into the Management of Oil Reservoirs with Horizontal Wells between Fluid Contacts. Paper presented at the Offshore Europe Oil and Gas Exhibition and Conference, Aberdeen, United Kingdom. September 2, 2003 - September 5, 2003
- Emerick, A. A., Moraes, R. and Rodrigues, J. 2007. History Matching 4D Seismic Data with Efficient Gradient Based Methods. Paper presented at the SPE Europec/EAGE Annual Conference and Exhibition, London, United Kingdom. 11-14 June 2007
- Falahat, R., Obidegwu, D., Shams, A. and MacBeth, C. 2014. The interpretation of amplitude changes in 4D seismic data arising from gas exsolution and dissolution. *Petroleum Geoscience*, **20**(3), 303–320.
- Floridich, M. 2006. *An engineering-consistent approach for pressure and saturation estimation from time-lapse seismic data*. PhD thesis, Heriot Watt University.
- Gosselin, O., Aanonsen, S. I., Aavatsmark, I., Cominelli, A., Gonard, R., Kolasinski, M., Ferdinandi, F., Kovacic, L. and Neylon, K. 2003. History Matching Using Time-lapse Seismic (HUTS). Paper presented at the SPE Annual Technical Conference and Exhibition, Denver, Colorado, U.S.A. 5 - 8 October, 2003
- Govan, A. H., Primmer, T., Douglas, C. C., Moodie, N., Davies, M. and Nieuwland, F. 2006. Reservoir Management in a Deepwater Subsea Field--The Schiehallion Experience. *SPE Reservoir Evaluation and Engineering*, **9**(04), 382–390.
- Jack, I., Barkved, O. I., and Kommedal, J. H. 2010. The Life-of-Field Seismic System at Valhall, Norwegian Sea. In Chapter 6: The Road Ahead. In Johnston, D. H. (ed.) *Methods and Applications in Reservoir Geophysics*. SEG Investigations in Geophysics, 15. Society of Exploration Geophysicists, Tulsa, OK, 483–625
- Hamming, R. W. 1950. Error detecting and error correcting codes. *Bell System technical journal*, **29**(2), 147–160.
- Hatchell, P., Kelly, S., Muerz, M., Jones, T., Engbers, P., Van der Veecken, J. and Staples, R. 2002.

- Comparing time-lapse seismic and reservoir model predictions in producing oil and gas fields. Paper presented at the 64th EAGE Conference & Exhibition, Florence, Italy. 27 - 30 May, 2002
- Huang, X. and Lin, Y. 2006. Production Optimization Using Production History And Time-lapse Seismic Data. Paper presented at the SEG Annual Meeting, New Orleans, Louisiana, U.S.A. 1 - 6 October, 2006
- Jin, L., Castineira, D., Fu, S., Van Den Hoek, P., Pirmez, C., Fehintola, T., Tendo, F. and Olaniyan, E. 2011. 4D seismic history matching using flood front information. Paper presented at the SPE Europec/EAGE Annual Conference and Exhibition, Vienna, Austria. 23 - 26 May, 2011
- Jin, L., Weber, D., van den Hoek, P., Alpak, F. O. and Pirmez, C. 2012. 4D Seismic history matching using information from the flooded zone. *First Break*, **30**(7), 55–60.
- Kazemi, A., Stephen, K. D. and Shams, A. 2011. Improved Normalization of Time-lapse Seismic Data using NRMS Repeatability Data to Improve Automatic Production and Seismic History Matching in the Nelson Field. Paper presented at the SPE Europec/EAGE Annual Conference and Exhibition, Austria, Vienna. 23 -26 May, 2011
- Kragh, E. and Christie, P. 2001. Seismic Repeatability, Normalized RMS And Predictability. Paper presented at the SEG International Exposition and Annual Meeting, San Antonio, Texas. 9 - 14 September, 2001
- Kretz, V., Le Ravalec-Dupin, M. and Roggero, F. 2004. An Integrated Reservoir Characterization Study Matching Production Data and 4D Seismic. *SPE Reservoir Evaluation and Engineering*, **7**(02), 116–122.
- Lancaster, S. and Whitcombe, D. 2000. Fast-track 'coloured' Inversion. Paper presented at the SEG Annual Meeting, Calgary, Alberta. 6 - 11 August 2000
- Landa, J. L. 1997. *Reservoir parameter estimation constrained to pressure transients, performance history and distributed saturation data*. PhD thesis, Stanford University.
- Landa, J. L. and Horne, R. N. 1997. A Procedure to Integrate Well Test Data, Reservoir Performance History and 4-D Seismic Information into a Reservoir Description. Paper presented at the SPE Annual Technical Conference and Exhibition, San Antonio, Texas, U.S.A. 5 - 8 October, 1997
- Landa, J. L., Kalia, R. K., Nakano, A., Nomura, K. and Vashishta, P. 2005. History Match and Associated Forecast Uncertainty Analysis - Practical Approaches Using Cluster Computing. Paper presented at the International Petroleum Technology Conference, Doha, Qatar. 21 - 23 November, 2005
- Landa, J. L. and Kumar, D. 2011. Joint Inversion of 4D Seismic and Production Data. Paper presented at the SPE Annual Technical Conference and Exhibition, Denver, Colorado, U.S.A. 30 October - 2 November 2011
- Landrø, M. 2001. Discrimination between pressure and fluid saturation changes from time-lapse seismic data. *Geophysics*, **66**(3), 836–844.
- Le Ravalec, M., Da Veiga, S., Derfoul, R., Ench ry, G., Gervais, V. and Roggero, F. 2012. Integrating data of different types and different supports into reservoir models. *Oil & Gas Science and Technology–Revue d'IFP Energies nouvelles*, **67**(5), 823–839.
- Liu, N., Betancourt, S. and Oliver, D. S. 2001. Assessment of Uncertainty Assessment Methods. Paper presented at the SPE Annual Technical Conference and Exhibition, New Orleans, Louisiana, U.S.A. 30 September - 3 October 2001
- Lygren, M., Halvorsen, K. ., Randen, T., Sønneland, L., Dahl, G. V., Lindeberg, E. and Bergmo, P. 2002. History Matching of CO2 Flow Models Using Seismic Modeling And Time-lapse Data. Paper presented at the SEG International Exposition and Annual Meeting, Salt Lake City, Utah, U.S.A. 6 - 11 October, 2002

- MacBeth, C., Soldo, J. and Floricich, M. 2004. Going Quantitative With 4D Seismic Analysis. Paper presented at the SEG International Exposition and Annual Meeting, Denver, Colorado, U.S.A. 10 - 15 October, 2004
- Martin, K. and Macdonald, C. 2010. The Schiehallion field: applying a geobody modelling approach to piece together a complex turbidite field. Paper presented at the DEVEX conference, Aberdeen, Scotland, U.K. 12 - 13 May 2010
- Obidegwu, D. C., Chassagne, R. L. and Macbeth, C. 2014. Using 4D Seismic Surveys and History Matching to Estimate Critical and Maximum Gas Saturation. Paper presented at the International Petroleum Technology Conference, Kuala Lumpur, Malaysia. 10 - 12 December, 2014
- Oliver, D. S. and Chen, Y. 2011. Recent progress on reservoir history matching: a review. *Computational Geosciences*, **15**(1), 185–221.
- Pele, O. and Werman, M. 2008. Robust real-time pattern matching using bayesian sequential hypothesis testing. *Pattern Analysis and Machine Intelligence, IEEE Transactions*, **30**(8), 1427–1443.
- Portella, R. C. M. and Emerick, A. A. 2005. Use of Quantitative 4D-Seismic Data in Automatic History Match. Paper presented at the SPE Latin American and Caribbean Petroleum Engineering Conference, Rio de Janeiro, Brazil. 20 - 23 June 2005
- Roggero, F., Ding, D. Y., Berthet, P., Lerat, O., Cap, J. and Schreiber, P.-E. 2007. Matching of Production History and 4D Seismic Data--Application to the Girassol Field, Offshore Angola. Paper presented at the SPE Annual Technical Conference and Exhibition, Anaheim, California, U.S.A. 11 - 14 November, 2007
- Roggero, F., Lerat, O., Ding, D. Y., Berthet, P., Bordenave, C., Lefevre, F. and Perfetti, P. 2012. History Matching of Production and 4D Seismic Data: Application to the Girassol Field, Offshore Angola. *Oil & Gas Science and Technology--Revue d'IFP Energies nouvelles*, **67**(2), 237–262.
- Romero, C. E., Carter, J. N., Zimmerman, R. W. and Gringarten, A. C. 2000. Improved Reservoir Characterization through Evolutionary Computation. Paper presented at the SPE Annual Technical Conference and Exhibition, Dallas, Texas, U.S.A. 1 - 4 October, 2000
- Rukavishnikov, V. and Kurelenkov, S. 2012. Dynamic Cluster Analysis for Updating Simulation Model Using Time-lapse Seismic. Paper presented at the SPE Europe/EAGE Annual Conference and Exhibition, Copenhagen, Denmark. 4 - 7 June 2012
- Sahni, I. and Horne, R. N. 2006. Generating Multiple History-Matched Reservoir-Model Realizations Using Wavelets. *SPE Reservoir Evaluation and Engineering*, **9**(3), 217–226.
- Schulze-Riegert, R. and Ghedan, S. 2007. Modern techniques for history matching. Paper presented at the 9th International Forum on Reservoir Simulation, Abu Dhabi, United Arab Emirates. 9 - 13 December, 2007
- Soleng, H. H. 1999. Oil reservoir production forecasting with uncertainty estimation using genetic algorithms. Paper presented at the Evolutionary Computation, Washington DC, U.S.A. 6 - 9 July, 1999
- Staples, R., Hague, P., Cooke, G., Ashton, P., Stammeijer, J., Jolley, S., Stevens, T. and Marshall, J. 2002. Integrating 4D Seismic to Optimize Production. Paper presented at the SPE European Petroleum Conference, Aberdeen, Scotland, U.K. 29 - 31 October 2002
- Staples, R., Stevens, T., Leoutre, E., Jolley, S. and Marshall, J. 2005. 4D seismic history matching—the reality. Paper presented at the 67th EAGE Conference & Exhibition, Madrid, Spain. 13 - 16 June 2005
- Stephen, K. D. and MacBeth, C. 2006. Seismic history matching in the UKCS Schiehallion field. *First Break*, **24**(4), 43–49.

- Stephen, K. D., Soldo, J., Macbeth, C. and Christie, M. A. 2005. Multiple Model Seismic and Production History Matching: a case study. Paper presented at the 14th Europec Biennial Conference, Madrid, Spain. 13 - 16 June, 2005
- Tillier, E., Da Veiga, S. and Derfoul, R. 2013. Appropriate formulation of the objective function for the history matching of seismic attributes. *Computers and Geosciences*, **51**, 64–73.
- Tillier, E., Le Ravalec, M. and Da Veiga, S. 2012. Simultaneous inversion of production data and seismic attributes: Application to a synthetic SAGD produced field case. *Oil & Gas Science and Technology—Revue d'IFP Energies nouvelles*, **67**(2), 289–301.
- Vasco, D. W., Datta-Gupta, A., Behrens, R., Condon, P. and Rickett, J. 2004. Seismic imaging of reservoir flow properties: Time-lapse amplitude changes. *Geophysics*, **69**(6), 1425–1442.
- Waggoner, J. R., Cominelli, A. and Seymour, R. H. 2002. Improved Reservoir Modeling With Time-Lapse Seismic in a Gulf of Mexico Gas Condensate Reservoir. Paper presented at the SPE Annual Technical Conference and Exhibition, San Antonio, Texas, U.S.A. 29 September - 2 October, 2002
- Walker, G., Allan, P., Trythall, R., Parr, R., Marsh, M., Kjelstadli, R., Barkved, O., Johnson, D. and Lane, S. 2006. Three case studies of progress in quantitative seismic-engineering integration. *The Leading Edge*, **25**(9), 1161–1166.
- Walker, G. J. and Lane, H. S. 2007. Assessing the Accuracy of History-Match Predictions and the Impact of Time-Lapse Seismic Data: A Case Study for the Harding Reservoir. Paper presented at the SPE Reservoir Simulation Symposium, Houston, Texas, U.S.A. 26 - 28 February 2007
- Wang, Y. and Kovscek, A. R. 2002. A Streamline Approach for Ranking Reservoir Models that Incorporates Production History. Paper presented at the SPE Annual Technical Conference and Exhibition, San Antonio, Texas, U.S.A. 29 September - 2 October, 2002
- Wen, X.-H., Lee, S. and Yu, T. 2006. Simultaneous integration of pressure, water cut, 1 and 4-D seismic data in geostatistical reservoir modeling. *Mathematical Geology*, **38**(3), 301–325.
- Williams, G. J. J., Mansfield, M., MacDonald, D. G. and Bush, M. D. 2004. Top-Down Reservoir Modelling. Paper presented at the SPE Annual Technical Conference and Exhibition, Houston, Texas, U.S.A. 26 - 29 September 2004
- Zhao, Y., Wang, S., Feng, G. and Tang, Z. 2010. A robust image hashing method based on Zernike moments. *Journal of Computational Information Systems*, **6**(3), 717–725.
- Zubarev, D. I. 2009. Pros and Cons of Applying Proxy-models as a Substitute for Full Reservoir Simulations. Paper presented at the SPE Annual Technical Conference and Exhibition, New Orleans, Louisiana, U.S.A. 4 - 7 October, 2009



We LHR2 14

Comparative Analysis of Binary and Conventional Seismic Assisted History Matching

D. Obidegwu* (Heriot-Watt University), C. MacBeth (Heriot-Watt University) & R. Chassagne (Heriot-Watt University)

SUMMARY

A comparative analysis of seismic assisted history matching techniques using binary image matching and conventional seismic modelling methods is performed. This analysis is conducted on field data from a United Kingdom Continental Shelf (UKCS), and has production data available for ten years. There is a seismic baseline that was acquired preproduction, and six seismic monitor surveys were acquired between one and two year intervals. The production data objective function is calculated using the least squares method between the historical production data and simulation predictions. The seismic data objective function is calculated using the *Current* measurement metric in the binary approach, and compared to the conventional seismic modelling route. Seismic modelling shows some improvement in the match, but not as significant as the binary approach which demonstrates a better forecasting capability. The study also found that a greater proportion of the parameters converge towards the correct solution when using the binary approach. It is observed that for both methods, combining both production and seismic data improves the history match and reduces uncertainties, as opposed to not combining them.



Introduction

In order to implement a seismic assisted history matching scheme, the 4D seismic data has to be integrated into the history matching loop. This paper explores the integration of 4D seismic data using gas and water binary representations, and compares this to the seismic modelling route. The *Current* measurement metric is used to determine the mismatch between the binary seismic and the binary simulation images of saturation (gas and water) distribution predictions, while the modelled 4D seismic data response is compared to the observed 4D seismic data. The production data is also matched using the least squares objective function calculated between the historical production data and the simulation predictions. The field data analysed is from the United Kingdom Continental Shelf (UKCS) (Martin and MacDonald, 2010). The main feature of the data is that the reservoir pressure is close to its bubble point pressure, such that the commencement of production activities leads to depressurisation and gas ex-solution, and that there is a subsequent pressure maintenance scheme in place by the use of water injector wells, so there will be water sweep expected in the reservoir. The reservoir permeability is in the range of 200 mD to 2000 mD, with a reservoir porosity ranging from 25% to 30%. The pore compressibility is $7 \times 10^{-6} \text{ psi}^{-1}$, oil viscosity is 3.5 cp at reservoir temperature, water viscosity is 0.5 cp at reservoir temperature, and the oil formation volume factor is 1.16 rb/stb. There are 10 years of production activity from 1998 to 2008, and it should be noted that the history matching will be implemented for the first seven years, while the remaining three years will be used to validate the history matching process and forecasting ability.

Description of overall methodology

When conducting a history matching exercise, pertinent reservoir parameters have to be perturbed such that the result of the simulation model output corresponds to the observed historical data. Over the years of production in this reservoir, it has been observed that the major challenges to the field development and management plan are the field connectivity and the representation of its numerous geobodies. These geobodies were derived from the 3D seismic interpretation and used for geological model construction. A sensitivity study starting with 104 parameters was implemented to determine which parameters and geobodies were most significant to the seismic assisted history matching objective function. Combining the geobody regions and global parameters, 35 parameters were identified for the history matching exercise. These include the permeability multipliers, porosity multipliers, net-to-gross multipliers, pore volume multipliers, geobody transmissibility multipliers, connate water saturation and critical gas saturation. The starting values of the parameters are the initial values, while the ranges are selected generally based on engineering judgement, and such that the perturbed model remains physically and geologically meaningful and consistent with the present understanding of the field. An initial ensemble of fluid flow simulation models is created where the full range of uncertain parameters are acknowledged using experimental design methods, and an evolutionary algorithm is used for optimization in the history matching process.

Binary approach

The proposed approach converts the observed 4D seismic data to binary seismic gas and water maps. The observed 4D seismic data is initially clustered and separated into 'softening' and 'hardening' signals; historical production data are then superimposed on the maps to aid the interpretation and deciphering of potential gas and water signals due to the injector/producer positioning, as well as the volumes produced that are represented by the size of the bubble plots. Application of these processes leads to the final binary seismic gas and water maps as shown in Figure 1. The softening and hardening signals on seismic data are represented by red and blue colours respectively. The softening signal is as a consequence of pressure increase or gas saturation increase. In broad terms, a drainage process will give rise to a softening signal due to the different elastic properties of the fluids, as a non-wetting phase fluid displaces a wetting phase fluid, i.e. gas displacing oil or water, or oil displacing water. Conversely, a hardening signal is as a consequence of pressure decrease or an imbibition process, where a wetting phase fluid displaces a non-wetting phase fluid, i.e. water displacing oil or

gas, or oil displacing gas. For binary seismic gas and water maps, a change in the saturation values are represented by a value of one, while no change is represented by a value of zero. A region exists that is characterised as ambiguous signal or noise, and this is not captured by this binary approach. The pore volume weighted gas and water saturation difference maps (monitor year minus baseline year) are also generated from the simulation model and then converted to binary simulation gas and water maps, where a value of one represents presence of gas or water respectively, and zero represents an absence of gas and water respectively. In order to convert the pore-volume weighted gas and water saturation from the simulation model and the 4D seismic data to binary maps, cut-off values representing thresholds need to be obtained. These can be derived from a calibration exercise using seismic forward modelling, or by interactive interpretation which requires a clear understanding of the 4D seismic response in terms of the dynamic behaviour of the reservoir (Jin et al., 2012). A combination of both methods is utilised here, where seismic forward modelling is used to determine the initial threshold values in collaboration with *k*-means clustering; then integration of reservoir engineering knowledge, injector and producer well activities, reservoir geology and structural contour, as well as 4D seismic concepts are applied to generate the final binary maps.

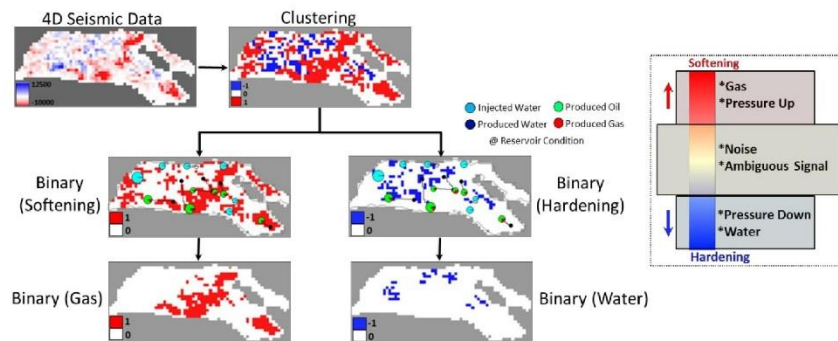


Figure 1 The process of generating the binary (gas and water) maps from the 4D seismic data. The 4D seismic data are initially clustered and separated into ‘hardening’ and ‘softening’ signals; historical production data are then introduced to aid the interpretation and deciphering of potential gas and water signals due to the injector/producer positioning, as well as the volumes produced which are represented by the size of the bubble plots. Application of these processes leads to the final seismic binary gas and water maps. Inset shows the 4D seismic colour bar and the associated physical interpretation.

The binary seismic maps (gas and water) are compared to those predicted from the simulation maps using a binary seismic objective function - *Current* measurement metric. This metric is more flexible in detecting a wide range of differences between two images as opposed to a more traditional metric. The objective function is calculated on the simulation model scale, so the 4D seismic data is arithmetically upscaled to the simulation model scale. The *Current* measurement metric (Glaunès, 2005) between two images can be computed as the Euclidean norm of a filtered difference between the two images, where the filter is similar to a smoothing kernel. Mathematically, the *Current* measurement metric for binary images is represented by equation (1).

$$H_{CMM} = \sum_{i,j=1}^N K_{ij} |\widehat{A}_{ij} - \widehat{B}_{ij}|^2 \quad (1)$$

where \widehat{A}_{ij} and \widehat{B}_{ij} denote the (i,j) -th Fourier coefficients of A and B , and K is the aforementioned smoothing kernel. Production data and binary seismic data (gas and water) are history matched, and the combined objective function is normalised such that the effect of the production data and binary

seismic data (gas and water) are equal. After history matching to both production data and binary seismic data (gas and water), the production profiles and the updated binary simulation maps have improvement (Figure 2). The parameters converge towards a solution, and the objective function and uncertainty reduces. The forecast period will be used in the comparative forecast analysis.

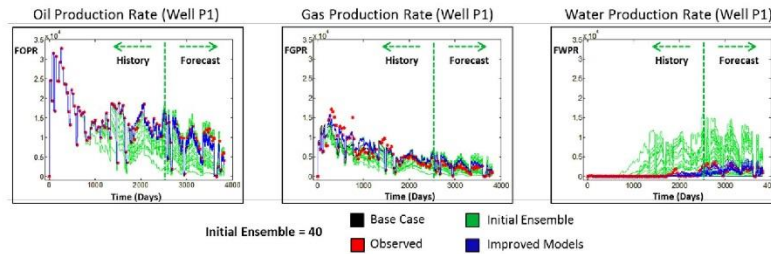


Figure 2 Normalized production profiles for well P1 history matched to production data and binary seismic maps.

Seismic modelling approach

For the seismic modelling, the relationship between seismic data and average maps of reservoir dynamic properties (pressure distribution, water saturation and gas saturation) derived from MacBeth et al. (2004) and Fursov (2015), and shown in equation (2) is used

$$\Delta A = \begin{pmatrix} a_p \Delta P + a_{sw} \Delta Sw + a_{sg} \Delta Sg + a_{pSw} \Delta P \Delta Sw + a_{pSg} \Delta P \Delta Sg + \\ a_{pp} \Delta P^2 + a_{swsw} \Delta Sw^2 + a_{sgsg} \Delta Sg^2 \end{pmatrix} A_o \quad (2)$$

where, ΔA is the time lapse seismic map, ΔP is the change in pressure distribution, ΔSw and ΔSg are the change in water and gas saturation respectively, A_o is the baseline seismic map which captures the effects of the static properties. The coefficients for the linear and quadratic terms are determined by regression between the data ΔA and the individual simulation model predictions. The production data and modelled seismic data are jointly history matched, and there is improvement in the history match. Interestingly, the modelled seismic data are able to capture the major hardening and softening signals on the observed seismic data as shown in Figure 3. The first 4 monitors (the first four rows) are used for the history matching exercise, while the last 2 monitors (the last 2 rows) are used for the forecasting analysis. Some of the parameters converge towards a solution, and the objective function and uncertainty reduces. The forecast period will be used in the comparative forecast analysis.

Comparative analysis and conclusions

A comparison of the results of the binary seismic assisted history matching approach and conventional seismic assisted history matching approach is done in terms of convergence of parameters, objective function and uncertainty, and the forecast capabilities. The parameters converge to a solution when using the binary approach, but do not fully converge to a solution when using the conventional approach. Also, the binary approach shows a better reduction in the objective function and uncertainty, as opposed to a fair reduction when using the conventional approach. The overall forecast percentage improvement for the binary approach is 46%, while that for the conventional approach is 38%. The well data forecast improvement for the binary approach is 58%, in contrast with the well data forecast improvement for the conventional approach which is 44%. The binary approach gives a good match to the gas saturation distribution and water saturation distribution, and the conventional approach captures the hardening and softening signals in some areas in the seismic data.

Based on the analysis, it is concluded that the binary approach for seismic assisted history matching is the preferred method, and seems more suitable as a quick look reservoir management tool, as it circumvents the use of the complex seismic modelling approach, however, the conventional approach explored here has shown positive potential and will be further investigated.

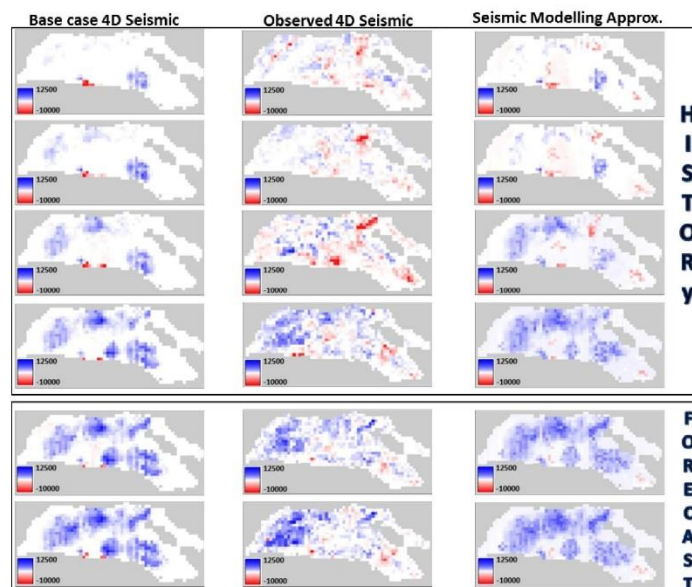


Figure 3 The base case 4D seismic maps, observed 4D seismic maps, and history matched maps using seismic modelling for all the relevant time-steps.

Acknowledgements

We thank the sponsors of the Edinburgh Time-Lapse Project Phase V and VI (BG, BP, CGG, Chevron, ConocoPhillips, ENI, ExxonMobil, Hess, Ikon Science, Landmark, Maersk, Nexen, Norsar, Petoro, Petrobras, RSI, Shell, Statoil, Suncor, Taqa, TGS and Total) for supporting this research. Special thanks to BP for providing the data set. We thank Schlumberger for their Petrel, Eclipse and Mepo Software.

References

- Fursov, I. 2015. Quantitative application of 4D seismic data for updating thin-reservoir models. PhD thesis, Heriot Watt University.
- Glaunès, J. 2005. Transport par difféomorphismes de points, de mesures et de courants pour la comparaison de formes et l'anatomie numérique. PhD thesis, Université Paris.
- Jin, L., Weber, D., van den Hoek, P., Alpak, F. O. and Pirmez, C. 2012. 4D Seismic history matching using information from the flooded zone. *First Break*, **30** (7), 55-60.
- MacBeth, C., Soldo, J. and Floricich, M. 2004. Going Quantitative With 4D Seismic Analysis. Paper presented at the SEG International Exposition and Annual Meeting, Denver, U.S.A. 10 - 15 October, 2004
- Martin K. and MacDonald C., 2010. Schiehallion Field: Applying a geobody modelling approach to piece together a complex turbidite reservoir. 7th European Production and Development Conference, UK.

References

- Aanonsen, S. I., Aavatsmark, I., Barkve, T., Cominelli, A., Gonard, R., Gosselin, O., Kolasinski, M. and Reme, H. 2003. Effect of Scale Dependent Data Correlations in an Integrated History Matching Loop Combining Production Data and 4D Seismic Data. Paper presented at the SPE Reservoir Simulation Symposium, Houston, Texas, U.S.A. 3 - 5 February 2003
- Aggio, A. and Burns, S. 2001. Seismic visualization for dynamic and static reservoir characterization. Paper presented at the EAGE 63rd Conference and Technical Exhibition, Amsterdam, The Netherlands. 11 - 15 June, 2001
- Ahmed, T. 2006. Reservoir engineering handbook (3rd edition), Gulf Professional Publishing.
- Aki, K. and Richards, P. 1980. Quantitative Seismology: Theory and Methods. *Volume I: WH Freeman & Co.*
- Alerini, M., Ayzenberg, M., Ek, T., Feng, T., Hustoft, L., Lie, E., Liu, S., Skjei, N. and Skjervheim, J. A. 2014. Utilization of time-lapse seismic for reservoir model conditioning. Paper presented at the SPE Europec/EAGE Annual Conference and Exhibition, Amsterdam, Netherlands. 16-19 June 2014
- Alsos, T., Osdal, B. and Høiås, A. 2009. The many faces of pressure changes in 4D seismic at the Svale Field and its implication on reservoir management. Paper presented at the 71st EAGE Conference & Exhibition, Amsterdam, The Netherlands. 8 - 11 June, 2009

- Amini, H. 2014. A pragmatic approach to simulator to seismic modelling for 4D seismic interpretation. PhD thesis, Heriot Watt University.
- Amini, H., MacBeth, C. and Shams, A. 2011. Calibration of Simulator to Seismic Modeling for Quantitative 4D Seismic Interpretation. Paper presented at the 73rd EAGE Conference & Exhibition, Vienna, Austria. 23–26 May 2011
- Aranha, C., Tanabe, R., Chassagne, R. and Fukunaga, A. 2015. Optimization of oil reservoir models using tuned evolutionary algorithms and adaptive differential evolution. Paper presented at the IEEE Congress on Evolutionary Computation (CEC), 2015
- Arenas, E., van Kruijsdijk, C. and Oldenziel, T. 2001. Semi-Automatic History Matching Using the Pilot Point Method Including Time-Lapse Seismic Data. Paper presented at the SPE Annual Technical Conference and Exhibition, New Orleans, Louisiana, USA. 30 September - 3 October 2001
- Avansi, G. D. and Schiozer, D. J. 2011. Quantitative Analysis Involving Scaling Procedures for Integration Between History Matching and 4D Seismic. Paper presented at the SPE Europec/EAGE Annual Conference and Exhibition, Vienna, Austria. 23-26 May 2011
- Avansi, G. D., Souza, R. M. and Schiozer, D. J. 2010. Scaling Issues Through Quantitative Analysis Between Reservoir Simulation. Paper presented at the SPE EUROPEC/EAGE Annual Conference and Exhibition, Barcelona, Spain. 14-17 June, 2010

- Ayzenberg, M., Hustoft, L., Skjei, N. and Feng, T. 2013. Seismic 4D Inversion for Quantitative Use in Automated History Matching. Paper presented at the SPE Europec/EAGE Annual Conference and Exhibition, London, UK. 10 - 13 June, 2013
- Bäck, T. 1996. Evolutionary algorithms in theory and practice: Evolution strategies, evolution programming, genetic algorithms, Oxford University Press, Oxford.
- Bagley, G., Saxby, I., McGarrity, J., Pearse, C. and Slater, C. 2004. 4D/time-lapse seismic: examples from the Foinaven, Schiehallion and Loyal Fields, UKCS, West of Shetland. *Geological Society, London, Memoirs*, **29** (1), 297-302.
- Bansal, P. 1988. Sensitivity Of Simulation Results To PVT Data, Rock Compressibility And Critical Gas Saturation. *SPE Journal*.
- Baudrier, E., Millon, G., Nicolier, F. and Ruan, S. 2004. The adaptative local hausdorff-distance map as a new dissimilarity measure. *Pattern Recognition*, **41**, 1461-1478.
- Beecroft, W., Mani, V., Wood, A. and Rusinek, I. 1999. Evaluation of depressurisation, Miller field, North sea. Paper presented at the SPE annual technical conference, Houston, Texas, USA. 3–6 October 1999
- Bertolini, A. C. and Schiozer, D. J. 2011. Influence of the objective function in the history matching process. *Journal of Petroleum Science and Engineering*, **78** (1), 32-41.

- Blunt, M. J. 2000. An Empirical Model for Three-Phase Relative Permeability. *SPE Journal*, **5** (04), 435 - 445.
- Blunt, M. J. 2001. Flow in porous media — pore-network models and multiphase flow. *Current Opinion in Colloid & Interface Science*, **6** (3), 197-207.
- Boge, R., Lien, S. K., Gjesdal, A. and Hansen, A.-G. 2005. Turning a North Sea oil giant into a gas field - Depressurization of the Statfjord Field. Paper presented at the Offshore Europe, Aberdeen, UK. 6 - 9 September, 2005
- Bondino, I., McDougall, S. R. and Hamon, G. 2002. Pore network modelling of heavy oil depressurisation: a parametric study of factors affecting critical gas saturation and 3-phase relative permeabilities. Paper presented at the SPE International Thermal Operations and Heavy Oil Symposium and International Horizontal Well Technology Conference, Calgary, Alberta, Canada. 4-7 November, 2002
- Bouzarkouna, Z. and Nobakht, B. N. K. 2015. A Better Formulation of Objective Functions for History Matching Using Hausdorff Distances. Paper presented at the SPE Europec/EAGE Annual Conference and Exhibition, Madrid, Spain. 01-04 June, 2015
- Brun, B., Gosselin, O. and Barker, J. W. 2001. Use of Prior Information in Gradient-Based History-Matching. Paper presented at the SPE Reservoir Simulation Symposium, Houston, Texas, USA. 11-14 February, 2001
- Cairns, G., Jakubowicz, H., Lonergan, L. and Muggeridge, A. 2012. Using time-lapse seismic monitoring to identify trapping mechanisms during CO₂ sequestration. *International Journal of Greenhouse Gas Control*, **11**, 316-325.

- Calvert, M., Roende, H., Herbert, I., Za, J., Hickman, P. and Micksch, U. 2014. The impact of a quick 4D seismic survey and processing over the Halfdan Field, Danish North Sea. *First Break*, **32** (4), 43 - 50.
- Carlson, M. 2003. Practical reservoir simulation: using, assessing, and developing results, PennWell Books.
- Castro, S. A. 2007. A probabilistic approach to jointly integrate 3D/4D seismic, production data and geological information for building reservoir models. PhD thesis, Stanford University.
- Chassagne, R. L. and Hammond, P. 2012. Simulation of Drilling Fluid Filtrate Invasion Near an Observation Well. *SPE Journal*, **17** (04), 1047 - 1055.
- Chen, Y. 2008. Efficient Ensemble based Reservoir Management. PhD thesis, University of Oklahoma, USA.
- Chesseboeuf, J. 2015. Transport par difféomorphismes de points, de mesures et de courants pour la comparaison de formes et l'anatomie numérique. PhD thesis, Université Paris.
- Christie, M. A. and Blunt, M. J. 2001. Tenth SPE Comparative Solution Project: A Comparison of Upscaling Techniques. *SPE Reservoir Evaluation & Engineering*, **4** (04), 308 - 317.
- Clifford, P. J., Trythall, R., Parr, R. S., Moulds, T. P., Cook, T. and Allan, P. M. 2003. Integration of 4D Seismic Data into the Management of Oil Reservoirs with Horizontal Wells between Fluid Contacts. Paper presented at the Offshore

Europe Oil and Gas Exhibition and Conference, Aberdeen, United Kingdom.
September 2, 2003 - September 5, 2003

Closmann, P. 1987. Studies of critical gas saturation during gas injection. *SPE Reservoir Engineering*, **2** (03), 387-393.

Dake, L. P. 2001. The practice of reservoir engineering (revised edition), Elsevier.

Danesh, A. 1998. PVT and phase behaviour of petroleum reservoir fluids, Elsevier.

Davolio, A., Maschio, C. and Schiozer, D. J. 2014. A methodology to calibrate water saturation estimated from 4D seismic data. *Journal of Geophysics and Engineering*, **11** (5), 1 - 16.

Domenico, S. N. 1977. Effect Of Brine-gas Mixture On Velocity In An Unconsolidated Sand Reservoir. *Developments in Seismic Data Handling and Interpretation*, 235 - 245.

Dowson, N. and Bowden, R. 2004. Metric mixtures for mutual information (M 3 I) tracking. Paper presented at the 17th International Conference on Pattern Recognition, Cambridge, UK. 23 - 26 August 2004

Drummond, A., Fishlock, T., Naylor, P. and Rothkopf, B. 2001. An evaluation of post-waterflood depressurisation of the south Brae field, North Sea. Paper presented at the SPE Annual Technical Conference and Exhibition, New Orleans, Louisiana, USA. 30 September - 3 October 2001

- Edwards, J., Honarpour, M., Hazlett, R., Cohen, M., Membere, A., Pebdani, F., Clayton, C. and Al-Hussainy, R. 1998. Validation of gravity-dominated relative permeability and residual oil saturation in a giant oil reservoir. Paper presented at the SPE Annual Technical Conference and Exhibition, New Orleans, Louisiana, USA. 27 - 30 September 1998
- Elde, R. M., Haaland, A. N., Ro, H. E., Ystad, B. and Zachariassen, E. 2000. Troll West - Reservoir Monitoring by 4D Seismic. Paper presented at the SPE European Petroleum Conference, Paris, France. 24-25 October, 2000
- Emerick, A. A., Moraes, R. and Rodrigues, J. 2007. History Matching 4D Seismic Data with Efficient Gradient Based Methods. Paper presented at the SPE Europec/EAGE Annual Conference and Exhibition, London, United Kingdom. 11- 14 June 2007
- Enchery, G., Le Ravalec-Dupin, M. and Roggero, F. 2007. An Improved Pressure and Saturation Downscaling Process for a Better Integration of 4D Seismic Data together with Production History. Paper presented at the SPE Europec/EAGE Annual Conference and Exhibition, London, UK. 11-14 June, 2007
- Fagervik, K., Lygren, M., Valen, T., Hetlelid, A., Berge, G., Dahl, G., Sønneland, L., Lie, H. and Magnus, I. 2001. History Matching of Reservoir Flow Models using 4D Seismic. Paper presented at the 63rd EAGE Conference & Exhibition, Amsterdam, The Netherlands. 11 - 15 June, 2001
- Falahat, R. 2012. Quantitative monitoring of gas injection, exsolution and dissolution using 4D seismic. PhD thesis, Heriot Watt University.

- Falahat, R., Shams, A. and MacBeth, C. 2011. Towards quantitative evaluation of gas injection using time-lapse seismic data. *Geophysical Prospecting*, **59** (2), 310-322.
- Falcone, G., Gosselin, O., Maire, F., Marrauld, J. and Zhakupov, M. 2004. Petroelastic Modelling as Key Element of 4D History Matching: A Field Example. Paper presented at the SPE Annual Technical Conference and Exhibition, Houston, Texas, USA. 26 -29 September, 2004
- Faseemo, O. and Onyema, U. 2013. Saturation History Match Update of Ofon Field Reservoir Model Using Dynamic Parameters. Paper presented at the SPE Nigeria Annual International Conference and Exhibition, Lagos, Nigeria. 5-7 August, 2013
- Ferreira, C. J., Davolio, A., Schiozer, D. J., Vernon, I. and Goldstein, M. 2015. Use of Emulator and Canonical Correlation to Incorporate 4D Seismic Data in the Reduction of Uncertainty Process. Paper presented at the SPE Europec/EAGE Annual Conference and Exhibition, Madrid, Spain. 01-04 June, 2015
- Ferreira, C. J., Vernon, I., Schiozer, D. J. and Goldstein, M. 2014. Use of Emulator Methodology for Uncertainty Reduction Quantification. Paper presented at the SPE Latin America and Caribbean Petroleum Engineering Conference, Maracaibo, Venezuela. 21-23 May, 2014
- Firoozabadi, A., Ottesen, B. and Mikklesen, M. 1992. Measurements of Supersaturation and Critical Gas Saturation (includes associated papers 27920 and 28669). *SPE Formation Evaluation*, **7** (04), 337-344.

- Florich, M. 2006. An engineering-consistent approach for pressure and saturation estimation from time-lapse seismic data. PhD thesis, Heriot Watt University.
- Florich, M., MacBeth, C., Stammeijer, J., Staples, R., Evans, A. and Dijkstra, C. 2006. A New Technique for Pressure-Saturation Separation from Time-Lapse Seismic-Schiehallion Case Study. Paper presented at the 68th EAGE Conference & Exhibition, Vienna, Austria. 12 - 15 June, 2006
- Fursov, I. 2015. Quantitative application of 4D seismic data for updating thin-reservoir models. PhD thesis, Heriot Watt University.
- Gainski, M., Macgregor, A., Freeman, P. and Nieuwland, H. 2010. Turbidite reservoir compartmentalization and well targeting with 4D seismic and production data: Schiehallion Field, UK. *Geological Society, London, Special Publications*, **347** (1), 89-102.
- Glaunès, J. 2005. Transport par difféomorphismes de points, de mesures et de courants pour la comparaison de formes et l'anatomie numérique. PhD thesis, Université Paris.
- Goodfield, M. and Goodyear, S. G. 2003. Relative Permeabilities for Post-Waterflood Depressurisation. Paper presented at the Offshore Europe, Aberdeen, United Kingdom. 2-5 September, 2003
- Gosselin, O., Aanonsen, S. I., Aavatsmark, I., Cominelli, A., Gonard, R., Kolasinski, M., Ferdinandi, F., Kovacic, L. and Neylon, K. 2003. History Matching Using Time-lapse Seismic (HUTS). Paper presented at the SPE Annual Technical Conference and Exhibition, Denver, Colorado, U.S.A. 5 - 8 October, 2003

- Govan, A. H., Primmer, T., Douglas, C. C., Moodie, N., Davies, M. and Nieuwland, F. 2006. Reservoir Management in a Deepwater Subsea Field--The Schiehallion Experience. *SPE Reservoir Evaluation and Engineering*, **9** (04), 382 - 390.
- Hamming, R. W. 1950. Error detecting and error correcting codes. *Bell System technical journal*, **29** (2), 147-160.
- Han, D.-h. and Batzle, M. 2000a. Velocity, Density and Modulus of Hydrocarbon Fluids--Data Measurement. Paper presented at the Society of Exploration Geophysicist (SEG) Annual Meeting, Tulsa, Oklahoma, USA.
- Han, D.-h. and Batzle, M. 2000b. Velocity, Density And Modulus of Hydrocarbon Fluids--Empirical Modeling. Paper presented at the 2000 SEG Annual Meeting, Tulsa, Oklahoma, USA.
- Hatchell, P., Kelly, S., Muerz, M., Jones, T., Engbers, P., Van der Veecken, J. and Staples, R. 2002. Comparing time-lapse seismic and reservoir model predictions in producing oil and gas fields. Paper presented at the 64th EAGE Conference & Exhibition, Florence, Italy. 27 - 30 May, 2002
- Honarpour, M. and Saad, N. 1994. Influence of small-scale rock laminations on core plug oil/water relative permeability and capillary pressure. Paper presented at the University of Tulsa Centennial Petroleum Engineering Symposium, Tulsa, Oklahoma, USA. 29 - 31 August, 1994
- Huang, X. and Lin, Y. 2006. Production Optimization Using Production History And Time-lapse Seismic Data. Paper presented at the SEG Annual Meeting, New Orleans, Louisiana, U.S.A. 1 - 6 October, 2006

- Huang, Y. 2011. Integration of well data into dynamic reservoir interpretation using multiple seismic surveys. PhD thesis, Heriot Watt University.
- Huang, Y., MacBeth, C., Barkved, O. and van Gestel, J.-P. 2011. Enhancing dynamic interpretation at the Valhall Field by correlating well activity to 4D seismic signatures. *First Break*, **29** (3), 37-44.
- Huttenlocher, D. P., Klanderman, G. A. and Rucklidge, W. J. 1993. Comparing images using the Hausdorff distance. *Pattern Analysis and Machine Intelligence, IEEE Transactions on*, **15** (9), 850-863.
- Jack, I., Barkved, O. and Kommedal, J. 2010. The life-of-field seismic system at Valhall, Norwegian Sea. *Chapter*, **6**, 483-625.
- Jin, L., Tiller, G., Weber, D., Fu, S., Ferrandis, J., van den Hoek, P., Pirmez, C., Fehintola, T. O., Tendo, F. and Olaniyan, E. E. 2011. An Integrated Workflow for Quantitative 4D Seismic Data Integration: A Case Study. Paper presented at the International Petroleum Technology Conference (IPTC), Bangkok, Thailand. 7 - 9 February, 2012
- Jin, L., van den Hoek, P. J., Alpak, F. O., Pirmez, C., Fehintola, T., Tendo, F. and Olaniyan, E. E. 2012a. A Comparison of Stochastic Data-Integration Algorithms for the Joint History Matching of Production and Time-Lapse-Seismic Data. *SPE Reservoir Evaluation & Engineering*, **15** (04), 498 - 512.
- Jin, L., Weber, D., van den Hoek, P., Alpak, F. O. and Pirmez, C. 2012b. 4D Seismic history matching using information from the flooded zone. *First Break*, **30** (7), 55-60.

- Johann, P., Sansonowski, R., Oliveira, R. and Bampi, D. 2009. 4D seismic in a heavy-oil, turbidite reservoir offshore Brazil. *The Leading Edge*, **28** (6), 718-729.
- Johnston, D. H. 2013. Practical applications of time-lapse seismic data, Distinguished Instructor Short Course, SEG.
- Johnston, D. H. and Cooper, M. R. 2010. Methods and applications in reservoir geophysics.
- Johnston, D. H., Eastwood, J. E., Shyeh, J. J., Vauthrin, R., Khan, M. and Stanley, L. R. 2000. Using legacy seismic data in an integrated time-lapse study: Lena Field, Gulf of Mexico. *The Leading Edge*, **19** (3), 294-302.
- Joosten, G. J. P., Altintas, A., Van Essen, G., Van Doren, J., Gelderblom, P., van den Hoek, P. and Foreste, K. 2014. Reservoir Model Maturation and Assisted History Matching Based on Production and 4D Seismic Data. Paper presented at the SPE Annual Technical Conference and Exhibition, Amsterdam, The Netherlands. 27 - 29 October, 2014
- Kamath, J. and Boyer, R. 1995. Critical gas saturation and supersaturation in low-permeability rocks. *SPE Formation Evaluation*, **10** (04), 247-254.
- Kazemi, A. 2011. Optimal parameter updating and appropriate 4D seismic normalization in seismic history matching of the nelson field. PhD thesis, Heriot Watt University.
- Kazemi, A., Stephen, K. D. and Shams, A. 2011. Improved Normalization of Time-lapse Seismic Data using NRMS Repeatability Data to Improve Automatic

- Production and Seismic History Matching in the Nelson Field. Paper presented at the SPE Europec/EAGE Annual Conference and Exhibition, Austria, Vienna. 23 -26 May, 2011
- King, M. J. 2007. Upgridding and Upscaling: Current Trends and Future Directions. SPE Distinguished Lecture Series, Society of Petroleum Engineers.
- Kragh, E. and Christie, P. 2001. Seismic Repeatability, Normalized RMS And Predictability. Paper presented at the SEG International Exposition and Annual Meeting, San Antonio, Texas. 9 - 14 September, 2001
- Kretz, V., Le Ravalec-Dupin, M. and Roggero, F. 2004. An Integrated Reservoir Characterization Study Matching Production Data and 4D Seismic. *SPE Reservoir Evaluation and Engineering*, 7 (02), 116 - 122.
- Lancaster, S. and Whitcombe, D. 2000. Fast-track 'coloured' Inversion. Paper presented at the SEG Annual Meeting, Calgary, Alberta, Canada. 6 - 11 August 2000
- Landa, J. L. 1997. Reservoir parameter estimation constrained to pressure transients, performance history and distributed saturation data. PhD thesis, Stanford University.
- Landa, J. L. and Horne, R. N. 1997. A Procedure to Integrate Well Test Data, Reservoir Performance History and 4-D Seismic Information into a Reservoir Description. Paper presented at the SPE Annual Technical Conference and Exhibition, San Antonio, Texas, U.S.A. 5 - 8 October, 1997

- Landa, J. L. and Kumar, D. 2011. Joint Inversion of 4D Seismic and Production Data. Paper presented at the SPE Annual Technical Conference and Exhibition, Denver, Colorado, U.S.A. 30 October - 2 November 2011
- Landrø, M. 2001. Discrimination between pressure and fluid saturation changes from time-lapse seismic data. *Geophysics*, **66** (3), 836-844.
- Le Ravalec, M., Da Veiga, S., Derfoul, R., Enchéry, G., Gervais, V. and Roggero, F. 2012a. Integrating data of different types and different supports into reservoir models. *Oil & Gas Science and Technology—Revue d'IFP Energies nouvelles*, **67** (5), 823-839.
- Le Ravalec, M., Tillier, E., Da Veiga, S., Enchery, G. and Gervais, V. 2012b. Advanced integrated workflows for incorporating both production and 4D seismic-related data into reservoir models. *Oil and Gas Science and Technology*, **67** (2), 207-220.
- Li, H., Chen, S. N., Yang, D. and Tontiwachwuthikul, P. 2012. Estimation of Relative Permeability by Assisted History Matching Using the Ensemble Kalman Filter Method. *Journal of Canadian Petroleum Technology*, 205 - 214.
- Ligthelm, D., Reijnen, G., Wit, K., Weisenborn, A. and Scherpenisse, W. 1997. Critical gas saturation during depressurisation and its importance in the Brent field. Paper presented at the Offshore Europe, Aberdeen, Scotland, UK. 9–12 September 1997
- Link, P. K. 2001. Basic petroleum geology (3rd edition). *OGCI Publications*.

- Liu, N., Betancourt, S. and Oliver, D. S. 2001. Assessment of Uncertainty Assessment Methods. Paper presented at the SPE Annual Technical Conference and Exhibition, New Orleans, Louisiana, U.S.A. 30 September - 3 October 2001
- Liu, N. and Oliver, D. S. 2005. Critical Evaluation of the Ensemble Kalman Filter on History Matching of Geologic Facies. *SPE Reservoir Evaluation & Engineering*, **8** (06), 470 - 477.
- Lumley, D. E. and Behrens, R. A. 1997. Practical Geophysical Issues of 4D Seismic Reservoir Monitoring. *Society of Exploration Geophysicists*, 1945 - 1949.
- Lygren, M., Halvorsen, K. Å., Randen, T., Sønneland, L., Dahl, G. V., Lindeberg, E. and Bergmo, P. 2002. History Matching of CO₂ Flow Models Using Seismic Modeling And Time-lapse Data. Paper presented at the SEG International Exposition and Annual Meeting, Salt Lake City, Utah, U.S.A. 6 - 11 October, 2002
- MacBeth, C., Fursov, I. , Geng, C. J., Obidegwu, D. and Chassagne, R. 2015. A Seismic Modelling Proxy for Fast-Track SHM.(Journal manuscript in preparation).
- MacBeth, C., Huang, Y. and Falahat, R. 2013. 4D seismic interpretation with frequently acquired, multiple time-lapsed surveys. Paper presented at the Second EAGE Workshop on Permanent Reservoir Monitoring 2013 – Current and Future Trends, Stavanger, Norway. 2 - 5 July 2013
- MacBeth, C., Soldo, J. and Floricich, M. 2004. Going Quantitative With 4D Seismic Analysis. Paper presented at the SEG International Exposition and Annual Meeting, Denver, Colorado, U.S.A. 10 - 15 October, 2004

- MacKay, D. J. 2003. Information theory, inference and learning algorithms, Cambridge university press.
- MacQueen, J. 1967. Some methods for classification and analysis of multivariate observations. *Fifth Berkeley symposium on mathematical statistics and probability*, **1** (14), 281-297.
- Marsh, J. M., Bagley, G., Lewis, A., McGarrity, J., Nash, T., Parr, R., Saxby, I. and Whitcombe, D. 2001. The use of 4D seismic in reservoir management. Paper presented at the 63rd EAGE Conference & Exhibition, Amsterdam, The Netherlands. 11–15 June, 2001
- Martin, K. and Macdonald, C. 2010. The Schiehallion field: applying a geobody modelling approach to piece together a complex turbidite field. Paper presented at the DEVEX conference, Aberdeen, Scotland, U.K. 12 - 13 May 2010
- Maschio, C. and Schiozer, D. 2014. A method for reduction of uncertainties in reservoir model using observed data: application to a complex case. *Journal of the Brazilian Society of Mechanical Sciences and Engineering*, **36** (4), 901-918.
- Maschio, C. and Schiozer, D. J. 2003. A new upscaling technique based on Dykstra–Parsons coefficient: evaluation with streamline reservoir simulation. *Journal of Petroleum Science and Engineering*, **40** (1–2), 27-36.
- Maschio, C. and Schiozer, D. J. 2005. Development and Application of Methodology for Assisted History Matching. Paper presented at the SPE Latin American and Caribbean Petroleum Engineering Conference, Rio de Janeiro, Brazil. 20 - 23 June, 2005

- Maschio, C. and Schiozer, D. J. 2013. A new procedure to reduce uncertainties in reservoir models using statistical inference and observed data. *Journal of Petroleum Science and Engineering*, **110**, 7-21.
- Maschio, C., Vidal, A. C. and Schiozer, D. J. 2008. A framework to integrate history matching and geostatistical modeling using genetic algorithm and direct search methods. *Journal of Petroleum Science and Engineering*, **63** (1-4), 34-42.
- McCain, W. D. 1990. The properties of petroleum fluids, PennWell Books.
- McDougall, S. R. and Sorbie, K. S. 1999. Estimation of critical gas saturation during pressure depletion in virgin and waterflooded reservoirs. *Petroleum Geoscience*, **5** (3), 229-233.
- Mezghani, M., Fornel, A., Langlais, V. and Lucet, N. 2004. History Matching and Quantitative Use of 4D Seismic Data for an Improved Reservoir Characterization. Paper presented at the SPE Annual Technical Conference and Exhibition, Houston, Texas, USA. 26 - 29 September, 2004
- Mitchell, P., Paez, R., Johnston, D., Mohler, G. and Neto, C. d. C. 2010. 4D seismic in deep water at the Dikanza field, offshore Angola, West Africa. Paper presented at the 72nd EAGE Conference and Exhibition incorporating SPE EUROPEC 2010, Barcelona, Spain. 14-17 June 2010
- Mohamed, L., Christie, M. A. and Demyanov, V. 2010. Reservoir Model History Matching with Particle Swarms: Variants Study. Paper presented at the SPE Oil and Gas India Conference and Exhibition, Mumbai, India. 20-22 January, 2010

- Moulu, J. 1989. Solution-gas drive: experiments and simulation. *Journal of Petroleum Science and Engineering*, **2** (4), 379-386.
- Nielsen, L. K., Li, H., Tai, X.-C., Aanonsen, S. I. and Espedal, M. 2010. Reservoir description using a binary level set model. *Computing and visualization in science*, **13** (1), 41-58.
- O'Donovan, A. R., Smith, S. G. and Kristiansen, P. 2000. Foinaven 4D Seismic - Dynamic Reservoir Parameters and Reservoir Management. Paper presented at the SPE Annual Technical Conference and Exhibition, Dallas, Texas, USA. 1-4 October, 2000
- Obidegwu, D. and MacBeth, C. 2014a. Estimation of Critical and Maximum Gas Saturation Using Multiple 4D Seismic Surveys. Paper presented at the 76th EAGE Conference and Exhibition 2014, Amsterdam, The Netherlands. 16 - 19 June, 2004
- Obidegwu, D. and MacBeth, C. 2014b. Quantitative analysis of gas volumes using multiple 4D seismic surveys and material balance. Paper presented at the 5th International Geosciences Student Conference, Nizhny Novgorod, Russia. 28 July - 01 August, 2014
- Oliver, D. S. and Chen, Y. 2011. Recent progress on reservoir history matching: a review. *Computational Geosciences*, **15** (1), 185-221.
- Ouenes, A. and Bhagavan, S. 1994. Application of Simulated Annealing and Other Global Optimization Methods to Reservoir Description: Myths and Realities.

- Paper presented at the SPE Annual Technical Conference and Exhibition, New Orleans, Louisiana, USA. 25-28 September, 1994
- Pagano, T. A., Fanchi, J. R. and Davis, T. L. 2000. Integrated Flow Modeling: The Fusion of Geophysics and Reservoir Engineering. Paper presented at the SPE Annual Technical Conference and Exhibition, Dallas, Texas, USA. 1-4 October, 2000
- Pannett, S., Slager, S., Stone, G. and Dekker, S. 2004. Constraining a Complex Gas-Water Dynamic Model Using 4D Seismic. Paper presented at the SPE Annual Technical Conference and Exhibition, Houston, Texas, USA. 26-29 September, 2004
- Pazetti, B., Davolio, A. and Schiozer, D. J. 2015. The impact of rock and fluid uncertainties in the estimation of saturation and pressure from a 4D petro elastic inversion. *Journal of Geophysics and Engineering*, **12** (4), 686 - 701.
- Pele, O. and Werman, M. 2008. Robust real-time pattern matching using bayesian sequential hypothesis testing. *Pattern Analysis and Machine Intelligence, IEEE Transactions on*, **30** (8), 1427-1443.
- Portella, R. C. M. and Emerick, A. A. 2005. Use of Quantitative 4D-Seismic Data in Automatic History Match. Paper presented at the SPE Latin American and Caribbean Petroleum Engineering Conference, Rio de Janeiro, Brazil. 20 - 23 June 2005

- Risso, F. V. A., Risso, F. F. and Schiozer, D. J. 2008. Risk Assessment of Oil Fields Using Proxy Models: A Case Study. *Journal of Canadian Petroleum Technology*, **47** (08), 9 - 14.
- Risso, F. V. A., RISSO, V. F. and SCHIOZER, D. J. 2011. Risk analysis of petroleum fields using Latin hypercube, Monte carol and derivative tree techniques. *Journal of Petroleum and Gas Exploration Research*, **1** (1), 14 - 22.
- Rodrigues, J. R. P. 2005. Calculating Derivatives for History Matching in Reservoir Simulators. Paper presented at the SPE Reservoir Simulation Symposium, The Woodlands, Texas, USA. 31 January-2 February, 2005
- Roggero, F., Ding, D. Y., Berthet, P., Lerat, O., Cap, J. and Schreiber, P.-E. 2007. Matching of Production History and 4D Seismic Data--Application to the Girassol Field, Offshore Angola. Paper presented at the SPE Annual Technical Conference and Exhibition, Anaheim, California, U.S.A. 11 - 14 November, 2007
- Roggero, F., Lerat, O., Ding, D. Y., Berthet, P., Bordenave, C., Lefevre, F. and Perfetti, P. 2012. History Matching of Production and 4D Seismic Data: Application to the Girassol Field, Offshore Angola. *Oil & Gas Science and Technology--Revue d'IFP Energies nouvelles*, **67** (2), 237-262.
- Romero, C. E., Carter, J. N., Zimmerman, R. W. and Gringarten, A. C. 2000. Improved Reservoir Characterization through Evolutionary Computation. Paper presented at the SPE Annual Technical Conference and Exhibition, Dallas, Texas, U.S.A. 1 - 4 October, 2000

- Roshni, V. and Revathy, K. 2008. Using mutual information and cross correlation as metrics for registration of images. *Journal of Theoretical & Applied Information Technology*, **4** (6).
- Roy, S. S., Bøen, F., Sæbø, A. and Aanonsen, S. 2011. 4D Seismic Monitoring-A Case Study on the Grane Field, North Sea. Paper presented at the 73rd EAGE Conference and Exhibition incorporating SPE EUROPEC 2011, Vienna, Austria. 23–26 May, 2011
- Rukavishnikov, V. and Kurelenkov, S. 2012. Dynamic Cluster Analysis for Updating Simulation Model Using Time-lapse Seismic. Paper presented at the SPE Europec/EAGE Annual Conference and Exhibition, Copenhagen, Denmark. 4 - 7 June 2012
- Sahni, I. and Horne, R. N. 2006. Generating Multiple History-Matched Reservoir-Model Realizations Using Wavelets. *SPE Reservoir Evaluation and Engineering*, **9** (3), 217-226.
- Scheibe, T. and Yabusaki, S. 1998. Scaling of flow and transport behavior in heterogeneous groundwater systems. *Advances in Water Resources*, **22** (3), 223-238.
- Schulze-Riegert, R. and Ghedan, S. 2007. Modern techniques for history matching. Paper presented at the 9th International Forum on Reservoir Simulation, Abu Dhabi, United Arab Emirates. 9 - 13 December, 2007

- Schulze-Riegert, R. W., Axmann, J. K., Haase, O., Rian, D. T. and You, Y. L. 2002. Evolutionary Algorithms Applied to History Matching of Complex Reservoirs. *SPE Reservoir Evaluation and Engineering*, 163 - 173.
- Sen, M. K., Datta-Gupta, A., Stoffa, P. L., Lake, L. W. and Pope, G. A. 1995. Stochastic Reservoir Modeling Using Simulated Annealing and Genetic Algorithm. *SPE Formation Evaluation*, **10** (01), 49 - 56.
- Sengupta, M. and Mavko, G. 2003. Impact of flow-simulation parameters on saturation scales and seismic velocity. *Geophysics*, **68** (4), 1267-1280.
- Skauge, A. and Ottesen, B. 2002. A summary of experimentally derived relative permeability and residual saturation on North Sea reservoir cores. Paper presented at the International Symposium of the Society of Core Analysts, Monterey, California, USA. September 22 - 25, 2002
- Soleng, H. H. 1999. Oil reservoir production forecasting with uncertainty estimation using genetic algorithms. Paper presented at the IEEE Conference on Evolutionary Computation, Washington DC, U.S.A. 6 - 9 July, 1999
- Souza, R. M., Machado, A. F., Munerato, F. P. and Schiozer, D. J. 2010. Iterative History Matching Technique for Estimating Reservoir Parameters from Seismic Data. Paper presented at the SPE EUROPEC/EAGE Annual Conference and Exhibition, Barcelona, Spain. 14-17 June, 2010
- Staples, R., Hague, P., Cooke, G., Ashton, P., Stammeijer, J., Jolley, S., Stevens, T. and Marshall, J. 2002. Integrating 4D Seismic to Optimize Production. Paper

presented at the SPE European Petroleum Conference, Aberdeen, Scotland, U.K.
29 - 31 October 2002

Staples, R., Stevens, T., Leoutre, E., Jolley, S. and Marshall, J. 2005. 4D seismic history matching—the reality. Paper presented at the 67th EAGE Conference & Exhibition, Madrid, Spain. 13 - 16 June 2005

Stephen, K. D. and MacBeth, C. 2006. Seismic history matching in the UKCS Schiehallion field. *first break*, **24** (4), 43 - 49.

Stephen, K. D., Shams, A. and Macbeth, C. 2007. Faster Seismic History Matching in a UKCS Reservoir. Paper presented at the SPE Europec/EAGE Annual Conference and Exhibition, London, UK. 11- 14 June, 2007

Stephen, K. D., Soldo, J., Macbeth, C. and Christie, M. A. 2005. Multiple Model Seismic and Production History Matching: a case study. Paper presented at the 14th Europec Biennial Conference, Madrid, Spain. 13 - 16 June, 2005

Stone, H. 1970. Probability model for estimating three-phase relative permeability. *Journal of Petroleum Technology*, **22** (02), 214-218.

Stone, H. 1973. Estimation of three-phase relative permeability and residual oil data. *J. Pet. Technol.:(United States)*, **12** (4).

Teshome, M., Zerubabel, L. and Dong Yoon, K. 2011. A simple binary image similarity matching method based on exact pixel matching. Paper presented at the International Conference on Computer Engineering and Applications, Singapore. 2011

- Tillier, E., Da Veiga, S. and Derfoul, R. 2013. Appropriate formulation of the objective function for the history matching of seismic attributes. *Computers and Geosciences*, **51**, 64-73.
- Tillier, E., Le Ravalec, M. and Da Veiga, S. 2012. Simultaneous inversion of production data and seismic attributes: Application to a synthetic SAGD produced field case. *Oil & Gas Science and Technology—Revue d'IFP Energies nouvelles*, **67** (2), 289-301.
- van Gestel, J. P., Best, K. D., Barkved, O. I. and Kommedal, J. H. 2011. Integration of the life of field seismic data with the reservoir model at the Valhall Field. *Geophysical Prospecting*, **59** (4), 673-681.
- Vasco, D. W., Datta-Gupta, A., Behrens, R., Condon, P. and Rickett, J. 2004. Seismic imaging of reservoir flow properties: Time-lapse amplitude changes. *Geophysics*, **69** (6), 1425-1442.
- Waggoner, J. R., Cominelli, A. and Seymour, R. H. 2002. Improved Reservoir Modeling With Time-Lapse Seismic in a Gulf of Mexico Gas Condensate Reservoir. Paper presented at the SPE Annual Technical Conference and Exhibition, San Antonio, Texas, U.S.A. 29 September - 2 October, 2002
- Walker, G., Allan, P., Trythall, R., Parr, R., Marsh, M., Kjelstadli, R., Barkved, O., Johnson, D. and Lane, S. 2006. Three case studies of progress in quantitative seismic-engineering integration. *The Leading Edge*, **25** (9), 1161-1166.
- Wang, Y. and Kocscek, A. R. 2002. A Streamline Approach for Ranking Reservoir Models that Incorporates Production History. Paper presented at the SPE Annual

Technical Conference and Exhibition, San Antonio, Texas, U.S.A. 29 September - 2 October, 2002

Watts, G. and Marsh, M. 2011. How Often Should you Acquire 4D Seismic Surveys to Optimise Value? Paper presented at the EAGE Workshop on Permanent Reservoir Monitoring (PRM) - Using Seismic Data, Trondheim, Norway. 28 February - 3 March 2011

Wen, X.-H., Lee, S. and Yu, T. 2006. Simultaneous integration of pressure, water cut, 1 and 4-D seismic data in geostatistical reservoir modeling. *Mathematical geology*, **38** (3), 301-325.

Williams, G. J. J., Mansfield, M., MacDonald, D. G. and Bush, M. D. 2004. Top-Down Reservoir Modelling. Paper presented at the SPE Annual Technical Conference and Exhibition, Houston, Texas, U.S.A. 26 - 29 September 2004

Wu, Z. 2001. A Newton-Raphson Iterative Scheme for Integrating Multiphase Production Data Into Reservoir Models. *SPE Journal*, **6** (03), 343 - 351.

Yan, T. 2014. History matching of production and 4D seismic data - Application to the Norne field. MSc thesis, Norwegian University of Science and Technology (NTNU).

Zhao, Y., Shuozhong, W., Xinpeng, Z. and Heng, Y. 2013. Robust Hashing for Image Authentication Using Zernike Moments and Local Features. *Information Forensics and Security, IEEE Transactions on*, **8** (1), 55-63.

Zhao, Y., Wang, S., Feng, G. and Tang, Z. 2010. A robust image hashing method based on Zernike moments. *Journal of Computational Information Systems*, **6** (3), 717-725.

Zubarev, D. I. 2009. Pros and Cons of Applying Proxy-models as a Substitute for Full Reservoir Simulations. Paper presented at the SPE Annual Technical Conference and Exhibition, New Orleans, Louisiana, U.S.A. 4 - 7 October, 2009